TESTING FOR COMPOSITIONAL CONVECTION IN SILICATE MELTS : CRYSTAL GROWTH EXPERIMENTS AND A PETROGRAPHIC STUDY OF A DIFFERENTIATED RING DYKE

Jonathan K. Seedhouse

A Thesis Submitted for the Degree of PhD
at the
University of St Andrews

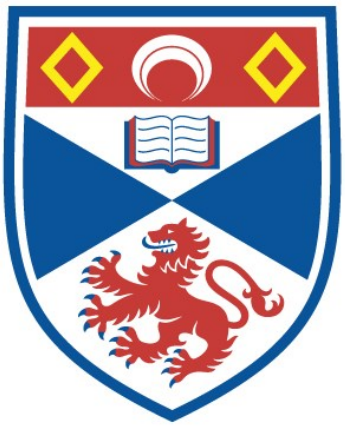

1994

Testing for compositional convection in silicate melts; crystal growth experiments and a petrographic study of a differentiated ring dyke.

Jonathan K. Seedhouse

Thesis presented in partial fulfilment for the degree of Doctor of Philosophy.

January 1994.

ProQuest LLC.
789 East Eisenhower Parkway
P.O. Box 1346
Ann Arbor, MI 48106 – 1346

Declaration

I, Jonathan Keith Seedhouse, hereby certify that this thesis has been composed by myself, that it is a record of my own work, and that it has not been accepted in partial or complete fulfilment of any other degree of professional qualification.

I was admitted to the Faculty of Science of the University of St. Andrews under Ordinance General No. 12 on 1st October, 1990 and as a candidate for the degree of Ph.D. on 1st October, 1991.

I hereby certify that the candidate has fulfilled the conditions of the Resolution and Regulations appropriate to the Degree of Ph.D.

In submitting this thesis to the University of St. Andrews I understand that I am giving permission for it to be made available for use in accordance with the regulations of the University Library for the time being in force, subject to any copyright vested in the work not being affected thereby. I also understand that the title and abstract will be published, and that a copy of the work may be made and supplied to any *bona fide* library or research worker.

Abstract

Convection in magma chambers, driven by compositional density differences, is thought to be a major process in fractionation of liquid from crystals in the differentiation of magmas. Compositional convection has been tested for by undertaking two sets of experiments in silicate melts, and by re-examining the vertically differentiated gabbro-granophyre Glen More ring dyke on the Isle of Mull.

Crystal growth quenching experiments have been carried out in a synthetic basalt in which iron is replaced by cobalt. Co-Mg olivine was overgrown on olivine seeds cemented in alumina crucibles and the glasses produced on quenching were analyzed by EPMA for compositional variation at and above the overgrowth-glass interface. Boundary layers upto 50 μm wide, and depleted in Co and Mg by upto 25 %, have been found at crystal-glass interfaces, and plumes of the same melt have been detected above the apexes of growing olivine crystals. The computed density difference which causes the convection of this boundary layer melt is in the region of 1 %. This phenomenon, known as compositional convection, has been seen associated with dissolving crystals in silicate melts, and around growing crystals in aqueous salt solutions, but this is the first time it has been reported accompanying crystal growth in silicate melts.

Other experiments in which hematite underwent dissolution in a natural basalt melt show that dense, Fe-enriched melt can be lifted above its origin by the buoyant rise of bubbles. In both sets of experiments a zone of buoyant boundary layer melt has been produced by side-wall crystallization of hercynite. This zone of melt has convected up and has ponded beneath the meniscus by a process that can be likened to side-wall crystallization in magma chambers.

Petrological, mineralogical, textural, and new geochemical evidence from the re-examination of the Glen More ring dyke strongly suggests that the petrological variation is the result of a magma mixing mechanism. It is proposed that this was produced by the injection of a basic magma which underwent partial consolidation. This was then followed by a second injection of a silicic magma which underwent partial mixing with the dioritic residual magma remaining after crystallization of gabbros from the initial magma.

Acknowledgements

It would have been impossible to complete this project without the considerable help of many people, whom I would like to take this opportunity to thank. The project has been supervised by Colin Donaldson, and I would like to thank him for our many stimulating discussions, for his critical reviews of early drafts of my work, for his encouragement, and most of all for persuading me to spend three more wonderful years in St Andrews. This studentship was funded by the NERC whose financial assistance is gratefully acknowledged.

The technical staff at St Andrews (Andy Mackie, Angus Calder, Richard Batchelor, Stuart Allison and Donald Herd) are thanked for their expert assistance in matters relating to computing and analytical work. Donalds help in operating the electron microprobe was invaluable. Peter Knott at the Leeds University School of materials is thanked for commenting on earlier drafts of experimental chapters and for his assistance in producing the clay, experimental crucibles. Ed Stephens and Simon Wathen are thanked for their assistance in understanding the Unimap computer package.

My fellow postgraduates are all thanked for their assistance and friendship. Mike Macdonald, Rick Yarr and Justin Dix are singled out for being such great company on the golf courses of St Andrews on many balmy summer evenings. I am very grateful to Florence McAndie for the typing lessons which have made many hours in front of a key board a little more bearable.

The many friends I have made during my time at Universtiy are thanked for making my years as a student so rewarding. Special thanks go to Fiona MacNaughtan, Stuart Cotton, Matt Wade, Richard and Chris Freeman, Jilly Adams, and Angus McLeod for their company and help over the past two rather rough years.

Finally I would like to offer my thanks to my father and my late mother for all their encouragement and assistance throughout my education.

Contents Page

List of figures.

Chapter 1 Introduction

1.1 Introduction

Processes which cause magmas to differentiate can be split into two groups; those that take place entirely in the liquid state (eg. liquid immiscibility, magma mixing, thermogravitational differentiation), and those involving fractionation of crystals from liquids. The latter group are believed to be the most important in bringing about magma differentiation *in situ* (i.e. in individual igneous intrusions) and also in deeper magma chambers before intrusion to higher crustal levels (Wilson, 1993). The processes responsible for the fractionation of crystals from liquids in magma chambers include crystal settling, and crystal growth on walls and floors with convective removal of residual liquid. The processes that drive the convection in this latter case are the subject matter examined in this thesis.

One of the earliest mechanisms proposed to explain the transfer of solute to crystals from surrounding liquid (a process that must be sustained for continued crystal growth) relies on chemical diffusion transferring crystallizing components towards zones of crystallization at the margins of igneous bodies (Harker, 1894 and 1909). However, modelling of cooling rates of magma chambers has shown that calclulations of times required for bodies to cool are much bigger than those observed. From this convection has been invoked in magma chambers to explain more rapid cooling than is allowed by diffusion alone (Hofmann, 1980).

If diffusion is too slow to transfer crystallizing components to crystallization zones, then other processes are needed to fractionate crystals from liquid, and to allow continued crystal growth and compositional evolution of magma. Crystal settling was therefore proposed as a mechanism for this (eg. Darwin, 1844; Harker, 1909; Daly, 1933; Wager and Deer, 1939). Evidence for gravitational crystal settling is found in many layered igneous intrusions which show modal layering with dense minerals at the bottom and lighter phases at the top of individual layers (eg. Irvine, 1980).

To aid gravitational crystal settling, convection driven by density variations in liquids, associated with temperature changes and crystal content was proposed (Grout, 1918; Wager and Deer, 1939; Hess, 1960). Magma convection may work both with and against crystal settling, causing crystal-rich currents to sink in a magma chamber, aiding settling, or keeping crystals in suspension. Bartlett (1969) noted that crystal distribution depends on the competition between settling and convective fluxes. This is still thought to be an active mechanism by Sparks *et al*, (1993) who propose that crystals have critical concentrations in a magma at which sedimentation of these minerals can occur.

However, McBirney and Noyes (1979) showed that layering in mafic intrusions cannot be solely modelled by crystal settling and instead they proposed *in situ* crystallization on chamber floors and walls as the dominant mechanism responsible for crystal-liquid fractionation and layering in igneous intrusions. The main factor that led petrologists to reject the crystal settling model was recognition of the "plagioclase flotation problem" in the 1970's (Bottinga and Weill, 1970; Morse, 1973; Campbell, 1978; Campbell *et al*, 1978), namely that plagioclase cannot sink in many basic magmas, and therefore cannot become part of layering by settling from magmas. Also, turbulent thermal convection, driven by temperature variations in magmas, is thought to take place in all but the most viscous of magmas (eg. Hess, 1989) and is probably responsible for keeping crystals in suspension in magma chambers, i.e. preventing crystal settling.

When heated magma expands and becomes less dense, allowing it to convect due to buoyancy. Conversely, when cooled, as at the top of a magma chamber where heat is lost by conduction, magma becomes denser allowing it to sink. Convection patterns during thermal convection depend on values of the thermal Rayleigh number, Ra_T, defined as

$$Ra_T = g\,\alpha(T_2 - T_1)d^3/vD$$

and the Prandtl number, Pr, defined as

$$Pr = v/K$$

where d is the depth of the fluid layer, (T_2-T_1) is the temperature difference across it, g is the acceleration due to gravity, α is the coefficient of thermal expansion of the fluid, v is the kinematic viscosity of the fluid, and D is the thermal diffusivity of the fluid (Tritton, 1977). Magmas have very high values of Pr and it has been shown that turbulent convection does not occur until $Ra_T = 4.5 \times 10^{12}$ (Rohsenow and Choi, 1961), however since d is very large in most magma chambers, convection can be expected to be fully turbulent (Hardee, 1983). During turbulent thermal convection, strong thermal gradients exist near the walls, while the chamber interior is kept essentially isothermal by stirring of the magma (Tritton, 1977). Flow is driven by dense or buoyant packets of melt from the walls, known as "thermals" (Howard, 1966; Sparrow *et al*, 1970).

Temperature differences in magma bodies have long been suggested as a cause of crystal-liquid fractionation (eg. Wager, Brown and Wadsworth, 1960). More recently, however, density variations due to compositional differences in melts have been proposed as an important mechanism bringing about transfer of matter in magma bodies (eg. Sparks *et al*, 1984; Martin, Griffiths and Campbell, 1987). Investigations into these processes have been carried out with the aid of experiments in which tanks of saturated, aqueous salt solutions are cooled to simulate crystallization in magma

chambers (see reviews by Sparks, Huppert and Turner, 1984, and Turner and Campbell, 1986). It is thought likely that compositional effects will generally have a greater effect on melt density than thermal ones (Murase and McBirney, 1973) because basic magmas have low values of the coefficient of thermal expansion.

Fractionation of crystals from liquids leads to density changes in the liquid (Sparks *et al*, 1983; Grove and Baker, 1983; Sparks and Huppert, 1984). This has led to the term "fractionation density" being introduced (Sparks *et al*, 1983; Sparks and Huppert, 1984), defined as the density of the liquid components being removed by crystallization. Fractionation in an area of crystallisation (eg. chamber side-walls and floors) can produce either a local reduction or an increase in liquid density (McBirney, 1980; Sparks *et al*, 1983; Sparks and Huppert, 1984), depending on the composition of the system being examined. Dense or light fluid produced by crystallization in boundary layer zones adjacent to chamber walls can convect and form stratified fluid at the top or bottom of a chamber (see figure 1.1) (Turner and Gustafson, 1978). It has been proposed that this process can produce extreme differentiation of magmatic liquids (McBirney, 1980; Turner, 1980; Turner and Gustafson, 1981). Evidence of the existence of zoned magma chambers comes in several forms; compositional zoning in acidic-intermediate eruptive products (Hildreth, 1981), bimodal basalt-rhyolite eruptions (eg. Sigurdsson and Sparks, 1981), and mixed magma ring intrusions in subterranean igneous complexes (eg. Bell, 1983; Sparks and Marshall, 1984; Marshall, 1984).

Convective processes have been observed in experimental tanks and produce compositionally and thermally stratified liquid end-products which have been likened to layered igneous intrusions. The convective processes observed in these experiments have been used to predict convective behaviour in magma chambers; they suggest that compositional and thermal differences will both drive vigorous convection in all but the smallest and most viscous magma chambers. Figure 1.1 summarizes some of the convective processes thought to be active in evolving magma chambers.

1.2 Compositional Convection

Compositional differences in magmas (and therefore density and buoyancy differences) are produced by crystallization, crystal dissolution, by contamination as a result of magma mixing, and by contamination caused by rock assimilation. Work in this thesis aims to examine one of these processes, crystallization, in more detail.

In aqueous salt-solution experiments, differentiation into compositionally contrasting liquids is brought about by convective removal of light residual liquids from growing crystals. Compositional differences that drive magma convection arise whenever a

FIGURE 1.1. Schematic diagram showing convective processes in magma chambers.

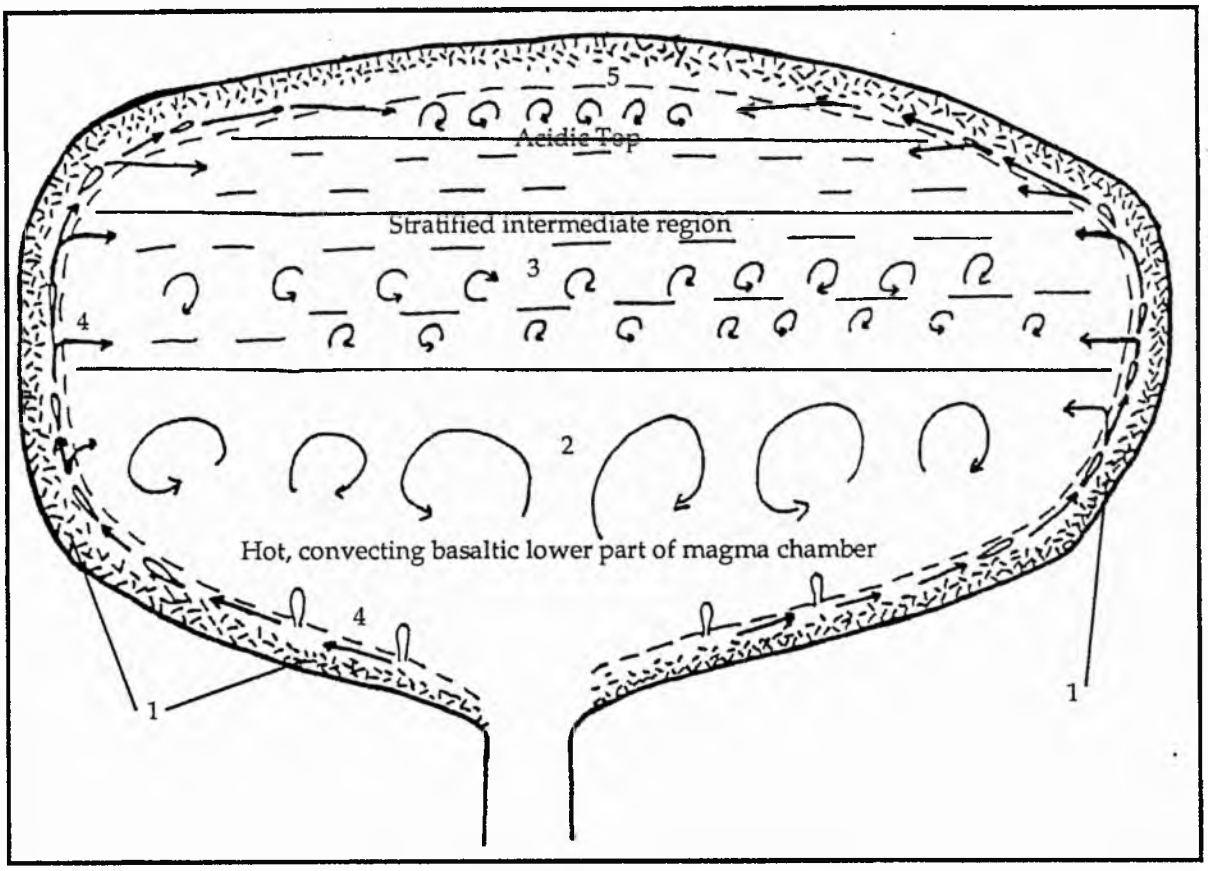

1= Side-wall, floor, and roof crystallization produces a compositionally-discrete boundary layer zone (McBirney, 1980)

2= Turbulent convection in hot basaltic lower layer (Turner and Campbell, 1986)

3= Stratified part of chamber, with double-diffusive convection in individual layers (cf. Turner *et al*, 1983)

4= Release of buoyant, residual magma in plumes from the floor and in a side-wall boundary layer zone. This magma rises until it reaches a layer of equivalent density, where it enters and mixes by convection (cf. Helz *et al*, 1989)

5= The most acidic melt, produced by side-wall crystal-liquid fractionation and partial melting of the country rocks, rises to the top of the chamber and ponds beneath the roof (cf. Brophy, 1989; Huppert and Sparks, 1988).

crystal grows or dissolves because the crystal and melt differ in composition, thus melt at the crystal-liquid interface becomes enriched or depleted in certain elements creating a compositional boundary layer (see figure 1.2). For example, enrichment in iron in a melt surrounding a growing plagioclase crystal forms a denser boundary layer which should flow downward from the crystal, whereas depletion in iron about growing mafic minerals creates a boundary layer that moves buoyantly upwards because it is less dense than the host liquid.

Whereas boundary layer formation and convection have been observed in crystallizing aqueous salt solution experiments, similar experiments using silicate melts have not been reported. Therefore it is one of the aims of this study to examine the production and convection of boundary layers around individual growing crystals in experimental silicate systems.

In this study the process of boundary layer release is referred to as COMPOSITIONAL CONVECTION, a term introduced to the petrological literature by Tait *et al*, (1984). Previous literature in other fields has referred to the same process as *solutal convection* (Carruthers, 1976), *thermosolutal convection* (Coriell *et al*, 1980), and *chemical convection* (Rosenberger, 1979). In some studies (eg. Sparks *et al*, 1984) the petrological process involving the accumulation of boundary layer melt from many crystals, to form a zone of compositionally-discrete melt at the margins of the magma chambers, has been described and the zone of melt has been referred to as the *boundary layer* . In this study the term *boundary layer* is used to describe the film of melt around an individual crystal, while the term *boundary layer zone* is adopted to describe compositionally discrete zones of melt comprising boundary layers from many individual crystals.

Figure 1.2 outlines the manner of release of boundary layers from growing or dissolving crystals. Release of melt may be as a continuous stream or as punctuated packets. Fast crystal growth or dissolution in low viscosity melts favours continuous plume activity, while slow growth or dissolution in a viscous melt is more likely to produce periodic release of boundary layers from the top or bottom of the crystal. Martin, Griffiths and Campbell (1989) discussed a model which involves small, equant crystals growing on a horizontal surface, each producing a boundary layer which contributes to a boundary layer zone overlying the layer of crystals. Only when this zone has thickened to be sufficiently buoyant can it convect (see figure 1.2e). The unstable thickness is governed by the compositional Rayleigh equation which assesses the stability of a compositional boundary layer on a horizontal surface, and is defined as

$$Ra_C = g\Delta\rho_C d^3 / \nu D$$

FIGURE 1.2. Production and convection of compositional boundary layers around growing and dissolving crystals

a) Production of a high density boundary layer by dissolution of mafic minerals (eg. olivine) or growth of felsic minerals (eg. feldspar).

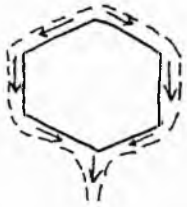

b) Production of a low density boundary layer by dissolution of felsic minerals or by growth of mafic minerals.

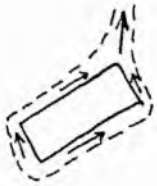

c) Convection of a dense boundary layer in a low viscosity melt occurs in a continuous stream of melt.

d) Convection of a dense boundary layer in a high viscosity melt occurs in individual packets of melt.

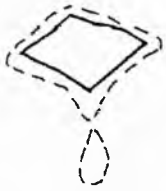

e) convection of a thick buoyant boundary layer zone overlying a layer of equant crystals ona horizontal surface (Martin, Griffiths and Campbell, 1987).

(i) Boundary layer thickness increases with time. Rate of its increase is governed by chemical diffusion rates.

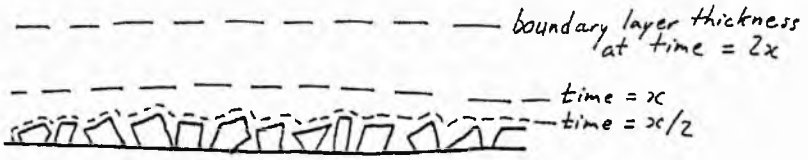

(ii) Boundary layer becomes unstable and convects buoyantly when its compositional Rayleigh number exceeds 1000.

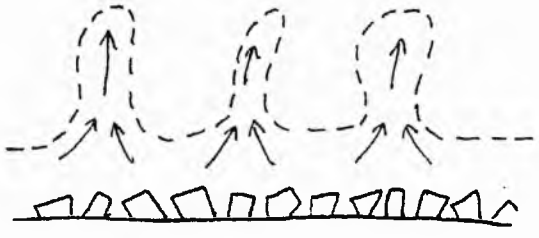

where Ra_C = Compositional Rayleigh Number

g = Acceleration due to gravity

$\Delta\rho_C$ = Density difference across boundary layer. Calculated from EPMA data.

d = Width of compositional boundary layer

v = Melt viscosity

D = Diffusion coefficient (10^{-5} - 10^{-8} $cm^2.s^{-1}$. Hofmann, 1980).

This equation is used in chapters 3 and 4 to compare observed boundary layer widths with those calculated. Calculated d values can be used in conjunction with the equation, $\tau = d^2/D$, to estimate the times (τ) necessary to produce unstable boundary layers on horizontal surfaces. However, the crystal surfaces in the experiments in this study are sloping to aid boundary layer instability, and so the calculated times will be maximum ones.

Sparks *et al* (1984) described *in situ* crystallization at the margins of magma chambers with the convection of the residual liquid due to its density difference with the melt in the rest of the chamber. They called this process "Convective Fractionation". The convecting melt may mix with the rest of the chamber, so that the magma evolves, even in areas where it is not crystallizing (Langmuir, 1989; Tait and Jaupart, 1990), or it may remain discrete in a boundary layer zone at the chamber margins, convecting to produce an evolved top to a magma chamber (see figure 1.1) (cf. Brophy, 1990). In this latter process the boundary layer zone remains discrete and is progressively stripped of solute as it convects over other side-wall crystals.

It appears to be generally agreed that most magma bodies will convect throughout most of their crystallization histories. This convection is driven by both thermal and compositional effects on density, with compositional effects thought to be greater than thermal ones. Marsh (1988, 1989a, 1989b) has stated that convection will be suppressed by slow heat conduction through surrounding country rocks, and has questioned whether temperature driven convection is as turbulent as is widely thought. However, Huppert and Turner (1991) have questioned the validity of Marsh's calculations on the grounds of his assumption that the absence of superheat from a magma makes it impossible to sustain convection except in the very earliest stages of cooling. Turner *et al* (1986) have shown that the temperature flux, and hence the vigour of convection, will vary with time as the temperature in the magma decreases. Although temperature-driven density differences may vary in importance with time, it would seem likely that the effects of compositional density differences will ensure that convection in magmas is the norm.

Compositional variations in glass around olivine crystals in pillow basalts were reported by Donaldson (1975), and chemical gradients were seen to increase or decrease exponentially (increase in SiO2 of 0.5 wt %, and decreases in MgO and FeO of

2.5 and 0.5 wt % respectively) towards the interface over a narrow region (20μm). Compositional boundary layers in glass around partially dissolved crystals have been reported for silicate systems by Zhang et al (1989) and Donaldson (1990) and their convective behaviour has been studied by Donaldson (1993). Lasaga (1981) reports that the motion of melt relative to a crystal decreases to zero at the crystal-melt interface due to surface tension, and therefore diffusion is the only mechanism responsible for mass transfer right at the interface. This means that the most solute-depleted melts will not be able to detach and convect away from their source. The experiments described in part A of this study follow on from these dissolution experiments, and aim to investigate the role that compositional convection plays in magma systems while crystals are growing.

1.2 Aims of this project

1) To undertake a series of crystal-growth, quenching experiments with silicate melts and to examine the products for evidence of compositional convection associated with the growth of mafic minerals. This is done by examining vertically-aligned, polished thin sections of quenched run products by optical microscopy and electron-probe micro analysis, to search for evidence of compositional convection driven by crystallization in silicate melts.

2) To evaluate the scale and magnitude of compositional variation in glasses in boundary layers at crystal-liquid interfaces, and its effect on melt density in experimental run products.

3) To re-examine a vertically-differentiated igneous body (the Glen More gabbro-granophyre ring dyke on Mull) as a potential site of *in situ* fractional crystallization of basaltic magma with release of buoyant, residual melt that formed the intermediate and acidic rocks in the upper reaches of the intrusion. This was thought to be the best possibility of testing for compositional convection in an igneous body in the British Isles.

4) To examine naturally-occurring porphyritic glasses for evidence of boundary layer development and its convective behaviour, adjacent to phenocrysts.

A collection of porphyritic glasses from Iceland, Pantelleria, Hawaii, and from the glassy rinds of deep-sea pillow basalts was assembled and examined. Much of the glassy material has undergone extensive devitrification, especially at crystal-glass interfaces. This makes microprobe analysis of boundary layers at interfaces impossible. The Hawaiian samples were riddled with vesicles which caused a similar problem. Some of the Pantellerian samples were analyzed but it was soon realized that

compositional variations at crystal-glass interfaces are very small, and could have been produced by quench crystallization and not by growth of the phenocrysts. Another problem with examining these rocks is that the phenocrysts have probably not grown from the melts at their interfaces, and so evidence of boundary layer convection cannot be expected. Also, the orientation of the samples is not known so we do not know which way to expect any boundary layer melt to convect. For these reasons this part of the study was halted at an early stage.

1.4 Organisation of this thesis.

This thesis splits into two sections; part A (chapters 2-5) and part B (chapters 6-12). Part A describes experimental methods used (chapter 2) in two sets of experiments; one growing olivine in a synthetic basalt (chapter 3) and the other aiming to grow magnetite in a natural basalt (chapter 4). The findings of the experimental study are summarized in chapter 5 and similarities with natural magma systems are suggested. Part B is a petrographic and petrogenetic study of the Glen More ring dyke. The problems of its petrogenesis are introduced and previous work and field relations are presented in chapter 6. Petrography, mineral chemistry and geochemistry are presented and discussed in chapters 7, 8, and 9, respectively. The evidence is summarized in chapter 10, and major element computer modelling is presented in chapter 11, before the findings of the study are summarized in chapter 12. Chapter 13 is a summary of the thesis.

PART A.
EXPERIMENTAL TESTING FOR COMPOSITIONAL CONVECTION

Chapter 2 Experimental Procedure

2.1 Introduction

In this chapter the techniques and materials used in two sets of high-temperature, crystal-growth quenching experiments are described, and the reasons for their use are explained. 41 experiments have been carried out using a synthetic basalt to overgrow olivine seeds with Co-Mg olivine, and 29 runs were made in an attempt to overgrow hematite with an iron-oxide in a natural basaltic melt. The problems associated with the various experimental techniques are outlined, as is the appearance and possible source of metallic blebs which contaminate the synthetic basalt. The concentration and distribution of these blebs may be used as an optical tracer of boundary layer movement in olivine growth experiments.

2.2 Melt systems used

2.2.1 Introduction

Olivine is probably the easiest silicate mineral to nucleate and grow from a melt and so an olivine-normative basaltic system was chosen. This was also used because its low viscosity at 1200°C will not discourage boundary layer movement.

In an attempt to avoid problems with iron oxidation, and the associated compositional change of melts at high temperatures, systems have been chosen which will not oxidize in an uncontrolled atmosphere. The first of these is a synthetic basalt in which iron is replaced by cobalt to avoid iron oxidation and iron loss to noble metal containers in the wire-loop runs (Coons, Holloway and Navrotsky, 1976; Coons and Holloway, 1979). This system is used in the experiments described in chapter 3. The second system, used in the experiments described in chapter 4, is the melt of a roasted and powdered dolerite. This section gives details of phase relations and preparation techniques of the melts used in the two sets of experiments.

2.2.2 Synthetic Cobalt-Basalt

This system was proposed as an analogue for natural basalts in experimental petrology because the amount of cobalt lost to noble metal containers is negligible compared to iron, and because Co^{2+}, unlike Fe^{2+}, does not oxidize at high temperatures in an atmospheric furnace (Coons, Navrotsky and Holloway, 1976). In iron-bearing systems, up to 95% of Fe^{2+} is lost to platinum, and up to 50% to $Ag_{30}Pd_{70}$ capsules and containers (Merrill and Wyllie, 1973). Iron and molybdenum capsules reduce iron loss but are limited to certain oxygen fugacities (Stern and Wyllie, 1975).

Coons *et al* (1976) report that an equimolar replacement of Fe^{2+} by Co^{2+} produces a system which is not troubled by the iron loss problem, and in which equilibrium is obtained over a wide range of oxygen fugacities without any deviation from Fe-bearing phase relations. They also report that analyses of Pt wire that has been in contact with this cobalt-basalt contains only 0.04 wt % Co, and that Co^{2+} loss could be eliminated by saturating the sample holder with Co before use.

The phase relations and composition of the cobalt-basalt are shown in figure 2.05, along with those of the original 1921 Kilauea basalt on which the synthetic composition is based. This figure illustrates the systematic shift of stability temperatures of all mineral phases by approximately +50°C from the iron to the cobalt system.

The minerals produced in this analogue system are vividly coloured in thin section due to the coordination state of Co^{2+} in the crystal lattice. Whereas tetrahedrally coordinated Co^{2+} produces a blue colour (eg. in glass), in the octahedrally coordinated state (eg in olivine) the colour is pink.

The synthetic basaltic melt was produced by combining and fusing oxides, carbonates and bicarbonates of the component elements (see appendix A). After fusing the mixture twice, chips of glass were checked for any remaining heterogeneity using EPMA. The composition of the cobalt-basalt glass is given in table 2.01.

2.2.3 Problems with the synthetic cobalt basalt

During EPMA of the glass, tiny (<10μ) rounded blebs of a highly reflecting phase were noticed scattered through it (see plate 2.01) An analytical scan has been made of one of these blebs and it contains a combination of Pt, Au and Co. The form of this metallic phase and its distribution throughout the glass indicates that it was originally present as molten blebs of metal in the silicate melt. Previous workers using this Co-bearing melt have not mentioned this phenomenon.

On close inspection of the $Pt_{95}Au_5$ crucibles in which the cobalt-basalt was fused, a line is seen around the inner crucible wall, marking the level of the meniscus contact with the crucible. Along this line the crucible has a shinier appearance, and below it the crucible has a more polished appearance than above it. No such platinum contamination has been reported using natural basalts, in fact the opposite occurs (with iron being absorbed in the Pt crucible).

The composition of the metallic blebs and the appearance of the crucibles after cobalt-basalt fusion, points towards the blebs originating from the crucible walls. This is

FIGURE 2.05. Comparison of liquidus phase equilibria in the 1921 Kilauea basalt (dashed curves) and the Cobalt analogue basalt (solid curves) at atmospheric pressure (from Coons, Holloway and Navrotsky, 1976).

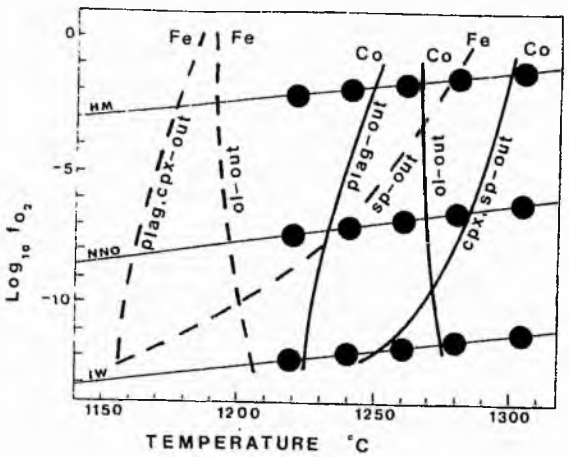

Table 2.01. Composition of the Co basalt starting material in experiments in chapter 3

Data accurate to 1d.p.

	1921 basalt (Hill, 1969)	Co basalt									
SiO2	49.4	47.97	48.05	48.05	48	47.63	48.04	47.51	48.02	47.94	47.94
TiO2	2.78	3.42	3.3	3.32	3.21	3.44	3.25	3.4	3.34	3.53	3.3
Al2O3	13	12.55	13.52	13.43	13.25	13.15	13.42	13.3	13.33	13.36	13.27
FeO tot	12.3										
CoO		11.89	11.62	11.77	11	11.59	11.13	11.45	11.88	11.06	11.66
MgO	8.1	8.46	8.54	8.45	8.35	8.51	8.53	8.39	8.48	8.65	8.55
CaO	11.3	12.91	12.73	12.63	12.78	13.07	12.86	11.97	12.69	12.83	13.11
Na2O	2.15	0.63	0.61	0.56	0.57	0.57	0.64	0.65	0.59	0.66	0.58
K2O	0.52	0.29	0.32	0.35	0.29	0.3	0.3	0.3	0.32	0.33	0.33
Total	99.55	98.12	98.69	98.56	97.45	98.26	98.17	96.97	98.65	98.36	98.74

Plate 2.01. Backscattered electron image showing the bright Co-olivine overgrowth separated from the dark olivine seed by a line of tiny Pt blebs. This plate also shows the region of bleb-free melt around the crystal seed. Scale bar = 100 μm.

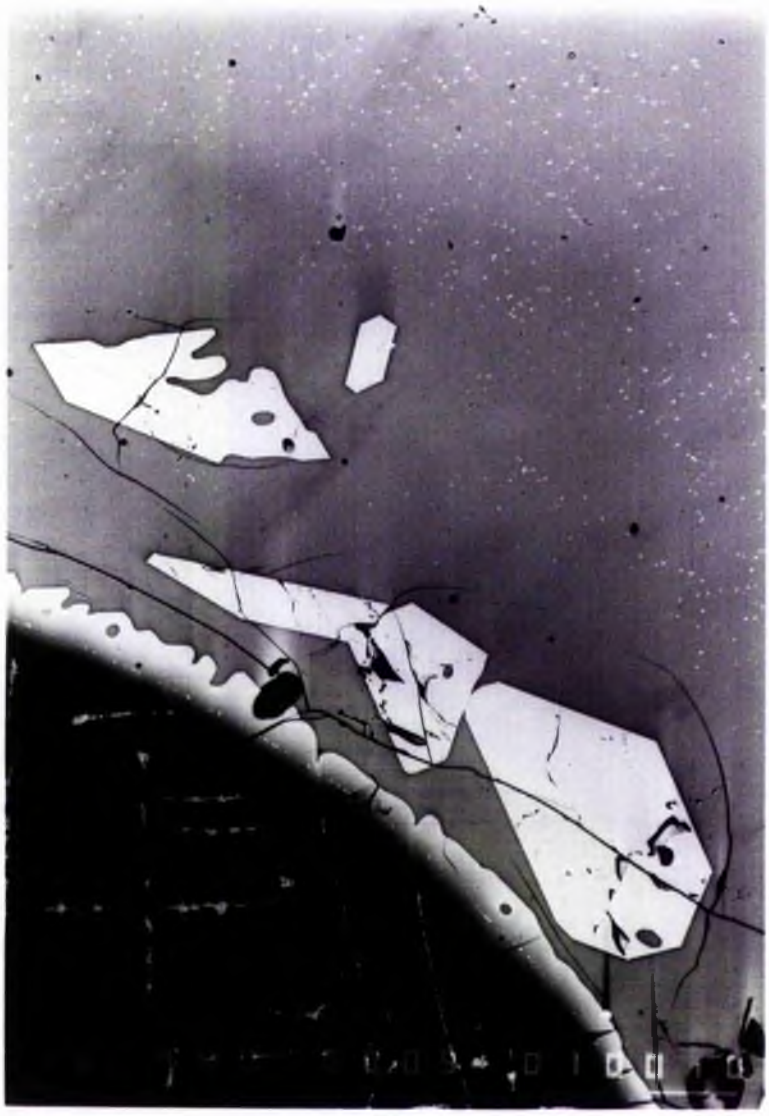

possibly because cobalt alloys with the $Pt_{95}Au_5$ crucible to form a mixture whose melting point is less than 1320°C. In olivine growth experiments using this glass, a rim of these blebs can be seen around the original olivine seeds, but only inside the Co-Mg olivine overgrowths (see plate 2.1).

2.2.4 Natural basaltic system

In an attempt to produce an overgrowth of an iron-oxide on a seed of hematite, a doleritic rock powder roasted in air was used as the starting material in a second series of experiments (see chapter 4). A sequence of Pt-wire loop runs was carried out in air to investigate the phase relations of this melt optically. This was followed by a set of experiments with hematite seeds cemented in alumina crucibles.

The sample used to produce the starting powder is a dolerite from an intrusive sheet in the Cleish Hills in West Fife. The rock was powdered and roasted in air at 800°C in order to oxidize Fe^{2+} to Fe^{3+}. This produces a system which will not change composition by iron oxidation in high temperature experiments in alumina crucibles. Due to the problems of fusing basaltic melts in platinum containers, the powder was used as the starting material and was pressed into the alumina crucibles and fused, with no refilling of charges. As powder has been used, gas bubbles are abundant in the fused melt in short duration runs, however, due to the low viscosity of the melt, these escape readily from the melt and, in doing so, cause some interesting convective phenomena which are discussed in chapter 4.

2.2.5 Furnace details

The pressed powder pellets, fused to Pt-wire loops, were suspended from ceramic rods and held in the hotspot of a vertical quenching furnace at atmospheric pressure. As the hotspot of this furnace is measured at 10mm long it can be assumed that no thermal gradient exists in the molten beads. These charges were quenched by rapid removal from the furnace to room temperature (Quench rate = $200°Cs^{-1}$). Quenching by dropping charges into water was not attempted as this causes shattering of the glass bead (eg Curry 1989).

In experimental runs using fixed crystals in crucibles a furnace with a hydraulically-operated, elevator-hearth mechanism was used. This has a smooth mechanism and therefore prevents sudden movements and forced convection as the charge is taken out of the furnace. The crucible, in a containing Pt boat, was loaded onto the plinth on the furnace floor, which was then raised up into its sealed position in the furnace. To quench the charges the bottom of the furnace was lowered and the Pt boat lifted onto a silica plinth at room temperature. This quench rate was estimated visually as $60°Cs^{-1}$

by the time taken for the meniscus to stop glowing. Crucibles have a vertical temperature difference of about 4°C (hottest at the top). This vertical gradient will prevent thermal convection of the melt.

2.3 Experimental Design

2.3.1 Factors influencing experimental design

The original aims of these experiments were to promote the formation of compositional boundary layers adjacent to growing crystals and to analyse the extent and scale of compositional variation across the boundary layers using electron-probe microanalysis and optical microscopy. In order to maximise the chances of observing compositional boundary layers convection driven by temperature differences and surface tension is suppressed in the experimental charges. Convection driven by temperature variation is eliminated in these experiments as they are carried out in a temperature gradient in which the top of the crucible is hotter than the bottom. Therefore in a compositionally-homogeneous crucible, the melt at the bottom has a higher density than that at the top and the density gradient is stable. Another convective phenomenon, surface-tension-driven convection (Donaldson, 1993), is eliminated here (except in wire-loop experiments) by ensuring that the crystal seed does not come into contact with the melt's meniscus.

For the above reasons, and in order to keep the crystal seed in a fixed position, the original intention was to carry out experiments in alumina crucibles (18 mm in diameter and 24 mm in height) in which drilled crystals could be suspended by threading them with platinum wire passed through holes in the crucible walls (see figure 2.04). Whereas this technique has been successful for short duration, high-temperature, dissolution experiments in silicate melts (Donaldson 1993), problems arose with it in the crystal growth experiments reported here. These problems are outlined in section 2.3.2b.

The loss of iron to noble metal containers is a problem that has been confronted by Corrigan and Gibb (1979) and by Donaldson (1979). This problem is avoided here by the choice of melt system (see section 2.2 above) and by using alumina crucibles for the experimental runs. The choice of magma system used in the experiments rules out the need for a controlled atmosphere in the furnace.

2.3.2 Development of a suitable experimental system

This section outlines the experimental designs used during this project, and the problems associated with each. As will become clear in chapters 3 and 4, even the most successful method in this study (cementing crystal seeds to the crucible floor using alumina cement) has problems which have not yet been overcome.

Technique a) The Pt wire loop technique

A $Pt_{80}Rh_{20}$ wire loop is used as a sample holder (Weill and McKay 1975, Lofgren *et al* 1974). The sample consists of a pressed pellet (figure 2.01a) of powdered glass and chips of the mineral to be overgrown. The pellet is attached to the wire by heating the wire with an electrical current which melts the outside of the pellet (figure 2.01b). The loop is then slung from a rod and inserted in the furnace. This technique was used in two series of preliminary experiments checking the phase relations of both melts used in this study. The chips of crystal sink to the bottom of the bead if they are denser than the melt. In theory they should remain here during the experiment, but there is a possibility that they may move in the bead of liquid, especially if buoyant, escaping air bubbles attach to them. This risk is minimal as most air is expelled from the pellets when they are pressed during preparation, however this technique provides no guarantee of fixing crystal seeds during experiments.

The main problem with the technique, however, involves the effect of differential surface tension at the points where crystal seeds come into contact with the meniscus of the bead. Variations in surface tension at these points may override the buoyancy forces in a compositional boundary layer and cause the melt at the crystal-liquid interface to be dragged away from the crystal onto the meniscus (Donaldson, 1993). For these reasons this technique has not been used for all experiments in this study. The wire-loop technique does, however, provide a ready method of testing phase relations in order to identify the most suitable temperature conditions for further experiments.

Pressed powder pellets (3 mm in diameter), mounted on 2.5 mm diameter loops of $Pt_{80}Rh_{20}$ wire (0.2 mm thick) (see figure 2.01), were fused to form spherical beads of melt in a quenching furnace, held above the liquidus of the system (1300°C for the cobalt basalt and 1270°C for the natural basalt) for 10 minutes, and then cooled rapidly to a subliquidus temperature to allow crystal overgrowths to form on the seeds. The beads were quenched in air, and vertically-aligned, polished thin sections were made for optical and electron-probe micro-analysis.

FIGURE 2.01. Sketches outlining the wire-loop technique.

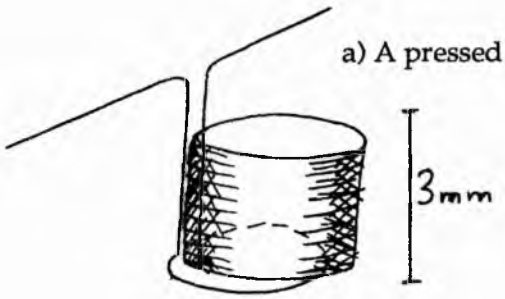

a) A pressed powder pellet is mounted on the wire loop

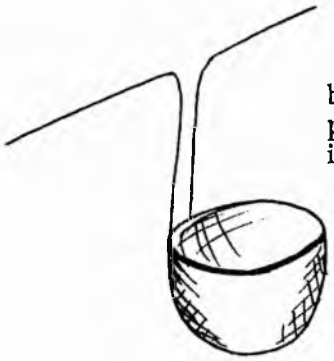

b) After attaching the wire to a vertical ceramic rod, the pellet is fused in the furnace to form a bead of melt which is held on the wire by surface tension.

c) Vertically-alligned thin sections through beads show how crystals have settled at the bottom of the charge. The indentations on the meniscus are the points at which the bead was attached to the wire.

FIGURE 2.02. Phase diagram for a typical mineral showing solid solution (eg. olivine). There is a bigger compositional difference (y>>x) between the original melt composition and melt at the crystal-liquid interface at lower temperatures.

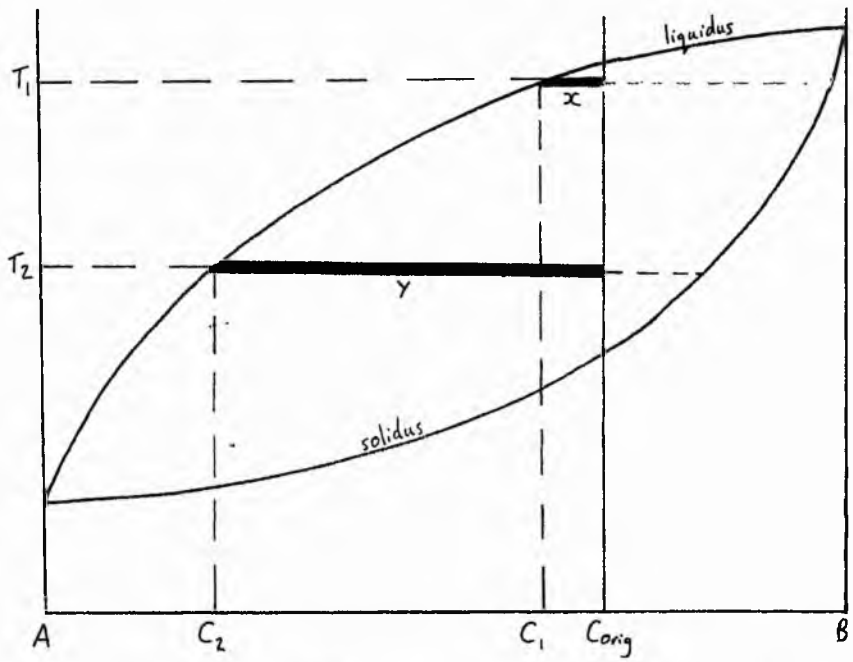

FIGURE 2.03. Summary of the change in olivine morphology with varying cooling rates and degrees of supercooling (from Donaldson, 1974).

Cooling Rate	0·5	2·5	7	15	40	80	300	1450
ΔT (°C)		10	20	30	50	80	140	
Morphology								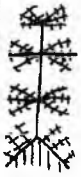

FIGURE 2.04. Cross section of an alumina crucible in which an olivine seed is suspended by platinum wire.

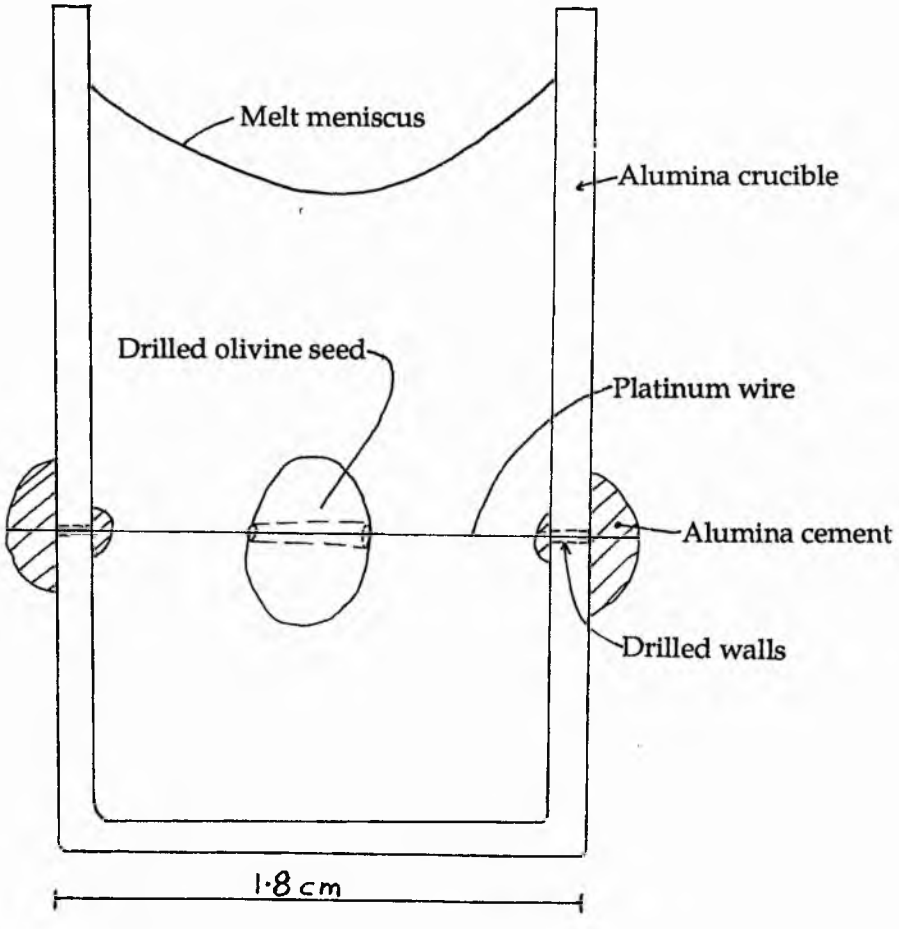

This technique provides an estimate of the rate of crystal growth at a given temperature, and indicates the morphology of the crystals that will grow at that temperature. If the temperature is too low then crystals will nucleate throughout the melt and interfere with analysis of the resultant glass because compositional gradients are established adjacent to all crystals, not just in the glass adjacent to the central crystal seed. This is especially relevant in the cobalt-basalt, as olivine nucleates readily in this melt when it is supercooled.

Figure 2.02 illustrates the importance of finding the optimum temperature conditions for overgrowing crystal seeds in these experiments. If an experimental run is made at temperature T_1, using an initial melt composition of C_{orig}, the composition of melt in equilibrium with the growing crystal at the crystal-liquid interface is given by C_1. At a higher degree of supercooling in the same liquid composition, (i.e. at T_2), the melt at the crystal-liquid interface has the composition C_2. At T_2 the interface melt has a larger compositional difference with C_{orig} than at T_1 (denoted by the length of X and Y in figure 2.02). If convection does not remove it, the boundary layer at T_2 will have a larger compositional contrast with C_{orig}. However, at greater supercoolings crystal nucleation rate is higher, and more elongate and skeletal crystal morphologies grow (Donaldson, 1976, and Lofgren 1974). This will produce a complex interface along which boundary layer movement will be potentially hard to trace. At smaller supercoolings (eg T_1 in figure 2.02), a thinner boundary layer will be produced due to the slower crystal growth rates, but the crystal overgrowth will have a simple morphology and so examination of the boundary layer and crystal morphology is not complicated by a complex crystal morphology (see figure 2.03) whereas at lower temperature it might be.

If convection does not interfere with boundary layer development then the width of boundary layers will be controlled by chemical diffusion rates. At large supercoolings, where interface melt has a bigger compositional difference with the original melt composition, diffusion rates will be relatively slow. In this case diffusion rates will not be able to smooth out the compositional gradients formed by crystal growth, and so the large compositional difference is spread over a wide boundary layer. At small supercoolings diffusion rates are faster and so boundary layers will not develop to the same thickness as they do at larger supercoolings. In such cases small compositional variations will exist across thin boundary layers. Therefore a problem exists in choosing the degree of supercooling at which boundary layer development should be studied. At small supercoolings small compositional differences will develop in thin boundary layers, if convection does not interfere with their development, while at larger supercoolings a bigger, and possibly more easily detectable, boundary layer will form with a larger compositional difference. From this it may seem that larger supercoolings are advantageous in the search for boundary layers, however the

aforementioned problems of crystal morphology come into play more at larger supercoolings. In this study runs are made at small degrees of supercooling.

In examining the glasses produced on quenching crystal-growth experiments, using either optical or electron microscopy, it should be easier to detect larger compositional differences in melts. This suggests that a larger degree of supercooling should be used. However the problems of extra crystal nucleation and increasingly complex crystal-liquid interface morphologies then need to be considered. An intermediate temperature (1230°C for the synthetic basalt, and 1250°C for the basalt) would therefore seem to be the most suitable condition for developing and observing compositional boundary layers in these experiments.

In summary, experiments using the wire-loop technique serve a dual purpose:-
1) They allow phase relations of a magma system to be checked.
2) They allow crystal growth rates and crystal morphologies at different temperatures to be gauged.
From this information a suitable temperature can be selected for experiments, one at which boundary layer thickness and compositional differences across it should be sufficient to be detected, and at which nucleation of extra crystals in the charges will not interfere unduly with glass analysis.

Technique b) Crystals suspended by Pt wire in alumina crucibles

This technique has been used successfully in high-temperature, short-duration, crystal-dissolution experiments in silicate melts (Donaldson 1993). It involves suspending a drilled crystal (olivine in the cobalt-basalt) in an alumina crucible, by threading the two together with 0.05mm diameter Pt-Rh wire through drilled holes in the crucible walls (see figure 2.04). Holes were drilled in the crucible walls with a 0.8mm diameter, diamond tipped dental drill bit. The wire is looped around the crystal once, to keep the seed in a fixed position, and the wire-ends are tied together on the outside wall of the crucible. The holes in the sides of the crucible are plugged using alumina cement, and a 2-3 mm thick layer of this cement is applied to the outside of the charge to prevent leakage of melt through the crucible walls. After adding the alumina cement, the charges were allowed to dry at 100°C for several hours.

The crucibles were filled with chips of cobalt-basalt glass, held at 1300°C until the glass had fused, removed from the furnace and refilled if the melt level fell to anywhere near the upper surface of the crystal (to avoid any surface-tension driven convection). The glass was then remelted and held above the liquidus for 10 minutes before being cooled to the appropriate subliquidus temperature. At the end of the experimental runs the charges were quenched in air (to avoid the shattering that occurs in water-quenched

experiments). Polished thin sections, cut vertically through crystal seeds, were made for optical and electron microscope analysis.

This technique was successful for short-duration runs (<5 hours), but after longer periods of time the pores in the alumina cement became saturated with melt, and then the melt leaked onto the outside of the crucible, forcing runs to be aborted. Long duration runs (which are necessary to produce any noticeable differentiation in the charges) are therefore not possible using this technique. After several failures due to melt leakage this method was abandoned. Another problem of the technique involves contamination of the melt by a certain amount of dissolution of alumina cement, this is discussed further in chapters 3 and 4.

Technique c) Crystals suspended in clay crucibles

With the aid of the School of Materials at Leeds University clay crucibles were made in which crystals could be suspended internally, without the problem of weaknesses caused by holes in the crucible walls. These crucibles were made using clay slip provided by the technique described in appendix A. This technique involves attaching small handles of clay to the inner walls of a clay crucible before the crucible is fired in a furnace. The clay handles are pierced vertically with a needle to form holes two-thirds of the way down the walls of the crucible. Olivine seeds can be hung in the crucible by threading them with Pt wire, passing this through the holes in the handles, and tying the wire at its ends (see appendix B for details).

Several experiments using the cobalt-basalt were run in these crucibles. However problems arose due to dissolution of the crucibles in this melt. This type of crucible is usually used for glass and ceramic experiments at 1000°C, with only minimal contamination of melts being reported. It appears that a combination of higher temperature in these experiments, and the corrosive properties of basaltic melts causes increased dissolution of the crucible walls. Making the walls thicker only prolongs the life of the crucible before leakage occurs from the charge, while the melt becomes more contaminated with dissolved clay.
However the dissolution does cause convection in the crucibles by producing a less dense melt at the walls and on the floor (see plate 3.04 in chapter 3). Dissolution of the crucible takes place at all liquid-clay interfaces, but is fastest at the meniscus-wall contact where flux-line attack causes accelerated wall thinning. In some of the runs using these crucibles dissolution causes clay handles to detach from crucible walls so that the crystal seed does not retain its fixed position during the run. This is discussed further in chapter 3.

Technique d) Crushed olivine seeds in alumina crucibles

This technique aims to simulate crystal growth in a zone of crystal-liquid mush on the crucible floor, and relies upon the crushed olivine crystals remaining on the bottom of the crucible during the run. The crucible floor was covered to a depth of 3-4 mm with olivine chips (<1 mm diameter), and then the crucible was filled up with chips of the synthetic basalt glass before fusion at 1300°C, followed by supercooling to a sub-liquidus temperature. On vertical slicing of these charges it was obvious that the olivine chips did not remain on the crucible floor. Some crystals lay on the floor but many had floated due to attachment to air bubbles (see plate 3.11 in chapter 3). For this reason it is not certain that even the crystals on the crucible floor remained in place throughout the run. One approach to overcome this problem might be to hold the charge at 1300°C for longer, in order to allow the air bubbles to escape and crystals to resettly to the floor before the run begins. However bubbles have remained preferentially attached to crystal seeds in the experiments of several days duration and superheating for such a length of time is impractical. Due to the nature of these experiments (i.e. they cannot be monitored without interrupting and changing the temperature conditions) it is impossible to know when all bubbles may have escaped from the charges.

Another attempt, based on this method, was made by pressing a covering of olivine chips into a layer of alumina cement on the crucible floor. However again many of the crystals detached from the cement and floated in the melt with the aid of air bubbles. Crystals that have remained on the floor can be analysed for boundary layer development but their small size in relation to the amount of alumina cement close to them means that the chemical differences in individual boundary layers are masked by the effects of a boundary layer caused by alumina cement dissolution .

Technique e) Crystals cemented to the floor of alumina crucibles

Previous experimental work (Donaldson 1993) indicates that this method, which involves fixing a crystal seed to the crucible floor with alumina cement, should be restricted to short-duration runs because basaltic melt attacks the cement and dissolves it so that the crystal seed may not remain in its fixed position. This judgement is based upon the findings of crystal dissolution experiments using natural basalts, and is therefore from higher temperature experiments than used here. When this technique is used at the temperatures used in this study(1200°C to 1255°C), the cement remains coherent and the crystal seed retains its original orientation.

As the aim of this series of experiments is to produce detectable, buoyant, boundary layers, elongate crystals of olivine and hematite are cemented to crucible floors with

their long-axes vertically-aligned . This means that horizontal crystal surfaces, on which buoyant boundary layers may be temporarily stable, are not present in these experiments. On a vertical or inclined face the boundary layer is instantly unstable and should therefore convect away from its source. Vertical alignment of crystals therefore enhances boundary layer instability and increases the chance of identifying boundary layer convection.

In some experiments using this method elongate crystals were ground to give the shape illustrated in plates 3.17 to 3.26 in chapter 3. This triangular cross section provides steep sides and a sharp point at which buoyant boundary layer melt from the sides of the crystal should converge and detach from the crystal.

This cemented-seed method has been the most successful one used in the crystal growth experiments of this study, however it does have a problem because a certain amount of alumina dissolution occurs. This problem is discussed in chapters 3 and 4.

2.4 Experimental Details

2.4.1 Introduction

70 experiments were undertaken using the cobalt basalt and Cleish Hills dolerite melts, using the various techniques described in section 2.3. Details of these runs are given in chapters 3 and 4. Each set of experiments is of two kinds. The first kind use the wire-loop technique to check phase relations and crystal growth and nucleation rates in the system, while the second kind uses the clay and alumina crucibles with fixed-position crystal seeds in an attempt to form compositional boundary layers in the melt adjacent to crystal overgrowths on these seeds.

2.4.2 Olivine crystallization in synthetic cobalt basalt.

Details of experimental runs are given in chapter 3. Wire-loop experiments used chips (upto 1mm diameter) of gem-grade peridote olivines (Fo 88) (3 in each charge), while the runs with suspended crystals used rounded, drilled crystal seeds. Cemented seed runs used the polished, rounded, vertically aligned olivine crystals too, but in later runs the olivines were ground to provide pyramid-shaped seeds. All of the runs in this set of experiments were superheated at 1300°C for 10 minutes after complete fusion of the glass, before being supercooled to the run temperature at a rate of 0.3-0.5°Cs^{-1}.

2.4.3 Iron oxide development in Cleish Hills dolerite

Experimental details are given in chapter 4. The hematite seeds in the wire-loop experiments were chips (<1mm) from euhedral hematite crystals (2.8 wt % TiO_2, <0.1 wt % Al_2O_3, <0.1 wt % MnO). These same euhedral crystals were used in the cemented-seed experiments, after being ground to elongate, pyramidal shapes to provide steep sides for oxide overgrowth. The liquidus temperature of this system is approximately 1260°C. Runs were superheated at 1300°C for ten minutes in the wire-loop experiments, and for 15 minutes after fusion in the runs using alumina crucibles. Cooling to run temperatures was again at 0.3-0.5°Cs^{-1}.

2.5 Analysis of Experimental Charges

2.5.1 Thin section preparation

Charges were sliced vertically using a diamond-coated saw, and vacuum impregnated with epoxy resin to avoid loss of glass fragments during thin section production. Vertical surfaces were ground to reveal suitable sections of the crystal seeds; this was usually the highest exposure of the seed. This surface was then ground using 600 and 1200 grade carborundum powders and affixed to a microscope slide, before being ground down to 0.5 mm thickness, then to 100μ using 600 grade carborundum powder, and approximately 50μ using 1200 grade powder. All thin sections were finally polished with diamond paste. The final thickness varies from section to section because some charges which had cracked during quenching were intentionally left thicker than others to avoid plucking of glass fragments during polishing. For this reason, and because of the difficulty in preparing a uniform thickness of section for all charges, colour intensity in glasses from different runs is not a good indication of relative cobalt or iron concentrations in each run. Colour density in each thin section, assuming even thickness across the slide, is however a guide to relative cobalt or iron concentration variation in each experimental run. In these slides some slight colour change can be detected adjacent to crystal seeds and crucible walls (see chapters 3 and 4).

2.5.2 Optical analysis

The concentration of Co^{2+} in the synthetic basaltic glass is reflected in the intensity of the blue colour of the glass. It was originally hoped that if a boundary layer, depleted in Co^{2+}, was formed adjacent to the crystal overgrowth then it would be detectable as a paler blue colour.

In iron-based melts the intensity of the brown colour in the glass makes compositional variation hard to detect optically. From the cobalt basalt experiments it was soon realized that the intensity of the blue colour of the glass, combined with the small compositional difference at the crystal-liquid interface makes boundary layers very hard to detect using optical techniques.

In the basalt-hematite experiments colour variations are detectable optically, and in the cobalt-basalt system the distribution of platinum blebs is possibly influenced by the fluid dynamics of the system. In the latter case, areas close to the crystal-liquid interface are frequently devoid of Pt blebs, which are relatively evenly distributed throughout the rest of the melt see plate 2.1. These metallic blebs are seen incorporated in the crystal overgrowths. The blebs are seen along a plane dividing the olivine seed from the Co-Mg overgrowth, but not within the overgrowth. They could have adopted this position due to a surface tensional effect which has attracted blebs around the seed to the interface during superheating of the melt. If this is the case then the melt around the seed will be stripped of blebs, in contrast to that further from the seed which will still contain blebs. The melt near the crystal-liquid interface will subsequently have Co and Mg taken from it by olivine crystallization and should therefore form a buoyant boundary layer. If this occurs then identifying the areas of Pt-free melt may help to trace the movement of the crystal-liquid interface melt.

2.5.3 Electron microscopy and microprobe investigations

The JEOL JCXA 733 Superprobe microanalyser at St Andrews University was used to carry out all of the analytical work for this project. Back-scattered-electron imagery (BSEI) and wavelength-dispersive spectrometry were used to examine compositional variations in the glasses and crystals produced by quenching of experimental runs. Operating conditions for analysis were 15kV and 20nA throughout, using pure metals, oxides and minerals as reference standards. Apparent concentrations were corrected using the conventional ZAF correction procedures.

Backscattered electrons rebound off a sample with an intensity which is a function of the mean atomic number of the sample. Areas with high mean atomic numbers backscatter more electrons and appear brighter in BSEI. If the variation in mean atomic number is sufficient in the glasses then it will be reflected in the intensity of backscattered image.

Quantitative analysis was carried out to determine both glass and mineral compositions. Both were analysed using a 1-micron, fully-focused beam. 8-element chemical analysis (SiO_2, TiO_2, Al_2O_3, CoO, MgO, CaO, Na_2O, and K_2O) was carried out on the first runs of the cobalt basalt, and in all runs of the Cleish dolerite.

FIGURE 2.06. Calibration graph for Co count rate data versus CoO wt %.

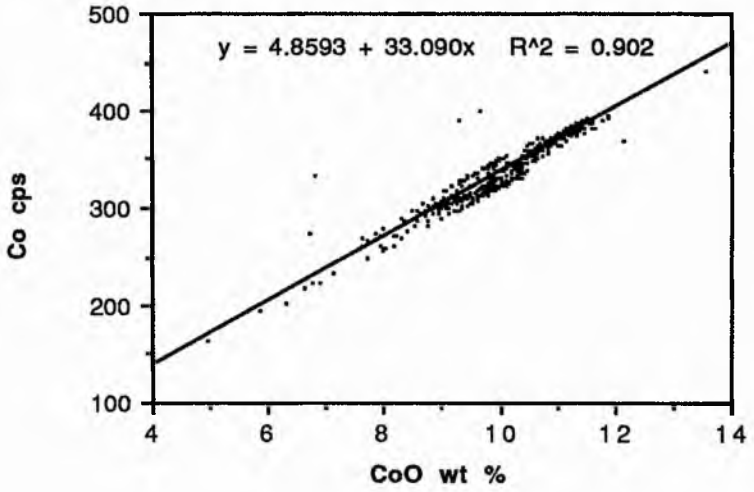

FIGURE 2.07. Calibration graph for Mg count rate data versus MgO wt %.

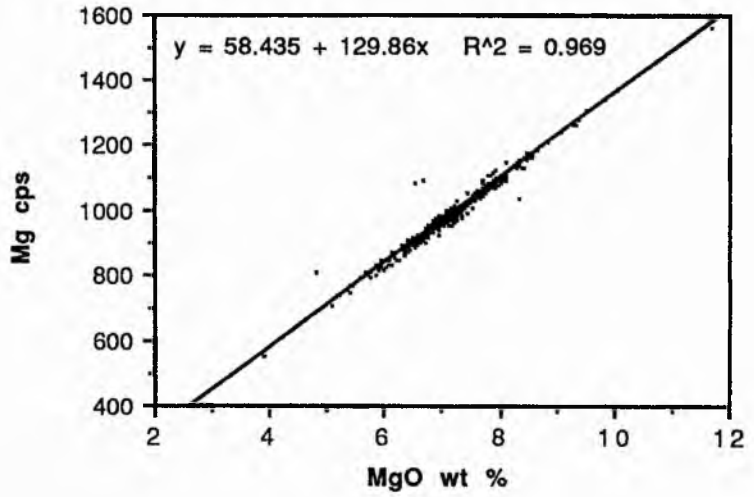

Preliminary analysis of glass in the cobalt-basalt experiments indicated that compositional variation at the crystal-liquid interface is small, and is limited to very narrow zones (<50μ). This led to the use of a different method of quantitative analysis involving closely-spaced points being analysed for Co, Mg, Fe, Si and Al X-ray count rates. In this latter method Co, Mg, Al and Si x-ray count rates at closely-spaced points are calculated by analyzing spots for 5-second peaks and 5-second backgrounds. The x-ray count rates can be calibrated with those from full analyses for an indication of wt % equivalents. Stage movement between points is dictated by the computer programme and can be controlled down to a lower limit of 1 micron in any direction by controlling x and y coordinates so that the width of boundary layers, and their compositional variations, can be delineated down to the nearest few microns. A peak-seeking facility was used, with counts for peak and background being carried out for 10 and 5 second durations respectively. The count rate data for Co and Mg are calibrated by comparisons with count rates for full chemical analyses, and is shown for Co and Mg in figures 2.06 and 2.07 respectively. The analytical data are displayed graphically and as contoured maps in the following two chapters. The contoured maps were produced using a programme called "UNIRAS UNIMAP 2000" on a SUN workstation. This allows data from several analytical traverses to be brought together on a single map, and has been very successful in producing contoured maps of Co, Mg and Al concentrations around apexes of crystal seeds(See Appendix E).

Melt density and viscosity are calculated from glass compositions using the methods of Bottinga and Weill (1970) and Shaw (1972), respectively. This allows the fluid dynamical behaviour of boundary layers to be predicted using the Compositional Rayleigh equation (see chapter 1).

Chapter 3. Olivine growth in a synthetic basalt

3.1 Introduction

The work described in this chapter is a study of experiments in which Co-Mg olivine was grown in a synthetic basaltic melt. The melt around the crystal seed is examined for compositional variation and for signs of convection of boundary layer melt from around the seed.

Chemical analysis has been carried out on charges using all the techniques outlined in chapter 2 to evaluate the effects of cement and clay dissolution, and to examine individual olivine crystallites for evidence of boundary layer development and its movement. Extensive chemical analysis has been carried out on charges that used the most successful technique; cemented olivine seeds in alumina crucibles. The discussion of results of these experiments includes sections on crystallization, glass compositional variation, melt density and viscosity changes, and melt convection within the charges.

3.2 Experimental runs using the wire-loop technique

7 runs were made using this technique to establish the following:-
1) Phase relations.
2) Rates of nucleation and growth of olivine crystallites in the melt, and rate of overgrowth on the seed.
3) Whether or not compositional variation in boundary layers around olivine crystals is detected as a colour change in thin sections of charges.
The details of runs using this technique are given in table 3.01. From these initial runs a temperature of between 1200°C and 1230°C was chosen for suspended-seed experiments. These are temperatures at which crystallite development is slow enough not to interfere with glass analysis at the overgrowth-melt interface.

Electron-probe micro-analysis has been carried out on thin sections of the quenched products of these runs. As mentioned in chapter 2, surface tension-driven convection may affect the movement of boundary layer material in wire-loop charges, making them unsuitable for the main series of experiments. EPMA was carried out adjacent to an overgrowth on one of the olivine seeds in run number C-O 7. A map of analytical points in C-O 7 is given in figure 3.01 and the analytical data are displayed in table 3.02, along with density and viscosity calculations for these melts. Graphs in figure 3.02 indicate that relative to the bulk glass the interface melt is depleted in CoO and MgO, and enriched in Al_2O_3, TiO_2 and SiO_2 in a layer of melt only 20 microns thick at the crystal-liquid interface. These chemical variations are expected, as the overgrowth on the seed is Co-Mg olivine (see analyses 8 and 9 in table 3.02). They result in an

TABLE 3.01. Run details for olivine growth experiments

Experiment Number	Experimental method	Temperature (°C)	Run duration (hours)
Co basalt-oliv 3	Wire loop	1219	21.58 (21h35")
Co basalt-oliv 4	Wire loop	1219	Run aborted due to furnace failure.
Co basalt-oliv 5	Wire loop	1238	1.417 (1h 25m)
Co basalt-oliv 6	Wire loop	1238	2.167 (2h 10m)
Co basalt-oliv 7	Wire loop	1217	41.833 (41h 50m)
Co basalt-oliv 8	Wire loop	1238	27.667 (27h 40m)
Co basalt-oliv 9	Wire loop	1205	70.833 (70h 50m)
Co basalt-oliv 10	Seed suspended in Al2O3 crucible	1230	4.883 (4h 50m)
Co basalt-oliv 11	Seed suspended in clay crucible	1230	22
Co basalt-oliv 12	Seed suspended in clay crucible	1210	5
Co basalt-oliv 13	Seed suspended in clay crucible	1210	10
Co basalt-oliv 14	Seed suspended in clay crucible	1205	5
Co basalt-oliv 15	Seed suspended in clay crucible	1195	4
Co basalt-oliv 16	Seed suspended in clay crucible	1195	8
Co basalt-oliv 17	Seed suspended in clay crucible	1195	24
Co basalt-oliv 18	Seed suspended in clay crucible	1190	22
Co basalt-oliv 19	Crushed seeds in alumina crucibles	1210	65
Co basalt-oliv 20	Crushed seeds in alumina crucibles	1210	116
Co basalt-oliv 21	Crushed seeds in alumina crucibles	1200	209
Co basalt-oliv 25	Crushed seeds in alumina crucibles	1200	416
Co basalt-oliv 27	Crushed seeds cemented in	1210	119
Co basalt-oliv 22	Al2O3 crucible with no seed or cement	1200	0.083 (5minutes)
Co basalt-oliv 23	Al2O3 crucible with no seed or cement	1200	0.083 "
Co basalt-oliv 24	Al2O3 crucible with no seed or cement	1300	0.083 "
Co basalt-oliv 26	Cemented olivine seed	1200	45
Co basalt-oliv 28	Cemented olivine seed	1200	154
Co basalt-oliv 29	Cemented olivine seed	1230	24
Co basalt-oliv 30	Cemented olivine seed	1240	24
Co basalt-oliv 31	Cemented olivine seed	1230	72
Co basalt-oliv 32	Cemented olivine seed	1230	557
Co basalt-oliv 33	Cemented olivine seed	1230	71
Co basalt-oliv 34	Cemented olivine seed	1235	Furnace failure
Co basalt-oliv 35	Cemented olivine seed	1240	72
Co basalt-oliv 36	Cemented olivine seed	1245	72
Co basalt-oliv 37	Cemented olivine seed	1250	72

Figure 3.01. Thin section through charge CO 7 showing positions of analytical points, olivine seeds, and crystallites. Bead diameter = 3mm.

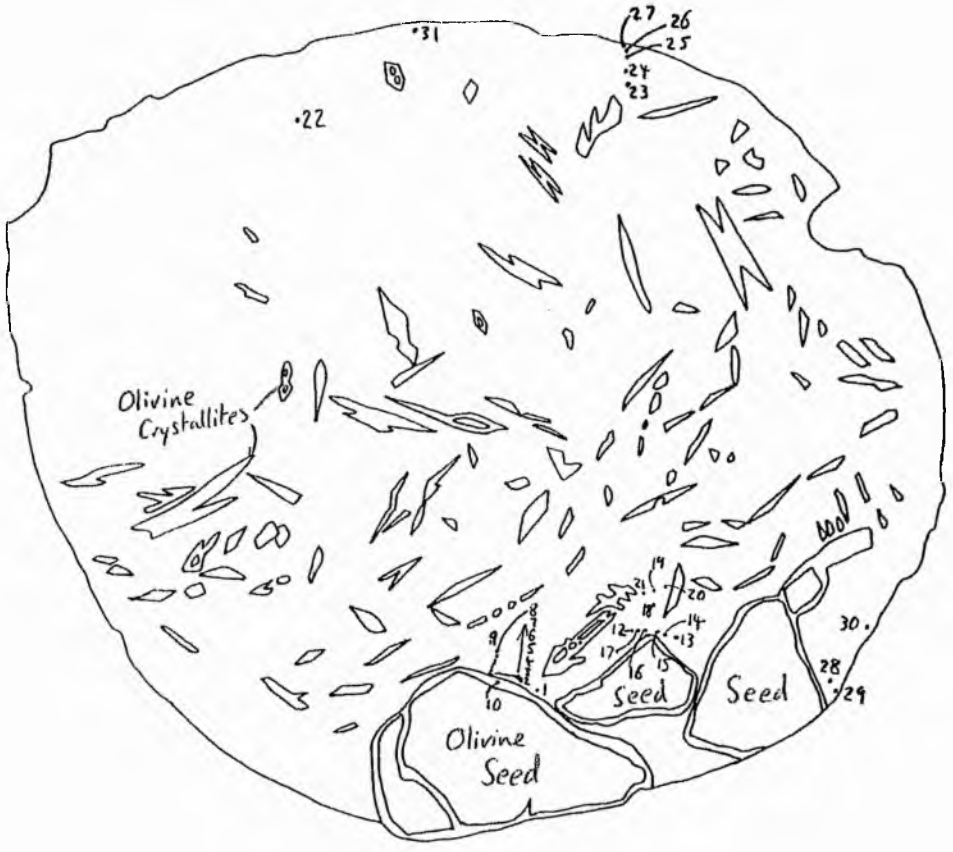

Table 3.02. Analytical data from CO 7

Analysis Number	SiO2	TiO2	Al2O3	CoO	MgO	CaO	Na2O	K2O	Total	Density @ 1217°C (g/cc)	Viscosity @ 1217°C (poise)	X (mm)	Y (mm)
3	48.9	3.8	14.9	7.6	5.1	14.4	2.3	0.7	98.2	2.69	333	12.96	12.71
4	48.7	3.6	14.5	8.8	6.3	14.2	2.1	0.7	99.3	2.72	213	12.95	12.69
5	48.8	3.6	14.5	8.7	6.3	14.3	2.0	0.7	99.3	2.72	221	12.95	12.68
6	48.4	3.5	14.4	8.8	6.3	14.2	2.1	0.7	98.7	2.72	208	12.95	12.67
7	48.8	3.6	14.4	8.9	6.4	14.0	2.1	0.7	99.2	2.72	216	12.94	12.67
8	48.8	3.5	14.5	9.1	6.3	13.8	2.2	0.7	99.3	2.72	218	12.93	12.67
9	48.4	3.5	14.4	9.0	6.4	14.1	2.2	0.7	99.0	2.72	200	12.90	12.67
10	37.4	0.1	0.0	27.0	35.4	0.5	0.0	0.0	100.8			12.94	12.74
11	37.2	0.0	0.0	29.4	33.9	0.5	0.0	0.0	101.2			12.55	12.90
12	48.9	3.6	14.4	9.0	6.5	14.3	2.1	0.7	100.0	2.72	199	12.43	13.05
13	48.0	3.6	14.5	8.7	6.4	14.0	2.1	0.6	98.4	2.72	198	12.01	13.22
14	48.3	3.6	14.5	8.9	6.6	14.1	2.2	0.7	99.2	2.72	189	12.06	13.17
15	47.9	3.7	14.5	9.0	6.4	14.0	2.2	0.7	98.7	2.72	187	12.08	13.14
16	48.4	3.7	14.6	9.1	6.4	13.9	2.2	0.6	99.3	2.72	199	12.13	13.10
17	48.9	3.6	14.4	8.9	6.5	14.0	2.1	0.6	99.4	2.72	215	12.17	13.07
18	48.4	3.6	14.2	8.9	6.4	14.1	2.3	0.7	99.0	2.72	195	11.99	13.07
19	48.2	3.5	14.4	8.7	6.4	14.0	2.2	0.7	98.6	2.72	203	11.93	13.00
20	47.8	3.7	14.3	8.6	6.6	14.0	2.3	0.7	98.3	2.72	182	11.90	13.02
21	48.6	3.6	14.5	8.8	6.5	14.1	2.2	0.7	99.3	2.72	207	11.99	12.95
22	48.5	3.7	14.2	9.2	6.6	14.1	2.2	0.7	99.3	2.73	187	11.42	10.95
23	48.0	3.6	14.3	9.0	6.4	13.9	2.2	0.7	98.3	2.72	192	10.55	11.60
24	48.5	3.5	14.0	9.2	6.5	14.0	2.2	0.7	98.8	2.72	194	10.43	11.60
25	48.0	3.6	14.0	9.1	6.4	14.0	2.1	0.6	98.1	2.72	193	10.41	11.58
26	46.8	3.6	14.1	9.2	6.2	13.9	2.0	0.7	96.7			10.40	11.57
27	43.9	3.4	12.9	8.8	5.7	13.3	1.9	0.6	90.6			10.39	11.57
28	48.7	3.6	14.5	8.6	6.6	14.0	2.3	0.7	99.3	2.71	207	11.74	13.76
29	49.0	3.7	14.5	8.6	6.6	13.9	2.2	0.6	99.6	2.71	218	11.24	13.79
30	48.3	3.5	14.4	8.6	6.4	13.9	2.2	0.7	98.6	2.72	211	11.24	13.71
31	44.0	3.5	13.1	9.0	6.2	13.8	2.2	0.6	92.8			11.59	10.42
1	48.5	3.5	14.5	8.9	6.2	14.2	2.0	0.6	98.8	2.72	224	12.93	12.79
0	47.5	3.3	13.1	11.3	8.5	12.5	2.0	0.6	98.8	2.76	103		

Figure 3.02. Profiles of oxide concentrations and calculated densities and viscosities in the glass above the olivine seed in CO 7.

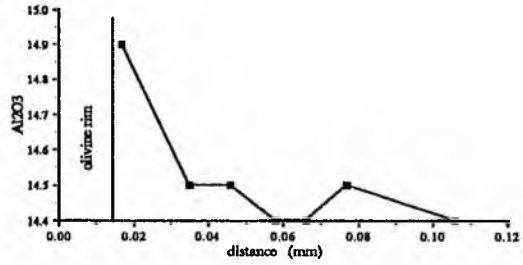

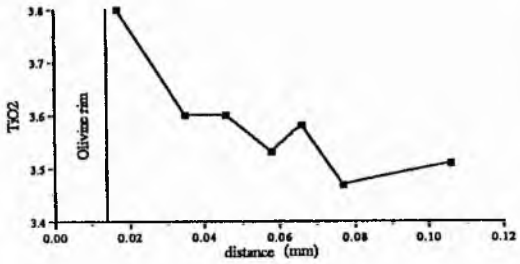

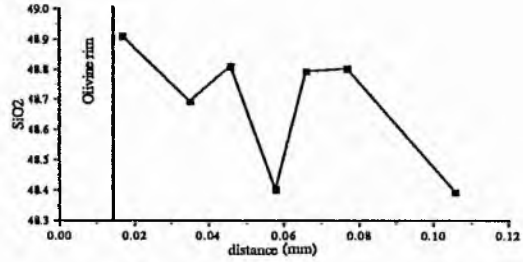

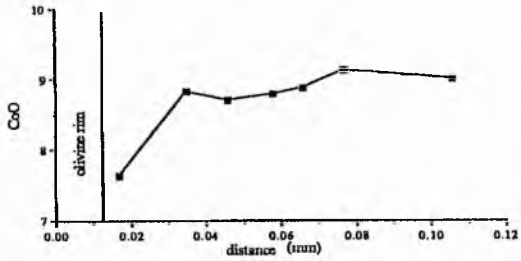

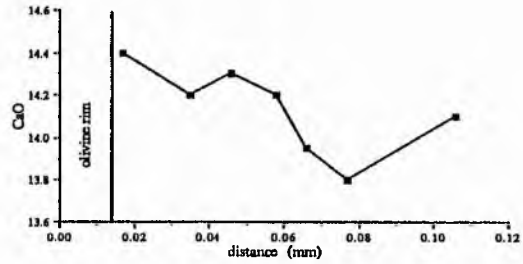

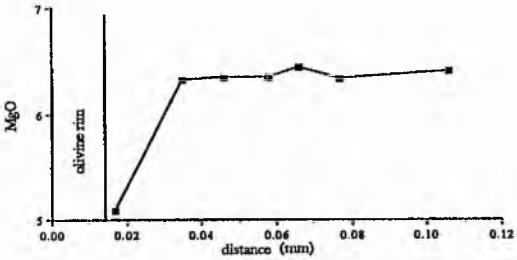

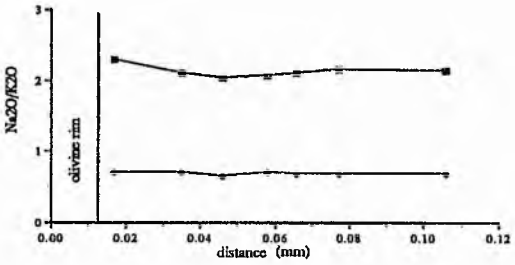

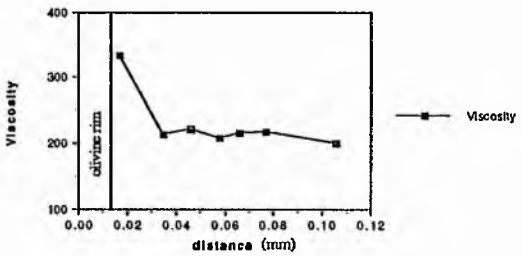

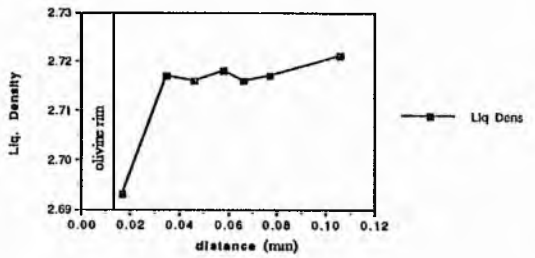

increased viscosity and decreased density in melt in the boundary layer. Chemical variation was not detected at the meniscus in this charge, pointing to the fact that longer runs (>2 days) need to be carried out in order to give any buoyant, boundary-layer melt an opportunity to migrate to, and accumulate at, the uppermost parts of the experimental charge, i.e. for melt differentiation to occur. Experiments in sections 3.3-3.6 are aimed at producing melt differentiation by providing longer run durations.

3.3 Olivine seeds suspended in alumina crucibles

3.3.1 Introduction

Due to the porous nature of the alumina cement this technique has been unsuccessful in allowing long-duration, crystal overgrowth experiments to be undertaken. It did however provide further information on olivine nucleation and growth rates, and EPMA was carried out on one of the experimental charges to examine compositional gradients around an individual olivine crystallite, and also to check for vertical differentiation in the crucible.

The charge examined (CO 10) is shown in plate 3.01. Figure 3.03 shows the position of analyses in the charge and around the crystallite examined, and the EPMA data are displayed in table 3.03. The crystallite was examined for boundary layer development and for evidence of crystallite movement relative to such a boundary layer.

3.3.2 Vertical differentiation of melt in C-O 10

Variations in glass composition above or below the olivine seed are small (see figure 3.04). The only noticeable chemical variation is that of Al_2O_3 which shows a sharp increase in concentration at the crucible floor, suggesting that the melt has been contaminated by crucible dissolution. The calculated density and viscosity reflect this chemical variation. Enrichment of melt in Al_2O_3 should produce a lower-density melt, capable of convecting in the crucible if it attains a thickness that is buoyantly unstable. The existence of such melt at the bottom of the charge suggests that it had not built up to an unstable thickness (see section 3.7.5).

3.3.3 Chemical profiles around an olivine crystallite

Concentration profiles around the olivine crystallite are displayed as maps in figure 3.05. These show decreases in CoO and MgO, and increases in CaO, Al_2O_3, SiO_2 and TiO_2 as the crystal-glass interface is approached. These changes are responsible for a density decrease and a viscosity increase in the melt in this boundary layer. Most of the compositional variation is seen in melt only 20-30 microns from the interface and

no trail of boundary layer melt is seen above the crystal. However the wide-spacing of the analyses in relation to the width of the boundary layer (20-30μ) mean that it is feasible that these data points have not detected escaping boundary layer melt (i.e. a plume of boundary layer melt could have passed between the analytical points. Also, there is no evidence to suggest that the crystallite has not moved during the run. Its density could have caused it to sink through the charge, and left boundary layer melt behind. Any boundary layer still remaining could therefore be the remains of a once thicker boundary layer. This provides enough problems to suggest that this method should not be pursued any further.

Plate 3.01. Thin section of charge CO 10 (1230°C 4.9 hours) with overlay showing points analysed by EPMA. Note how the glass is riddled with olivine crystallites, preventing a thorough search for compositional variation in the glass in this charge.

Plate 3.02. Thin section of charge CO 11 (1230°C 22 hours) showing dissolution of crucible walls to form pale melt at the side-wall. This layer of melt is thicker close to air bubbles and has formed a buoyant plume that can be seen rising in the crucible.

Plate 3.03. Thin section of charge CO 12 (1210°C 5 hours) showing pale-blue melt beginning to pond beneath the meniscus.

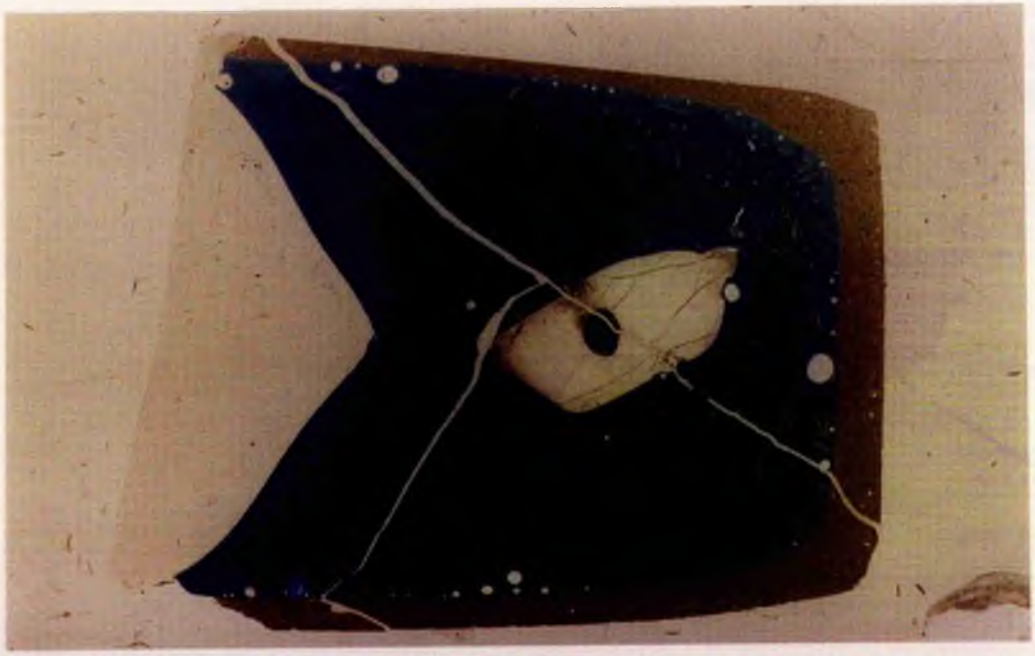

Table 3.03. Analytical data from CO 10

Analysis	X (mm)	Y (mm)	SiO2	TiO2	Al2O3	CoO	MgO	CaO	Na2O	K2O	Density @ 1230°C (g/cc)	Viscosity @ 1230°C (poise)
1	15.998	20.994	48.0	3.4	13.8	9.9	6.9	13.4	2.1	0.6	2.67	165
2	15.998	21.032	48.6	3.3	13.9	9.8	7.0	13.3	2.1	0.6	2.66	181
3	15.968	21.032	47.9	3.4	13.4	9.4	6.9	13.3	2.2	0.6	2.66	183
4	15.958	21.032	48.0	3.4	13.8	9.9	6.9	13.6	2.0	0.6	2.59	733
5	15.944	21.032	48.5	3.6	14.0	9.6	6.5	14.1	2.2	0.6	2.67	179
6	15.936	21.032	49.4	3.8	15.2	7.9	5.1	13.7	2.4	0.7	2.64	347
7	15.935	21.032	50.3	3.6	16.0	7.7	4.8	13.1	2.6	0.8	2.63	455
8	16.008	20.990	48.2	3.4	13.8	9.7	6.9	13.2	2.0	0.7	2.66	184
9	15.991	20.990	48.2	3.4	13.6	9.9	6.7	13.7	2.0	0.6	2.67	182
10	15.984	20.990	47.9	3.6	13.7	9.5	6.9	13.6	2.0	0.6	2.67	172
11	15.968	20.990	48.1	3.5	13.9	9.6	6.6	13.8	1.9	0.5	2.67	197
12	15.973	20.990	48.1	3.4	13.9	9.6	6.8	13.6	2.0	0.6	2.67	185
13	15.964	20.990	47.9	3.4	13.8	9.3	6.5	13.8	2.1	0.6	2.66	191
14	15.955	20.990	48.2	3.5	13.7	9.4	6.9	13.8	1.9	0.6	2.67	187
15	15.948	20.990	48.3	3.2	13.7	9.8	6.9	13.7	2.0	0.6	2.67	179
16	15.941	20.990	48.6	3.5	13.9	9.9	6.9	13.5	2.0	0.6	2.67	181
17	15.924	20.990	47.9	3.5	13.7	9.8	7.0	13.5	2.0	0.6	2.67	167
18	15.924	21.000	48.0	3.2	13.7	9.6	6.9	13.4	1.9	0.6	2.66	188
19	15.943	21.000	48.1	3.5	13.8	9.2	6.6	13.6	2.1	0.6	2.66	203
20	15.947	21.000	48.6	3.5	14.0	8.7	6.4	13.6	2.0	0.5	2.65	247
21	15.952	21.000	48.5	3.6	14.2	9.1	6.1	13.9	2.2	0.6	2.66	223
22	15.962	21.000	49.1	3.6	14.7	8.5	5.6	13.9	2.3	0.6	2.65	284
23	15.968	21.000	48.8	3.7	14.4	8.6	5.9	14.0	2.2	0.7	2.65	251
24	15.977	21.000	47.9	3.5	13.9	9.0	6.4	13.5	1.9	0.6	2.66	219
25	15.991	21.010	48.5	3.4	13.8	9.8	6.9	13.6	2.0	0.6	2.66	185
26	15.984	21.010	48.2	3.5	13.9	9.0	6.3	13.9	2.1	0.5	2.66	209
27	15.978	21.010	48.6	3.2	14.6	8.1	5.7	13.7	2.2	0.6	2.64	303
28	15.975	21.010	49.1	3.7	15.1	7.8	5.1	13.5	2.5	0.8	2.64	358
29	15.971	21.010	49.7	3.4	15.8	8.0	5.2	10.8	2.5	0.9	2.61	546
30	15.913	21.032	47.9	3.4	13.8	9.4	6.8	13.6	2.0	0.5	2.66	188
31	15.919	21.032	48.6	3.4	14.0	9.3	6.2	13.6	2.0	0.6	2.66	244
32	15.921	21.032	49.3	3.7	14.5	8.8	5.9	13.9	2.2	0.6	2.65	265
33	15.924	21.032	49.3	3.7	15.3	7.6	5.2	13.4	2.3	0.7	2.63	385
34	15.914	21.022	48.3	3.4	13.6	9.5	6.9	13.6	2.0	0.6	2.66	184
35	15.920	21.022	48.0	3.2	13.6	9.3	6.3	13.7	2.0	0.6	2.66	218
36	15.925	21.022	48.0	3.5	13.9	9.3	6.4	13.7	1.7	0.6	2.67	218
37	15.929	21.022	48.3	3.6	14.3	8.9	5.8	13.8	1.6	0.6	2.66	277
38	15.930	21.022	48.6	3.5	14.4	8.3	5.7	13.8	1.4	0.6	2.65	340
39	15.912	21.080	47.6	3.3	13.4	10.0	6.9	13.3	1.5	0.6	2.67	198
40	15.918	21.080	47.9	3.4	13.7	9.2	7.1	13.1	1.8	0.6	2.66	197
41	15.928	21.080	47.9	3.4	13.7	9.9	7.2	13.3	1.8	0.6	2.67	171
42	15.935	21.080	48.1	3.3	13.1	9.7	7.1	13.5	2.0	0.6	2.67	172
43	15.939	21.080	47.8	3.3	13.7	10.1	7.0	13.0	2.0	0.6	2.67	174
44	15.941	21.080	48.0	3.4	13.7	9.5	7.2	13.6	2.2	0.6	2.67	161
45	15.946	21.080	49.0	3.1	13.8	10.0	7.2	13.7	2.2	0.6	2.66	173
46	15.947	21.080	48.0	3.1	13.5	9.9	6.8	13.3	2.0	0.6	2.66	187
47	15.951	21.080	47.7	3.4	13.5	8.7	6.9	13.4	2.0	0.6	2.66	201
48	15.957	21.080	47.8	3.4	13.7	10.0	7.0	13.2	2.1	0.6	2.67	163
49	15.968	21.080	48.0	3.4	13.5	9.7	6.9	13.6	2.1	0.6	2.67	171
50	15.975	21.080	47.7	3.4	13.7	9.4	6.5	13.6	2.1	0.6	2.67	177
51	15.979	21.059	47.9	3.3	13.6	10.1	6.8	13.4	2.1	0.6	2.67	173
52	15.979	21.065	48.2	3.3	13.8	9.9	7.0	13.5	2.0	0.6	2.67	174
53	15.971	21.065	47.7	3.6	13.5	9.6	6.9	13.6	2.0	0.6	2.67	180
54	15.956	21.065	47.9	3.3	13.5	9.5	7.0	13.2	1.9	0.6	2.66	190
55	15.946	21.065	47.9	3.3	13.4	10.0	6.8	13.5	2.1	0.6	2.67	174
56	15.936	21.065	48.0	3.3	13.6	9.9	7.1	13.5	2.0	0.6	2.67	164
57	15.924	21.065	47.7	3.6	13.7	9.9	7.1	13.5	2.1	0.7	2.67	151
58	15.923	21.071	47.8	3.4	13.5	9.8	6.9	13.4	2.1	0.6	2.67	172
59	15.929	21.071	48.5	3.4	13.6	9.9	7.0	13.4	2.0	0.6	2.67	182
60	15.937	21.071	47.6	3.3	13.5	9.3	6.9	13.5	1.9	0.7	2.67	183
61	15.947	21.071	48.1	3.0	13.6	9.7	6.7	13.5	2.1	0.6	2.66	194
62	15.955	21.071	47.9	2.7	13.6	9.7	7.0	13.5	2.0	0.6	2.66	172
63	15.897	21.051	49.1	3.2	14.0	9.9	7.0	13.6	2.1	0.6	2.66	186
64	15.911	21.051	48.1	3.0	13.6	9.7	7.0	13.3	2.1	0.6	2.66	182
65	15.917	21.051	47.7	3.2	13.7	9.7	7.0	13.4	1.9	0.6	2.67	175
66	15.920	21.051	48.0	3.3	13.6	9.3	7.0	13.1	2.1	0.7	2.66	191
67	15.920	21.060	47.9	3.3	13.6	10.0	7.0	13.2	2.0	0.6	2.67	176
73	14.166	17.494	47.7	3.4	13.4	8.3	6.9	13.1	2.1	0.6	2.65	212
74	14.163	17.595	48.3	3.2	13.8	9.9	7.1	13.3	2.1	0.6	2.66	179
75	14.163	17.749	48.1	3.3	13.5	9.9	7.1	13.2	2.1	0.6	2.67	168
76	14.163	18.685	47.6	3.4	13.6	9.8	6.9	13.5	2.0	0.7	2.67	166
77	14.162	19.015	47.6	3.4	13.8	10.0	7.2	13.0	2.0	0.6	2.67	158
78	14.152	19.980	48.1	3.4	13.7	10.1	7.1	13.4	2.2	0.6	2.67	160
80	14.203	23.305	48.1	3.3	13.8	10.0	7.1	13.4	2.0	0.6	2.67	167
81	14.221	28.973	48.0	3.3	13.7	10.1	6.5	13.5	2.0	0.7	2.66	192
82	14.215	29.424	47.8	3.1	13.5	9.8	6.8	13.4	2.0	0.6	2.67	179
83	14.207	29.991	47.7	3.4	13.7	10.0	6.6	13.4	2.1	0.6	2.67	180
84	14.212	31.752	47.1	3.4	15.7	9.9	6.8	13.0	2.2	0.6	2.68	162
86			48.0	3.3	13.5	9.1	6.7	13.4	2.0	0.7		
87			49.9	3.6	15.8	7.0	4.3	13.4	2.7	0.8		

Figure 3.04. Variations in oxide concentrations and calculated densities and viscosities across the vertical range of charge CO 10.

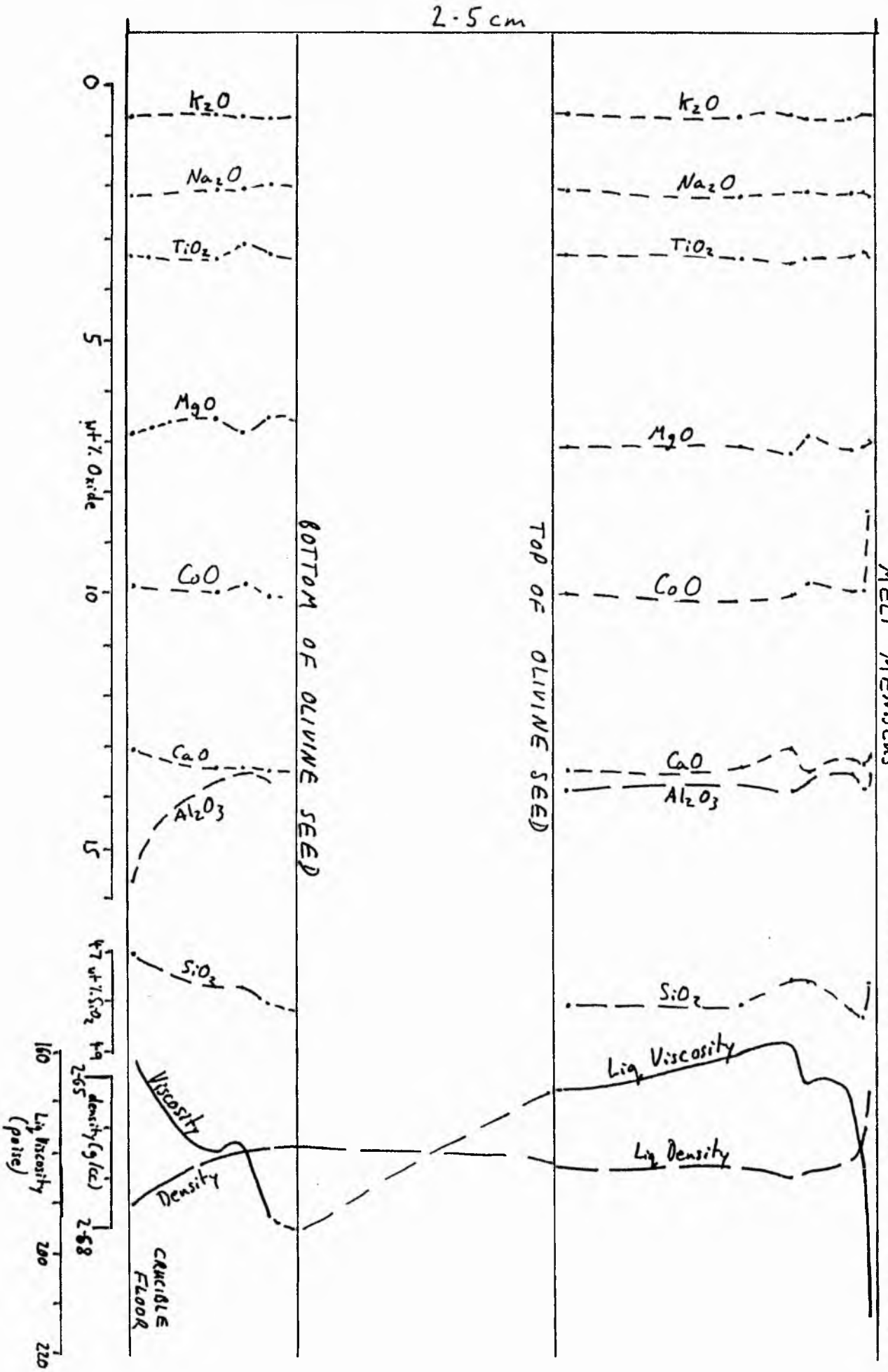

Figure 3.03. Map of points analysed around the olivine crystallite in CO 10.

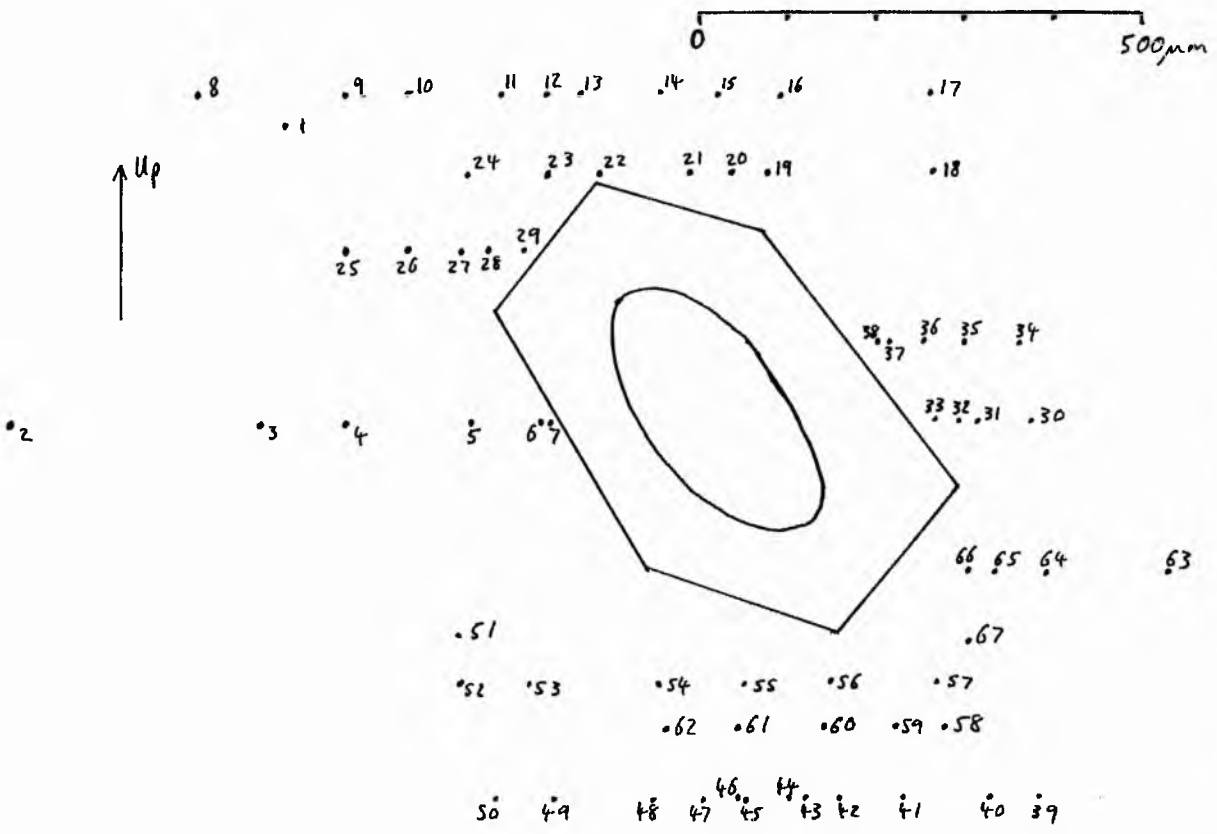

Figure 3.05. Maps of oxide concentrations and calculated density and viscosty around the olivine crystallite in CO 10.

Figure 3.05a. SiO_2 wt % map.

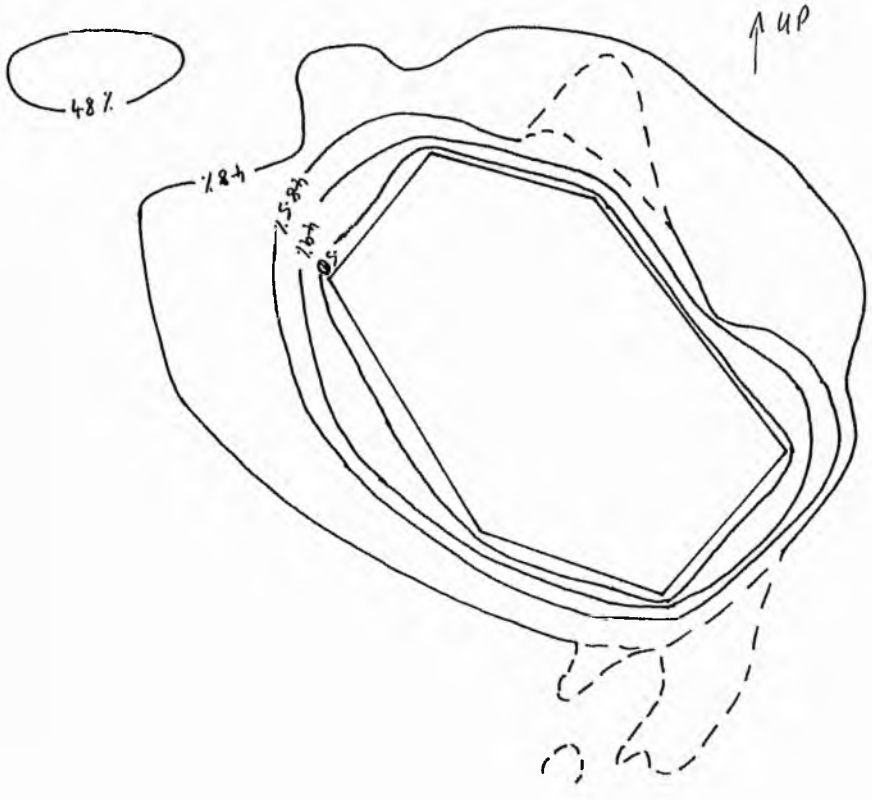

Figure 3.05b. TiO_2 wt %map

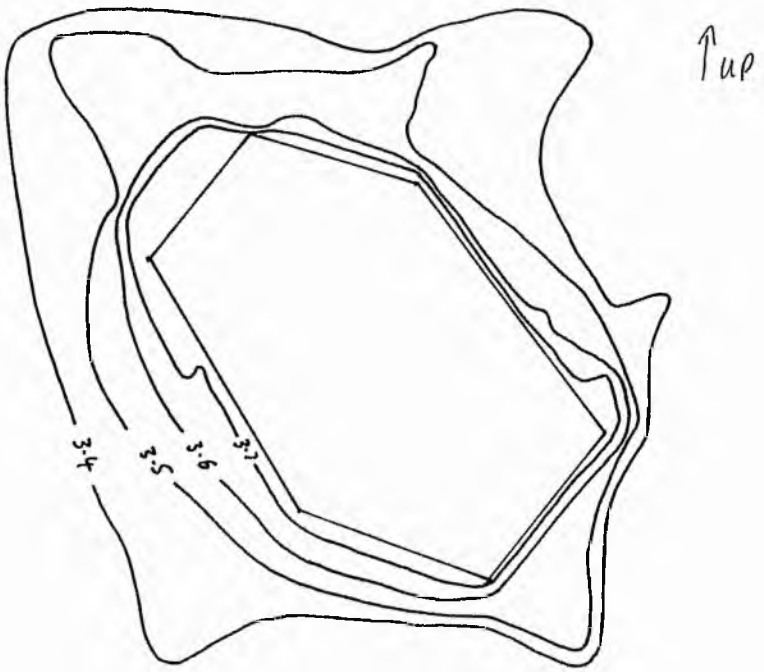

Figure 3.05c. CoO wt % map.

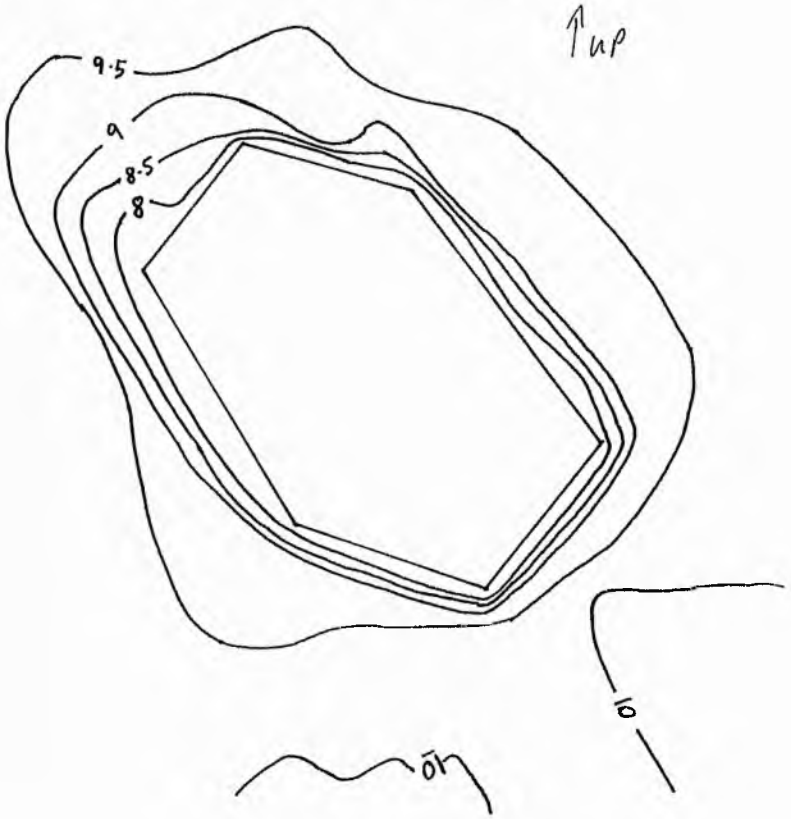

Figure 3.05d. MgO wt % map.

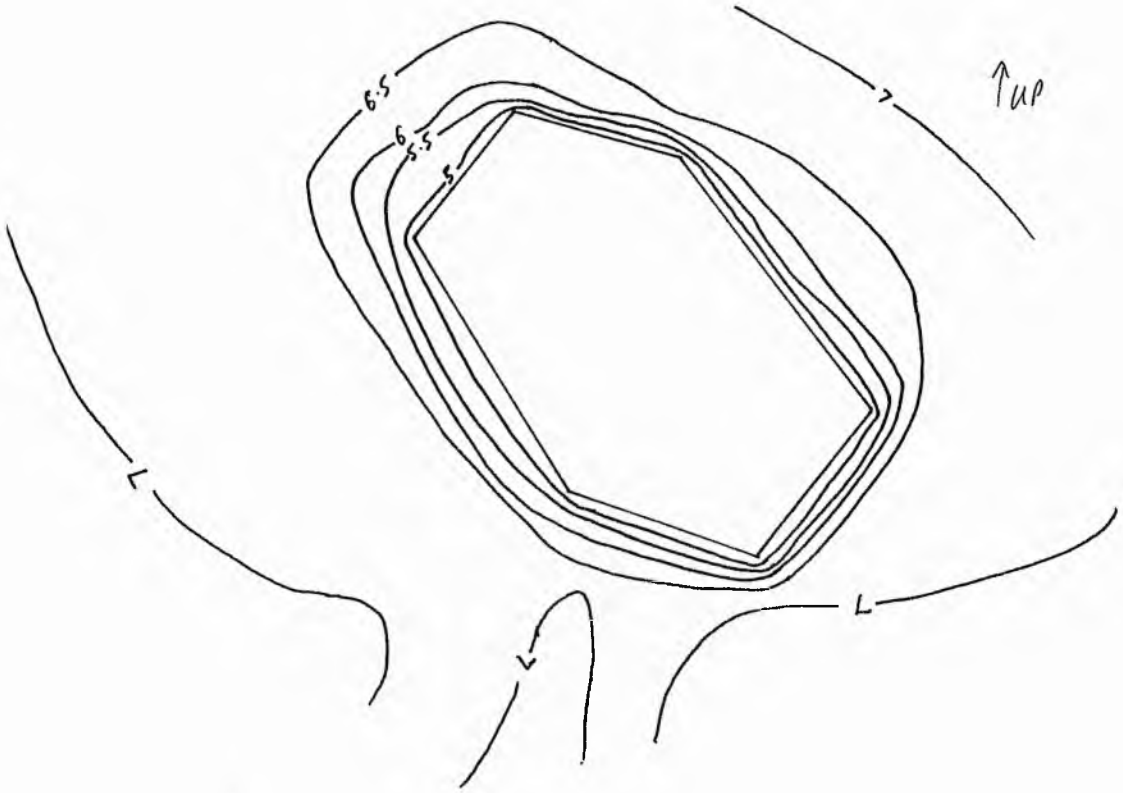

Figure 3.05e. Al_2O_3 wt % map.

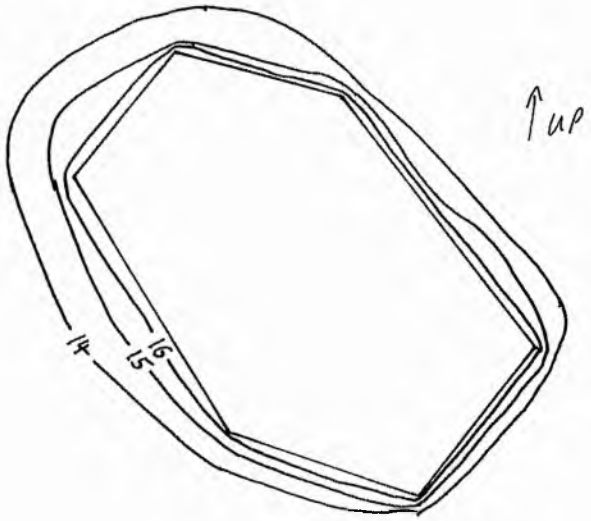

Figure 3.05f. Viscosity map (poise).

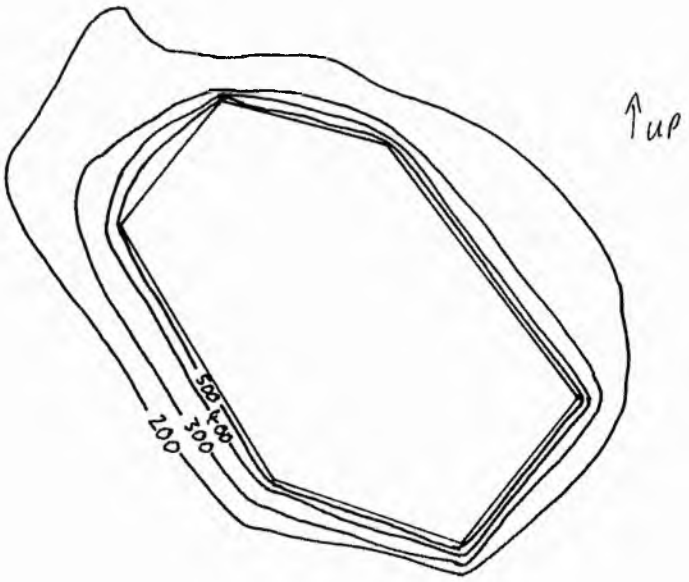

Figure 3.05g. Density map (g/cc).

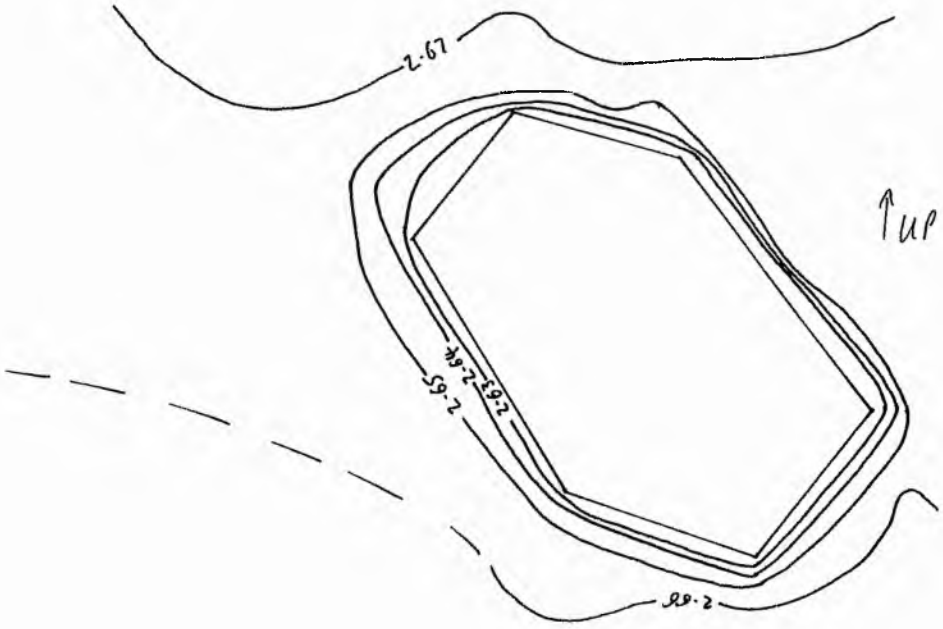

3.4 Olivine seeds suspended in clay crucibles

Details of experimental runs using this technique are summarized in table 3.01. On inspection of thin sections of these charges (plates 3.02 to 3.09) it is obvious that the clay has dissolved into the melt, contaminating the system and producing a pale melt beside the walls of the crucible. Melt with a similar colour is also seen at the meniscus and has probably convected to this position due to a density difference with the bulk melt. Dissolution of crucibles has, in several runs, caused the handles to detach from the inner-crucible walls so the crystal seed has not remained *in situ* during the run, making this technique unsuitable for experiments longer than 1-2 hours.

From the features present in thin section the following processes can be inferred to have occurred in the charges:-

1) Melt at the crucible walls is pale blue in colour, due to dissolution of clay. This pale melt is also seen at the meniscus, having risen buoyantly in a layer up the side walls and as buoyant plumes from the crucible floor.

2) Skeletal olivine crystallites, which have nucleated throughout the melt, display parallel alignment (see to plates 3.02 to 3.09). This is suggested to be caused by the currents in the crucibles. The most obvious causes of such currents are bubble ascent and compositional-driven convection of the buoyant side-wall melt.

To quantify the compositional changes in the clay-contaminated melt, C-O 13 (figure 3.06) was examined. A visual indicator of compositional variation is visible in the glass where the melt is paler and the concentration of Co^{2+} is reduced. Probe data in table 3.04 and maps in figure 3.06 show the pale glass to contain a difference of >2 wt % less CoO and of >3 wt % more SiO_2 than in the uncontaminated glass.

Plate 3.04 and the maps in figure 3.06 reveal the following points, as surmized in figure 3.07:-

1) Clay-crucible dissolution enriches the melt at the wall in SiO_2 and Al_2O_3, reducing melt density.
2) Dissolution was faster where there were air bubbles adjacent to the side wall.
3) A thicker layer of pale Co-depleted glass exists at the meniscus than at the crucible floor. This suggests that the melt rose buoyantly in the crucible and ponded beneath the meniscus. This layer of pale melt thickens with time (compare plates 3.06 and 3.07).
4) Convection takes place readily in this low-viscosity melt. After only 5 minutes, there is evidence that melt ascended along the walls (see plates 3.02-3.09).

5) Erosion of the crucible wall is accelerated at the wall-meniscus-air contact. This is analogous to flux-line attack - the process which accelerates erosion of refractory bricks in the manufacture of glass and steel by producing locally variable redox conditions (Towers and Chipman, 1957).

6) The distribution of olivine and plagioclase crystallites in runs at 1195°C varies with time. Plagioclase crystallites are only visible in the lowest temperature runs (<1200°C) close to crucible walls, while olivine crystallites are seen in all experiments. Olivine crystallites are observed below an upper limit in the charge. This upper limit is lower in longer duration experiments (compare plates 3.06 and 3.07). The level of this upper limit could be due to:-

a) Crystallites sink through the charge due to their density difference with the melt.

b) As buoyant melt rises up the crucible walls and ponds beneath the meniscus, a counter-current is produced which pushes the melt in the centre of the crucible downwards.

c) Crystallites are not stable in the SiO_2- and Al_2O_3-enriched melt and re-dissolve in CoO-poor melt. As the thickness of pale blue glass beneath the meniscus increases so too does the thickness of melt in which crystallites are not found.

d) A combination of the above processes.

Over the relatively short times of the experiments complete dissolution of crystallites in the buoyant melt would not be expected, without production of resorption textures- these are not seen. A combination of processes a and b is therefore preferred to explain the crystallite distribution pattern. The crystallite distribution variation with timeis best seen in the runs at 1195°C, as these were at a low-enough temperature for crystallites to nucleate, but this temperature is also high enough for rapid wall-dissolution. At lower temperatures wall dissolution is too slow to have a noticeable effect on crystallite distribution with time (see plate 3.08), while at higher temperatures the abundance of crystallites is much smaller and so the line marking the upper crystallite limit is not as clear.

7) This set of experiments shows that temperatures of roughly 1230°C are needed if excessive crystallite nucleation is to be avoided. Such experiments are not possible in these charges because dissolution of the crucible is fast and so a closed system is not maintained in the crucibles.

8) Crucible dissolution shows the following characteristics:-

a) Two discrete boundary layers exist close to the crucible walls; a very thin, pale layer close to the crystal-liquid interface, and a wider, slightly darker layer further from the wall than the first layer. The second layer often contains vesicles that have attached preferentially to the crucible wall.

b) The boundary layer bulges around the vesicles. The surface tension difference where the vesicles touch the side-wall may cause the most SiO_2-enriched part of the boundary layer to be dragged away from the side-wall, encouraging accelerated dissolution.

c) Where boundary layers bulge around bubbles on the crucible floor, the bulges may build up to such a thickness that they become buoyantly unstable and can detach and rise as plumes from the crucible floor.

d) Feldspar crystallites nucleate within the side-wall boundary layer, indicating that the composition of the melt here has altered sufficiently to change the phase relations of the melt.

9) There is no optically-visible evidence that CoO-depleted boundary layers were produced next to the crystal seeds on which Co-Mg olivine has overgrown. EPMA reveals a region of slight CoO- and MgO-depleted melt around the crystal seed in C-O 13, however analyses are not closely-enough spaced to explore this further here.

Plate 3.04. Thin section of charge CO 13 (1210°C 10 hours) showing crystallite concentration in the bottom third of the crucible and pale melt near the side walls and in the top right corner.

Plate 3.05. Thin section of charge CO 14 (1205°C 5 hours)

Plate 3.06. Thin section of charge CO 15 (1195°C 4 hours). Note alignment of elongate olivine crystallites above the olivine seed and at top right. This could be caused by convection within the charge.

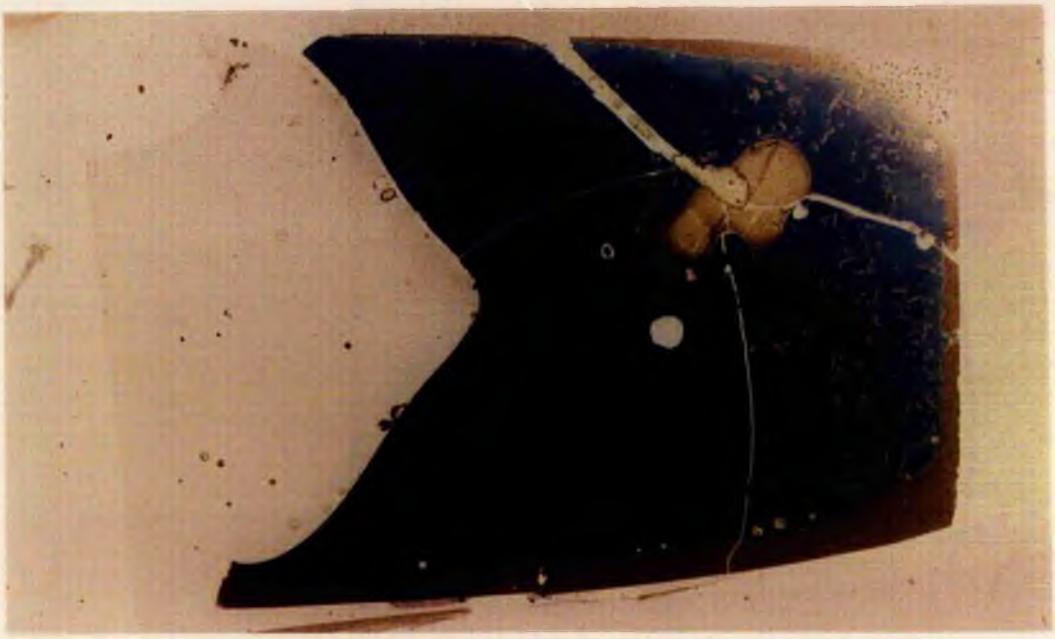

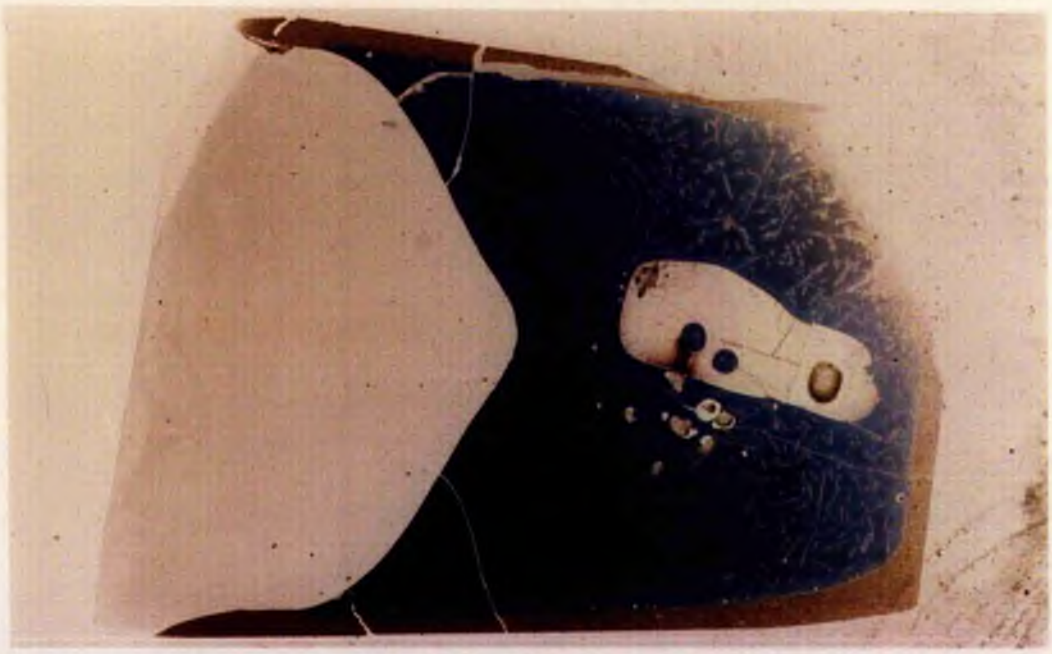

Plate 3.07. Thin section of charge CO 17 (1195°C 24 hours). Note the alignment of crystallites on the left of the seed, the discrete layer of pale-blue melt at the meniscus, and the two densities of pale blue colour in the side wall boundary layer zone.

Plate 3.08. Thin section of charge CO 18 (1190°C 22 hours), showing the appearance of plagioclase crystallites close to the pale side wall melt in this lower temperature experiment.

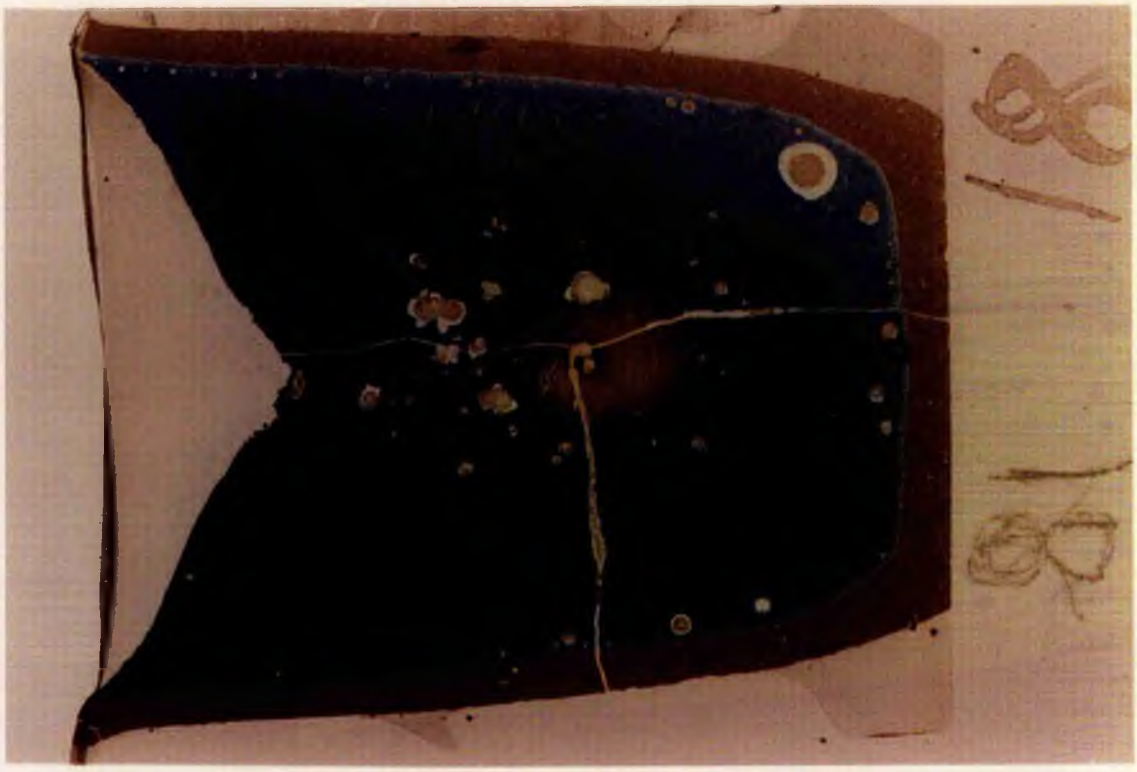

Table 3.04. Analytical data from CO 13

X (mm)	Y (mm)	Analysis	SiO2	TiO2	Al2O3	FeO	MnO	CoO	MgO	CaO	Na2O	K2O	Total
4.95	20.95	1	51.5	2.6	15.0	0.4	0.0	7.9	6.3	9.5	0.5	0.7	94.2
4.97	20.95	2	51.4	2.8	15.2	0.4	0.0	7.7	5.8	9.6	0.5	0.7	94.1
5.32	19.69	3	55.0	2.5	15.5	0.5	0.0	7.1	5.4	9.8	0.6	0.9	97.3
4.97	19.69	4	54.1	2.7	15.8	0.5	0.0	6.6	5.9	9.9	0.5	0.8	97.0
5.04	20.27	5	54.3	2.6	15.8	0.5	0.0	6.1	5.6	9.8	0.5	1.0	96.3
4.91	20.96	6	51.7	2.5	14.9	0.4	0.0	7.7	6.0	9.4	0.4	0.7	93.7
13.01	13.95	7	51.7	2.9	14.8	0.1	0.0	9.1	7.0	11.1	0.6	0.6	97.9
13.07	13.33	8	51.4	2.9	14.6	0.3	0.0	9.6	7.4	12.2	0.5	0.5	99.3
13.07	12.82	9	50.2	3.2	14.5	0.2	0.0	10.3	7.5	12.4	0.6	0.4	99.3
13.02	12.31	10	50.2	3.1	14.4	0.2	0.0	10.8	7.6	12.4	0.5	0.4	99.7
13.00	11.81	11	49.7	3.4	14.2	0.2	0.1	10.3	7.3	12.6	0.5	0.4	98.7
13.04	11.02	12	49.7	3.4	14.3	0.1	0.0	10.4	7.2	12.8	0.4	0.4	98.9
13.03	10.53	13	49.1	3.5	14.3	0.0	0.0	10.7	7.5	13.1	0.6	0.4	99.2
13.00	10.05	14	48.8	3.3	14.0	0.1	0.0	10.0	7.4	13.2	0.5	0.3	97.6
12.99	9.51	15	49.2	3.5	14.2	0.0	0.1	9.9	7.2	13.4	0.6	0.4	98.3
12.99	9.00	16	49.2	3.7	14.4	0.1	0.1	10.3	7.3	13.5	0.6	0.3	99.5
12.96	8.14	17	49.4	3.5	14.4	0.1	0.0	10.4	7.2	13.8	0.6	0.3	99.8
12.93	7.50	18	49.9	3.5	14.2	0.0	0.0	10.0	7.4	14.0	0.6	0.3	99.9
12.86	7.03	19	49.3	3.7	14.3	0.0	0.0	10.3	7.2	13.8	0.6	0.3	99.5
12.84	6.28	20	49.1	3.7	14.1	0.0	0.0	10.0	7.1	13.8	0.6	0.3	98.8
12.86	5.90	21	49.1	3.3	14.1	0.1	0.0	9.4	7.2	14.0	0.5	0.3	98.1
12.85	5.39	22	49.1	3.6	13.7	0.0	0.0	9.7	7.0	13.3	0.6	0.3	97.4
12.86	4.92	23	49.3	3.6	14.2	0.0	0.0	10.3	7.0	13.6	0.6	0.3	99.0
12.84	4.43	24	49.5	3.5	14.4	0.1	0.0	10.4	7.0	13.7	0.6	0.3	99.6
12.84	3.91	25	49.4	3.7	14.4	0.1	0.0	10.2	7.0	13.6	0.5	0.3	99.2
12.83	3.40	26	49.7	3.6	14.4	0.1	0.1	10.2	7.0	13.6	0.5	0.4	99.5
12.85	2.90	27	49.3	3.5	14.3	0.2	0.1	9.9	7.0	13.6	0.5	0.3	98.8
12.78	2.35	28	49.7	3.5	14.6	0.1	0.0	10.0	7.1	12.9	0.5	0.3	98.7
12.65	1.76	29	49.2	3.6	14.4	0.1	0.0	9.3	7.1	12.8	0.4	0.4	97.4
12.61	1.02	30	49.6	3.8	14.6	0.1	0.1	9.3	7.0	12.5	0.3	0.4	97.7
12.64	0.62	31	47.3	2.7	13.6	0.6	0.0	8.4	5.1	10.0	0.5	0.8	88.9
21.05	14.01	32	55.8	2.9	16.2	0.6	0.0	6.8	5.2	9.7	0.6	1.0	98.9
20.00	14.01	33	50.8	3.2	14.5	0.3	0.0	9.3	7.1	11.8	0.4	0.5	97.8
19.01	14.01	34	51.0	3.3	14.6	0.3	0.0	9.9	7.3	11.7	0.4	0.5	98.9
18.02	14.04	35	50.3	3.4	14.3	0.3	0.0	10.3	7.3	11.9	0.5	0.5	98.8
17.00	14.04	36	50.7	3.1	14.7	0.3	0.1	9.8	7.4	11.7	0.4	0.5	98.5
15.98	14.04	37	49.7	3.1	14.6	0.2	0.0	9.9	7.3	11.5	0.5	0.4	97.3
14.97	14.06	38	51.2	2.9	14.7	0.3	0.0	8.7	6.7	11.6	0.6	0.6	97.2
14.00	14.06	39	51.9	3.0	15.0	0.2	0.0	9.0	6.8	11.2	0.6	0.7	98.2
21.02	15.02	40	55.2	2.7	15.8	0.6	0.0	6.8	5.4	9.7	0.6	1.0	97.8
19.99	15.02	41	50.7	3.1	14.9	0.2	0.0	9.4	7.1	11.4	0.5	0.6	97.8
19.01	16.02	42	52.9	2.8	15.2	0.3	0.0	9.1	6.7	11.3	0.5	0.7	99.6
18.02	16.02	43	53.0	3.0	15.3	0.4	0.0	8.5	6.5	11.1	0.6	0.7	99.2
17.00	16.02	44	53.7	2.9	15.4	0.3	0.0	7.9	6.3	10.6	0.7	0.8	98.6
16.07	16.02	45	53.0	2.5	15.1	0.4	0.0	8.7	6.6	11.0	0.6	0.8	98.7
8.35	17.11	46	53.2	2.7	15.7	0.5	0.0	8.0	6.1	10.0	0.6	0.8	97.8
8.35	16.13	47	53.4	2.8	15.3	0.4	0.0	8.2	6.5	10.5	0.6	0.7	98.5
8.35	16.11	48	51.5	3.0	14.7	0.2	0.0	9.8	6.7	11.7	0.5	0.6	98.7
8.35	14.12	49	50.9	3.2	14.4	0.3	0.0	10.2	7.4	11.7	0.5	0.5	99.1
8.33	13.10	50	50.0	3.2	14.4	0.2	0.0	9.4	7.3	12.2	0.5	0.4	97.6
8.31	12.11	51	47.8	3.2	13.5	0.1	0.1	10.0	6.7	12.0	0.4	0.4	94.3
8.30	11.09	52	49.6	3.2	14.4	0.2	0.1	10.0	7.3	12.6	0.5	0.4	98.2
8.30	10.14	53	49.1	3.3	14.0	0.1	0.1	10.4	7.5	12.7	0.5	0.4	98.1
8.28	9.11	54	49.4	3.4	14.3	0.1	0.1	10.1	7.4	13.0	0.5	0.4	98.7

X (mm)	Y (mm)	Analysis	SiO2	TiO2	Al2O3	FeO	MnO	CoO	MgO	CaO	Na2O	K2O	Total
8.23	8.10	55	47.4	3.4	13.7	0.1	0.1	10.5	7.3	12.7	0.5	0.3	95.9
8.21	7.14	56	49.3	3.4	14.1	0.0	0.1	10.1	7.3	12.9	0.5	0.3	98.1
8.19	6.17	57	48.2	3.4	13.9	0.1	0.0	10.4	7.1	12.9	0.5	0.4	97.1
8.16	5.08	58	49.0	3.5	14.4	0.1	0.1	10.3	6.9	13.3	0.4	0.4	98.3
8.16	4.08	59	48.6	3.6	14.3	0.1	0.1	10.4	7.2	13.4	0.5	0.4	98.5
8.15	3.10	60	48.7	3.6	14.2	0.1	0.0	9.9	6.6	13.1	0.4	0.3	96.9
8.08	2.11	61	53.8	3.3	16.2	0.2	0.0	9.4	7.4	12.2	0.6	0.5	103.6
8.06	1.19	62	51.8	2.6	15.5	0.5	0.0	7.9	6.2	9.8	0.6	0.8	95.7
6.45	5.25	63	53.3	2.4	15.4	0.3	0.1	7.7	6.0	10.4	0.6	0.9	97.1
6.51	5.23	64	53.6	2.6	15.3	0.4	0.0	8.0	6.0	10.8	0.5	0.9	98.1
6.60	5.25	65	53.4	2.5	15.4	0.4	0.0	8.0	6.0	11.0	0.6	0.9	98.1
6.97	5.24	66	49.0	3.4	14.4	0.1	0.0	10.2	7.2	13.2	0.4	0.3	98.1
6.98	5.65	67	49.0	3.6	14.3	0.1	0.0	9.5	7.2	12.9	0.5	0.4	97.5
6.50	5.64	68	53.4	2.7	15.6	0.4	0.0	8.3	6.1	11.0	0.5	0.8	98.8
6.04	5.63	69	51.6	3.1	15.3	0.5	0.1	7.9	6.3	10.1	0.5	0.7	96.1
7.18	18.07	70	52.5	2.6	15.1	0.4	0.0	7.3	5.9	9.9	0.5	0.8	95.0
6.13	18.09	71	52.5	2.9	14.8	0.4	0.0	9.0	6.8	10.4	0.4	0.7	97.9
5.12	18.11	72	52.1	3.0	15.2	0.4	0.0	8.7	6.3	10.5	0.5	0.6	97.3
4.89	18.11	73	55.5	2.6	16.0	0.7	0.0	6.9	5.4	8.9	0.7	1.0	97.5
14.09	10.04	74	49.0	3.1	14.1	0.1	0.0	10.3	7.2	13.0	0.5	0.3	97.6
15.12	10.04	75	49.8	3.2	14.4	0.1	0.0	10.3	7.5	13.0	0.5	0.4	99.1
16.13	10.05	76	49.4	3.5	14.1	0.1	0.1	11.0	7.7	13.1	0.6	0.3	99.9
17.11	10.05	77	49.2	3.4	13.9	0.1	0.0	10.5	7.5	12.9	0.4	0.4	98.4
18.12	10.04	78	49.8	3.5	14.4	0.1	0.0	10.4	7.5	12.8	0.5	0.4	99.5
18.72	10.04	79	49.0	3.3	13.9	0.1	0.0	10.6	7.5	12.9	0.5	0.4	98.2
19.52	10.04	80	49.6	3.3	14.4	0.1	0.1	10.7	7.3	12.5	0.5	0.4	98.8
20.13	10.04	81	51.2	3.4	14.6	0.2	0.0	10.0	6.9	12.4	0.5	0.5	99.5
13.01	9.02	82	49.4	3.6	14.3	0.1	0.0	10.4	7.1	13.7	0.6	0.3	99.5
14.02	9.02	83	49.6	3.2	14.4	0.1	0.1	10.3	6.9	13.6	0.5	0.3	99.1
15.00	9.03	84	49.2	3.3	14.4	0.2	0.0	10.2	7.3	13.6	0.6	0.3	99.0
16.03	8.98	85	49.3	3.4	14.2	0.1	0.0	10.3	7.1	13.3	0.6	0.4	98.7
17.07	8.97	86	49.6	3.6	14.3	0.0	0.0	10.1	7.2	13.5	0.5	0.3	99.2
16.55	8.97	87	49.5	3.5	14.1	0.1	0.0	10.4	7.6	13.1	0.5	0.4	99.2
19.52	8.96	88	49.3	3.4	14.4	0.1	0.0	10.0	7.2	12.7	0.4	0.3	97.8
20.48	8.99	89	53.6	2.8	15.4	0.3	0.0	8.4	6.3	11.7	0.5	0.7	99.7
20.72	8.98	90	55.3	2.6	15.8	0.5	0.0	7.1	5.4	10.2	0.6	1.0	98.3
14.00	12.01	91	50.7	3.4	14.4	0.1	0.0	10.6	7.5	12.4	0.5	0.4	99.9
15.01	12.01	92	50.2	3.4	14.4	0.2	0.0	10.3	7.5	12.3	0.4	0.4	99.2
15.96	12.01	93	50.6	3.3	14.4	0.2	0.0	9.8	7.3	11.7	0.6	0.4	98.5
17.01	12.01	94	48.9	3.2	14.3	0.1	0.0	9.9	7.4	12.3	0.5	0.4	97.2
18.01	11.99	95	50.3	3.3	14.3	0.2	0.0	10.5	7.4	12.4	0.5	0.5	99.4
19.01	11.98	96	50.9	3.3	14.6	0.2	0.0	10.2	7.3	12.5	0.4	0.4	99.8
20.02	11.98	97	50.7	3.7	14.6	0.2	0.0	10.4	7.6	12.2	0.5	0.4	100.3
20.67	12.00	98	52.3	3.0	15.0	0.4	0.0	7.6	6.4	10.6	0.6	0.6	96.4
17.33	6.87	99	49.4	3.7	14.2	0.1	0.0	9.9	7.1	13.2	0.5	0.3	98.4
18.31	6.85	100	49.4	3.6	14.4	0.1	0.0	10.4	7.3	13.4	0.5	0.3	99.5
19.30	6.86	101	49.3	3.5	14.0	0.1	0.0	9.5	7.3	13.2	0.4	0.4	97.7
20.31	6.86	102	53.0	3.3	15.8	0.5	0.0	8.2	6.1	10.9	0.5	0.8	99.1
15.01	8.68	103	48.9	3.8	14.9	0.2	0.0	9.3	5.8	14.3	0.7	0.4	98.2
15.18	8.71	104	36.7	0.1	0.0	0.0	0.0	30.2	32.4	0.4	0.0	0.0	99.8
11.09	3.32	105	36.6	0.1	0.0	0.0	0.0	30.3	32.6	0.3	0.0	0.0	99.9

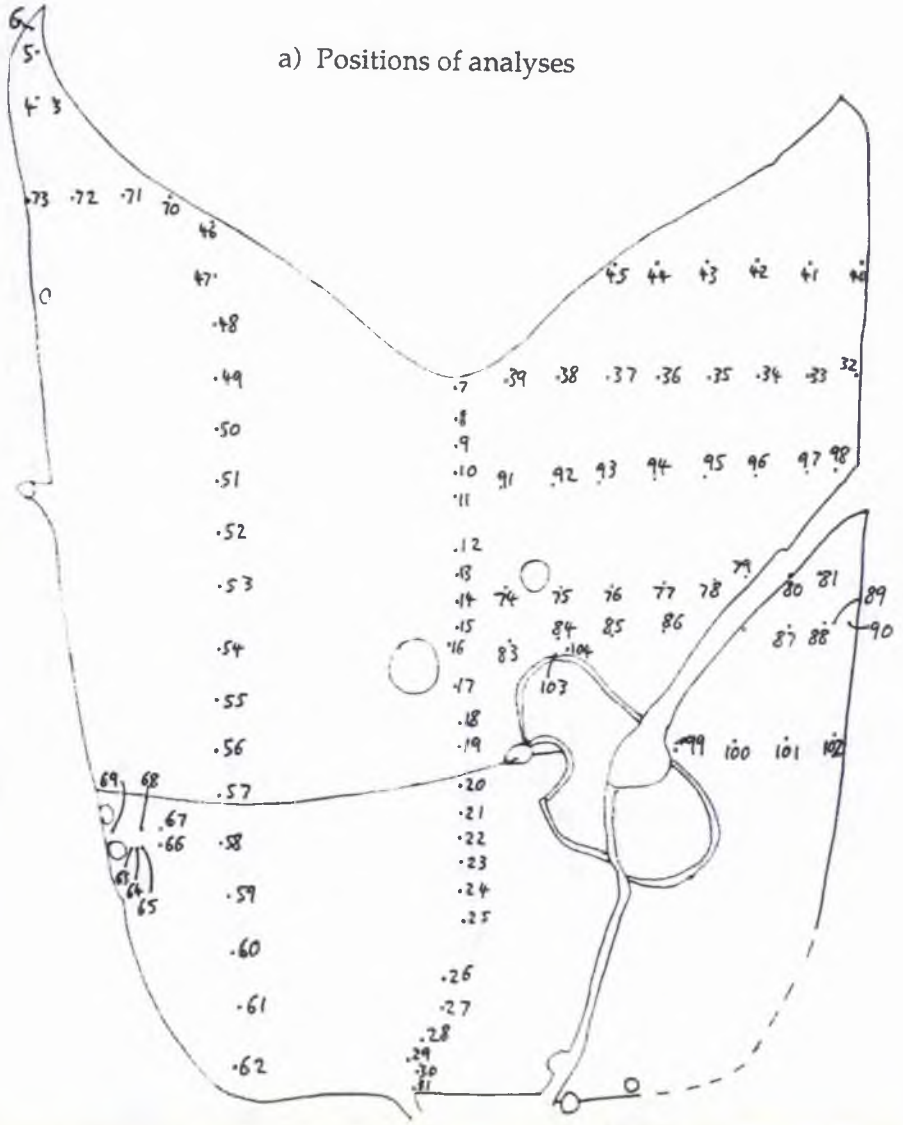

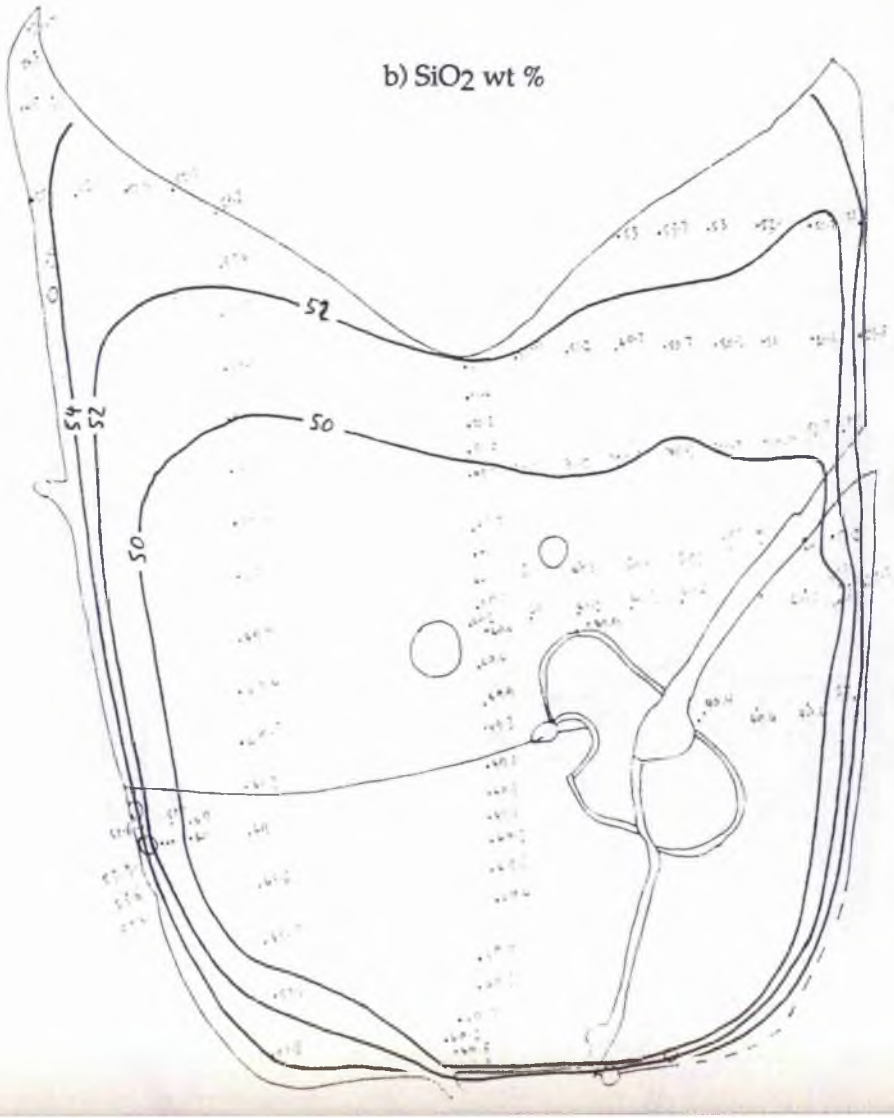

Figure 3.06. Oxide concentration maps of charge CO 13.

c) TiO_2 wt %

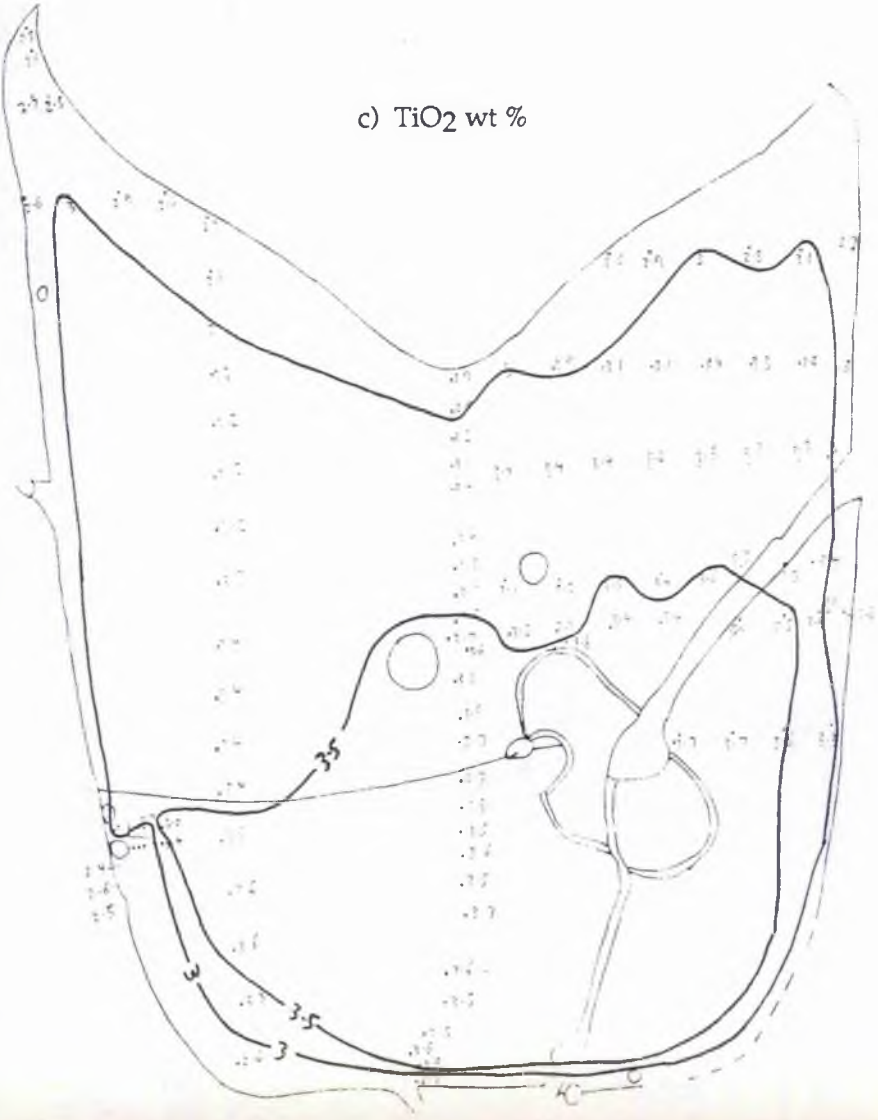

d) Al_2O_3 wt %

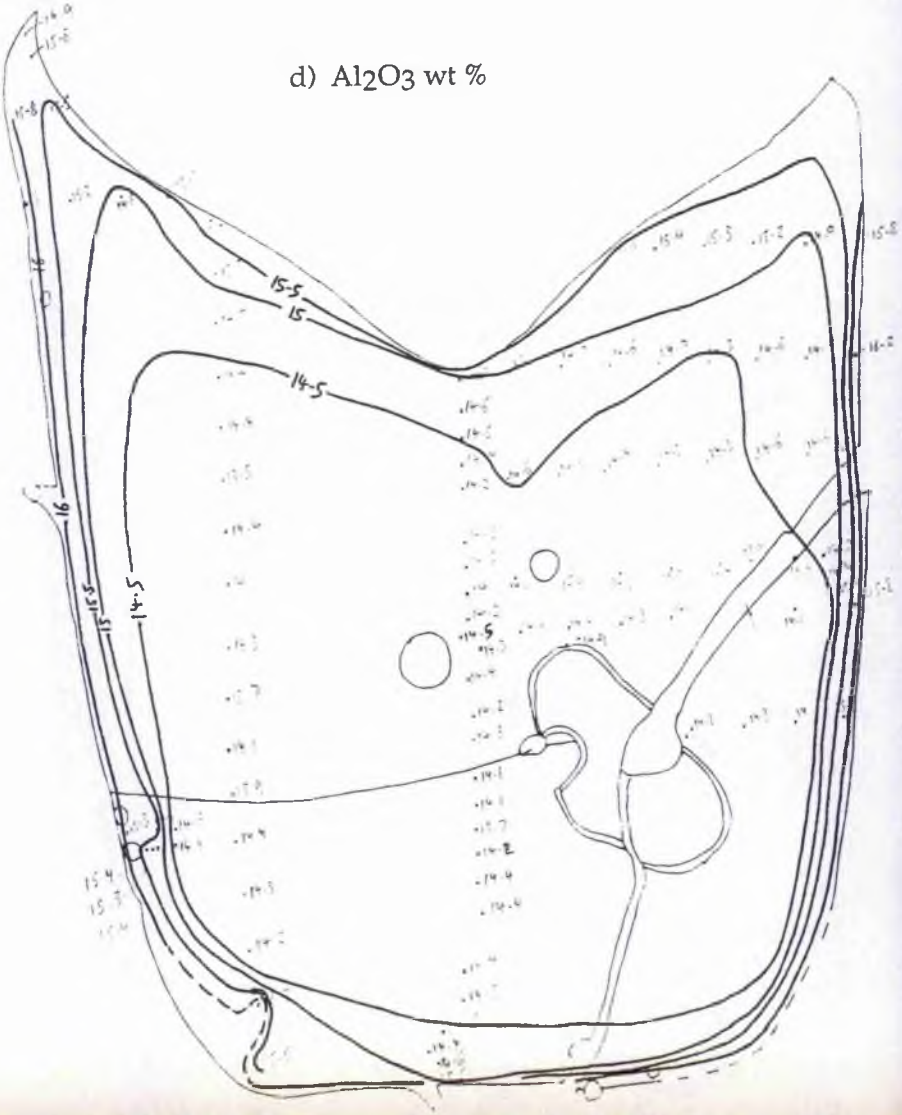

e) FeO wt %

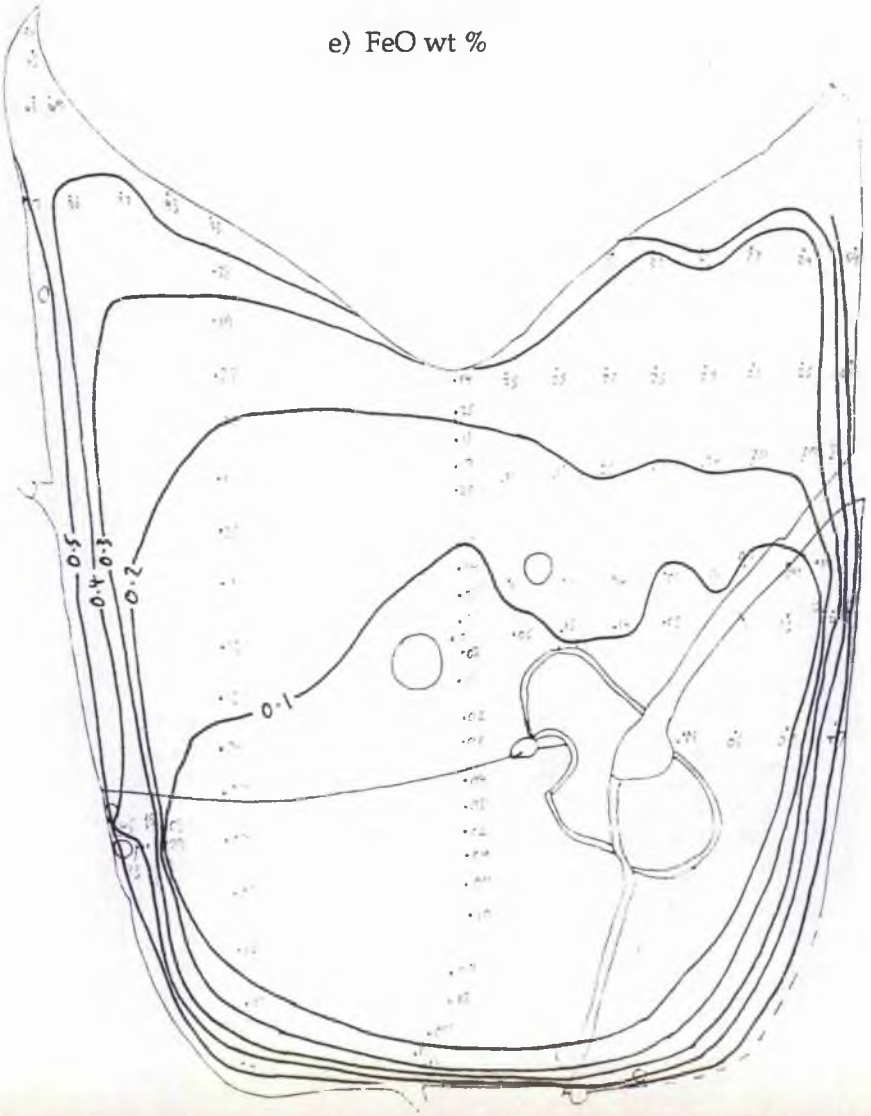

f) CoO wt %

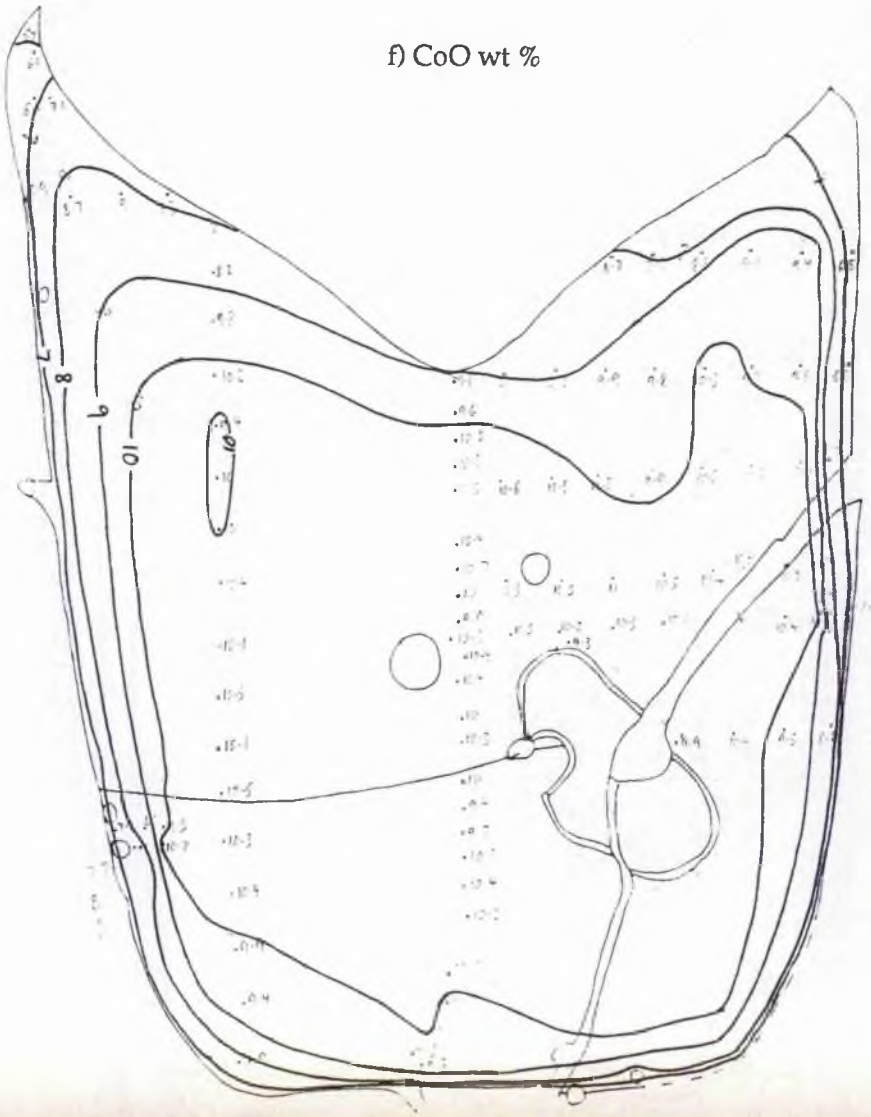

g) MgO wt %

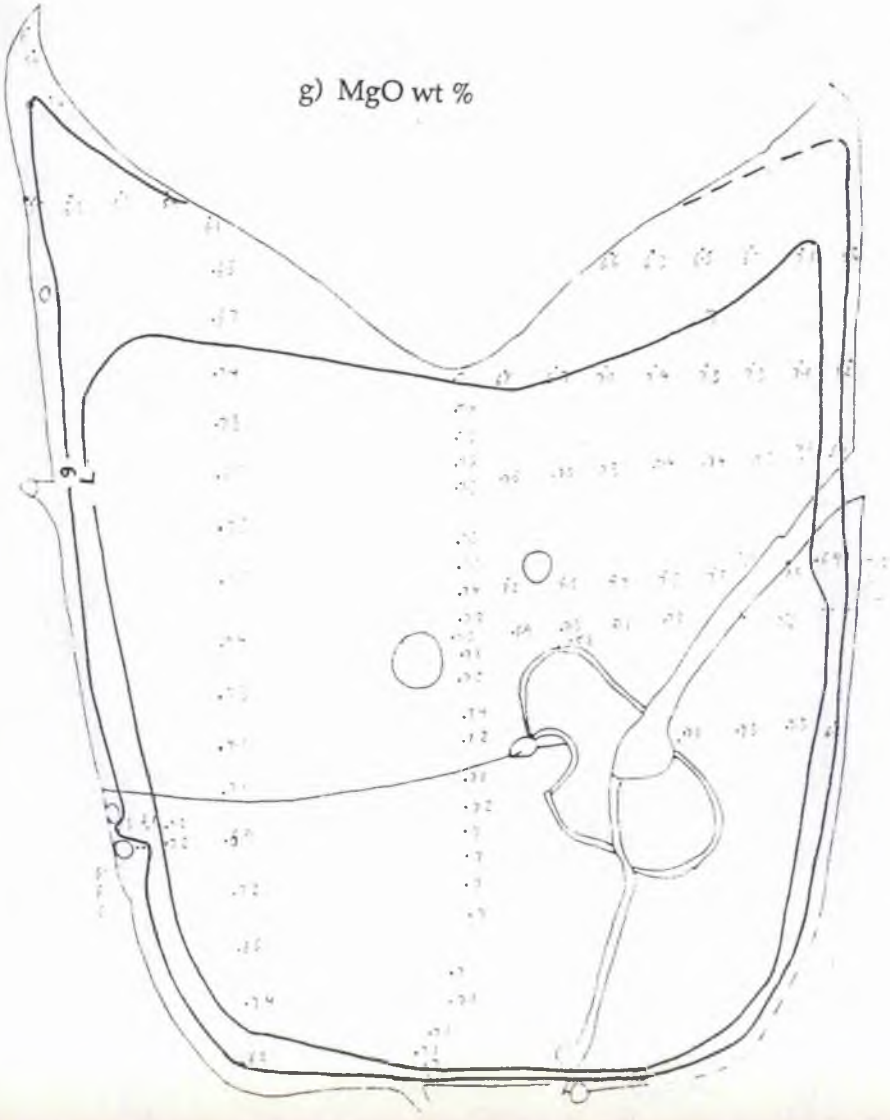

h) CaO wt %

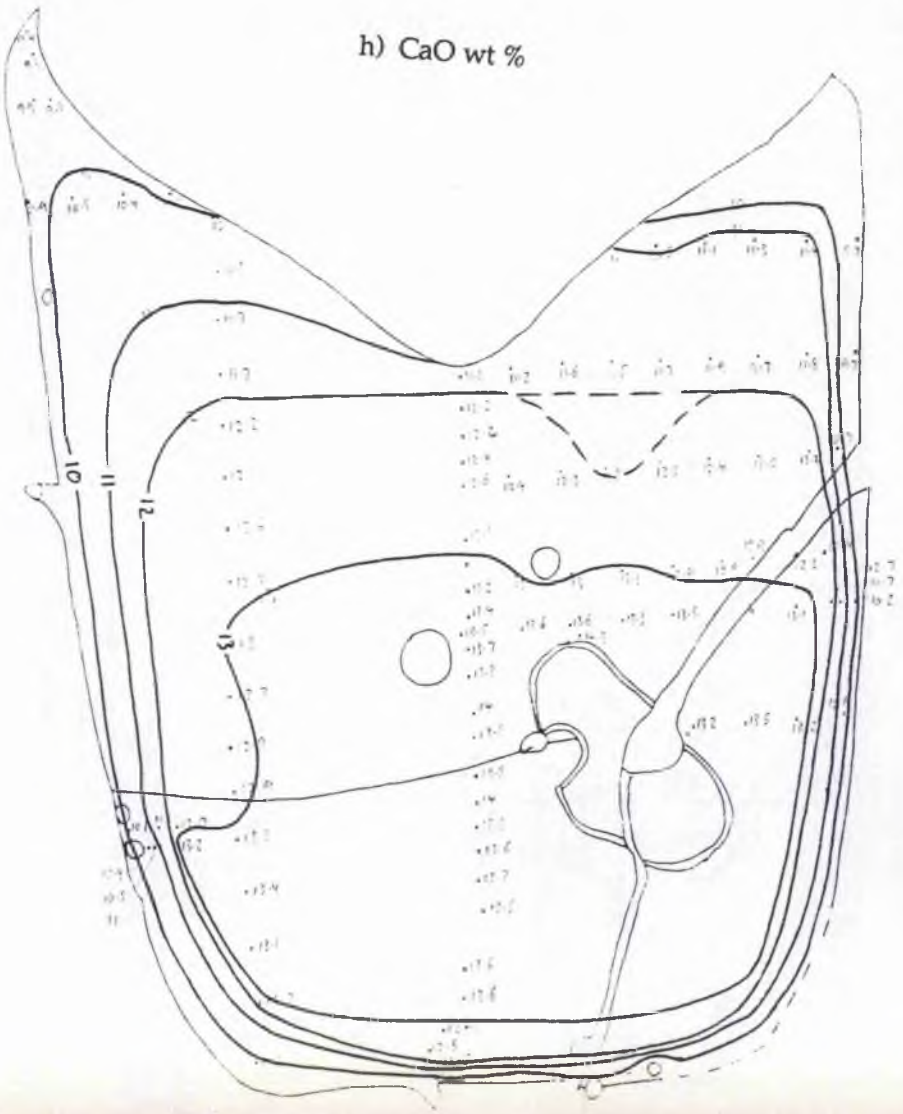

Figure 3.07. Sketch summarizing proposed convective processes in clay crucibles.

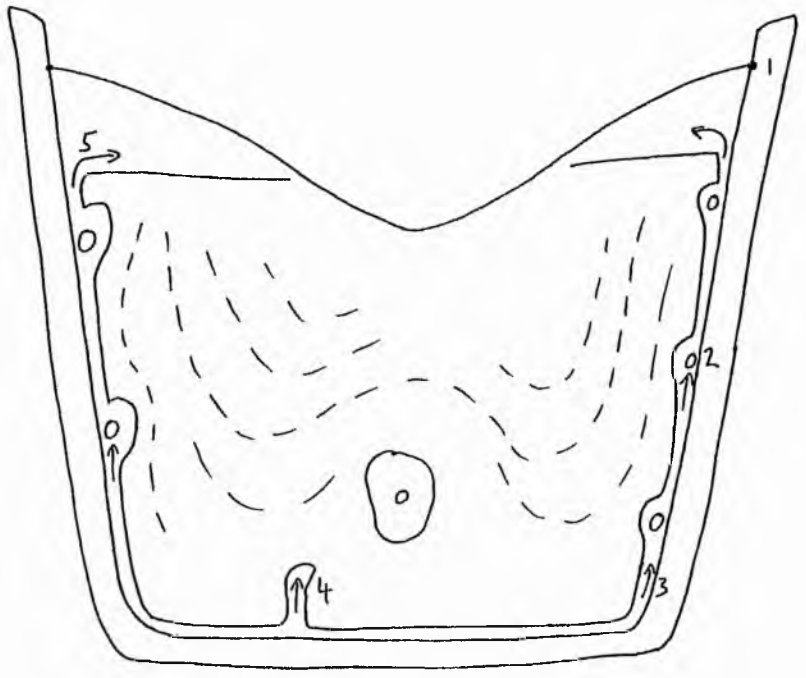

1) Flux line attack at the meniscus-wall contact.

2) Bubbles accelerate dissolution of crucible walls.

3) Convection of Si-enriched melt is inferred by arrows.

4) Buoyant plume of Si-enriched melt produced on crucible floor.

5) Si-enriched melt is produced by crucible dissolution. Its low density allows it to rise buoyantly and pond beneath the meniscus.

Dashes denote allignment of olivine crystallites due to convective flow of melt in the charge.

3.5 Crushed olivine seeds on the crucible floor

3.5.1 Introduction

This section deals with analysis of several experiments using loose olivine chips in alumina crucibles. It had been hoped that the olivine would remain on the crucible floor as they are denser than the melt, but this did not occur, rendering this technique unsatisfactory.

3.5.2 Observations

Plates 3.10 to 3.15 show thin sections of runs made with loose olivine chips in alumina crucibles. Post-experiment, none of the chips lies on the crucible floors in the quenched charges, indeed there is no way of telling whether or not their final positions were maintained throughout the run. Even in the longest run of 416 hours (C-O 25) some air bubbles remain in the melt, their movement may well have caused crystals to move.

In plate 3.16 tiny, euhedral crystals of hercynite can be seen coating the crucible. Although there is no visible sign of alumina dissolution (i.e. no pale blue glass near the wall), EPMA of glass close to crucible walls indicates alumina enrichment in this melt (see figures 3.10 and 3.11). This Al_2O_3 has only one possible source, from dissolution of the crucible wall. Therefore it is suggested that Al concentration in the melt rose to allow hercynite saturation with crystals nucleating heterogeneously on the crucible wall. The growth and influence on melt composition of side-wall crystals is discussed further in chapter 4, but the development of Al-rich melt may effect the melt composition at the meniscus if it can convect up the walls.

3.5.3 Analysis of experiments

The maps in figures 3.08 and 3.09 show the distribution of points analysed in charges C-O 20 and C-O 25, respectively. These data are presented in table 3.05a and b and have been used to construct the chemical variation maps in figure 3.10 and 3.11). The following observations are made from examination of these data:-

C-O 20 (116 hours at 1210°C)

- Na_2O, K_2O, TiO_2 and CaO show no systematic variation through the crucibles.
- Al_2O_3 and SiO_2 are slightly enriched in glass at the meniscus and in close proximity to the crystal seeds. SiO_2 is most enriched near crystal-liquid interfaces.
- MgO and CoO show slight depletion in the lower half of the crucible. This is most pronounced close to olivine seeds.
- Apart from Al2O3-enrichment close to crucible walls, and slight CoO and MgO depletion close to olivine, there is no systematic compositional change in this charge.

C-O 25 (416 hours at 1200°C)

- This lacks any pattern of compositional variation.
- Crystallites are again limited to the lower parts of the crucible.

3.5.4 Summary

If crystal growth in these charges produced buoyant, CoO- and MgO-depleted melt, then one would expect such melt to have accumulated at the top of the charge, beneath the meniscus. It would be expected that such an accumulation would remain discrete from the rest of the melt and be detectable using EPMA. This is not the case. Therefore, either compositionally discrete boundary layer melt has not been produced around the seed crystals, or chemical diffusion has homogenized the melt. The production of Al2O3-rich melt by hercynite crystallization on crucible walls is expected to produce a buoyant melt that should pond at the meniscus. Due to the lack of analyses in the glass near the meniscus, such melt has not been detected here. Side-wall hercynite crystallization and production of Al-rich melt is discussed later in this chapter and in chapter 4.

Plate 3.10. Thin section of charge CO 19 (1210°C 65 hours) showing how loose olivine seeds do not remain on the crucible floor during experiments. They are possibly lifted with the aid of air bubbles.

Plate 3.11. Thin section of charge CO 20 (1210°C 116 hours), again showing the failure of the loose olivine chip technique, with crystals floating in the melt.

Plate3.12. Thin section of charge CO 21 (1200°C 209 hours). Note visible hercynite rim between crucible and glass, crystals nucleating at the meniscus, and the line above which no crystallites appear in this long duration run.

Plate 3.13. Thin section of charge CO25 (1200°C 416 hours). Gas bubbles still persist in this long duration run. They have possibly aided olivine chips in floating in the melt as they remain above the crucible floor.

Plate 3.14. Charge CO 27 (1210°C 119 hours). Many gas bubbles remain in the very porous crystal-liquid mush in the bottom half of this crucible.

Plate 3.15. Charge CO 33 (1230°C 71 hours). An attempt to produce a crystal-liquid mush on the crucible floor by cementing a layer of olivine chips in alumina cement has failed as olivine seeds have become untethered from the crucible floor.

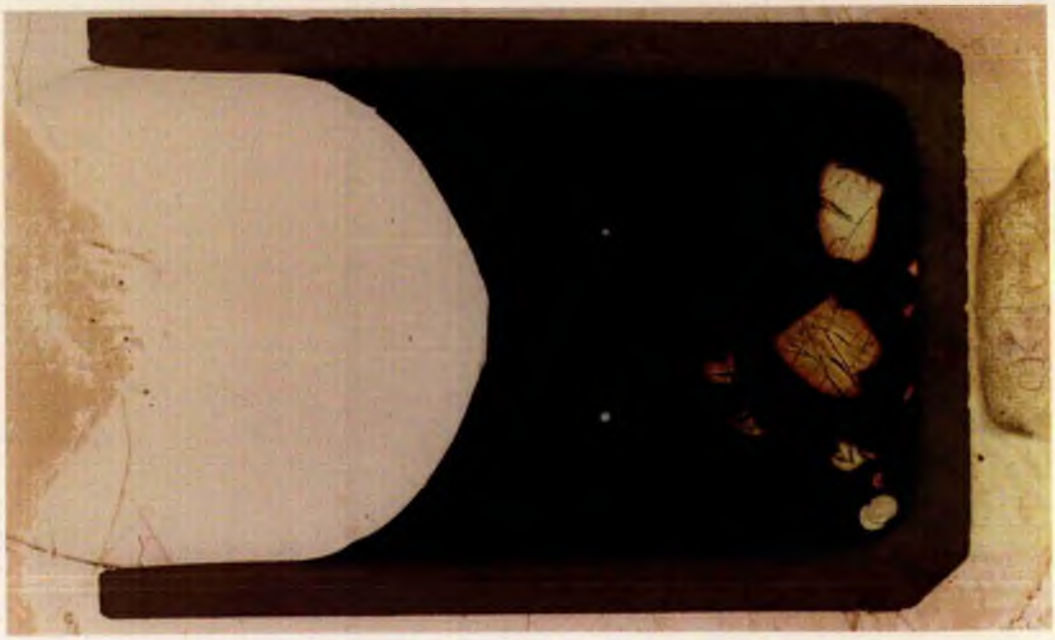

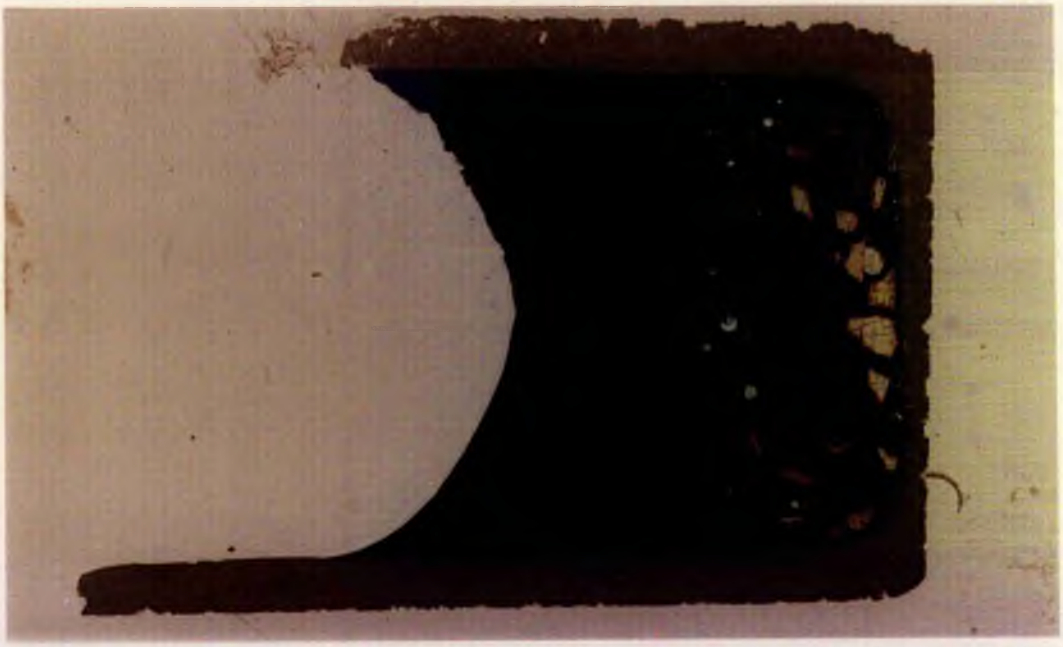

Plate 3.16. PPL photomicrographs showing
a) Layer of elongate hercynite crystals at the crucible-glass interface (magnification x 40).

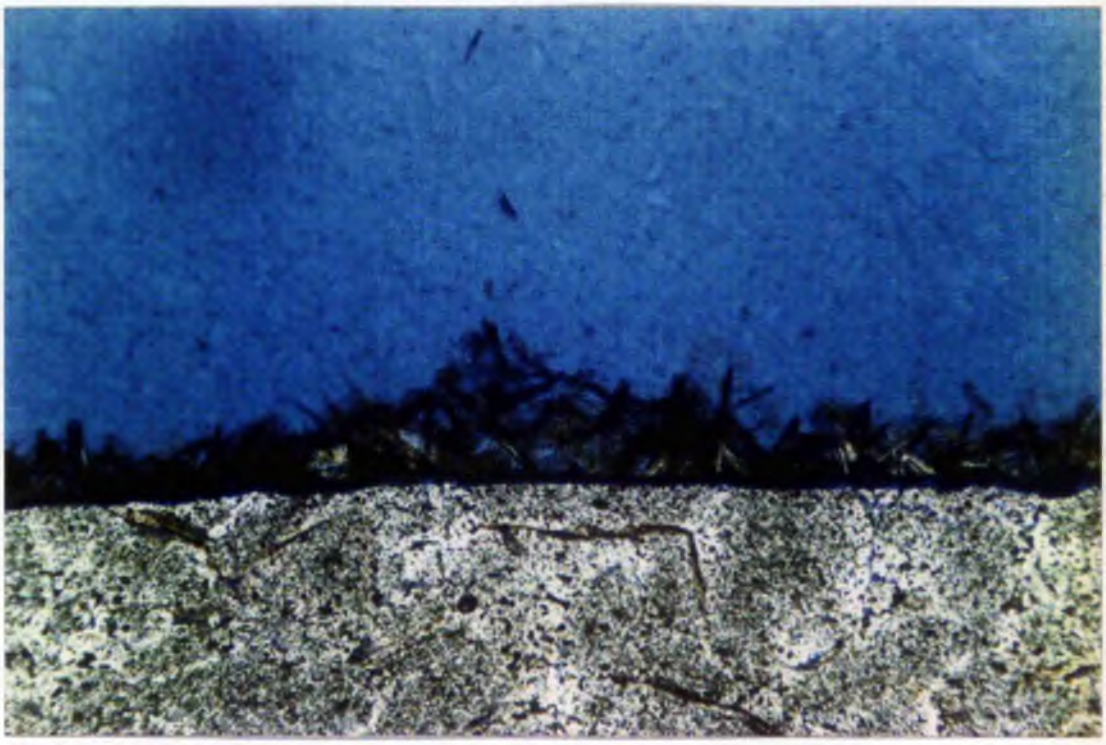

b) Layer of hercynite crystals that has grown between the alumina cement (left) and the blue glass. Some crystals appear to have broken away from the overgrowth layer, possibly due to convection currents (magnification x 40).

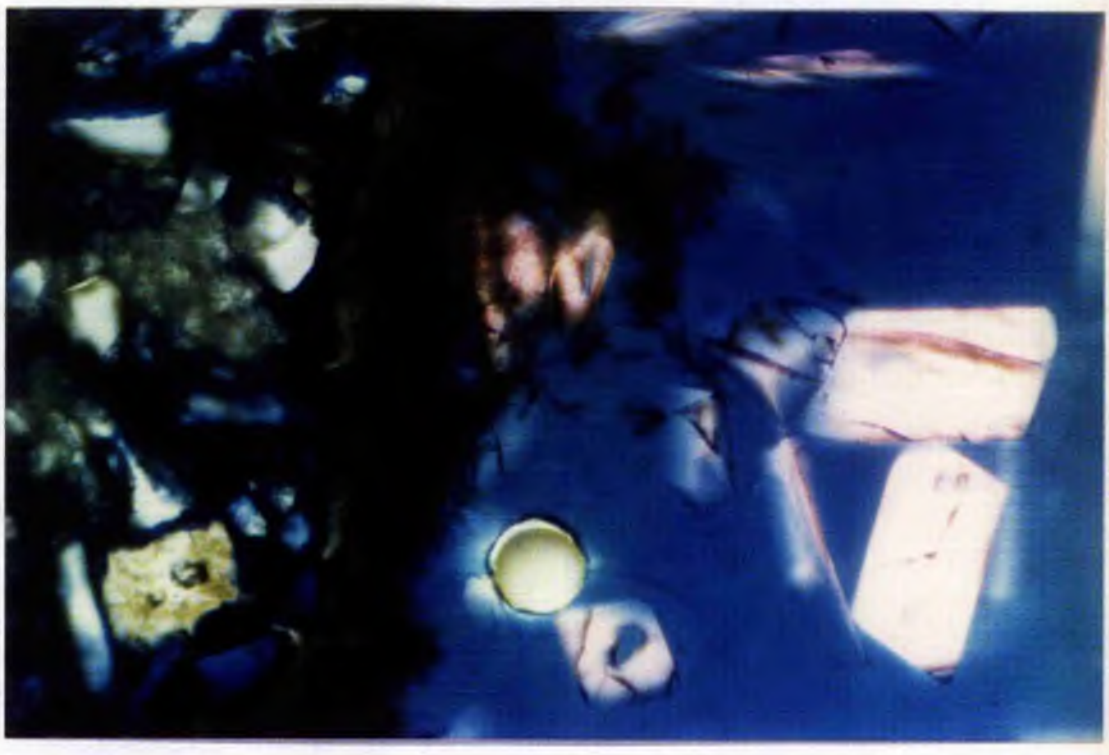

Figure 3.08. Map of points analysed in charge CO 20.

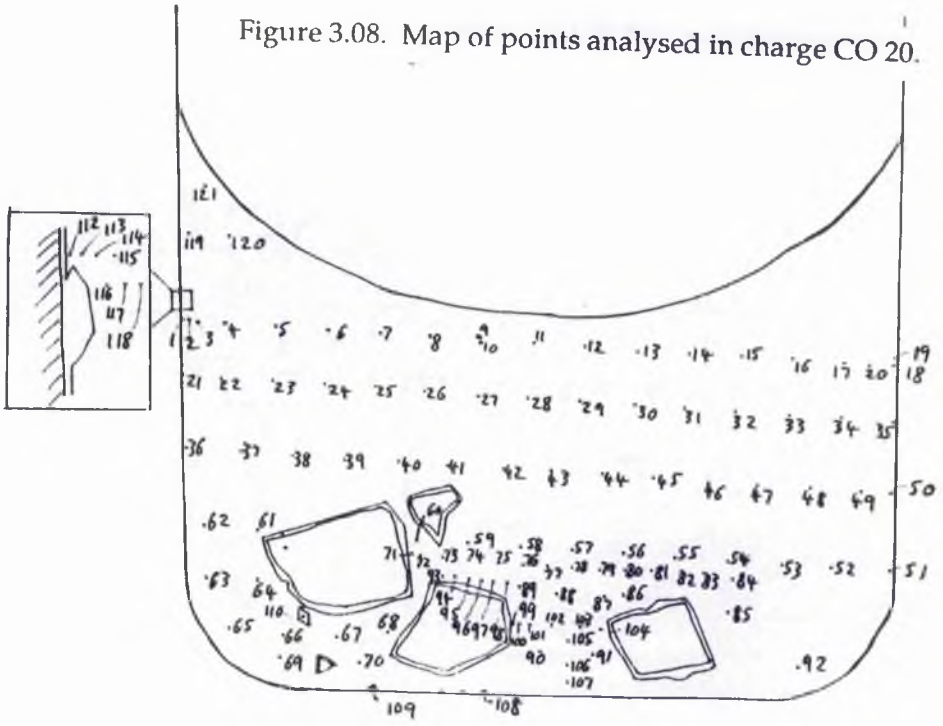

Figure 3.09. Map of points analysed in charge CO 25.

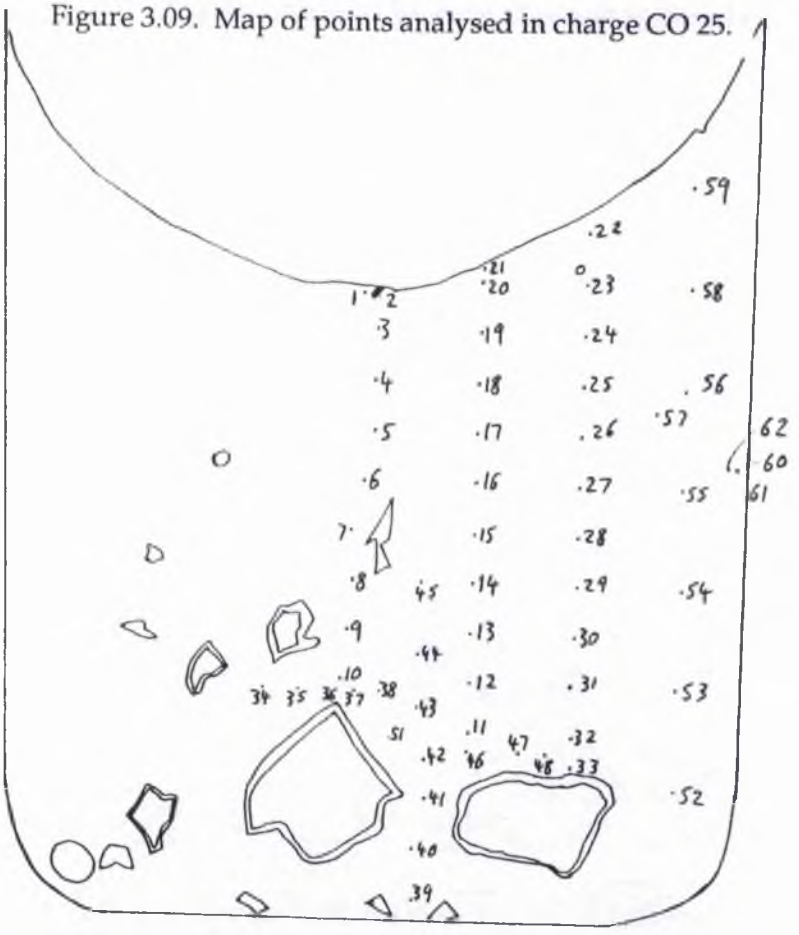

Table 3.05a. Analytical data from CO 20.

Analysis	X (mm)	Y (mm)	SiO2	TiO2	Al2O3	CoO	MgO	CaO	Na2O	K2O	Total
1	6.1	9.5	49.2	3.4	13.9	10.2	7.0	12.6	0.3	0.2	96.9
2	6.3	9.5	49.7	3.5	13.6	9.5	7.0	12.9	0.3	0.2	96.7
3	6.5	9.5	50.2	3.5	14.1	10.2	7.1	12.7	0.2	0.2	98.1
4	7.0	9.5	49.9	3.4	14.2	10.1	7.1	12.8	0.3	0.2	98.0
5	8.0	9.5	49.6	3.5	14.0	10.4	7.2	12.9	0.2	0.2	97.9
6	9.0	9.5	49.5	3.5	13.8	9.9	7.0	12.5	0.2	0.2	96.7
7	10.0	9.5	49.6	3.5	13.9	9.9	7.1	12.4	0.4	0.3	96.9
8	11.0	9.5	49.8	3.3	14.0	10.4	7.1	12.6	0.2	0.2	97.7
9	12.0	9.5	50.2	3.5	14.0	10.2	7.1	12.6	0.2	0.2	98.0
10	12.0	9.5	49.2	3.4	13.9	10.1	7.1	12.6	0.3	0.2	96.8
11	13.0	9.5	49.5	3.5	13.8	10.0	7.1	12.7	0.2	0.2	97.1
12	14.0	9.5	49.8	3.5	13.9	10.4	7.2	12.6	0.3	0.2	97.9
13	15.0	9.5	49.6	3.2	13.8	10.0	7.2	12.8	0.2	0.2	97.0
14	16.0	9.5	49.5	3.6	14.0	10.1	7.2	12.6	0.2	0.2	97.3
15	17.0	9.5	49.6	3.5	14.0	10.4	7.2	12.6	0.2	0.2	97.7
16	18.0	9.5	49.5	3.2	13.7	10.1	7.1	12.7	0.1	0.2	96.8
17	19.0	9.5	49.5	3.5	14.1	10.2	7.1	12.4	0.2	0.2	97.1
18	20.0	9.5	49.4	3.6	13.8	10.2	7.0	12.5	0.2	0.2	96.8
19	20.0	9.5	48.5	2.4	21.1	8.0	3.9	14.3	0.4	0.2	98.6
20	19.5	9.5	49.1	3.6	14.1	10.1	7.1	12.6	0.2	0.2	97.1
21	6.3	8.4	49.7	3.6	14.2	10.1	6.7	12.9	0.1	0.1	97.5
22	7.0	8.4	47.9	3.3	13.9	9.5	7.0	12.6	0.3	0.2	94.7
23	8.0	8.4	49.3	3.5	13.8	9.5	7.1	12.9	0.2	0.2	96.4
24	9.0	8.4	49.5	3.1	14.1	10.1	7.1	12.9	0.1	0.2	97.1
25	10.0	8.4	48.5	2.2	13.6	10.2	7.2	12.5	0.3	0.1	94.6
26	11.0	8.4	49.2	2.9	13.8	9.9	7.1	12.7	0.2	0.2	95.9
27	12.0	8.4	49.4	3.4	13.9	10.3	7.1	12.8	0.2	0.2	97.2
28	13.0	8.4	49.3	3.6	14.1	10.1	7.0	12.5	0.2	0.2	97.0
29	14.0	8.4	49.4	3.5	14.2	9.9	7.2	12.8	0.3	0.2	97.4
30	15.0	8.4	49.5	3.4	13.8	10.3	7.0	12.6	0.3	0.3	97.2
31	16.0	8.4	49.3	3.5	13.8	9.8	7.2	12.8	0.2	0.3	96.8
32	17.0	8.4	49.1	3.4	13.8	9.4	7.0	12.7	0.2	0.2	95.8
33	18.0	8.4	49.3	3.5	14.2	10.2	7.0	12.6	0.3	0.2	97.4
34	19.0	8.5	49.2	3.4	13.8	10.3	7.0	12.4	0.2	0.2	96.4
35	20.0	8.5	48.9	3.4	13.9	9.9	6.9	12.6	0.2	0.2	95.9
36	6.5	7.0	49.7	3.5	13.9	9.8	7.2	12.9	0.1	0.2	97.3
37	7.5	7.0	49.1	3.5	13.8	9.1	6.8	12.8	0.2	0.2	95.5
38	8.5	7.0	50.0	3.5	14.0	10.0	7.2	12.5	0.2	0.2	97.4
39	9.5	7.0	49.5	3.4	13.9	9.5	6.9	12.8	0.2	0.2	96.3
40	10.5	7.0	49.2	3.5	14.0	9.9	7.1	12.6	0.1	0.2	96.7
41	11.5	7.0	49.2	3.5	13.8	9.2	6.9	13.0	0.2	0.2	96.1
42	12.5	7.0	49.3	3.4	13.9	10.0	7.0	12.6	0.2	0.2	96.7
43	13.4	7.1	49.0	3.5	14.0	10.2	7.2	12.8	0.2	0.2	97.2
44	14.5	7.1	49.3	3.4	13.8	9.6	7.2	12.7	0.2	0.2	96.5
45	15.4	7.1	48.8	3.4	13.8	9.7	7.0	12.6	0.2	0.2	95.8
46	16.5	7.1	48.9	3.4	13.9	10.0	7.2	12.8	0.2	0.2	96.5
47	17.5	7.1	49.1	3.4	13.9	10.4	7.2	12.8	0.2	0.2	97.2
48	18.5	7.1	48.9	3.6	14.0	10.3	7.2	12.8	0.2	0.1	97.2
49	19.5	7.1	49.3	3.5	13.9	10.1	7.0	12.6	0.2	0.2	96.8
50	20.1	7.0	49.4	3.3	13.9	9.9	7.0	12.6	0.2	0.2	96.6
51	20.1	5.5	48.0	3.3	13.5	10.2	6.6	12.9	0.3	0.2	95.0
52	19.0	5.5	49.1	3.5	13.9	10.2	7.1	12.6	0.2	0.2	96.8
53	18.0	5.5	49.1	3.5	13.8	10.0	7.0	12.6	0.1	0.2	96.4
54	17.0	5.5	49.3	3.3	13.9	10.0	7.0	12.6	0.2	0.2	96.4
55	16.0	5.5									
56	15.0	5.5	49.0	3.5	14.0	9.5	7.0	12.3	0.3	0.2	95.9
57	14.0	5.6	49.4	3.4	13.9	9.9	7.2	12.5	0.2	0.2	96.7
58	13.0	5.6	49.4	3.4	14.0	10.1	7.1	12.5	0.2	0.2	97.0
59	12.0	5.6	49.2	3.5	13.9	9.8	7.2	12.5	0.2	0.2	96.6
60	11.0	5.6	49.1	3.5	14.0	9.2	7.2	12.8	0.2	0.1	96.1
61	7.9	5.6	49.2	3.4	14.0	9.4	7.4	12.6	0.2	0.1	96.3
62	6.9	5.6	48.7	3.5	13.7	9.3	7.2	12.6	0.2	0.2	95.2
63	7.0	4.5	49.1	3.5	14.0	9.2	7.3	12.6	0.1	0.2	96.0
64	8.0	5.5	49.6	3.5	14.2	9.6	7.3	12.4	0.1	0.2	96.9
65	7.4	3.5	49.1	3.4	14.1	9.4	7.2	12.4	0.2	0.2	96.1
66	8.5	3.5	49.0	3.2	14.0	9.3	7.2	12.6	0.2	0.2	95.6
67	9.5	3.5	49.3	2.8	13.9	9.2	7.4	12.5	0.2	0.2	95.4
68	10.5	3.6	49.6	3.3	14.0	8.9	7.2	12.6	0.2	0.2	95.9
69	8.5	3.0	49.4	3.1	13.9	8.8	7.3	12.5	0.2	0.2	95.5
70	10.0	3.0	49.3	3.6	14.1	9.3	7.4	12.5	0.2	0.2	96.5
71	10.9	5.3	49.6	3.4	13.7	9.9	7.3	12.0	0.2	0.2	96.3
72	11.1	5.3	49.7	3.7	13.9	10.0	7.4	12.7	0.2	0.2	97.9
73	11.5	5.2	49.4	3.4	13.9	9.8	7.2	12.5	0.2	0.2	96.5
74	12.0	5.2	49.4	3.4	13.9	9.8	7.0	12.4	0.2	0.2	96.1
75	12.5	5.3	49.3	3.4	13.8	9.8	7.2	12.3	0.2	0.2	96.3
76	13.0	5.2	50.2	3.4	14.1	9.6	7.3	12.8	0.2	0.2	97.8
77	13.5	5.2	49.9	3.4	14.0	9.7	7.1	12.6	0.2	0.2	97.2
78	14.0	5.2	49.7	3.4	13.9	9.4	7.1	12.8	0.1	0.2	96.7
79	14.5	5.3	49.4	3.3	13.9	9.4	7.1	12.8	0.2	0.2	96.4
80	15.0	5.3	49.7	3.5	14.0	9.8	7.2	11.7	0.2	0.2	96.2
81	15.5	5.3	49.7	3.6	14.0	9.9	7.2	12.6	0.2	0.2	97.4
82	16.1	5.3	50.1	3.5	14.1	10.0	7.1	12.4	0.3	0.2	97.8
83	16.5	5.3	50.1	3.3	14.2	10.1	7.2	12.3	0.2	0.2	97.6
84	17.1	5.1	49.8	3.5	13.8	9.7	7.1	12.6	0.2	0.2	96.8
85	17.0	4.5	50.1	3.5	14.0	9.9	6.9	12.2	0.2	0.2	97.1
86	15.0	4.7	50.2	3.6	14.1	9.3	7.0	12.9	0.2	0.2	97.5
87	14.6	4.7	50.1	3.2	13.9	9.3	7.3	12.8	0.2	0.2	96.9
88	13.7	4.7	50.0	3.5	14.2	9.4	7.3	12.7	0.2	0.2	97.4
89	13.0	4.8	49.8	3.6	14.1	9.6	7.2	12.6	0.2	0.2	97.3
90	13.5	3.5	49.7	3.6	14.1	9.4	7.3	12.0	0.2	0.2	96.4
91	14.5	3.5	49.7	3.5	14.0	8.7	7.2	12.5	0.3	0.2	96.0
92	18.5	3.5	49.5	3.4	14.0	10.0	7.2	12.7	0.2	0.2	97.1
93	11.5	5.1	50.3	3.5	14.1	9.5	7.2	12.9	0.2	0.2	97.9
94	11.7	5.1	50.3	3.4	14.2	9.3	7.2	13.0	0.2	0.2	97.8
95	12.0	5.1	49.8	3.5	14.1	9.4	7.1	12.7	0.2	0.2	97.1
96	12.2	5.1	49.9	3.4	13.9	9.5	7.3	12.9	0.2	0.2	97.3
97	12.5	5.1	50.0	3.4	14.0	9.8	6.9	12.4	0.2	0.2	96.9
98	12.7	5.1	55.3	4.0	15.5	10.7	7.9	14.1	0.2	0.2	108.0
99	12.8	4.0	50.5	3.3	14.5	9.1	6.6	12.9	0.2	0.2	97.3
100	13.0	4.0	49.8	3.5	14.0	9.2	7.3	12.8	0.2	0.2	97.1
101	13.0	4.0	49.8	3.5	14.1	9.5	7.2	12.4	0.2	0.2	97.0
102	13.7	4.0	49.7	3.6	14.0	9.6	7.3	12.5	0.2	0.2	97.0
103	14.2	4.1	50.0	3.3	13.6	9.3	7.4	12.6	0.2	0.2	96.5
104	14.7	4.1	49.5	3.6	13.9	9.8	7.3	12.7	0.3	0.2	97.3
105	14.0	3.8	50.0	3.5	14.1	9.3	7.4	12.4	0.2	0.2	97.2
106	14.0	3.3	49.8	3.6	14.1	9.6	7.2	12.6	0.1	0.2	97.3
107	14.0	2.9	48.5	3.4	13.5	9.2	6.6	11.9	0.1	0.2	93.6
108	12.3	2.7	48.2	3.2	17.1	8.9	5.9	13.3	0.2	0.2	97.0
109	10.7	2.7	44.7	0.1	33.5	0.5	0.4	18.5	0.2	0.0	98.1
110	8.8	4.0	36.4	0.1	0.1	30.5	32.6	0.2	0.0	0.0	99.8
111	8.9	5.8	37.6	0.1	0.0	22.5	37.1	0.2	0.0	0.0	97.6
112	6.1	9.6	48.5	3.6	13.6	10.5	7.5	12.3	0.2	0.2	96.3
113	6.1	9.6	49.4	3.5	13.8	9.7	7.1	12.5	0.2	0.2	96.3
114	6.1	9.6	49.9	3.6	14.2	10.0	7.2	12.7	0.2	0.2	98.0
115	6.1	9.6	49.0	3.5	13.8	9.9	7.1	12.0	0.2	0.2	95.7
116	6.1	9.6	49.9	3.7	14.0	9.8	7.2	12.5	0.2	0.2	97.5
117	6.1	9.6	49.8	3.5	13.6	10.2	7.3	12.5	0.2	0.2	97.3
118	6.2	9.6	49.9	3.6	13.9	9.9	6.8	12.6	0.2	0.2	97.2
119	6.2	11.2	50.0	3.5	14.2	9.8	7.2	12.1	0.2	0.2	97.1
120	7.0	11.2	49.7	3.5	14.1	10.2	7.2	12.1	0.2	0.2	97.1
121	8.0	11.0	49.6	3.5	14.0	9.8	7.2	12.5	0.2	0.2	96.8
122	6.5	12.2	49.9	3.7	14.1	10.3	7.0	12.6	0.2	0.2	98.0

Table 3.05b. Analytical data from CO 25

Analysis	X (mm)	Y (mm)	SiO2	TiO2	Al2O3	CoO	MgO	CaO	Na2O	K2O	total
1	12.70	21.71	49.8	3.4	14.0	9.2	7.1	13.5	0.2	0.2	97.3
2	12.63	21.71	45.3	0.1	33.5	0.6	0.4	18.5	0.3	0.0	98.7
3	12.99	20.98	50.5	3.8	14.1	9.7	6.9	13.0	0.2	0.2	98.5
4	12.99	19.98	49.5	3.5	13.9	9.2	6.9	13.2	0.2	0.2	96.6
5	12.97	18.98	49.6	3.8	14.0	9.4	6.9	13.1	0.2	0.2	97.2
6	12.85	18.03	49.4	3.5	13.8	8.9	6.8	13.0	0.2	0.2	95.8
7	12.62	16.98	49.8	3.6	13.9	9.3	6.8	13.1	0.2	0.2	96.9
8	12.64	15.96	49.1	3.3	13.9	8.3	6.8	13.2	0.2	0.3	95.0
9	12.59	14.97	49.8	3.5	13.9	8.8	7.0	13.3	0.2	0.2	96.7
10	12.55	13.98	49.9	3.6	14.1	8.0	7.0	13.4	0.1	0.1	96.2
11	14.98	13.01	49.9	3.8	14.1	9.2	7.0	13.2	0.2	0.3	97.6
12	14.97	13.96	49.7	3.6	14.2	9.2	7.1	13.1	0.2	0.2	97.3
13	14.96	14.97	50.0	3.4	14.1	9.3	6.7	13.4	0.1	0.2	97.1
14	14.96	15.97	50.6	3.6	14.2	9.6	6.9	13.1	0.2	0.2	98.4
15	14.99	17.00	50.2	3.5	14.1	9.7	6.9	13.5	0.2	0.2	98.2
16	14.99	17.98	49.8	3.6	14.0	9.4	6.8	13.3	0.3	0.2	97.4
17	14.99	18.98	55.9	4.2	15.6	10.7	7.6	14.5	0.2	0.3	108.9
18	14.97	19.98	50.3	3.5	14.1	9.4	7.0	13.5	0.2	0.2	98.1
19	14.97	20.98	50.2	3.5	13.9	9.6	7.1	13.3	0.2	0.3	97.9
20	14.97	21.98	50.3	3.3	13.9	8.7	6.5	13.1	0.2	0.2	96.2
21	14.97	22.41	49.8	3.7	13.9	9.9	6.8	13.3	0.2	0.2	97.8
22	16.99	22.98	50.3	3.7	13.8	9.3	7.0	13.2	0.2	0.2	97.7
23	16.97	21.97	49.8	3.6	14.0	9.5	6.9	13.2	0.2	0.2	97.3
24	16.95	20.98	49.8	3.6	13.6	8.9	6.8	12.7	0.3	0.3	95.9
25	16.95	20.01	49.9	3.6	13.9	9.7	6.9	13.0	0.2	0.2	97.4
26	16.93	18.98	50.1	3.6	13.9	9.7	7.0	12.6	0.1	0.2	97.4
27	16.93	17.99	49.9	3.6	13.8	9.8	6.9	13.4	0.3	0.2	97.9
28	16.96	16.95	49.5	3.7	13.8	9.3	6.8	13.1	0.2	0.2	96.7
29	16.97	15.98	50.2	3.6	14.1	9.6	7.0	13.4	0.2	0.2	98.4
30	16.92	14.99	49.8	3.7	14.2	9.7	6.7	13.3	0.2	0.2	97.8
31	16.89	14.02	49.6	3.6	14.0	8.9	6.8	13.3	0.2	0.2	96.6
32	16.88	13.01	50.5	3.5	14.1	9.6	7.0	13.2	0.3	0.2	98.3
33	16.96	12.38	49.3	3.4	13.8	9.4	7.0	13.1	0.2	0.2	96.3
34	10.99	14.06	46.2	3.5	12.9	9.0	7.1	12.7	0.1	0.2	91.8
35	11.49	14.13	50.0	3.8	14.2	9.0	7.1	13.5	0.2	0.2	98.0
36	11.88	14.13	50.0	3.6	14.0	9.7	7.0	12.9	0.1	0.2	97.6
37	12.46	13.96	50.4	3.7	14.0	9.2	7.1	13.2	0.2	0.2	97.9
38	12.82	14.00	50.1	3.6	14.0	9.3	7.1	13.3	0.1	0.2	97.7
39	13.55	9.73	50.2	3.3	13.8	9.0	7.2	13.4	0.3	0.2	97.4
40	13.54	10.70	50.6	3.4	14.1	8.8	7.0	13.4	0.1	0.3	97.6
41	13.68	11.68	50.1	3.4	14.1	8.9	7.1	13.2	0.2	0.2	97.3
42	13.77	12.49	50.4	3.6	14.0	9.3	7.1	13.1	0.2	0.2	97.8
43	13.77	13.51	50.1	3.4	14.1	9.5	7.1	13.3	0.2	0.2	97.8
44	13.77	14.59	49.7	3.4	14.0	9.1	7.0	12.9	0.2	0.2	96.5
45	13.75	16.01	50.0	3.7	13.9	9.1	7.1	13.3	0.2	0.3	97.6
46	14.60	12.80	50.2	3.5	14.0	9.3	6.9	13.4	0.2	0.2	97.9
47	15.49	12.80	50.3	3.7	14.0	9.3	6.9	13.1	0.2	0.2	97.7
48	16.53	12.80	50.4	3.4	13.8	8.7	6.8	13.1	0.3	0.2	96.6
49	15.99	13.51	50.0	3.4	14.0	9.1	7.0	13.2	0.2	0.2	97.2
50	15.91	14.89	49.7	3.5	14.1	9.2	6.9	13.2	0.3	0.2	97.1
51	13.44	12.96	50.2	3.7	14.0	9.0	7.0	13.4	0.2	0.2	97.8
52	18.99	12.03	50.1	3.7	13.8	9.8	7.0	13.2	0.2	0.2	98.1
53	19.01	14.01	50.0	3.6	13.7	9.5	6.9	12.7	0.2	0.2	96.8
54	19.04	16.03	50.2	3.7	13.9	9.4	6.8	13.1	0.2	0.2	97.5
55	19.04	18.01	49.4	3.6	13.8	9.5	6.8	13.0	0.2	0.2	96.5
56	19.04	20.03	49.7	3.6	13.7	9.8	6.9	13.1	0.1	0.2	97.1
57	19.04	20.03	50.2	3.6	13.8	9.2	6.8	12.5	0.0	0.2	96.4
58	19.04	22.02	49.6	3.8	14.0	9.7	7.0	12.9	0.2	0.2	97.5
59	19.04	24.02	49.5	3.6	13.8	9.7	7.0	13.4	0.2	0.3	97.4
60	19.91	18.46	44.1	0.0	34.1	0.5	0.4	19.2	0.3	0.0	98.5
61	19.86	18.44	50.2	3.5	13.8	9.9	7.0	13.1	0.2	0.2	98.0
62	19.82	18.44	49.9	3.3	13.9	9.7	6.9	13.2	0.2	0.2	97.3

Figure 3.10. Maps of oxide concentrations in charge CO 20

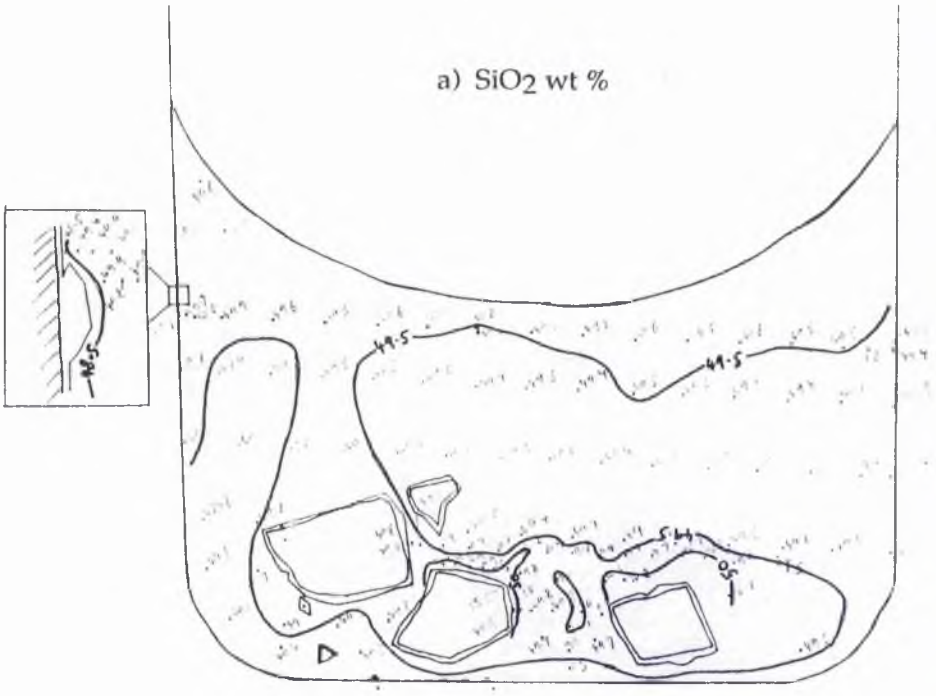

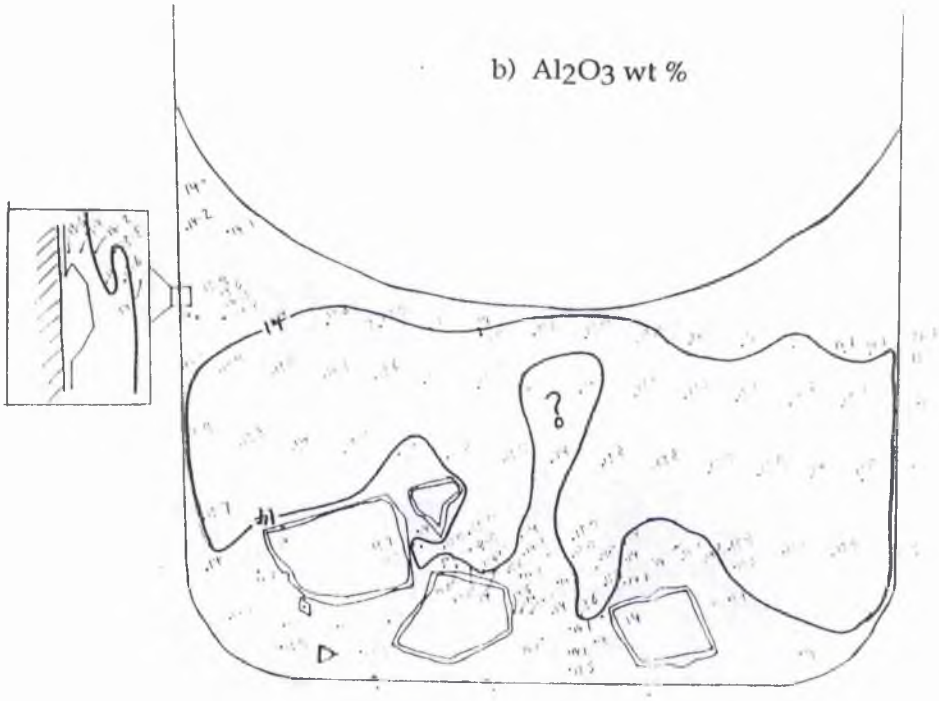

c) CoO wt %

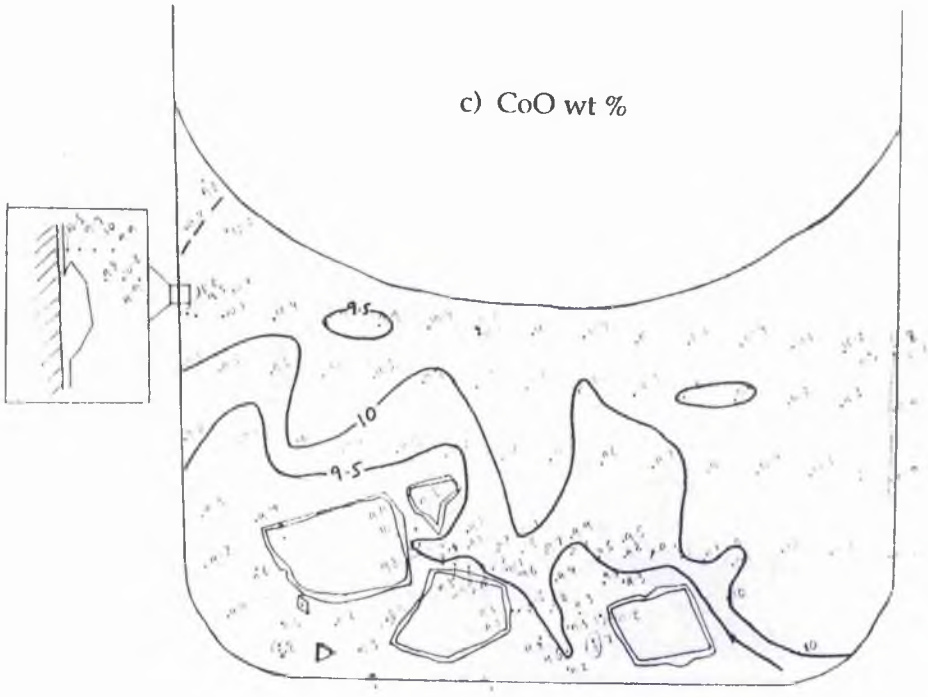

d) MgO wt %

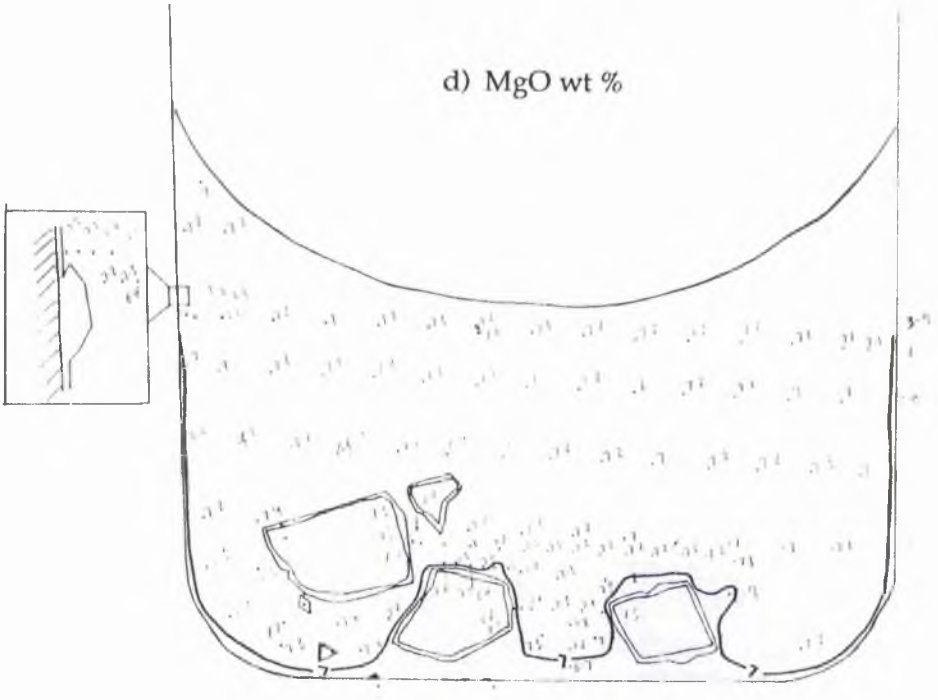

Figure 3.11. Maps of oxide concentrations in charge CO 25.

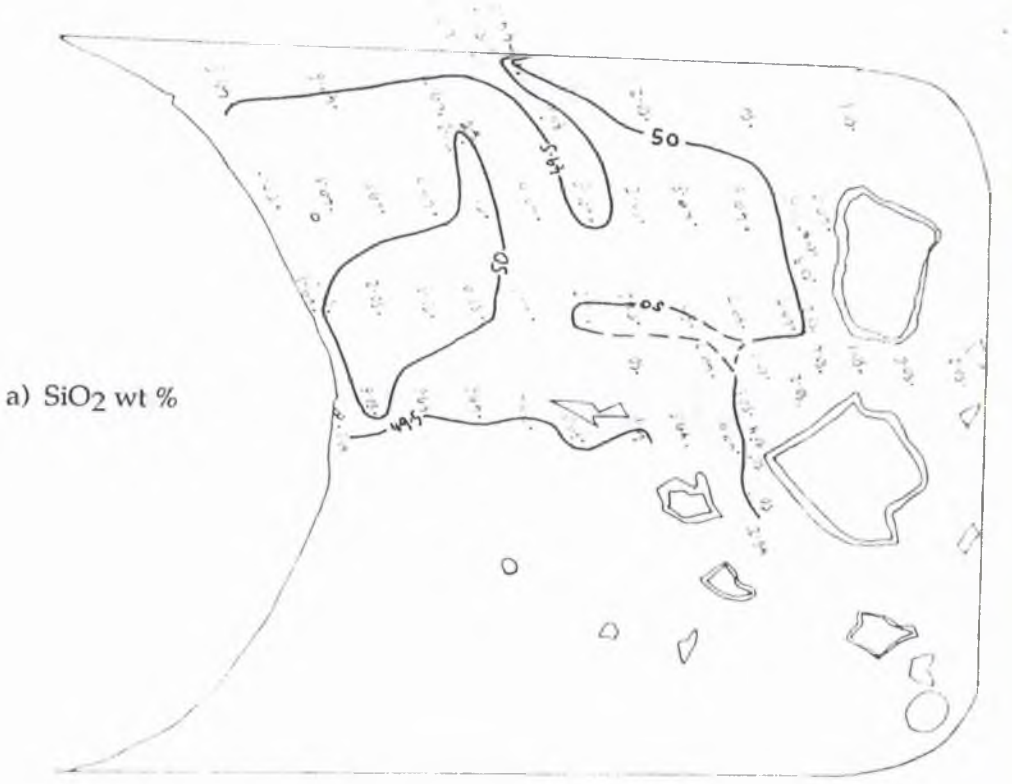

a) SiO_2 wt %

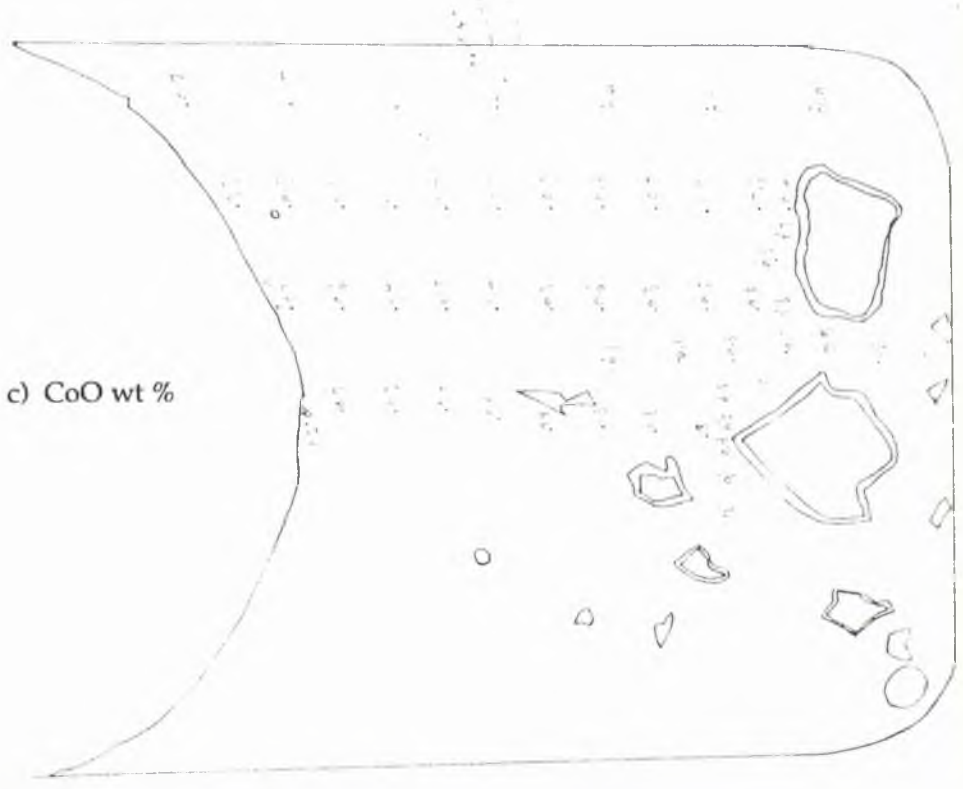

c) CoO wt %

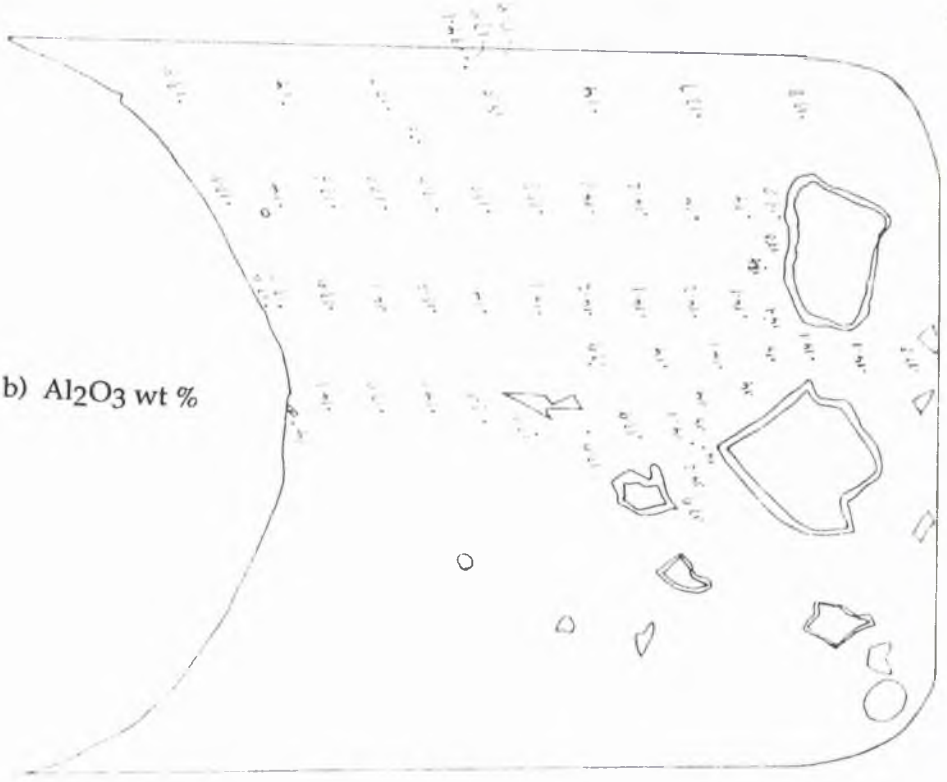

b) Al_2O_3 wt %

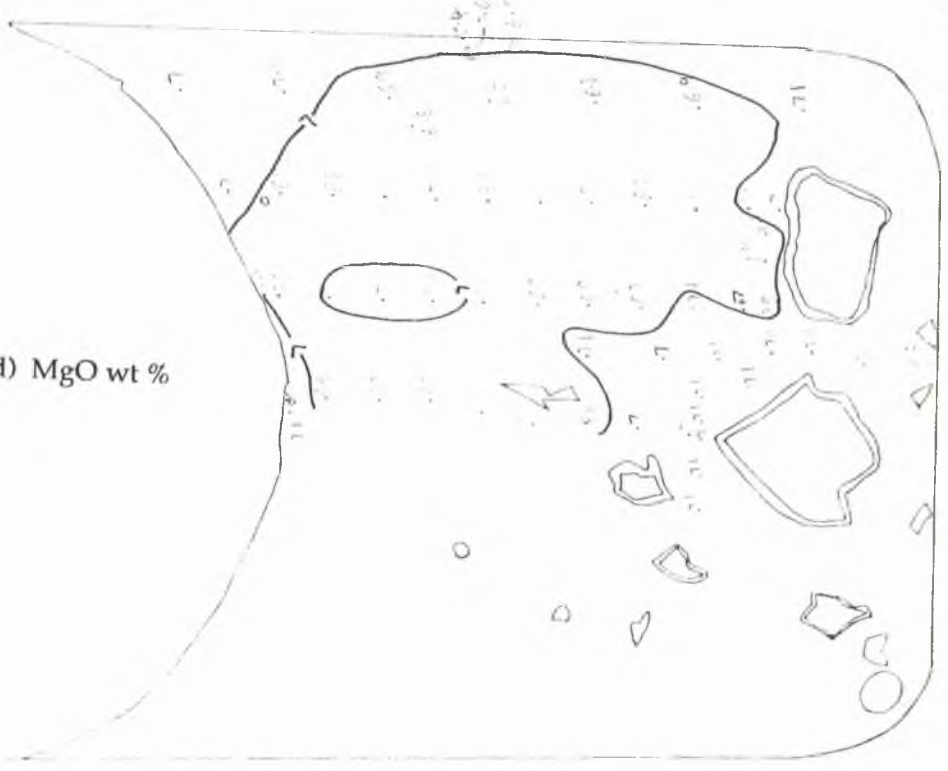

d) MgO wt %

3.6 Olivine seeds cemented in alumina crucibles

3.6.1 Introduction

Following the failures of other techniques to fix crystal seeds this technique was used in a final attempt to establish a suitable experimental arrangement. Previous work using this technique (Donaldson, 1992) reported it as unsuitable because basaltic melt dissolved the cement rapidly releasing the crystal seed. However, this work was at higher temperatures. Hence, it was hoped that at the lower temperatures used in the current experiments the rate of cement dissolution would be slow enough to hold the crystals in place.

3.6.2 General Observations

Polished thin sections of these runs (plates 3.17-3.26) were analysed optically and by EPMA both in full chemical oxide analyses (appendix C) and in recorded Mg, Co, Al and Si X-ray count-rates at closely spaced points on preset traverses. EPMA was only carried out on runs above 1230°C, as lower temperature runs contain too many crystallites which interfere with analyses on traverses across boundary layers. The positions of full chemical analysis points and count-rate tracks in the charges C-O 29, 30, 31a, 31b, 32, 35, 36, and 37 are shown in figures 3.13, 3.15, 3.18, 3.19, 3.24, 3.26, 3.28, and 3.30 respectively. Plates 3.17 to 3.26 illustrate the following general points which help to identify areas worthy of closer inspection:-

- At temperatures of 1230°C and above, crystallites occur at or below the level of the apex of the seed crystal, and so do not hamper the search for buoyant boundary layer release from the seed.
- A pink overgrowth of Co-Mg olivine has developed on all crystal seeds. This overgrowth becomes wider with increasing time (see plate 3.23). As boundary layers of melt next to crystal overgrowths do not increase greatly in width with time, some other process must transport matter to and from the interface. Crystal growth rates therefore appear to be controlled by convection rather than diffusion.
- Melt penetrated into the alumina cement but did not weaken the grip of the cement on the crystal seed enough to allow seeds to move.
- In charges C-O 29, 30 and 31 (plates 3.19-3.22) an area of paler glass is detectable in thin section in the lower parts of the crucibles. This is in the region close to the olivine seed but it is also close to areas of alumina cement. EPMA was therefore used to test whether or not the colour difference is due to olivine growth stripping Co^{2+} from the melt, or whether it is caused by alumina cement dissolving into the melt, and diluting the blue coloration caused by Co^{2+} (section 3.7.1.4).
- At the contact between crucible and melt, a layer of hercynite crystals has developed (cf. section 3.5).

• There is a layer of Pt blebs between the original seed and the new pink overgrowth (see plate 3.27). Whereas glass distant from the interface also contains blebs that at the overgrowth contains none. Apparently the blebs have been stripped from the interface melt during crystal growth. If bleb-free glass can be traced beyond the limit of the interface, then it will indicate the path of movement of this melt away from the interface.

• Plate 3.28 shows an area of melt free of blebs, directly above the crystal apex in C-O 31. If this is CoO and MgO depleted it may represent a buoyant boundary layer that is rising from the crystal seed. Alternatively it could also be Al_2O_3-enriched due to cement dissolution, although data in section 3.3.3 revealed Al enrichment around olivine crystallites, showing that olivine crystalliazation produces an increase in aluminium concentration at the crystal-liquid interface.

Using these optical observations to locate areas of particular interest, EPMA was carried out in the areas indicated in figure 3.12 to quantify the following phenomena:-

• Compositional boundary layer development adjacent to the olivine overgrowth.
• Compositional boundary layer development adjacent to olivine crystallites.
• The presence or absence of buoyant boundary layer melt above the seed apexes.
• The extent of side-wall hercynite crystallization and its associated boundary layer production.
• The presence or absence of zoning in olivine overgrowths as an indication of temperature variation.
• The effect of alumina dissolution.
• Vertical chemical differentiation of melt in the crucibles.

3.6.3 Presentation of analytical data

3.6.3a Run C-O 29

• Data from analytical tracks 1, 2, 3, 6, and 7 have been used to produce the maps of Co and Mg concentrations in figure 3.14 a and b respectively. These diagrams clearly show a vertically elongate region of Co and Mg depleted glass above the crystal apex in CO 29.

• Track 7 detects vertical compositional variation in this plume of glass, causing the contours in the maps to form boudinaged patterns. This may reflect an irregular 3-dimensional structure in this plume, but could also be caused by pulses of melt leaving the crystal apex, as opposed to one continuous stream.

•The presence of the most depleted glass 4 mm above the seed apex provides evidence that chemical diffusion is not fast enough to smooth out compositional gradients in these experiments, and that boundary layer melt has a high enough viscosity and low enough density contrast with the bulk melt to enable it to remain discrete.

- 0.3 mm above the seed (track 2) the width of CoO and MgO depleted glass is 4.2 mm. Here CoO dips from 11.5 wt % at the edges of the track to 9.7 wt % in the centre of the track and MgO dips from 8.1 to 7.7 wt % across the same distance.
- 1.3 mm above the seed (track 1) the depleted glass is 2mm wide and CoO falls from 11.3 to 10.2 wt % across it while MgO falls from 8 to 7.6 wt %. In Plate 3.29 the pale, bleb-free glass is only 0.5 mm across at the same height above the seed, indicating that CoO and MgO depletion is not limited to the bleb-free glass.
- Above the crystal seed is a 1 mm thick region of CoO- and MgO-depleted melt (track 7). CoO falls from 7.1 wt % to 6.5 wt % across this region while MgO drops from 7.3 to 6.9 wt % as the top of the seed is neared. This indicates that the depleted melt has built up to a thickness of 1mm on this roughly horizontal surface.
- Data from track 5 (figure 3.14 c and d) indicate a narrow zone of CoO and MgO depletion adjacent to the overgrowth on the olivine seed. MgO is depleted over a distance of 14 microns from the interface, and falls from 6.8 to 5.3 wt % over this distance compared with an average value of 7.2 wt % further from the seed, while CoO is only depleted for 8 microns and falls from 6.5 to 5.3 wt % over this distance, compared with an average value of 7.1 wt %.
- Probe data from a vertical transection of the charge (track 4) indicates a drop in CoO and MgO concentrations towards the bottom of the crucible. There is no marked decrease in CoO or MgO beneath the meniscus, where buoyant, CoO- and MgO-depleted melt would be expected to have accumulated. The dramatic reductions in CoO and MgO values at the bottom of the charge are due to an increase in the amount of Al2O3 from cement dissolution, and from CoO and MgO being taken out of the melt here by crystallite growth.

Plate 3.17. Charge CO 26 (1200°C 45 hours). The first experiment in which olivine remained tethered throughout the run duration. Note the slightly paler blue colour of the glass in the right of the crucible. This is possibly caused by dissolution of the alumina cement in this part of the charge.

Plate 3.18. Charge CO 28 (1200°C 154 hours) showing a white line of hercynite on the right hand side wall, and the presence of too many crystallites in the glass to check thoroughly for heterogeneity of glass composition.

Plate 3.19. Thin section of charge CO 29 (1230°C 24 hours). Note the decreasing abundance of olivine crystallites at this higher temperature, and the appearance of slightly paler blue melt above and around the olivine seed.

Plate 3.20. Thin section of charge CO 30 (1240°C 24 hours). Note the absence of olivine crystallites at this temperature and the variation in depth of blue colour, with pale glass being present around and above the olivine crystal seed, and near to the alumina cement. The pink speck above the olivine seed is one of the few crystallites in this charge.

Plate 3.21. Charge CO31a (1230°C 72 hours) showing development of pale, Co-depleted glass in the vicinity of olivine crystallites near the base of the crucible and around and above the pink overgrowth on the olivine seed. A plume of pale blue melt can be detected above the apex of this seed.

Plate 3.22. Charge CO31b (1230°C 72 hours). The area of pale blue glass in the bottom left of this plate is due to thinning of the slide on polishing. No other colour variation is seen in the glass.

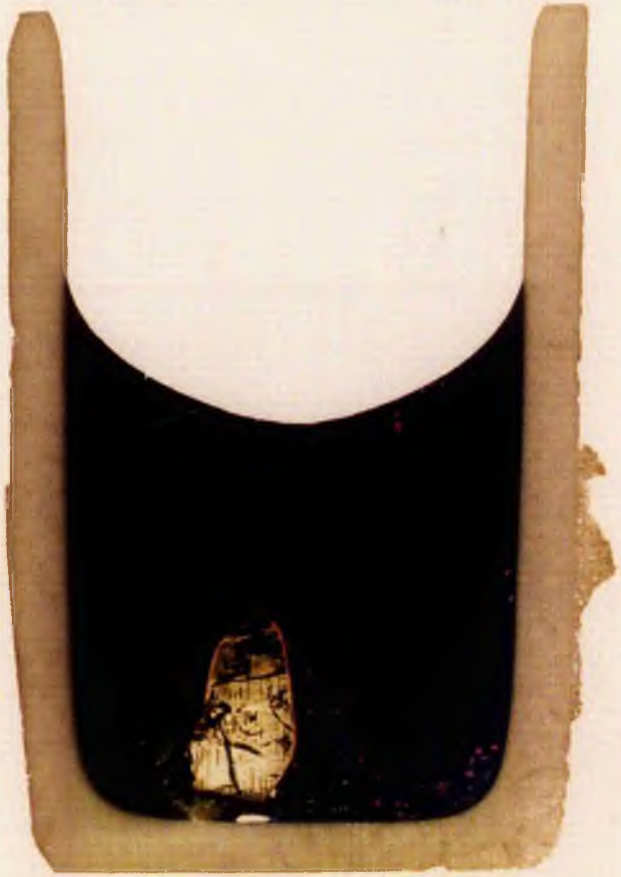

Plate 3.23. Charge CO 32 (1230°C 557 hours). Note the width of the pink olivine overgrowth on the seed, and the absence of pale glass above and around the seed in this long duration run. It appears, from this slide, that Co-depleted melt is not being produced by crystallization at the time of quenching but this may be due to the plane of section not bisecting any such glass.

Plate 3.24. Charge CO 35 (1240°C 72 hours). No pale blue, Co-depleted melt can be detected optically in this section, however compositional variation is detected using EPMA.

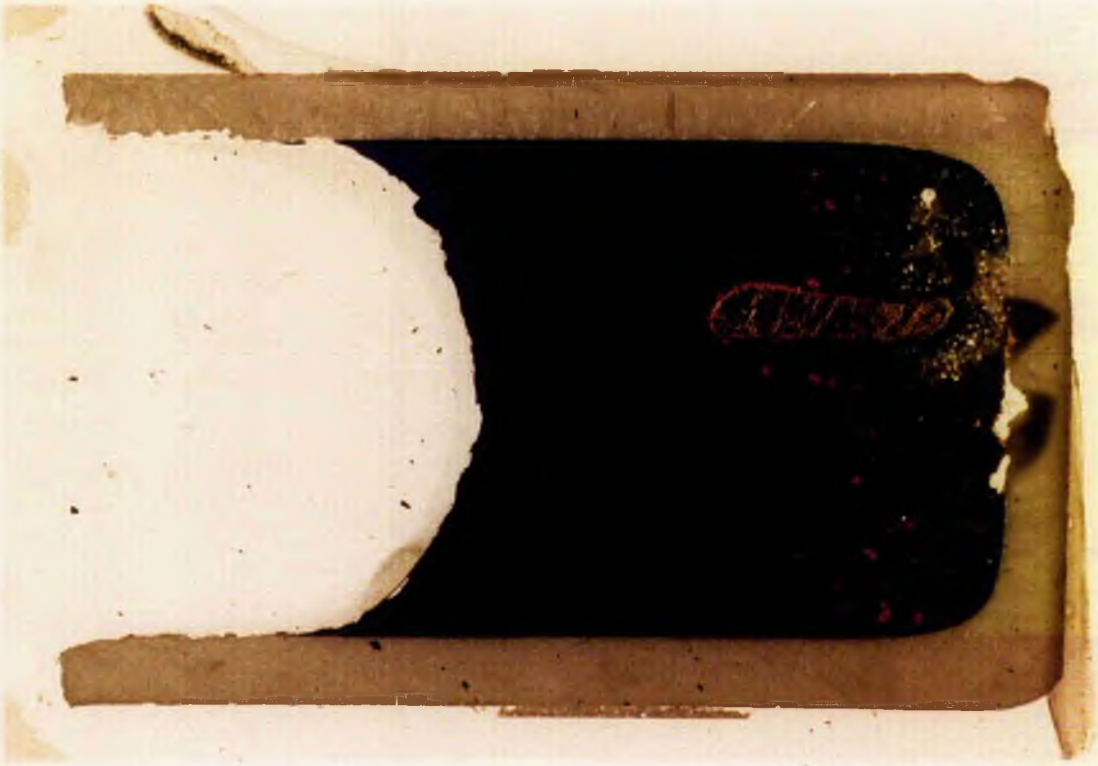

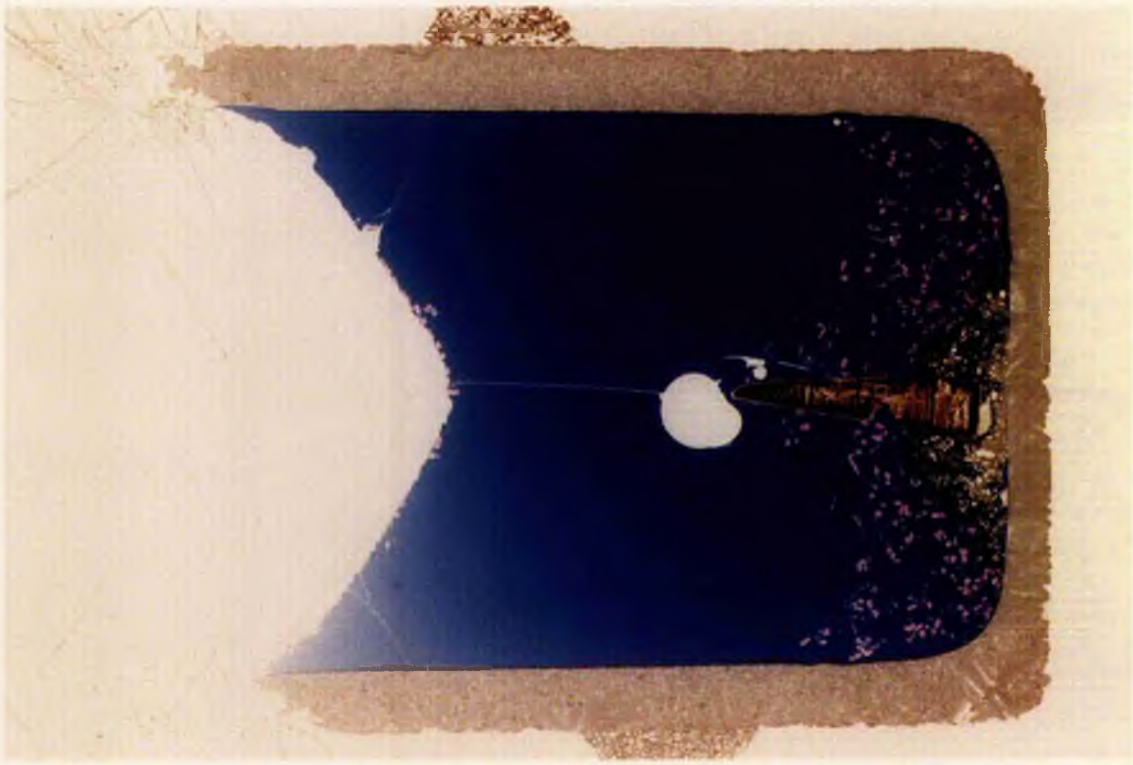

Plate 3.25. Charge CO36 (1245°C 72 hours) showing how an air bubble remains above the crystal apex. This obscures an optical search for compositional variation in the glass above the seed. The air bubble may, in the third dimension, be attached to the seed apex.

Plate 3.26. Charge CO37 (1250°C 72 hours). No pale blue melt can be detected around this seed. Pale melt on the right hand side may be due to thinning of the slide during polishing.

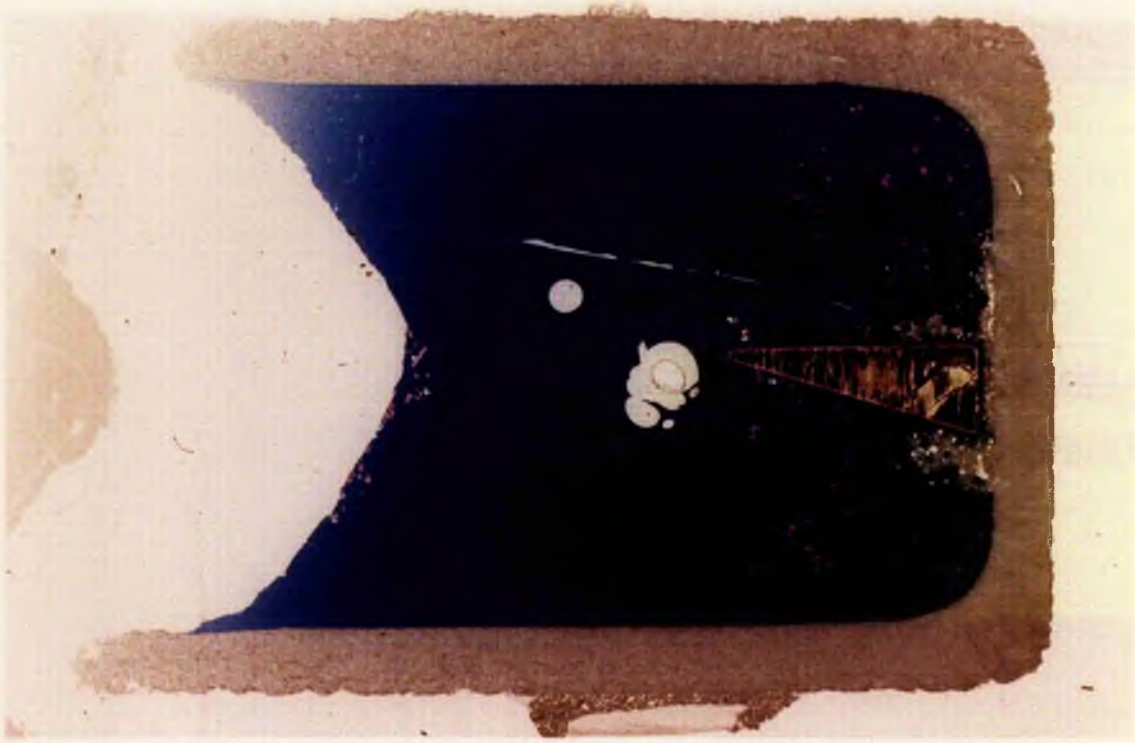

Plate 3.27. PPL photomicrograph showing the line of dark Pt blebs separating the pink Co-Mg olivine overgrowths from the pale olivine seed. The concentration of Pt blebs in this area is responsible for producing pale, Pt-free glass at the crystal-glass interface, which can also be detected above crystal seeds. Magnification x 50.

Plate 3.28a. PPL photomicrograph of the crystal apex in slide CO 31a. Note the pale blue melt on either side of the seed and its appearance directly above the crystal apex. Streakiness can also be detected to the right of the crack above the seed. A lack of Pt blebs is largely responsible for this colour variation, but Co-depletion in the glass will also have an effect. Magnification x 15.

up ↑

Plate 3.28b. Photomicrograph showing variations in depth of blue colour in glass directly above the olivine seed in slide CO 31b. This plate is orientated sideways so that the crystal seed lies to the left and the up direction is to the right. Magnification x 30.

→ up

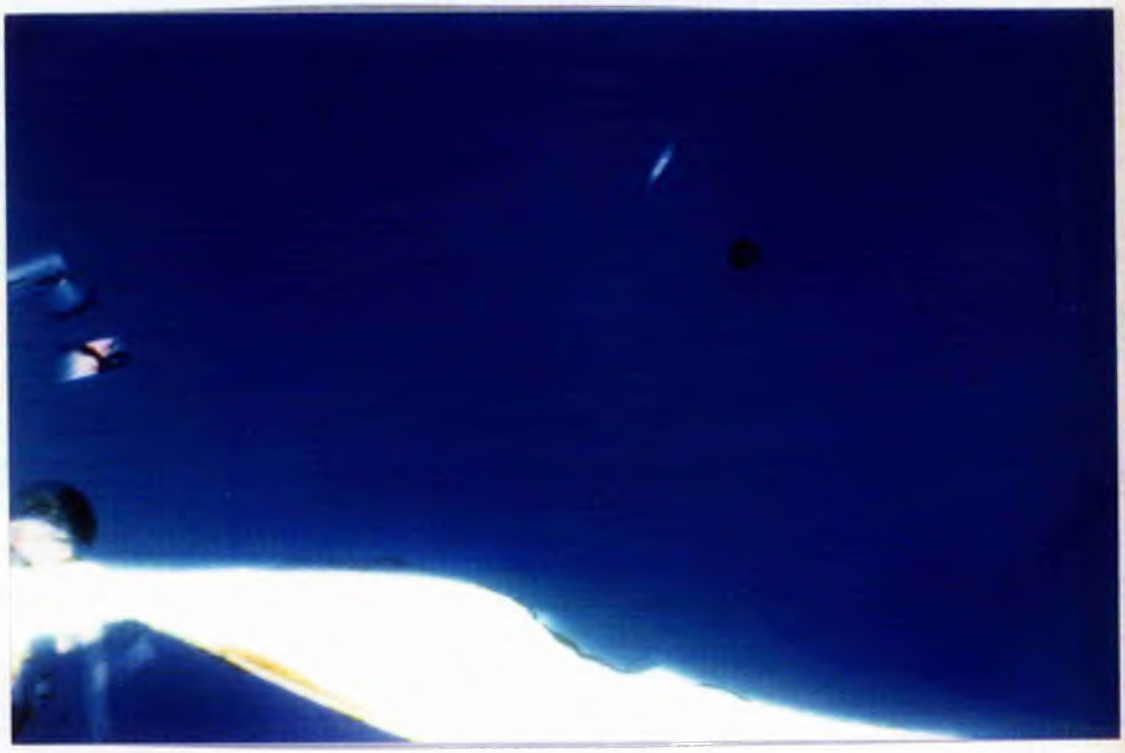

Figure 3.12. Sketch of areas examined by EPMA for compositional variation.

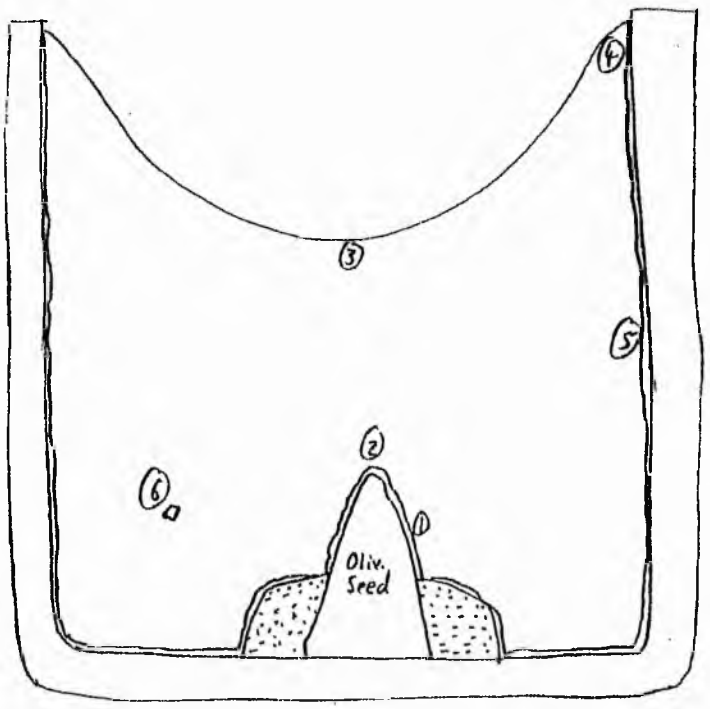

1) Glass adjacent to olivine overgrowths on crystal seeds. To test for horizontal extent of boundary layer development.

2) Glass directly above crystal apex. To test for buoyant release of boundary layer melt from the highest point on the seed.

3) and 4) Glass at the meniscus to test for accumulation of buoyant melt in a compositionally-discrete layer beneath the meniscus.

5) Glass adjacent to the hercynite layer on the inner wall of the crucible.

6) Glass around olivine crystallites.

Figure 3.13. Map of analytical points and positions of count rate tracks in charge CO 29.

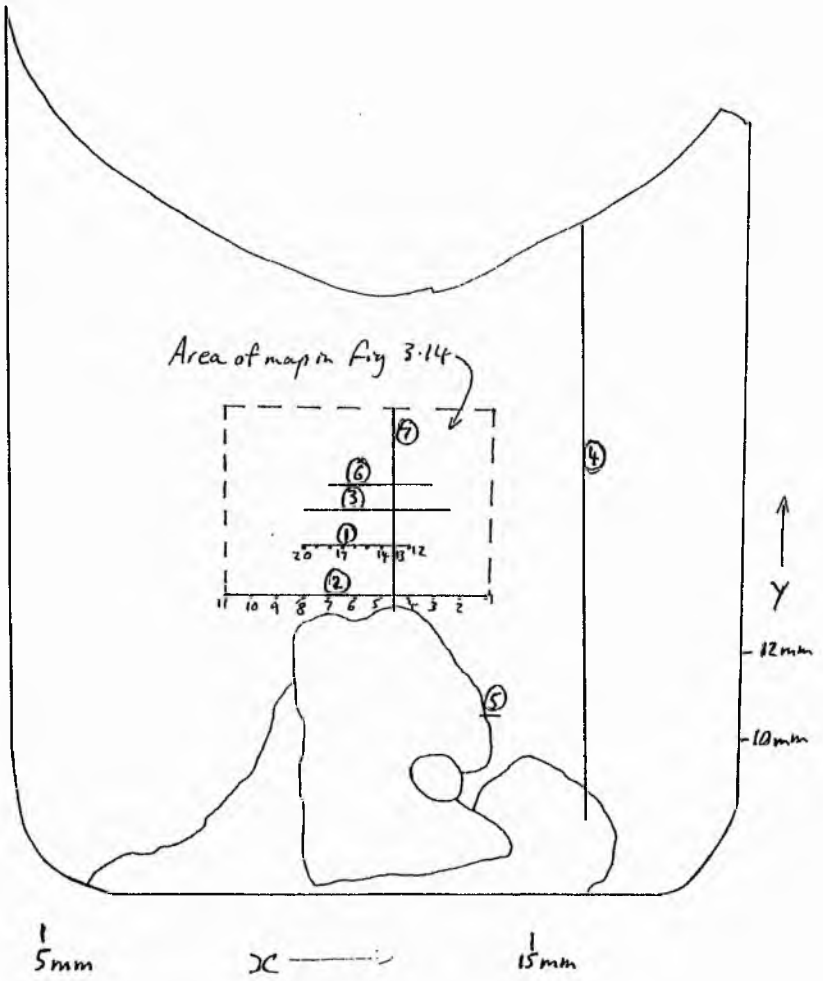

Track details

Number	Data points	Interval (μm)	X (mm)	Y (mm)
1	100	20	10.5-12.5	13.35
2	250	20	9-14	11.96
3	100	20	10.5-12.5	14
4	110	100	15.9	19.8-7.8
5	100	2	13.86 -14.26	9.47
6	63	20	11-13	14.5

Plate 3.29. PPL photomicrograph showing the variation in blue glass colour above the crystal seed and overgrowth in charge CO 29. Magnification x 15.

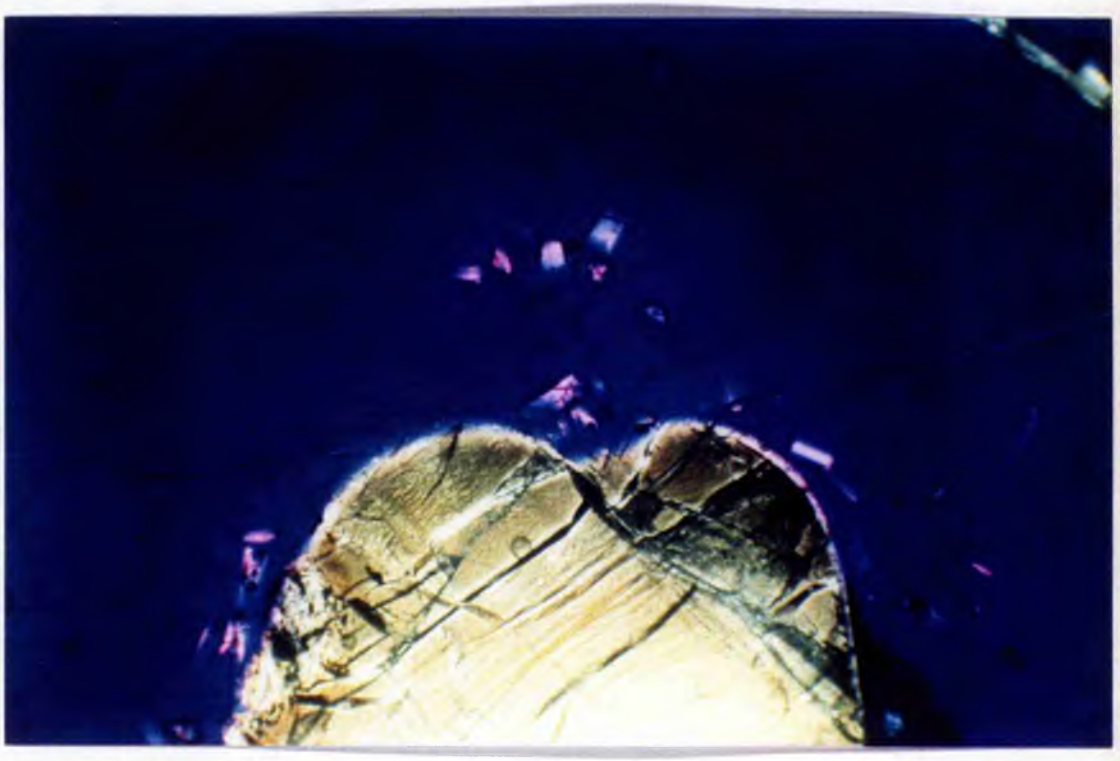

Figure 3.14a. Map of Co concentrations in glass above the crystal apex in charge CO 29. Note the lume of Co-depleted melt directly above the crystal apex. Its boudinaged appearance may reflect the 3-dimensional nature of the plume. Area covered in map is indicated in figure 3.13. 713 Data Points

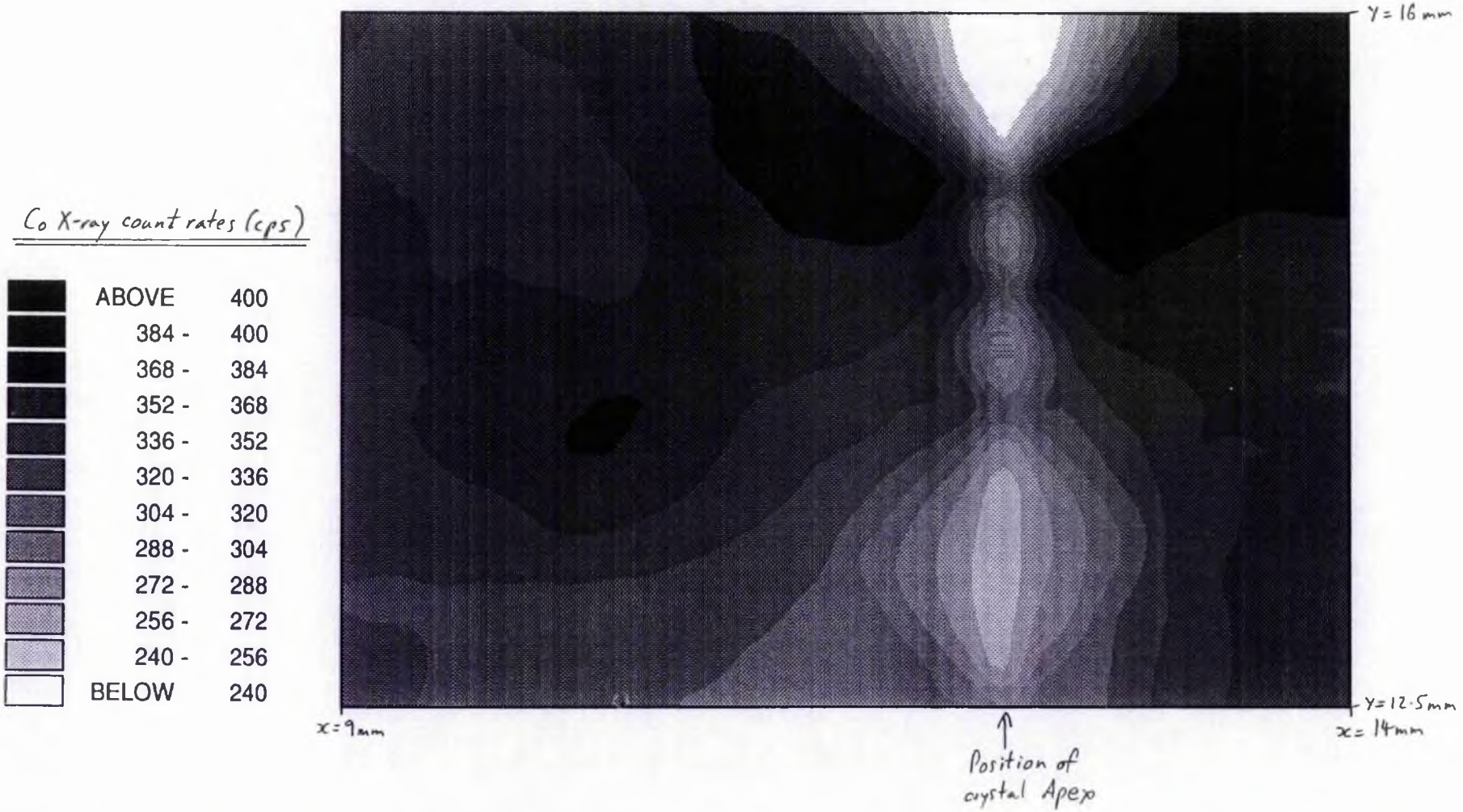

Figure 3.14b. Map of Mg concentrations in glass above the crystal apex in charge CO 29. Note the lume of Mg-depleted melt directly above the crystal apex. Its boudinaged appearance may reflect the 3-dimensional nature of the plume. Area covered in map is indicated in figure 3.13. 713 Data Points

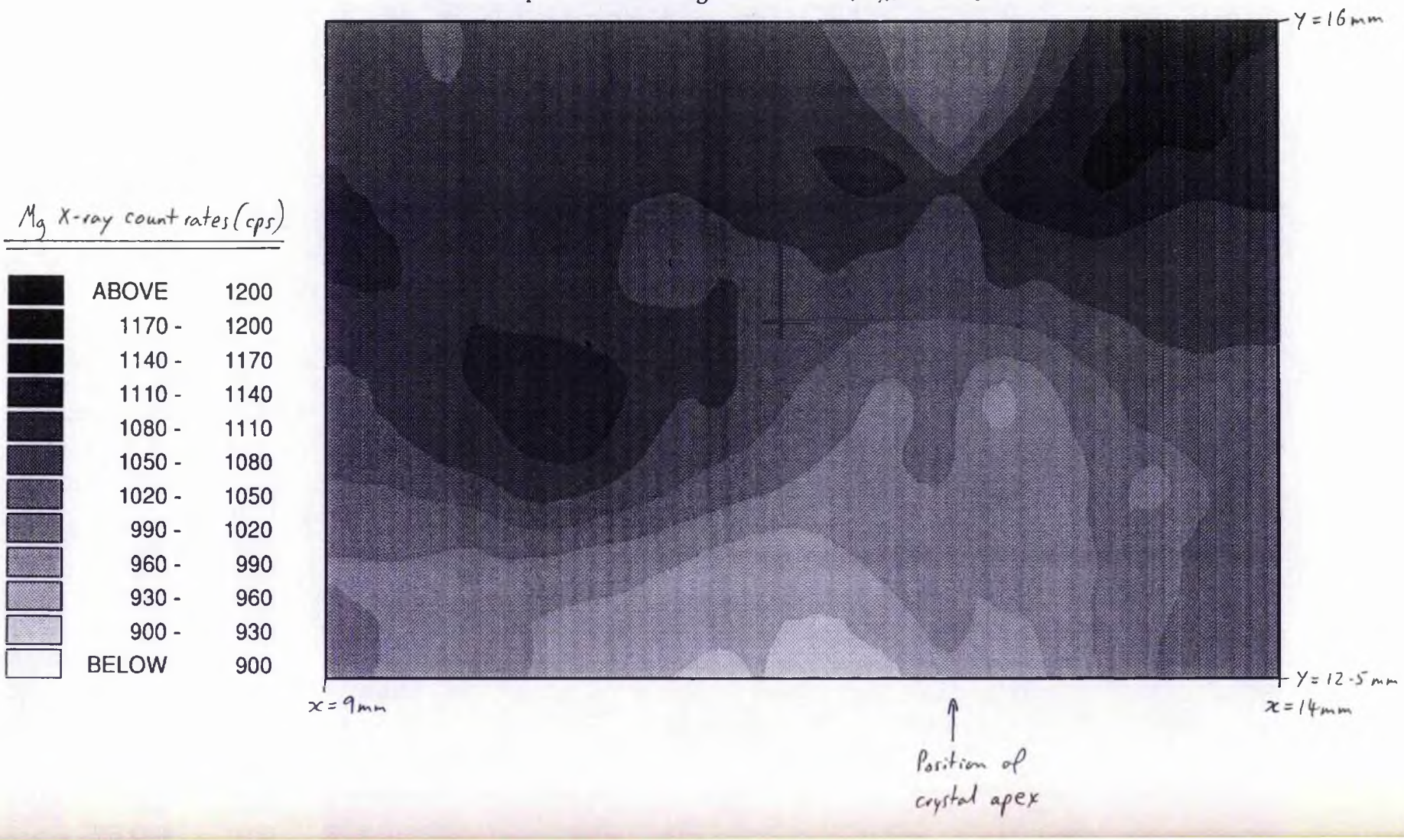

Figure 3.14c. X vs Co from track 5 in CO 29.
From left to right the track moves away from the crystal overgrowth.

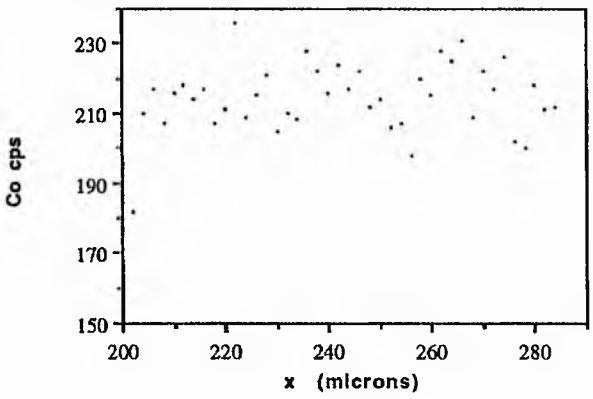

Figure 3.14d. X vs Mg from track 5 in CO 29.
From left to right the track moves away from the crystal overgrowth.

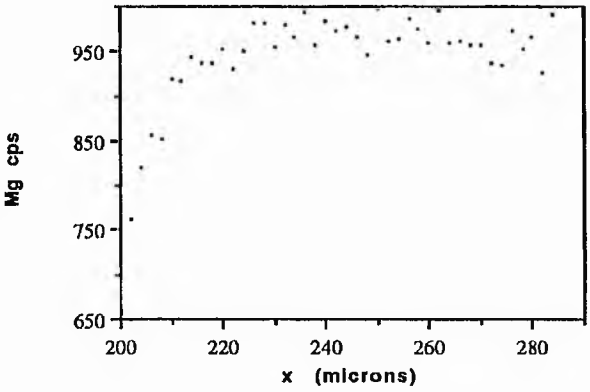

Figure 3.14f. Y vs Mg on track 4 in CO 29

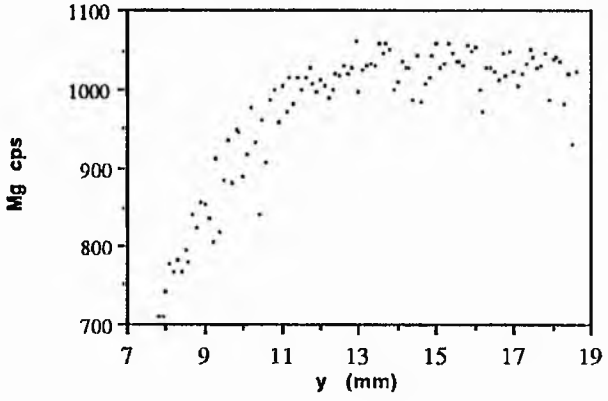

Figure 3.14e. Y vs Co on track 4 in CO 29

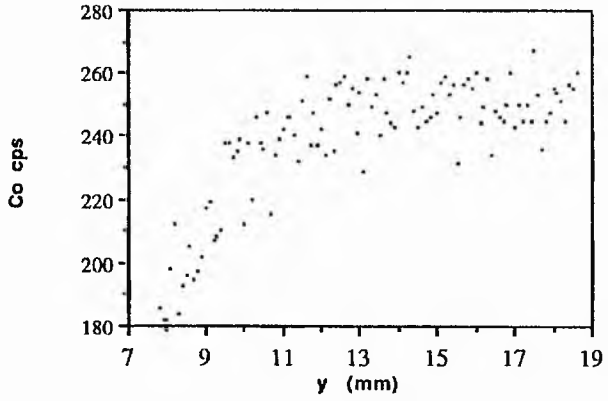

3.6.3b Run C-O 30

The maps in figure 3.16 and the graphs in figure 3.17 demonstrate the following points about this run product:-

- Maps of Co and Mg concentration around the crystal seed show an obvious zone of depletion in glass around the crystal and directly above the crystal apex.
- A narrow area of CoO- and MgO-depleted glass extends upwards from the apex of the crystal seed. It is visible as paler, bleb-free glass for 3 mm.
- Maximum CoO and MgO depletion occurs directly above the seed apex and at the crystal-glass interfaces.
- 0.25 mm above the seed apex (track 2) the zone of depletion is roughly 1.5 mm wide. MgO falls from 8.4 wt % at the ends of this track to 7.4 wt % at its centre. Across the same range CoO falls from 11.5 to 10.3 wt %. The computed melt densities across this track vary by just 0.02g/cc (0.7 %) at the most, with the lowest values being in the centre of the track.
- 1 mm above the apex (track 1) the zone of depletion is narrower and chemically less pronounced. Across this track MgO falls from 8.2 wt % to 8.0 wt % while CoO falls from 11.6 to 10.7 wt %. The maximum depletion appears at x =13.5 mm.
- Plate 3.29 shows that the zone of bleb-free melt is only 0.3 mm and 0.5 mm wide in the same places as tracks 1 and 2 respectively, indicating that the zone of CoO and MgO depletion is wider than the bleb-free melt, but is centred on the bleb-free glass.
- Data from tracks 3, 4, 6, and 8 indicate a narrow zone of CoO and MgO depletion at the olivine-glass interface. Its width decreases up the crystal seed, from 30 to 12 microns for MgO, and from 20 to 9 microns for CoO. Across this narrow boundary layer CoO falls from 10.7 to 8.3 wt %, and MgO falls from 8.0 to 5.2 wt %. The reason for the variation in the amount of CoO and MgO depletion across boundary layers in tracks 3, 4, 6, and 8 probably lies in the precise position of the analytical points closest to the crystal-glass interface. The steep compositional gradient in this glass means that a positional difference of only a few microns could result in a difference of tens of cps in X-ray count-rates.
- Track 6 passes over the apex of an olivine crystallite. Directly above the crystallite a drop in CoO and MgO concentrations is seen in the glass, indicating that this individual crystallite has produced a boundary layer depleted in CoO and MgO.
- Vertical traverses (tracks 5 and 7) through the crucible reveal no signs of CoO and MgO depletion beneath the meniscus. The fall in CoO and MgO concentrations as the bottom of the crucible is approached is due to a slight de-focusing of the electron beam as the charge is descended, giving lower X-ray count rates.

Figure 3.15. Map of analytical points and positions of count rate tracks made in charge CO 30.

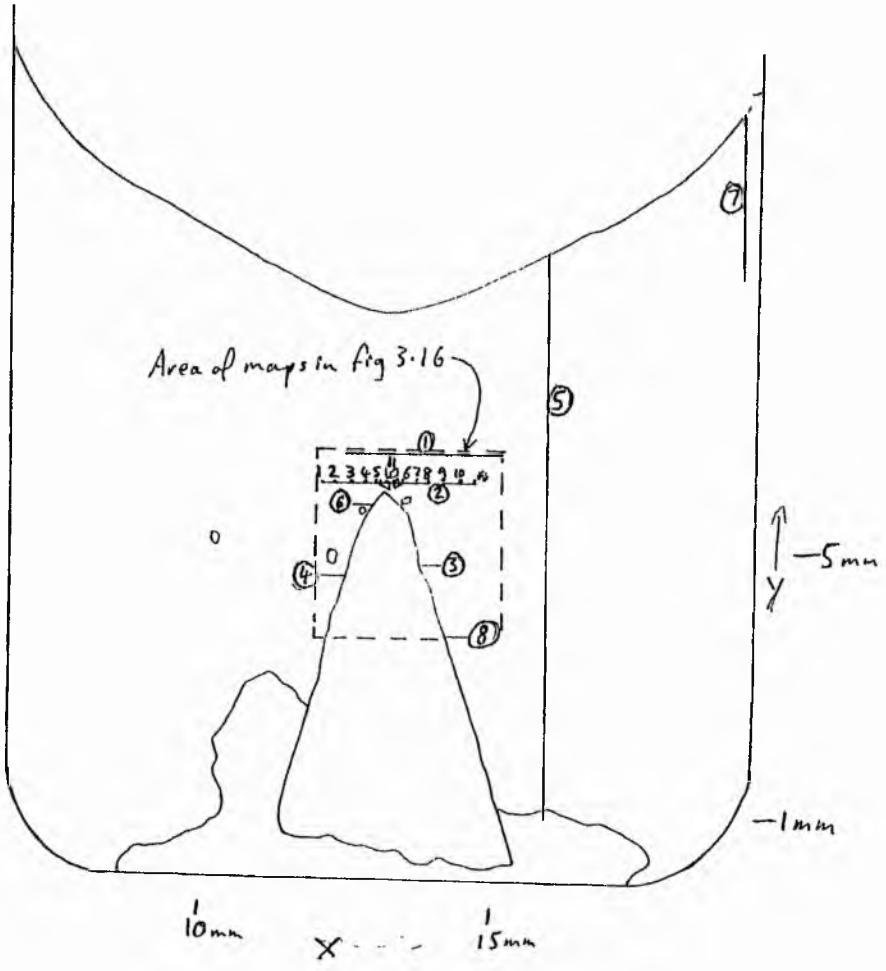

Track details

Number	Points analysed	Interval (μm)	X (mm)	Y (mm)
1	150	20	12.52-15.5	7.5
2	100	30	12-15	6.98
3	150	3	14 -14.5	5.25
4	100	5	12 -12.5	5.1
5	220	50	16.5	0 -11.5
6	100	3	12.5 -13	6.5
7	100	30	20.2	11 -14
8	100	5	14.4 -14.9	3.9

Plate 3.30. Photomicrograph of olivine seed and pink overgrowth in charge CO 30. Note the pale blue glass at the left hand side crystal-glass interface and around and above the pink crystallite above the seed apex. Magnification x 10.

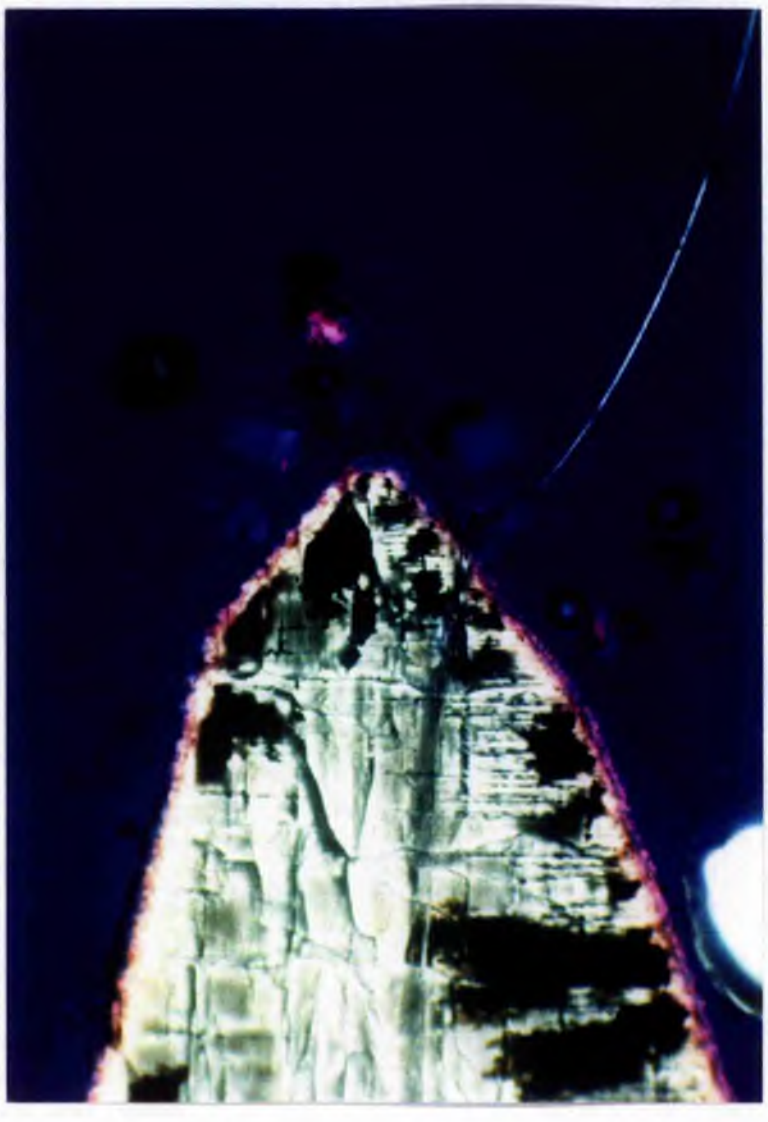

Figure 3.16a. Map of Co concentrations around the olivine seed in CO 30. 700 Data Points

Note that the glass above + around the olivine seed is depleted in Co

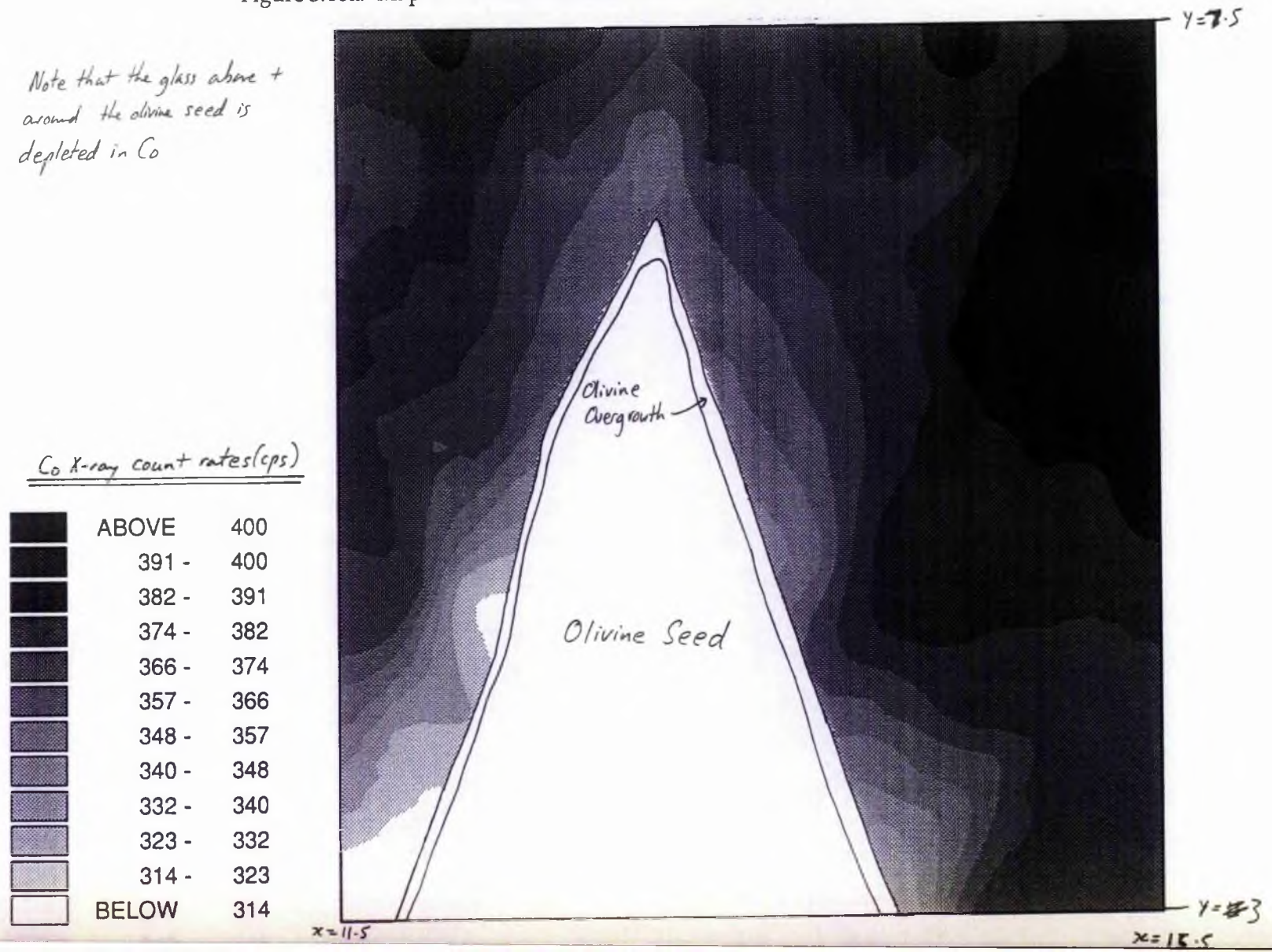

Figure 3.16b. Map of Mg concentrations around the olivine seed in CO 30. 700 Data Points

Note that the glass above + alongside the seed is depleted in Mg.

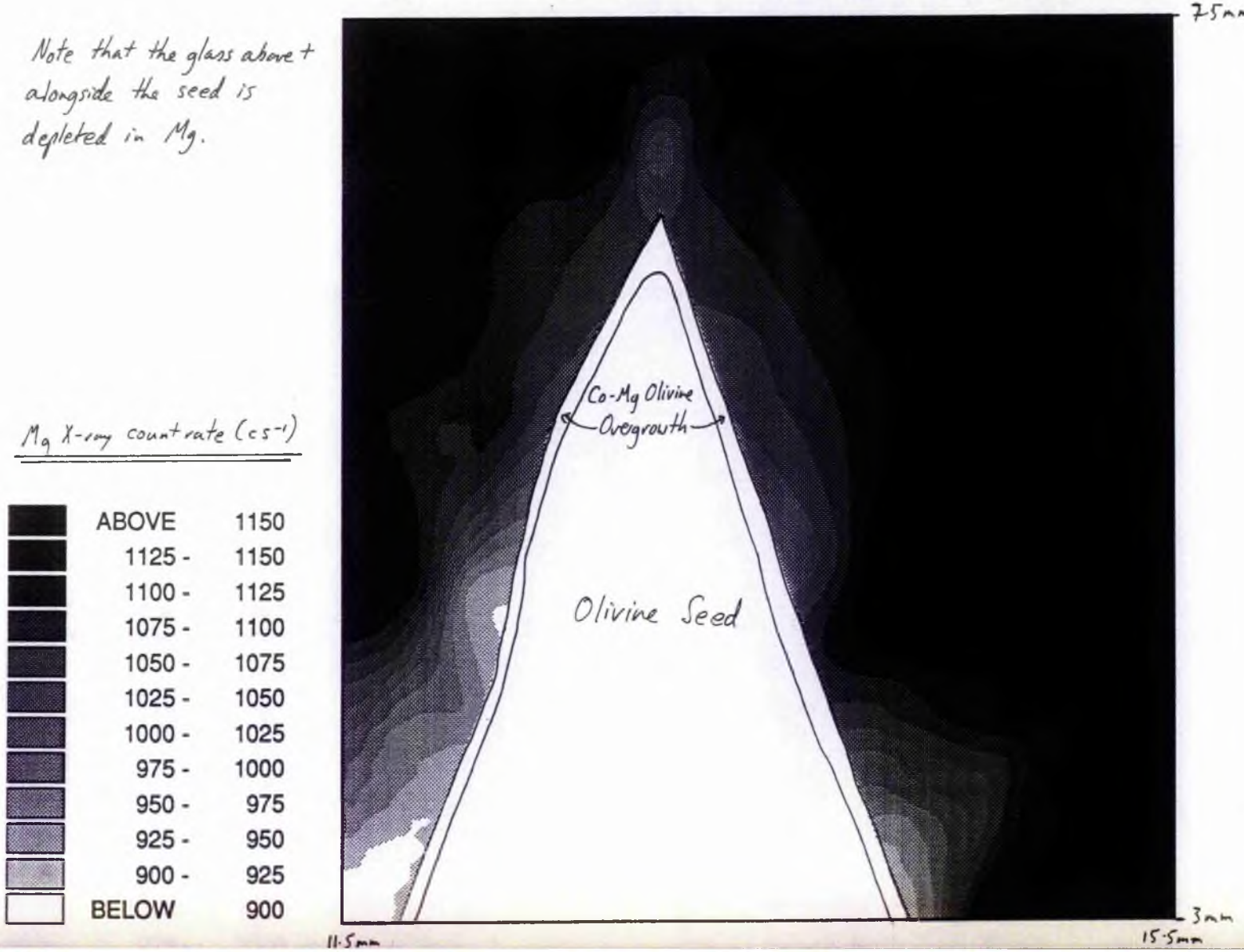

Mg X-ray count rate (cs^{-1})

ABOVE	1150
1125 -	1150
1100 -	1125
1075 -	1100
1050 -	1075
1025 -	1050
1000 -	1025
975 -	1000
950 -	975
925 -	950
900 -	925
BELOW	900

Figure 3.17a. X vs CoO wt % in the glass above the olivine apex in CO 30

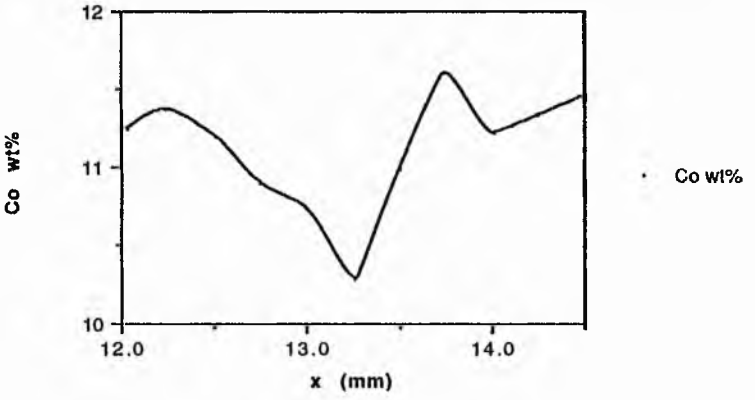

Figure 3.17b. X vs MgO in the glass above the crystal apex in CO 30.

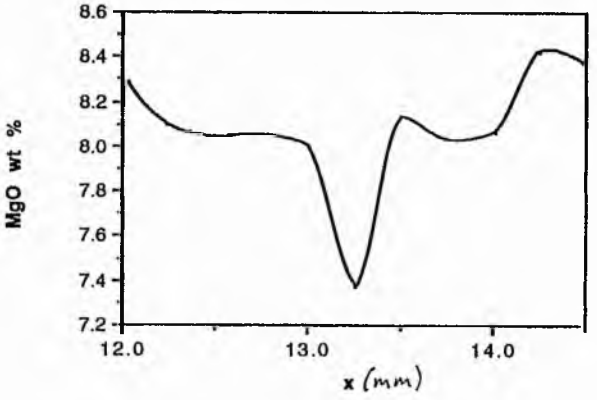

Figure 3.17c. Co count rate data from track 6 in CO 30.
The right hand side of the graph represents the edge of the olivine overgrowth.

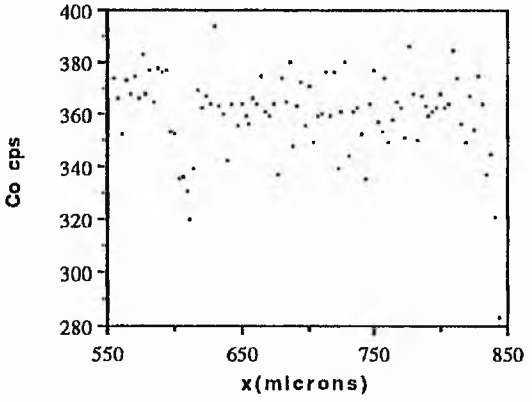

Figure 3.17d. Mg count rate data from track 6 in CO 30.
The edge of the olivine overgrowth lies at the right hand side of the graph.

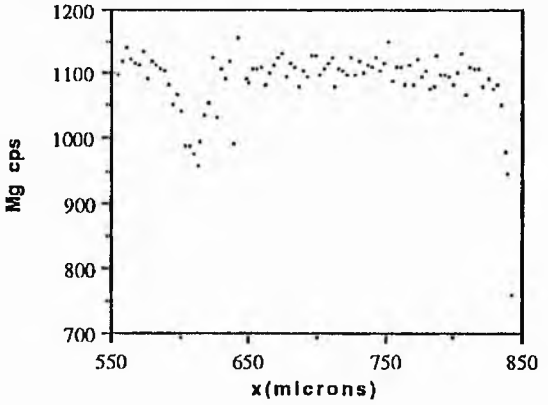

Figure 3.17e. Co count rate variation in track 8 from CO 30.
The left edge of the graph represents the edge of the olivine overgrowth.

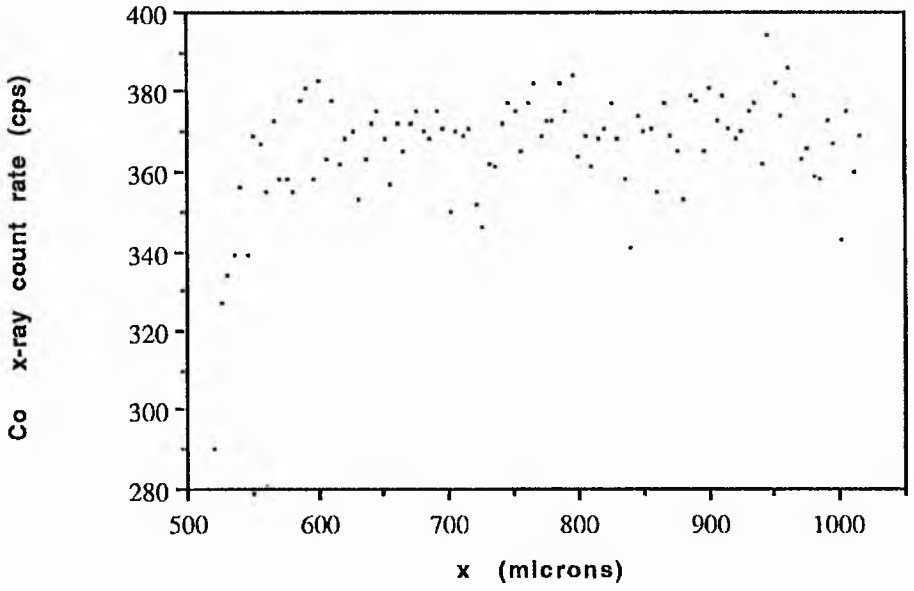

Figure 3.17f. Mg count rate variation in track 8 from CO30.
The left edge of the graph represents the edge of the olivine overgrowth.

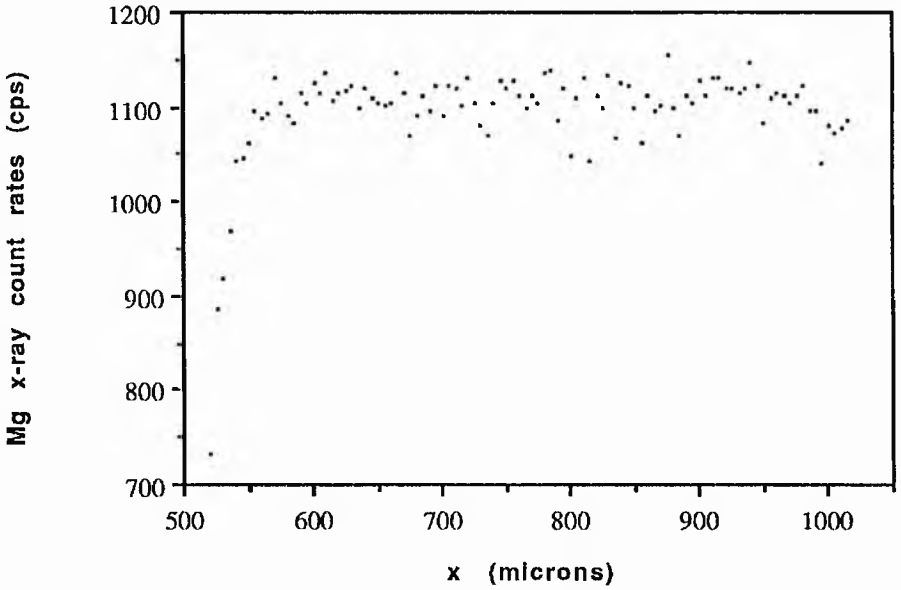

Figure 3.17g. Vertical Co variation in track 7 on CO 30.
Meniscus at right hand side of graph.

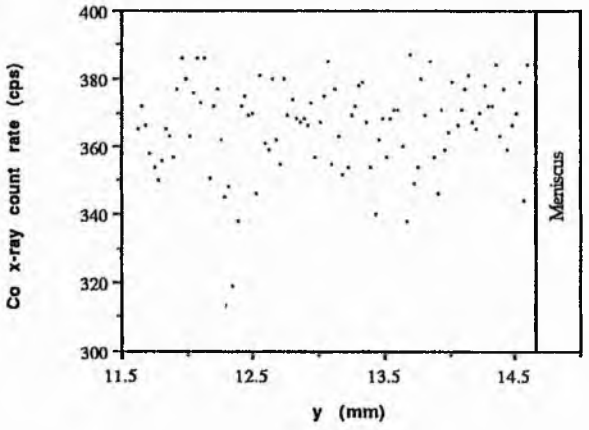

Figure 3.17h. Vertical Mg variation in top 3mm of charge. Track 7, CO 30.

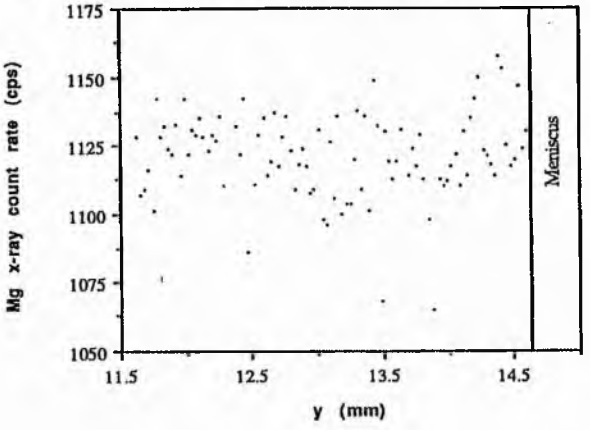

Figure 3.17i. Vertical Mg variation through CO 30 (track 7).
Right edge of graph represents meniscus.

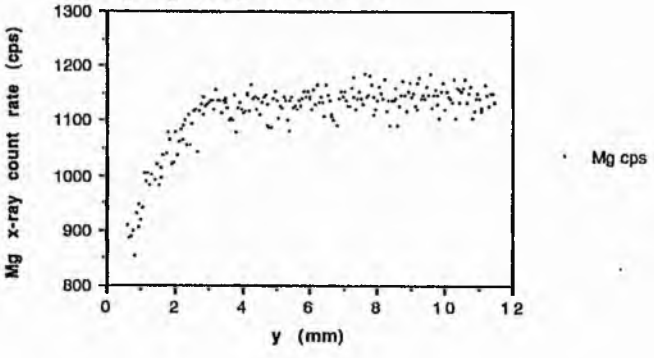

Figure 3.17j. Vertical variation in Co through charge CO30 (track 5).
Meniscus at right edge of diagram.

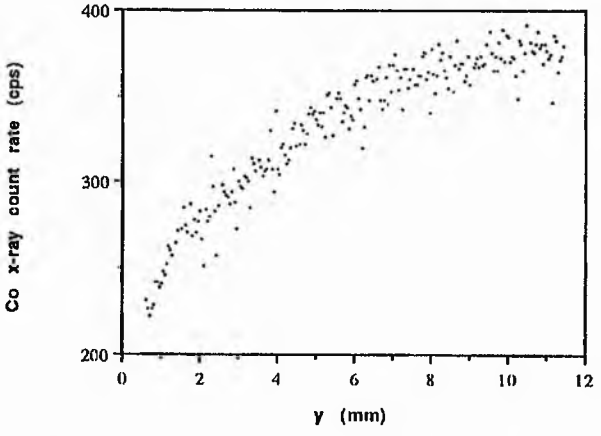

3.6.3c Run C-O 31

From point-analysis of glass chemistry (Maps in figures 3.20 and 3.21, data in appendix C) :-

- SiO_2 concentration increases closer to the crystal-glass interface (in overgrowths and crystallites) (e.g. 48.5 wt % to 50.6 wt %. C-O 31a points 15-20). SiO_2 increases are also evident above the crystal-seed apex (49.5 to 50.2 wt %. C-O 31a points 1-8) and close to the melt meniscus (C-O 31b). SiO2 depletion is noted towards the bottom of the crucibles.
- CoO depletion is evident at crystal-liquid interfaces (10.6 to 8.5 wt %), above the seed apex (across the zone of bleb-free glass), towards crucible walls, and near the meniscus of the melt. All bleb-free glass examined has a CoO concentration of less than 11 wt %.
- MgO depletion (by upto 25 %) is seen at crystal-liquid interfaces and at crucible walls.
- Al_2O_3 shows the following variation patterns; a15 % increase in concentration approaching crystal-liquid interfaces and a 9 % increase approaching crucible walls. A slight increase is seen above the crystal apex (13.7 to 14.1 wt %. i.e. 6 %). Al_2O_3 generally increases in concentration towards the bottom of the crucible.

Figure 3.18. Map of analytical points and tracks in slide CO 31 a

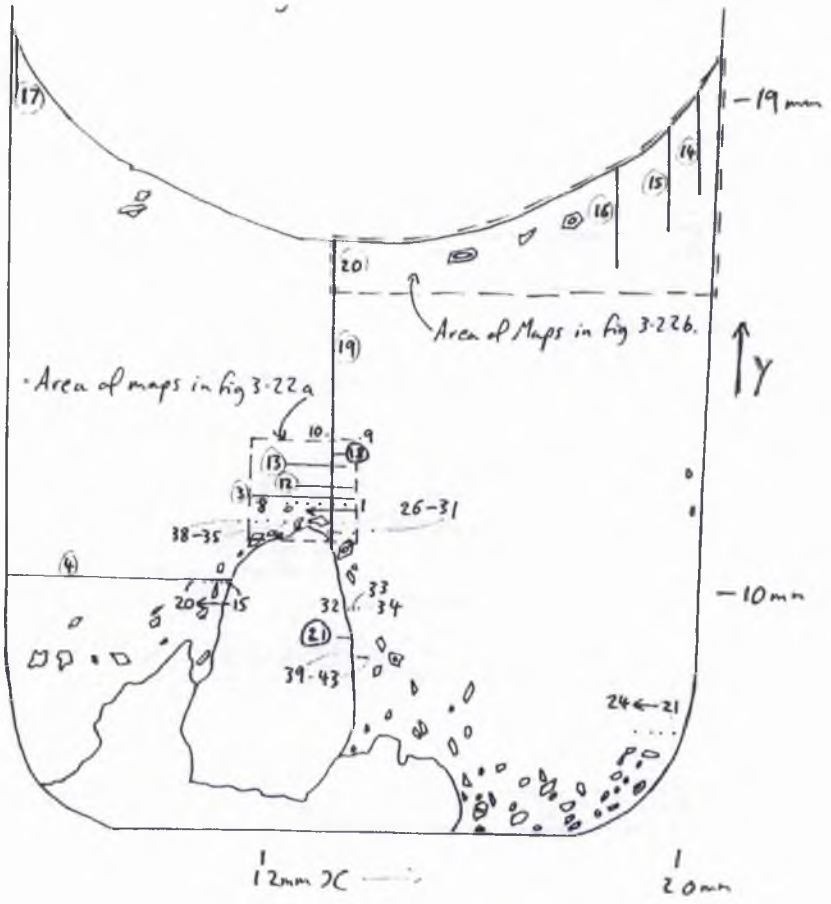

Track details

Number	Points analysed	Interval (μm)	X (mm)	Y (mm)
3	100	20	12-14	7.8
4	210	20	7.3-11.5	6.1
12	100	10	12.8-13.8	8
13	100	10	12.6-13.6	8.4
14	220	10	19.5	17.25-19
15	100	20	19	16-17.5
16	100	20	18	15.5-17
17	50	20	6.5	19-20
18	100	20	12.75	10-12
19	60	50	12.75	12-15.5
20	50	20	12.75	15.5-16.5
21	40	1	13-13.04	8.5

Figure 3.19. Map of analytical points and tracks in slide CO 31b.

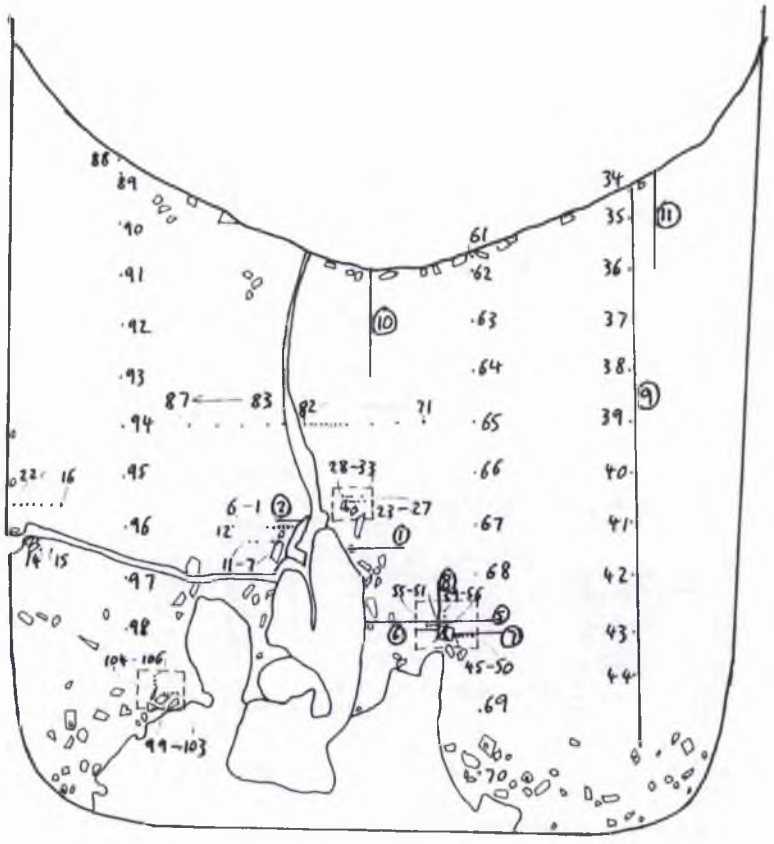

Track details

Number	Points analysed	Interval (µm)	X (mm)	Y (mm)
1	100	10	9.35-10.34	12.58
2	50	10	7.85-8.34	13.1
5	95	20	11.49-13.37	11.07
6	30	10	12.73-13.01	10.97
7	55	10	13.24-13.78	10.76
8	20	20	13.114	10.95-11.33
9	125	100	15.09	8.05-20.45
10	110	20	11.5	15.94- 18.12
11	100	20	15.52	19.27-17.29

Figure 3.20. Maps of oxide variation in slide CO31a

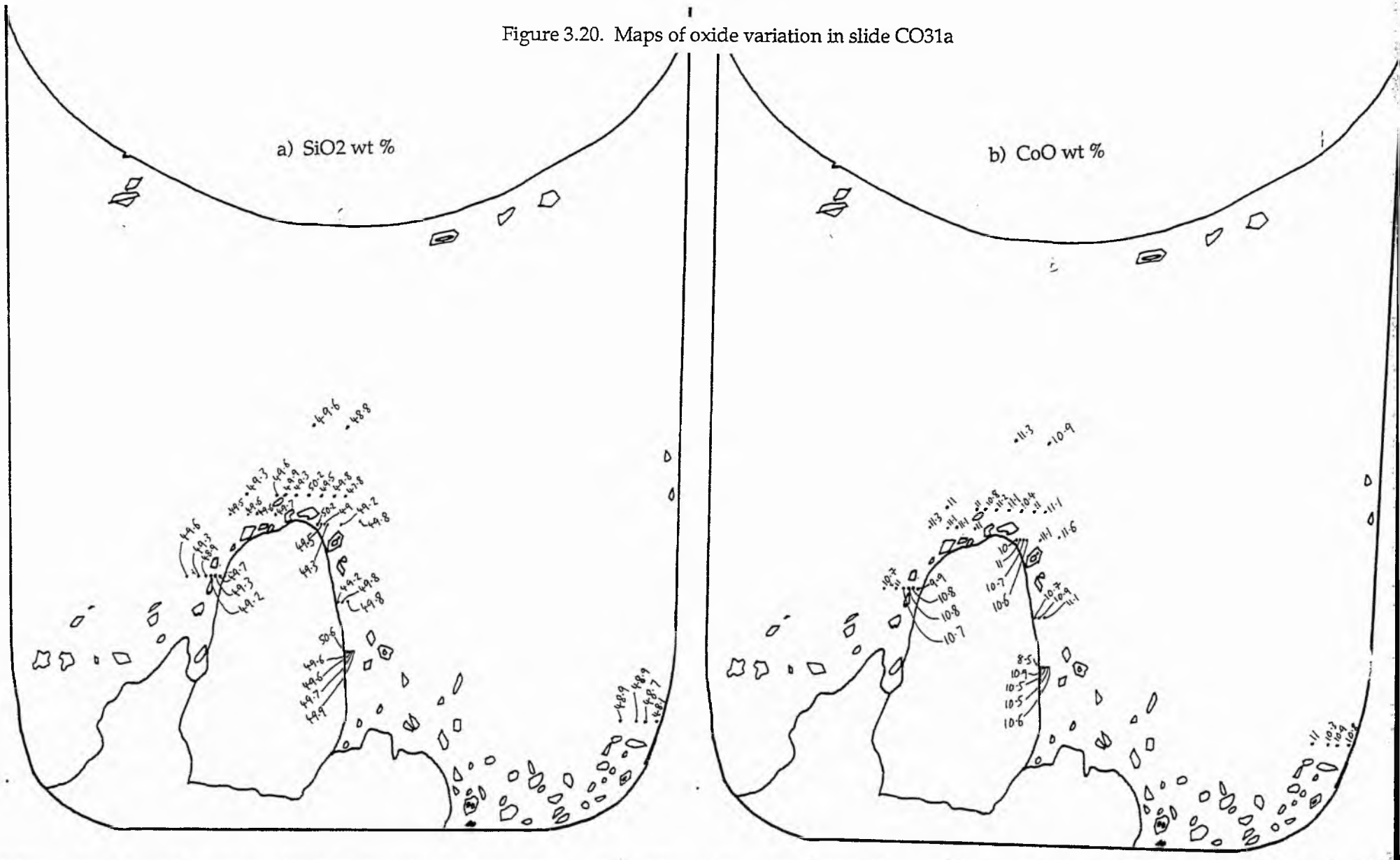

3.20 c) MgO wt %

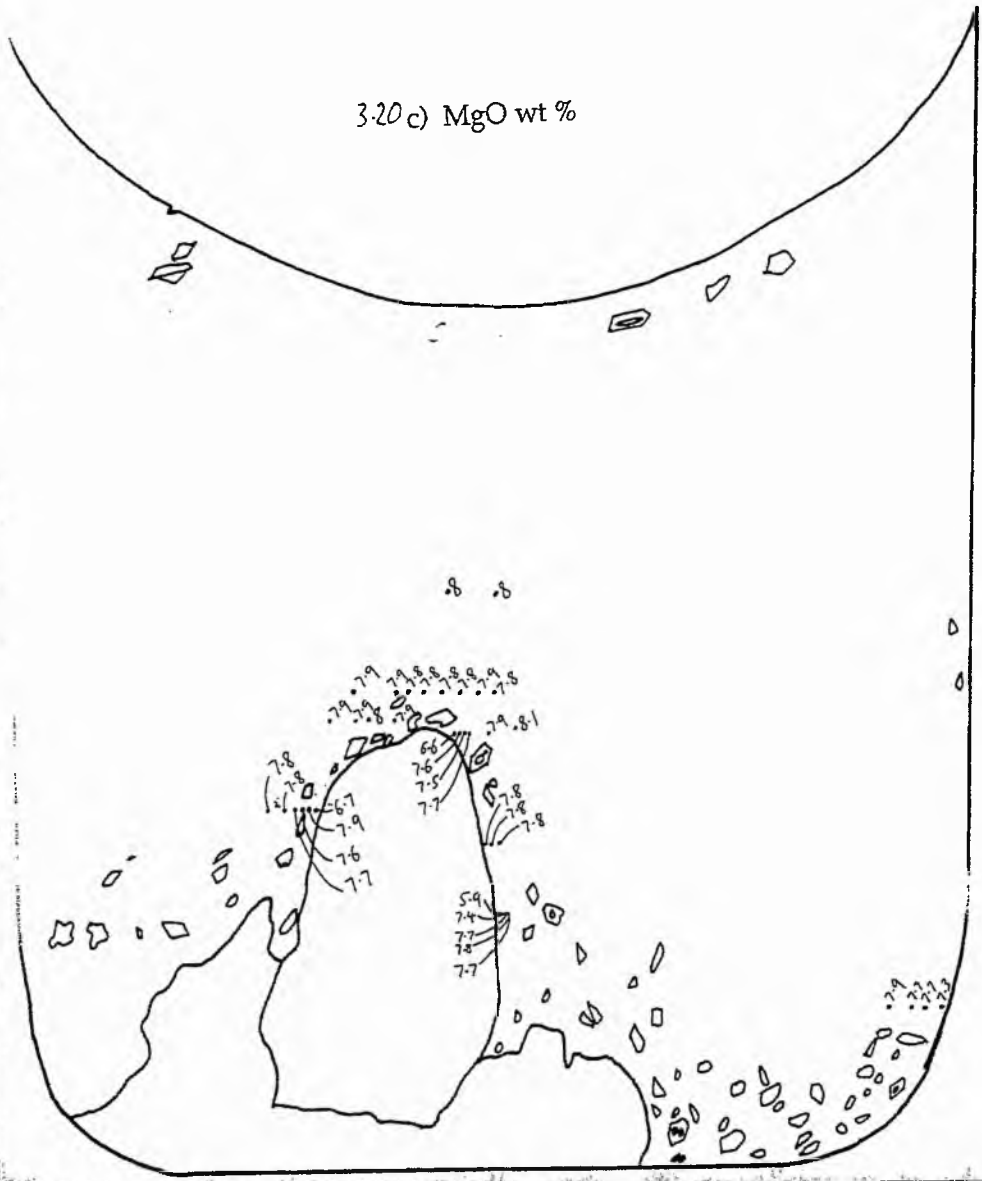
7.9
7.8
7.9
7.8
7.9
7.8

3.20 d) Al2O3 wt %

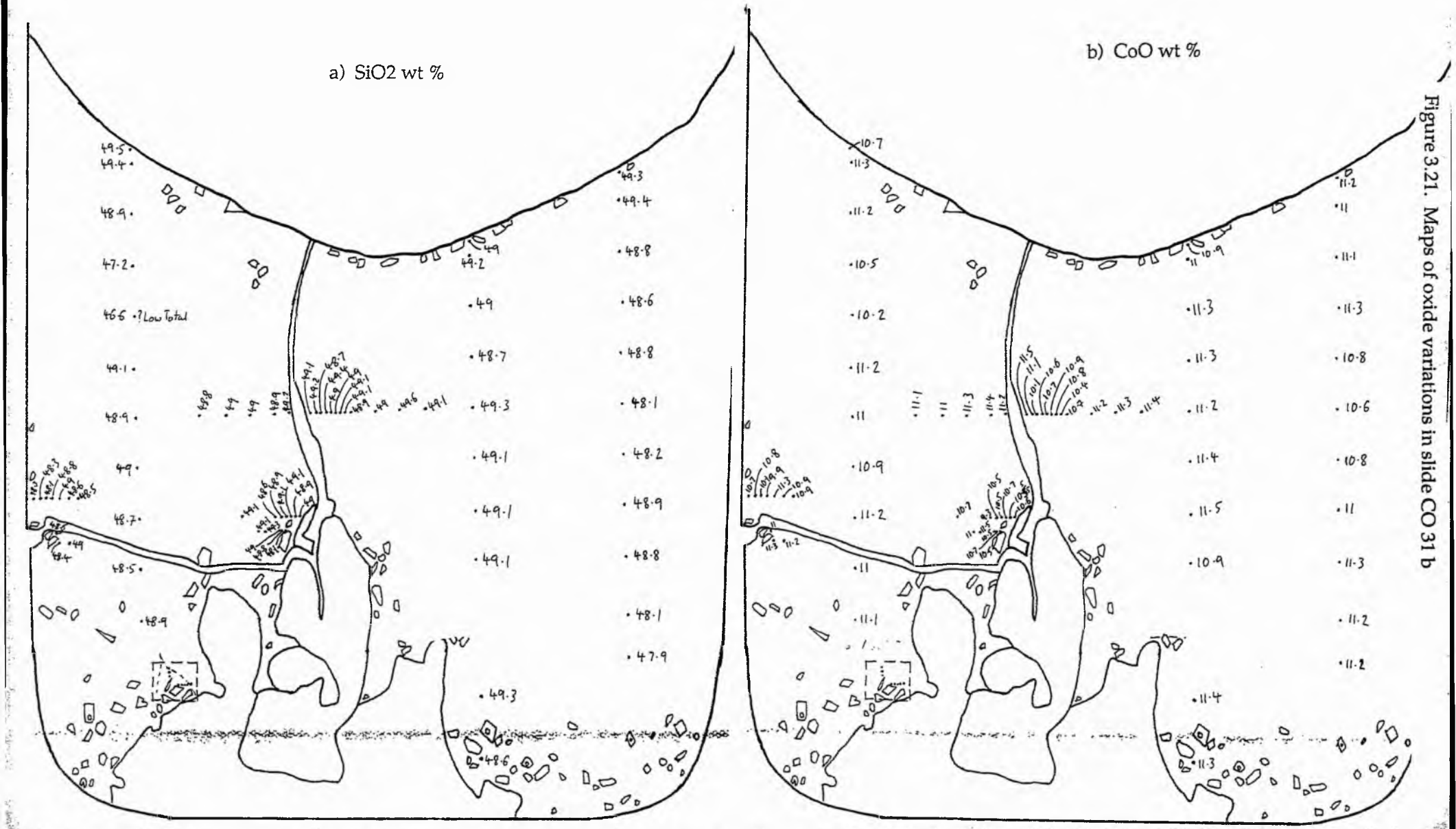

Figure 3.21. Maps of oxide variations in slide CO 31 b

c) MgO wt %

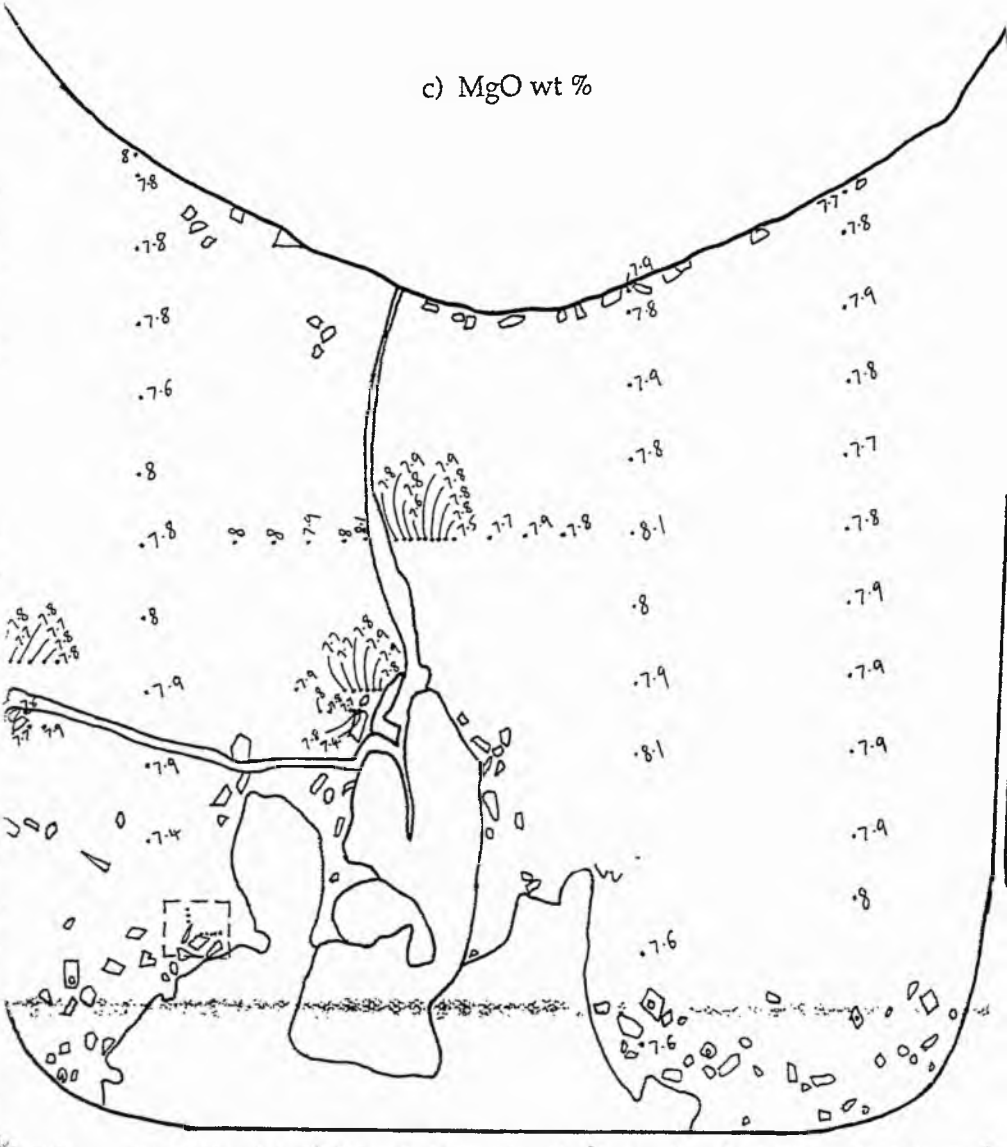

d) Al2O3 wt %

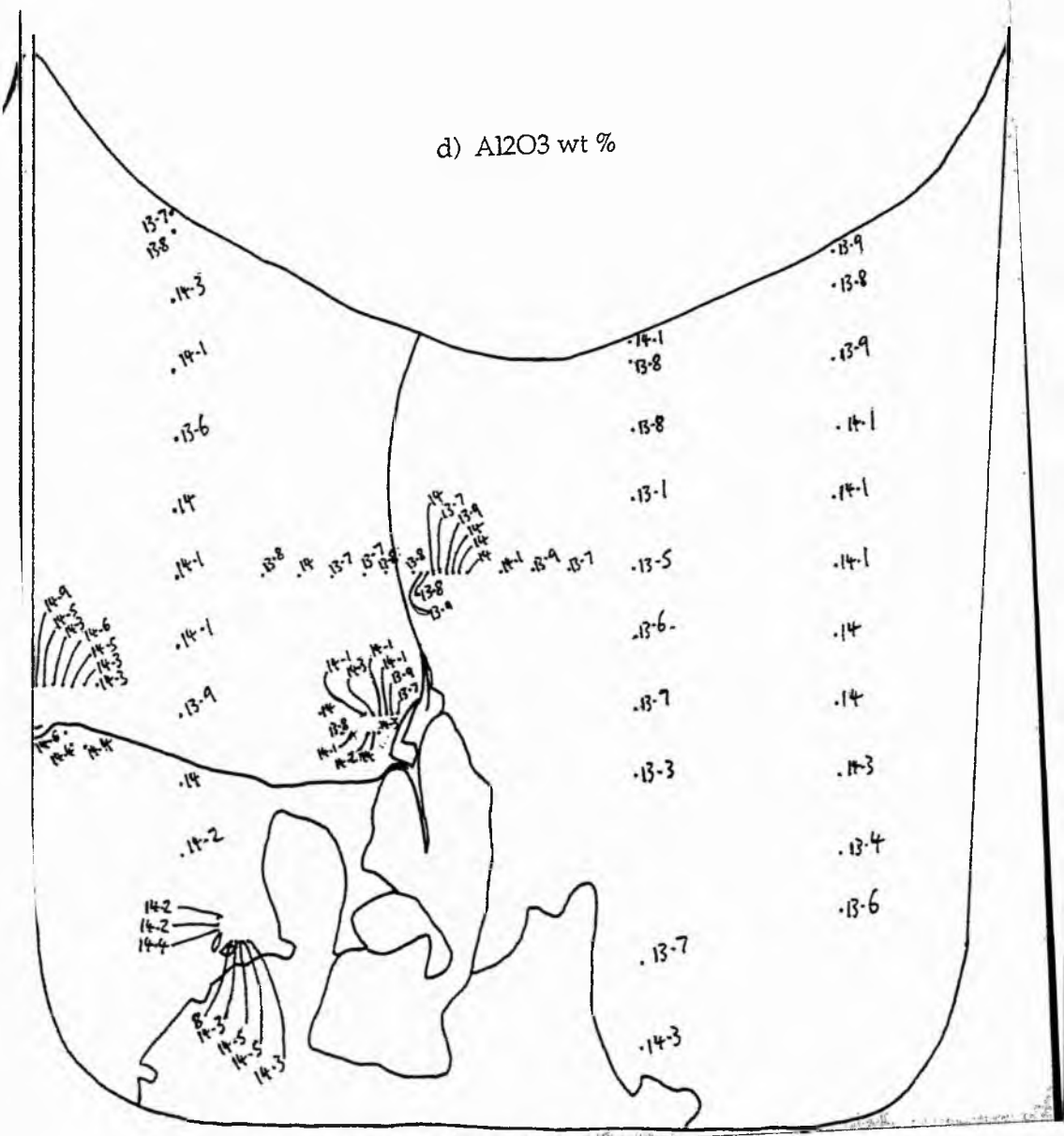

From X-ray count-rate data (maps and graphs in figures 3.22 and 3.23)

- There are signs of slight depletion of CoO- and MgO in glass below the lowest part of the meniscus (track 10. see left side of figure 3.22b), however other vertical tracks (9, 11, 20, 14, 15, 16, and 17) show a stronger depletion in CoO in the uppermost parts of this experimental charge beneath the higher points of the meniscus. In the top 3mm CoO concentration drops from 11.0 wt % to 10.4 wt % and MgO falls from 8.0 wt % to 7.6 wt % (falls of 5.4% and 7.6 % respectively).
- The glass in the lowermost 3mm of the charge is depleted in CoO (3 %) and MgO (4.5 %) (track 9). This could be caused by CoO and MgO being preferentially taken out of the melt by crystallite formation in this area, or by melt dilution by Al_2O_3 dissolution from the cement in the bottom of the charge.
- A plume of pale, bleb-free glass is seen directly above the crystal-seed apex in thin section C-O 31a (see plate 3.29). Tracks 3, 12, and 13 run horizontally across this area and indicate CoO and MgO depletion in the glass across a 1.3 mm wide zone above the crystal apex (see map in figure 3.22a). 0.5 mm above the apex (track 3), depletion occurs over a 2mm wide zone, across which MgO falls from 8.2 wt % to 7.5 wt % (8.5 %), while CoO falls from 11.3 wt % to 10.6 wt % (6.4 %). 1.3 mm above the seed apex (track 13) the depleted zone is only 0.5 mm wide and MgO falls from 8.0 wt % to 7.4 wt % (7.6 %) across it, while CoO drops from 11.2 wt % at the edges to 10.2 wt % (18 %) at its centre.
- CoO and MgO are depleted in glass across a narrow boundary layer next to the olivine overgrowth (tracks 2 and 4). MgO falls from 8.0 wt % to 6.1 wt % (a fall of 15 %) across a zone 45 microns wide, while CoO drops from 11.3 wt 5 to 9.2 wt % (a fall of 19 %) across a much narrower zone (25 microns wide).
- CoO and MgO depletion is also seen next to an olivine crystallite (tracks 1, 2, 5, 6, and 7). Again the depleted layer is narrow, and is narrower for CoO than it is for MgO (30 microns as opposed to 50 microns). Tracks 5, 6, and 7 also indicate that there is no sudden compositional change between glass which contains metallic blebs, and glass which does not. Above this crystallite (near tracks 5, 6, and 7) there is a general increase in CoO and MgO concentration with increasing distance from the interface.
- CoO and MgO depletion, and Al_2O_3 enrichment are detected close to the crucible walls (track 4).
- Across the olivine overgrowth (track 21), concentration of MgO increases and CoO decreases with increasing distance from the crystal-glass interface.

Figure 3.22 a (i) Map of Co concentration in glass above the olivine crystal apex in CO 31. Note the areas of Co depletion derectly above the seed apex

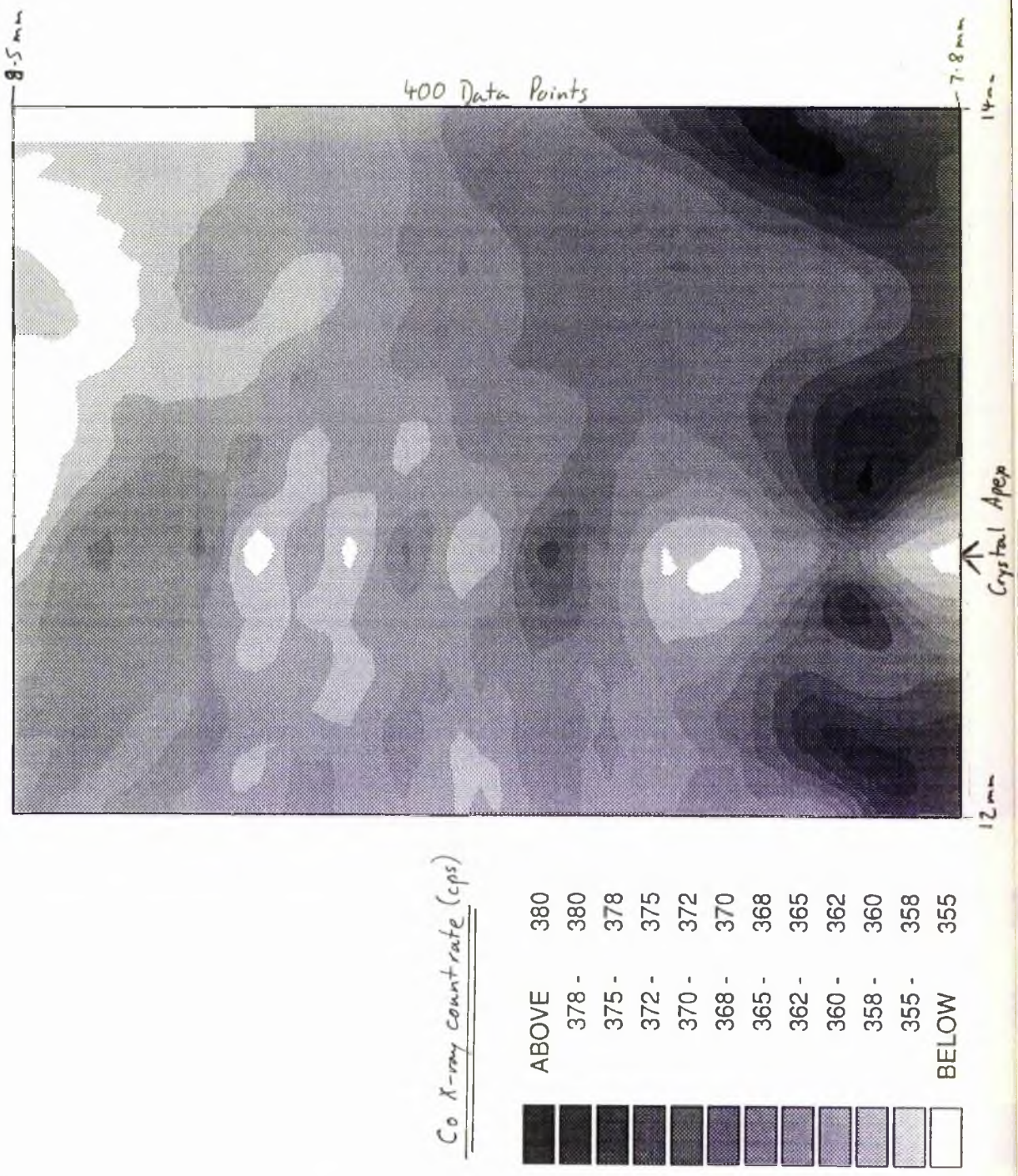

Figure 3.22 a (ii) Map of Mg concentration in glass above the olivine crystal apex in CO 31. Note the areas of Mg depletion directly above the seed apex

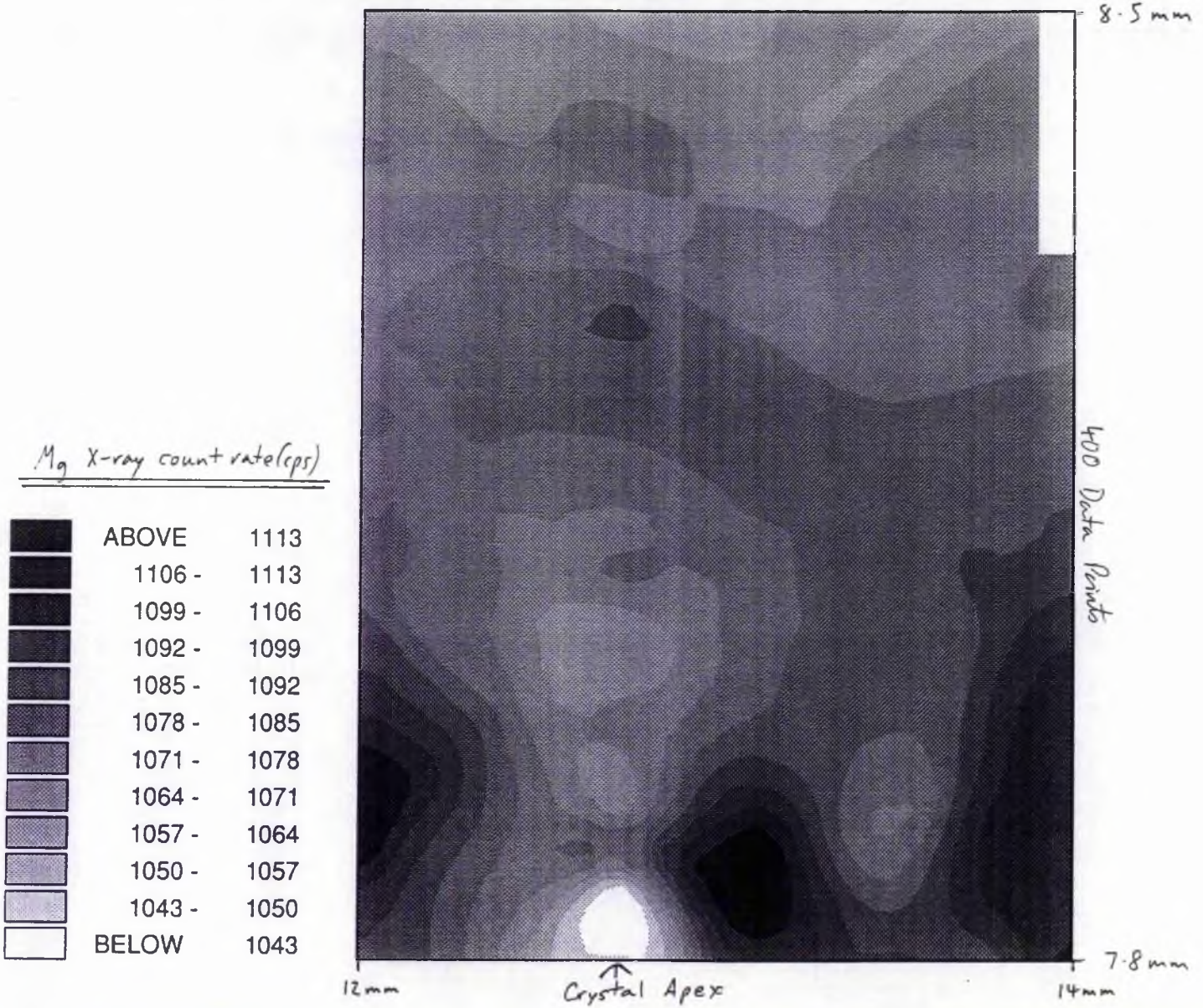

Figure 3.22b (i). Map of Co concentration in glass beneath the meniscus in CO 31.
Note that the lowest concentrations are in the highest parts of the crucible.

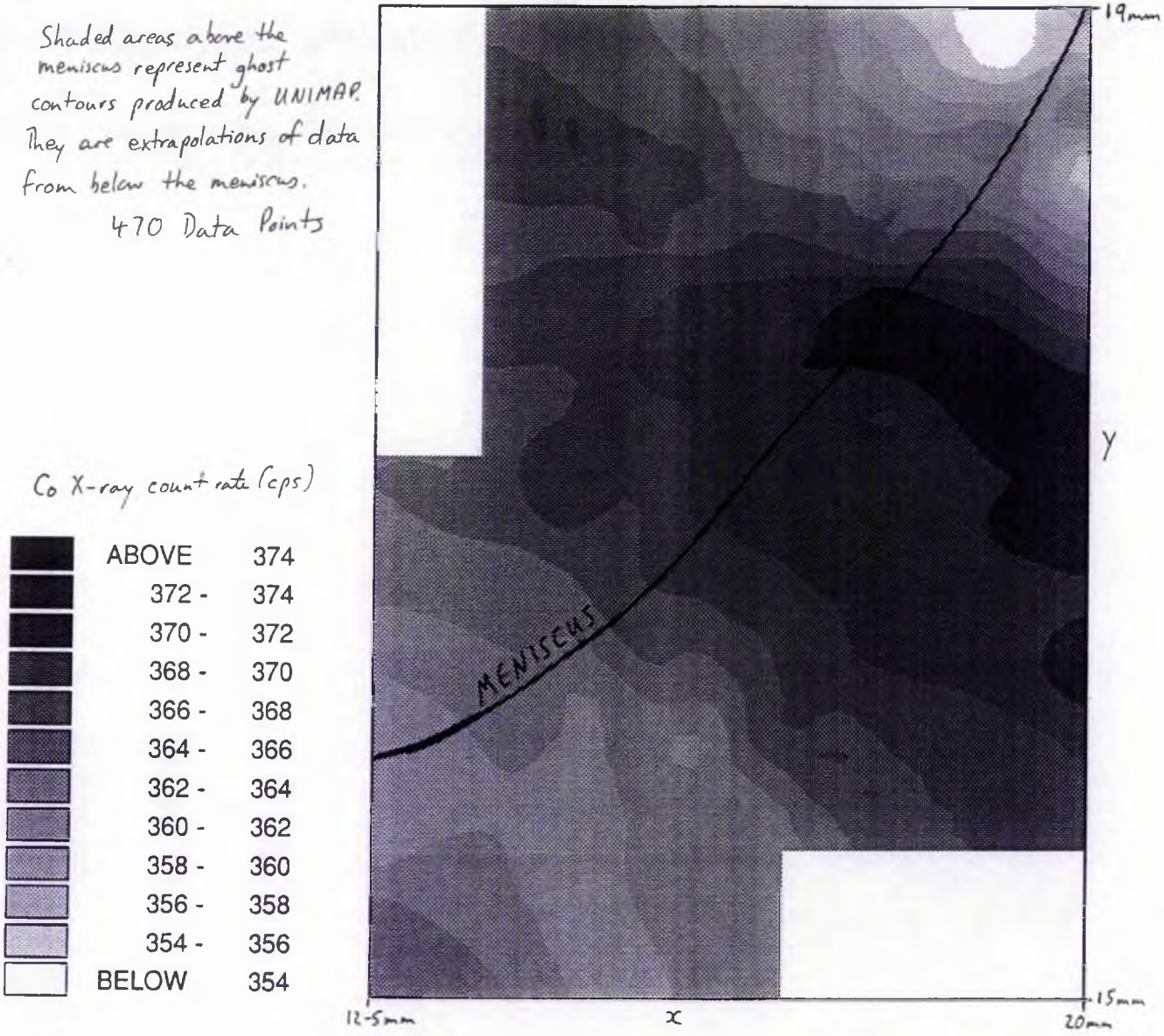

Figure 3.22b (ii). Map of Mg concentration in glass beneath the meniscus in CO 31. Note that the lowest concentrations are in the highest parts of the crucible.

See note on previous page. for explanation of contours above meniscus.

470 Data Points

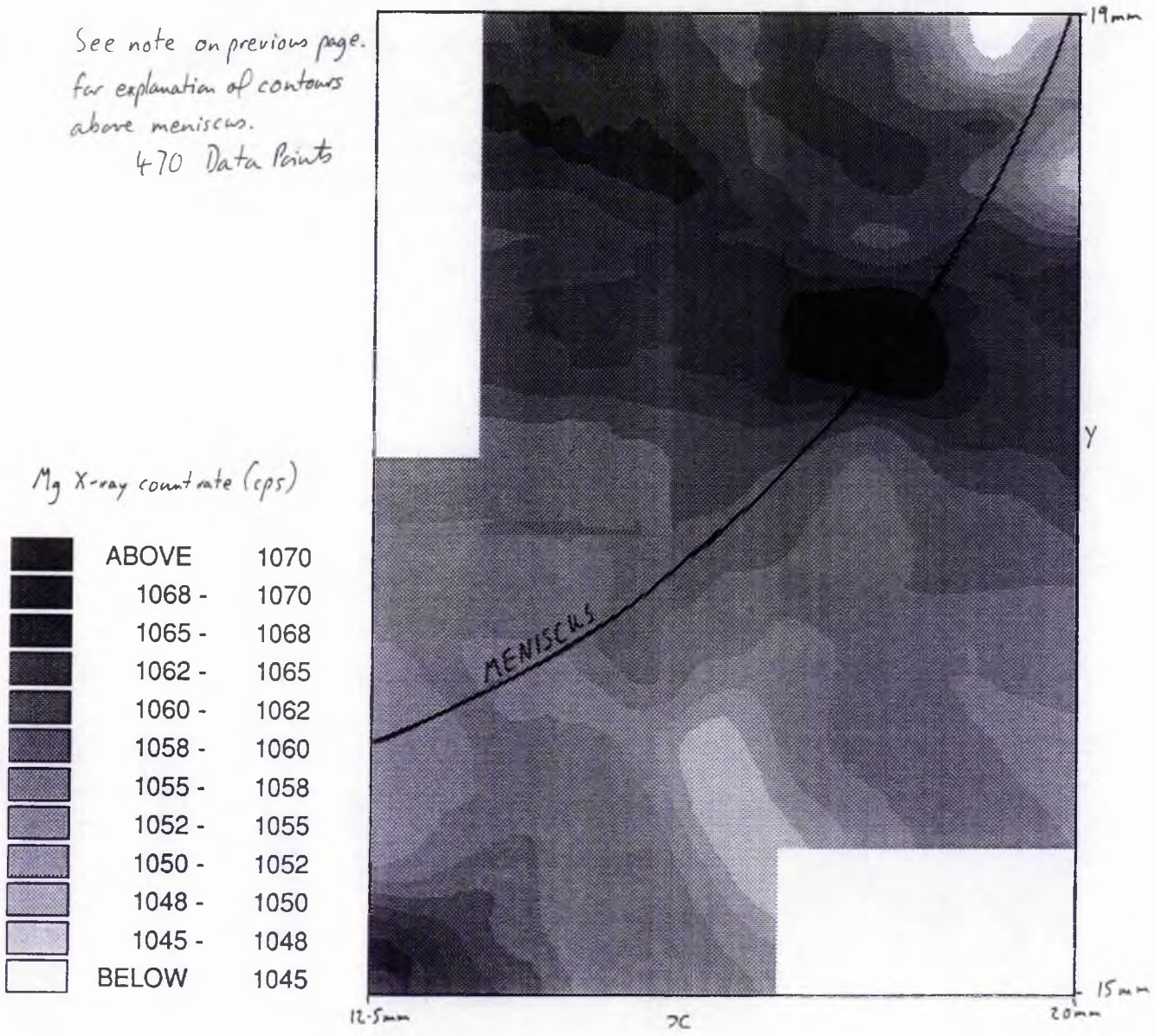

Figure 3.22c. Co variation in the glass directly beneath the meniscus in CO 31 (track 4), showing a slight drop in Co count rate at the top (right hand side of the graph).

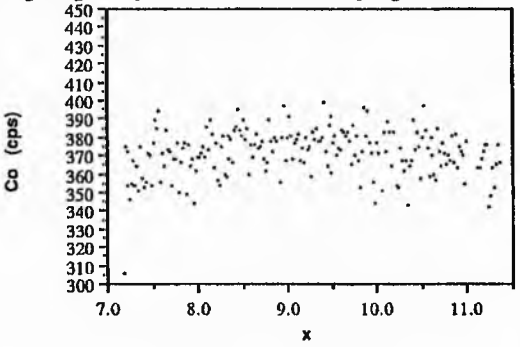

Figure 3.22d. Mg variation beneath the meniscus of CO 31 (track 4), showing a slight drop in Co concentration towards the top (right hand side).

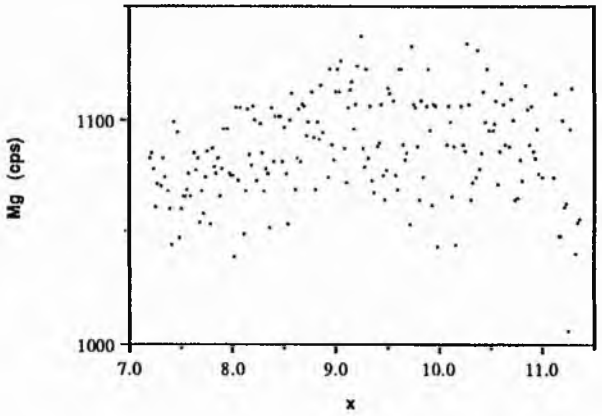

Figure 3.22e. Y vs Mg and Co count rates from track 14 in CO31. The track runs horizontally from the crucible wall (Left) to the olivine seed (right).

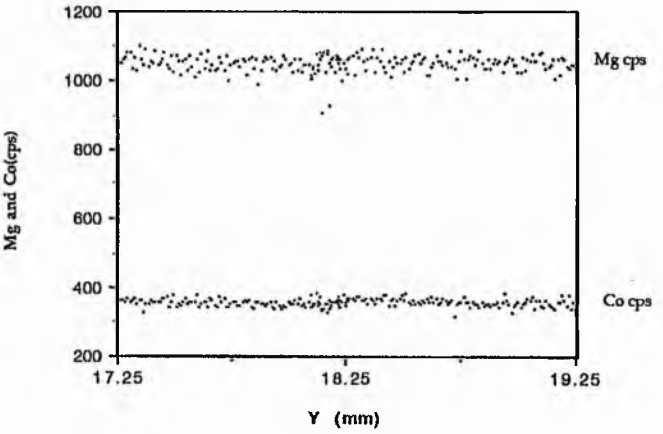

Figure 3.22f. Co and Mg data (cps) from track 15. This shows minimal variation beneath the meniscus.

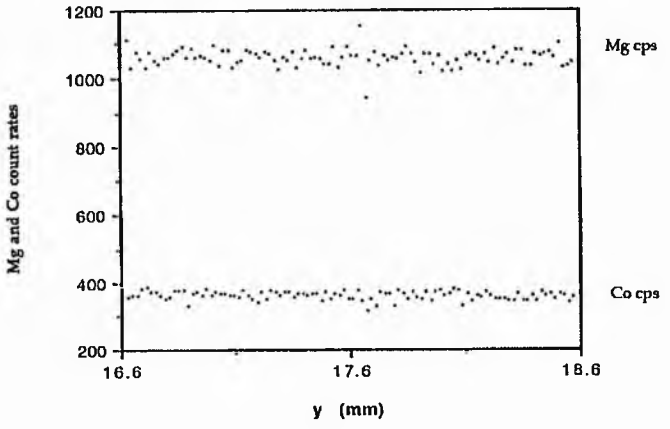

Figure 3.22g. Y vs Mg and Co count rates from track 16, showing variation beneath the meniscus (right hand side).

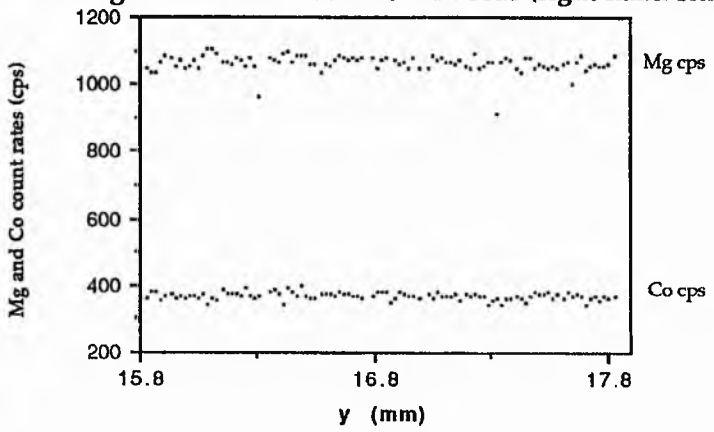

Figure 3.22h. Y vs Co and Mg count rates in track 17.
Showing minimal variation beneath the highest part of the meniscus (right).

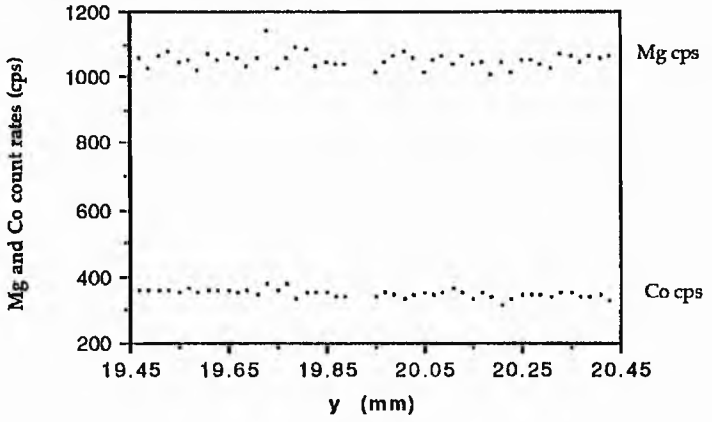

Figure 3.22i. X vs Co and Mg count rates from track 21.
This shows compositional variation across the olivine overgrowth and in the glass at the crystal interface.

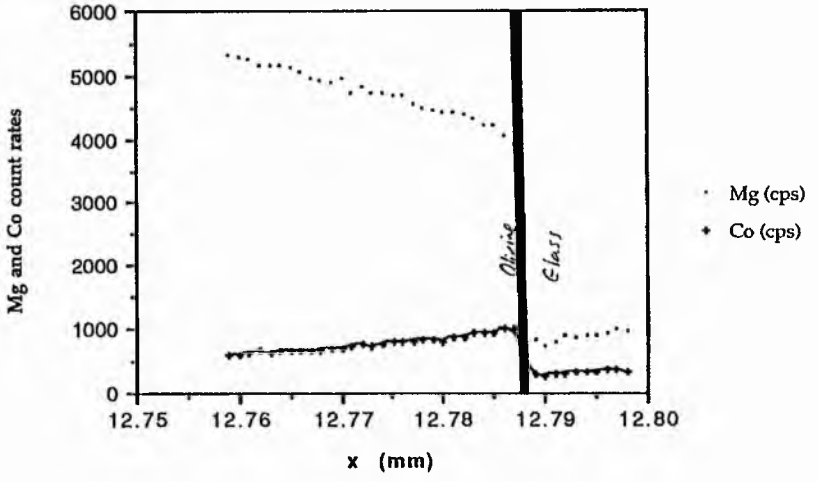

Figure 3.23a. Co variation moving away from the olivine crystallite (left hand side) at the end of track 1 (CO31)

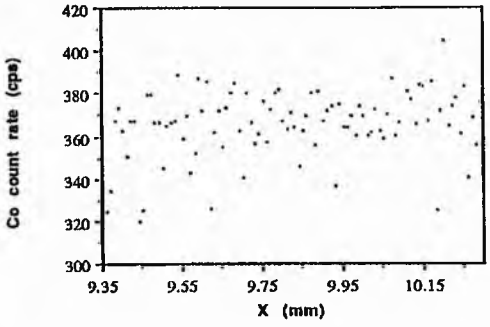

Figure 3.23a. Mg variation approaching the crystallite in track 1 (CO31). Showing the fall in Mg close to the crystallite (left).

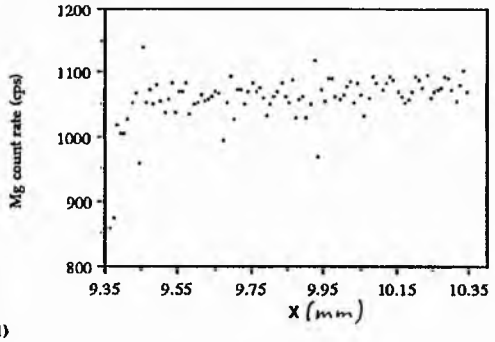

Figure 3.23b. Co variation approaching the olivine overgrowth in track 2 (CO31)

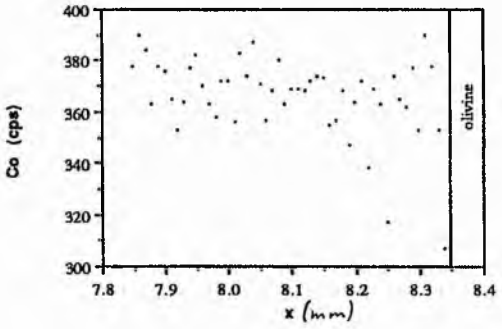

Figure 3.23b. Mg variation approaching the olivine overgrowth in track 2 (CO31)

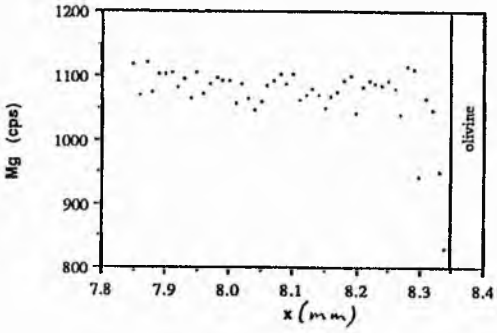

Figure 3.23c. Co variation moving away from the olivine overgrowth in track 5 (CO31)

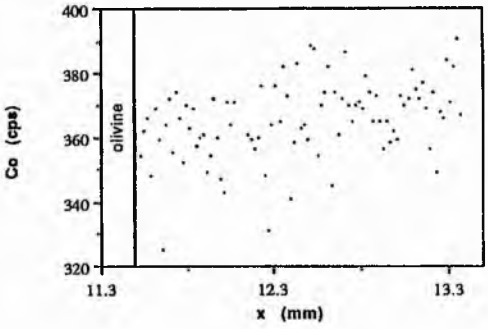

Figure 3.23c. Mg variation approaching the olivine overgrowth in track 5 (CO31)

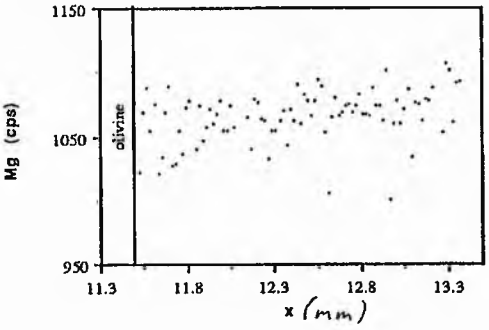

Figure 3.23d. Co variation approaching the olivine crystallite in track 6 (CO31)

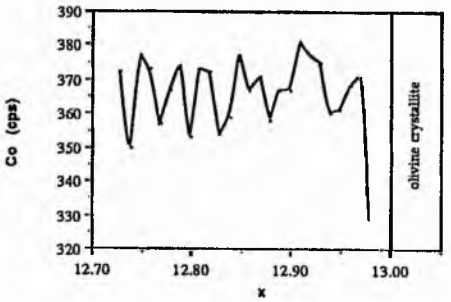

Figure 3.23d. Mg variation approaching the olivine crystallite in track 6 (CO31)

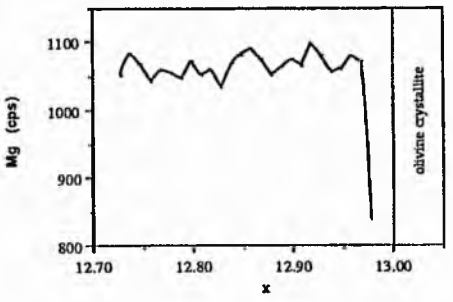

Figure 3.23e. Co variation approaching the olivine crystallite in track 7 (CO31)

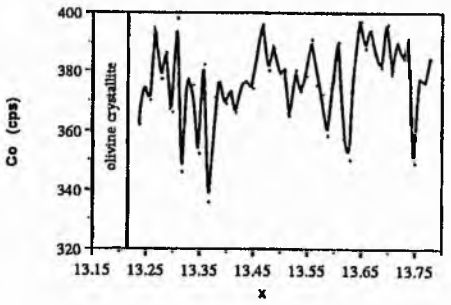

Figure 3.23e. Mg variation approaching the olivine crystallite in track 7 (CO31)

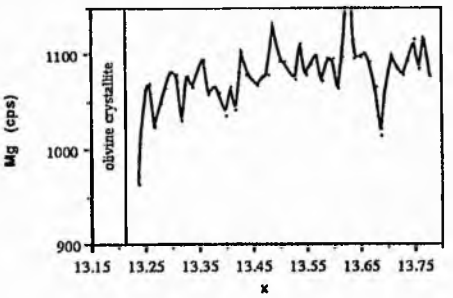

Figure 3.23f. Co variation in the glass above the crystallite in track 8 (CO31)

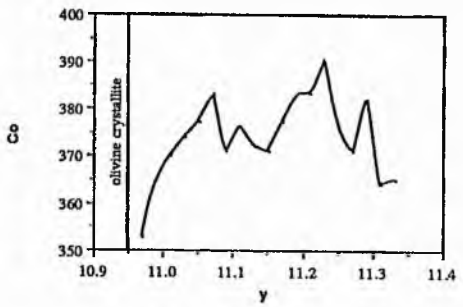

Figure 3.23f. Mg variation above the crystallite in track 8 (CO31)

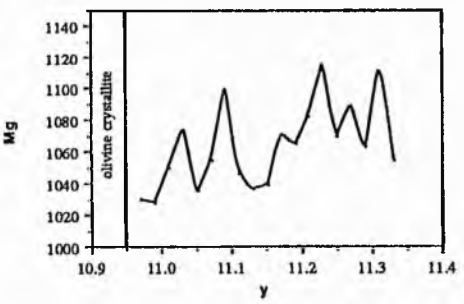

3.6.3d Run C-O 32

The following points can be made from the data in figure 3.24 and 3.25 (see appendix C for full chemical analyses):-

- The data from tracks 1 and 3, directly above the crystal apex, provide no evidence of CoO or MgO depleted melt from a compositional boundary layer convecting above the seed.
- Track 8 shows that MgO depletion from 8.0 wt % to 5.3 wt % (a fall of 33 %) occurs across glass roughly 40μ from the crystal-liquid interface. CoO is depleted over a narrower distance (30μ), from 10.4 wt % to 8.0 wt % (a fall of 23 %). Across the crystal overgrowth (moving from the glass-crystal interface inwards) MgO increases while CoO decreases (see figure 3.25f). Zonation therefore exists across the olivine overgrowths.
- Data from track 2 show a decrease in CoO and MgO concentrations at the top and bottom of the crucible. The fall at the top is over a 4mm range where CoO falls from 10.7 wt % to 9.8 wt % (8.3 % change), and MgO falls from 7.6 wt % to 7.2 wt % (15 %). Over the lowermost 4 mm of this track, as the bottom of the crucible is approached, a slight drop in MgO is accompanied by a drop in CoO from 7.6 wt % to 6.4 wt % (15 %). These changes are accompanied by a rise in Al_2O_3 concentration in the bottom 4 mm and top 0.75 mm of the track (4 % and 3 % respectively).
- The Co map in figure 3.25 indicates that CoO concentrations fall as the meniscus is approached. SiO_2 also decreases in concentration, as Al_2O_3 increases, over the 4mm towards the top of the charge. One would expect SiO_2-enriched melt to pond at the top of the crucible, as it should be of lower density. The reduced SiO_2 concentration actually observed (figure 3.25e) may be a reflection of the increase in Al_2O_3 (also a low density oxide) with SiO_2 concentration being diluted. Melt depleted in CoO and MgO, and enriched in Al2O3 is less dense than the original melt in these experiments and should therefore rise buoyantly to the upper reaches of the charge. It appears that differentiation of melt, driven by compositional (and therefore density) differences in the melt, has occurred over the 557 hours of this run. This phenomenon is seen better in the graphs than in the map in figure 3.25c.

Figure 3.24. Map of analytical points and tracks in charge CO 32

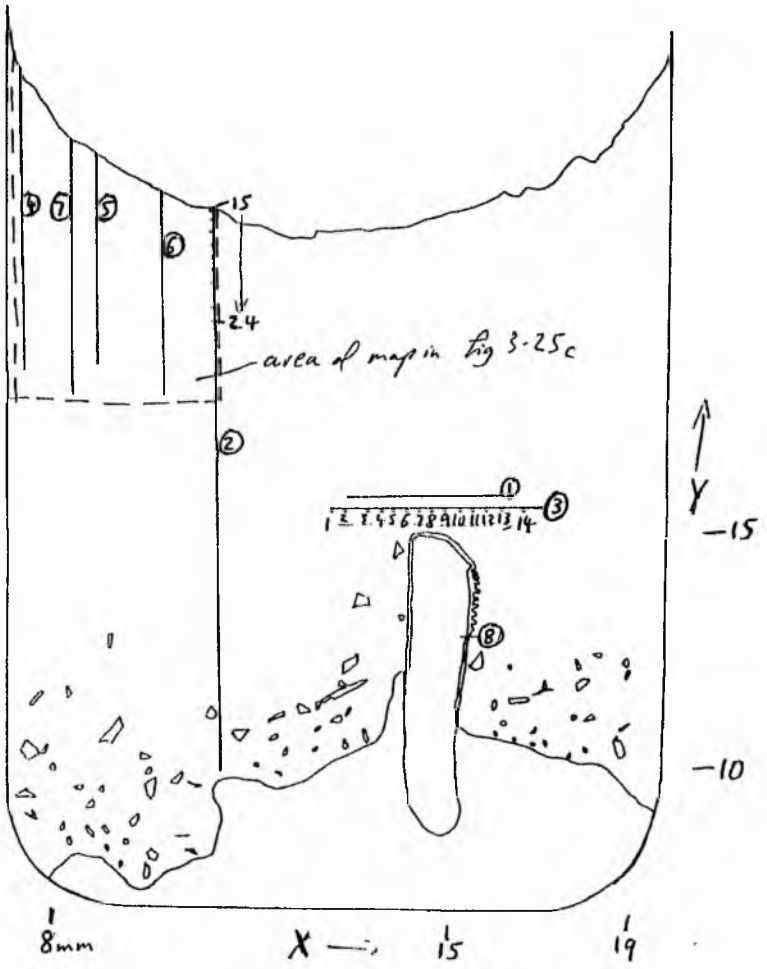

Track details

Number	Points analysed	Interval (μm)	X (mm)	Y (mm)
1	100	30	13.5-16.5	15.4
2	220	50	11	10-21.2
3	200	20	13.2-16.2	15.2
4	120	50	7.2	18-24
5	80	50	8.7	18-22.2
6	160	25	10	17.5-21.5
7	100	50	8.2	17.5-22.5
8	150	2	15.7-16	12.6

Figure 3.25a. Mg count rate data from track 3 in CO 32, showing the lack of compositional variation in the glass above the crystal seed.

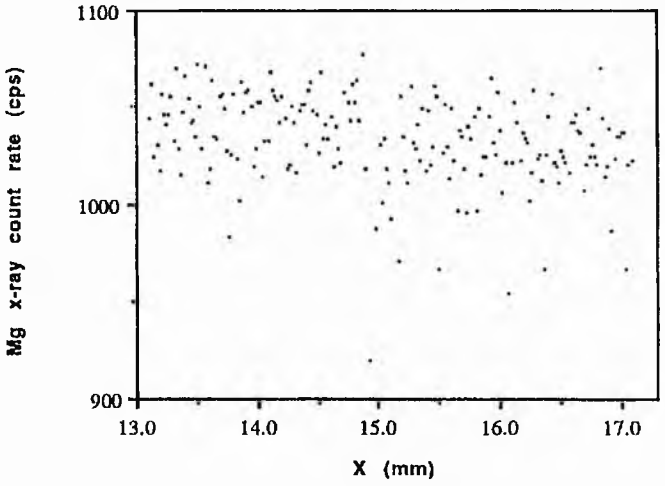

Figure 3.25a. Co data from track 3 in CO 32, showing the lack of compositional variation in the glass above the crystal seed.

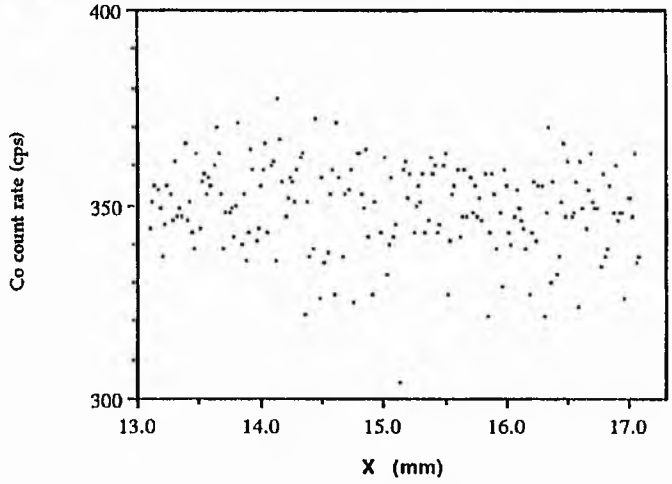

Figure 3.25b. Y vs Al count rate along track 2 of charge C-O32, showing the increase in Al concentration at the top and bottom of the crucible.

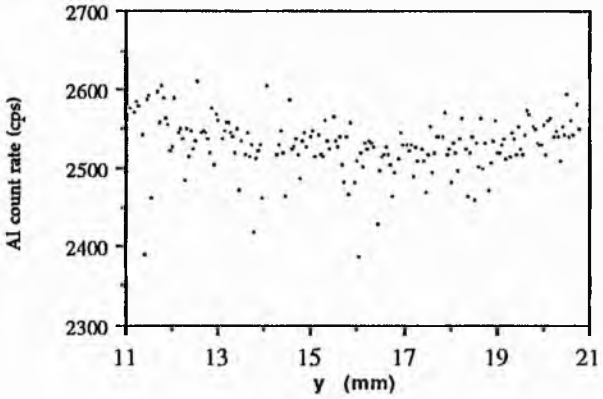

Figure 3.25c. Map of Mg concentration beneath the meniscus in charge CO 32

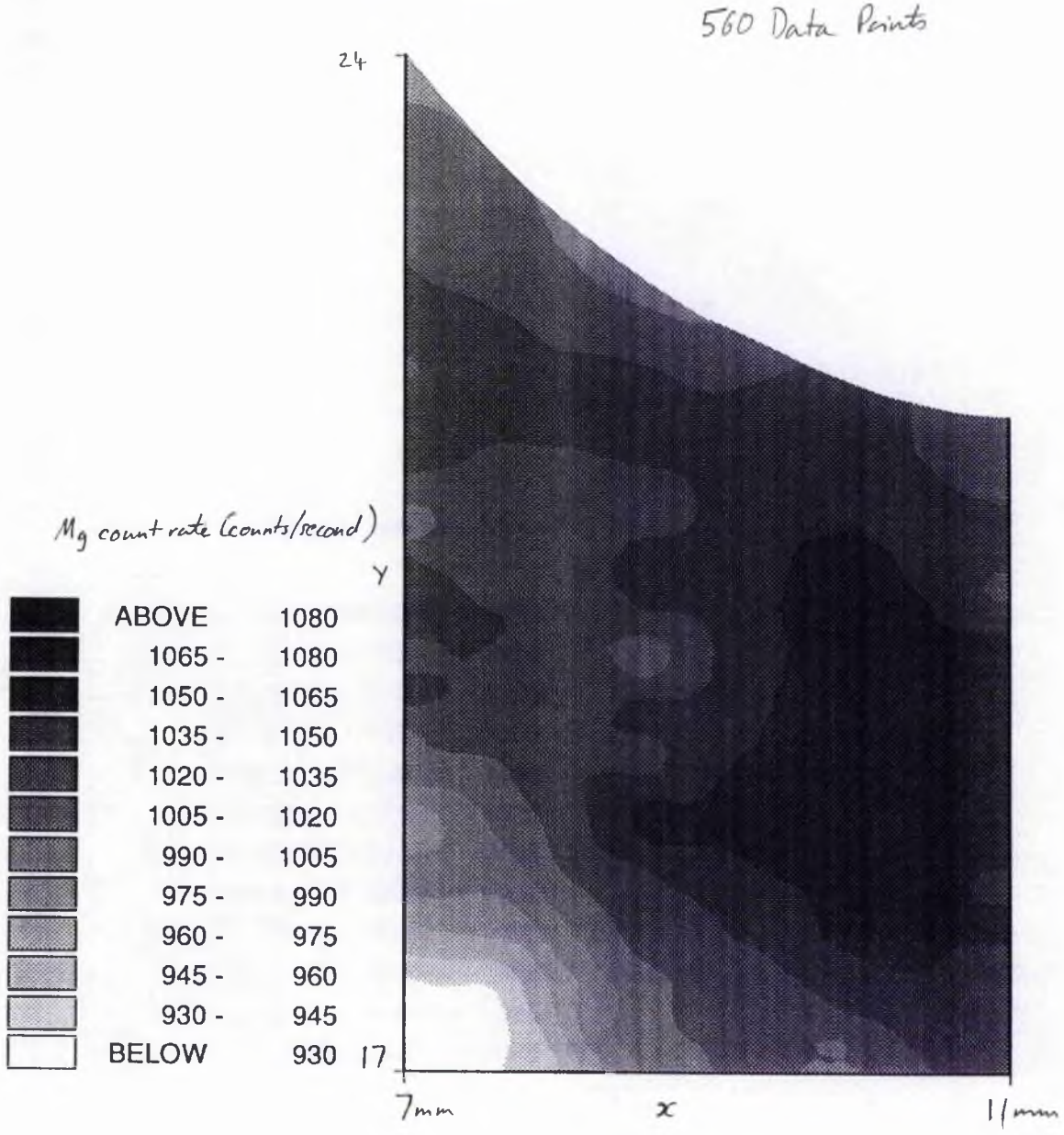

Figure 3.25d. Y vs Si count rate on track 7 in CO 32, indicating a drop in Si concentration towards the meniscus (right edge of graph).

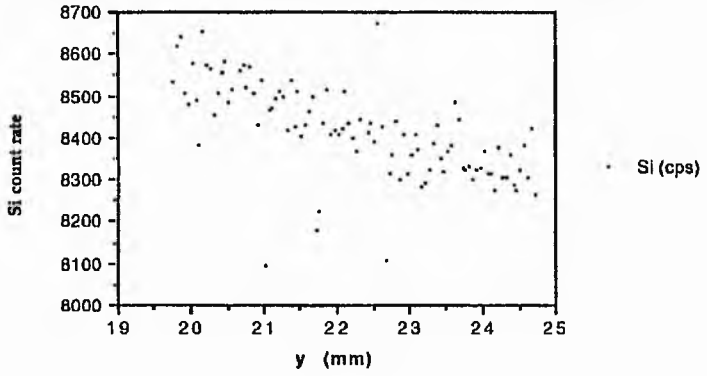

Figure 3.25e. X vs Co and Mg count rates across the olivine overgrowth and its' adjacent glass.

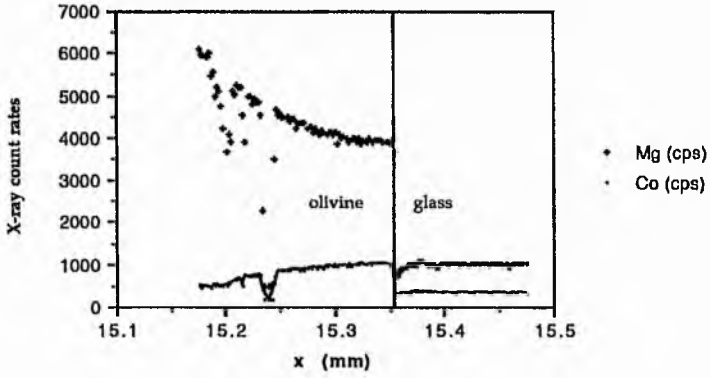

Figure 3.25f. CoO variation approaching the meniscus in CO 32

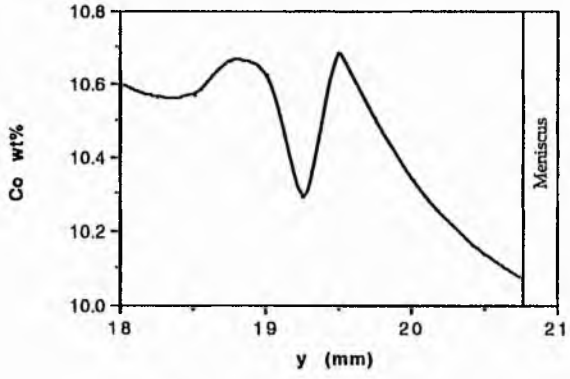

Figure 3.25g. MgO variation approaching the meniscus in CO 32.

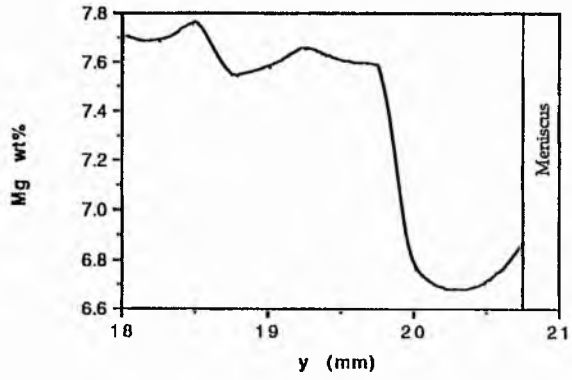

3.6.3e Run C-O 35 (figures 3.26 and 3.27)

- In the olivine overgrowth MgO increases while CoO decreases as the overgrowth is traversed towards the original seed.
- A narrow zone of CoO and MgO depletion is evident at the overgrowth-liquid interface. MgO falls by 26% (950cps to 700 cps) over a 20μm-thick zone, while CoO falls by 26% (350cps to 260cps) over a 10μm-wide zone.
- Track 1 shows no evidence of a buoyant plume of CoO- and MgO-depleted melt rising this far above the crystal apex. Also, the bubble visible in thin section does not appear to have been responsible for dragging boundary layer melt away from the apex by surface-tension-driven convection.
- There is a slight decrease in CoO and MgO towards the crystal apex in track 3, 3.7% for CoO and 2.8 % for MgO.

Figure 3.26. Positions of analytical tracks in CO 35

Track details

Number	Points analysed	Interval (μm)	X (mm)
1	100	20	9-13.5
2	140	2	10.9-11.17
3	120	10	11.36-12.56

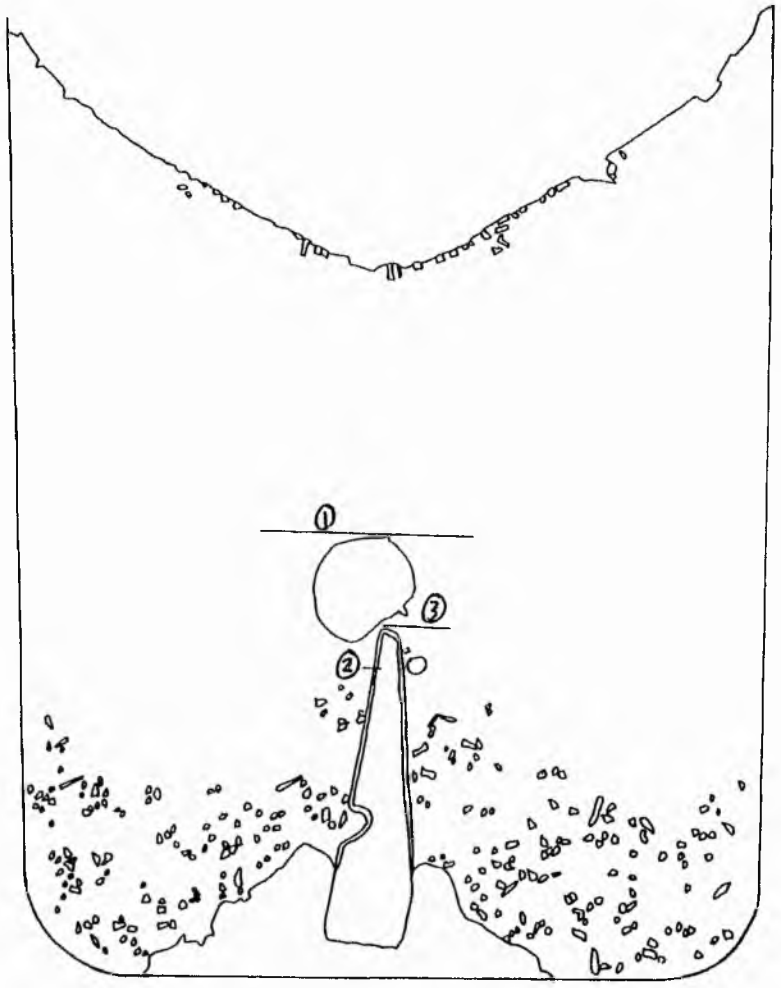

Figure 3.27a. X vs Co and Mg count rates from track 1 of CO 35, showing a lack of depletion above the crystal seed.

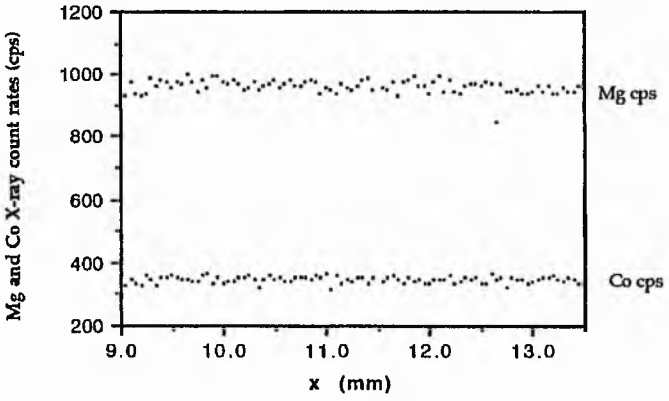

Figure 3.27b. X vs Mg and Co count rates from track 3 in CO-35.

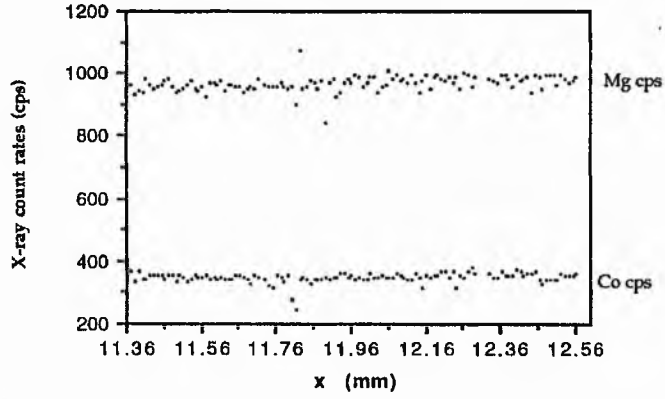

Figure 3.27c. Co and Mg count rates across the olivine overgrowth and its' adjacent glass in track 2 from CO 35.

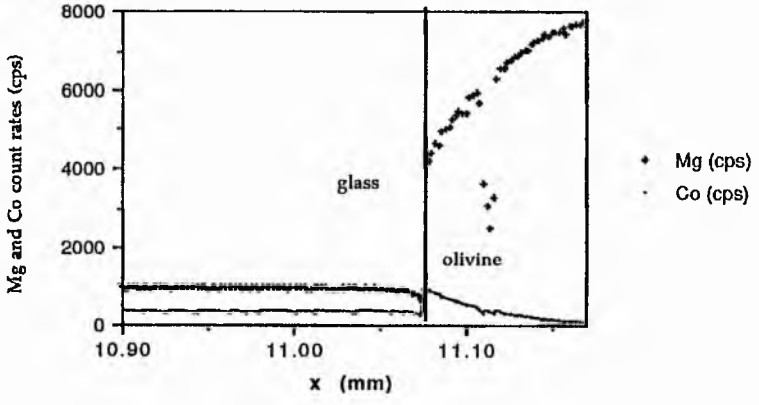

3.6.3f Run C-O 36 (figures 3.28 and 3.29)

- A thin boundary layer, depleted in CoO and MgO, exists adjacent to the pink olivine overgrowth on the seed (Track 7). The boundary layer is only 20μm-wide for both CoO and MgO. CoO falls by 17 % and MgO by 26 % across the layer.
- In track 3 there is an increase in Al_2O_3 concentration in the glass at the bottom of the charge. Alumina-enriched melt is not seen at the meniscus.
- No depletion of CoO or MgO is detected beneath the meniscus (track 4).
- Maps 3.29d and e, comprising data of Co and Mg concentrations respectively from tracks 1, 2, 5, and 6, show clearly an area of glass, directly above the crystal apex that is depleted in Co and Mg. The area of depletion grows wider above the bubble that is seen above the apex of the crystal.

Figure 3.28. Positions of analytical tracks in charge CO 36

Track details

Number	Points analysed	Interval (μm)	X (mm)	Y (mm)
1	120	50	8-14	12.3
2	60	100	8-14	15
3 + 4	90	100	5	6-24
5	56	50	11.3-14	13
6	120	50	8-14	14.5
7	150	10	11.2-12.6	10

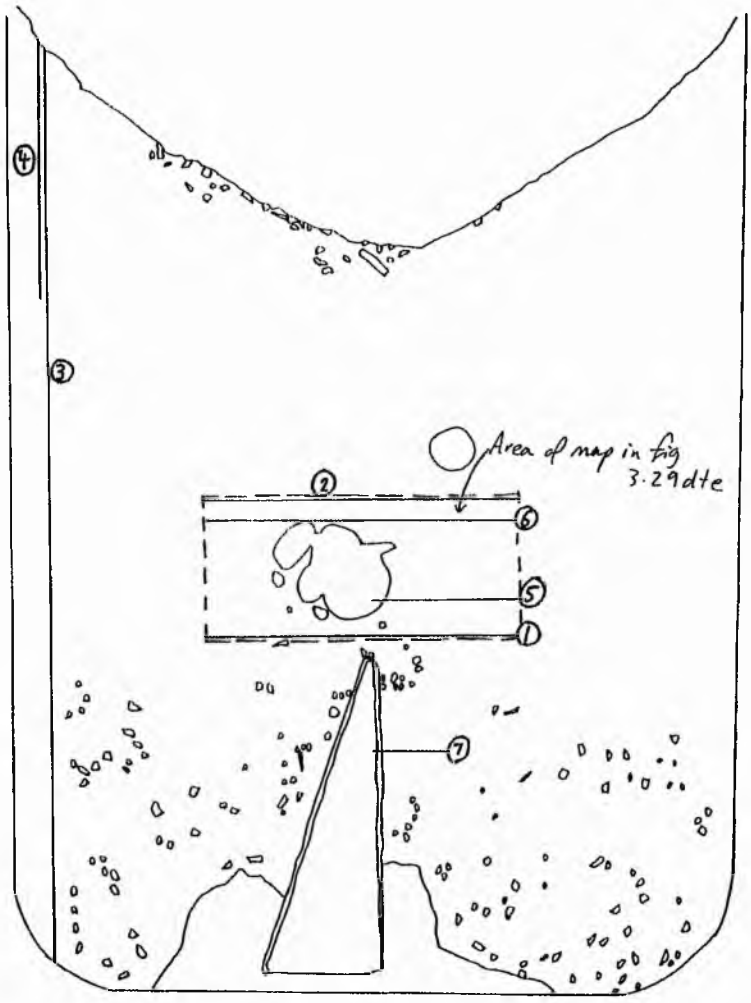

Figure 3.29a. X vs Co and Mg count rates in the glass adjacent to the crystal-liquid interface in track 7 CO36.

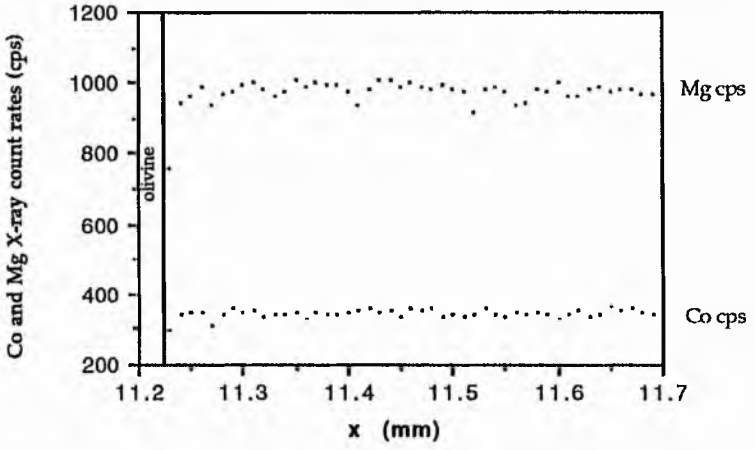

Figure 3.29b. Al count rate variation vertically through the charge CO-36

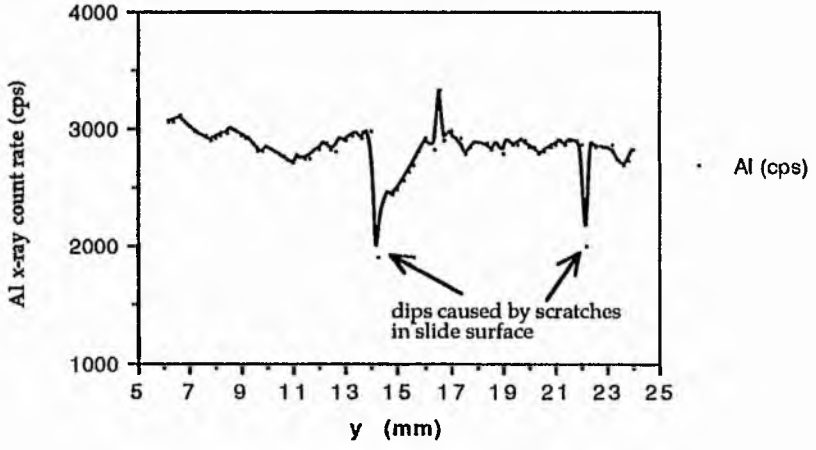

Figure 3.29c. Co and Mg count rate variation beneath the meniscus in track 4 in charge CO-36

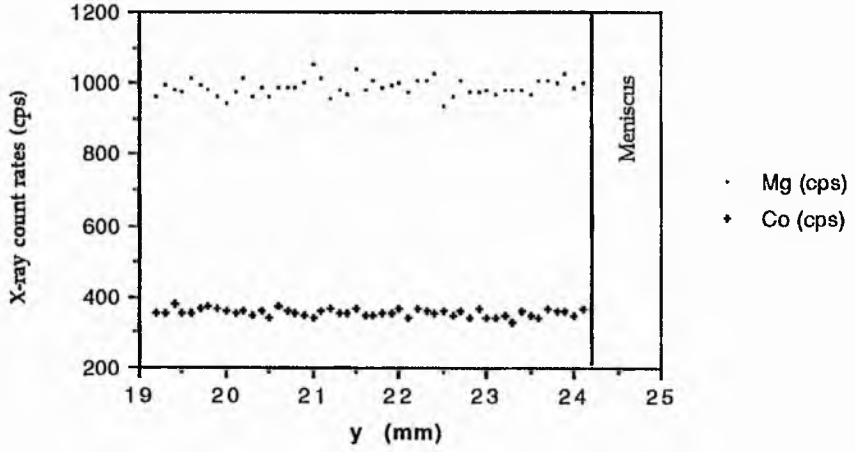

Figure 3.29d. Map of Co concentration above the crystal seed in CO 36

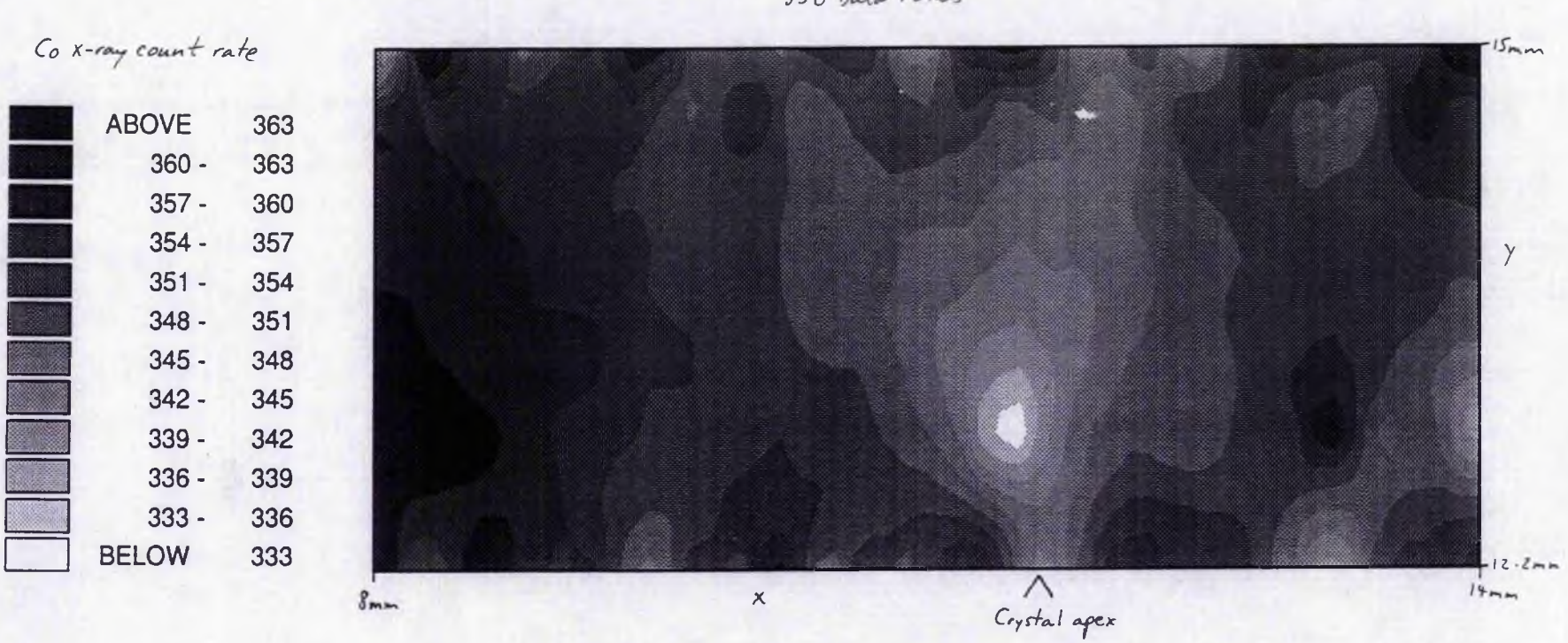

Figure 3.29e. Map of Mg concentration above the crystal seed in CO 36

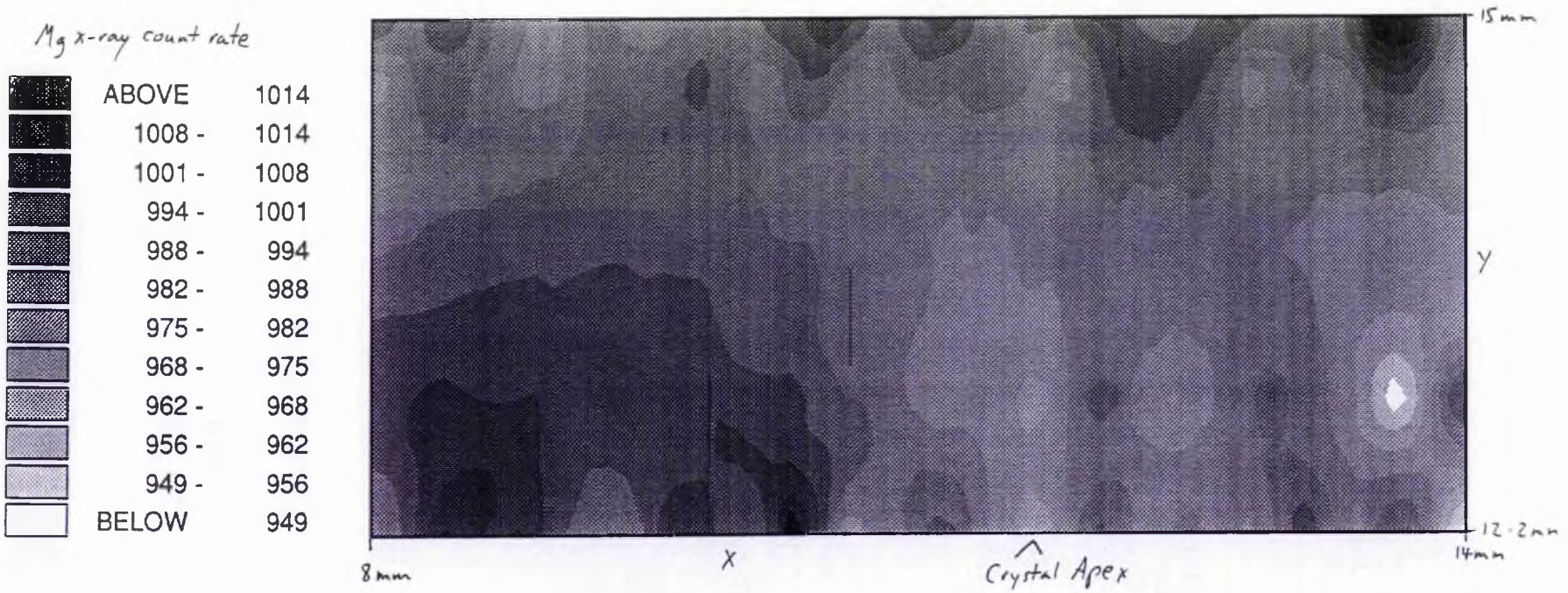

3.6.3g Run C-O 37 (figures 3.30 and 3.31)

- In glass close to the crucible walls Al_2O_3 concentration increases, while that of CoO and MgO decreases.
- Tracks 1, 3, and 4 (maps in figure 3.31b, c, and d) show an area of CoO- and MgO-depleted glass above the crystal apex. This same area also has low concentrations of aluminium.

Figure 3.30. Positions of analytical tracks in charge CO 37

Track details Number	Points analysed	Interval (μm)	X (mm)	Y (mm)
1	120	25	11-14	13.5
3	125	25	11-14	13
4	120	25	11-14	12.6
6	142	100	4.5-18.5	13

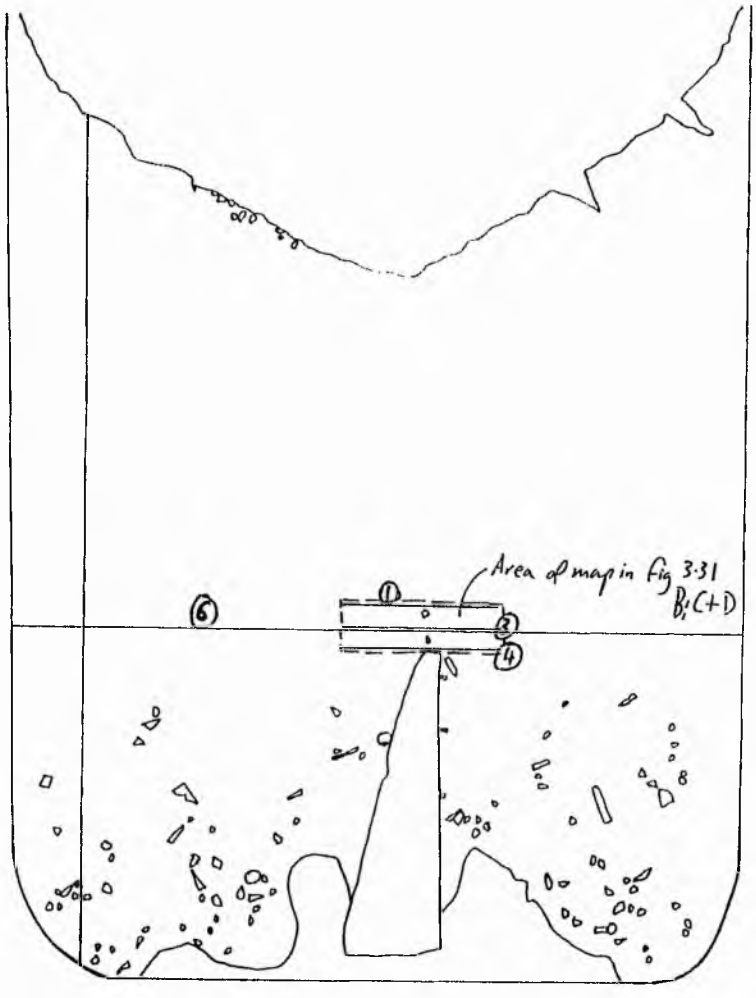

Figure 3.31a. Co, Mg and Al variation across the crucible in track 6 of CO-37

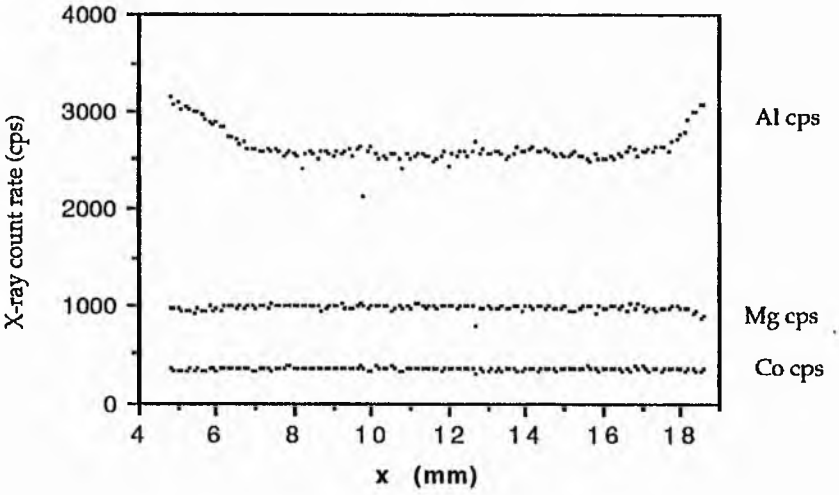

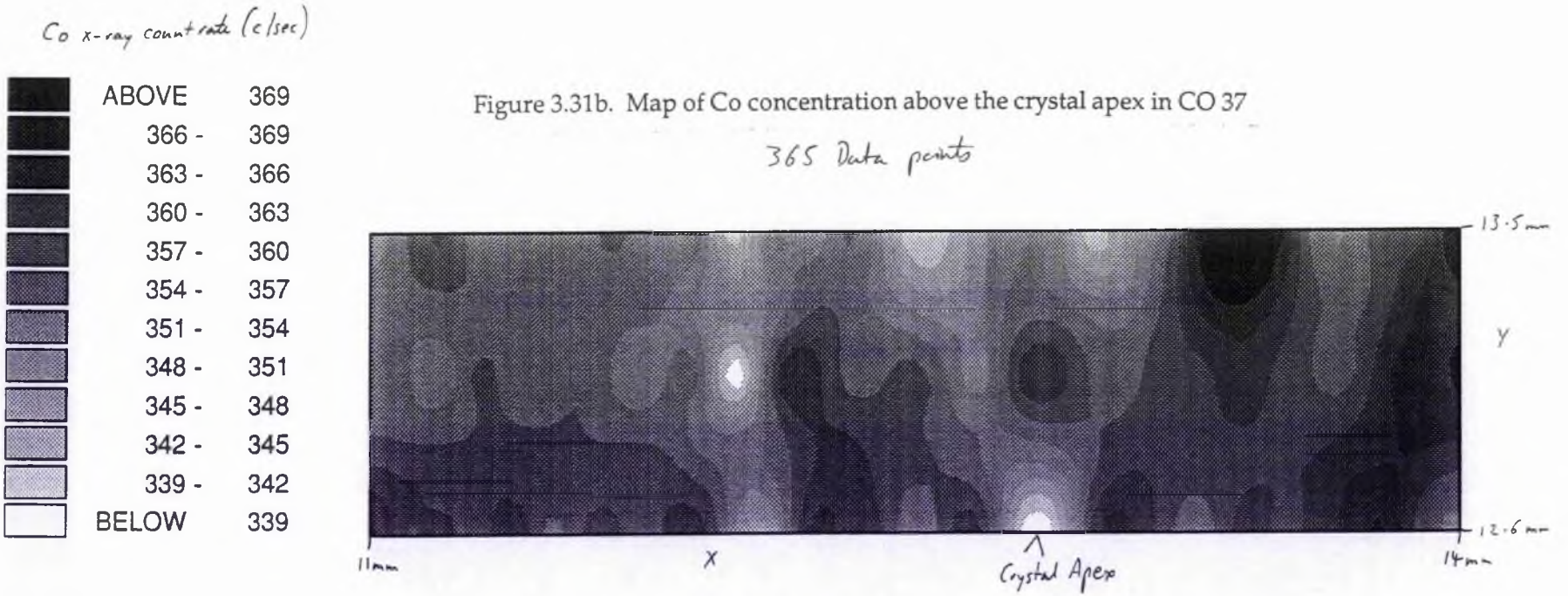

Figure 3.31b. Map of Co concentration above the crystal apex in CO 37

Figure 3.31c. Map of Mg concentration above the crystal apex in CO 37

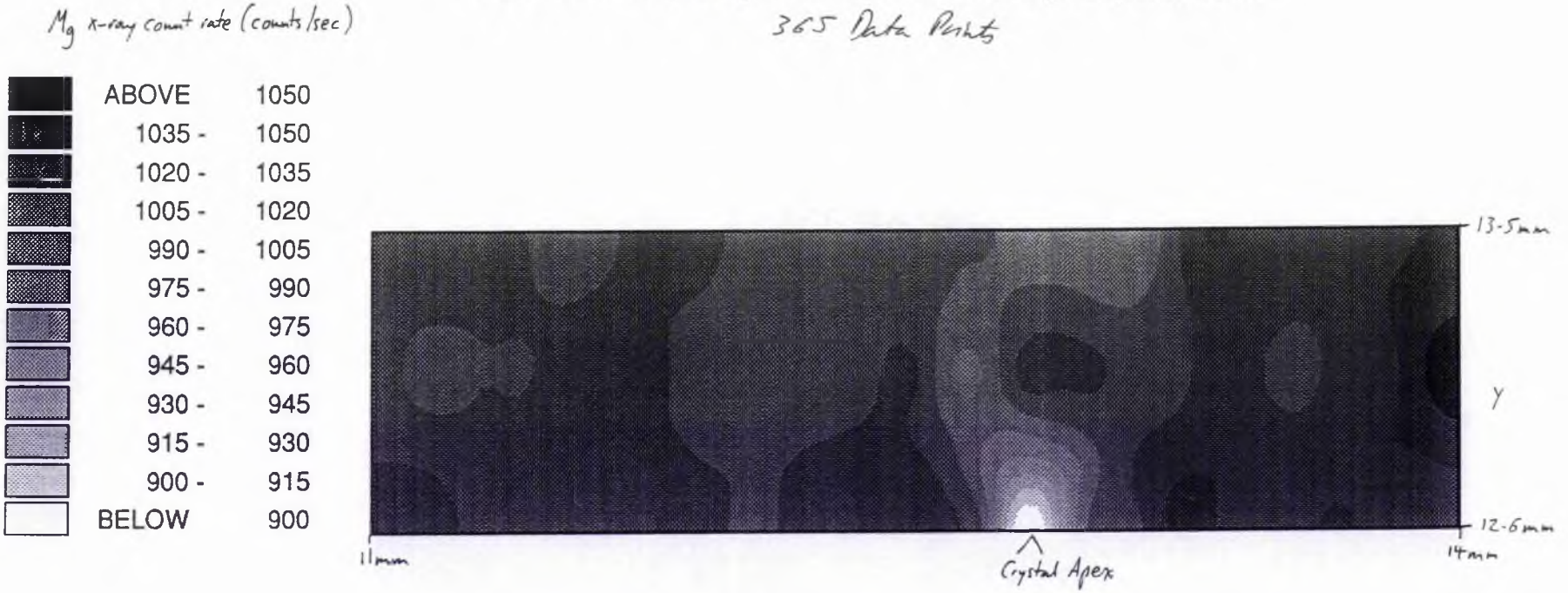

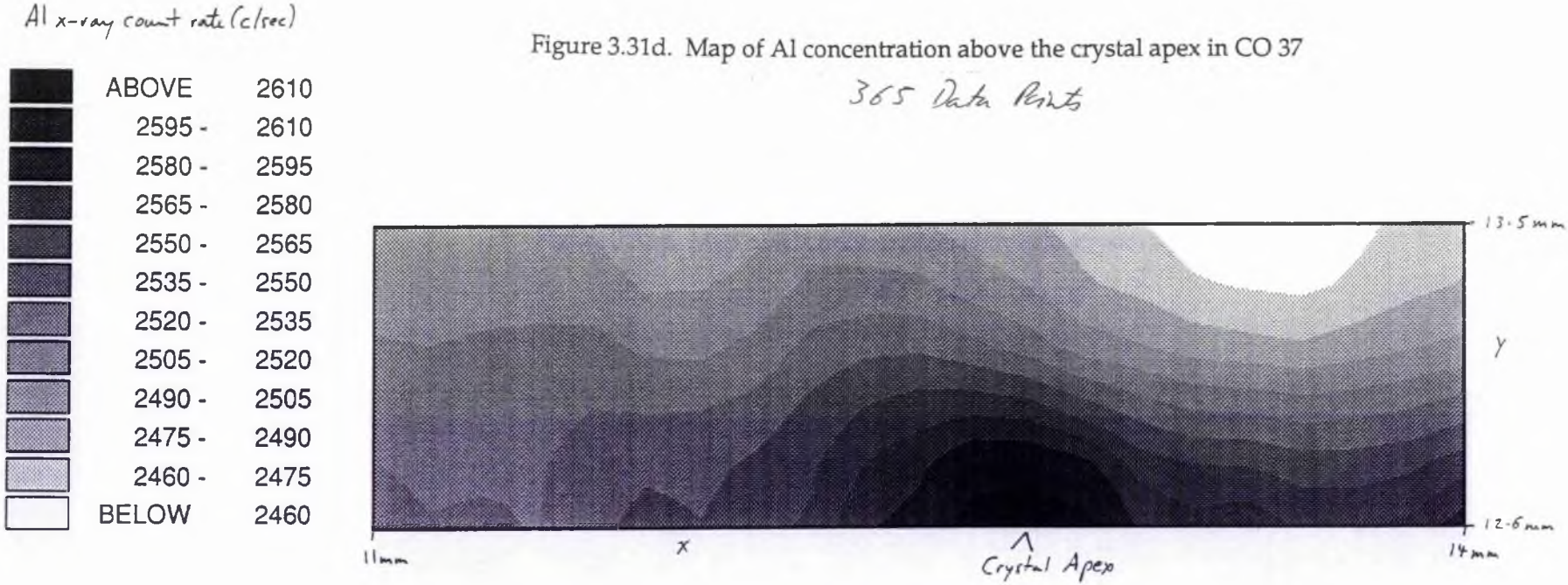

Figure 3.31d. Map of Al concentration above the crystal apex in CO 37

365 Data Points

3.6.4 Summary of results

The following section contains a list of points that summarize the data presented in the preceding section. These are discussed further in section 3.7.

1) Glass that is free of metallic blebs, at the crystal-liquid interface and above the crystal-seed apex, is depleted in CoO and MgO, and enriched in SiO_2. These compositional differences indicate that this melt had a lower density than the original melt in the crucible.

2) Platinum blebs are re-distributed from their original regular distribution in the melt by being incorporated into the crystal overgrowth (possibly by a surface tensional effect). This produces a bleb-free melt at the crystal-liquid interface by 'sucking' the Pt blebs out of the melt. As the overgrowth develops the bleb-free boundary layer becomes depleted in CoO and MgO, making it less dense than the original melt and enabling it to convect buoyantly. The occurrence of bleb-free glass above the seed apex results from the buoyant flow of this boundary layer away from the seed.

3) The compositional boundary layer is depleted in CoO and MgO by upto 25 %. This area of sharp depletion is narrower for CoO than for MgO.

4) In long duration runs vertical, compositional differentiation of melt has occurred. The melt directly beneath the meniscus and near the floor of the crucible is depleted in CoO and MgO, and slightly enriched in Al_2O_3.

5) Density calculations indicate that the CoO- and MgO-depleted, and Al_2O_3-enriched melt has a lower density than the original melt and should therefore be buoyant. This buoyant melt, which is produced in the lower half of the crucibles, is able to migrate to the upper parts of the charges. Clearly the low melt viscosity (around 200 poise) at these run temperatures does not hinder the movement of this melt.

6) Depletion of the melt in CoO and MgO is primarily caused by olivine crystallization. This takes place both on the crystal seed and as crystallites in the lower parts of the charge. Preferential formation of crystallites in the lower parts of the charge, may be due to the temperature gradient in the furnace. The crucibles are 4°C hotter at the top and so the cooler temperature at the bottom will make crystal nucleation more likely here.

7) Crystallization of hercynite on the crucible walls, and alumina dissolution from the crucible walls produce a CoO-, MgO- depleted, Al_2O_3-enriched side-wall boundary

layer with a lower density than the original melt in the charges. This can rise buoyantly up the side-walls, and gather in the uppermost parts of the charge.

From data presented in this study it is impossible to determine the relative contributions of (6) and (7) above, to the overall compositional variation in the charges. Crystallization rates of both hercynite and olivine are temperature dependent and so their contribution will vary with run temperature, however at higher temperatures alumina dissolution will be more rapid, therefore having a bigger input into the compositional evolution of the charges. Without using noble metal containers, an an inert cement material there is no way of stopping side-wall contamination completely. One possible way of estimating the contribution of hercynite growth and crucible dissolution would be to run experiments at temperatures above the olivine liquidus.

3.7 Discussion

3.7.1 Crystallization in experimental charges

3.7.1.1 Crystal overgrowths on olivine seeds

Overgrowth morphology is a function of degree of supercooling, while overgrowth width is controlled by both degree of supercooling and time (see figure 3.32). At larger supercoolings overgrowths have a complex, porous, skeletal morphology, with rounded corners. With decreasing degree of supercooling the overgrowth morphology becomes more euhedral and less porous, and corners are more angular. At small supercoolings the overgrowth comprises hexagonal crystals with no holes (see figure 3.32 for summary). This morphological change is consistent with the experimental results of Donaldson (1975) for olivines and Lofgren (1974) for feldspars and pyroxenes, whose findings are summarized in figure ~~3.33~~ 3-03. Overgrowth morphology is always similar to that of the crystallites that grow throughout the charges. The fact that olivine morphology does vary with run temperature allows us to infer that crystallites grew during each experiment. If they were the products of quench-induced crystallization then morphology would be consistent for all run temperatures if quenching rates had been equal throughout.

3.7.1.2 Variation in MgO/CoO across the olivine overgrowth

CoO and MgO X-ray count rate analysis across olivine overgrowths shows that a decrease in the MgO/CoO ratio occurs as the crystal-melt interface is approached. The first crystal overgrowth to form is MgO rich and CoO poor. Chemical analyses of the olivine overgrowth in table 3.07 show that the rim can contain upto 5 wt % FeO. The amount of FeO in the overgrowth probably increases as the seed-overgrowth interface

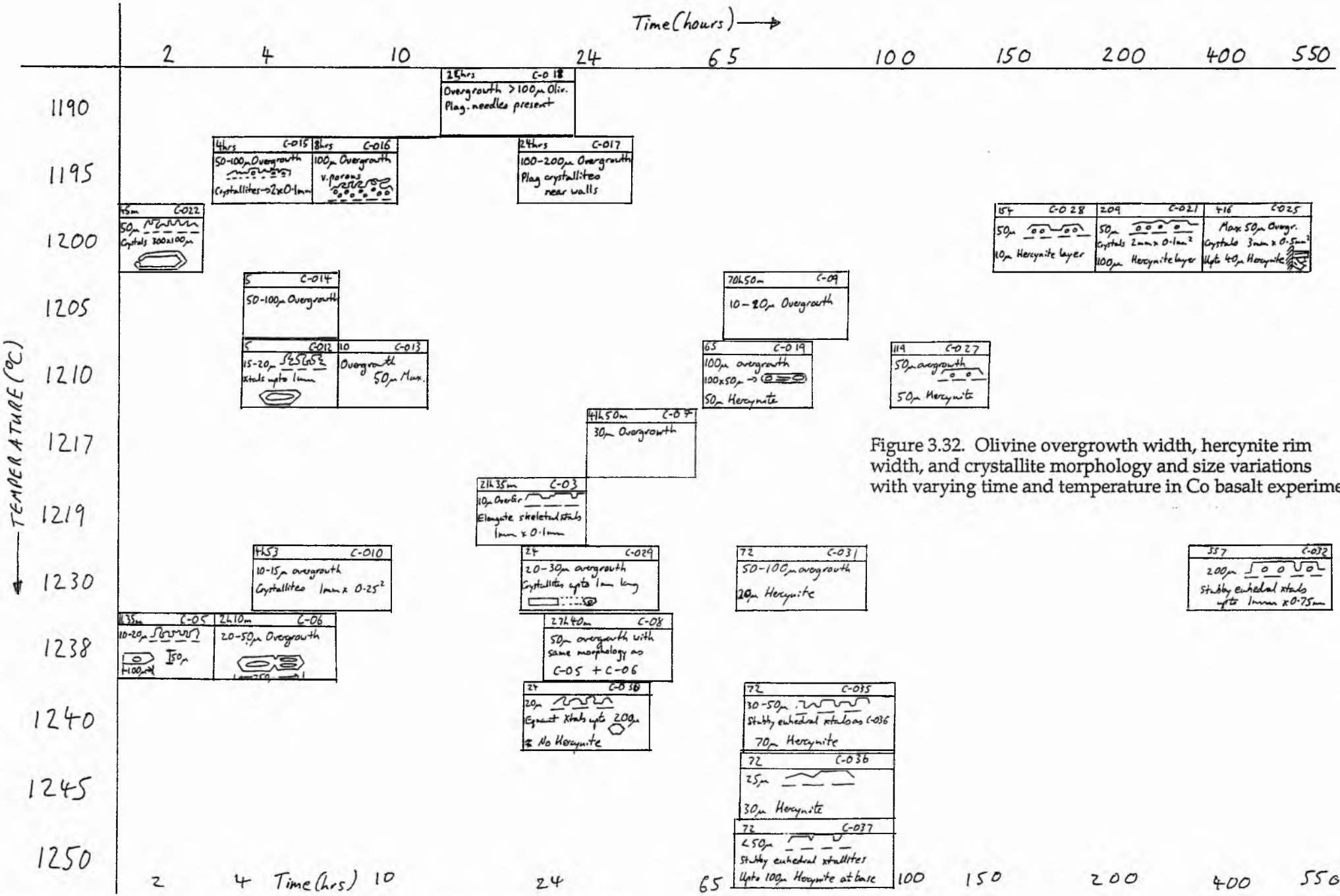

Figure 3.32. Olivine overgrowth width, hercynite rim width, and crystallite morphology and size variations with varying time and temperature in Co basalt experiments

Table 3.07 Representative analyses of olivine crystallite and overgrowth compositions from runs in chapter 3.

temperature (°C)	1188	1195	1205	1210	1210	1210	1217	1219	1230	1238	1240	1245
crystal or overgrowth	crystal	crystal	crystal	crystal	crystal	crystal	crystal	crystal	crystal	crystal	crystal	crystal
SiO2	37.3	37.6	37.3	36.4	36.7	36.6	37.1	36.6	37.6	36.2	36.8	37.7
TiO2	0.1	0.1	0.2	0.1	0.1	0.1	0.1	0.1	0	0.1	0.1	0.1
Al2O3	0	0	0.1	0.1	0	0	0	0	0	0	0.1	0
CoO	28	31.1	29.1	30.5	30.2	30.3	29.4	29.7	30.7	29.7	30.4	29
MgO	34.8	33.2	33.6	32.6	32.4	32.6	33.9	33.6	34	32.4	33.3	33.6
CaO	0.5	0.3	0.5	0.2	0.4	0.3	0.5	0.5	0.3	0.4	0.2	0.3
Na2O	0	0	0	0	0	0	0	0	0.1	0.1	0	0
K2O	0	0	0	0	0	0	0	0	0	0	0	0
total	101.3	102.4	101	99.8	99.8	99.9	101.2	100.64	102.9	99	100.9	100.9
% Co olivine	44	48	46	48	48	48	46	47	47	48	48	46
% Mg olivine	56	52	54	52	52	52	54	53	53	52	52	54
% Fe olivine												

1210	1217	1245
overgrowth	overgrowth	overgrowth
37.6	37.4	39.5
0.1	0.1	0
0	0	0
22.5	27	17.5
37.1	35.4	42.5
0.2	0.5	0.2
0	0	0.1
0	0	0
97.6	100.8	102.9
38	43	28
62	57	67
		5

is neared. It is also likely that MgO from the seed will contaminate the overgrowth in the same way, thus causing an increase in the MgO/CoO ratio close to the seed-overgrowth interface. This may be the cause of the MgO/CoO variation across the overgrowth.

3.7.1.3 Position and morphology of olivine crystallites

Representative analyses of olivine crystallites is displayed in table3.07. These data show a minimal variation in olivine crystallite composition across a range of temperatures of 57°C. This lack of compositional variation could indicate that the Co_2SiO_4-Mg_2SiO_4 phase diagram has a very steep loop, or that the temperature range examined was not large enough for the solid solution series of this system to show up.

Olivine crystallites have grown in all the experimental charges. Their position in clay crucibles is dependent upon the position of SiO_2-rich melt produced by side-wall dissolution; crystallites are absent from this pale melt but are abundant throughout the rest of the charge. The morphology of the crystallites is governed by the degree of supercooling; increasingly more elongate and skeletal morphologies grow at lower temperatures. The crystallites are aligned, presumably by a current in the charges.

In alumina crucibles the same crystallite morphology variation occurs, with simpler, more equant crystallites forming at smaller supercoolings (see figure 3.32), but the position of these crystallites is problematic. In the cemented-seed runs crystallites only appear in the lower third of the crucibles. In clay crucibles the upper level of the crystallites is determined by the lower level of the pale alumina- and silica-enriched glass. There is no such obvious compositional limitation in the alumina crucible runs and so it may seem reasonable to consider that the crystallite level is due to olivine settling through the charges by virtue of its higher density than the melt. However the upper crystallite level does not decrease with increasing time; the level of crystallites in 3-day runs remains roughly the same at 1230, 1240, 1245, and 1250°C. The number and size of these crystallites does, however, decrease with increasing temperature (as nucleation density and growth rates decrease).

As the crystallites are restricted to the bottom of the crucibles, and do not appear to have reached there by crystal settling from the top of the charge (no crystallites are seen between the meniscus and the upper crystallite level) the question must be asked; why do crystallites only nucleate and grow in the lower regions of the crucibles and at the meniscus? The temperature gradient within the charges could be significant. The 4°C vertical gradient means that the lowest temperatures are at the bottom of the crucibles. This makes nucleation most likely in these areas. In the upper parts of the

charges the higher temperatures make crystallite nucleation rate low and so very few crystallites are seen in these areas, except at the meniscus where heterogeneous nucleation is seen.

3.7.1.4 Crystal growth on crucible walls

A more detailed study of the processes occurring at the wall-melt interface is given in chapter 4, but a brief discussion is presented here. In thin sections of these charges a dark line is seen between the glass and the pale alumina crucible wall. This line is split into two parts and comprises a blue line of alumina impregnated by cobalt-basaltic melt next to a layer of tiny crystals of spinel. The crystallites in this layer are hercynite and the layer generally becomes wider towards the bottom of the crucible. The hercynite layer contains tiny needles, frequently alligned at right angles to the wall. The width of the hercynite zone increases with run duration, and thickens faster at lower temperatures. Hercynite is seen in wider zones at the bottom of the crucibles, possibly due to the lower temperature causing more rapid crystal growth.

For hercynite to grow, CoO and MgO have to combine with Al_2O_3. CoO and MgO are readily available in the melt and the melt close to the crucible walls is enriched in Al_2O_3. This enrichment is probably due to side-wall dissolution and produces an Al_2O_3-enriched melt in which hercynite can grow, with the side-wall providing a nucleation surface for the hercynite needles. The presence of the blue line shows that the crucible wall is slightly porous and has allowed the Cobalt-basalt melt to infiltrate it before the growth of the hercynite.

3.7.2 Compositional variation in melt in experimental charges.

3.7.2.1 Compositional variation in glass adjacent to olivine overgrowths on cemented crystal seeds

Olivine overgrowth on an olivine seed takes CoO, MgO and SiO_2 from the melt. This strips the heavy elements (CoO and MgO) from the melt at the interface, enriching it with the lighter elements (Al_2O_3, CaO, Na_2O, K_2O). CoO and MgO are the elements that have been examined most closely in this study, and are the ones which show the strongest compositional variation patterns in glass at crystal-glass interfaces, both being strongly depleted over a narrow (Max 50μm) boundary layer. Typically the boundary layer is wider for MgO than it is for CoO. It is also enriched by 1 wt % in both Al_2O_3 and SiO_2.

3.7.2.2 Compositional variation in melt adjacent to olivine crystallites

The study of compositional variations around an olivine crystallite in C-O 10 reveals sharp oxide variations across a narrow zone of glass at the crystal-glass interface. The chemical, and resultant physical, variations in the melt around the olivine crystallite in C-O 10 were discussed in section 3.3. The maps in figure 3.05 provide no evidence that this low-density boundary layer has built up in thickness on the upper surfaces of the crystallite and detached from the crystal-liquid interface. If it is assumed that the crystallite's current position is the one that it has been in throughout its growth, then any buoyant layer of melt should have risen to the upper surfaces of the crystal forming a thickness of melt that became unstable. Various possibilities exist for the apparent absence of evidence of boundary layer movement in relation to the crystal seed:-

1) The crystallite has not been in its current position throughout the run duration. It could have sunk through the charge, and boundary layer melt may have been left behind and replaced by fresh melt from below.
2) The current boundary layer may be a product of quench-related crystal growth- although rapid growth crystal textures are not seen in contact with the melt.
3) The analytical points may not be close enough together to detect a thin boundary layer leaving the top of the crystal. The very depleted glass at the interface is less than 50μ wide - this is approximately the spacing between the data points and so it is feasible that boundary melt could have passed through the network of analytical points, although boundary layer thickness calculations (see section 3.7.5) indicate that huge thicknesses of this compositional boundary layer are needed before it will become buoyantly unstable. When this part of the study was carried out the technique of analysing closely spaced points by x-ray count rates had not been devised.

Glass around the olivine crystallites is often bleb-free, and Pt blebs are seen within the crystallites. This suggests that metallic blebs are incorporated into the crystallite, producing a layer of bleb-free melt at the crystal-liquid interface. This is the same process that occurs next to the olivine overgrowth.

3.7.2.3 Compositional variation in melt above the crystal-seed apexes

If CoO- and MgO- depleted glass, detected as a boundary layer at the overgrowth-glass interface, was buoyantly unstable when molten, then it should be detectable above the crystal-seed apex. Glass depleted in CoO and MgO has indeed been detected above crystal-seed apexes. It is not however as depleted in CoO and MgO, or as enriched in SiO_2, as the glass closest to the very interface, and so is harder to detect

in the analytical tracks above the seed apexes than in those at the crystal-liquid interfaces.

The absence of the very depleted melt above the crystal seed could be caused by a lack of movement of the melt at the interface. It could be held in place by surface-tension which makes it unable to detach from the seed. Martin, Griffiths and Campbell (1987) suggest that melt in an unstable boundary layer moves faster with increasing distance from the crystal-melt interface, while Lasaga (1981) reports that the motion of the melt relative to the crystal decreases to zero at the interface. If this work is applied here then the melt that can detach from the crystal apex is the least depleted melt (from the outer limits of the boundary layer). Due to its smaller compositional contrast with the original melt it is harder to detect above the seed than the boundary layer is at the crystal-liquid interface. Also the thin section probably does not intersect the core of the plume, which may contain glass more depleted in CoO and MgO than that examined in this study, so that even though CoO- and MgO-depleted melt is not detected above all seed apexes, this does not rule out compositional convection and plume activity in such charges. Although thin sections cut through the centres of seeds, they may not bisect a plume of buoyant melt above the seed. A comprehensive search for a plume above a seed would necessitate multiple sections through charges, a rather time consuming process.

The presence or absence of boundary layer melt above the apex may also be affected by the manner of release of melt around the growing crystals. Different rates of crystallization and boundary layer production will result in either continuous or punctuated release of melt (Donaldson, 1993), with fast growth encouraging melt to be drained continuously from the seed, and slow growth inhibiting this. The latter results in punctuated release of melt, and could explain the erratic appearance of boundary layer plumes in some charges.

Only a very thin layer of melt around the crystal seeds has a compositional variation of more than 1.5 wt % absolute of any oxide. This is the melt in contact with the overgrowth and is therefore, according to Martin, Griffiths and Campbell (1987) and Lasaga (1981), the part of the boundary layer that will move slowest. It should therefore not be surprising that glasses with large compositional variations are not detected above the crystal apex.

3.7.2.4 Compositional variation in melt at the meniscus

If buoyant compositional boundary layers have been formed by olivine growth, and they have had time to convect upwards, then it is beneath the meniscus that ponding

will occur. Therefore as a test for compositional-driven convection in long-duration experiments vertical chemical differentiation of charges was looked for.

It is also necessary to take into account the input of other processes before the differentiation effect of crystallization-driven compositional-convection can be evaluated. Another factor that produces CoO and MgO depletion in melt is the growth of hercynite crystals on the crucible walls. This produces slight CoO and MgO depletion in a narrow region of melt at the crucible wall. In experimental runs using clay crucibles side-wall dissolution takes place, contaminating the melt near the wall by enriching it in SiO_2 and Al_2O_3. This produces a buoyant melt that rises in the crucibles and ponds as a discrete layer below the meniscus. Any accumulation at the top of charges of Co- and Mg-depleted boundary layer melt released from around olivine seeds will be masked in these crucibles by the compositionally contrasting melt produced by this side-wall dissolution and hercynite growth. The use of alumina crucibles cuts down the amount of side-wall contamination but does not prevent it completely. Alumina enrichment is seen close to the side-walls and to the cement at the bottom of the crucible.

Examination of crystal-liquid interfaces reveals no enrichment of the boundary layer in Al_2O_3 - and Al_2O_3 depletion is seen above the crystal apex of runs - so we can assume that all alumina enrichment beneath the meniscus is a product of side-wall and cement dissolution. From this it can also be deduced that CoO and MgO depletion at the meniscus is produced by buoyant release of Co-Mg depleted boundary layers from the crystal-liquid interfaces of growing hercynite and olivine.

The region of CoO and MgO depletion at the meniscus increases in depth with increasing run duration. If crystallization of olivine and hercynite continue throughout the run, buoyant melt will be produced all the time. However, as mentioned in 3.7.2.3, its presence above the seed apex is often hard to detect. Long run durations are therefore necessary to allow compositional differentiation of melts with different densities. Long run duration gives the maximum opportunity for segregation of boundary layer melt into density-controlled stratified units.

3.7.2.5 Compositional variation at crucible walls

As mentioned previously, the dissolution rate of clay crucibles makes them unsuitable for long-duration runs, which are necessary if compositionally-variable melt is to collect in the upper reaches of these charges. A more detailed study of side-wall crystallization and dissolution is made in chapter 4, where the combined effect of the two processes is to produce an optically-visible, pale boundary layer which ponds beneath the meniscus.

3.7.2.6 Compositional variation near the crucible floor

EPMA has revealed CoO and MgO depletion and Al_2O_3 enrichment in glass in the bottom third of experimental charges. This is the region closest to the alumina cement, at the coolest temperature (4°C less than the top of the charge), and containing the highest concentration of olivine crystallites. These factors can be used to explain the compositional variations in the bottom of the crucibles in the following ways:-

1) Dissolution of the nearby alumina cement enriches the melt in Al_2O_3.
2) Olivine crystallite growth in this area depletes the melt in CoO and MgO.
3) The slight temperature gradient causes more olivine crystallites to nucleate and grow at the bottom of the charge than at the top. This gradient also causes slight density differences between melts at the top and bottom of the crucible. Melts of the same composition will therefore be denser at the bottom of the crucible than at the top, where it is hotter, and so the unstable density gradient caused by compositional variations may not be sufficient to overcome the stable, temperature-governed density gradient.

3.7.3 Density and viscosity variations in experimental charges

3.7.3.1 Introduction

This section summarizes density and viscosity variations produced by crystallization and dissolution processes in the experimental charges. Viscosities and densities were calculated using the methods of Shaw (1976) and Bottinga and Weill (1970) respectively, from EPMA data.

3.7.3.2 Density and viscosity variations at the overgrowth-melt interface.

Figure 3.3 shows density and viscosity profiles for melts adjacent to olivine overgrowths in experimental run 31a (1230°C for 72 hours). These profiles show clearly that melt density decreases and viscosity increases in a narrow zone at the interface. This zone is approximately 50μ wide for both density and viscosity. The problems of analysing closely spaced points, using EPMA as opposed to X-ray count rates, mean that this is only a rough estimate of the thickness. Across this narrow zone density decreases from 2.750 to 2.703 g/cc (1.7 %) and viscosity increases from 240 to 480 poise.

3.7.3.3 Density and Viscosity variations above the crystal seeds

Figure 3.3 displays horizontal profiles of melt density and viscosity variations derived from glass above crystal apexes in runs 29, 30, and 31. Each of these profiles shows a

density decrease and viscosity increase in glasses at the centre of CoO- and MgO-depleted regions. Viscosity generally increases and density decreases by about 1 % across these areas. If this melt originates from the overgrowth-melt boundary layer, then its appearance above the seed crystal indicates that small density differences (<1 %) can cause convection in low-viscosity silicate melts. Although the variations are small, the same pattern of variation is seen in all charges and therefore seems to reflect the physical properties of the melt above the crystal apex at the time of quenching.

3.7.3.4 Vertical density and viscosity variations in experimental charges

The graphs in figure 3.3~~7~~5 display density and viscosity variations along vertical profiles through experimental charges. These data indicate that melt density decreases and viscosity increases towards the top of the charge (higher Y values). Most of this variation is in the top 2mm, directly beneath the meniscus.

3.7.4 Compositional convection within the experimental charges

Compositional variations in melts affect the two physical properties which govern convection - density and viscosity. In this series of experiments three factors produce compositional variation in the silicate melts; alumina dissolution from side-walls and cement, olivine crystallization on the seed and as crystallites, and hercynite crystallization on crucible walls.

Contamination by crucible dissolution is minimized in this study by using alumina crucibles, however a degree of contamination does occur and partially obscures the search for crystallization-dependent, compositional convection. Without using expensive noble metal containers there is no way of avoiding this contamination and so the inconvenience must be persevered with. Al_2O_3 contamination of the basaltic melt causes a decrease in melt density and therefore produces a buoyant melt which can convect upwards adjacent to the crucible walls. On reaching the uppermost parts of the charge the melt can rise no further and as more Al_2O_3-rich melt rises the thickness of this layer increases downwards. This process is seen best in the clay crucibles, where dissolution and convection is rapid and is marked clearly by a more compositionally contrasting melt than that produced by dissolution in alumina crucibles. Dissolution also takes place of the crucible floor and a layer builds up rapidly in clay crucibles that is buoyantly unstable and can therefore break away and convect upwards (see section 3.7.5). In alumina crucibles the build up of such a layer on the floor is much slower and plumes have not been detected.

Hercynite crystallization on crucible walls produces a melt which is depleted in CoO and MgO. This depletion exaggerates the buoyancy of the melt which is already

Fig 3.33a. Density and viscosity profiles in the glass adjacent to olivine overgrowth in CO 31.

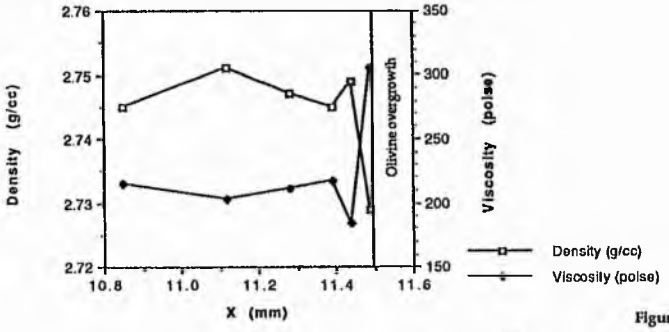

Figure 3.33b.

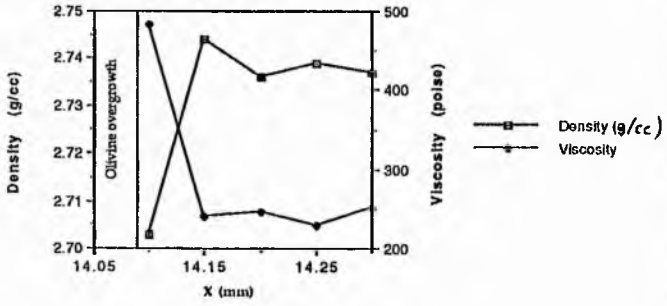

Figure 3.34a. Density and viscosity variations in glass above the olivine seed apex in CO-30

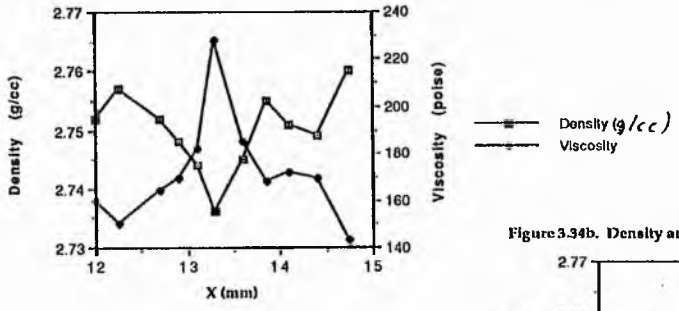

Figure 3.34b. Density and viscosity variation above the olivine seen in CO-31

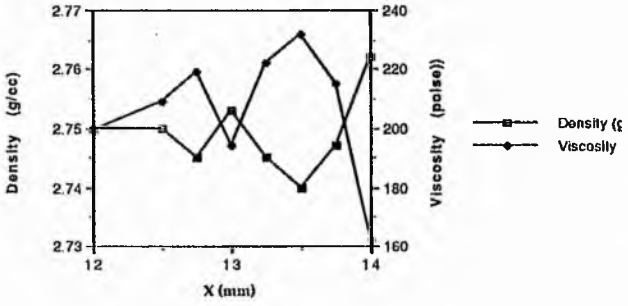

Figure 3.35a. Density and viscosity variations approaching the meniscus in CO-32

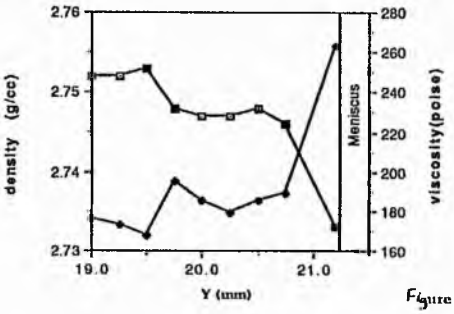

Figure 3.35b. Vertical density and viscosity variations through the charge CO32

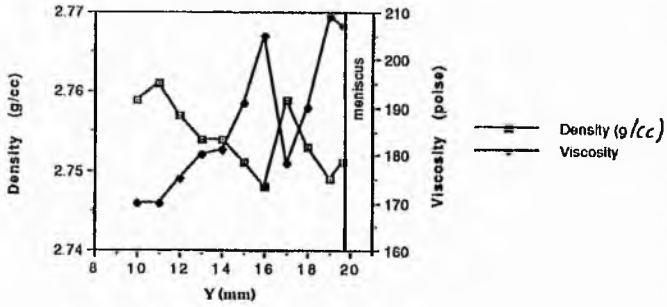

alumina enriched from slight wall dissolution. The rise of this buoyant melt to the top of the charge means that compositional variation in the charges is not caused entirely by the release of compositional boundary layers produced by olivine growth. This means that monitoring the build up of CoO-MgO-depleted melt beneath the meniscus cannot be used as a measure of boundary layer release solely from olivine growth. Hercynite growth on side-walls does, however, provide an example of the production of buoyant, boundary layers of melt by crystal growth, and is discussed in more detail in chapter 4.

Crystallization of olivine (as an overgrowth on olivine seeds and as crystallites in the lower regions of the crucibles) produces a very thin (<50μm) layer of buoyant melt which is depleted in CoO and MgO, and enriched in SiO_2. Its low density causes it to rise up the crystal seed and detach from the seed apex. The migration of this melt to the meniscus in the charges is partially responsible for vertical compositional variation in these experiments. It is impossible, however, to assess the total volume of boundary layer melt produced by olivine crystallization, due to the effects of hercynite growth and alumina dissolution.

The compositional variations, along with the resultant variations in density and viscosity, produced by crystal growth are small but these experiments prove that in low-viscosity silicate melts these variations are sufficient to produce buoyancy differences which drive compositional convection in a stable temperature gradient. Differences in colour of boundary layer melt in thin section are not detected by optical or back-scattered electron analysis; probably because Co^{2+} variations are so small, and because the most depleted part of the boundary layer is very thin.

It has been shown that a 1% density decrease is sufficient to produce convection, and so it is not surprising that colour variations are not detected in convecting compositional boundary layers. As soon as, or possibly before, a 1 % density decrease is produced convection can occur. The boundary layer around a growing olivine crystal therefore never becomes sufficiently depleted in Co^{2+} to produce a colour variation. If a melt with a higher viscosity was used, then a bigger compositional and density variation would be needed to produce an unstable boundary layer. The boundary layer would not be unstable at such a low density difference and would therefore need to develop a bigger compositional difference or a thicker layer before convecting buoyantly. This would possibly be seen more readily as a colour variation in the melt.

3.7.5 Compositional Rayleigh number calculations

The stability of a boundary layer on a horizontal surface is governed by the compositional Rayleigh number, Ra_C, where;

$$Rac = g\Delta\rho_c d^3/vD.$$

This value must exceed 1000 for boundary layer instability (Rosenberger, 1979). In the above equation g is the gravitational constant, $\Delta\rho_C$ is the compositional density difference across the film, d is the film thickness, v is the kinematic viscosity, and D is the chemical diffusion coefficient. Values for v and $\Delta\rho_C$ have been calculated from melt compositions. Values for D are in the range 10^{-5}-10^{-8} cm^2s^{-1} (Hofmann, 1980).

Calculations have been carried out for four scenarios in this study:-
1) A compositional boundary layer forming on the horizontal floor of an alumina crucible by hercynite growth.
2) A compositional boundary layer on the floor of a clay crucible, produced by wall dissolution.
3) A boundary layer forming on a horizontal olivine surface.
4) A boundary layer forming around an olivine crystallite.

The calculations in table 3.06 show the thicknesses of boundary layer necessary to produce melt instability (i.e. Rac exceeds 1000), and the times needed for a boundary layer to reach these thicknesses. The computed widths of boundary layers (800-10,000μm), and the minimum times necessary for them to be unstable are not consistent with observed boundary layer thicknesses.

The thicknesses of boundary layers produced on the floors of experimental charges do not begin to approach the calculated thicknesses, probably explaining why plumes are not seen rising from the floors of crucibles in this chapter (cf. chapter 4). Even in clay crucibles, boundary layers do not reach the minimum width needed for convection, but buoyant plumes have been observed. In such cases bubbles could have induced boundary layer instability.

The convection of side-wall melt in alumina crucibles, in relatively short duration runs, can be explained because the calculations here are for horizontal surfaces. On inclined surfaces boundary layers are instantaneously unstable.

The calculations for boundary layers around the crystallite reveals a very thick boundary layer is needed for convection, with the crystallite being only 500μm in diameter. Even though the calculation is for a horizontal surface, and boundary layer

Table 3.06. Compositional Rayleigh number calculations for boundary layers in experiments in chapter 3

Position of boundary layer examined		Interface melt density (g/cc)	bulk melt density (g/cc)	density difference (kg/m³)	v (m2/s)	D(m2/s)	Ra comp	d (mm)	Time (hours)= d2/D
Boundary layer on floor of alumina crucible in CO 20	a	2.707	2.743	36	237	10(-9)	1000	8000	76,702
	b	2.707	2.743	36	237	10(-10)	1000	4065	165,000
	c	2.707	2.743	36	237	10(-11)	1000	1536	356,000
	d	2.707	2.743	36	237	10(-12)	1000	875	760,000
Boundary layer on floor of clay crucible in CO 13	a	2.622	2.747	125	980	10(-9)	1000	9000	81000
	b	2.622	2.747	125	980	10(-10)	1000	4310	186000
	c	2.622	2.747	125	980	10(-11)	1000	2000	400000
	d	2.622	2.747	125	980	10(-12)	1000	928	861000
Boundary layer above olivine seed in CO 31	a	2.746	2.752	6	74	10(-9)	1000	10740	116424
	b	2.746	2.752	6	74	10(-10)	1000	5000	250000
	c	2.746	2.752	5	74	10(-11)	1000	2320	538240
	d	2.746	2.752	6	74	10(-12)	1000	1079	1164241
Boundary layer around crystallite in CO 10	a	2.63	2.66	30	173	10(-9)	1000	8380	70224
	b	2.63	2.66	30	173	10(-10)	1000	3889	151243
	c	2.63	2.66	30	173	10(-11)	1000	1805	325802
	d	2.63	2.66	30	173	10(-12)	1000	838	702244

melt from vertical sides of the crystal may contribute to more rapid boundary layer build up, it is no wonder that compositional convection is not observed around crystallites.

For a horizontal boundary layer above an olivine seed, a minimum thickness of 23 cm is required before it becomes buoyant. No such thickness of boundary layer could be observed in this chapter, although compositional convection has taken place. Again the explanation of this inconsistency lies in the fact that calculations are for horizontal surfaces. Donaldson (1993) discusses evidence for boundary layer melt on inclined surfaces flowing round crystals and increasing boundary layer thickness at the bottom of dissolving crystals. If this situation is turned upside down it can be applied to the growing olivine crystals here, causing rapid thickening of a boundary layer above the crystal seed, and so convection occurs within the duration of these experiments. Also, any horizontal surface on the crystal seeds in these experiments has been almost removed by crystal grinding and careful alignment, so no horizontal sides exist on the seeds.

3.8 Summary and Conclusions

The following list summarizes the findings of the experiments in this chapter:-

- Compositional variation in experimental charges is produced by olivine crystallization, hercynite crystallization and alumina dissolution.
- Alumina dissolution melt near walls and cement produces a lower density than the original melt.
- Growth of olivine crystallites produces a 20-30μm wide, low-density boundary layer around each crystallite. Conclusive evidence for convection of these boundary layers has not been observed.
- The compositional variations, produced in melts by crystallization, are not sufficient to cause a colour difference in quenched glasses. In higher viscosity silicate systems, colour variation may be observed because a bigger compositional variation across a wider zone is required to produce boundary layer instability.
- Surface-tension driven convection (eg. near bubbles and at the meniscus) causes accelerated side-wall dissolution.
- Compositional variation greatly affects the distribution of nucleating crystallites.
- The study of fluid dynamics associated with crystallization requires small supercoolings so that excessive crystallization does not interfere with observation of glass compositions.
- Air bubbles aid the rise of crystals in melts, even if the crystals have a higher density than the melt.

- Olivine growth produces a 30μm-wide, low-density, boundary layer (depleted in CoO and MgO, but enriched in SiO2) around the crystal seed. This boundary layer is detectable by EPMA above the crystal apex.
- Across the boundary layer CoO and MgO are depleted by 25 %. The most depleted part of the boundary layer remains at the crystal-liquid interface and is not seen above the crystal seed.
- With longer run duration, vertical compositional differentiation occurs, producing CoO and MgO depletion and Al2O3 enrichment at the top and bottom of crucibles.

This chapter has described the existence of compositionally-discrete plumes of Co- and Mg-depleted melt above growing olivine crystal apexes. However, due to the unsolved problem of melt contamination the results of this series of experiments are not entirely satisfactory, as crystal growth is not the only process causing compositional variation in the experimental charges. This means that differentiated end-products are not produced solely by crystallization of Co- and Mg-bearing crystals.

In a body of magma several mechanisms produce compositional and density variations (eg. crystal dissolution, side-wall melting, temperature variations, contamination by another magma injection). This study has shown that crystallization in low-viscosity silicate systems does produce compositional variation in boundary-layer melts, and that the change is large enough to drive melt convection. The quantative evaluation of this process is difficult to assess due to contamination. In a magma chamber the effect of crystallization-driven convection may also be impossible to assess due to the influence of other processes. These include:-

1) Side-wall melting and later magma injection.
2) The crystal assemblage being produced at the margins of chambers. For example, olivine will produce a low density boundary layer if crystallized alone, but if enough plagioclase is crystallized in the assemblage then the density of the boundary layer zone may be greater than the original melt.
3) Other convective processes (eg temperature-driven convection) may wash away boundary layers before they are unstable, accelerating crystal growth by bringing fresh, undepleted melt into contact with the crystals. This would prevent maximum depletion of boundary layer melt being reached, and so the process would have a lesser effect on the composition of the magma which is washed away from the crystals.

In basaltic magma chambers at high temperatures the low viscosity will not inhibit compositional-driven convection, but under such conditions crystal growth rates are small and so boundary layer melt is produced slowly. In lower temperature basaltic chambers, or with a more evolved magma, melt viscosity is higher and bigger

compositional differences are needed to produce boundary layer instability, however the increase in viscosity will also hinder convective processes.

Composition-driven convection is therefore probably most active in the early evolution of a basaltic magma body, and should decrease in importance with increasing time and decreasing temperature.

Chapter 4 Iron-oxide development in a basaltic melt

4.1 Introduction

This chapter examines compositional variation in liquids adjacent to hematite seeds cemented in alumina crucibles. The results section of this chapter (4.3) illustrates that the melt at iron-oxide-melt interfaces has a higher density than the melt in the rest of the experimental charge. If the iron-oxide rim is a true overgrowth then one would expect the melt at the oxide-melt interface to be depleted in iron and therefore to be less dense than the melt in the rest of the crucible. This is not the case in these experiments, suggesting that dissolution of the seed has occured, and the convection associated with this is examined. Convection in the experimental charges is driven by two processes; the first process is crystallization of iron-oxide at the meniscus and on the surfaces of air bubbles, and the second is iron-oxide production on the seed and hercynite growth on the side-walls. The latter is accompanied by a small amount of alumina dissolution.

4.2 Experimental Details

Iron oxide (hoegbomite) has been produced as crystallites (see analysis 13 of B-H 14 in table 4.02) and as a rim on the hematite seed (see analysis 1 of B-H 14 in table 4.02) in a basaltic melt in 29 experiments. Most used the wire-loop and cemented seed techniques, at temperatures of between 1217°C and 1306°C, for run durations of 11 minutes to 4 days (run details in table 4.01).

A sequence of short-duration (45 minutes to 24 hours), wire-loop experiments at between 1217°C and 1306°C, pinpoint the liquidus temperatures of mineral phases that crystallize from this melt system. Details of these runs, and the minerals produced in each are displayed in table 4.01. These indicate that the iron oxide liquidus lies between 1258°C and 1271°C. As discussed in chapter 2, a small degree of supercooling is desirable in crystal growth experiments, and so a run temperature of between 1250°C and 1270°C is used here.

The cemented-seed technique, which has proved relatively successful in the cobalt-basalt experiments, is used with hematite crystals as the seeds on which a layer of iron-oxide develops. Because a powder is being used as the starting material for these experiments, it is pressed down gently in the charges before fusion, to expel as much air as possible, and also so that the meniscus level does not fall too low on fusion of the powder. Cemented-haematite runs were made at between 1238°C and 1255°C for durations of between 11 minutes and 4 days. In early experiments (B-H 1 and 2a) the glass in vertical thin sections of the resultant charges is riddled with tiny, euhedral

Table 4.01. Experimental details for runs with basalt melt.

Experiment Number	Technique	Temperature (°C)	Time (hours)	Notes
B-H A	Wire loop	1286	2.083	No crystallization observed
B-H B	Wire loop	1260	0.75	Star-shaped oxide crystallites visible in glass. Possibly formed on quenching.
B-H C	Wire loop	1238	0.917	Both star-shaped and euhedral oxide crystallites visible.
B-H D	Wire loop	1251	1.883	Star-shaped oxide crystallites visible. Possibly a quench product.
B-H E	Wire loop	1197	1.917	Crystallites of plagioclase, iron-oxide and a ferromagnesian silicate mineral.
B-H F	Wire loop	1222	1	Crystallites of plagioclase, iron-oxide and a ferromagnesian silicate mineral.
B-H G	Wire loop	1230	1.17	Plagioclase and iron oxide crystallites have grown in the melt.
B-H H	Wire loop	1240	24	No crystallization seen in thin section of experimental charge.
B-H 1	Cemented seed	1238	2	Preliminary run with single hematite seed cemented in alumina crucible.
B-H 2a	Cemented seed	12445	4	Single seed cemented in alumina crucible. Charge refilled after fusion of powder.
B-H 2b	Just crucible and melt	1245	4	No seed or cement in crucible. Just powder. Not refilled after fusion of powder.
B-H 2c	Melt and cement. No seed	1245	4	No seed in crucible. Just powder and cement. Not refilled after fusion.
B-H 2d	Same as 2a	1245	4	Same set-up as B-H 2a.
B-H 3	Cemented seed	1250	48	Single hematite seed cemented to crucible floor. No refilling of charge.
B-H 4	Cemented seed	1250	96	Single hematite seed cemented to crucible floor. No refilling of charge.
B-H 5	Cemented seed	1260	48	Single hematite seed cemented to crucible floor. No refilling of charge.
B-H 6	Cemented seed	1245	0.5	Single hematite seed cemented to crucible floor. No refilling of charge.
B-H 7	Cemented seed	1255	96	Single hematite seed cemented to crucible floor. No refilling of charge.
B-H 8	Cemented seed	1255	48	Single hematite seed cemented to crucible floor. No refilling of charge.
B-H 9	Cemented seed	1255	24	Single hematite seed cemented to crucible floor. No refilling of charge.
B-H 10	Cemented seed	1255	12	Single hematite seed cemented to crucible floor. No refilling of charge.
B-H 11	Cemented seed	1255	6	Single hematite seed cemented to crucible floor. No refilling of charge.
B-H 12	Cemented seed	1255	3	Single hematite seed cemented to crucible floor. No refilling of charge.
B-H 13	Cemented seed	1255	1.5	Single hematite seed cemented to crucible floor. No refilling of charge.
B-H 14	Cemented seed	1255	0.75	Single hematite seed cemented to crucible floor. No refilling of charge.
B-H 15	Cemented seed	1255	0.37	Single hematite seed cemented to crucible floor. No refilling of charge.
B-H 16	Cemented seed	1255	0.183	Single hematite seed cemented to crucible floor. No refilling of charge.
LT 713 a	Ceramic finger in large crucible	1238	4.217	Alumina tube inserted into fused basalt in large alumina crucible.
LT 713 a	Ceramic finger in large crucible	1238	72	As above. Crystal growth not induced on wall of fingers.

Table 4.02. Chemical analyses from basalt-hematite experiments and computed melt densities and viscosities

B-H 8	SiO2	TiO2	Al2O3	FeO	MnO	MgO	CaO	Na2O	K2O	Original Total	Liquid Density (g/cc)	Liquid Viscosity (poise)	Mineral
1	0.11	3.33	1.86	82.77	0.09	0.73	0	0	0	88.68			hematite
2	0.34	0.86	8.11	66.22	0.3	13.49	0.1	0.01	0.01	89.44			hoegbomite
3	0.15	0.27	1.29	85.22	0.02	0.03	0	0	0.02	87.00			hematite
4	0.22	0.17	3.33	76.82	0.21	9.86	0.03	0.18	0	90.81			hoegbomite
5	51.07	1.77	14.9	10.6	0.08	5.82	9.78	2.98	0.98	97.99	2.664	293	
6	52.17	1.75	15.51	10.43	0.103	5.98	10.05	3.05	0.96	98.14	2.66	305	
7	51.46	1.73	17.78	9.13	0.1	5.68	9.92	3.19	1.01	97.64	2.646	342	
8	52.35	1.83	16.47	9.44	0.15	5.95	9.92	2.84	1.04	97.23	2.648	371	
9	52.15	1.82	15.91	10.19	0.08	5.93	9.78	3.18	0.96	96.46	2.655	320	
10	51.33	1.94	17.72	8.7	0.16	5.85	10.37	2.9	1.02	95.75	2.649	332	
12	51.96	1.81	15.47	10.47	0.16	6	9.9	3.24	0.98	98.56	2.661	285	
13	52.14	1.75	15.77	9.95	0.13	6.09	9.94	3.26	0.96	97.00	2.654	306	
15	52.83	1.9	15.64	9.79	0.06	6.21	9.6	2.92	1.04	96.15	2.647	366	
16	50.5	1.75	18.3	8.44	0.13	6.36	9.8	3.55	1.11	93.20	2.644	255	
17	0.12	0.04	65.58	8.59	0.09	22.9	0.03	0	0	97.30			low Fe hercynite
18	0.35	0.26	45.5	27.4	0.2	21.2	0.1	0.01	0.02	95.10			High Fe hercynite
19	51.86	1.87	18.8	8.27	0.11	4.83	10.02	3.22	1.04	96.86	2.63	484	
21	52.66	1.86	18.32	8.148	0.14	5.3	9.28	3.28	1.05	93.10	2.622	532	
22	51.96	1.82	17.71	9.04	0.13	5.5	9.67	3.14	1.03	97.46	2.64	401	
23	52.63	1.91	16.6	9	0.08	6.05	9.4	3.29	1.04	96.80	2.635	391	
24	51.75	1.91	17.07	9.17	0.14	5.68	9.86	3.33	1.08	97.40	2.643	351	
25	52.47	1.98	15.56	9.24	0.19	6.26	9.96	3.35	0.99	97.32	2.645	321	
26	53.87	1.72	17.88	7.1	0.06	5.73	9.36	3.28	1.01	93.01	2.603	670	

B-H 7	SiO2	TiO2	Al2O3	FeO	MnO	MgO	CaO	Na2O	K2O	Original Total	Liquid Density	Liquid Viscosity (poise)	Mineral
1	51.25	1.75	17.97	9.39	0.13	5.62	9.58	3.32	0.98	97.88	2.648	330	
2	52.52	1.99	16.48	9.04	0.24	6	9.64	3.06	1.03	97.22	2.642	383	
3	52.15	1.88	16.14	9.77	0.15	5.93	9.79	3.15	1.04	97.45	2.651	331	
4	52.27	1.7	15.84	9.97	0.16	6.19	9.82	3.09	0.97	98.36	2.654	316	
5	51.97	1.85	18.25	8.01	0.06	5.4	9.94	3.57	0.96	96.74	2.626	426	
6	52.16	1.83	16.3	9.55	0.11	5.8	9.5	3.72	1.03	99.13	2.641	332	
7	51.52	1.91	17.81	9.69	0.06	5.74	9.82	3.38	1.06	99.53	2.639	347	
8	52.5	2	16.5	9.51	0.12	5.68	9.52	3.23	0.95	98.21	2.643	392	
9	52.18	1.89	17.04	8.94	0.14	5.83	9.78	3.19	1.01	98.86	2.64	378	
10	51.8	1.85	18.07	8.63	0.11	5.39	9.63	3.47	1.04	99.27	2.634	400	
11	51.53	2.06	18.66	8.48	0.14	4.9	9.52	3.69	1	98.22	2.631	423	
12	52.36	1.96	16.74	8.86	0.16	5.78	9.7	3.35	1.1	99.16	2.636	383	
13	51.63	1.74	15.9	10.56	0.14	5.95	10.1	3.02	0.97	98.38	2.666	279	
14	52.07	1.82	16.3	9.57	0.11	6.02	9.84	3.25	1	98.92	2.649	325	

Data only accurate to 1d.p

Table 4.02. Chemical analyses from basalt-hematite experiments, with computed densities and viscosities.

	SiO2	TiO2	Al2O3	FeO	MnO	MgO	CaO	Na2O	K2O	Original Total	Liquid Density (g/cc)	Liquid Viscosity (poise)	
Original Melt	49.01	1.72	14.99	10.95	0.12	6.27	9.81	3.05	0.97				
B-H 14													Mineral
1	0.27	0.83	5.47	61.65	0.22	12.38	0.09	0	0.1	80.92			hoegbomite
2	50.71	1.81	16.03	10.65	0.09	5.75	10.38	3.48	1.1	94.88	2.67	223	
3	52.36	1.89	15.56	9.36	0.11	6.48	9.88	3.28	1.07	99.03	2.646	304	
4	51.4	1.95	15.42	10.23	0.06	6.32	10.28	3.33	1	97.00	2.665	237	
5	52.32	1.81	15.45	9.6	0.11	6.45	10.07	3.08	1.09	97.38	2.651	301	
6	52.56	1.89	15.15	9.42	0.12	6.8	9.91	3.07	1.07	96.94	2.649	296	
7	52.09	2	15.4	9.48	0.15	6.7	9.92	3.26	0.98	97.42	2.653	272	
8	51.6	2.1	15.66	8.79	0.08	6.87	11.16	2.86	0.84	98.76	2.659	251	
9	52.56	1.87	16.41	8.74	0.1	6.24	9.85	3.21	1.02	99.51	2.637	368	
10	51.83	2.05	17.15	8.87	0.13	5.92	9.78	3.17	1.1	98.59	2.642	348	
11	52.08	1.96	15.71	9.87	0.15	6.41	9.58	3.15	1.09	98.39	2.654	291	
12	51.94	1.86	15.62	9.59	0.19	6.43	9.85	3.46	1.07	99.17	2.651	271	
13	0.37	12.38	2.78	67.53	0.16	4.73	0.12	0.03	0	88.10			hoegbomite
14	52.17	2.16	15.97	9.08	0.11	6.59	9.84	2.97	0.91	97.88	2.649	318	

B-H 13	SiO2	TiO2	Al2O3	FeO	MnO	MgO	CaO	Na2O	K2O	Original Total	Liquid Density	Liquid Viscosity (poise)	Mineral
1	51.99	1.69	15	10.94	0.14	5.86	10.1	3.21	1.03	96.62	2.666	276	
2	51.93	1.69	15.12	10.87	0.07	5.96	10.02	3.3	1.03	98.19	2.664	270	
3	52.23	1.85	15.16	10.29	0.06	6.27	9.9	3.21	1.03	97.22	2.657	286	
4	52.38	1.72	15.6	9.4	0.06	6.54	9.89	3.3	1.1	98.11	2.645	302	
5	0.311	0.831	5.887	69.046	0.311	12.461	0.093	0	0.015	89.00			hoegbomite
6	0.543	0.132	59.287	13.015	0.15	20.775	0.169	0	0	94.07			hercynite
7	1.13	0.884	9.697	56.238	0.329	14.555	0.288	0.049	0.048	83.22			hoegbomite
8	51.54	2.16	15.77	9.73	0.06	6.44	9.93	3.23	1.13	95.26	2.657	256	
9	52.01	1.95	15.7	9.23	0.08	6.51	10.11	3.36	1.06	96.90	2.648	281	
10	52.79	1.98	15.55	9.19	0.16	6.34	9.93	3.14	0.98	98.48	2.644	347	
11	52.39	1.96	15.6	9.42	0.11	6.34	9.8	3.34	0.98	98.17	2.646	315	
12	52.64	1.95	15.57	9.11	0.15	6.4	10.21	2.97	1.01	97.28	2.646	338	

B-H 10	SiO2	TiO2	Al2O3	FeO	MnO	MgO	CaO	Na2O	K2O	Original Total	Liquid Density	Liquid Viscosity (poise)	Mineral
27	52.92	1.84	14.92	9.93	0.06	6.03	10.08	3.19	1.03	96.67	2.648	344	
28	51.98	1.64	15.79	10.37	0.12	5.78	10.05	3.31	0.96	96.90	2.658	303	
29	52.54	1.87	15.6	10.1	0.1	6.16	9.39	3.2	1.01	98.00	2.65	333	
30	52.57	1.86	15.97	6.67	0.12	6.49	10.12	3.16	1.02	96.23	2.612	471	
31	52.18	1.77	18	8.05	0.08	5.62	9.79	3.43	1.09	97.72	2.625	428	
32	52.37	1.81	15.63	9.49	0.11	6.33	10.02	3.22	1.03	98.83	2.648	312	
33	52.9	1.86	15.69	8.59	0.15	6.68	9.96	3.17	0.99	97.39	2.637	350	
34	51.83	2.03	17.91	8.63	0.16	5.19	9.49	3.64	1.12	97.61	2.631	406	
35	52.81	1.95	16.44	8.73	0.13	5.78	9.72	3.42	1.02	97.54	2.632	416	
36	51.89	1.98	17.79	8.26	0.11	5.55	9.8	3.51	1.11	98.64	2.63	392	
37	52.41	2.09	15.98	9.14	0.14	6.26	9.61	3.47	0.91	97.74	2.642	331	
38	52.19	1.97	15.79	9.27	0.18	6.23	9.9	3.4	1.08	96.33	2.646	307	
39	52.85	1.88	15.49	9.03	0.1	6.52	9.86	3.16	1.1	97.26	2.64	344	
40	52.63	1.9	15.57	9.37	0.11	6.38	9.73	3.25	1.04	97.15	2.644	332	
41	51.84	1.79	15.28	10.77	0.14	5.67	10.11	3.39	1.01	97.71	2.663	278	
42	52.3	1.84	15.3	10.24	0.09	5.82	10	3.34	1.05	97.50	2.654	313	
43	52.12	1.92	15.44	9.8	0.21	6.33	9.8	3.23	1.11	99.20	2.653	288	
44	52.66	1.95	15.69	9.39	0.06	6.23	9.88	3.17	0.97	97.63	2.645	348	
45	52.41	1.93	15.81	9.09	0.04	6.45	10.02	3.25	1.01	106.69	2.644	320	
46	51.98	1.99	15.34	9.77	0.22	6.37	10.15	3.15	1.03	96.26	2.658	274	
47	52.07	1.92	17.37	8.37	0.13	5.87	9.86	3.35	1.07	96.13	2.634	378	

Data only accurate to 1d.p.

iron-oxide crystallites. To examine whether these are influenced by crucible refilling, or the presence of either alumina cement or the crystal seed, runs 2 b, 2c, and 2d were made at identical conditions without a seed, cement, and both seed and cement respectively. Iron-oxide crystallites are seen in thin sections of each of these three charges and so their appearance is apparently not influenced by any of the above factors. The flow-patterns formed by allignment of these crystallites are discussed in section 4.3.

Two larger-scale experiments were attempted at Leeds University using a bigger crucible without a crystal seed. Basalt powder was fused at 1300°C and ceramic tubes were placed in the crucibles in an attempt to provide a surface for side-wall crystal nucleation and growth with associated boundary layer formation in the melt. The objective was to simulate side-wall crystallization in bodies of magma. Due to the fact that the ceramic tubes extended out of the hot-spot of the furnace, it had been hoped that this would be sufficient to induce a temperature difference between the tube and the melt, and so would provoke crystallization on the melt-tube interface. However, crystallization on the tube walls is not seen in thin sections of these experimental charges and iron-oxide crystallites again form throughout the melt. Such a technique could be developed in further work by using a longer tube with an internal cooling mechanism which would produce a temperature difference between the melt and this 'cold finger'. As shown later in this chapter another problem exists with using an alumina tube as a cold finger. Alumina dissolves slightly into the melt contaminating it, possibly masking any effect of boundary layer melt production due to crystallization on the tube. A tube for any such future experiments should be inert when it comes into contact with a basaltic melt. Noble metals could be used for this purpose but would inevitably be costly and could not be re-used.

4.3 Results

4.3.1 Summary of processes taking place in experimental charges

1255°C was adopted as the run temperature for the main sequence of experiments (B-H 7-16), with durations between 11 minutes and 96 hours, to examine the following phenomena which were first identified in experiments B-H 1 to 6 (see figure 4.01 for outline of processes):-

- Iron-oxide crystallites form in the melt, and regions of melt in the charge that are enriched in these crystallites convect due to their increased density. EPMA shows that regions of glass with high concentrations of crystallites have almost identical compositions to those without crystallites. Therefore the melt does not convect on its

FIGURE 4.01. Typical thin section of a short-duration experimental charge using basalt melt and a cemented hematite seed.

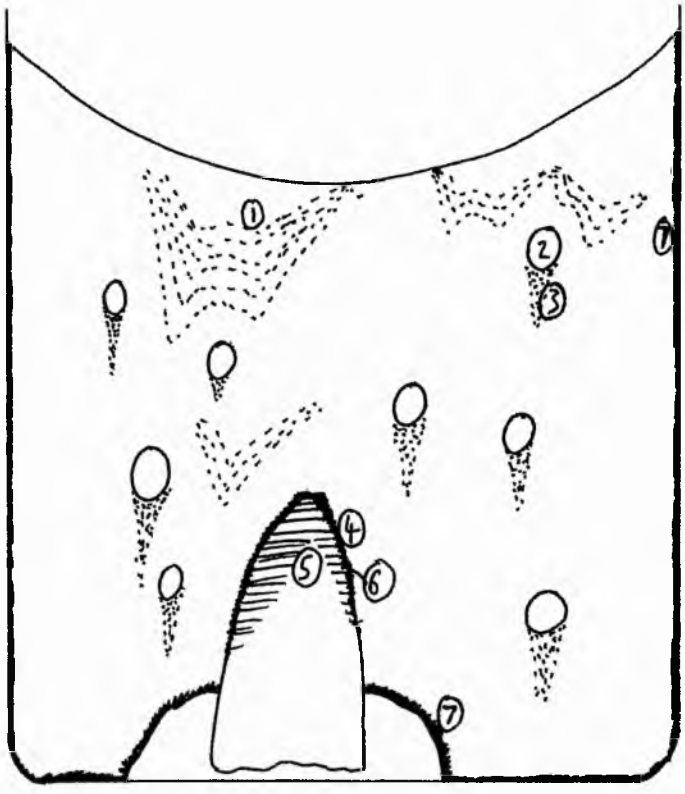

1 = Fe-oxide crystallites nucleate at the meniscus and sink. Their flow patterns are re-alligned by rising bubbles.
2 = Air bubbles escaping.
3 = Trails of oxide crystallites beneath air bubbles.
4 = Dark, Fe-rich melt surrounding crystal seed.
5 = Lamellae of hoegbomite run horizontally into the seed.
7 = Hercynite growth on side walls and cement.
6 = Hoegbomite rim developed at seed-melt interface

own, convection is instead caused by an increased density in packets of melt containing melt and crystals.

- Dark glass develops at the seed-liquid interface, and has moved from its original position at the interface; possibly due to its high concentration of iron.
- Air bubbles escape and effect flow patterns of the crystallites in the charges.
- Side-wall crystallization of hercynite, and its effect on the density of the melt at the crucible-melt interface.

These phenomena all have an effect on the convective regime within experimental charges, and this series of experiments illustrates how the relative importance of each of these processes develops with time.

Plates 4.01 to 4.10 are plane-polarized light photographs of vertical thin sections through the experimental crucibles B-H 7-16, arranged in order of increasing run duration. Points marked on figures 4.02 to 4.11 are those analysed by EPMA. These chemical analyses are displayed, with totals of all original glass analyses recast as 100%, in table 4.02, along with calculated melt density and viscosity at 1255°C. The following observations are made from these plates and tables and are annotated in the sketches in figures 4.02 to 4.11:-

4.3.1A Bubbles

1) Most air bubbles escape from the melt during the first 90 minutes. Bubbles remaining after this time cling to crystal-seed interfaces and get larger by aggregation.
2) Iron-oxide crystallites nucleate on the surface of the bubbles (see plate 4.11), and at the meniscus.
3) In short duration runs the buoyant rise of bubbles through the melt causes deformation of streams of crystallite-rich melt (see plate 4.11).
4) As they rise, bubbles leave a trail beneath them, rich in iron-oxide crystallites (see plate 4.11).

4.3.1B Iron-oxide crystallite formation

1) Crystallites of hoegbomite nucleate at the meniscus and on the surfaces of air bubbles in the melt, indicating a possible redox, surface tension, or temperature effect in their nucleation process.
2) Crystallites are ubiquitous in runs upto 90 minutes long, then become scarcer, and are barely detectable after 6 hours.
3) Crystallite-rich melt forms dense currents which sink in the charges, and are folded and distorted by obstructions in their path. These obstructions include rising air bubbles and the central hematite seed. For this downward convection there must be an opposing upward flow of matter producing currents which may further distort the density currents of crystallites.

FIGURE 4.04 and plate 4.03. 45 minute duration.
1) Widening of hercynite layer.
2) Increased development of Fe-rich melt.
3) Fewer vesicles but crystallites remain in folded sheets.

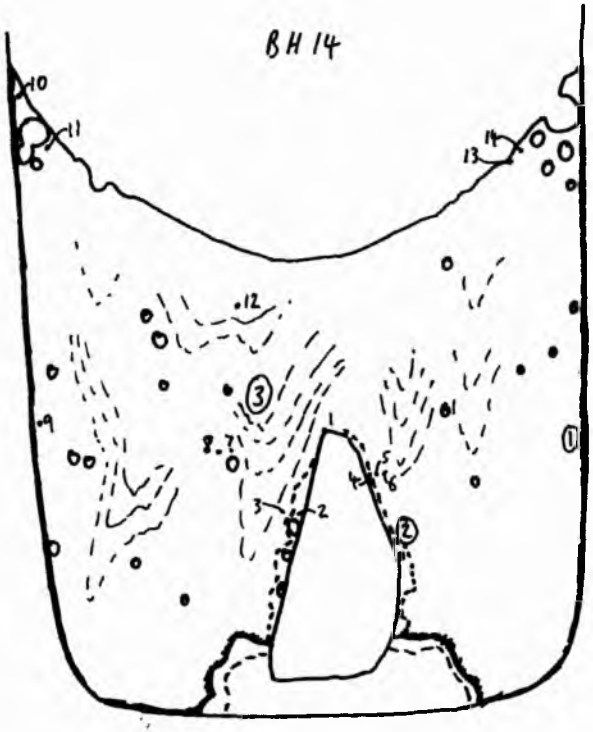

FIGURE 4.03 and plate 4.02.. 22 minute duration.
1) Streams of crystallites rain down from the meniscus and their trails are contorted.

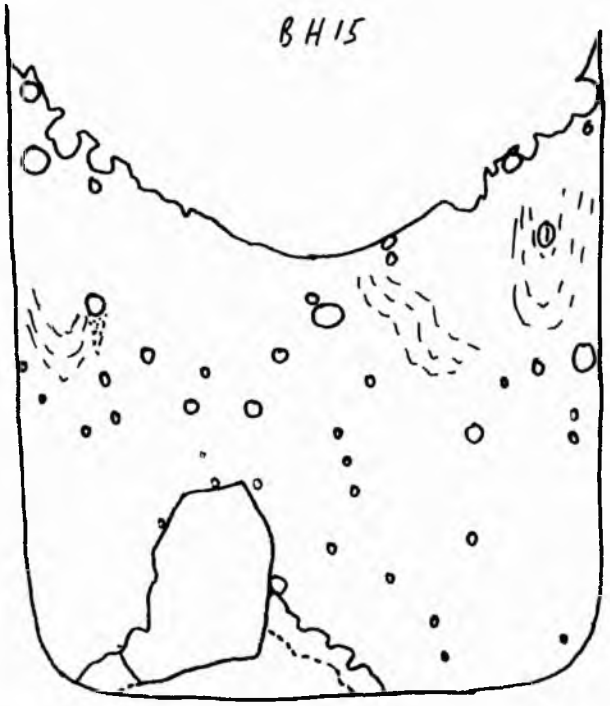

FIGURE 4.02 and plate 4.01. 11 minute duration.
1) Vesicles with trails of crystallites beneath them.
2) slight development of Fe-rich melt around seed.
3) Dark line of hercynite.
4) Trails of crystallites contorted by rising bubbles.

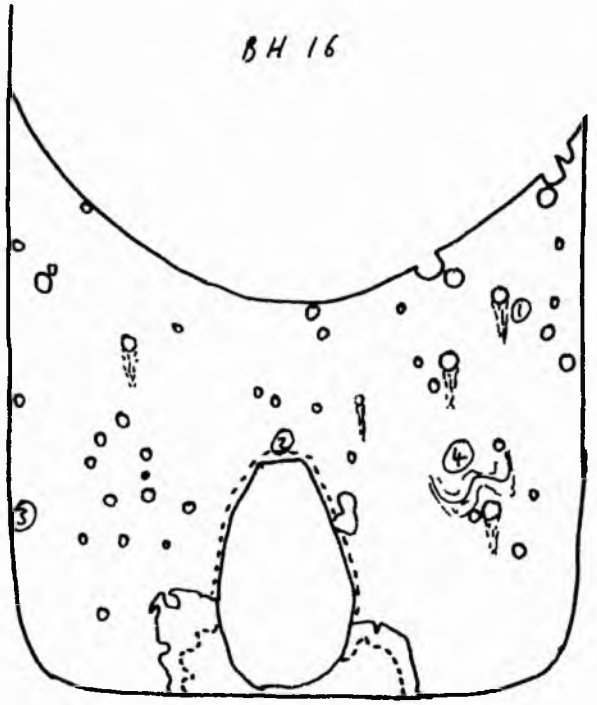

FIGURE 4.07 and plate 4.06. 6 hours duration.
1) Layer of pale, Al2O3-rich melt at crucible wall.
2) Layer of darker, FeO-rich melt up the sides of he crucible. Could possibly have been dragged there by the buoyant Al2O3-rich melt or by escaping bubbles.

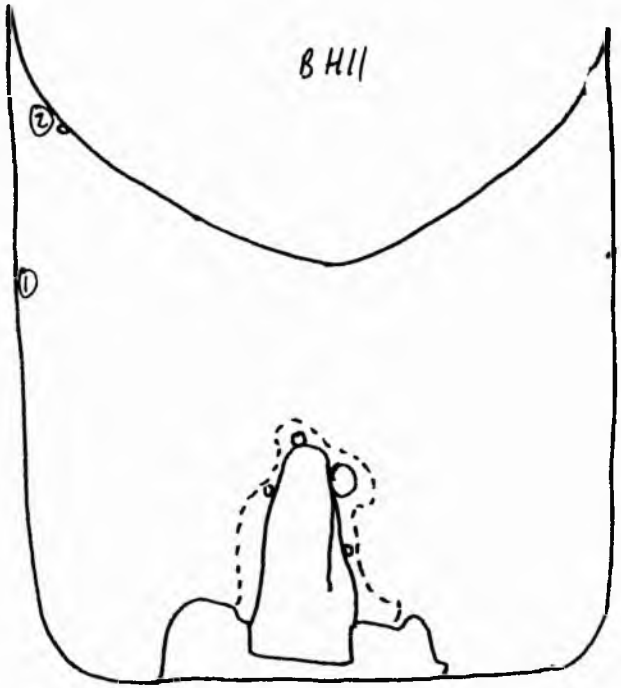

FIGURE 4.06 and plate 4.05. 3 hours duration.
1) Fe-rich melt clearly seen around crystal seed.
2) Wide hercynite rim around Al2O3 cement.
3) Pale, Al2O3-rich melt developes next to the growing layer of hercynite.

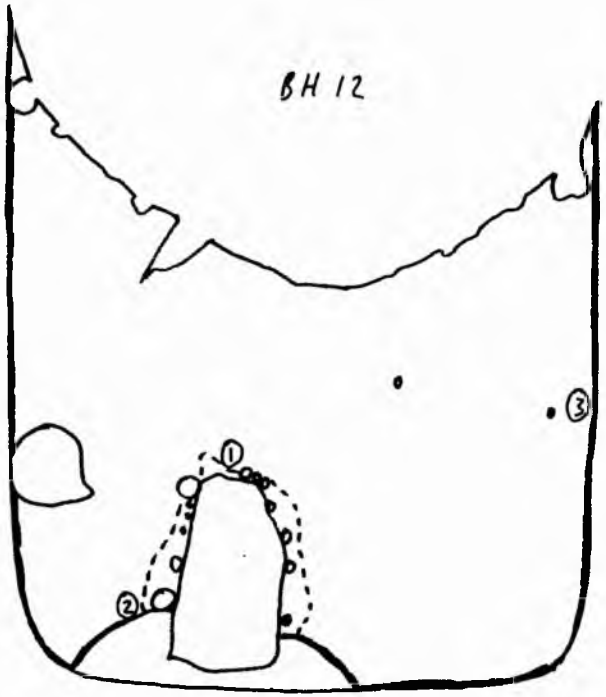

FIGURE 4.05 and plate 4.04. 90 minute duration.
1) Fe-rich melt appears above the seed but is absent from the seeds right-hand side.
2) Very few vesicles remain, therefore crystallite sheets are not folded but appear to form in U-shaped patterns between the seed and the crucible walls.

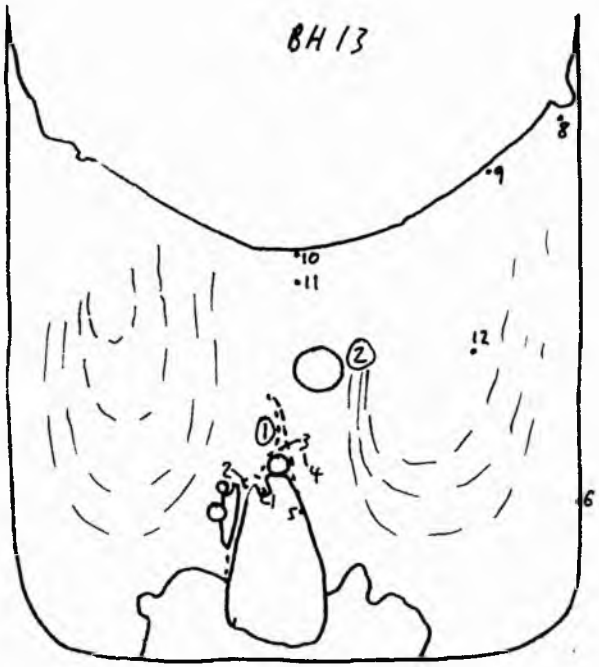

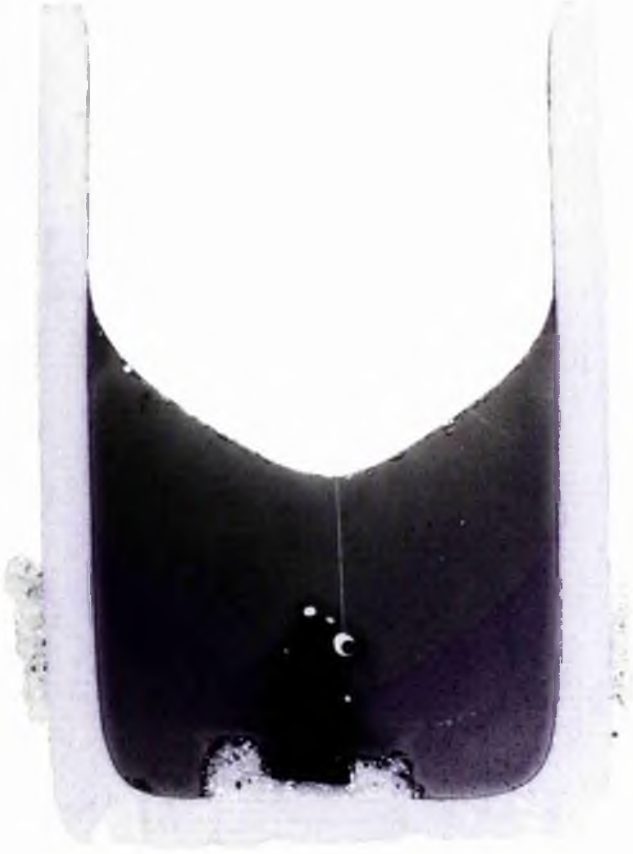

FIGURE 4.09 and plate 4.08. 24 hours duration.

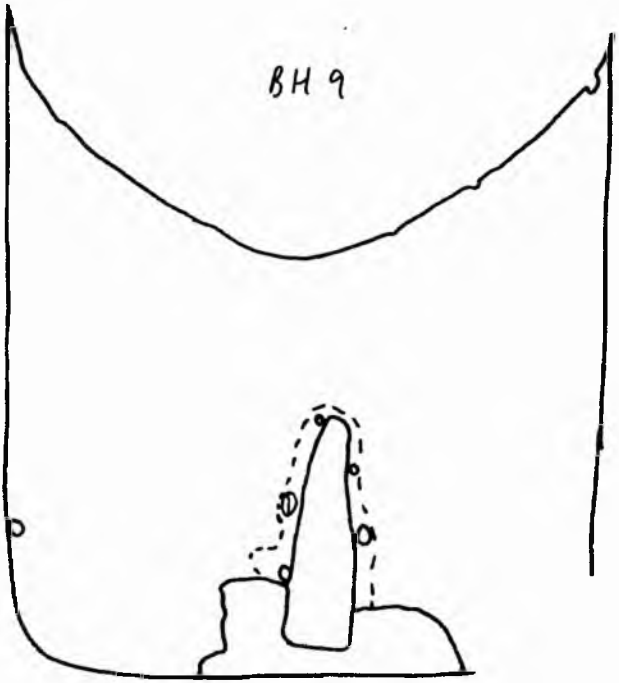

FIGURE 4.08 and plate 4.07. 12 hours duration.

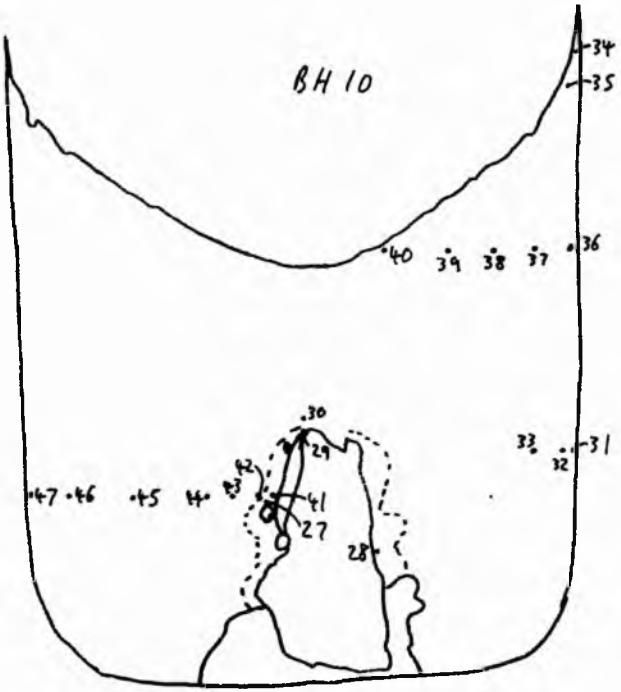

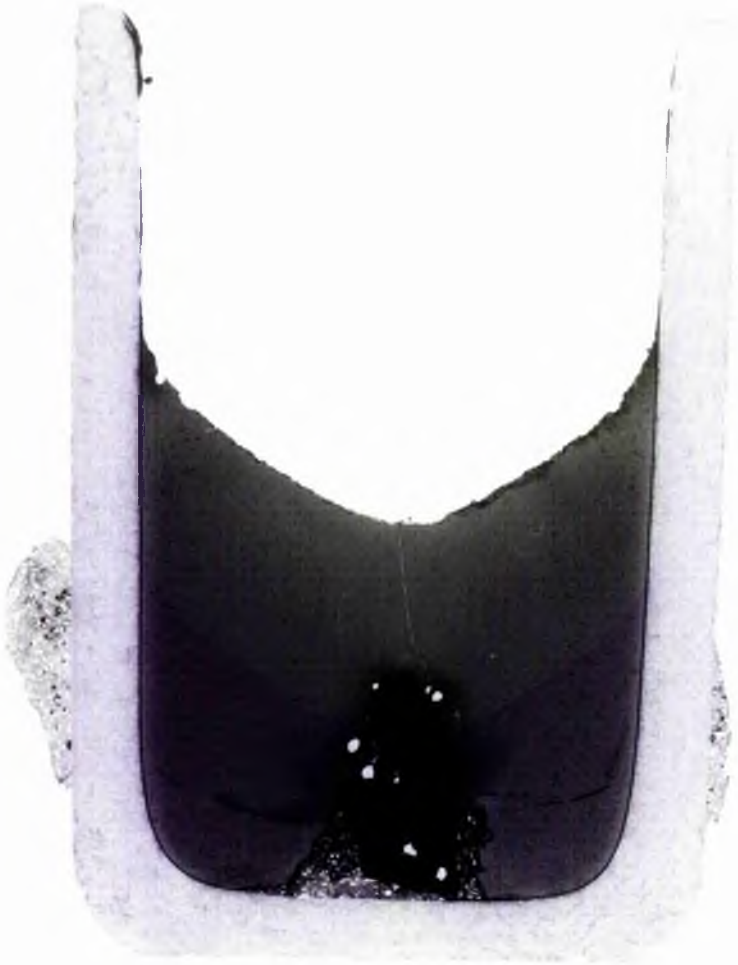

FIGURE 4.11 and plate 4.10.

1) Fe-rich melt has risen up the side wall, possibly dragged by the buoyant Al2O3-rich melt, or by bubble escape.
2) Fe-rich melt has sunk, due to its high density, and has spread across the crucible floor.

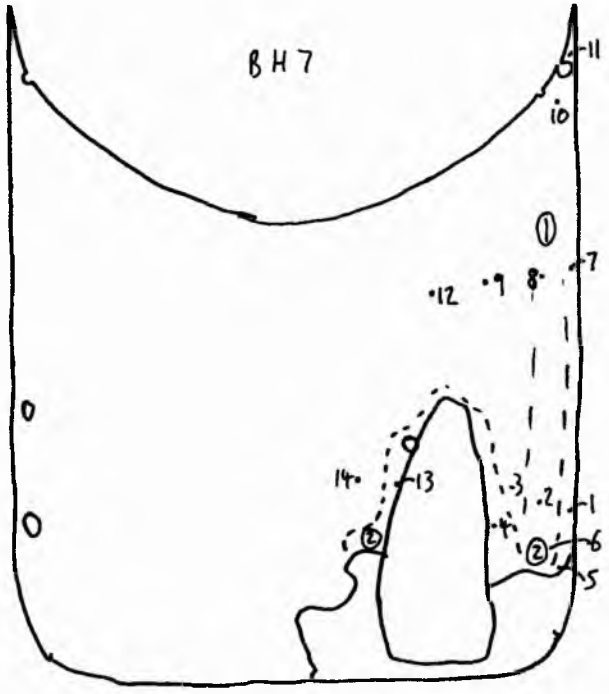

FIGURE 4.10 and plate 4.09. 48 hours duration.
1) Al2O3-rich melt has rised up the crucible walls and spread out horizontally beneath the meniscus.
2) A buoyant plume of Al2O3-rich melt is produced by cement dissolution and hercynite growth.

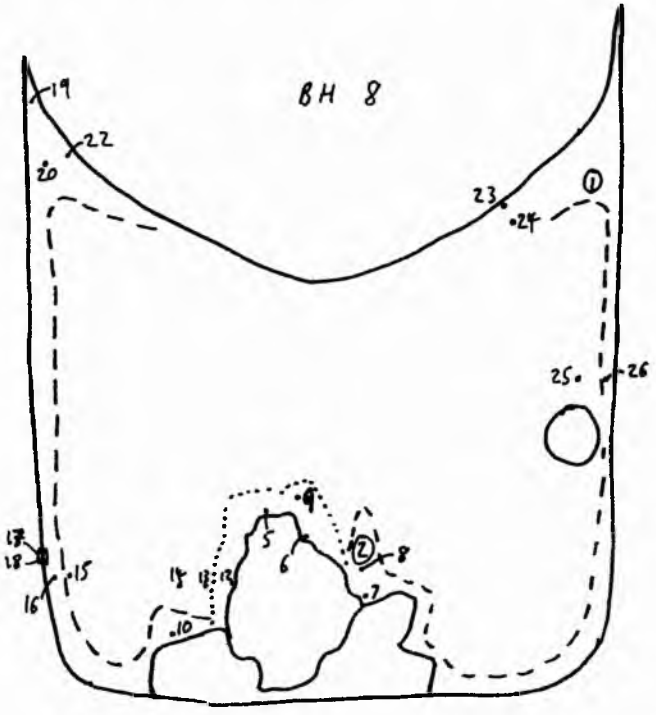

Plate 4.11. PPl photomicrograph of air bubbles and hoegbomite crystallites in the brown glass in charge BH 15. The dark rim around the bubbles comprises nucleating crystallites. Trails of crystallites are seen beneath the bubbles, and folding of crystallite trails above the bubbles can be detected. Magnification x 50.

4) The crystallites do not settle to the bottom of the crucibles. Their disappearance coincides with the reduction in the number of gas bubbles in the melt, lending weight to the observation that their crystallization is connected with a surface tension, redox, or temperature effect at the meniscus and on bubble surfaces.

4.3.1C Development of dark, iron-rich melt

1) An area of darker glass is seen around the seeds in all of the experiments in this series. This becomes more pronounced with time (compare B-H 11 and 12 with B-H 15 and 16 in plates 4.05, 4.06, 4.02 and 4.01 respecively). EPMA shows that this glass is enriched in iron and hence is denser (by 1.5%) than the original melt in the charge (see analyses 3, 4, 6, 13, and 14 in B-H 7 in table 4.02).

2) In B-H 13 a plume of this darker glass is seen above the top of the bubble overlying the crystal seed. Calculations indicate that this dark melt is denser than melt in the rest of the charge (compare analyses 3 and 4 in run B-H 13 in table 4.02) and is therefore defying gravity in being above its source region. Mechanisms responsible for this could include a convective response to the sinking currents of crystallites and melt, or the action of bubbles escaping from the charge. The convective response to sinking of crystals and liquid must be a counter-flow of matter somewhere else in the crucible. If this takes place close to the crystal seed then the upward flow of melt may overcome the higher density of the iron-rich melt and drag it upwards in the crucible. More likely is that the buoyant escape of bubbles from the seed-liquid interface has dragged some of this iron-enriched melt up as the bubbles rise in the charge. When this bubble escapes at the meniscus the denser melt would be left above its source.

3) In longer runs (eg B-H 7 and 9) the dark glass has sunk and spread out across the floor of the crucible (bottom right corner in plate 4.10). It is also seen up the sides of the crucible and close to the meniscus, next to an area of pale glass, in runs B-H 7, 8, 9, 10, and 11. This again conflicts with density calculation evidence.

4.3.1D Hercynite crystallization and alumina dissolution at crucible walls.

1) At the interfaces between the glass and the crucible walls and the cement on the floor a dark line is seen in thin sections. This line (plates 4.12 to 4.17) is comprised of a layer of euhedral hercynite crystals (see analysis 6 in B-H13 in table 4.02) and a layer of dark alumina which has soaked up some of the basaltic melt.

2) This dark line becomes thicker and therefore more visible with increasing run duration (compare plates 4.01 to 4.10).

3) Immediately adjacent to the hercynite layer the glass is a paler colour than the original melt. This is more pronounced in runs exceeding 90 minutes, after hoegbomite crystallite formation has ceased and bubbles have escaped. EPMA indicates that this melt is enriched in Al_2O_3, and depleted in SiO_2 and FeO, giving it a lower density than the melt in the centre of the crucible. Hercynite development has depleted the melt in iron, but an Al_2O_3 depletion, which would be expected if Al_2O_3

Plates 4.12, 4.13 and 4.14. Backscattered electron images of the hercynite rims between crucibles and glass in runs of 45 minutes, 3 hours, and 6 hours (from top to bottom) respectively. Note the constant width of elongate needles (a quench product) and the increasing width of the layers of brighter hercynite between the dark alumina wall and the layer of quench crystals. Scale bar = 10 μm.

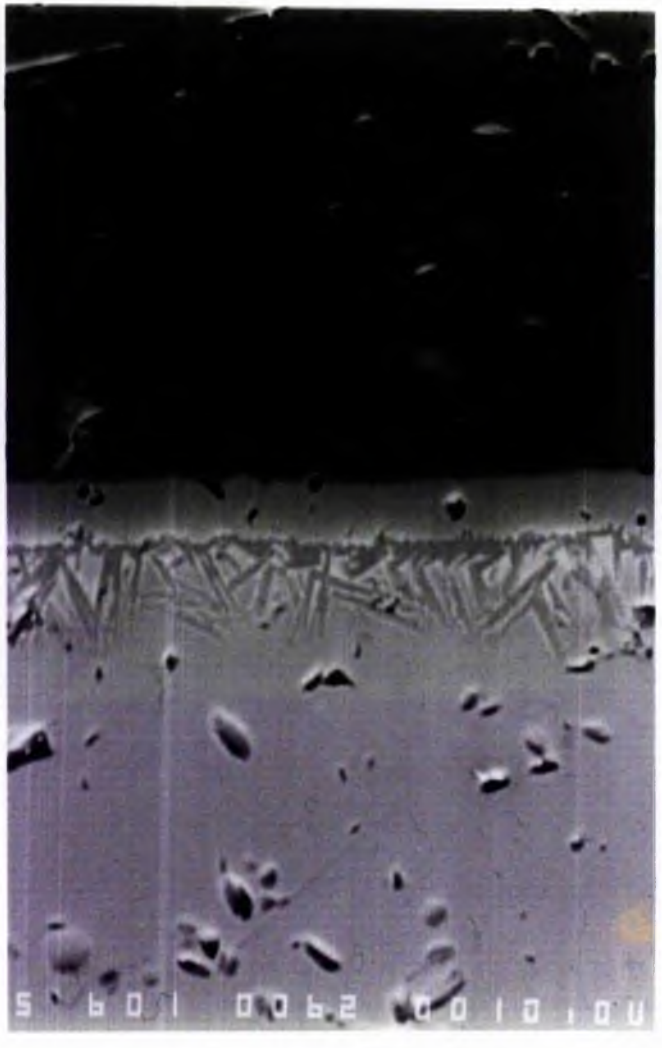

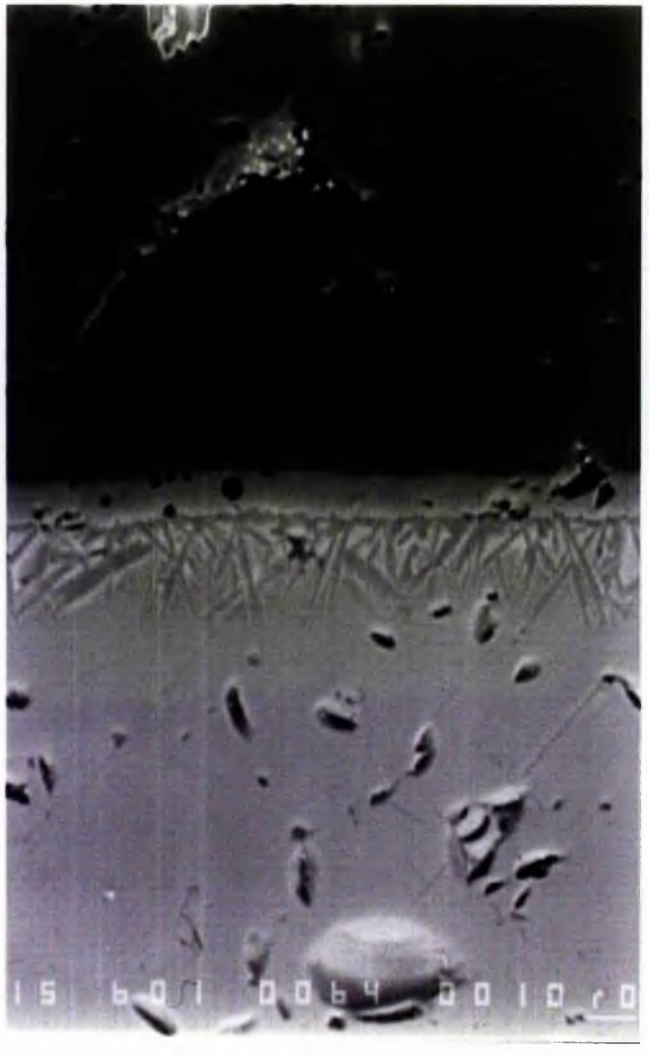

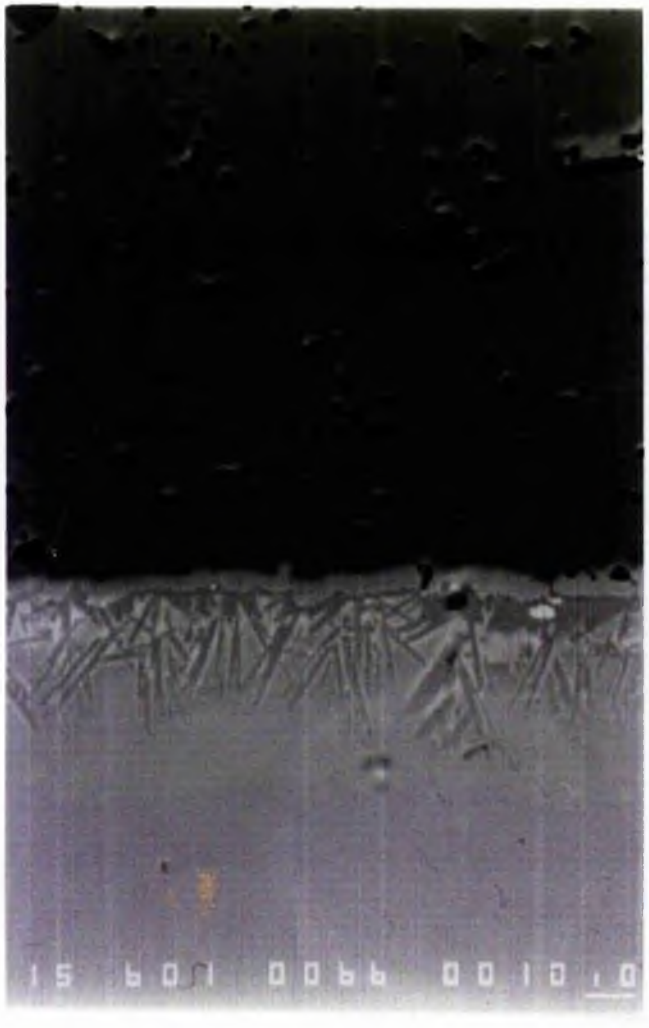

Plates 4.15, 4.16 and 4.17. Backscattered electron images of the hercynite rims between crucibles and glass in runs of 12, 48, and 96 hours (from top to bottom) respectively. Note the constant width of elongate needles (a quench product) and the increasing width of the layers of brighter hercynite between the dark alumina wall and the layer of quench crystals. Scale bar = 10 μm.

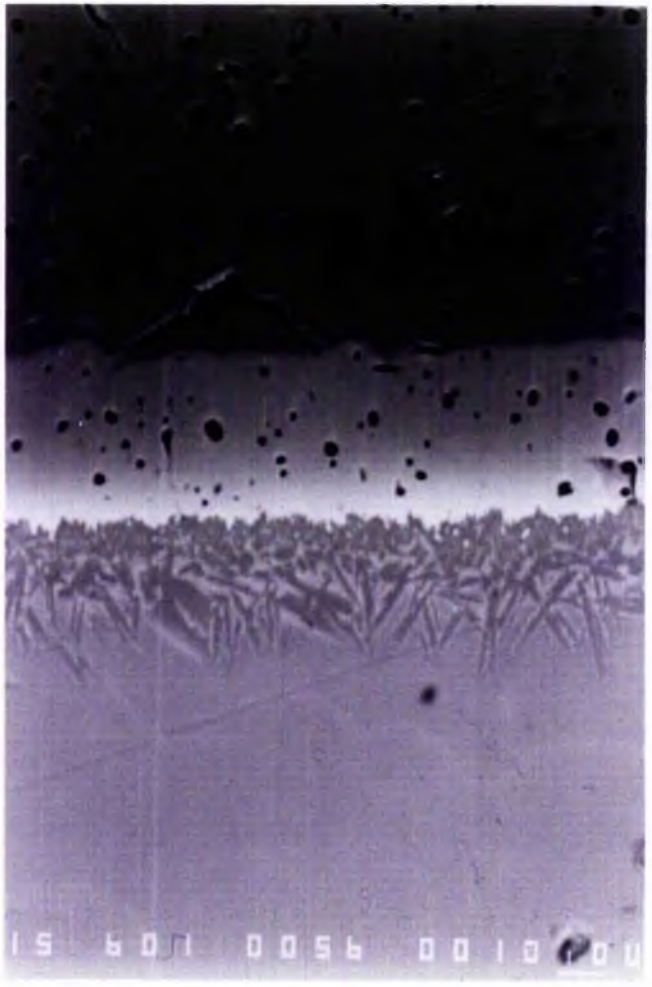

was stripped from the melt and incorporated with iron and magnesium in hercynite, is not seen, pointing towards a contamination of the melt near the wall with dissolved alumina from the crucible and cement.

4) The aluminium-rich melt is buoyant (see density calculations in table 4.02) and, in runs of 6 or more hours, is seen to have ponded beneath the meniscus.

5) Dissolution of the alumina cement on the crucible floor produces buoyant melt that rises in plumes from its source (see plate 4.06 and 4.09). These plumes cannot be traced far through the crucible, and so they are either young, and just developing, or they become quickly homogenized in the charges by chemical diffusion and, or, physical mixing.

6) In experiments B-H 11, 8 and 7 the denser, iron-rich melt (produced at the seed-liquid interface) has spread across the crucible floor as expected, but also occurs up the crucible walls, inside the alumina-rich melt. EPMA and density calculations indicate that this dark melt is not buoyant. Perhaps the buoyant aluminium-rich melt, on rising up the crucible walls, has dragged the denser, iron-rich melt up to the meniscus, or the buoyant rise of bubbles may have lifted the denser melt above its original position.

4.3.1E Density Differences

From EPMA and density calculations displayed in table 4.02 the following points can be made. These are listed under the headings of three experiments of varying durations to outline the difference in processes at different times.

B-H 14 (45 minutes) (plate 4.03)

1) The melt at the crystal-liquid interface is depleted in SiO_2 and MgO, is relatively enriched in Al_2O_3 and FeO in comparison with the original melt, and has a higher density than the surrounding melt. This layer is upto 1 mm thick in places but is unevenly developed.

2) Melt at the crucible walls is enriched in Al_2O_3 and depleted in FeO, giving it a lower density than the original melt. This experiment has not run for long enough for the buoyant melt to have ponded visibly beneath the meniscus.

3) The melt which is rich in iron oxide crystallites is depleted in SiO_2 andFeO, but is enriched in CaO. It is not noticeably different in density from crystallite-free melt.

B-H 13 (90 minutes) (plate 4.04)

1) Iron-rich melt is poorly developed adjacent to this crystal seed (right hand side of the seed on plate 4.04) but is seen on the upper and left-hand sides. As mentioned earlier, there is a plume of iron-rich melt above the seed. This plume has probably been dragged up by a convection current or by bubble action which could have eroded the dark melt from the right-hand side of the crystal.

2) Buoyant, Al_2O_3 rich, melt has developed at the crucible wall, but not enough has been produced to be identified optically as a distinct layer beneath the meniscus.

B-H 10 (12 hours) (plate 4.07)

1) The density differences described in B-H 13 and 14 are also seen in longer runs, with the appearance of buoyant melt, produced by side-wall crystallization and alumina dissolution, and denser, iron-rich melt, produced by the reaction at the seed-liquid interface. Al_2O_3-rich melt has risen in the crucible and ponded beneath the meniscus.

2) Compositional differences in the glasses produced in this experiment are relatively small (FeO varies from 10.4 wt % at the crystal interface to 8.3 wt % at the crucible wall, while Al_2O_3 varies from 15.8 wt % to 17.8 wt % in the same places) but are differences in the heaviest and lightest oxides (FeO and Al2O3 respectively), and so have a noticeable effect on the density of melts in these positions.

3) The maximum density difference in melts in run B-H 10 is 0.05 gcm^{-3}, between Al2O3-rich melt at the crucible wall and Fe-rich melt at the crystal-liquid interface. The density difference between the melt at the crucible wall and the original melt in the charges is only half of this (0.025 gcm^{-3}) but is obviously sufficient to cause compositional-driven convection in this low-viscosity melt. This fact is important when considering composition-driven convection in magmas, as it shows that small density differences (<0.05 $g.cm^{-3}$) are sufficient to cause convection in low-viscosity melts.

To summarize, the compositional differences which drive convection in these experiments appear to be produced by the following processes. These processes are examined in closer detail in the next two sections.

a) Crystallization of hercynite and dissolution of alumina at the alumina-melt interface. These two processes combine to produce a buoyant melt enriched in aluminium but depleted in iron.

b) A dissolution reaction at the seed-liquid interface which produces a hoegbomite rim on the seed and causes iron-enrichment in the adjacent melt.

4.3.2 Processes at the crystal-liquid interface

Reflected light microscopy reveals an outer layer of iron-oxide, with a lower reflectivity than hematite on all crystal seeds. The back-scattered electron images in plates 4.18 to 4.23 illustrate the morphology and width of this layer in runs from 11 minutes to 96 hours in length. As well as this rim, horizontal lamellae of the same mineral penetrate into the hematite seed.

Both the oxide rim and the lamellae in the crystal seed have the same composition (see analyses 2 and 4 from B-H8 in table 4.02) and are connected at the edge of the crystal seed. Table 4.03 presents measurements of oxide-rim width, lamellae development, and overgrowth morphology at different times and these data are displayed in figure

Plate 4.18. BSEI of hoegbomite rim in run of 45 minute duration. Note the simple, euhedral morphology of the dark rim.

Plate 4.19. BSEI of hoegbomite dissolution rim after 3 hours. Rim has become wider, and slightly skeletal, and is wider at the top of the seed. Lamellae of dark hoegbomite have begun to penetrate into the hematite seed.

Plate 4.20. BSEI of hoegbomite rim and lamellae development on the hematite seed after 6 hours. Note the increase in length of lamellae as the seed is ascended.

Plate 4.21. BSEI of hematite seed and hoegbomite development after 12 hours. lamellae are longer and the rim is more skeletal than in plate 4.20.

Plate 4.22. BSEI of hoegbomite dissolution rim after 48 hours. Note the porous appearance of the rim and the penetration of the lamellae right across this crystal seed.

Plate 4.23. Hoegbomite dissolution rim and lamellae development after 96 hours. Note the shortening of lamella length as the seed is descended.

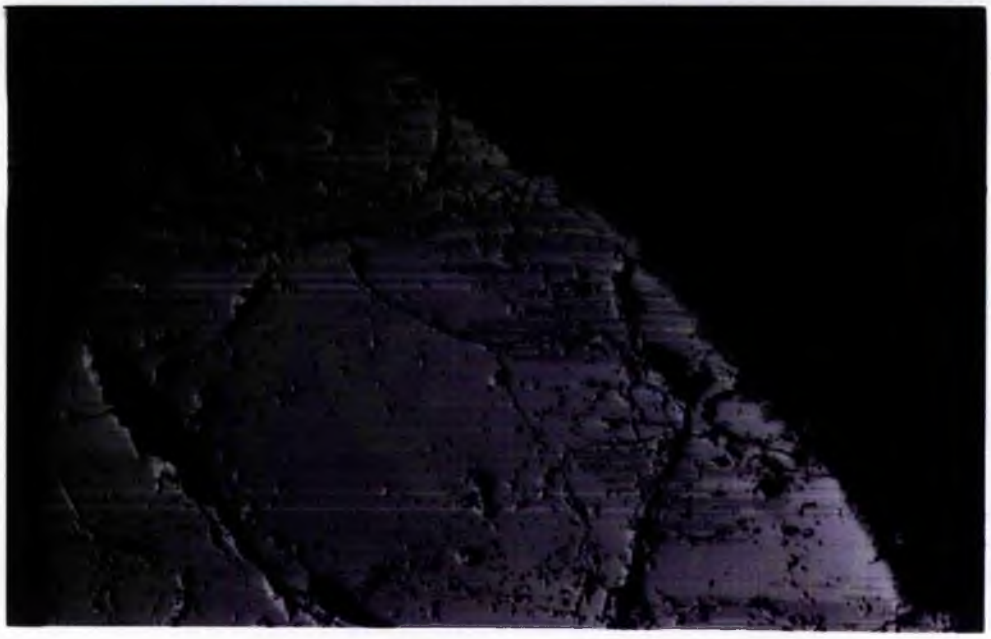

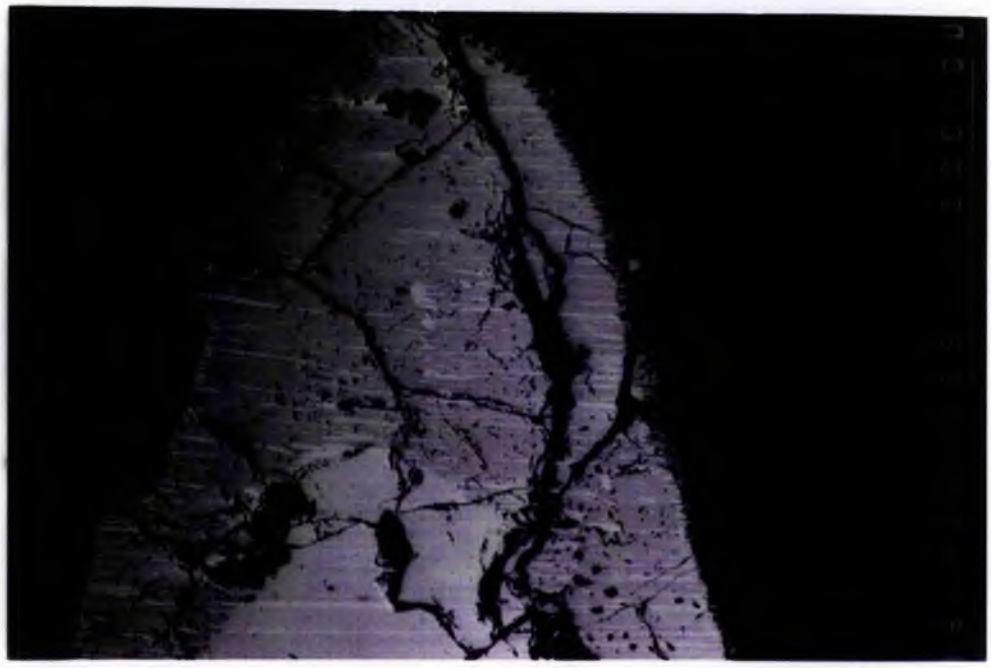

Table 4.03. Hoegbomite rim and lamella development in basalt-hematite experiments

Run Number	B-H 14	B-H 12	B-H 11	B-H 10	B-H 8	B-H 7
Time (hours)	0.183	3	6	12	48	96
Temperature (hours)	1255	1255	1255	1255	1255	1255
Maximum width of oxide rim (μm)	10	10	25	25	100	100
Maximum lamellae width (μm)	40	100	150	200	600	800
Average oxide rim growth rate (μm/hr)	54.6	3.3	4.16	2.1	2.08	1.04
Oxide rim growth rate since last run (μm/hr)	54.6	1.8	5	1.7	2.1	0.5
Overall rate of lamellae development (μm/hr)	219	33.3	25	17	12.5	8.3
Rate of lamellae development since last run(μm/hr)	219	21.3	16.7	8.3	11.1	4.2
Sketch of oxide rim morphology	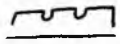	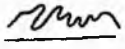	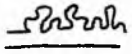	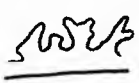	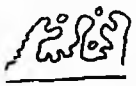	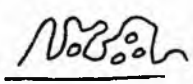

Figure 4.12a. Variation in width and growth rate of hoegbomite rim with time.

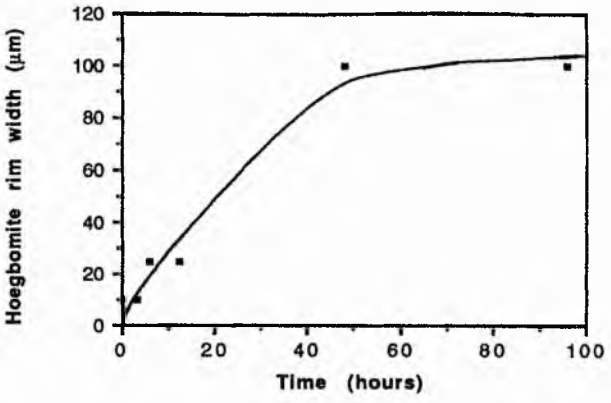

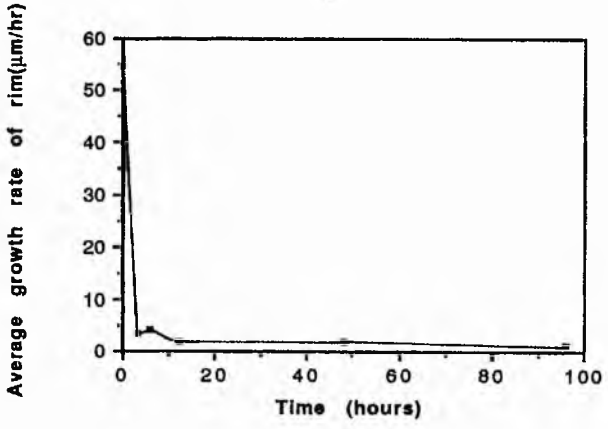

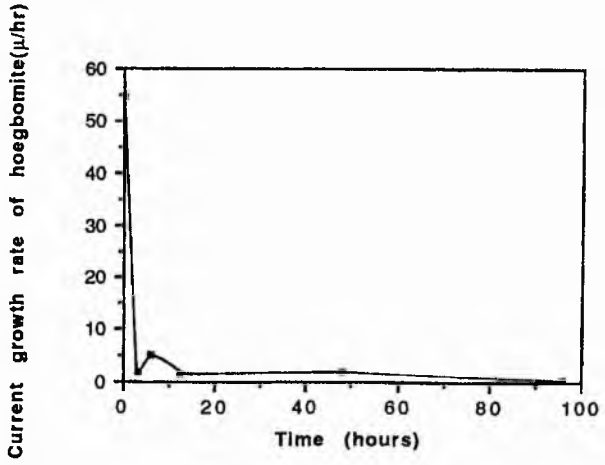

Figure 4.12b. Length and rates of lamellae development

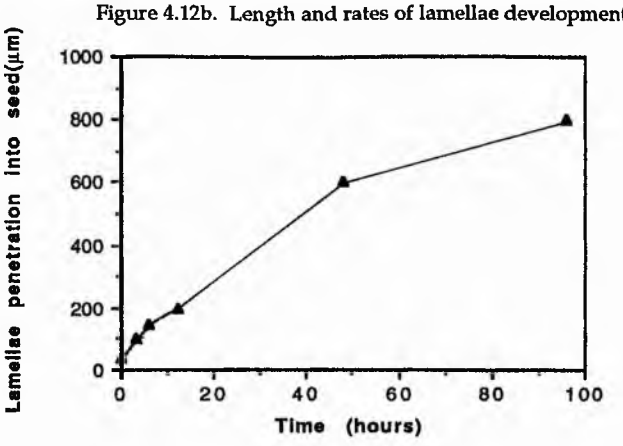

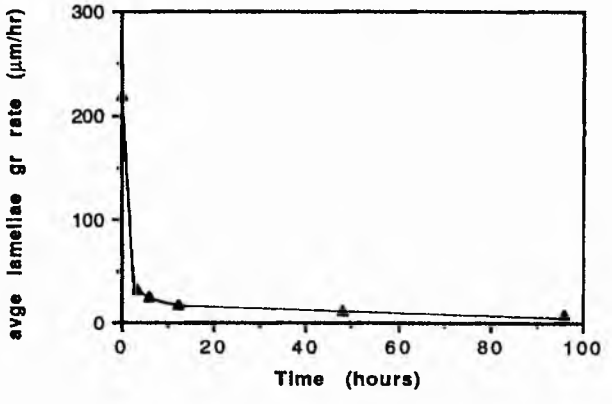

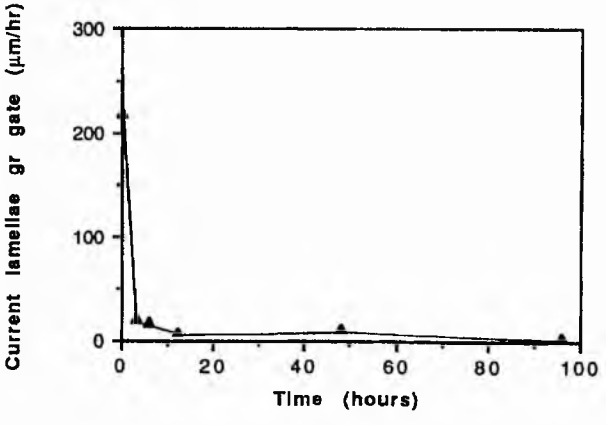

4.12. The following points summarize the oxide-rim and lamellae development and distribution in this series of experiments:-

- Oxide-rim width increases with increasing run duration.
- Oxide-rim morphology becomes more complex with increasing run duration.
- The oxide-rim is thicker at the top of the crystal seeds, thinning to absence near the base of the seed.
- Lamellae of the overgrowth mineral penetrate horizontally into the seed. They increase in length in longer runs and in all cases penetrate further into the seed near its top, becoming shorter near to the base.

If this iron-oxide has grown on the crystal seed, one would expect the melt at the interface to be depleted in iron; this is not the case. Instead an iron-enriched halo of melt is seen around the crystal seeds in all experimental runs.

The increasingly complex rim morphology is seen to consist of a network of rounded crystals. If this rim was an overgrowth it should contain euhedral crystals. This, combined with the fact that the adjacent melt is enriched in iron, and the only source of extra iron is in the hematite seed, points towards the rim being an intermediate in the dissolution of the hematite seed.

Due to the destructive nature of the methods used to analyse these crucibles, there is no means of testing whether an individual seed grows or shrinks during experimental runs. The iron-oxide dissolution intermediate has the same composition as the crystallites that are ubiquitous in short-duration runs. After 3 hours these crystallites re-dissolve in the melt; it appears that the same happens to the iron-oxide rim too.

The iron-oxide rim, and the lamellae contain upto 14 wt % MgO and 6 wt % Al2O3. The original hematite seed contains no MgO and very little Al_2O_3 (see analysis 1 from B-H8 in table 4.02). This suggests strongly that an exchange reaction has taken place at the crystal-liquid interface, with MgO and Al_2O_3 infiltrating into the seed to form this rim and the lamellae, while FeO migrates out into the melt. The rim is a zone of hoegbomite that is therefore an intermediate in the dissolution of hematite. The sketches in figure 4.13 summarize the processes taking place at the seed-melt interface.

Assuming the hottest temperatures exist at the top of the experimental charges, one would expect overgrowth rate and lamella development on the crystal seed to increase from top to bottom. Plates 4.18 to 4.23 show that this is not the case, with rim and lamellae development being fastest at the top and decreasing downwards. An explanation of this may lie in the convective behaviour of the iron-rich melt at the seed-melt interface. In long duration runs this melt sinks in the charges due to its increased density. When this happens the melt at the top of the seed is replaced by

FIGURE 4.13. Summary of processes at hematite seed-melt interface

a) Development of hoegbomite rim, with increasingly complex morphology and longer lamellae with increasing run duration.

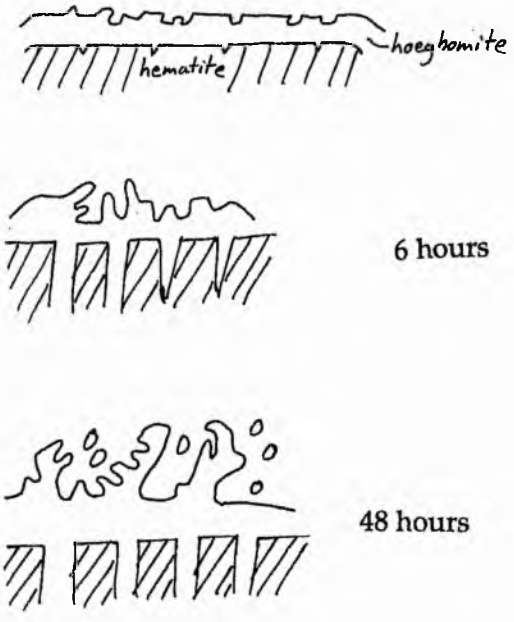

b) Chemical exchange processes at the interface. Lamellae width and hoegbomite rim width decrease as the seed is descended.

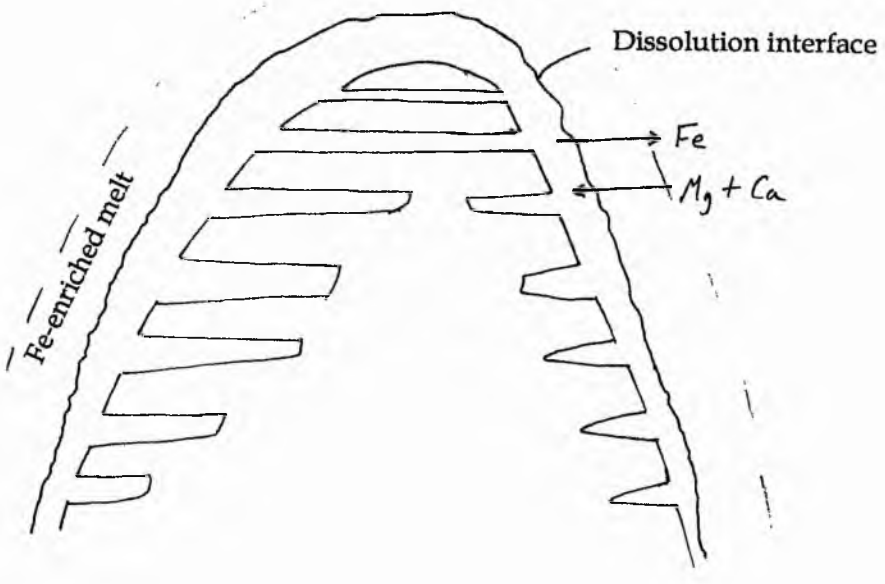

fresh melt from other parts of the crucible (i.e. from above the seed. See figure 4.14). This melt is relatively enriched in MgO and Al_2O_3, and is depleted in FeO; thus development of the dissolution intermediate continues because chemical disequilibrium exists between hoegbomite and the melt. When the melt at the bottom of the seed sinks, it is replaced by iron-rich melt from above. This melt is enriched in iron and so dissolution rate here is slow as chemical equilibrium is maintained.

4.3.3 Crystal Overgrowths on the crucible walls

In thin sections of all experimental charges, a dark rim is seen at the interface between the glass and the alumina cement and crucible wall. This rim thickens as run duration increases. Using BSEI it is seen to comprise of 2 portions (see figure 4.15). These are:-

1) A continuous brighter outer layer on the crucible wall of euhedral crystals. This layer does not contain any of the circular pits which appear in the crucible wall and in layer 2.

2) A layer which is duller in BSEI than layer 1 but is brighter than the alumina wall. This layer has a sharp contact with the alumina wall. It contains circular pits identical to those in the crucible.

A layer of needle-like crystals separates layer 1 from the glass. BSEI photographs of these layers from half-way up the wall in runs of different duration are presented in plates 4.12 to 4.17. EPMA of these overgrowths (see table 4.02) indicate the following points:-

- Both the bright and dark parts of the rim are hercynite, the brighter portion being richer in iron (see analyses 17 and 18 from B-H 8).
- The glass adjacent to the crucible walls is enriched in Al_2O_3 and depleted in FeO and MgO; as a melt it is therefore less dense than the rest of the melt and should convect upwards.

The widths of the different parts of the dark line are measured and presented in table 4.04, along with a simplified sketch of this region. Graphs in figure 4.16 show the growth rates of the different portions of the interface zone, and indicate the following points:-

- Layer D (the layer of needle-like quench crystals) does not increase in width with increasing run duration. Runs of 11 minutes and 12 hours produce layers of similar width. This, combined with the crystal morphology in this layer, indicates that the crystals are a product of fast cooling (i.e. quenching) of the charges as they are taken

FIGURE 4.14. Convection of an Fe-rich boundary layer and its effect on hoegbomite rim and lamellae development.

a) Dissolution begins as a thin hoegbomite layer forms around the seed and a boundary layer, rich in Fe, forms by diffusion of Fe out of and Ca and Mg into the rim. The boundary layer begins to convect down the sides of the seed as it is denser than its surrounding melt.

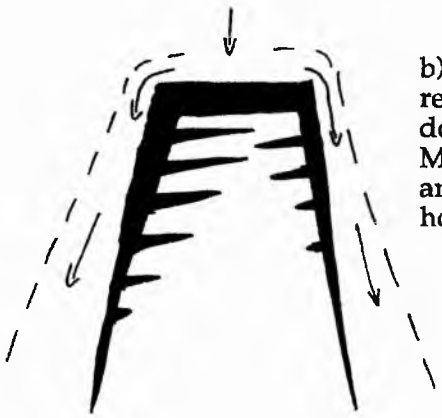

b) Boundary layer melt at the bottom of the seed is replaced by Fe-rich melt from above, therefore slowing down dissolution, and so the hoegbomite layer remains thin. Melt at the top of the crystal is replaced by Fe-poor melt and so dissolution can continue at a fast rate and a thick hoegbomite layer develops.

FIGURE 4.15. Distribution of mineralogical zones at the crucible-glass interface.

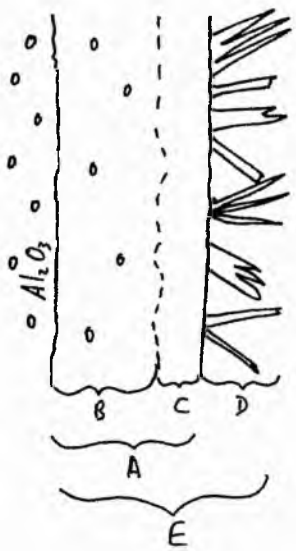

A = B + C
B = Hercynite layer with rounded pits
C = hercynite without pits and with a higher mean atomic number than B.
D = Elongate needles formed on quenching of charge
E = B + C + D

Table 4.04. Widths and growth rates of zones at side walls of crucibles.

Run Number	14	12	11	10	8	7
Duration (hours)	0.183	3	6	12	48	96
Temperature	1255	1255	1255	1255	1255	1255
Width of zone A (μm)	5	9	13	18	upto 35	40-55
Width of zone B (μm)	4	7	10	15	25	30 to 40
Width of zone C (μm)	1	2	3	3	10	10 to 15
Width of zone D (μm)	20 to 30	10 to 20	upto 20	20 to 30	upto 30	30 to 50
Width of zone E (μm)	20 to 35	upto 30	upto 35	upto 40	60	80
Average growth rate A(μm/hr)	27.3	3	2.2	1.5	0.7	0.4 to 0.6
Average growth rate B (μm/hr)	21.8	2.3	1.7	1.3	0.5	0.3 to 0.4
Average growth rate C (μm/hr)	< 5.5	0.7	0.5	0.25	0.2	0.11 to 0.14
Average growth rate D (μm/hr)	108 to 162	3.35 to 6.84	<3.3	1.66 to 2.52	<0.6	0.32 to 0.5
Average growth rate E (μm/hr)	108 to 190	<10	<5.8	<3.4	1.3	0.8
Current growth rate A (μm/hr)	27.3	1.4	1.3	0.8	0.5	0.4
Current growth rate B (μm/hr)	21.8	1.8	1	0.8	0.3	0.2
Current growth rate C (μm/hr)	5.5	0.4	0.3	0.2	0.2	0.1
Current growth rate D (μm/hr)	136.4	0	3.3	1.7	0.3	0.4
Current growth rate E (μm/hr)	163.7	3.6	1.6	0.8	0.6	0.4

Figure 4.16a. Development of side-wall layers with time

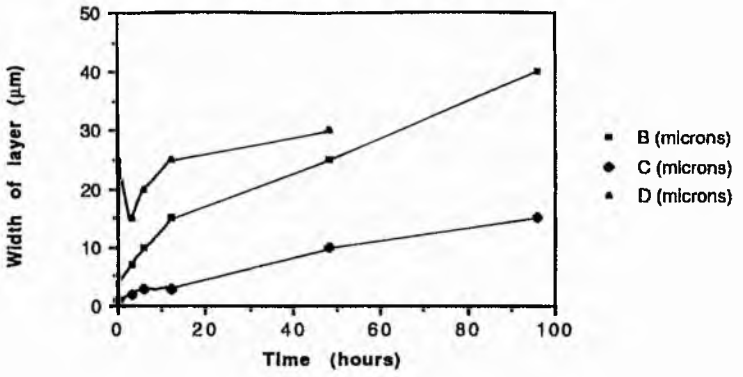

Figure 4.16b. Average growth rates of side wall layers with time

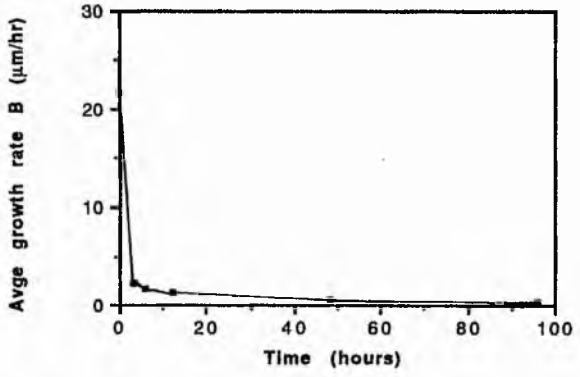

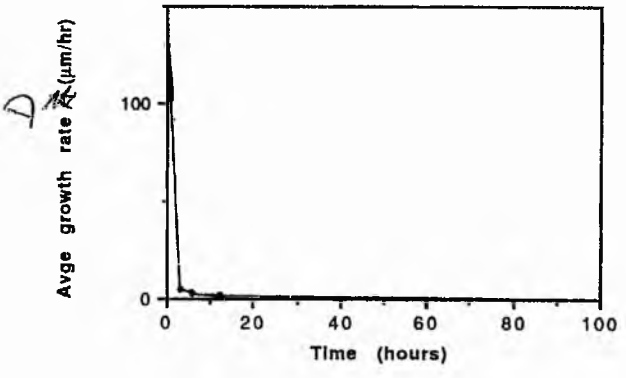

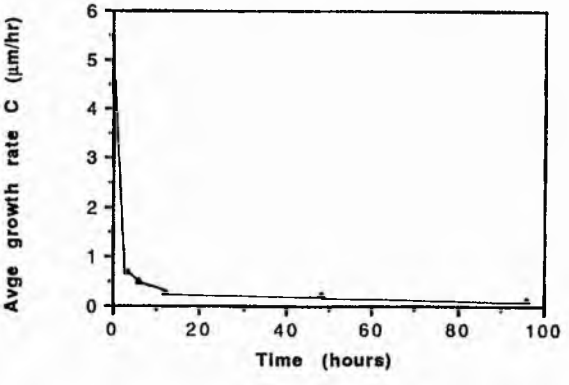

Figure 4.16c. Current (i.e. since last experiment) growth rates of layers B, C, and D from side wall overgrowth

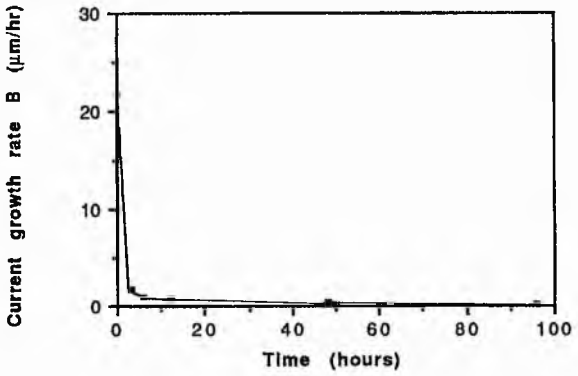

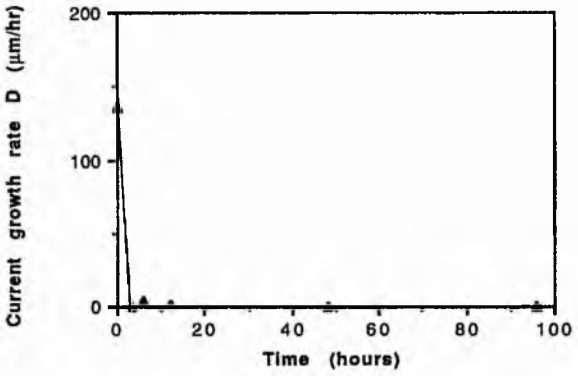

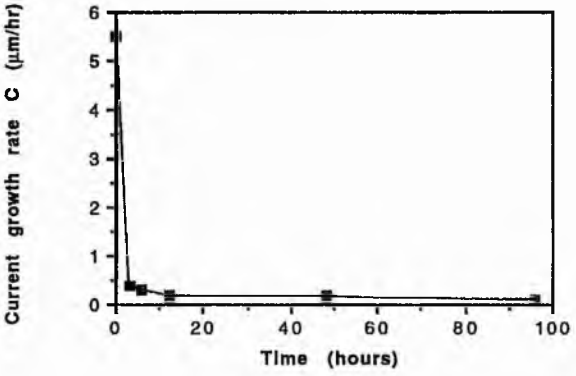

out of the furnace. Slight variations in the width of this layer may be caused by variations in the time taken to extract the crucibles from the furnace at the end of the runs.

- Layer B has a growth rate which is initially very high but decreases very rapidly and flattens out to almost zero after 3 hours. This layer contains circular pits, equivalent to those in the pure alumina crucible wall. Such pits are not be expected, and are not seen, in overgrowths on the wall (i.e. layer C). This indicates that layer B is part of the original crucible wall, and is not an overgrowth, but has been infiltrated by FeO and MgO from the melt. This process could have been caused by the porous nature of the crucible wall early in the run duration, but has not proceeded at the same rate with time.
- Layer C is a continuous rim of iron-rich hercynite crystals between the alumina crucible and the basaltic melt. The growth rate of this layer decreases exponentially with time, and so the width ultimately develops very slowly. The formation of this layer could be the reason for the slow development of layer B after its initial development. If layer B is caused by basaltic melt infiltrating into the porous crucible walls, and the growth of layer C forms an impermeable layer between the crucible and the basaltic melt, then as soon as layer C covers the crucible wall, layer B will be isolated from the melt and cannot continue to develop by melt infiltration. Any further development of layer B has to be by chemical diffusion of FeO and MgO into the wall. This is a much slower process than melt infiltration, and so the growth rate of layer B drops dramatically as soon as layer C has grown, and will drop further with time as FeO and MgO have further to diffuse into the crucible wall. This inward diffusion of FeO and MgO is probably countered in the opposite direction by outward diffusion of Al_2O_3, which enriches the melt at the interface and helps to make it buoyant.

This hercynite overgrowth, and the chemical exchange between the melt and the alumina crucible wall are jointly responsible for producing composition-driven convection in these experimental charges. Crystal growth takes iron and magnesium out of the melt and incorporates it, with aluminium from the crucible wall and cement, in hercynite. Meanwhile alumina is dissolving into the melt, causing dilution of FeO and MgO in the wall melt, and making it more buoyant. There is no noticeable thinning of the crucible walls and so it can be surmised that the walls do not dissolve but that aluminium removed from the wall is replaced by an equal amount of Fe or Mg. The process forming this buoyant melt is therefore a combination of both crystal growth on the walls, and partial dissolution of these walls.

4.4 Discussion and Petrological Applications

4.4.1 Summary

The intention of this series of experiments was to produce buoyant, iron-depleted boundary layers at seed-melt interfaces. Although this does not happen here, a number of processes are observed which cause convection in the experimental charges and which can be applied to the broader aspect of magma convection and compositional differentiation. The following is a summary of the important processes seen in this series of experiments, and the convective effects that they have:-

1) Bubbles in the melt cause heterogeneous nucleation of crystallites of hoegbomite. This nucleation also occurs at the meniscus.
2) Although the bubbles are buoyant, the crystallites on their surfaces are dense and so detach from the bubble surfaces and the meniscus, and then sink through the melt. Regions of glass enriched in these crystallites form high-density currents which sink and are distorted by the bubbles rising in the opposite direction.
3) Bubbles remaining in experimental charges after 3 hours are usually attached to crystal seeds. This preferential attachment could help dense crystals in magma bodies to be buoyant.
4) Iron-enriched melt at the seed-melt interface, produced by hematite dissolution through an intermediate layer of hoegbomite, is dense and sinks to the bottom of the experimental charges.
5) Convection currents in the opposite direction occasionally reverse the downward movement of this dense melt, lifting it above its source and, in longer runs, taking it to the top of the charge.
6) Crystallization of a layer of hercynite crystals, combined with alumina dissolution, produces a buoyant boundary layer of melt that is enriched in Al_2O_3 but depleted in FeO and MgO. This melt rises up the walls and ponds in the uppermost parts of the charge, beneath the meniscus. Dissolution of the cement in the bottom of the crucible forms buoyant plumes of Al_2O_3 rich melt which rise from the crucible floor.

For each of the processes which has been observed in this set of experiments an analogue in a body of magma can be suggested.

4.4.2 Action of Bubbles

Gas bubbles in magmas could cause heterogeneous nucleation of crystals in melts. If these crystals are dense, then they may detach from the bubbles and sink in the magma chamber. Dense crystals may, however, remain attached to bubbles and be dragged upto the top of the magma chamber. If conditions are different, and a relatively light mineral (eg Feldspar) nucleates on a bubble, then it could rapidly be transported to the

top of the magma body. One can imagine this happening if gas is escaping from a body of magma, possibly due to vesiculation associated with a pressure decrease.

4.4.3 Iron-rich melts

If dense, iron-enriched melt is formed (by dissolution of mafic xenoliths and xenocrysts, or by an injection of a less evolved magma) in a body of less dense magma it will sink due to its density difference. However, stronger convection currents (possibly driven by temperature) in the opposite direction, could reverse this and cause dense melts to appear higher up in the body. Such convection currents could also bring about mixing and promote homogenization of compositionally-contrasting melts.

4.4.4 Melting of, or crystallization on, the side wall of a magma chamber

Although crystallization on a single mineral seed does not occur here to produce a detectable buoyant boundary layer, the combined boundary layers of hundreds of small hercynite crystals can be detected rising in a boundary layer zone up the crucible walls. The crystallization of hercynite enriches this boundary layer in Al_2O_3 and depletes it in FeO and MgO. The visibility of boundary layers appears to depend greatly on the scale of observation. If a single crystal is being examined (as in chapter 3) and the boundary layer is very thin, then it is probably only detectable using EPMA at very closely spaced analytical intervals. However, if many crystals are grown closely together on a single surface then their boundary layers may merge together to produce a boundary layer zone of melt whose chemical and physical properties are a product of the properties of the individual boundary layers from single crystals, and will contrast with the original melt and cause composition-driven convection.

Table 4.05 displays compositional Rayleigh number calculations for the case of an alumina enriched boundary layer developing above a layer of hercynite crystals on a horizontal crucible floor. These data indicate that a minimum boundary layer thickness of 854μm needs to develop before it can convect buoyantly. The equation $\tau=d^2/D$ estimates that such a layer would take many days to develop if estimates of diffusion rates are accurate. This conflicts with the evidence seen in the basalt runs in this chapter, where buoyant Al_2O_3-enriched plumes are seen convecting within 6 hours. Two factors may have influenced the apparently premature convection of the Al_2O_3-enriched boundary layer. These are:-

a) Dissolution of alumina cement may aid thickening of the boundary layer.

b) Bubbles escaping from the crucible may have dragged the Al_2O_3-enriched melt with them.

A natural analogue of hercynite crystallization on side walls with an amount of dissolution can be imagined if the process is scaled up and applied to the walls of

Table 4.05. Boundary layer thickness calculations for a buoyant boundary layer forming on the crucible floor by hercynite growth

	Boundary layer density (g/cc)	Bulk melt density (g/cc)	$\Delta\rho$ (Kg/m3)	v (m2/s)	D cm2/s)	Ra comp	d(μm)	Time (hours)
a	2.603	2.645	42	257	10(-4)	1000	5547	73051
b	2.603	2.645	42	257	10(-5)	1000	3467	157358
c	2.603	2.645	42	257	10(-11)	1000	1847	339032
d	2.603	2.645	42	257	10(-12)	1000	854	730512

magma chambers. The temperature of country rocks surrounding a magma chamber is usually low enough to chill magma and induce nucleation and crystal growth on side-walls, floor and roof of the chamber first. Depending upon the proportions and growth rates of the minerals in this side-wall crystallization assemblage, the density of the overall boundary layer zone (the residue from crystallization) could be higher or lower than the melt in the interior of the chamber. If, for example, olivine and magnetite are the major minerals on the side-wall, then the residue in the boundary layer zone will be buoyant and will rise up the wall in the chamber. This provides a mechanism to bring fresh, undepleted melt alongside the side-wall crystallization zone, allowing continued growth. As the magma chamber loses heat by conduction so the country rock will become hotter. At 800-900°C silicic portions of the country rock will begin to melt and could penetrate into the chamber, further altering the composition of the melt close to the chamber wall, making it more silica-rich and therefore more buoyant.

Figure 4.17 is an attempt to apply the processes unveiled in this series of experiments to a natural system involving a basaltic magma chamber intruded into an area of mixed country rocks.

FIGURE 4.17. Convective processes from chapter 4 experiments applied to a basaltic magma chamber in a sequence of acidic country rocks.

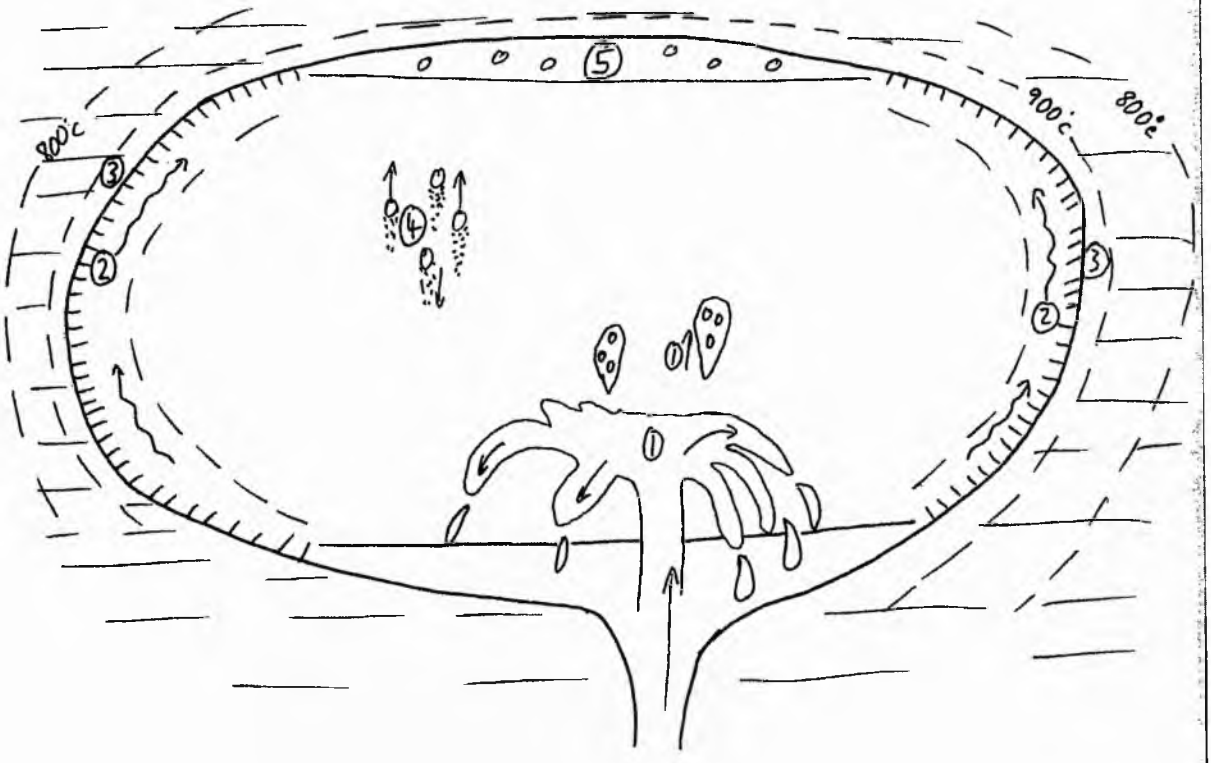

1) A pulse of hot, mafic, magma is injected into the magma chamber. Due to its higher density it sinks and ponds at the bottom of the chamber. However, if gas bubbles exist inthe chamber then these may cause dense melt to rise through the chamber.

2) Side-wall crystallization produces a boundary layer zone of melt depleted in FeO and MgO. This is less dense than the original melt and can convect buoyantly.

3) Heating of country rock causes partial melting of silicic material. This melting adds SiO2-enriched melt to the boundary layer zone, adding to its buoyancy.

4) Vesiculation of the magma may cause nucleation of crystals within the magma body. The vesicles will rise buoyantly in low-viscosity melts. The crystals will sink if they are denser than the magma and not kept afloat by temperature driven convection currents.

5) Fe- and Mg-depleted, Si-rich boundary layer zone melt has ponded at the top of the chamber to form an acidic top to the magma chamber. This may be gas-rich if volatiles have been unable to escape.

Chapter 5. Discussion of experimental results and petrological applications

5.1 Introduction

This chapter describes similarities between the convective processes observed in the experimental charges and natural analogues in magma chambers. The products of experimental runs cannot be regarded as models for magma chambers, as experiments only study convective fractionation around individual crystals on a very small scale. However the results show, for the first time, that compositional convection driven by crystallization can take place in silicate melts. The results of this study can be used as foundations from which to construct further experimental arrangements to investigate compositional convection in magmas at high temperature.

5.2 Convective fractionation associated with olivine crystallization

The experiments described in chapter 3 show that small density variations in thin boundary layers, produced by olivine crystallization, can drive convection in low-viscosity silicate melts. These experiments provide the first evidence that this can occur in a rock melt during its crystallization.

The compositional differences (5-20 % depletion of MgO and CoO) seen across the narrow boundary layers (maximum 40μ m wide) around the olivine overgrowths are not sufficient to produce colour variation in the melt. This is because boundary layer instability on inclined crystal faces is induced before Co-depletion is large enough to cause the brilliant blue colouration to fade. In order to observe colour variation across boundary layers, a larger depletion of Co in the melt is required. To produce this, boundary layer convection must be suppressed in experimental systems, conflicting with the aims of the experiments in this study. Suppression of convection could be achieved either using a more viscous melt system, or by developing boundary layers on horizontal surfaces, where a bigger thickness of boundary layer melt has to build up before it becomes unstable. These are both possibilities for further experimental work (see chapter 13).

As evidenced by the difference between Co and Mg count rates in glass at crystal-liquid interfaces and that in the plume of melt above olivine apexes, the most depleted melt in the boundary layer (i.e. that at the very interface between crystal and melt) does not convect away from the seed, but is instead held at the interface, presumably by surface tension.

In this study elongate crystal seeds have been used and the boundary layer melt that they produce feeds upwards to an individual plume that drains boundary layer melt

away from the crystal. Martin, Griffiths and Campbell (1987) envisaged individual plumes, each fed by the boundary layer of one crystal, developing on elongate crystals, while the boundary layers of more stubby, equant crystals would combine to produce a thicker boundary layer zone covering the layer of crystals (see figure 1.2 in chapter 1). In the latter case the boundary layer melt will only convect away from the zone of crystallization when it develops to an unstable thickness, while the elongate crystal feeds a continually-convecting plume of buoyant melt. The convection of plumes from individual crystals in this study is consistent with the former process.

The latter mechanism described above could be produced by a layer of equant, closely-spaced olivine crystals growing on the floor of a magma chamber with their individual boundary layers combining to produce a zone of MgO- and FeO-depleted melt, covering the crystals. The amount of FeO and MgO depletion in this boundary layer is dependent upon the degree of supercooling. This zone of melt could convect away either by building up to a thickness where its compositional Rayleigh number exceeds 1000, or it could be swept away by convective currents in the magma chamber. The net result is the addition of slightly evolved melt s (1-2 wt % depletion in MgO and FeO) to the bulk magma and their eventual mixing, . Only if this melt remains compositionally discrete could it contribute to a compositionally contrasting top to a magma chamber.

In the case of individual plumes of boundary layer melt convecting away from olivine crystals, the viscosity difference is relatively small, and so they will soon become homogenized in magma chambers. The rate of homogenization is probably largely dependent on other convective processes (eg. temperature driven convection and magma vesiculation) in the chamber, but the higher the contrast in viscosity between the escaping boundary layer melt and the magma, the better the chance that the escaping melt will remain discrete. If convection driven by temperature gradients is vigorous then the likelihood of boundary layer melt (in a plume or in a boundary layer zone) remaining discrete as it rises from the floor of the magma chamber is low. However, if temperature-driven convection is gentle, and the volume of melt that rises is large enough (probably in a boundary layer zone), then buoyant boundary layer melt may remain as a discrete packet of melt and rise through the body. The best chance of producing a large enough volume of boundary layer melt so that it will remain discrete on escape is probably as a zone of melt around a layer of crystals, rather than around individual crystals.

Although boundary layer production is a very small-scale process compared with the scale of magma chambers, if it is considered on a geological time-scale, with cooling occurring over a period of hundreds or thousands of year, and slightly evolved melt being produced throughout by continual crystal growth, then this process may have a

noticeable input into the gradual evolution of a basaltic magma to a more intermediate composition. Other processes (eg. side wall dissolution) would aid the compositional evolution. For boundary layer melt produced by crystallization of ferromagnesian minerals to evolve to an intermediate, or even acidic, composition, it needs to remain discrete from the rest of the magma chamber, and have solute continually extracted from it. This process cannot happen to melt released from crystallization on the floor of a magma chamber as it will not rise over other crystals, but is more likely near side-walls of magma chambers (see section 5.3).

The major finding from the experiments involving olivine growth in a synthetic basalt melt is that the boundary layers produced by olivine growth are buoyant enough to convect solely by compositional differences in low viscosity silicate melts. Production of crystal overgrowth and boundary layer instability on the timescale of these experiments necessitates fast crystal growth. It is therefore doubtful whether rates of individual boundary layer convection in these experiments can be applied directly to magma chamber processes where crystal growth rates are much smaller. In order to evaluate more realistically the effect of compositional convection on magma chambers further experiments at smaller supercoolings need to be attempted to observe boundary layer production and convection (i.e. under conditions more realistic to magma chambers). However, using the cemented seed technique, rates of boundary layer production can not be calculated due to the effects of other processes that produce compositional variation in melts (ie. side wall crystallization of hercynite, olivine crystallite formation, and cement dissolution).

Compositional convection driven by crystallization in magmas has previously been proposed as an active process in differentiation of magmas, by both theoretical studies, and by laboratory-based studies on aqueous salt solutions. Experiments in this study have proved that growth of ferromagnesian minerals (olivine and hercynite) produces low-density boundary layer melt that can convect buoyantly, driven solely by compositional density differences. The same process should be capable of occuring in magma chambers.

In these experiments, the convection of boundary layers is obscured by other processes (bubble escape, side-wall dissolution). In magma chambers many other convective processes have been suggested as active (eg. thermal convection, double-diffusive convection, turbulent stirring by later injections and by magma withdrawal from a chamber, contamination by other magmas and dissolving material, and vesiculation) providing a rather confusing picture of convection in magma chambers. All of the aforementioned processes have evidence to support their occurence and it would therefore seem that rather than a single process being responsible for convection and production of diverse magma compositions and zoning in igneous bodies, all of the

processes have an influence at some time in the evolution of some, if not all, igneous systems.

5.3 Convective fractionation associated with hercynite growth and alumina dissolution

One of the by-products of the experiments in chapters 3 and 4 is the formation of a rind of tiny hercynite crystals between the crucible wall and cement and the melt. This process has implications for natural processes in magma chambers, and can be likened to the process of side-wall crystallization (eg. Brophy, 1990).

The previous section (5.2) dealt with the behaviour of the boundary layer around individual crystals. The process in this section occurs on a much smaller scale (individual crystals in the experiments are only 10's of microns in diameter) but with many more crystals present, as is the case on the walls and floors of magma chambers.

The zone of pale-brown, Fe-depleted melt adjacent to crucible walls in the natural basalt experiments, and the Co-Mg-depleted melt in the synthetic basalt melt is produced by hercynite growth accompanied by a minimal amount of dissolution of the Al_2O_3 crucible walls. Dissolution of alumina is a slow process, as evidenced by the lack of wall thinning and flux-line attack at the meniscus and by the slow growth rates of layer 2 (the pock-marked hercynite) described in section 4.3.3, and so the majority of the compositional variation near crucible walls can be attributed to the growth of hercynite crystals. The product is a boundary layer zone of melt (2-3mm wide), enriched in SiO_2 and Al_2O_3, which has approximately a 1 % lower density than the bulk melt, allowing it to convect up the wall of the crucible. This zone of melt remains compositionally discrete, due to its higher viscosity and its density difference, and spreads out horizontally beneath the meniscus.

The pale boundary layer zone is the product of the amalgamation of boundary layers from hundreds of small hercynite crystals. As melt from one boundary layer at the bottom of the crucible wall rises upwards, it comes into contact with another hercynite crystal. Higher up in the crucible the boundary layer zone becomes thicker as more individual hercynite crystals contribute boundary layers to it. The width of the boundary layer zone and its compositional evolution, combined with the slight temperature increase, causes crystals higher up the crucible wall to grow more slowly.

When this process occurs on the crucible floor the zone of depleted melt thickens until it becomes unstable and rises as a plume through the crucible. This can be likened to the process suggested by Martin *et al* (1987), with small, equant crystals forming on a horizontal surface and their boundary layers feeding a thick boundary layer which

covers the whole layer of crystals and eventally convects away when its compositional Rayleigh number exceeds 1000, or when it is swept away by other convective currents. In this case convection is probably aided by the buoyant escape of bubbles as Rac calculations show that the boundary layer zone on the crucible floor should be stable at its observed thickness.

The density of the melt produced by side-wall and floor crystallization in magma chambers depends upon the crystallizing mineral assemblage (Sparks et al, 1980, and Stolper and Walker, 1980). If olivine is growing alone in basaltic melt in the side-wall assemblage then the boundary layer zone will be buoyant in the bulk melt. If only plagioclase is growing then the boundary layer zone will be relatively enriched in Fe and Mg and should be dense enough to sink in the chamber. Combinations of minerals in a crystallizing assemblage will produce a boundary layer zone which is either denser than, or less dense than the bulk melt, depending upon the proportions of the minerals crystallizing on the side-walls. Therefore, if additional experiments were carried out at lower temperatures, then hercynite would be joined by olivine and plagioclase in the crystallizing assemblage, this may produce a melt denser than the original one which could sink in the crucibles.

Another factor that will influence the density of the melt near the magma chamber walls is assimilation of country rock material. A basaltic magma chamber intruded into a series of acidic rocks (eg. sandstones, acidic gneisses, or granitic igneous rocks) will cool by conducting heat through the country rocks. If their temperature reaches 800-900°C then the acidic portion will begin to fuse. This is most likely if xenoliths are surrounded by basaltic magma as heat supply for fusion would be plentiful, but could also happen to side-wall rocks. The fusion of silicic portions of country rocks and xenoliths will produce a less dense melt close to the walls of a magma chamber. We can imagine this melt decreasing the density of the side-wall melt zone and therefore aiding compositional convection in the magma chamber. Such a process would also aid the compositional evolution of the magma chamber, producing even more compositionally discrete melt that can pond at the top of a magma chamber. Fusion of country rock could be likened to the process of crucible dissolution in the experiments in this study where alumina dissolution may be exaggerated the buoyancy of the compositionally discrete boundary layer zone and helping it to rise up the walls and pond at the meniscus.

Some country rock types will assimilate and fuse more readily than others and may have a more vigorous effect on convection in magma bodies. Hydrous minerals (eg. amphiboles, clays and micas) will let off gases into the magma when heated. The effect of bubbles in convective fractionation is discussed in section 5.5, but it is worth

mentioning here that they will accelerate the rise of buoyant melt and may even drag denser melt upwards in a magma body (Donaldson, 1993).

Side-wall melting will probably vary in importance at different times in the magma chamber development (see Huppert and Sparks, 1988). On initial intrusion of a basaltic magma the surrounding rocks will be cold, inducing crystallization near the margins of the chamber. The country rocks will heat up and eventually begin to fuse, adding silica-rich melt to the magma chamber near its walls. At the same time side-wall crystallization will be taking place and will eventually form an impermeable layer of crystals which separates any molten country rock from the magma chamber. Therefore side-wall melting will be most active at the intermediate stages of magma chamber development. Before this stage the country rocks will not be hot enough to fuse, and later an impermeable layer of side-wall cumulates could have developed to isolate the chamber from further contamination by this process.

5.4 Convective fractionation associated with hematite dissolution

Due to the fact that an iron-oxide overgrowth did not develop on the hematite seeds in these experiments, compositional driven convection associated with Fe-rich mineral crystallization is not seen. However, as discussed in the previous section, the hercynite crystallization on crucible walls in these experiments provides a good analogue for side-wall crystallization and release of buoyant boundary layer melt in magma chambers.

Instead of Fe-depleted boundary layers around the hematite seed the experiments in chapter 4 produce an Fe-rich melt at the crystal-liquid interface, with hematite dissolving through an intermediate breakdown product (hoegbomite). The convection of the dense boundary layer (with melt sinking to the bottom of the crucible and spreading out across the floor) is in agreement with the findings of deliberate dissolution experiments carried out in this laboratory (Donaldson, 1993). The dense liquid sinks, spreads out to fill the lower parts of the charge, can be dragged up above its origin by the action of bubbles, and appears to be pulled up the sides of the experimental charges either by bubbles that have since escaped, or by the dragging action of buoyant melt in the side-wall boundary layer zone, or even by being pushed upwards from behind by the sinking force of the dense melt following it down the sides of the dissolving crystal and across the bottom of the crucible (see figure 5.1).

The experiments in chapter 4 indicate that dense, Fe-rich melt can be produced by mineral dissolution at subliquidus temperatures. They show what will happen to dense melts produced by xenolith and xenocryst digestion (i.e. iron-rich melts will form dense melt currents sinking through magmas). In all the experiments in chapter

FIGURE 5.1. Diagram of proposed convective processes active in a basalt-hematite crucible from chapter 4, after a long run duration when iron-oxide crystallites have re-dissolved. Arrows inficate inferred movement of melt.

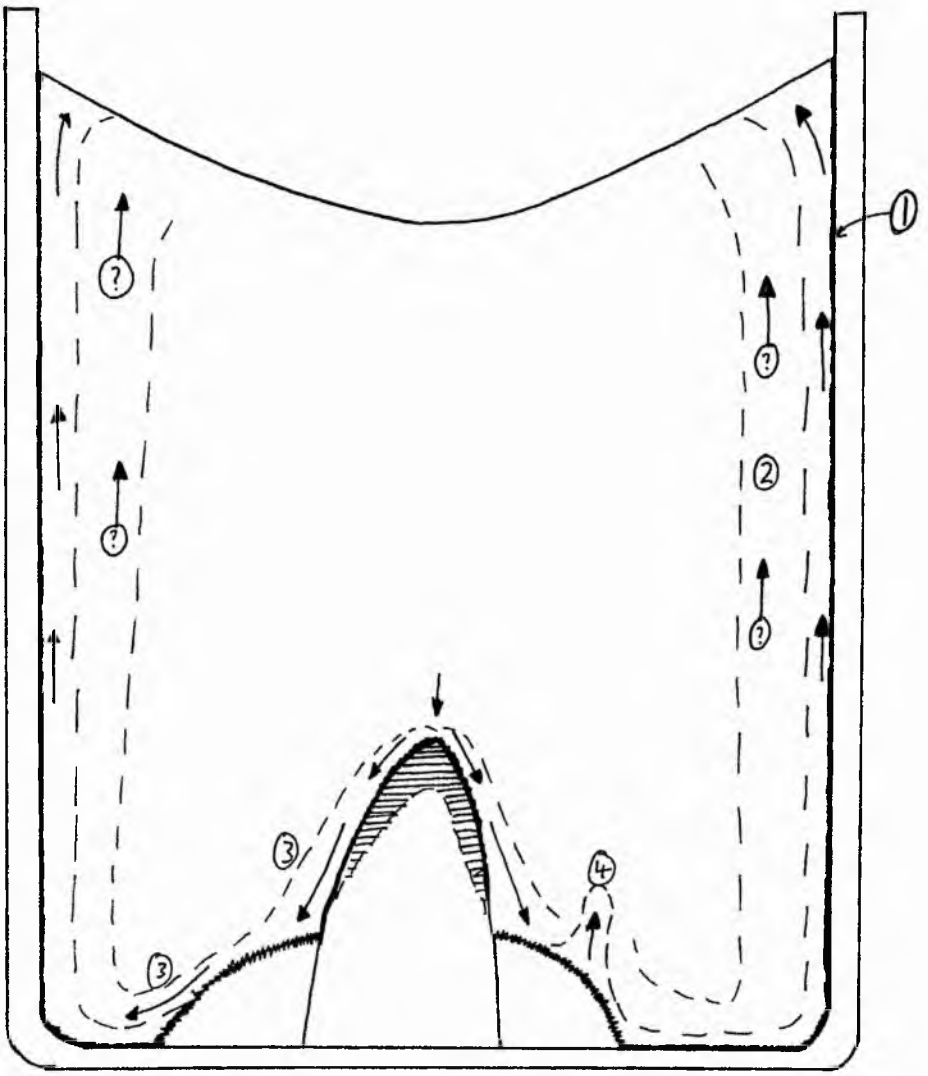

1) Side-wall hercynite crystallization produces a buoyant boundary layer zone.

2) Dark, Fe-rich melt is seen above its source. Perhaps air bubbles (now escaped) have been responsible for its apparently buoyant convection.

3) Dense, Fe-rich melt forms by hematite dissolution and sinks to spread across the crucible floor.

4) Buoyant plumes of Al-rich melt form as the boundary layer zone on the crucible floor thickens and becomes unstable.

4 the compositionally contrasting melts remain discrete, indicating that chemical diffusion rates are too slow to homogenize the melt in the charges in the times and at the temperatures used in these runs.

The phenomenon of the increasing width of hoegbomite rim and lamellae zone towards the top of the crystal seed, and the convective processes which may be responsible for it, may have implications for crystal growth rates, both of individual crystals and in zones of crystallization on side-walls of magma chambers. If the explanation for the width variation offered in chapter 4 (i.e. downward melt convection causes replacement of melt at the top with fresh, Fe-poor melt and therefore causes continued disequilibrium) and the situation is reversed and applied to a vertically-elongate growing crystal producing a buoyant boundary layer, the following sequence of events should occur (see figure 5.2):-

1) A buoyant boundary layer forms along the vertical side of the crystal.
2) It becomes unstable and convects upwards.
3) The boundary layer detaches from the crystal at the crystal apex.
4) The boundary layer near the top of the crystal is replaced by boundary layer melt from below so that the composition of melt in contact with the upper parts of the crystal remains roughly constant, and crystal growth is slow.
5) Towards the bottom of the crystal the boundary layer melt will be replaced by undepleted melt from beneath or alongside the crystal. This has a higher degree of supersaturation than the previously adjacent boundary layer melt and so should induce faster crystal growth at the bottom of the crystal.

The above could also be applied to crystallization on the side-walls of magma chambers with melt in the boundary layer zone at the bottom of side-walls being replaced by fresh magma as it convects, and that further up the chamber walls being replaced by already depleted melt. This could be responsible for thicker overgrowths being produced on the lower regions of magma chamber walls than further up the chamber walls. The compositions of crystallizing phases may also vary in this case, with more refractory minerals being produced further down the side-wall of the chamber at the same time as less refractory ones form at higher levels.

5.5 The effect of bubbles on convective fractionation in experimental charges

Air bubbles are present in the experimental charges described in chapters 3 and 4 because they are trapped in the melt during fusion and melt viscosity stops them from escaping instantaneously. The effects that bubbles have on crystallization, convection and dissolution within the crucibles as they rise towards the meniscus are summarized in this section and natural analogues are suggested.

FIGURE 5.2. Boundary layer convection and its possible effect on variable growth rates of individual crystals and of crystal assemblages on magma chamber walls.

A

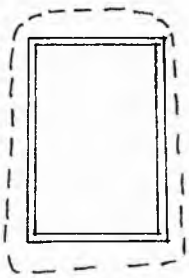

Olivine crystallization causes a boundary layer, depleted in MgO and FeO , to form.

B

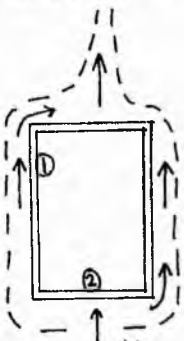

The boundary layer becomes unstable and convects buoyantly, leaving the crystal from its uppermost surface. Melt at point 1 is replaced by boundary layer melt from below, while that at 2 is replaced by melt distant from the interface which is therefore undepleted in MgO and FeO.

C

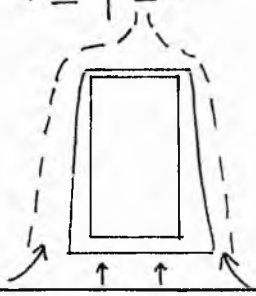

Crystal growth is faster at the bottom of the crystal where the interface melt is continually replenished with FeO and MgO.

D

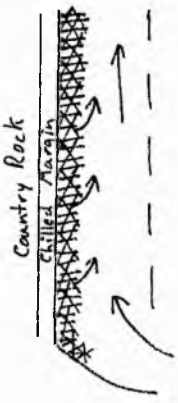

A basaltic magma has chilled against the country rock and an olivine-rich mineral assemblage has begun to form on the side-wall. This forms a buoyant boundary layer zone which rises up the side-wall. At the bottom the boundary layer zone melt is replaced by fresh basaltic magma from the interior of the chamber.

E

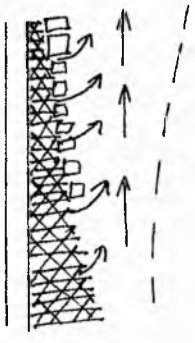

Olivine growth continues rapidly at the bottom of the wall as the crystals are bathed in fresh magma. Further up the wall, more refractory mineral phases will crystallize as the boundary layer zone is more evolved.

Vesicles can be produced in magma chambers by various mechanisms; magmas may vesiculate as pressure decreases, heating and fusion of country rocks rich in hydrated minerals will enrich magma in volatiles (Donaldson, 1993), and an influx of a volatile-rich, acidic magma into a magma body wil suddenly increase the volatile content of the body. Another situation is the addition of basalt to a chamber containing more acid magma which causes vesiculation due to heating (Huppert *et al*, 1986)

The following are convective phenomena involving air bubbles in experimental charges, and possible natural analogues for each process:-

1) The buoyancy of bubbles may overcome the gravitational effects on denser melt and cause it to rise above its source. This occurs in hematite dissolution experiments and could also be the cause of dark, Fe-rich melt being present above crystal seeds in the experiments in chapter 4. It has been suggested (Donaldson,1993) that such a process could be responsible for bringing dense Fe-Ti rich basalts to the tops of MORB chambers as the magma chambers vesiculate due to decreasing pressure (Bottinga and Javoy, 1990). Vesiculation could also reverse the flow of dense melt produced when plagioclase joins olivine in the crystalizing assemblage in a basalt (Sparks *et al* , 1980).

2) Vesicles appear to accelerate side-wall dissolution of clay crucibles. Where vesicles are attached to crucible walls in experiments in chapter 3, they are surrounded by a wide zone of pale melt, and indentations are seen in the walls, indicating accelerated erosion, possibly due to a surface tensional effect. This process is analogous to that described by Donaldson and Henderson (1988) where quartz dissolution is accelerated in places by vesicles, causing embayments in the dissolving crystals. The same process could operate during xenolith digestion, with accelerated erosion, if vesicles are present in the magma and attach themselves to xenoliths. Alternatively, a xenolith containing hydrated minerals could provoke heterogeneous nucleation of bubbles upon it.

3) As well as accelerating the rate at which buoyant melt is produced at clay crucible walls by dissolution, the bubbles accelerate convection of this melt by increasing its buoyancy. This accelerates the build up of evolved melt at the top of crucibles, and speeds up the dissolution of side-walls by removing SiO_2-rich melt more rapidly. This process can be envisaged occuring along the side-walls of a crystallizing chamber in contact with hydrated country rocks. If olivine or pyroxene is dominant in the crystallizing assemblage, then a boundary layer zone will be produced that is less dense than the original melt. This can rise buoyantly to the top of the charge and its rate of movement will be increased if vesicles form in the melt by volatiles given off from heating the country rocks.

4) The buoyancy of vesicles, and their tendency to attach preferentially to crystals in the experimental charges could cause crystals, whether denser or lighter than melts, to be carried to the top of magma chambers. However once the bubbles burst, denser crystals will sink. Helz *et al* (1989) suggest that bubbles have transported dense packets of melt and crystals to the top of the Kilauea Iki lava lake. Observations in this study provide evidence that supports the feasibility of this proposal.

5) The final observation of note regarding the effects of bubbles in the melts in these experimental charges, involves the nucleation of crystallites on the meniscus of the bubbles. This could be promoted by a surface tension, or temperature, or redox effect at the bubble surface, and could feasibly cause crystal nucleation in vesicle-rich magma bodies. The fact that the crystallites re-dissolve when bubbles have escaped from the melt implies that they are no longer stable once detached from the bubbles. However, if they remained in contact with the bubbles, or if the temperature continued to fall, then these crystallites could provide nuclei for further crystal growth, and indeed could seed nucleation throughout the magma.

5.6 Summary

The experiments described in chapters 3 and 4 have shown that convection driven by compositionally-induced density differences can occur in low-viscosity silicate melts. The processes responsible for the compositional variations are:-

- Hercynite crystallization on the side-walls of crucibles a solute-depleted boundary layer zone with a density decrease of 1 % from the original melt. This is sufficient to drive convection.
- Dissolution of alumina from side-walls and cement contributes to the above effect.
- Olivine crystallization produces a Co-Mg-depleted boundary layer capable of compositional convection.
- Hematite dissolution produces a dense, Fe-rich boundary layer.

Convection in the charges is aided in the early stages of runs by the buoyant escape of bubbles.

The experiments in chapter 3 have shown for the first time that solute-depleted boundary layer melt, produced by olivine crystallization, can convect buoyantly away from its source at the crystal-liquid interface. Melt in the buoyant plume shows between 5 and 20% depletion in CoO and MgO, which results in a 1 % density decrease. This is again sufficient to drive compositional convection.

In conclusion, experiments in section A of this thesis prove that compositional convection caused by crystallization can occur in silicate melts. The density differences

required to drive this convection are very small (<1 %). Compositional convection should therefore be an active process to transfer matter in the compositional development of magma chambers. However, it will rarely be the only convective process operating. In all but the slowest cooled bodies, temperature driven convection will take place and will have an effect of the boundary layer melts produced by crystallization, by homogenizing them with the rest of the magma, unless they can remain discrete in boundary layer zones. Also, even the most slowly cooled chambers will, at some stage, develop thermal gradients and temperature driven convection will occur. The chances of distinguishing between the effects of crystal-liquid fractionation on the residual melt, by in situ growth and boundary layer release, or by crystal settling, appear to be small as the net compositional effect will be the same.

PART B.
THE GEOLOGY OF THE GLEN MORE RING DYKE, MULL.

CHAPTER 6. Introduction, regional geology and field relations

6.1 Regional Geology

The Isle of Mull, on Scotland's west coast, lies on the axis of Tertiary igneous activity responsible for the formation of a wide variety of intrusive and extrusive igneous rocks on Skye, the Small Isles, Ardnamurchan, Arran and St Kilda between about 63 and 57 Ma (Mussett *et al* 1988) (see figure 6.01). Tertiary igneous activity on Mull can be divided into two episodes. The first, an extrusive episode, formed a sequence of basic lava flows 1800 m thick, comprising the Plateau and Central lava groups, each 900 m thick. The second episode was responsible for the subterranean intrusive igneous complex that is now exposed in central Mull (see figure 6.02) and has been described as possibly the most complicated area of igneous rocks in the British Tertiary igneous province (Emeleus, in Craig, 1991). This central intrusive complex comprises three intrusive centres aligned on a NW-SE axis (see figure 6.03). The focus of igneous intrusion (inferred from the circular outcrop pattern of the many ring intrusions, and the convergent point of cone sheets) migrated from SE to NW during the period of Tertiary igneous activity (Bailey et al. 1924). The positions of these centres, and the intrusions associated with each are shown in the maps in figure 6.02 and 6.03.

The earliest centre of igneous activity, in Glen More, is responsible for the deformation of Jurassic sediments in the south of the island (Rast *et al.* 1968), granophyric intrusions, acidic, intermediate and basic cone sheets, and the Beinn Buie layered gabbro. The third and youngest centre, focused on Loch Ba, is responsible for many acidic and intermediate intrusions, including the Loch Ba ring dyke, and a suite of basic cone sheets (Bailey *et al.* 1924).

The intrusion under examination in this study, the Glen More ring dyke, was intruded late in the history of the second intrusive centre, the Beinn Chaisgidle centre. Arranged around this centre are explosion vents in an early caldera, acid and basic cone sheets, the Corra Bheinn gabbro, and ring intrusions of variable composition (Emeleus in Craig. 1991). The largest, and probably latest, of these ring intrusions was the Glen More ring dyke which mostly comprises quartz and olivine gabbros (see figure 6.04). In two localities, at Cruach Choireadail and Choire Ghaibhre, however, these gabbros grade upwards, through rocks of intermediate composition, to acidic granophyres in their highest exposures. The origin of this compositional variation is the subject of this study.

FIGURE 6.01. Tertiary intrusive centres in Scotland. 1= St Kilda, 2= Skye, 3= Rum, 4= Ardnamurchan, 5= Mull, 6= Blackstones Bank, 7= Arran.

FIGURE 6.02. Map of the Central Intrusive complex on Mull (after Bailey *et al*, 1924)

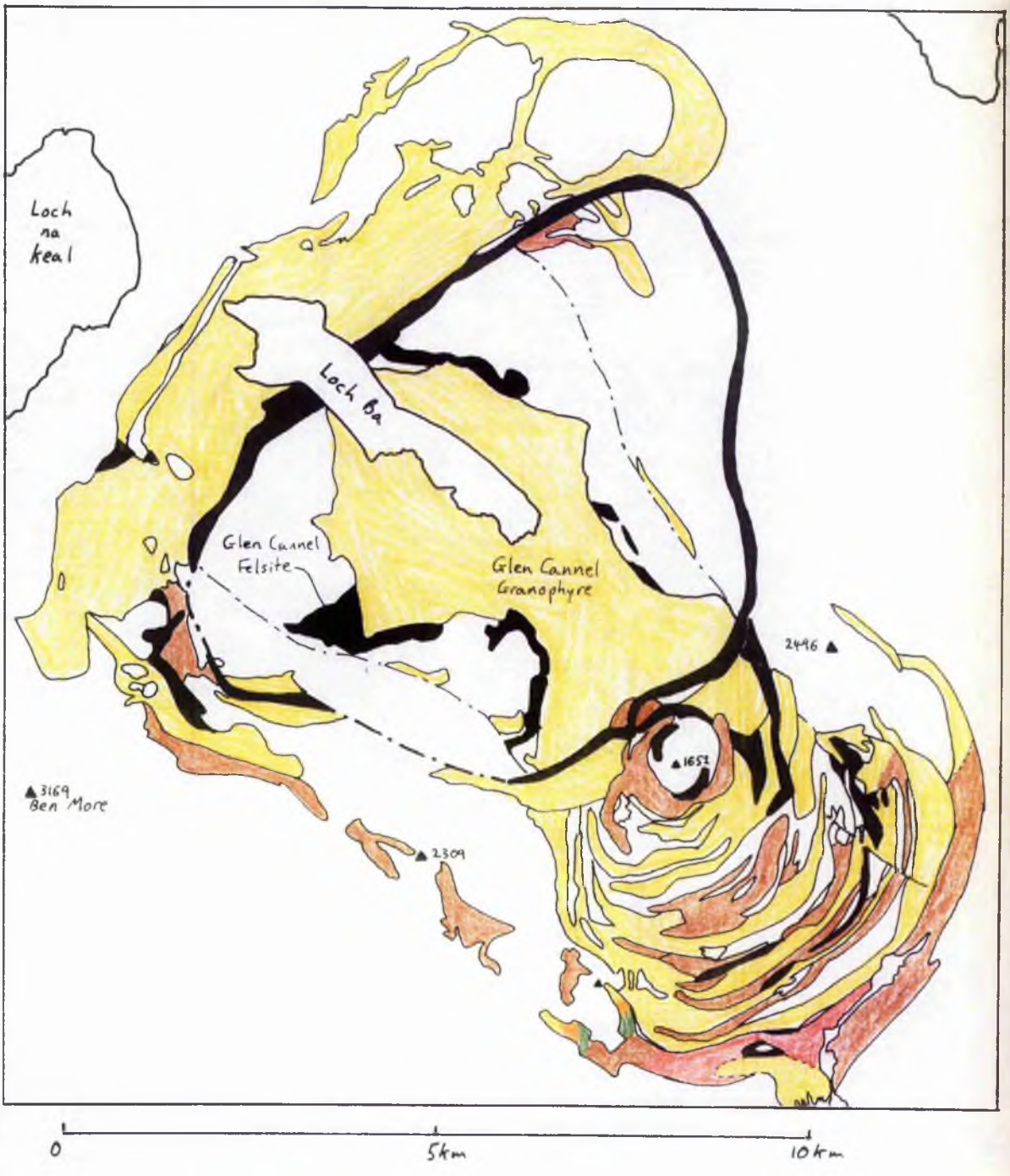

FIGURE 6.03. Distribution of intrusive centres, intrusive rocks, and lavas in the Mull Intrusive complex (after Walker, 1971, and British Geological Survey Map of East Mull, 1992).

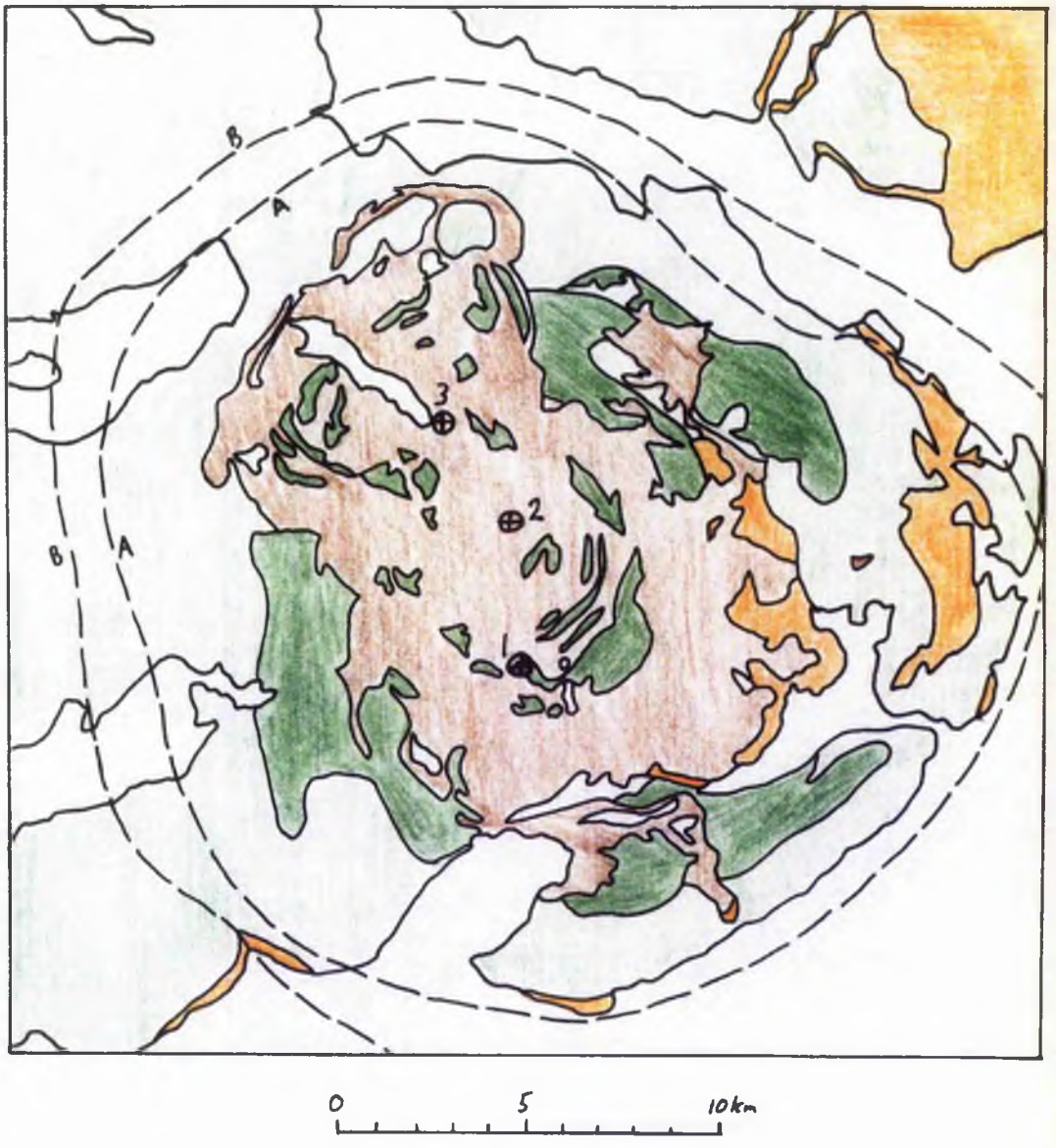

1= Glen More intrusive centre

2= Beinn Chaisgidle intrusive centre

3= Loch Ba intrusive centre

A= Limit of epidote zone of hydrothermal alteration (Walker, 1970)

B= Limit of prehnite zone of hydrothermal alteration (Walker, 1970)

Central Intrusive complex

Central group lavas and pyroclastics

Plateau group lavas

Pre-Tertiary rocks

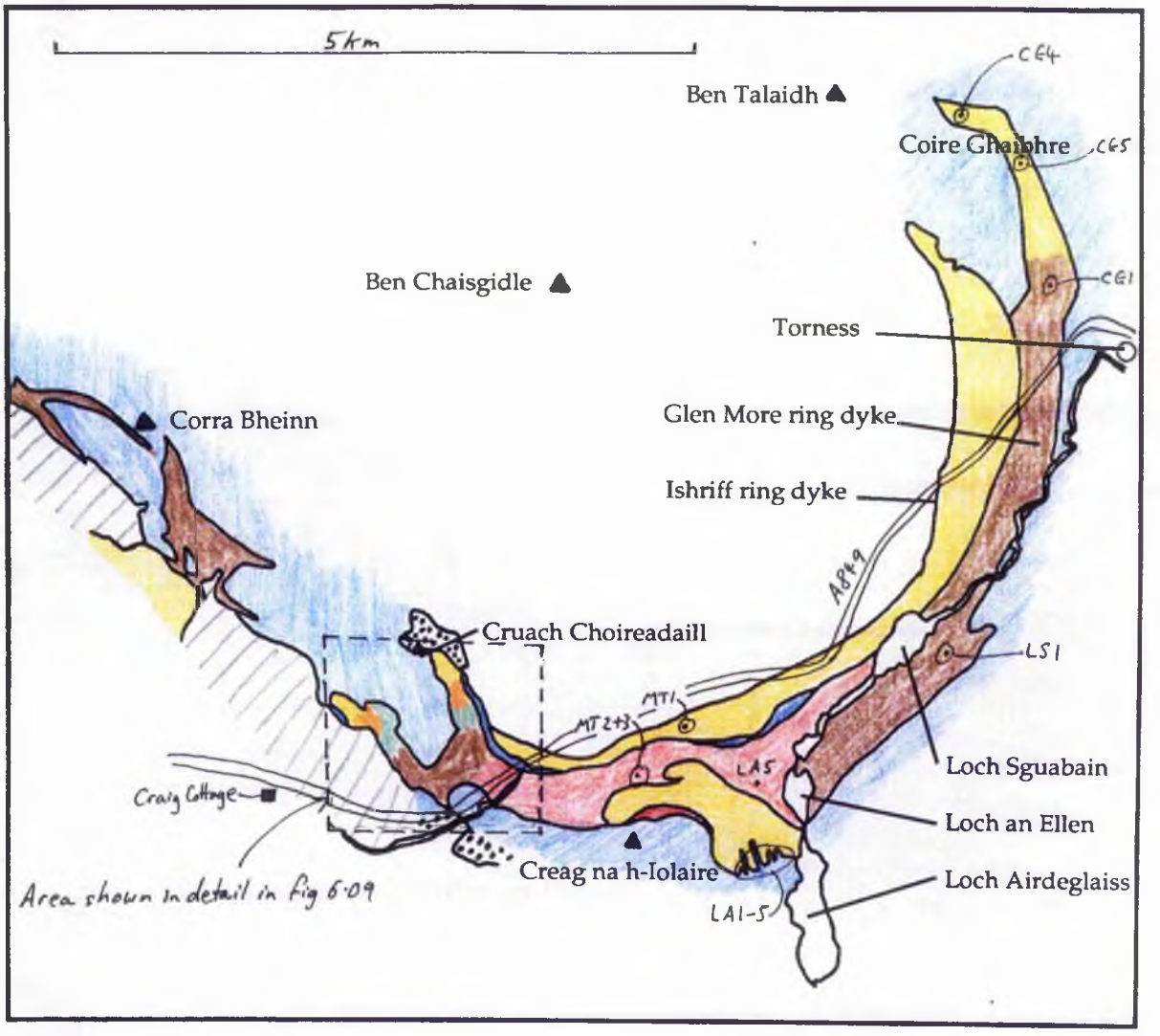

FIGURE 6.04. Map of the Glen More and Ishriff ring dykes, Mull (after British Geological Survey map of East Mull and this current study).

6.2 Object of study and methods used.

The original overall aim of this project was to investigate the nature and behaviour of compositional boundary layers in silicate melts adjacent to growing crystals (see chapter 1). Compositional-driven convection, associated with crystal growth, provides a possible mechanism for fractionation of liquid from crystals in magmas, may produce evolved melt from a more basic parental magma, and could therefore help to produce differentiation in magma chambers (see figure 1.1 in chapter 1). Compositional driven convection has been invoked as an active mechanism in magma bodies following recent work using aqueous salt solutions to simulate magma chamber processes (eg. Turner 1980, McBirney 1980, Huppert *et al* 1982).

The Glen More ring dyke at Cruach Choireadail provides an excellent example of a vertically-differentiated magma body. The distribution of rock types (densest at the base and lightest at the top) suggests that gravity played an important role in the petrogenesis of the body. The first investigation of the Glen More ring dyke (Bailey et al, 1924) proposed that the array of compositions in the body was a product of *in situ* fractionation of a single magma body, with buoyant, evolved, residual liquids separating from gabbroic cumulates to crystallize as the acidic rocks. Since this initial study other workers have published conflicting petrogenetic schemes for the ring dyke (see section 6.3.1). The present work re-investigated the Glen More ring dyke because of its potential as a site of magmatic differentiation by compositional driven convection associated with side-wall and floor crystallization.

Fieldwork involved extensive sampling and was followed by petrographic analysis, including whole-rock major and trace element analysis by XRF on 30 representative samples. Polished thin sections of these 30 rocks were made for electron-probe micro-analysis of mineral chemistry.

Evidence from this work has been used to test the validity of previously erected petrogenetic schemes, and petrogenetic modelling has been carried out on the most likely of these schemes using least-squares mixing programmes.

6.3 Previous work.

6.3.1 History of research on the Glen More ring dyke.

Since 1924 the vertically-differentiated nature of the Glen More ring dyke has been studied several times and contrasting petrogenetic schemes have been proposed to explain the distribution of rock types in the body. Petrogenetic schemes were based on hand specimen density, field relations, and microscopic evidence, with only limited whole-rock

wet chemical analysis being undertaken (6 analyses by Bailey et al [1924], 4 by Koomans and Kuenen [1938], and another 8 by Bor [1951]).

During the original geological survey of Mull "gravitational separation in a liquid emulsion" was tentatively proposed as the differentiation mechanism (Mull Memoir, page 51, Bailey *et al* 1924). Later this possibility was withdrawn and *in situ* differentiation was proposed as the active petrogenetic mechanism, involving crystallization accompanied by gravitational separation of buoyant, more evolved, residual liquids (Bailey et al, 1924). Holmes (1931 and 1936) and Fenner (1937) each raised objections to ideas put forward by Bailey *et al* (1924), and proposed that the differentiated nature of the Glen More ring dyke was a product of silicic and basic magmas being brought together in a single body, with mixing of these two magmas forming the intermediate rocks.

The objections made by Holmes and Fenner were based upon physical and chemical constraints that had not been considered by Bailey *et al* . These objections included:-

- Bailey *et al* propose a "pause in the process of crystallization" during which evolved, buoyant melt rises in the ring dyke. Holmes points out that crystallization is either complete or is still occurring, and a pause in crystallization is therefore not possible.
- The volume of granitic melt formed by crystallization of a basaltic magma is so small that its separation by gravitational filtration is mechanically impossible as crystallization must proceed a long way to produce this small amount of acidic residue (Holmes, 1936), and also produces a low-permeability crystalline framework.
- The gabbroic crystalline network in the Glen More ring dyke shows no evidence of having been deformed - one way by which interstitial melt could be squeezed upwards and so reach the upper parts of the body (Holmes 1936).
- Fenner objects to Baileys model on the grounds that in the passage from gabbroic to granitic liquid, the liquid portion should pass through intermediate compositions. Bailey makes no mention of intermediate residual liquids and instead suggests that the magma evolves from gabbroic to acidic liquids.

Investigation by Koomans and Kuenen (1938) provided additional chemical analysis of the rocks in the body. These authors supported the *in situ* crystallization and differentiation mechanism (with gravitational sinking of glomerophyric clots of augite, Fe-Ti oxide, and plagioclase) and suggested that kinks seen in chemical variation diagrams (see figure 6.05) could not be ascribed to magma mixing, which would produce straight mixing lines.

The most comprehensive study of the body was carried out by Bor (1951), who concluded that both crystal-liquid differentiation and magma mixing have been active processes. Bor proposed that gravitational settling of gabbroic minerals (augite, olivine, Fe-Ti oxide and calcic plagioclase) from a tholeiitic basaltic magma produced a more evolved residual magma which was partially hybridized with a granophyric magma at a later stage. This

FIGURE 6.05. Previous geochemical analysis of rocks from the Glen More ring dyke (Kooman and Kuenen, 1938). Note the kinks in trends which previous authors said could not be the product of magma mixing.

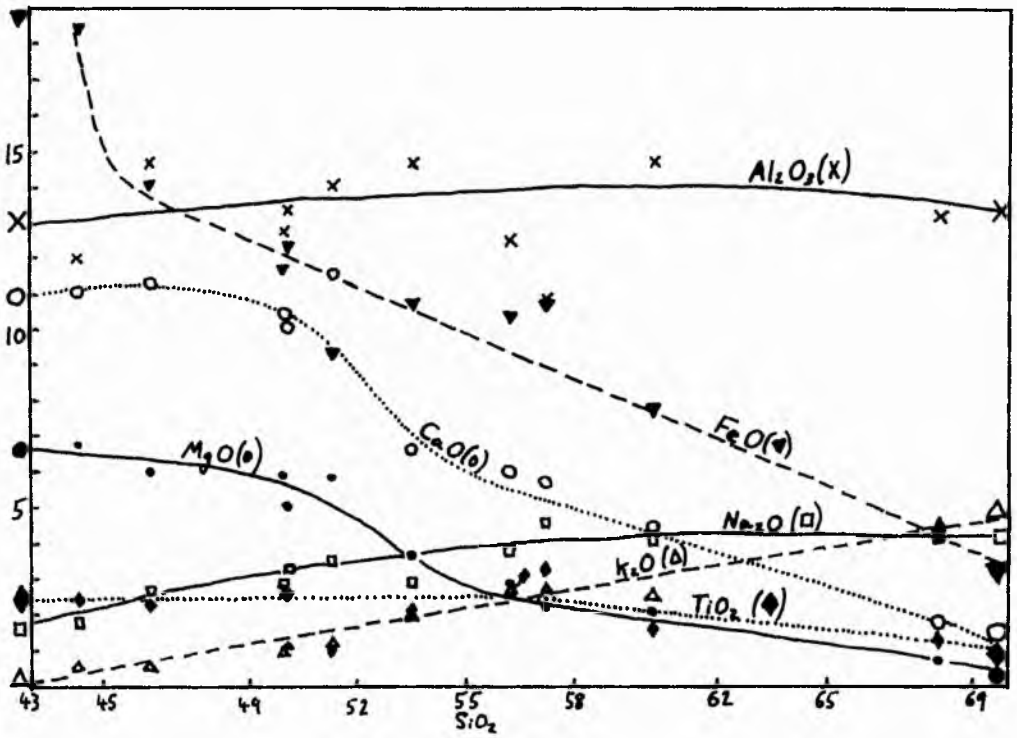

model was supported by Skelhorn *et al* (1969) who cited the lack of rhythmic layering, cumulate textures, and a chilled basaltic jacket around the granophyre as evidence which ruled out the petrogenetic schemes proposed by Bailey *et al* (1924) and by Koomans and Kuenen (1938).

The most recent commentary on the Glen More ring dyke (Marshall 1984) briefly compared it with other mixed-magma and net-veined composite intrusions in the British Tertiary igneous province (eg. Loch Ba ring dyke on Mull, the Mullach Sgar complex on St Kilda, and the Ardnamurchan ring dykes). Marshall invoked simultaneous injection of basic and acidic magmas from a compositionally-zoned magma chambers into ring dyke fissures (see figure 6.06) as the mechanism responsible for net-veined and mixed-magma bodies in the BTIP, although a subsequent paper (Marshall and Sparks, 1984) made no mention of the Glen More body when proposing this model for the Loch Ba, Ardnamurchan and St Kilda ring complexes. Marshall noted that the heterogeneous transition zone in the Glen More body is comparable with the hybrid Marscoite suite on Skye, with both bodies having the appearance of incompletely mixed silicic and mafic magmas. Recent work on Marsco (Bell, 1983; Vogel *et al*, 1984; Thompson, 1980) and on the Loch Ba ring dyke (Sparks 1988) has brought about an acceptance of mixing of magmas from zoned chambers beneath the Tertiary igneous centres as the process responsible for these net-veined and mixed magma intrusions. This scheme appears to be the currently accepted one for the Glen More ring dyke (Marshall, 1984), although little new work has been carried out on the body since Bor's study (1951).

6.3.2 Ring dyke intrusion mechanisms.

With the exception of Rum, each intrusive district in the British Tertiary igneous province includes at least one ring complex, containing both ring dykes and cone sheets, cropping out in concentric circular patterns around intrusive centres. Cone sheets dip inwards towards a subterranean focus of intrusion, thought to be the upper reaches of an underlying magma chamber, while ring dykes are cylindrical intrusions and dip steeply outward (Clough et al. 1909). Figure 6.07 illustrates the relationship between cone sheets and ring dykes.

In order to form a ring dyke, downward displacement of a cylindrical block of country rock, isolated by a ring fissure, is necessary (Richey 1932). The block drops into an underlying magma chamber and the resultant piston action forces magma into the fissure (see figure 6.08). For ring duke formation to occur, the subsiding block need not be denser than the underlying magma. It only has to sink into the magma, not through it. A block of equivalent density to the magma will therefore partially sink into the magma but will not be totally submerged in the magma chamber (like an iceberg floating in water), and its partial subsidence will displace magma into the ring fissure (Chapman, 1966). Due to

FIGURE 6.06. Ring dyke intrusion from a zoned magma chamber (from Marshall, 1984).

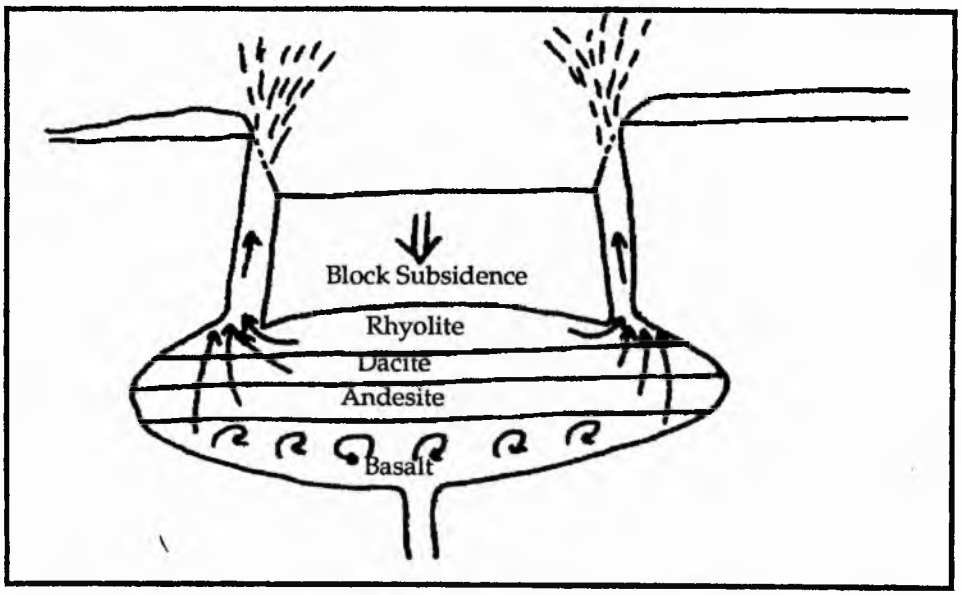

a) Ring dyke fissures reach the surface and feed mixed magma eruptions. This is the proposed interpretation for the Loch Ba ring dyke, Mull, and Askja, Iceland.

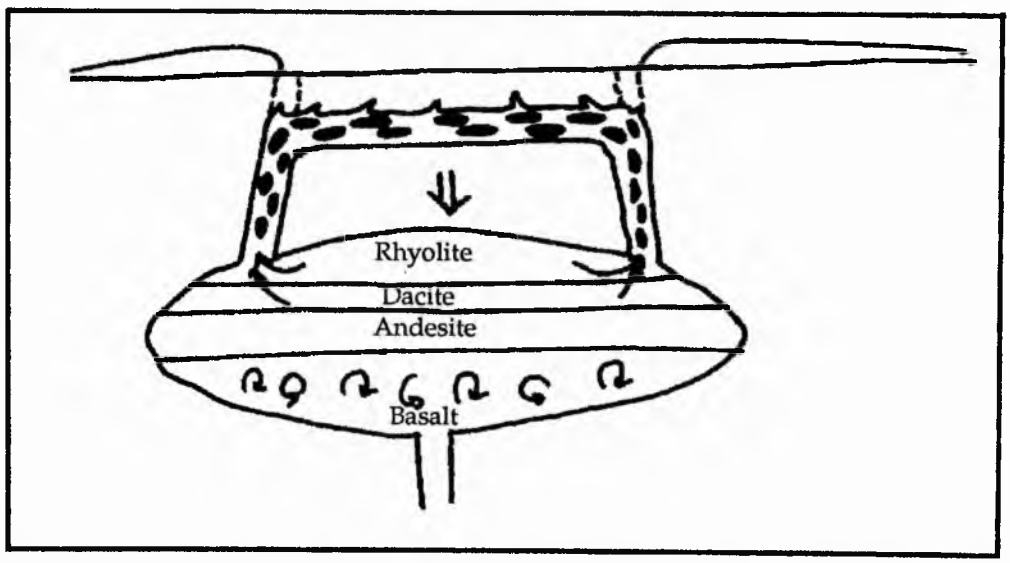

b) Block subsidence is entirely subterranean, feeds a mixed magma or net-veined ring intrusion and is capped by a horizontal sill. eg. Beinn a Chraig Granophyre, Mull.

FIGURE 6.07. Concentric arrangement of cone sheets and ring dykes. Cone sheets dip steeply inwards, while ring dykes dip steeply outwards (Clough *et al*, 1909; Richey, 1932).

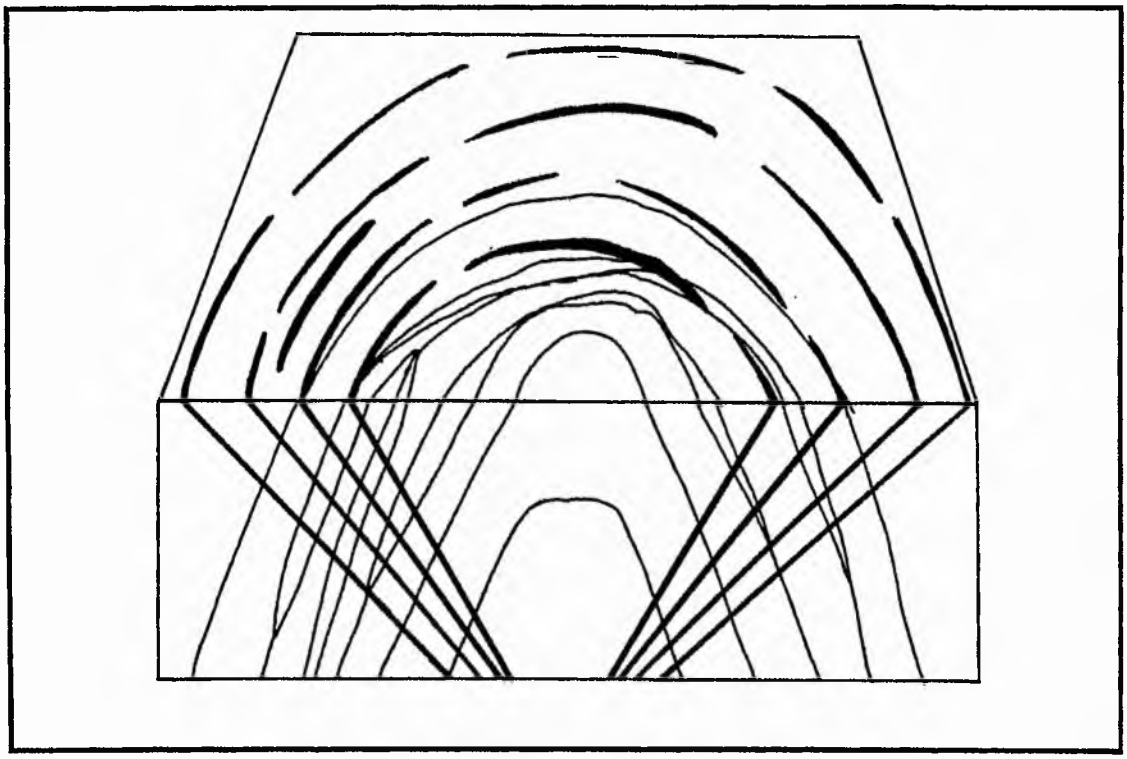

FIGURE 6.08. Ring dyke formation mechanism (Clough *et al*, 1909; Richey, 1932).

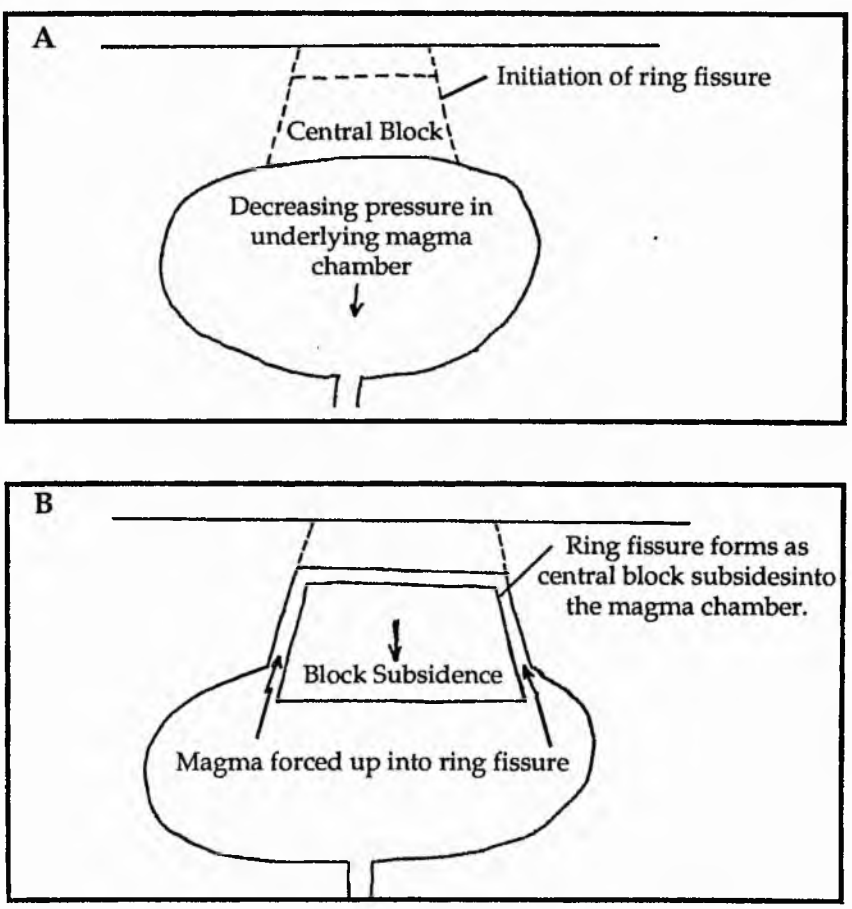

density differences subsidence of dense blocks of country rocks into acidic magma chambers is achieved readily, while subsidence into a basaltic magma chamber occurs less readily. Block subsidence is usually associated with decreasing pressure in the underlying chamber which subsequently provides less support for the crustal block. An increase in magma density with depth in an underlying chamber (for example in a polymagmatic chamber) may limit the depth to which central blocks can subside, thereby limiting the size of ring dyke intrusions (Chapman, 1966).

The form of ring dykes and their possible connections with surface calderas was first noted by Clough et al (1909) in Glen Coe. Ring dyke and cone sheet intrusion was later postulated as the formation mechanism for the Mull ring complexes (Bailey *et al,*. 1924). If ring dyke fissures connect with the surface they may be associated with vent eruptions and caldera collapse. If they do not then the steep sides of the fissure may be linked by a horizontal sill-like cap (eg. Beinn a' Ghraig granophyre on Mull).

Ring dykes very rarely form completely circular outcrop patterns. The circular outcrops of the Loch Ba ring dyke and those on Ardnamurchan are therefore exceptions rather than the rule. More frequently ring dykes have asymmetric outcrop patterns (see map in figure 6.02). The cause of this could be due to overprinting of part of the ring dyke by later intrusions if the intrusive centre migrates (as is probably the case on Mull). It could also be due to subsidence of an asymmetric central block with one vertical side which remains in contact with the country rock so that magma can only intrude around certain parts of the block (see Thompson, 1969).

Ring dykes form nested groups of intrusions whose maximum downward extent is presumed to be the underlying magma chamber. For this reason their lateral extent marks the minimum lateral extent of the underlying magma chamber (Richey, 1932). The range of compositions seen in groups of associated ring dykes points towards one of two possibilities:-

1) Ring dykes tap separate magma chambers of different compositions during the evolution of an intrusive centre.

2) The underlying magma chamber contains both acidic and basaltic magmas, possibly in a zoned body (eg. Sparks, 1988, Loch Ba).

6.4 Geological Setting.

The centre of intrusive igneous activity on Mull migrated in a north-westerly direction during the Tertiary period so that the youngest igneous rocks are associated with the Loch Ba centre in the north west while the oldest are arranged around the Glen More centre in the south east. Between the two lies the Beinn Chaisgidle intrusive centre. The Glen More ring dyke is the outermost and last intrusion associated with this centre (Walsh, 1979).

Each intrusive centre contains, or is bounded by, intrusions with circular outcrop patterns, indicating that cone sheet intrusion and block subsidence to form ring dykes was a very important process throughout the Tertiary on Mull.

Activity associated with the Beinn Chaisgidle centre began with explosion vents. Acidic and basic cone sheets, the Corra Bheinn gabbro, and numerous diorite, felsite, granophyre, dolerite and gabbro ring intrusions were then followed by a further suite of cone sheets overprinted by the Glen More ring dyke. The arcuate outcrop of the Glen More ring dyke follows Glen More from Coire Ghaibhre on Beinn Talaidh, near Torness ruins, to Cruach Choireadail near Craig Cottage (see figure 6.04). Three discrete bodies of gabbro also crop out to the northwest of Craig, on either side of Corra Bheinn. The petrology of these bodies is similar to that in the lower parts of the Glen More ring dyke. This caused Bailey et al (1924) to propose that they may belong to an extension of the Glen More ring dyke, although their structural alignment seems to owe more to the Loch Ba intrusive centre, and may be a product of the northwesterly migration of the Mull intrusive centre.

As mentioned in section 6.3.2, ring dyke formation is associated with central block subsidence due to pressure decrease beneath an intrusive centre. This, combined with the fact that the Glen More ring dyke is probably the last intrusion of the Beinn Chaisgidle centre, suggests that the ring dyke formed as the focus of igneous activity shifted from Beinn Chaisgidle to Loch Ba and the pressure beneath the former centre subsided. This may explain the lack of a northern half to the ring dyke, which could either be overprinted by the Loch Ba intrusions, or have involved subsidence of an asymetical block. This is discussed further in chapter 12.

6.5 Topography, exposure and physical form of the ring dyke.

The Geological Survey's mapping of Mull (Bailey et al, 1924) delineated the Glen More ring dyke over a 10 mile arc through Glen More. Most of the body comprises gabbro cropping out in the low lying land of the valley between Torness in the north-east and Craig Cottage in the south-west. At Cruach Choireadail the gabbro can be traced uphill through a series of intermediate rock types until granophyres are encountered (see figure 6.09). In Coire Ghaibhre on Ben Talaidh (figure 6.04 and 6.09), where exposure of the body is limited to the stream bed, basic gabbors are overlain by acidic rocks and intermediate rock types are not encountered.

Sampling in this study has concentrated on the southern slopes of Cruach Choireadail, although other localities have been examined for additional evidence. The low-lying areas of Glen More are covered by peat and drift, are boggy and so the ring dyke is poorly exposed. Much of the land to the northeast of Loch Sguabain has been afforested recently , all the way to the bottom of Coire Ghaibhre, which makes a thorough search for already

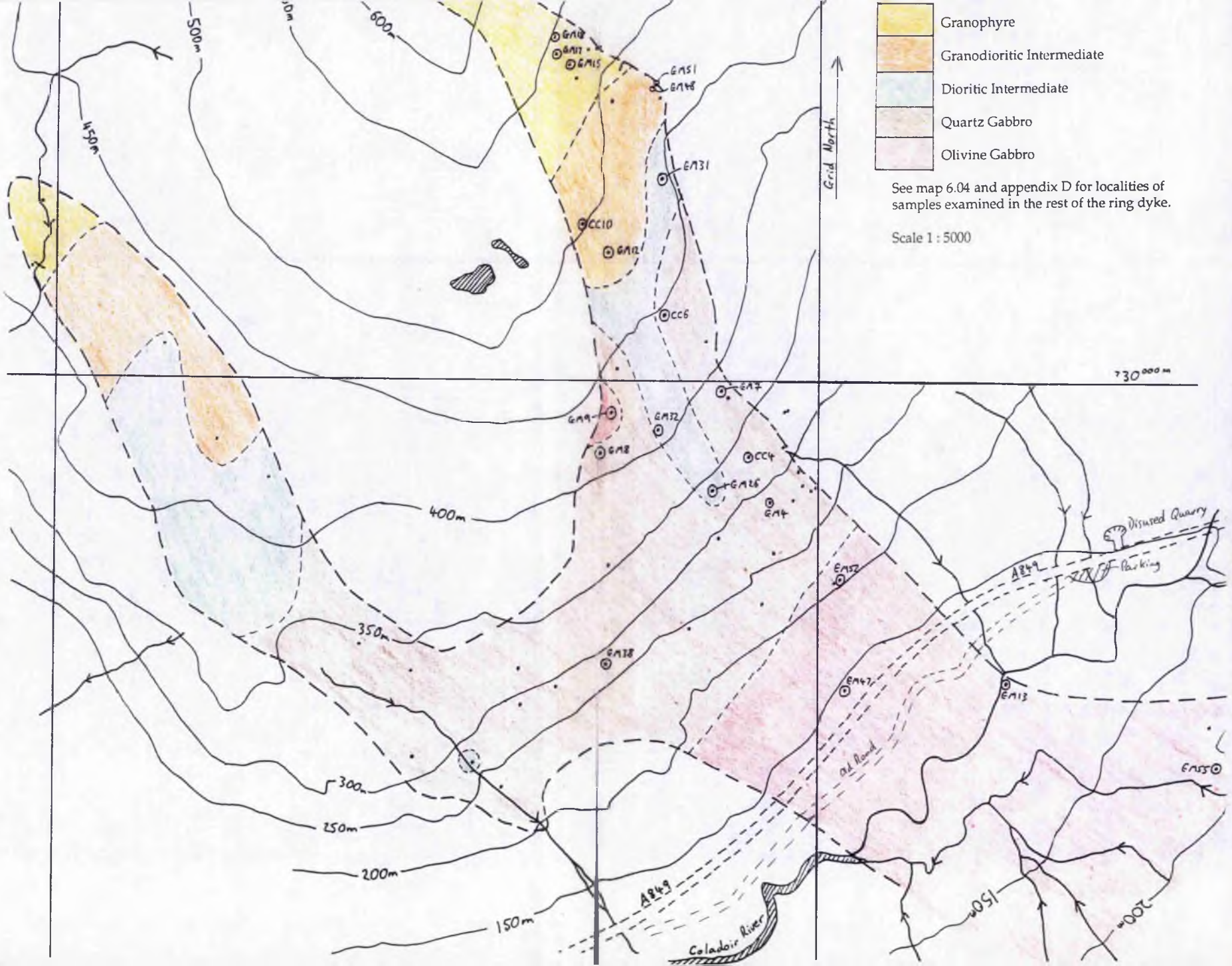
Granophyre
Granodioritic Intermediate
Dioritic Intermediate
Quartz Gabbro
Olivine Gabbro
See map 6.04 and appendix D for localities of samples examined in the rest of the ring dyke.
Scale 1 : 5000
Grid North
730 000 m
500m
600m
450m
400m
350m
300m
250m
200m
150m
GM18
GM17
GM15
GM51
GM48
GM31
CC10
GM12
CC6
GM7
GM9
GM32
GM8
CC4
GM26
GM4
GM52
GM38
GM47
GM13
GM55
Disused Quarry
Parking
A849
old road
Caladoir River

limited rock outcrop almost impossible. Apart from the higher ground of Coire Ghaibhre, Moal Tobar and Cruach Choireadail, exposure is limited to stream beds and occasional ice-scoured hummocks.

Previous investigations of the Glen More ring dyke have described the Cruach Choireadail area as comprising two vertical branches, linked by a vertically-jointed, sill-like body of gabbro (Bailey et al. 1924. See figure 6.10). Both vertical branches of the ring dyke contain gabbroic, intermediate, and granophyric rock types, and their outcrops are separated by an area of basaltic country rock.

Figure 6.10a attempts to illustrate how it is possible to do without the idea of a horizontal sill linking the two branches, and instead having the two branches ontop of a single dyke-like body. The vertical jointing in such a scheme would be caused by cooling joints at 90° to the irregular surface marked by the crosses in figure 6.10b.

6.6 Principal rock types and their field relations.

6.6.1 Introduction

In this section the various rock types seen in the Glen More ring dyke are described, together with their inter-relationships at the different field localities, brief petrographic descriptions are also presented. The only locality where all rock types are exposed, Cruach Choireadail, is discussed in order to provide a description of the full petrological range in the Glen More ring dyke. The outcrop patterns in the rest of the poorly exposed body are then outlined.

The southern slopes of Cruach Choireadail afford the most complete exposure of the petrological variations in the body, and have provided most of the observations made in previous work. However it is the outcrops at other localities which provide some of the best evidence for and against the proposed intrusion mechanisms for the ring dyke.

6.6.2 Rock Types at Cruach Choireadail

A 457m ascent of the south-eastern spur of Cruach Choireadail from the Coladoir River (see plate 6.01) passes from dark olivine gabbros at the base to buff-coloured granophyres at the top. In between are (from bottom to top) quartz gabbros and dolerites with increasing proportions of an acidic mesostasis, diorites with variable amounts of granophyre in patches and veins, and grey granophyres with decreasing amounts of fine grained melanocratic-enclaves. At Cruach Choireadail no sharp boundaries between adjacent rock types are exposed. Figure 6.11 is a summary of schematic petrographic sequences produced by previous authors, along with the classification system used in this study.

FIGURE 6.10. 3-dimensional sketch representing the branching outcrop pattern of the Glen More ring dyke at Cruach Choireadail.

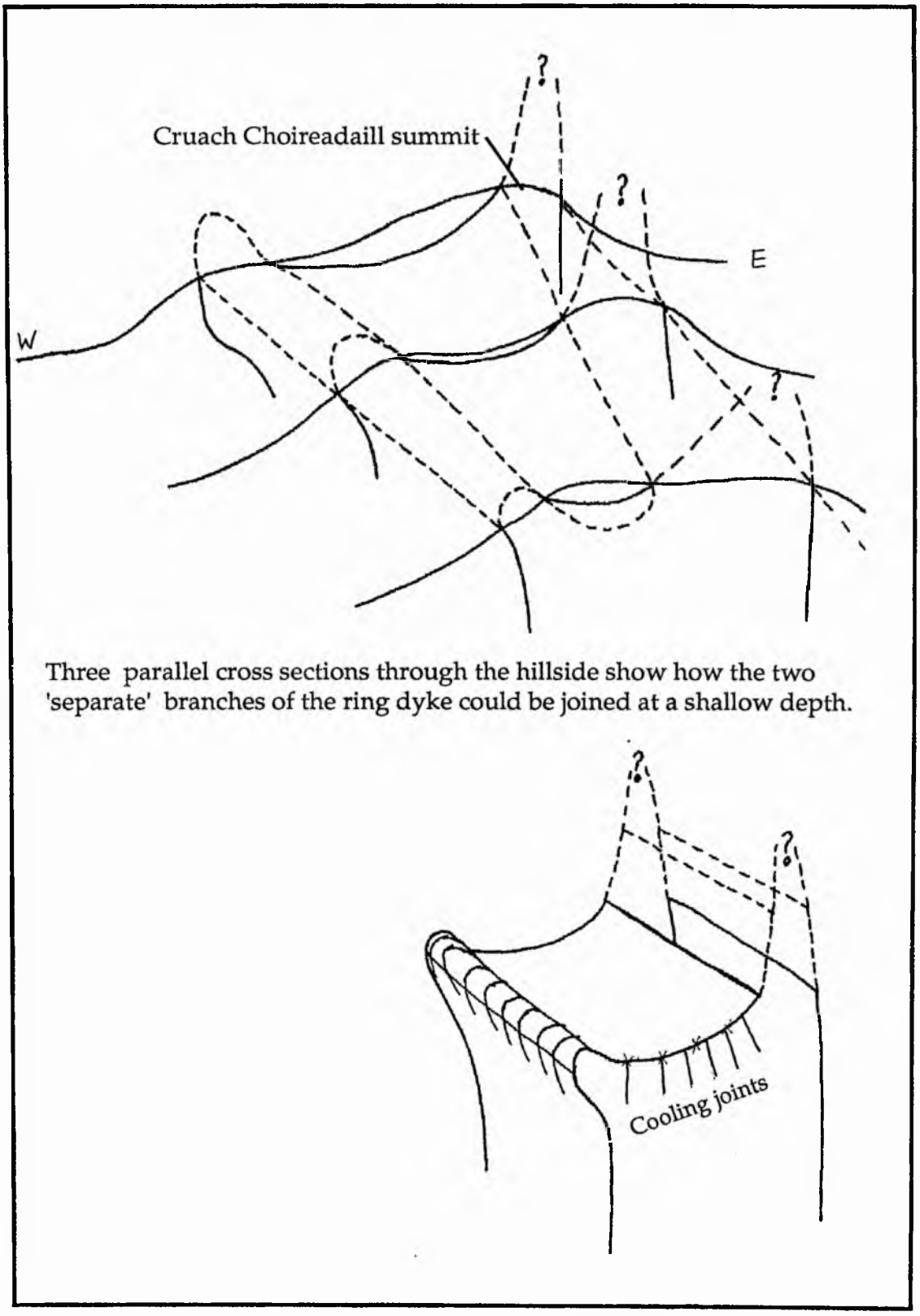

Plate 6.01. The southern slopes of Cruach Choireadail viewed from the south side of Glen More. Approximate outline of the Glen More ring dyke and petrological divisions within it are marked on the overlay.

1) Olivine gabbro
2) Quartz gabbro
3) Dioritic intermediate
4) Granodioritic intermediate
5) Granophyre
6) Country rocks

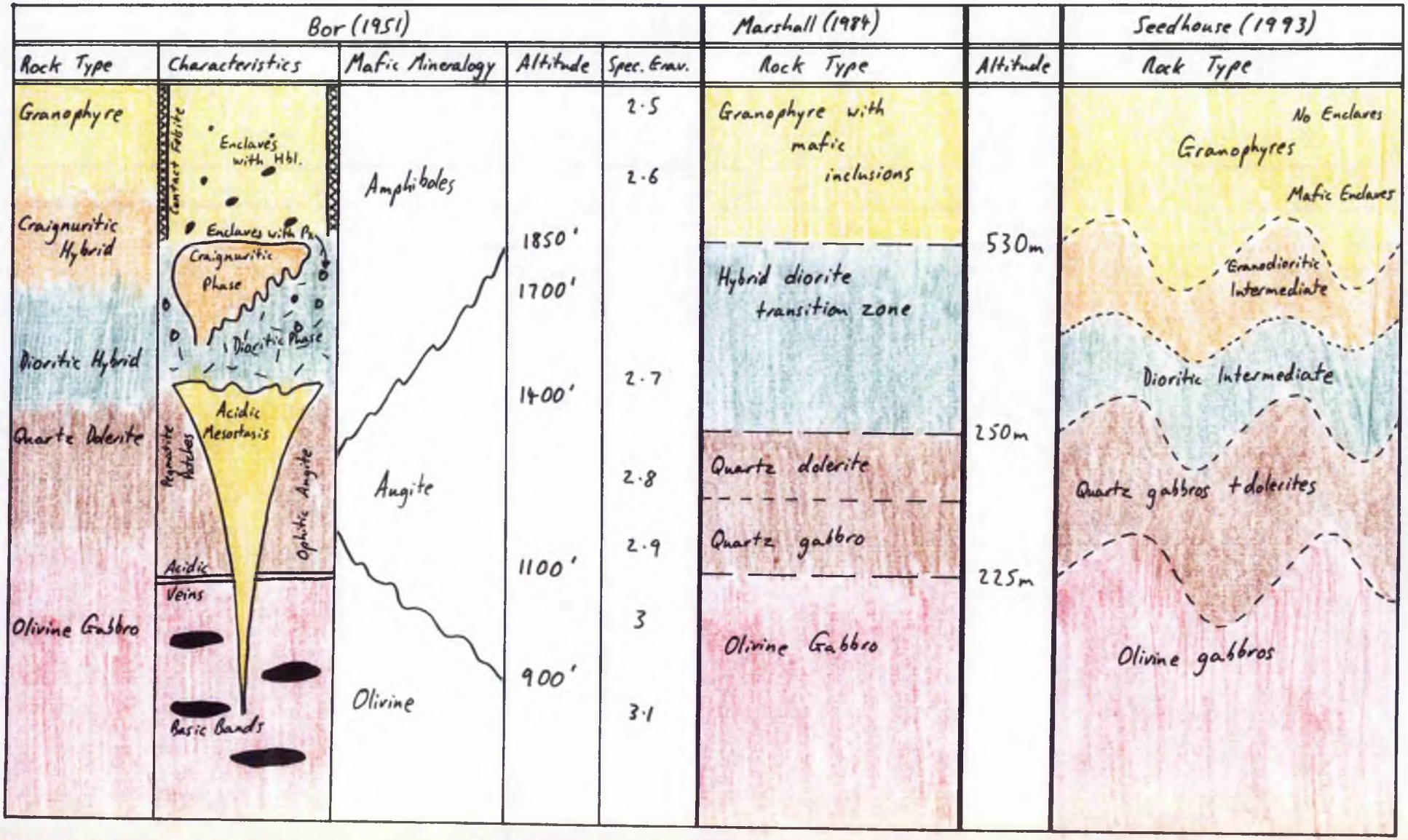

FIGURE 6.11. Table showing the various petrographic sequences proposed by previous workers for the rocks in the Glen More ring dyke.

Olivine gabbro crops out in the lowest exposed areas of the ring dyke. It is exposed in the Coladoir River and up to a height of 225m in rounded, hummocky outcrops. The rock has a moderate grain size (pyroxenes upto 5mm but 1-2mm on average) and is comprised of elongate prisms of plagioclase and pyroxene (see plate 6.02), with more equant crystals of Fe-Ti-oxides and olivine. Local concentration of mafic and felsic minerals gives rise to differences in appearance between specimens and accounts for the range of specific gravity values seen in this region of the ring dyke (Bailey et al (1924) and Koomans and Kuenen (1938)). Thin,poorly orientated, silicic veins (upto 3cm wide) run through these pale-green olivine gabbros. This green colouration is due to partial alteration of the pyroxene and olivine, largely to chlorite.

Above 225m olivine is absent from the gabbros and they are more leucocratic, with small aggregates of fine-grained acidic material present (see plate 6.03). These become more abundant and the spots of acidic material become larger up the intrusion. The leucocratic aggregates are upto 5mm in diameter at their coarsest. The acidic material appears as aggregates, discrete veins, and interstitially between gabbroic minerals.

Between 250m and 530m the rocks have a heterogeneous, mottled, dioritic appearance in a transition zone (plate 6.04). The mottling becomes more conspicuous uphill, consists of dioritic patches in a grey granophyric groundmass, and becomes more obvious as the melanocratic patches grow subordinate in abundance, and become finer grained with increasing altitude. The range in rock type in this transition zone is from diorites, with subordinate granophyric patches, to granophyres with fine-medium-grained, elongate, rounded, melanocratic enclaves (<5cm) (see plate 6.05).

Above 530m the body is entirely composed of granophyre, with occasional melanocratic enclaves (<< 1 %). The granophyre has a 2-3m-wide, enclave-free chilled margin with the country basalts (this boundary is planar as far as can be told from current outcrop), and grades from a grey to a buff colouration towards the top of the body, possibly due to an increased proportion of K-feldspar, or an increase in the degree of alteration of K-feldspar in the granophyre.

6.6.3 Mutual relationships of rock types

6.6.3.1 At Cruach Choireadail

Due to the poor exposure of the ring dyke at Cruach Choireadail, field evidence for a petrogenetic scheme has to be pieced together from a patchy network of information. For example, throughout the body there is no exposure of a boundary between the gabbros and the country basalts. As a consequence there is no evidence of a chilled margin which could be used as a potential parental magma composition in petrogenetic modelling. Also,

Plate 6.02. Hand specimen of course-grained olivine gabbro. Note elongate, euhedral laths of pale plagioclase, large black, skeletal oxide crystals, and grey subhedral clinopyroxene crystals penetrated by the plagioclase laths.

Plate 6.03. Hand specimen of quartz gabbro (LS1) showing local concentrations of pale minerals which appear as pale spots. These comprise of pools of acidic mesostasis interstitial between pyroxene and plagioclase laths.

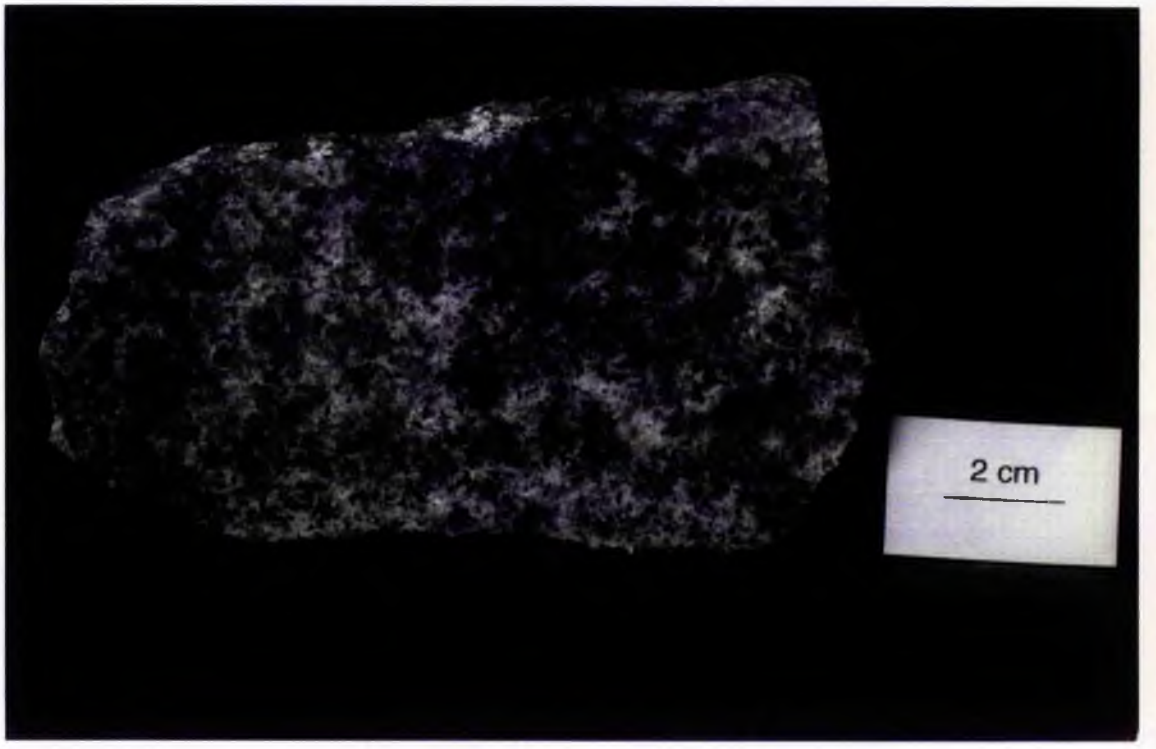

Plate 6.04. Photomicrograph of thin section of a dioritic intermediate sample from Cruach Choireadail. Note the pale patches of fine-grained acidic material within a network of course-grained diorite including laths of plagioclase and pyroxene and specks of oxide. Magnification x 4.

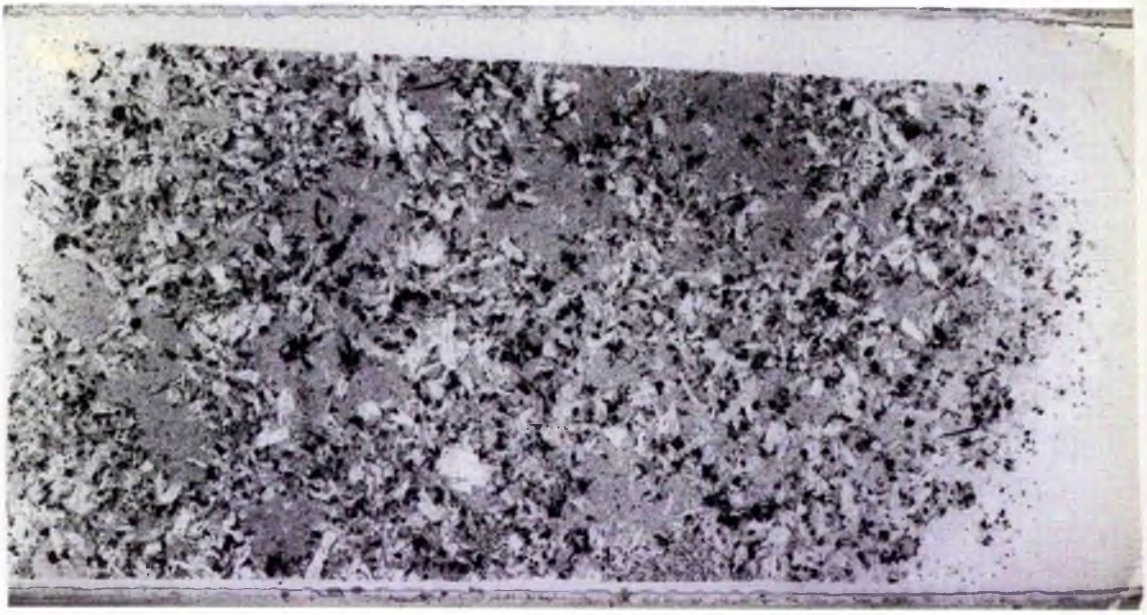

Plate 6.05. Hand specimen of granophyre (GM17). from the upper reaches of the Glen More ring dyke at Cruach Choireadail. This specimen clearly shows the contrast between the fine-grained pale granophyre and the dark, ferrodioritic enclaves. Note the rounded, ovoid shapes of the enclaves.

within the ring dyke at Cruach Choireadail no sharp internal boundaries between petrological units are seen. This could be due to the exposure limitations, but may also be a reflection of the rock types merging into one another, with sharp boundaries being absent. Field mapping reveals a very irregular distribution of rock types and these rock types are often found above or below the altitude zones in figure 6.11. These zones should therefore only be taken as a rough indication of rock type distribution at Cruach Choireadail.

Points to note from the field relations at Cruach Choireadail include the following:-

- Both branches of the ring dyke show a steady progression from gabbro to granophyre with increasing altitude (see figure 6.09)
- Granophyre above 450m is surrounded by a jacket of chilled, enclave-free felsite adjacent to the country basalts and there is no evidence of disruption of the country basalts (i.e. no xenoliths of basalt in the chilled jacket of felsite). This indicates that the enclaves in the rest of the granophyre do not originate from disruption of the adjacent country basalts.
- At locality CC6 (plate 6.06) rectilinear, perpendicular, granophyric veins (up to 10cm wide) are seen in gabbro. The veins branch and thin away from the main 'arterial' vein. There is no chilled margin in the granophyre or the gabbro, although the veins are very fine-grained throughout. In thin section the minerals in the gabbro are heavily altered close to the granophyre. This could indicate an intrusive origin for the granophyre veins into an already consolidated gabbro. The attitude of the veins indicates that they could have intruded along contraction joints in the gabbro.
- The acidic material found in spots and in veins is not visibly connected at any locality but microscopically the material in both is indistinguishable. Work on the filter-pressed late veins found in the Palisades sill (Shirley, 1987) shows that the veins in it are totally irregular; unlike the rectilinear ones seen here. This suggests that the veins in the Glen More body are not produced by filter pressing of the acidic mesostasis which is seen as spots here, and may be an indication that the vein material is not the same as that in the spots.

6.6.3.2 Other Localities

To supplement the field evidence at Cruach Choireadail other localities within the ring dyke were examined. These were located using descriptions by Bailey et al (1924) in the Mull Memoir.

The northern termination of the Glen More ring dyke at Choire Ghaibhre has limited exposure but shows vertical differentiation over a 210m section. In the low lying , now afforested, area near Torness ruins, the ring dyke comprises medium-grained quartz gabbro with narrow acidic veins (upto 3cm in width) (see plate 6.07) running through the

Plate 6.06. Rectilinear veins of granophyre in quartz gabbro at locality CC6 (Cruach Choireadail) in the Glen More ring dyke. Scale shown by camera lens cap.

Plate 6.07. Acidic veins in quartz gabbro at the base of Choire Ghairbe.

hummocky outcrop at locality CG1 (grid reference 642337). The ring dyke is sporadically exposed in the stream that runs down from Choire Ghaibhre. At 222m a pink granophyre is exposed, and above this, at 305m, the granophyre is of the grey-green variety seen at Cruach Choireadail. No contacts were seen between any of the rock types here, and no intermediate rock types were identified. Choire Ghaibhre provides evidence that vertical differentiation is not limited to one locality in the Glen More ring dyke.

Samples of gabbro were collected from east of Loch Sguabain and to the west of Loch an Ellen. The gabbros from throughout the body are relatively homogeneous, being slightly finer-grained to the north. West of Loch an Ellen, gabbro and granophyre outcrop at the same altitude (see figure 6.09). Contact relationships are not exposed but the boundaries are relatively sharp (<5m), and no intermediate rock types are seen in this area, although some development of intermediate, hybrid rocks (i.e. mixed magma in origin) is mentioned by Bor (1951) at this locality.

To the south, on the west of Loch Airdeglaiss the granophyre forms a crenulate, penetrating contact with the country basalts at 150 m (see figure 6.09). One cannot envisage a mechanism which could produce this contact if the granophyre were formed by *in situ* fractionation of the parental magma of the basal gabbros, as suggested by Bailey *et al.*

One other locality in the Glen More ring dyke, a spur of high ground directly between Loch an Ellen and Cruach Choireadail known as Moal Tobar, was examined. On an ascent of this spur from the A849 road at the high point in Glen More, one crosses the Ishriff granophyre ring-dyke, lying adjacently to the north of the Glen More body. Exposed above and to the south of the Ishriff ring dyke is the Glen More gabbro. At a higher altitude granophyre is seen overlying and intruding the Glen More gabbro (see plate 6.08). The intrusive veins of granophyre are upto 30cm wide, are rectilinear, and have fragmented the host gabbro into xenoliths and xenocrysts at the contacts of the two (see plate 6.09).

Bailey *et al*, (1924) examined two other areas of gabbro to the north-west of Cruach Choireadail which have not been examined here. These areas lie to the NW and SE of Corra Bheinn. The southeastern outcrop, in Choire a Mhaim, shows slight uphill decrease in basicity of gabbro (from olivine- to quartz-normative), but never reaches dioritic or granophyric compositions. The other outcrop, in Coir an-t Sailen, displays uphill branching (see figure 6.02) and gabbro becomes less basic, with granophyre exposed in the uppermost parts of one of the branches of the body (Bailey et al. 1924).

Plate 6.08. Granophyric veins intruding into olivine gabbro on the northern slopes of Maol Tobar. See plate 6.09 for detail.

Plate 6.09. Photomicrographs of granophyre veins intruding into and fracturing the olivine gabbro in sample MT2 from Maol Tobar. Note the reaction textures (clinopyroxene altered to hornblende) on the edge of the yellow clinopyroxene crystals in contact with the acidic veins. Magnification x 10.

6.6.4 3-Dimensional structure of the granophyre

The map in figure 6.09 shows the positions of granophyre outcrops in the Glen More ring dyke. The three major outcrops (at Cruach Choireadail, Loch Airdeglaiss and Moal Tobar, and at Choire Ghaibhre) appear at very different altitudes, and are several kilometers apart. An attempt has been made in figure 6.12 to link the areas of granophyre into a single body within the ring dyke. Granophyre is only seen on the outermost edge of the body at one point (at Loch Airdeglaiss) while wherever the ring dyke is exposed at high altitudes granophyre appears. We can therefore envisage a body of granophyre running up the outer side of the dyke and spreading out laterally in the uppermost parts of the ring dyke fissure. The low-level granophyre outcrop could be the remnants of a feeder pipe of granophyre - it lies almost equidistance between the two high-level granophyre outcrops, and a feeder pipe is not seen anywhere closer to the high-level outcrops. This indicates that the only visible means of getting the granophyric magma to the top of the ring dyke is by its intrusion through this feeder-pipe.

FIGURE 6.12. Sketch linking the granophyre outcrops in the Glen More ring dyke in three dimensions, showing how they could feasibly all be linked.

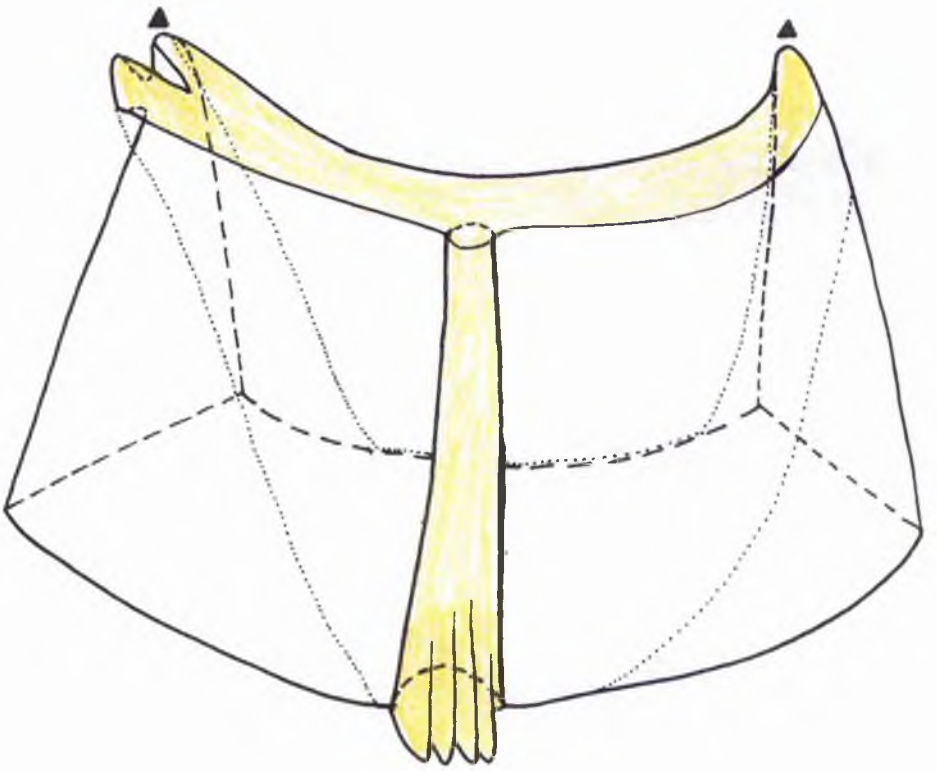

CHAPTER 7. Petrography

7.1 Introduction

Petrographic descriptions of the major rock types outlined in the previous section are presented here. In this section it has been necessary to classify the rocks in the ring dyke, however it should be emphasised that previous work has mentioned the continuum of petrological variation at Cruach Choireadail. The rocks at both the bottom and top of the body (the gabbros and granophyres respectively) have a homogenous appearance in hand specimen and thin section, while the intermediate petrologies have a mottled and blotchy appearance, comprising both acidic and basic patches. It should be remembered that few internal petrological boundaries exist, and so the classification system does not contain sharp divisions; instead a more continuous progression is present. For convenience the rocks at Cruach Choireadail have been split into lower, intermediate, and upper zones. These zones are, however, only applicable to the col.umn of rocks at Cruach Choireadail. The rock types are relevant at other localities but the vertical order of their appearance is variable, as described in chapter 6.

Table 7.1 displays modal mineral proportions for representative rocks from Cruach Choireadail and other localities within the Glen More ring dyke. The acidic granophyres are very fine-grained and are heavily altered, making modal analysis very difficult. For acidic and intermediate samples, where point counting is difficult due to the heterogeneous nature of grain size and rock type, the proportions of acidic and intermediate patches in section of hand specimens are given.

A. THE LOWER ZONE

7.2 Olivine gabbro

7.2.1 Introduction

This melanocratic, medium-coarse grained granular rock forms the lowest exposures of the Glen More ring dyke and crops out upto a height of 250m at Cruach Choireadail (see figure 6.09). The grain size decreases slightly with altitude. The rock is typified by the sample GM 13, collected from the north bank of the Coladoir River in Glen More. Bor reported horizontal acidic veins, upto 2 feet thick, resembling the intermediate rocks, cutting through these olivine gabbros. Only thin, randomly-aligned felsic veins were found in this study.

TABLE 7.1. Modal mineral proportions for representative samples from the Glen More ring dyke.

Sample Number	CC4	CC6	CC10	CG1	LS1	MT3	MT1	GM55	GM52	GM38	GM32	GM8	CG5	GM9	
Rock Type	Quartz gabbro	Quartz gabbro	Granodioritic Intermediate	Quartz gabbro/ diorite	Olivine gabbro	Quartz gabbro	Granophyre	Olivine gabbro	Olivine gabbro	Quartz gabbro	Dioritic Intermediate	Quartz gabbro	Granophyre	Olivine gabbro	
Altitude (m)	342	442	518	137	200	344	290	195	210	270	352	415	222	430	
Mineral content (volume %)															
Quartz	6.5	5.5	11.3	9.1	0	1.9	17.7	0	0	2.8	4.9	2	12.2	0	
Plagioclase	39.1	51.9	37.8	41.7	48.9	48	22.4	62.7	44.1	49.9	39.8	34.8	26.6	34.2	
K feldspar	12.7	0	14.2	6.1	8	2.8	21.8	6.6	6	6.7	8.9	3.4	21.7	5.1	
Clinopyroxene	12.3	9.4	1.2	16.3	19.8	23.8	0	15.2	26.5	19.4	17.5	26.7	0	20.3	
Chlorite	7.9	27	6.6	6.8	10.4	12	10.1	3.1	11.2	10.2	11.6	20.5	11	19.6	
Oxides	8.9	0	9.3	9.8	5.6	4.6	2.8	5.9	4.8	4.8	11.4	3.4	2.7	12	
Olivine	0	0	0	0	1.9	0	0	3	2.1	0	0	0	0	1.3	
Accessories	1.1	0	2.7	0	1	0.4	0	1.4	0.8	1.5	1.4	0.1	1.2	0	
Granophyre	11.5	0	8.7	4.7	0.6	1.7	23.8	0	0.8	0	1.7	0	20.3	0	
Hornblende	0	6.2	8.2	5.4	3.8	4.8	1.4	2.1	3.7	4.7	2.8	9.1	4	7.2	
Sample	GM32	GM26	GM30	GM31	GM12	GM16	CC10	CG5	MT1	CG4	GM48	GM20	GM15	GM18	GM19
Rock Type	Diorite	Dioritic Intermediate	Dioritic Intermediate	Granodioritic Intermediate	Granodioritic Intermediate	Granophyre	Granodioritic Intermediate	Granophyre	Granophyre	Granophyre	Granophyre	Granophyre	Granophyre	Granophyre	Granophyre
Altitude (m)	352	335	450	455	485	500	518	222	290	305	420	490	525	550	630
% Granophyre	30	30	32	60	50	90	80	95	100	100	98	100	90	94	100
% Diorite or mafic enclave	70	70	68	40	50	10	20	5	0	0	2	0	10	6	0
Locality Legend															
CC= Cruach Choireadail															
GM= Cruach Choireadail															
MT= Maol Tobar															
CG = Choire Ghaibre															
LS = Loch Steisevat															

7.2.2 Mineralogy and textures. (see plates 7.01 and 7.02)

The olivine gabbro has an interlocking prismatic character of moderate grain size with pyroxenes occasionally upto 5mm in length but averaging 2mm. In hand specimen it comprises pale-grey plagioclase, steely blue pyroxene (often altered to a rusty brown alteration product), green altered olivine, red weathered oxide and a small amount of interstitial acidic mesostasis (a fine-grained intergrowth of orthoclase feldspar, chlorite, oxide specks, apatite needles, and mIcrographic quartz-feldspar). There are some local concentrations of mafic and felsic minerals and some oxide-enriched bands. This accounts for the local specific gravity variations described by previous authors in these basic rocks.

In thin section plagioclase forms euhedral, twinned prisms (upto 4mm x 1mm x 1mm) of labradorite (approximately An 65), often albitized on crystal faces, especially those adjacent to patches and veins of quartz-rich, granophyric mesostasis. Plagioclase is intergrown with, and often poikilitically encloses, clinopyroxene, while some of the smaller plagioclases are completely enclosed by clinopyroxenes. In the olivine gabbros and many quartz gabbros plagioclase is the principal mineral and frequently occurs as aligned piles of elongate laths (see plate 7.02), with other minerals (augite, opaques, and granophyric mesostasis) being subordinate and occurring interstitially. This locally gives the rocks a plagioclase-rich adcumulate appearance, although they generally resemble orthocumulates due to the higher proportions of intercumulus minerals (stubby pyroxene and feldspar, and quartz-rich granophyric mesostasis).

The clinopyroxene in these rocks is calcic augite and displays pale purple-pale-brown pleochroism. It is ophitic, appears intergrown with plagioclase and opaques in glomerophyric aggregates, and has occasional small inclusions of magnetite and chlorite. Some augites contain olivine chadacrysts (upto 1mm diameter) and their edges are frequently penetrated by elongate plagioclase laths. Alteration of clinopyroxene to hornblende has occurred and hydration of clinopyroxene is seen adjacent to patches of acidic mesostasis and on cleavage traces. Optical and wet chemical work by Bor showed that clinopyroxene has an essentially uniform composition throughout the whole of the Glen More ring dyke (a=1.69 B=1.695 gamma=1.718 +2V=48° z:c=42°. Bor 1955). Clinopyroxene composition has been explored further by EPMA in chapter 8.

Olivine in thin section is heavily cracked and serpentinized, with pale-green, faintly pleochroic, residual cores in only a few rocks. Most crystals have been altered to serpentine and chlorite plus magnetite. Olivine pseudomorphs are either enclosed in clinopyroxene crystals, or form glomerophyric areas containing several touching pseudomorphed crystals. Optic axial figures were obtained from suitable crystals, producing relatively straight isogyres, indicating a composition of Fo >70; EPMA indicates a uniform composition of Fo 68 (see section 8.2).

Plate 7.01. PPL photomicrograph of glomerophyric aggregate of olivine and its alteration products (magnetite and serpentine) in sample GM13. Also note the skeletal opaque crystals comprising intergrown magnetite and ilmenite lamellae. Magnification x 15.

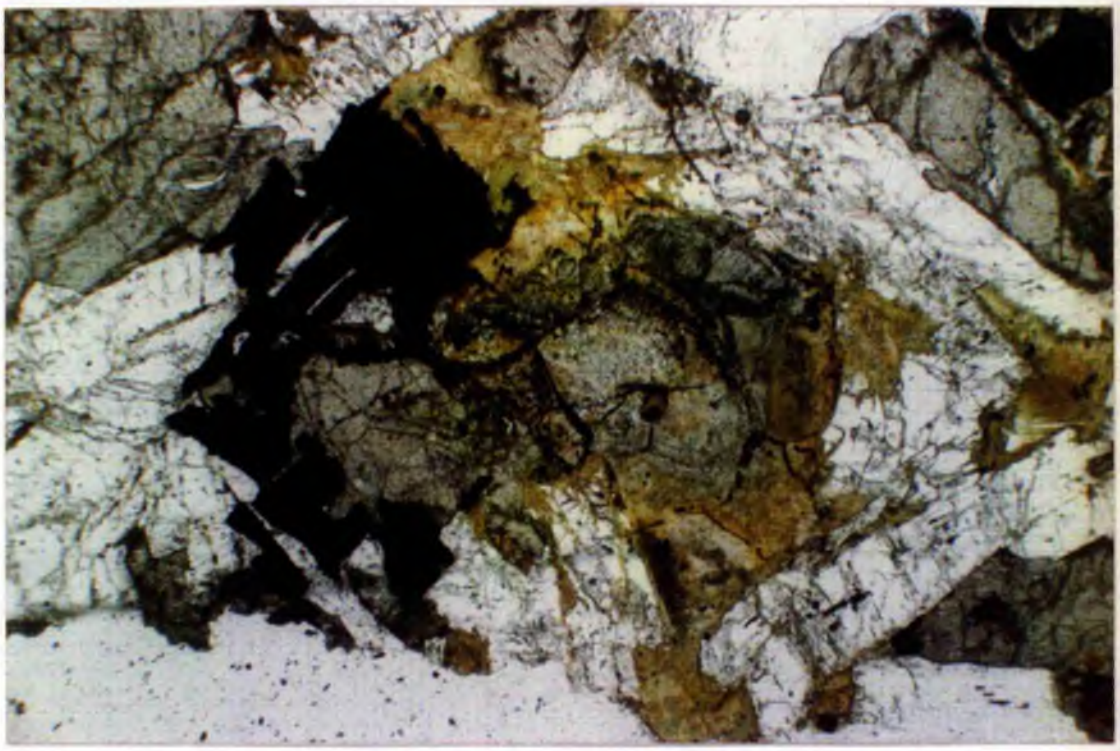

Plate 7.02. XPL photomicrograph of horizontally-aligned, piles of plagioclase laths in sample GM55, a quartz gabbro from Cruach Choireadail. Note the appearance of intersertal areas of acidic mesostasis. Magnification x 15.

The oxide minerals in the olivine gabbros are skeletal intergrowths of magnetite and ilmenite, with a small amount of pyrite. These oxides form large (upto 2mm) skeletal and euhedral crystals, between and within clinopyroxene crystals, and often forming glomerophyric aggregates with clinopyroxene.

Other minerals present in the olivine gabbros are alteration products, accessory minerals (apatite and zircon), and quartz, plagioclase and cloudy orthoclase in very fine grained patches of acidic mesostasis. The acidic mesostasis is intersertal in voids in the plagioclase and pyroxene orthocumulates. There is no evidence of enstatite being formed by silicic melt reacting with olivine. Alteration products include chlorite (replacing olivine, clinopyroxene and parts of plagioclase), hornblende (from pyroxene hydration) and epidote and prehnite in thin (< 1mm) veins. The area of study lies within the zone of late-stage hydrothermal alteration around the central Mull complex (Walker 1971), so this alteration is to be expected, and should be taken into account when whole-rock chemistry is analysed.

7.3 Quartz Gabbros and Quartz Dolerites (see plates 7.03 and 7.04)

7.3.1 Introduction.

The quartz gabbro (Type specimen CC6) is dark in colour with pale spots of acidic mesostasis. It becomes paler with increasing altitude due to the increase in this acidic material and is very pale in some outcrops due to local increases in plagioclase concentration. The decrease in grain size with increasing altitude in the body produces both quartz gabbros and quartz dolerites. The gabbros and dolerites have essentially the same mineralogy but vary texturally. The division between these rocks and the olivine gabbros, as indicated by the nomenclature, is made on the presence or absence of olivine or its alteration pseudomorphs (chlorite, epidote, and magnetite). Quartz gabbros and dolerites are generally found above 250m. Quartz dolerite is more prevalent towards the ring dyke margins with the country basalts, and at increasing altitude, indicating a faster cooling rate. This petrological unit merges upwards into the basic dioritic intermediates. The quartz gabbros and dolerites contain spots (5-10 mm, see plate 6.03) of acidic material which are picked out well on a weathered surface; in the intermediate rocks an interlinking network of quartz-rich, acidic material surrounds the dioritic patches. The quartz gabbros decrease in basicity with altitude due to an increase in the size and abundance of patches, veins and pools of acidic mesostasis composed of quartz, chlorite, apatite and orthoclase (compare modal analyses for samples CC6 and CC4).

Plates 7.03 and 7.04. PPL and XPL photomicrographs of stubby pyroxene crystals, skeletal opaques, and subhedral plagioclase in sample CC5, a quartz gabbro from Cruach Choireadail. Note also the alteration rims around clinopyroxene crystals. This is most prevalent close to patches of acidic mesostasis (top ~~right~~ left corner). Magnification x 20.

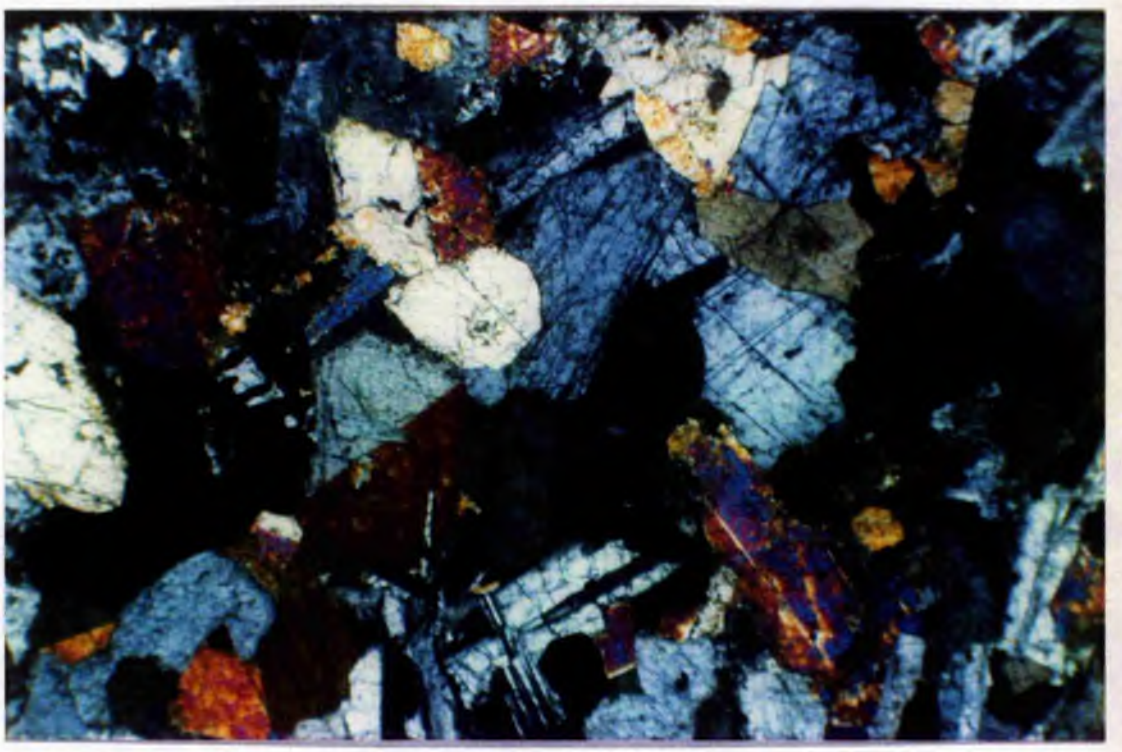

7.3.2 Mineralogy and textures

Clinopyroxene is euhedral, pale-brown pleochroic calcic augite (upto 3mm x $1mm^2$), makes up approximately 30% by volume of the rocks, has an ophitic texture, with most of the crystals having boundaries deeply penetrated by plagioclase laths, and forms glomerophyric aggregates with oxide minerals. Alteration of pyroxene to hornblende and chlorite is seen along cleavage traces and crystal edges, especially those in contact with acidic mesostasis. Magnetite is evident as specks along cleavage planes in clinopyroxene crystals; this is probably a product of a reaction between pyroxene and a later hydrothermal fluid.

Plagioclase forms elongate (3mm x 1mm x 1mm), subhedral, twinned laths with dusty brown albitized edges, especially on faces adjacent to acidic mesostasis. Optical analysis reveals a labradorite/andesine composition of An 50 for the cores of laths. The ophitic textural relationship indicates co-precipitation of pyroxene and plagioclase, in contrast to the relationships seen in the olivine gabbro where the relationship is sub-ophitic.

The oxide minerals in these rocks appear as both elongate-skeletal (2mm x 1mm x 1mm) and stubby, euhedral morphologies ($1mm^3$) of magnetite with ilmenite lamellae. Both are glomerophyrically associated with clinopyroxene, indicating co-precipitation.

The fine-grained (<0.5 mm), acidic interstitial material contains dusty orthoclase crystals, anhedral quartz, cloudy plagioclase, a micrographic quartz-feldspar intergrowth, chlorite flecks and apatite needles. The proportion of this material increases upwards to give the quartz gabbros and dolerites a more leucocratic and spotted appearance. Crystallization of the gabbroic minerals appears to have left behind an acidic residue which has crystallized in the interstices and ponded in pools throughout the rock to form the acidic spots.

Above 300 m the rocks in the dyke have undergone extensive alteration. At around this height the blotchy intermediate rock type becomes abundant and acidic material appears as a pervasive network around dioritic patches, as opposed to the spots seen in the quartz gabbros. If the acidic material in the quartz gabbros has the same origin as that in the intermediate rocks then one might expect the same alteration to be seen in the gabbros. This is not the case. On the other hand, if the acidic material in the intermediate rocks and the granophyres differs in origin, and has been brought into its position above the gabbros as a fluid-rich acidic melt, then the fluids associated with it could cause alteration in rocks with which it is in close contact, but not those further away (i.e. not the gabbros at the bottom of the exposed body).

B. The Intermediate Zone.

Introduction.

Blotchy rocks ranging from dolerites and microdiorites with subordinate amounts of interstitial granophyric material, through to granophyres with fine-grained microdioritic inclusions occur in this zone. This unit has been described as a physical mix of gabbroic and dioritic magmas with granophyric magma, made up of "scattered mafic and intermediate clots, inclusions and xenocrysts in a fine-grained quartzofeldspathic host" (Marshall. 1984).

The rocks in this zone are divided into two groups in this study; Basic(dioritic) intermediate rocks (see plate 7.05), and acidic (granodioritic) intermediate rocks (see plate 7.06). It should again be emphasised that boundaries between these rock units are indefinite.

In hand specimen the junctions between acidic and more basic portions become sharper upwards. These boundaries are diffuse in the basic intermediates but are sharper in the acidic intermediates and granophyres (compare plates 7.05 and 7.06); this is apparently a function of grain size contrast. This can be explained by considering the colour differences between course and fine-grained basic and acidic igneous rocks. Gabbros and granites may both appear quite pale in colour due to the abundance of large amounts of plagioclase and quartz respectively. However their fine-grained equivalents, basalt and felsite/rhyolite, have a bigger colour contrast due to their faster cooling rates, which an increased nucleation and growth rate of ferromagnesian minerals in the basalt, with plagioclase becoming subordinate in size and abundance.

7.4 Dioritic Intermediate Rocks (see plates 7.05 and 7.07)

7.4.1 Introduction

The type specimen for this petrological unit is GM 32. In hand specimen this has the appearance of a plagioclase-rich micro-diorite with fine-grained, pale-grey acidic patches. This material is first encountered at 250m, and is dominant upto 400m in the eastern branch at Cruach Choireadail. The basic groundmass of the rock resembles the quartz gabbro. The acidic portion appears as spots upto 5-10 mm in diameter at 250m. These spots generally become more abundant with altitude (compare the proportions of the two in samples GM32 and GM31 in table 7.1). The mottled appearance of these rocks increases upwards with the melanocratic portion becoming finer grained and more dioritic. This decrease in grain size causes a more marked colour contrast with the pale acidic patches.

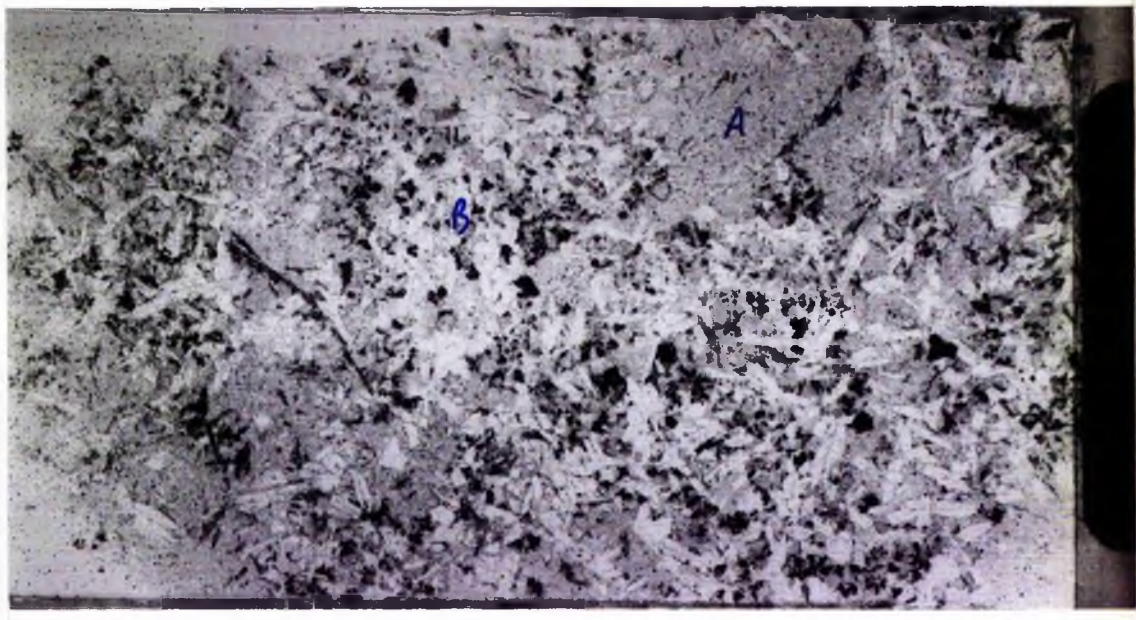

Plates 7.05 and 7.06. Thin sections of dioritic (GM 32, top) and granodioritic (GM 30, bottom) intermediates. Note the decrease in grain size of the dioritic portions (B) in contrast with the fine-grained acidic portions (A). Both slides magnified x 4.

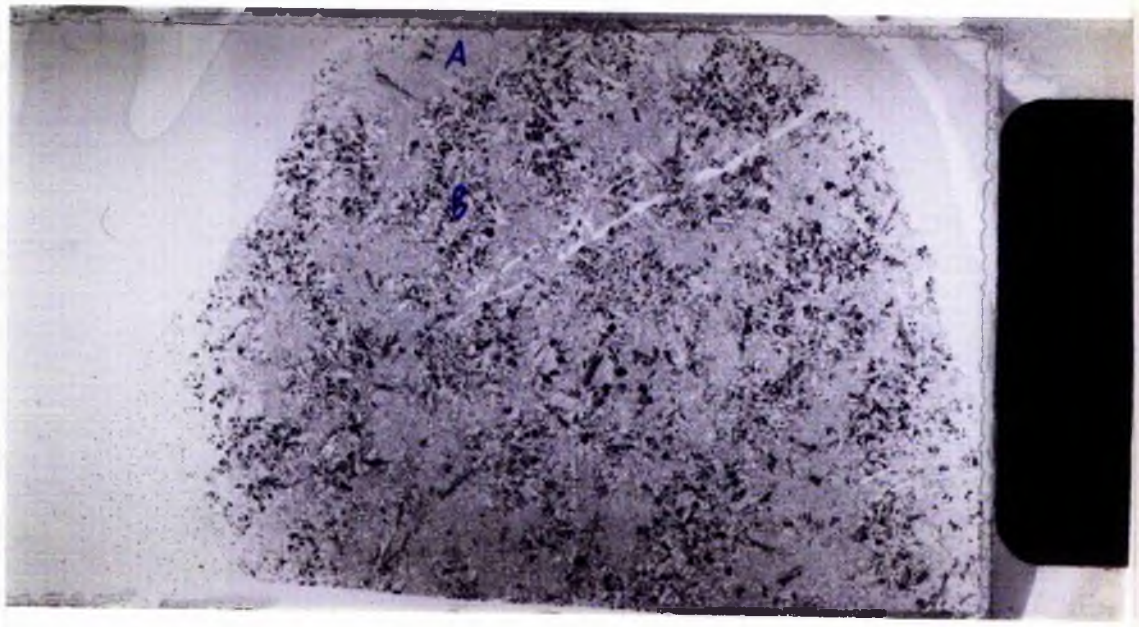

Plate 7.07. PPL photomicrograph (magnification x 20) of the contact between acidic (RHS) and dioritic (LHS) portions in a dioritic intermediate sample. Note the hydration textures around edges of plagioclase and pyroxene crystals in dioritic patches in contact with the fine-grained granophyre.

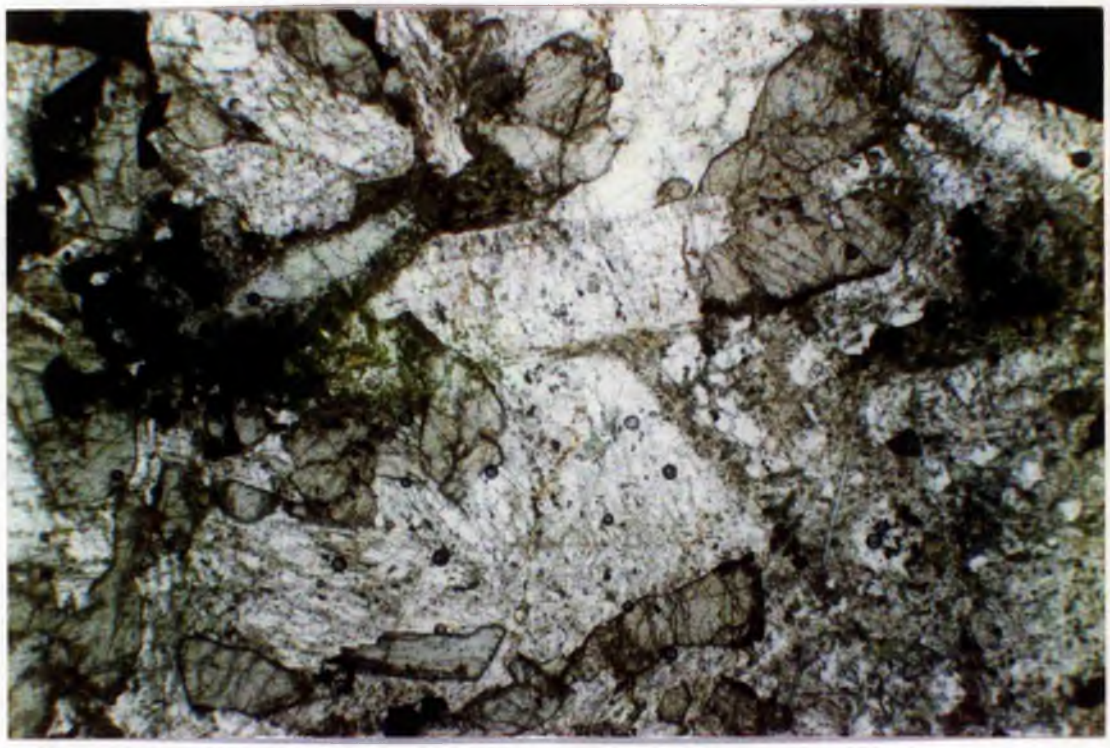

Plate 7.08. XPL photomicrograph (magnification x 30) showing the contrast between acidic and dioritic portions in a granodioritic intermediate. Note the finer grain size of the dioritic portion compared with that in plate 7.07.

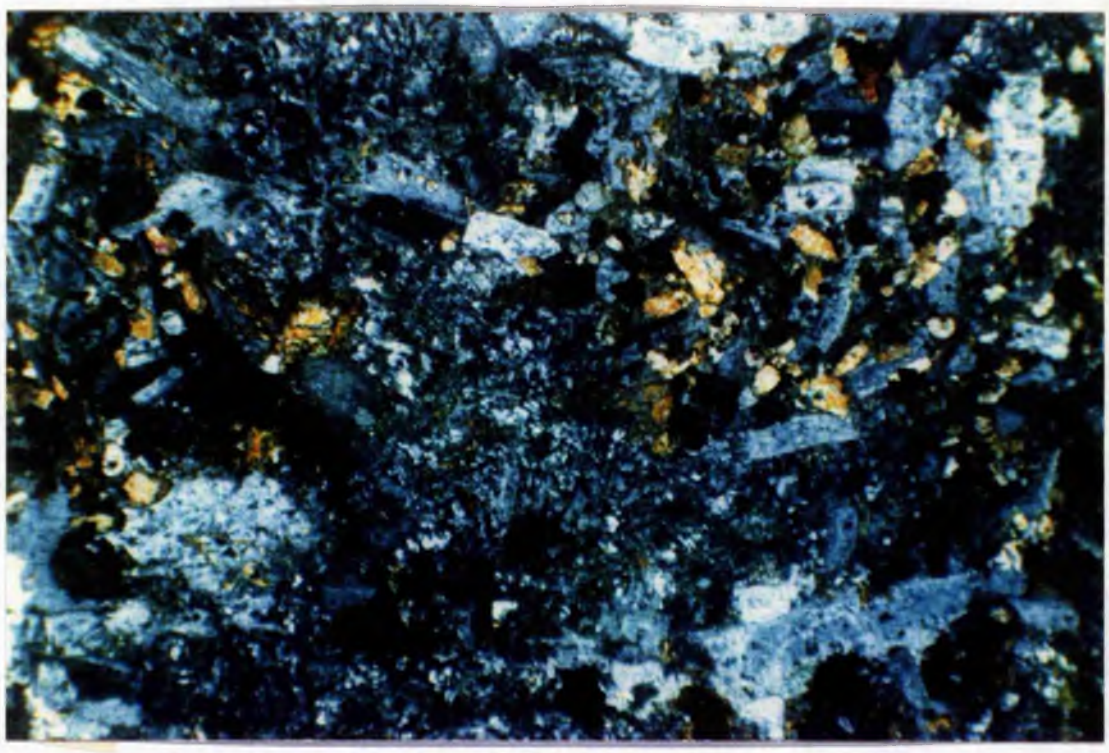

7.4.2 Mineralogical and Textural relationships

In thin section (plate 7.7) the dioritic portion resembles the quartz gabbros, however there is an increase in the degree of alteration. The possible cause of this alteration was discussed in the introduction to this section. In contact with the acidic material, plagioclase has albitized rims, and clinopyroxene has been hydrated to hornblende and chlorite with magnetite specks along cleavage traces. Plagioclase in the dioritic groundmass forms dusty, altered, elongate laths upto 2mm x 1mm x 1mm. It is more sodic in composition (An35) than plagioclase in the gabbros. Clinopyroxene has two forms; stumpy, subhedral collumns (averaging 1mm ^{2}) and larger, euhedral ophitic crystals (upto 2mm x 1mm x 1mm). The small, stumpy, subhedral columns are twinned augite with pale-brown pleochroism and are discrete from plagioclase laths. The scarcer ophitic pyroxenes are heavily cracked and altered, and form intergrowths with primary opaque minerals and with plagioclase laths. The different relations of each of these with plagioclase suggests that the euhedral crystals have co-precipitated with plagioclase while the other group has formed either before or after this co-precipitation. As the stubby pyroxene appears in interstitial voids it appears that it grew after the co-precipitation phase. Opaques are stubby crystals of magnetite and ilmenite (rarely more than 0.5mm^3) The granophyric portion contains plagioclase prisms (upto 1mm x 0.5mm x 0.5mm), and very fine-grained (0.1 mm^3)amounts of anhedral quartz, apatite needles, chlorite, dusty orthoclase , plumose plagioclase needles (indicating fast growth and quick cooling), oxide specks, and a micrographic intergrowth of quartz triangles set in cloudy albite. Occasional elongate (1mm x 0.2mm x 0.2mm) needles of hornblende with pyroxene remnants is seen. The amount of cloudy feldspar and chlorite gives the rock a pale-green tinge, and is a result of the increased alteration in these rocks.

7.5 Granodioritic Intermediate Rocks (see plates 7.06 and 7.08)

7.5.1 Introduction

This unit of the intermediate zone, typified by specimen GM 12 (see plate 7.08), contains >50% granophyre. It is composed of dark, fine-medium-grained, dioritic spots (upto 1cm across) surrounded by an acidic portion. The contacts between the acidic and basic portions of the rock are sharper than those in the basic intermediate rocks (compare plates 7.05 and 7.06) because the basic portion of the rock is finer grained and therefore darker than the acidic portion. Bor (1951) noted that these resemble hybrid rock types of supposed mixed magma origin, on Skye (Marsco), Arran and Ardnamurchan.

7.5.2 Mineralogy and Texture

The acidic portion, which makes up a majority of this rock unit and increases in proportion with altitude, contains fine-grained (all <2mm) oxide specks, anhedral quartz, apatite

needles, pale-green chlorite, micrographically intergrown quartz and feldspar, stubby orthoclase laths and radiating plagioclase needles. Plagioclase laths (upto 2 x 1 x 1 mm) are of the same composition as those in the granophyre (i.e. low An content. Chloritized hornblende (upto 1mm x 0.2mm x 0.2mm) is also present in this acidic portion. Hornblende may have been chloritized from primary hornblende or could be remnants of altered pyroxene. No unaltered pyroxene remains in the acidic portion, however dactylitic grains of chlorite and hornblende specked with opaques are possibly pseudomorphs of altered pyroxene crystals.

The medium-grained dioritic patches within the acidic portion consist of opaques and pyroxene in fine-medium-grained (upto 2mm max) glomerophyric aggregates with orthoclase and plagioclase laths in between the aggregates. The dioritic patches are similar in modal composition to the melanocratic portion of the dioritic intermediate rocks, but are finer-grained and less abundant.

C. THE UPPER ZONE

7.6 The Granophyres (see plate 7.09)

7.6.1 Introduction

Above 450m at Cruach Choireadail fine-medium-grained granophyre is the dominant rock type in the Glen More ring dyke. The rock contains fine-grained, ovoid, melanocratic inclusions (upto 5cm long but usually less than 2cm) (see plate 7.09), which become scarcer with increasing altitude (see table 7.1). There is an increase in silica content with altitude (see chapter 9), possible due to the decreasing proportion of mafic inclusions. The granophyre is generally pale-grey--pale-green, although it varies in colour and texture throughout the body, and in some places has a buff pink colouration where there is a higher concentration of unaltered potassium feldspar. The grey granophyre has a cloudy/dusty appearance in thin section, similar to that described in the Memoir in craignuritic rocks (glass rich rhyodacites) (Bailey et al. 1924). At its contact with the country basalts the granophyre has a 2-3m chilled margin of very fine-grained pale brown/pink felsite, containing no melanocratic inclusions.

7.6.2 Mineralogy and texture of the granophyres

The grey granophyre, typified by sample GM17 (see plate 7.09) from 535m on Cruach Choireadail, is very similar in appearance to the acidic portion of the intermediate rocks, but comprises >95% of the rock. The melanocratic enclaves are smaller ,less than 1cm to 3cm, and finer grained than the dioritic portion of the intermediate zone and have sharp boundaries with the acidic portion. The enclaves contain opaque needles (upto 2mm long), elongate hornblende crystals (upto 2mm x 0.5mm^2), interstitial plagioclase, quartz,

Plate 7.09. XPL photomicrograph (magnification x 40) of granophyric sample GM19 from the upper reaches of the Glen More ring dyke at Cruach Choireadail. Note the very fine-grain size, elongate K-feldspar lath and the thin elongate needles of opaque minerals.

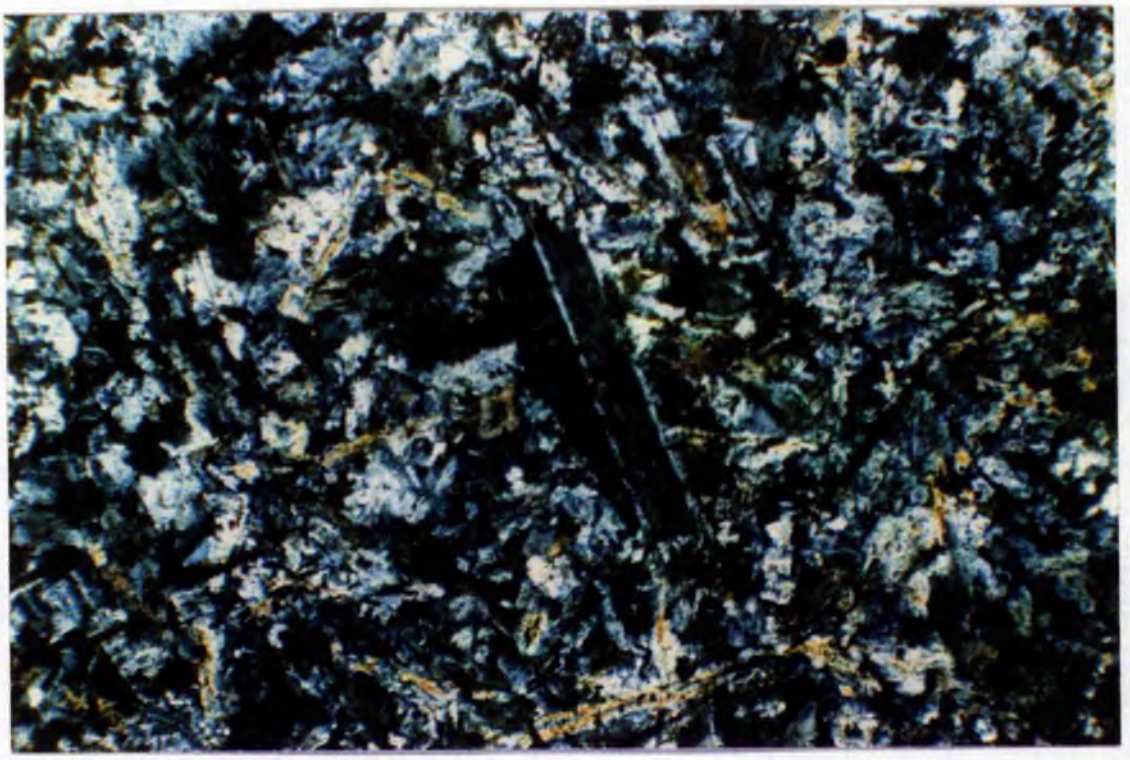

Plate 7.10. PPL photomicrograph (magnification x 10) showing the contact between a mafic enclave and its granophyric host. Note the rim of opaque minerals at the edge of the enclave, and the elongate, skeletal morphology of plagioclase and opaques in the enclave. Such morphologies are indicative of fast crystal growth, possibly caused by growth on quenching.

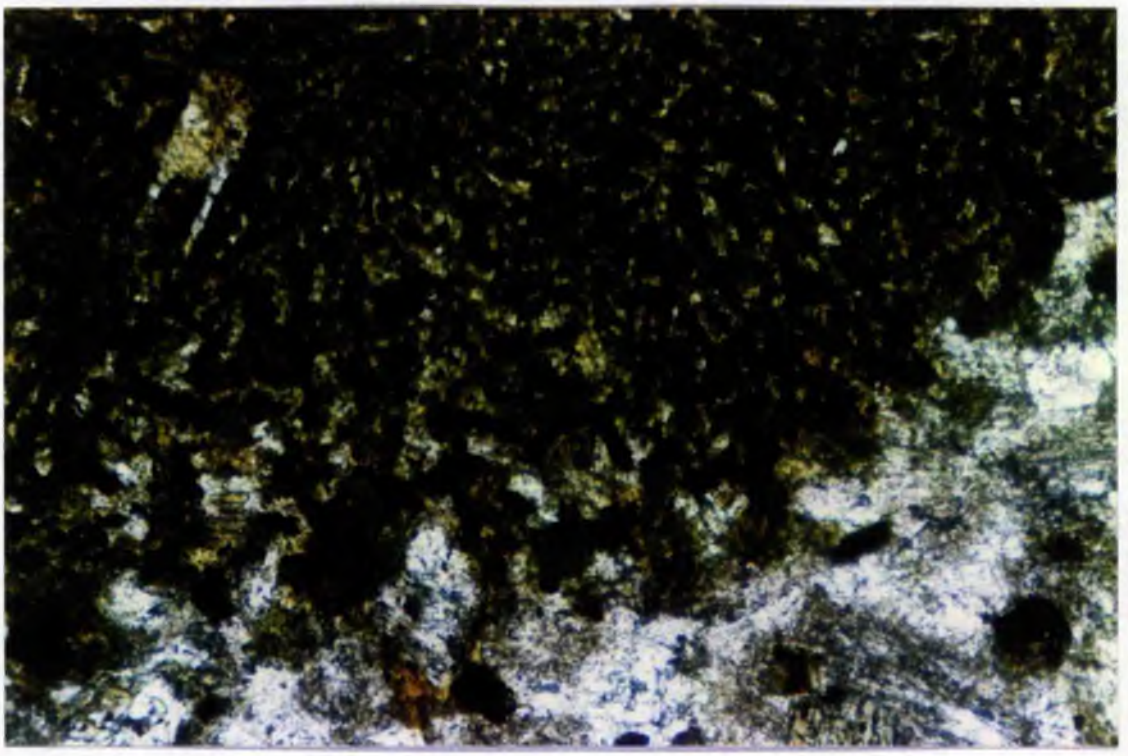

orthoclase, apatite and chlorite (all <1mm). Hornblende is also seen to have partially replaced the clinopyroxene. The rim of these xenoliths is often rich in elongate dendrites of Fe-Ti oxides, and occasional plagioclase laths show elongate skeletal morphologies (see plate 7.09). These crystal morphologies indicate rapid crystal growth from the melt, possibly caused by quenching of basic magma in an acidic host.

The grey-green granophyre contains prismatic, inclusion-rich, plagioclase laths (upto 2 x 0.5 x 0.5 mm) with albitized rims, and pink oligoclase laths (upto 2mm ^{2}) set in a very fine-grained groundmass of plumose plagioclase (upto 3mm x 0.5mm^2) with perthite, K-feldspar, chlorite, apatite, sphene, hornblende, magnetite, and micrographically intergrowth of quartz and feldspar. Hornblende and magnetite form elongate intergrowths (upto 3mm x 0.5mm^2), possibly pseudomorphing pyroxene. In thin section the rock is riddled with chlorite. The overlying pink granophyre is slightly coarser grained than the grey granophyre, and consists of a medium-grained mosaic of pink orthoclase, hornblende and chlorite flecks, interstitial quartz, and a granophyric intergrowth of quartz embedded in plagioclase. Pyroxene xenocrysts have been reported in these rocks (Bor 1951), but have not been observed in this study.

7.7 Summary

The petrographic descriptions in this chapter indicate the following points:-

- The interstitial spots of acidic mesostasis in the gabbros is distinct from the acidic portion of the intermediate rocks. It has essentially the same content but little alteration is associated with the interstices of the gabbros. In contrast, alteration is extensive in the intermediate and upper zones of the dyke, the probable cause being the fluids associated with the acidic magma that was the parent of the acidic parts of the intermediate and granophyric rocks. If this magma was the source of the acidic patches in the gabbros we would expect to see the same degree of alteration in the gabbros.
- The acidic portion of the intermediate rocks is very similar to the granophyric rocks at the top of the ring dyke.
- The dark, fine-grained enclaves could be the product of quenching of dioritic melt, similar to that which forms the dioritic patches in the intermediate rocks.
- From the data presented in this chapter it is impossible to evaluate the origin of the dioritic portion of the intermediate rocks. Various possibilities exist however:-

1) Dioritic magma was the parent from which the gabbros have crystallized as cumulates, leaving a dioritic residue which has been brought into contact with an acidic magma in the intermediate zone.

2) Basic and intermediate magmas were intruded simultaneously into the ring dyke in a zoned sequence. These crystallized to produce gabbro cumulates and a residue of dioritic magma. The granophyre was then injected into the ring dyke fissure and underwent partial mixing with the dioritic magma before cooling to produce the rocks seen now.

3) The gabbros crystallized as cumulates from a basic magma. As crystallization proceeded the residual magma evolved to an intermediate composition. Acidic magma was then brought into contact with this dioritic residue.
4) A 3-layer (basic overlain by intermediate, overlain by granophyric) magma system was injected into the body. A limited degree of mixing has occured between the top two layers (acidic and intermediate), and the whole system has crystallized with little further mixing.

The fourth possibility is the least likely due to some of the field relations reported in chapter 6. Granophyre is seen to intrude gabbros after substantial consolidation, indicating that the granophyre was intruded into the ring dyke during a later intrusive event. The first three possibilities are therefore favoured here but it is difficult to assess each one at this early stage.

CHAPTER 8. Mineral Chemistry

8.1 Introduction

Major element analyses of primary magmatic minerals in rocks from Cruach Choireadail and other localities within the Glen More ring dyke are presented in this chapter. Compositional variations in clinopyroxene and plagioclase are discussed with respect to the petrogenetic development of the body. Olivine composition is discussed with respect to the possible composition of the parental magma and depth of cooling of the ring dyke. Minerals in a mafic microgranular enclave in a granophyre sample were examined in an attempt to establish the provenance of the enclaves, their mineralogy is displayed in table 8.7.

Microprobe analyses were carried out on a Jeol JCXA 733 electron probe micro analyser at St Andrews using standard wavelength-dispersive techniques and a fully focused beam (1 micron diameter) at a specimen current of between 5×10^{-6} and 5×10^{-7} A, and 20kV accelerating potential. Pure metals, oxides and minerals were uaed as reference standards, and apparent concentrations were corrected using the conventional ZAF procedures. The accuracy of wavelength dispersive microprobe analysis has been determined by Dunham and Wilkinson (1978) to be +/- 2.4 %.

The combination of decreasing grain size and increasing degree of alteration with altitude means that most of the granophyres are unsuitable for EPMA. This explains the apparent bias towards analysis of minerals in gabbros and intermediate rocks in this chapter.

8.2 Olivine (table 8.2)

Magnesium-rich olivine has the highest liquidus temperature of the common rock-forming silicate minerals. It is therefore the least stable mineral at low temperatures and pressures, and so is the most susceptible to hydrothermal alteration. The Glen More ring dyke lies within the epidote zone of hydrothermal alteration outlined by Walker (1971) on Mull (see figure 6.03 in chapter 6). Much of the olivine in this body has therefore undergone alteration and most evidence for primary magmatic olivine lies in the existence of pseudomorphs, upto 2mm across, comprising serpentine, chlorite, and magnetite. However, fresh olivine is found in gabbros close to localities where the only evidence for primary olivine existence is in the presence of its pseudomorphing alteration products. This points towards very localized alteration, possibly close to fluid pathways in the body (Thompson 1982). Fresh olivine is seen in thin sections of two gabbros, GM13 and GM 24, from 130m and225m, respectively, at Cruach Choireadaill. Analyses from these olivine crystals are displayed in table 8.2.

Table 8.2. Olivine Compositions from Glen More gabbros

	GM 13-1	GM 13-4	GM 24-2	GM 24-5	GM 24-8
Altitude (m)	130	130	235	235	235
SiO2	36.5	37.4	36.7	37.5	37.5
TiO2	0.0	0.0	0.0	0.0	0.0
Al2O3	0.0	0.0	0.0	0.0	0.0
FeO	30.0	24.9	28.6	26.7	28.5
Cr2O3	0.0	0.0	0.0	0.0	0.0
MnO	0.6	0.4	0.5	0.5	0.6
NiO	0.0	0.0	0.1	0.1	0.1
MgO	31.8	35.8	33.5	35.1	33.7
CaO	0.1	0.2	0.1	0.1	0.2
Na2O	0.0	0.0	0.0	0.0	0.0
K2O	0.0	0.0	0.0	0.0	0.0
Total	99.1	98.9	99.5	100.0	100.5
% Forsterite	65	72	67	70	68
% Fayalite	35	28	33	30	32

Table 8.6. Oxide compositions from representative samples in the Glen More ring dyke.

Sample	CC4 (11)	CC4 (12)	CC4 (9)	CC4 (10)	GM47 (10)	GM52 (8)
Rock type	Quartz gabbro	Quartz gabbro	Quartz gabbro	Quartz gabbro	Basic intermediate	Olivine gabbro
Altitude (m)	342	342	342	342	148	210
Mineral	Magnetite	Ilmenite	Magnetite	Ilmenite	Ilmenite	Magnetite
wt % oxide						
SiO2	0.3	0.6	0.2	0.2	1.3	0.4
TiO2	3.9	50.7	4.5	38	50.7	3.4
Al2O3	0.6	0	0.7	0	0.2	1.1
FeO	85.2	43.1	86.5	56.6	42.6	84.1
MnO	0.4	3.6	0.4	1.8	3.5	0.2
MgO	0	0	0	0	0	0
CaO	0	0	0	0	1.4	0
Na2O	0	0	0	0	0	0
K2O	0	0	0	0	0	0
total	90.4	98	92.3	96.6	99.7	89.3

Sample	GM52 (9)	GM52 (16)	GM52 (17)	GM7 (15)	GM7 (16)	M48 (3) in enclave	CG1 (3)
Rock type	Olivine gabbro	Olivine gabbro	Olivine gabbro	Quartz gabbro	Quartz gabbro	ferrodioritic encla	Quartz gabbro
Altitude (m)	210	210	210	385	385	420	135
Mineral	Ilmenite	Magnetite	Ilmenite	Magnetite	Ilmenite	Magnetite	Ilmenite
wt % oxide							
SiO2	0.2	0.3	0.3	0.3	0.2	0.5	0.1
TiO2	50.9	3.9	51	5.6	51.1	1	48.1
Al2O3	0	1	0	1.8	0	0.2	0
FeO	45.4	82.2	44.8	82.5	45.6	88.2	47.3
MnO	2.4	0.2	2	0.3	1.9	0.2	2.4
MgO	0	0	0	0	0	0	0
CaO	0	0	0	0	0.1	0.1	0.1
Na2O	0	0	0	0	0	0	0
K2O	0	0	0	0	0	0	0
total	98.8	87.8	98.2	90.6	99	90.1	98.1

The compositional range of olivine in GM13 is Fo 65-72. In GM24 it is Fo 67-70. The mean value is Fo 68.2 which correlates well with the optical compositional estimate. No zoning is evident in the olivine crystals examined. The relatively high CaO content of the olivines in the body (range 0.08-0.2 wt %, average 0.142 wt %) places them above the 0.1 wt % dividing line defined by Simkin and Smith (1970), which separates olivines from a plutonic environment (with low CaO content), from olivines which have crystallized in an extrusive or hypabyssal environment. This indicates that the olivines in the Glen More ring dyke crystallized in a hypabyssal environment.

Roeder and Emslie (1970) took results of olivine-liquid equilibrium experiments and produced a graph (figure 8.01) which allows the composition of olivine crystallizing from a magma of known mole% FeO and MgO to be predicted or *vice versa*.. This model shows us that olivine of composition Fo 68 will crystallize from a magma with a molar MgO/FeO ratio of 0.65. The MgO/FeO ratio has been calculated for whole rock analyses of gabbros in this study (see table 8.3). The MgO/FeO ratio values for gabbros from the Glen More ring dyke range from 0.32 to 1.75. Samples LS1, GM52, and MT3 have molar MgO/FeO ratios closest to 0.65 (0.748, 0.56 and 0.664 respectively). Whole rock chemistry of these samples (chapter 9) shows that they are not the most primitive whole rock compositions found in the body (SiO_2 ranges from 48.6 to 49.6 wt % in these samples, while the lowest SiO_2 content is 47 wt %). This indicates that the least-evolved samples are not the most suitable parental magma compositions. This could indicate that the parental magma was of a more evolved composition than the samples with lowest SiO_2 content.

The gabbros in which olivine and its alteration products are found are often plagioclase-rich cumulates. If olivine was also a cumulus phase then the molar MgO/FeO ratio from whole-rock chemistry will not be representative of the parental magma composition. Rocks in which the olivine has accumulated will have the parental MgO/FeO ratio preserved in the olivine composition (eg. Fo_{68} comes from a parental magma with a ratio of 0.65) as long as the olivine composition has not been altered by postcumulus processes. On the other hand rocks representing the parental magma composition will not be present because olivine has fractionated out of the original liquid, depleting it in MgO and FeO. This means that the search for a parental magma composition in one of the whole -rock compositions may be futile.

Other problems may also lead to inaccuracies in calculations involving MgO/FeO ratios. FeO whole-rock values have been calculated using $Fe^{2+/3+}$ values calculated assuming the value from Bor's (1951) wet chemical analytical data. These ratios have been applied to rocks in this study on the basis of similar petrographic descriptions (ie. the ratio for Bor's olivine gabbro has been used for olivine gabbros in this study). Every effort has been made to match sample types but, due to the heterogeneous nature of the rocks and possible analytical error in Bor's data, innacuracies may exist. Also, Fe^{2+} is readily

Table 8.3. MgO/FeO ratios for gabbros from Glen More

Sample	FeO Mole %	MgO Mole %	MgO/FeO
GM 4	6.74	5.88	0.872
GM 8	6.93	12.12	1.75
LS 1	6.8	5.03	0.748
GM 9	7.43	11.4	1.53
GM 13	5.4	13.2	0.41
GM 32	4.9	9.94	0.49
GM 52	5.4	9.7	0.56
GM 55	8.84	4.34	1.12
CC 6	4.5	7.9	0.316
MT 3	6.4	5.36	0.664
GM 7	9.35	5.43	0.95

FIGURE 8.01. Roeder and Emslie (1970) model showing the relationships between mole % of MgO and FeO in the liquid, to olivine and temperature of crystallization at 1 atmosphere. The composition of olivine in the Glen More gabbros is shown, with an MgO/FeO value for the liquid from which it crystallized, of 0.65.

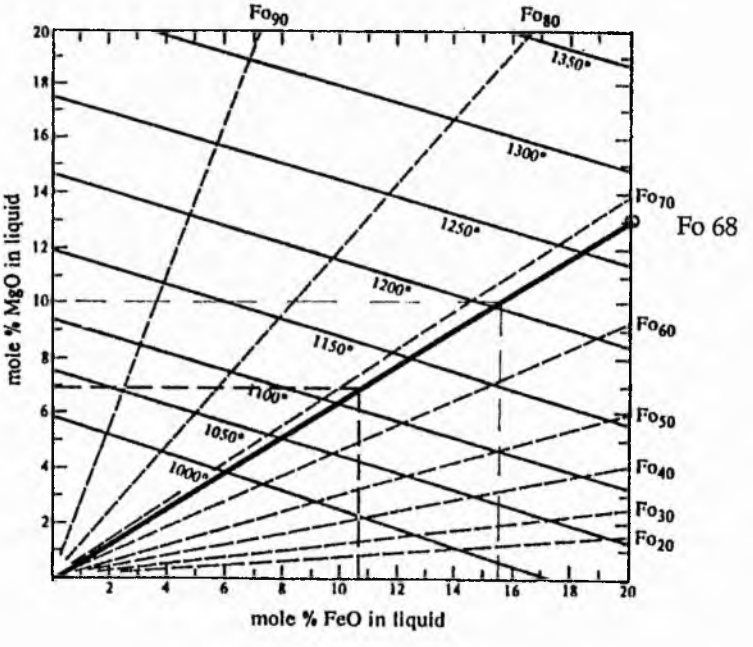

oxidized to Fe^{3+} during the hydrothermal alteration of these rocks. Fe^{2+} content in the whole-rock analysis is therefore not always a good guide to Fe^{2+} content in the original magma, or even the initial whole-rock. The heterogeneous nature of the alteration further complicates this problem.

8.3 Clinopyroxene (table 8.4)

32 optical and 5 wet-chemical analyses of pyroxenes made by Bor (1951) suggest that the clinopyroxenes have a fixed composition (diopsidic augite) throughout the ring dyke. Any variations seen were attributed to variable amounts of magnetite and chlorite in analysed crystals. Bor reported xenocrystic clinopyroxene in the granophyre at Cruach Choireadaill, however most is now completely altered to hornblende, chlorite and magnetite, making analysis very difficult. Increased alteration and decreasing grain size with increasing altitude make suitable crystals hard to locate in many intermediate and acidic rocks.

Clinopyroxene analyses from olivine and quartz gabbros, dioritic and granodioritic intermediates, and from an enclave in a granophyre (GM48) are displayed in table 8.4. The overall range of clinopyroxene composition is Wo 28-48, En 27-47, Fs 13-36. No zoned clinopyroxene, and no orthopyroxene is seen in any of the rocks analysed.

Figure 8.02 illustrates where the pyroxenes from the Glen More body plot on the pyroxene quadrilateral. Although not falling on a very well defined trend the clinopyroxenes in this study do show a general Fe-enrichment and Mg-depletion, with slight Ca-depletion, in the progression from olivine gabbros, through quartz gabbro, to dioritic intermediates.

The pyroxene analysed in GM 48 is from one of the mafic enclaves in a granophyre from the upper reaches of the dyke and has the most evolved composition of all pyroxenes analysed. As mentioned in chapter 7, the enclaves contain opaques and plagioclases with elongate skeletal morphologies which suggest rapid growth - possibly from quenching of blobs of mafic melt when it was surrounded by cooler granophyric melt. If this is how the mafic enclaves have formed then it suggests that blobs of an intermediate magma have been entrained in granophyric magma.

The Al content in these clinopyroxenes is relatively low for augites and decreases slightly as the augite becomes more Fe-enriched. In all cases Si and Al is sufficient to satisfy the numerical requirements of the Z group in the clinopyroxene formula, Ti is therefore free to occupy the Y site. The more evolved pyroxenes (>20 % Fs) have relatively low TiO_2 concentrations (<0.4 wt %) for augite (Deer, Howie and Zussmann, 1966), while some of the least evolved samples contain relatively high concentrations (>0.8 wt %). This

Table 8.4. Representative Clinopyroxene analyses

Rock Type	Olivine Gabbro	Olivine Gabbro	Olivine Gabbro	Olivine Gabbro	Quartz Gabbro	Quartz Gabbro	Quartz Gabbro	Quartz Gabbro	Quartz Gabbro
Sample Number	GM 13	GM 55	GM 52	GM 9	CG 1	GM 4	CC 4	MT 3	GM 7
altitude (m)	130	195	210	430	137	287	342	344	385
Weight % oxide									
SiO2	51	50.5	51.1	49.5	51.2	51.8	50.2	51.1	50.6
TiO2	1	0.8	0.7	1.1	0.4	0.1	0.7	0.8	0.9
Al2O3	1.8	2.2	1.8	3.5	1	0.3	1.3	2.7	2.7
FeO total	9.2	10.4	11.1	10.5	15.5	14.4	13.6	8.7	10.2
MnO	0.3	0.3	0.3	0.2	0.6	0.6	0.5	0.2	0.3
Cr2 O3	0.1			upto 0.2		upto 0.02			
MgO	15.2	15.3	14.4	13.5	11.8	11.6	13.4	14.5	14.7
CaO	20	18.6	18.9	20	18.7	20.2	18.1	20.2	19.3
Na2O	0.4	0.3	0.3	0.3	0.3	0.2	0.3	0.3	0.3
Total	98.8	98.5	98.7	98.7	99.6	99.3	98.1	98.4	99
Number of ions on the basis of 6 oxygens									
Si4+	1.904	1.906	1.936	1.876	1.962	1.99	1.92	1.925	1.89
Al3+	0.088	0.094	0.064	0.124	0.038	0.01	0.069	0.075	0.11
Ti4+	0.028	0.023	0.02	0.031	0.012	0.003	0.02	0.023	0.026
Al3+	0	0.004	0.016	0.032	0.008	0.004	0	0.045	0.01
Mn2+	0.01	0.01	0.01	0.006	0.019	0.02	0.016	0.006	0.01
Fe2+	0.357	0.394	0.382	0.384	0.526	0.478	0.499	0.28	0.393
Mg2+	0.85	0.861	0.813	0.763	0.674	0.664	0.768	0.814	0.828
Na+	0.029	0.022	0.022	0.022	0.022	0.015	0.022	0.022	0.022
Ca2+	0.803	0.752	0.767	0.812	0.768	0.832	0.746	0.815	0.782
Wo %	41	38	39	41	40	43	38	42	40
En %	46	47	44	43	36	35	41	45	45
Fs %	13	15	17	16	24	22	21	13	15

Table 8.4. Representative Clinopyroxene analyses

Quartz Gabbro	Basic Intermediate	Basic Intermediate	Basic Intermediate	Basic Intermediate	Acidic Intermediate	Mafic enclave
CC 6	GM 47	GM 26	GM 32	GM 31	GM 12	GM 48
442	148	335	352	455	485	420
50.5	50.3	49.6	51.4	52.6	49.9	49.8
0.9	0.7	0.4	0.9	0.2	0.9	0.2
2.8	1.3	0.8	1.7	1.3	2.6	0.3
9	17	15.3	12.2	19.4	9.6	18.8
0.2	0.6	0.8	0.4	1.2	0.2	0.6
	0	upto 0.05	upto 0.05			
14.9	10.9	8.4	14.2	10.4	14.4	8.5
20	18.3	21.5	18.6	11.9	19.4	18.9
0.3	0.3	0.2	0.4	0.2	0.4	0.3
98.7	99.3	97.2	99.9	97.3	97.5	97.4
1.899	1.944	1.979	1.931	2.101	1.903	1.991
0.101	0.056	0.021	0.069	-0.101	0.092	0.009
0.025	0.02	0.012	0.025	0.006	0.026	0.006
0.023	0.003	0.016	0.006	0.162	0.02	0.005
0.006	0.02	0.027	0.013	0.041	0.006	0.02
0.333	0.585	0.507	0.425	0.389	0.361	0.643
0.835	0.628	0.5	0.795	0.619	0.819	0.507
0.022	0.022	0.015	0.029	0.015	0.03	0.023
0.806	0.758	0.919	0.749	0.509	0.793	0.81
41	39	48	39	28	41	43
46	34	27	43	36	45	27
13	27	25	18	36	14	30

FIGURE 8.02. Pyroxene quadrilateral diagram illustrating the variation in clinopyroxene composition in the Glen More ring dyke. (Red= olivine gabbro, green= quartz gabbro, orange= intermediate rock type, yellow= pyroxene in mafic enclave in granophyre.)

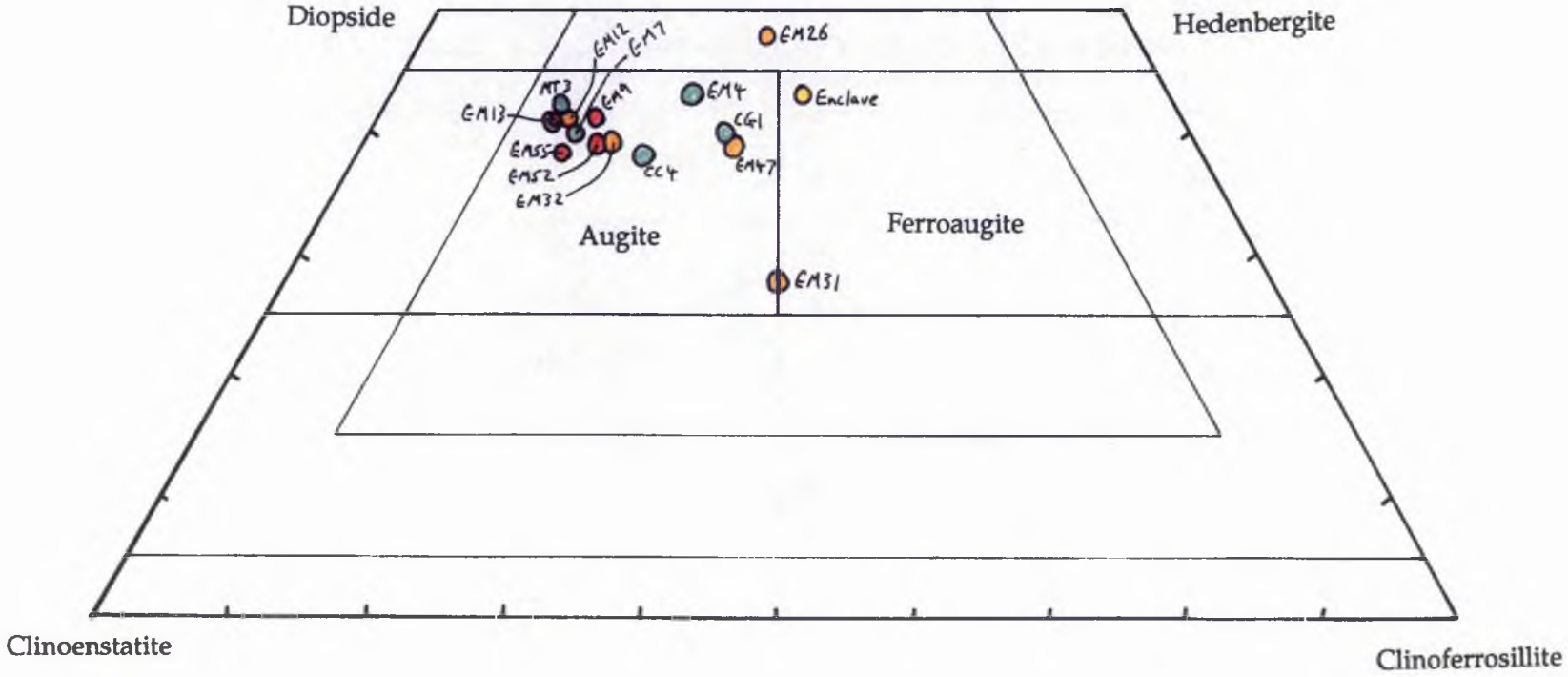

indicates a possible fractionation trend involving Ti depletion during magma fractionation, and could be caused by TiO_2 being removed from the melt by clinopyroxene and ilmenite crystallization.

8.4 Plagioclase (table 8.5)

Figure 8.03 (a +b) illustrates the data from table 8.5. Both graphs show a bimodal distribution of plagioclase compositions. Figure 8.03a plots the average core compositions of plagioclase on an An-Ab-Or triangle. Plagioclase from both olivine and quartz gabbros and basic portions of intermediates plots between An 51-75 while plagioclase from granophyres, and acidic portions of intermediate rocks plot between An 2-17. Figure 8.03b shows ranges of An % in individual samples plotted against altitude. This displays the same bimodal distribution of compositions.

Albitisation, caused by the introduction of a sodium ions into a rock by a secondary fluid, has occurred on the rims of many feldspars in the body, and is attributable to either the hydrothermal alteration around the central intrusive complex on Mull (Walker, 1971), or to late-stage fluids associated with the introduction of an acidic magma, possibly parental to the granophyres.
The following points summarize these data:-

• The dioritic-intermediate group of rocks contains both calcic and sodic plagioclases. Sodic plagioclase is seen in the granophyric portion of the rocks while calcic plagioclase occurs in the basic portions of the rocks. This implies plagioclase crystallization from contrasting melt compositions in close association with each other. The two portions may have been brought together when both were melts, or one may have been intruded when the other was partially solidified. In the latter case we could expect refusion of the acidic portion when basic magma came into contact with it or some form of fracturing of one as the other was intruded into it. Neither of these is seen. However, if acidic magma was brought alongside partially solidified basic or intermediate magma then it would cause quenching of the latter magma, and further mixing could not take place. This latter process is therefore favoured here.

• Plagioclase composition varies considerably within the gabbros and dioritic intermediates over a 350 m vertical range (An 51-75). However the plagioclase composition does not appear to be altitude controlled, and rock samples from one altitude (352 m) have two distinct plagioclase compositions. This range of compositions implies a wide range of crystallizing temperatures and compositions of parental magmas. Below 450 m plagioclase compositions of An65+ are seen at both the top and bottom of the exposed collumn of rocks. Between these samples there is a slight decrease in An in the plagioclase (down to An 50). This could indicate crystallization at a higher temperature at

Table 8.5. Representative Plagioclase Analyses

Rock Type	Olivine Gabbro	Olivine Gabbro	Olivine Gabbro	Olivine Gabbro	Quartz Gabbro	Quartz Gabbro	Quartz Gabbro	Quartz Gabbro	Quartz Gabbro	Quartz Gabbro	Basic Intermediate
Sample Number	GM 13	GM 55	GM 52	GM 9	CG 1	GM 4	CC 4	MT 3	GM 7	CC 6	GM 47
Altitude (m)	130	195	210	430	135	287	342	344	385	442	148
PLAG CORE											
Weight % oxide											
SiO2	51.3	54.3	55.2	53.7	57.2	55.3	58.8	52.5	54.6	53.3	58.6
TiO2	0.1	0.1	0.1	0.1	0.1	0.1	0.1	0.1	0.1	0.1	0
Al2O3	29.6	27.9	26.7	27.7	26.5	26.9	25.9	29.3	27.4	28.5	25.5
FeO total	0.7	0.7	0.7	0.7	0.5	0.7	0.5	0.5	0.6	0.8	0.3
MnO	0	0	0	0	0	0	0	0	0	0	0
MgO	0	0	0	0.1	0	0	0	0	0	0	0
CaO	12.9	11.1	9.6	11.2	8.8	9.8	7.9	12.2	10.7	12	7.7
Na2O	4.1	4.8	5.7	4.9	6.2	5.9	6.2	4.4	5.4	4.8	6.6
K2O	0.2	0.3	0.4	0.3	0.5	0.3	0.4	0.3	0.3	0.15	0.7
Total	99	99.26	98.4	98.7	99.8	99.3	99.71	99.11	99.27	99.59	99.5
Core Average											
% An	76	69	61	67	56	60	52	71	60	70	53
% Ab	23	29	36	32	41	39	45	27	37	29	43
% Or	1	2	3	1	4	1	3	2	3	1	4
Core Range	An 75-76	An 67-71		An 61-72	An 54-57	An 58-61	An 44-57	An 69-72	An 47-65	An68-73	An 51-57
Rim Average											
% An	70	44				17		41			50
% Ab	29	52				80		51			49
% Or	1	4				3		8			1
Rim Range	An 65-75					An 16-18		An 40-43			An 47-52

Table 8.5. Representative Plagioclase Analyses

Basic Intermediate	Basic Intermediate	Basic Intermediate	Acidic Intermediate	Acidic Intermediate	Acidic Intermediate	Granophyre	Mafic enclave
GM 26	GM 32	GM 31	GM 12	GM 15	GM 17	GM 19	GM 48
335	352	455	485	530	535	630	420
66.1	55.1	67.1	67	68.2	67.5	68	71.1
0	0.1	0	0	0	0	0	0.1
21.7	27	22	21.2	20.4	20.3	20.2	20.5
0.1	0.8	0.1	0.4	0.1	0.1	0	0.6
0	0	0	0	0.1	0	0.1	0
0	0.1	0	0	0	0	0	0
1.8	10.1	1.7	1.4	0.5	0.5	0.2	0.2
10.5	5.7	10.3	10.8	11.4	11.9	11.6	7.4
0.1	0.4	0.1	0.1	0.03	0.1	0.1	0.2
100.21	99.35	101.3	100.77	100.71	100.6	100.11	100.18
15	60	16	13	5	5	2	3
85	37	83	86	94	94	97	92
0	3	1	1	1	1	1	5
An 8-16	An 58-62	An14-18	An 11-15	An 4-6	An 4-5	An 2-3	An 3-5
23	13	16	17		4		
76	84	83	81		96		
1	3	1	2		0		
An 17-32	An 7-18		An 16-19				

FIGURE 8.03. Variation in plagioclase composition in the Glen More ring dyke.

a) An-Ab-Or triangle showing average plagioclase core compositions. Note the range of compositions in gabbros and intermediates, the gap in compositions between An16 and An52, and the range of compositions in the granophyres and acidic intermediates. (Red= olivine gabbro, brown= quartz gabbro, green = intermediate, yellow = granophyre).

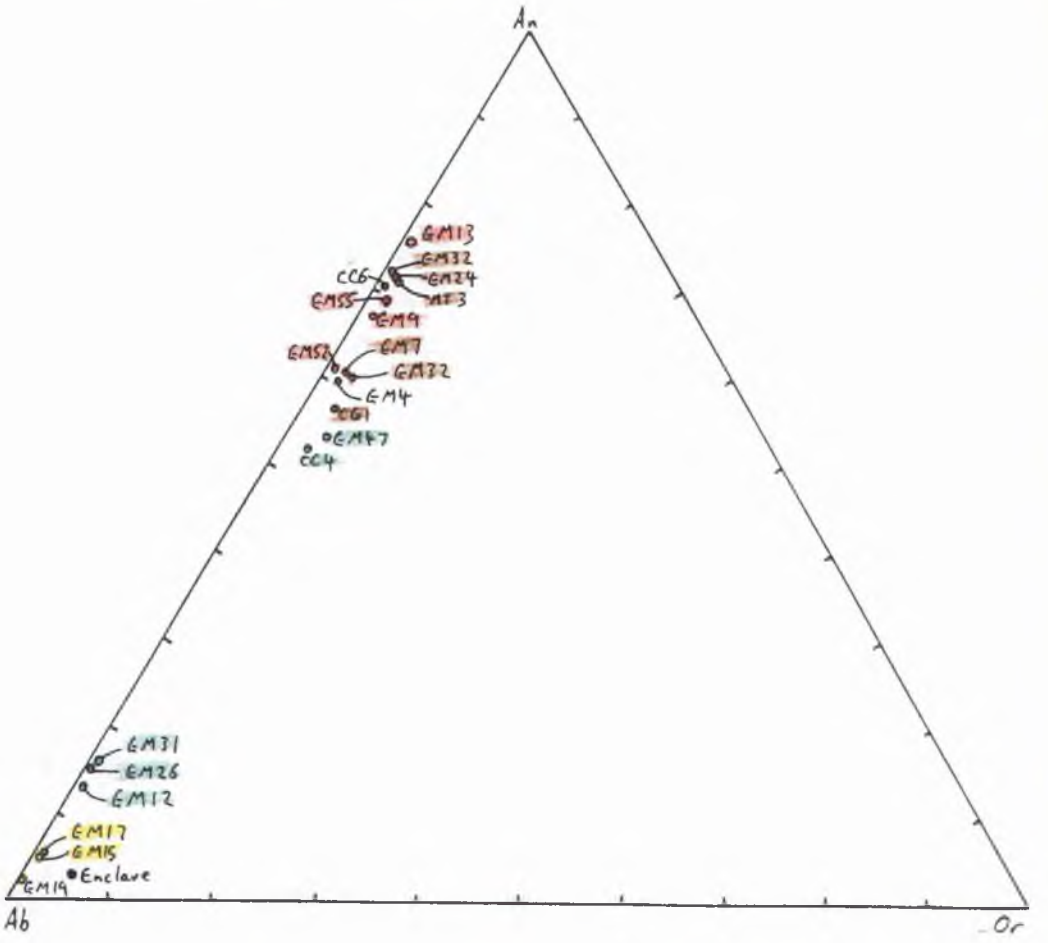

b) Graph showing the ranges of plagioclase compositions at different altitudes in the different rock types. Note the range of compositions in the intermediate rocks between 300 and 400m.

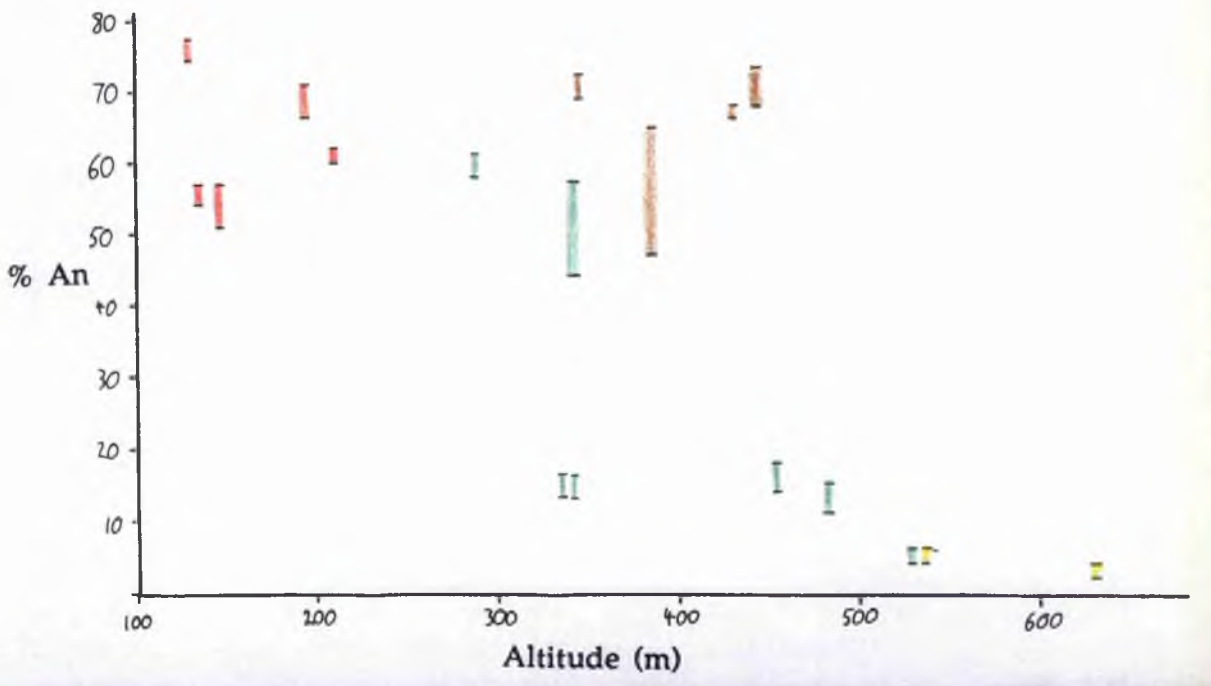

the top and bottom of the exposed gabbro pile. As crystallization progressed plagioclase in the interior (250-400 m) of the body could have crystallized at lower temperatures and so has a more albitic composition.

• Compositional variation is seen in the plagioclase in the granophyres, acidic intermediates and acidic portions of the basic intermediates, over a vertical range of 300m at Cruach Choireadaill. Intermediate and granophyric rocks (GM31, 26, 12, 17, 15, 19) contain plagioclase which shows a decrease in An content with increasing altitude (An16 - An 2 from 455 to 630m). This indicates a gravity controlled fractionation sequence with the most acidic magma being at the very top of the body. If this group of samples is considered separately from the rest (gabbros and basic intermediates) we can imagine it either crystallizing from the bottom (450m) upwards, with the more evolved residual magma being at the top of the body, or the various plagioclase compositions crystallizing from a magma that was already compositionally zoned when it intruded into its current position.

• There is not a continuous variation in plagioclase composition as the ring dyke is ascended. A large gap appears between An_{51} (at 342m) and An_{16} (at 455m) in which no plagioclase compositions plot. This is a sudden jump in composition in a very short area and would not be expected if plagioclase variation in the body was caused by fractionation of a single magma.

If the rocks in the ring dyke had evolved from one parental magma by fractional crystallization one would expect a continuous variation of plagioclase composition, ranging from calcic in the gabbros to sodic in the granophyres. High anorthite plagioclases are seen in the gabbros, and low anorthite in the granophyres, but no intermediate plagioclase compositions (An 16-45) exist. This hiatus implies an abrupt change in solidification, of such a size that only a change in magma composition of the can account for.

8.5 Opaque Minerals (table 8.6)

Opaques comprise of intergrowths of magnetite and ilmenite. Compositions of the two phases are uniform throughout the body, although their proportions vary

8.6 Dioritic Enclaves in the Granophyres

The mineralogy of these inclusions was described in section 7.6. Mineral analyses from an enclave in GM48 are shown in table 8.7.

Table 8.7. Mineral analyses from the mafic enclave in GM48

	Feldspar	Feldspar	Amphibole	Amphibole	Clinopyroxene	Chlorite	Magnetite	Ilmenite
SiO2	71.1	66.5	47.5	48.2	49.8	27.7	0.5	0.6
TiO2	0.1	0.1	1.4	1.0	0.2	0.3	1.0	50.7
Al2O3	20.5	19.7	4.9	4.2	0.3	16.3	0.2	0.0
FeO total	0.6	0.6	17.5	16.7	18.8	32.1	88.2	43.1
MnO	0.0	0.0	0.3	0.4	0.6	0.4	0.2	3.6
MgO	0.0	0.0	11.9	12.3	8.5	9.6	0.0	0.0
CaO	0.2	0.7	10.2	9.8	18.9	0.1	0.1	0.0
Na2O	7.4	11.4	2.4	1.6	0.3	0.0	0.0	0.0
K2O	0.2	0.2	0.8	0.6	0.0	0.2	0.0	0.0
Total	100.2	99.1	95.9	94.9	97.4	86.7	90.1	98.0
%An	3	5						
%Ab	94	93						
%Or	3	2						

Plagioclase feldspar in the enclave is albitic (An 6-10) and occurs as unzoned, stubby laths. If this is a primary mineral composition then it should have crystallized from an acidic magma; however the enclave studied is actually of ferrodioritic composition (see chapter 9). Plagioclase crystallizing from a dioritic magma should have an intermediate composition. This is not the case here and suggests one of two things:-

1) The plagioclase grew at a low temperature, possibly induced by the chilling effect that the granophyric magma would have had on the bleb of dioritic magma. The textures in the enclaves suggest that quenching has taken place.

2) Deuteric alteration of the rocks has taken place. Widespread albitization of the rocks on Mull has taken place (Walker, 1971) and this could also be responsible for plagioclase alteration. The feldspar in the granophyre surrounding the enclaves is extensively altered and ferromagnesian minerals are heavily altered (see below) to hornblende and chlorite, so it seems reasonable to assume that this process has affected the plagioclase in the enclaves. Therefore evidence exists for both of the above processes affecting the composition of the plagioclase seen in the enclaves.

Ferromagnesian minerals in the enclaves have undergone considerable alteration. Primary magmatic pyroxene is largely hydrated to chlorite and hornblende, with specks of magnetite. A pyroxene analysis from an enclave in GM48 was mentioned in section 8.3. In figure 8.02 the enclave pyroxene from sample GM48 plots as the most evolved composition. Assuming that the pyroxene composition has not been altered by a deuteric reaction (it is not altered to hornblende or chlorite so this seems to be a reasonable assumption) it lies on the most evolved (Fe-enriched) end of the trend described in section 8.3. This could indicate that the melt from which the enclave crystallized was the residue left after fractional crystallization of the parental magma.

Amphibole pseudomorphing clinopyroxene, is a green, calcic-hornblende. Its composition (see table 8.6) is similar to secondary amphibole compositions formed from hydrothermally altered augites in gabbros from Skye (Ferry, 1985), suggesting that the calcic hornblende is produced by a deuteric reaction. Oxide minerals in the enclaves are magnetite and intergrowths of ilmenite and magnetite.

8.7 Summary and Conclusions from mineral chemistry

The following points arise from the preceding sections:-

- Olivine is largely altered to serpentine, chlorite and magnetite. However fresh remnants are unzoned and have a mean composition of Fo 68.
- The parental magma for this olivine has a MgO/FeO ratio of 0.675 (Roeder and Emslie 1970). Sample MT 3 is the most suitable sample for a potential parental composition using MgO/FeO ratios and rock type as the main criteria.

- Most clinopyroxene in the granophyre is altered to hornblende, chlorite and magnetite.
- Clinopyroxene composition follows an evolutionary trend involving Fe-enrichment (increasing Fs and decreasing En) progressing from olivine gabbro, through quartz gabbros, to dioritic intermediate rocks. This may reflect the compositional evolution of the residual magma during crystallization of gabbros in the ring dyke. The most evolved pyroxene composition is found in the dioritic enclave examined in one of the granophyric samples. This enclave composition may represent the most evolved composition reached during basic magma evolution in the ring dyke.
- Plagioclase composition displays a bimodal distribution. Compositions in gabbros and dioritic intermediates range from An_{45} to An_{76}, while those in granophyres and acidic portions of the intermediate rocks range from An_2 to An_{16}. No plagioclase compositions fall in the range An_{16} to An_{45}. Plagioclase in the basic rocks has a minimum An content at 350 m and a maximum above and below this. In the granophyres An% decreases regularly with increasing altitude, indicating possible fractionation or magma zonation in this upper part of the body.

The pyroxenes analysed in this study are from gabbros or from the basic portions of intermediate rocks, plus one from a mafic enclave in the granophyres. Pyroxene in the olivine gabbros displays no compositional variation, while that from both quartz gabbro and intermediates show wide-ranges in values of En and Fs. The variation could be caused by evolution of the parental magma from which the pyroxenes crystallize, but the pattern is irregular. Instead of pyroxene composition steadily becoming more Fe-enriched as the host rock varies from olivine-gabbro through quartz-gabbros to more dioritic composition rocks, pyroxenes in quartz-gabbros, at quite high altitudes (CC6 and GM7), have the same composition as those in the olivine-gabbros. Also, pyroxenes in the intermediate rocks do not follow a steady evolutionary trend.

One way of explaining the lack of systematic variation is to consider the effect on pyroxene composition that a surrounding magma with a different composition may have. Such a situation could be envisaged if a second injection into the ring dyke caused a more acidic magma to percolate into (or mix with) a partially consolidated crystal-liquid mush. If the previously intruded magma had consolidated then the new magma would only intrude into it in cooling joints. However if the gabbroic magma was still a crystal-liquid mush then the new acidic magma may be capable of infiltrating into the mush.

If this happened we could envisage a mixing zone in which the silicic magma has, in some places, infiltrated the dioritic mush. Where the gabbro was more consolidated, acidic magma would form veins within the gabbro's cooling joints. In other areas, where the mush was relatively unconsolidated, lumps of the mush may be surrounded by silicic magma. This latter case would be preserved in rocks as rounded areas (as fracture was not brittle) of basic/intermediate rock within a network of granophyre. The proportions of

granophyre:diorite would vary depending upon how far away we go from the initial contact between acidic magma and the pre-existing gabbroic/dioritic mush. Close to this contact the granophyre:diorite ratio will be highest but further from it this ratio will fall as granophyre has further to penetrate into the underlying mush, and the mush will be more consolidated.

If silicic magma is percolating through a dioritic crystal-liquid mush it will have an effect on the mineral compositions in the mush if they are in contact with it. The amount of contact that a pyroxene or plagioclase crystal in the mush has with the percolating silicic magma depends upon the position of the crystal in a patch of the dioritic mush. If a crystal from a solid solution series is at the edge of a dioritic patch, its composition is more likely to be adjusted by re-equilibration with the silicic magma than a crystal in the centre of a dioritic patch which has no direct contact with the silicic magma, and will therefore retain its primary magmatic composition. Therefore it is possible to have a range of plagioclase or pyroxene compositions within a rock sample in a given zone.

The mineral compositions that are in equilibrium with more evolved melt compositions are more iron-rich clinopyroxenes (higher Fs and lower En), and more albitic plagioclase (decrease in An). Figure 8.02 indicates that the most evolved clinopyroxene compositions appear in intermediate rocks, although some clinopyroxene compositions in intermediate rocks have the same compositions as those in olivine gabbros. The intermediate rocks with the higher Fs values in clinopyroxene are therefore probably from basic portions close to granophyric material, while the least evolved clinopyroxene samples in intermediate rocks are probably from the centres of the basic portions of the samples, where silicic magma has not been able to affect the composition.

For plagioclase compositions (see figure 8.03 a and b) the range and variation within samples of intermediate rocks could be explained by the same process. Infiltration of silicic magma can cause alteration of crystals that it comes into contact with. This produces a drop in the % An in crystals in dioritic portions of the rocks that would have originally had >75% An. In the same samples some crystals will have been unaffected by this infiltration and will retain their primary magmatic composition, because they are buffered by being in the centre of dioritic portions of rock and therefore have no contact with the silicic magma.

This explanation agrees with the field relations and petrography of the samples, and also explain the blotchy textures seen in the dioritic and granodioritic intermediate rocks in the Glen More ring dyke.

CHAPTER 9. Whole rock major and trace element geochemistry

9.1 Introduction

Major and trace element geochemical analysis, using XRF techniques, has been carried out on 28 whole rock samples representing all the major rock groups from Cruach Choireadail and other localities within the ring dyke. Whole-rock major and trace element analysis was carried out using an automated Phillips X-ray flourescence spectrometer. Major element concentrations were determined on fused Lithium borate-lanthanum oxide glass beads, and trace-element levels were determined from pressed powder pellets. Details of sample preparation techniques are given by Norrish and Hutton (1969). Precision estimates are displayed below, expressed as wt % for major elements and PPM for trace elements. Precision estimates are for the Phillips XRF spectrometer at St. Andrews

Element	Standard Deviation	Element	Standard Deviation
SiO_2	0.177	Sr	1.8
TiO_2	0.006	Rb	1.4
Al_2O_3	0.042	Th	4.2
Fe_2O_3	0.114	Pb	0.8
MnO	0.0003	Zn	0.7
MgO	0.035	Cu	0.8
CaO	0.01	Ni	1.2
Na_2O	0.099	Cr	1.4
K_2O	0.013	V	0.9
P_2O_5	0.011	Ba	8.0
Nb	2.0	Hf	0.41
Zr	6.9	Ce	2.0
Y	1.5	La	1.3

Analytical data, along with calculated CIPW normative mineral proportions, are presented in table 9.1, and are discussed in the following section. Possible petrogenetic schemes that may account for the patterns produced by these data are outlined in chapter 10 and are discussed in chapter 11

Whole-rock geochemistry from previous authors work (Bor, Bailey et al, and Koomans and Kuenen) is presented. When these data are plotted alongside the XRF data from this study they do not plot within the region of the well-defined trends described in the following sections and are therefore not used in geochemical modelling in chapter 11.

Major and trace element data from an analysis of a mafic microgranular enclave, extracted from the granophyre GM17, is also presented in table 9.1 and the geochemical plots in this chapter. The mafic enclave was extracted from the granopyric sample by taking slices through the rock and then grinding the granophyre away to produce slabs of the enclave. This particular enclave measures 5cm x 3cm x 2cm (see plate 6.05 in chapter 6) and therefore provided enough material, when powdered, for analysis. An attempt was made to extract smaller enclaves (<1cm) for analysis but the problems of grinding away all the surrounding granophyre, and still having enough material for reliable analysis proved

Table 9.1a. Major and Trace element analysis of Gabbros in the Glen More ring dyke

Data only accurate to 1 d.p.

GABBROS	GM 7	GM 13	CC 6	GM 9	GM 8	GM 52	GM 55	MT 3	GM 32	LS 1	CG 1	GM 4
altitude (m)	385	130	442	430	415	210	195	344	352	200	137	287
weight % oxide												
SiO2	46.96	47.92	47.93	48.31	48.36	48.63	48.67	48.92	49.41	49.61	52.24	53.45
TiO2	2.44	1.16	0.45	48.31	1.04	1.34	1.57	1.5	1.14	1.62	2.29	2.13
Al2O3	12.67	16.36	18.18	13.93	14.7	15.71	16.56	15.52	16.23	14.8	12.84	13.29
FeO total	18.73	11.99	9.04	12.57	11.77	12.09	13.64	12.79	10.73	13.55	15.85	14.62
MnO	0.22	0.17	0.14	0.18	0.17	0.16	0.15	0.19	0.16	0.19	0.27	0.23
MgO	5.43	8.1	7.9	7.01	7.49	6.02	4.34	5.36	6.02	5.03	3.34	3.53
CaO	10.02	10.44	10.74	12.02	12.08	10.62	10.26	10.38	10.95	10.1	7.06	7.24
Na2O	2.56	2.95	2.05	2.49	2.42	2.78	3.11	2.85	3.09	3.12	3.43	3.84
K2O	0.77	0.57	0.46	0.23	0.23	0.63	1.1	0.72	1.19	0.73	1.47	1.73
P2O5	0.16	0.16	0.06	0.13	0.1	0.17	0.12	0.2	0.16	0.19	0.45	0.34
total	99.96	100.72	96.95	101.19	100.07	98.15	99.52	98.43	100.59	98.94	99.24	101.32
Trace element ppm												
Nb	2	3	1	1	1	3	2	4	12	3	8	9
Zr	126	87	44	74	61	112	87	129	340	125	250	267
Y	34	26	12	28	25	30	26	34	71	35	71	61
Sr	263	341	305	202	203	299	353	319	287	315	241	274
U	0	0	0	0	0	0	0	0	2	0	2	0
Rb	22	14	16	7	6	15	30	20	74	18	44	48
Th	2	2	0	1	1	2	2	0	7	3	6	6
Pb	3	1	4	3	1	2	0	3	9	0	3	8
Ga	27	21	24	20	20	26	28	27	25	25	27	25
Zn	95	70	128	28	75	73	68	89	78	77	135	106
Ni	25	149	130	63	77	64	42	51	7	33	13	6
Ce	28	14	9	8	8	27	29	29	86	33	64	60
Sc	55	36	33	59	53	48	48	46	24	44	33	34
V	682	234	85	325	282	292	512	331	143	356	215	300
Ba	351	290	194	162	134	324	319	346	794	301	486	640
La	11	10	6	4	4	12	8	17	38	11	23	28
Normative Minerals												
Quartz	3.01	0	0.61	0	0	1.63	0	2.61	0	3.03	8.96	6.75
Orthoclase	4.55	3.37	2.72	1.36	1.36	3.72	6.5	4.25	7.03	4.31	8.69	10.22
Albite	21.65	24.95	17.34	21.06	20.47	23.51	26.3	24.1	26.13	26.39	29.01	32.48
Anorthite	20.81	29.72	39.05	26.16	28.57	28.53	27.98	27.43	26.9	24.23	15.3	13.92
Corundum	0	0	0	0	0	0	0	0	0	0	0	0
Diopside % Wo	11.63	8.78	5.77	13.62	12.81	9.62	9.24	9.5	11.01	10.28	7	8.25
Diopside % En	7.31	6.38	4.26	8.08	7.87	6.69	4.54	6.41	7.81	6.75	4.02	5.02
Diopside % Fs	3.6	1.59	0.96	4.85	4.22	2.13	4.53	2.37	2.23	2.81	2.67	2.78
Hypersthene % En	6.21	4.98	15.41	8.01	7.78	8.29	2.75	6.94	3.51	5.77	4.29	3.77
Hypersthene %Fs	3.06	1.24	3.48	4.81	4.17	2.63	2.74	2.57	1	2.41	2.85	2.09
Olivine % Forsterite	0	6.17	0	0.96	2.1	0	2.47	0	2.57	0	0	0
Olivine % Fayalite	0	1.69	0	0.63	1.24	0	2.71	0	0.81	0	0	0
Magnetite	12.09	7.71	5.86	5.03	4.71	7.79	5.51	8.24	6.95	8.68	10.18	9.55
Ilmenite	4.63	2.2	0.85	2.34	1.98	2.54	2.98	2.85	2.17	3.08	4.35	4.05
Apatite	0.38	0.38	0.14	0.31	0.24	0.4	0.28	0.47	0.38	0.45	1.07	0.81
H2O	1	0.9	2.6	3.1	1.7	1.6	1	0.6	1.5	0.4	0.4	0
Total	99.93	100.06	99.06	100.3	99.22	99.09	99.53	98.33	100	98.59	98.79	100.59
TTDI	29.21	28.32	20.67	22.42	21.83	28.87	32.8	30.97	33.16	33.73	46.65	49.49

Table 9.1 b. Major and Trace Element analysis of Granophyric and Intermediate petrologies (Data only accurate to 1d.p.)

	Sample Number	GM 31	CC 4	GM 38	GM 26	GM 48	GM 51	CC 10	GM 47	GM 12	CG 5	GM 18	GM 17	GM 19	GM 15	MT 1	CG 4	Mafic Enclave	H344 (Bell 1983)	MS201X (Bell 1983)
	altitude (m)	455	342	270	335	420	420	518	148	485	222	550	535	630	530	290	305			
weight % oxide	SiO2	56.64	56.84	58.82	59.52	60.05	60.47	60.69	61.36	63.57	67.37	67.49	67.9	68.23	68.47	68.82	71.72	56.9	52.93	58.37
	TiO2	1.75	1.68	1.59	1.47	1.34	1.34	1.37	1.4	1.13	0.67	0.82	0.81	0.76	0.79	0.48	0.52	1.63	2.35	1.69
	Al2O3	13.73	13.6	13.69	13.69	13.51	13.43	14.06	14.04	13.65	13.45	13.45	13.55	13.83	13.6	13.53	13.27	13.1	12.69	13.27
	FeO total	11.87	11.63	10.95	10.43	9.33	9.26	9.34	9.48	7.22	5.69	5.18	5.07	4.77	5.02	5.27	3.36	12.45	14.24	12.56
	MnO	0.21	0.2	0.19	0.21	0.18	0.18	0.19	0.2	0.17	0.15	0.14	0.14	0.14	0.14	0.09	0.1	0.3	0.3	0.23
	MgO	2.59	2.05	1.91	1.55	1.96	1.78	1.49	1.59	1.46	0.31	0.87	0.81	0.71	0.76	0.07	0.35	2.72	2.02	1.61
	CaO	5.61	4.79	4.88	4.04	3.27	3.68	3.8	3.87	3.37	1.64	2.22	2.13	1.91	2	0.35	0.55	4.96	6.23	5.72
	Na2O	4.03	4.19	4.1	4.89	3.91	4.08	4.34	4.49	4.11	4.15	4.33	4.53	4.3	4.52	4.4	4.16	5.22	3.43	3.72
	K2O	2.78	2.44	2.78	2.87	3.67	3.26	3.04	3.19	3.59	4.3	4.05	4.15	4.34	4.15	4.65	4.36	1.06	1.91	1.8
	P2O5	0.58	0.46	0.52	0.59	0.47	0.49	0.6	0.61	0.4	0.12	0.24	0.24	0.21	0.23	0.04	0.08	0.35	1.18	0.37
	total	100.66	97.88	99.73	100.07	99.48	97.97	98.92	100.52	99.57	97.85	99.59	100.5	100.61	100.3	97.7	98.47	100.87	97.28	99.34
Trace element ppm	Nb	16	14	3	16	16	16	17	16	17	21	20	21	22	21	23	21	18	21	21
	Zr	428	363	107	434	387	403	414	383	454	539	475	518	532	540	556	533	282	406	278
	Y	84	779	29	91	77	77	82	77	77	90	80	81	73	85	105	80	94	79	64
	Sr	236	244	336	223	198	195	237	226	191	109	123	127	112	126	57	72	166	260	188
	U	1	0	1	2	1	1	1	1	0	0	2	3	3	2	0	2	0	na	na
	Rb	97	74	29	86	126	94	92	84	118	144	133	135	140	140	139	148	37	39	61
	Th	11	7	2	10	7	10	9	11	12	13	13	13	14	13	12	12	13	2	7
	Pb	12	6	0	9	10	12	10	13	11	14	15	11	18	13	10	15	110	na	na
	Ga	23	27	22	24	25	25	26	23	23	24	20	20	20	22	26	22	24	na	na
	Zn	118	124	55	134	119	102	125	112	99	100	97	77	85	92	110	80	203	139	107
	Ni	8	13	65	9	18	16	16	8	11	19	5	9	9	9	20	16	16	6	10
	Ce	117	96	23	102	111	107	112	116	115	135	113	115	109	124	151	122	118	93	na
	Sc	16	24	45	12	22	21	17	22	16	9	9	7	6	10	3	4	27	na	na
	V	47	97	241	30	89	86	44	99	58	5	22	17	11	13	0	7	256	84	209
	Ba	949	783	402	980	994	855	926	903	903	1065	1078	1065	1062	1079	1194	1075	566	1646	537
	La	52	43	11	52	52	53	53	54	53	65	56	54	50	59	91	65	75	42	na
Normative Minerals	Quartz	9.26	11.41	12.95	9.85	10.72	11.51	14.8	14.01	16.96	20.37	20.87	20.23	20.04	19.73	22.99	28.39			
	Orthoclase	16.42	14.42	16.42	16.96	21.68	19.26	17.96	18.85	21.21	25.41	23.93	24.52	25.64	24.52	27.47	25.76			
	Albite	34.08	35.44	34.68	41.36	33.07	34.51	36.71	37.97	34.76	35.1	36.62	38.31	36.37	38.23	37.21	35.18			
	Anorthite	11.17	11.1	10.75	6.94	8.48	8.71	9.91	8.74	8.2	5.38	5.31	4.39	5.63	4.57	1.47	2.21			
	Corundum	c	c	c	c	c	c	c	c	c	c	0	c	c	0	0.72	0.9			
	Diopside % Wo	5.37	4.03	4.2	3.86	1.95	2.65	2.09	2.7	2.46	0.82	1.73	1.92	1.03	1.61	0	0			
	Diopside % En	3.13	2.19	2.25	1.46	0.62	0.79	1.09	1.43	1.11	0.09	0.7	0.78	0.26	0.42	0	0			
	Diopside % Fs	1.98	1.7	1.81	2.47	1.39	1.96	0.94	1.19	1.34	0.82	1.04	1.16	0.83	1.28	0	0			
	Hypersthene % En	3.31	2.91	2.5	2.4	4.26	3.64	2.61	2.53	2.52	0.68	1.47	1.24	1.51	1.48	0.17	0.87			
	Hypersthene %Fs	2.1	2.26	2.02	4.05	9.51	8.99	2.24	2.12	3.04	6.23	2.18	1.84	4.81	4.54	3.78	2.17			
	Olivine % Forsterite	0	0	0	0	0	0	0	0	0	0	0	0	0	0	0	0			
	Olivine % Fayalite	0	0	0	0	0	0	0	0	0	0	0	0	0	0	0	0			
	Magnetite	7.63	7.52	7.02	5.07	1.54	1.45	6.05	6.09	3.51	0.87	2.48	2.52	0.72	0.84	2.52	1.58			
	Ilmenite	3.32	3.19	3.02	2.79	2.54	2.54	2.6	2.66	2.15	1.27	1.56	1.54	1.44	1.5	0.91	0.99			
	Apatite	1.38	1.09	1.23	1.4	1.11	1.16	1.42	1.45	0.95	0.28	0.57	0.57	0.5	0.55	0.09	0.19			
	H2O	1.2	1.8	0.3	0.8	1.8	1.2	1.4	0.3	0.9	2.2	0.8	1.2	1.4	0.6	2	1.4			
	Total	100.36	99.07	99.15	99.39	98.69	98.38	99.84	100.04	99.11	99.53	99.25	100.2	100.18	99.85	99.35	99.65			
	TTDI	59.77	61.27	64.05	68.16	65.48	65.28	69.46	70.83	72.93	80.88	81.42	83.06	82.05	82.48	87.68	89.34			

prohibitive. The grain size of these smaller enclaves proved to be too big to allow broad-beamed probe analysis, another potential method of analysing the chemistry of the enclaves. Only one enclave large enough to be analysed could therefore be extracted and analysed using XRF analysis. Another method of analysing the chemistry of the enclaves could be to extract them and fuse them into glass. Polished thin sections of these glasses could then be analysed by EPMA. This method could be used in further work to shed more light on the origin and petrogenesis of the enclaves.

The chemical analysis of this enclave has similarities with both the ferrodiorite from the Marscoite suite on Skye, and the basic inclusions from the Loch Ba felsite on Mull (Sparks, 1988, and Bell 1983). Analyses of both of these (H344 and MS201X respectively) are shown in table 9.1b.

9.2 Major element geochemistry

9.2.1 Introduction

Major element variation diagrams are presented and important features outlined in the following section. The data are compared with those from previous studies of the Glen More ring dyke.

9.2.2 Major Element variation diagrams

Figure 9.1 shows the major element oxides plotted against MgO wt %. The following points can be noted from examination of these graphs:-

- TiO_2, MnO, FeO tot., P_2O_5, and, to a lesser degree, CaO display similar trends, involving a steady but slight increase in concentration from 8 to 4 wt % MgO, and a more rapid and more coherent decrease in concentration from 4 to 0 wt % MgO. The pattern of points is discontinuous at 4 wt % MgO where there is a sharp jump in the concentrations of TiO_2 and P_2O_5 between samples GM 55 and GM 4.
- SiO_2, Na_2O and K_2O show an increase with decreasing MgO. SiO_2 remains constant in the gabbros and then increases with decreasing MgO. Na_2O and K_2O concentrations also increase with decreasing MgO. Na_2O shows a broad scatter of data points about the general trends.
- Al_2O_3 has scattered values in the gabbros with lower values in the acidic rocks. Al_2O_3 concentration remains relatively constant within the acidic group of rocks.
- The variation diagrams show a bimodal distribution of data. Data points plot on two, seemingly-unconnected, coherent trends; granophyres and intermediate rocks plot on one trend, while gabbros plot on another. A split between the two groups appears at roughly 4 wt % MgO and 50 wt % SiO_2. From this chemical data, combined with the petrographic

Figure 9.1. Major element variation diagrams for rocks analysed from the Glen More ring dyke. (■ = gabbros, □ = intermediates, △ = granophyres, • = dioritic enclave)

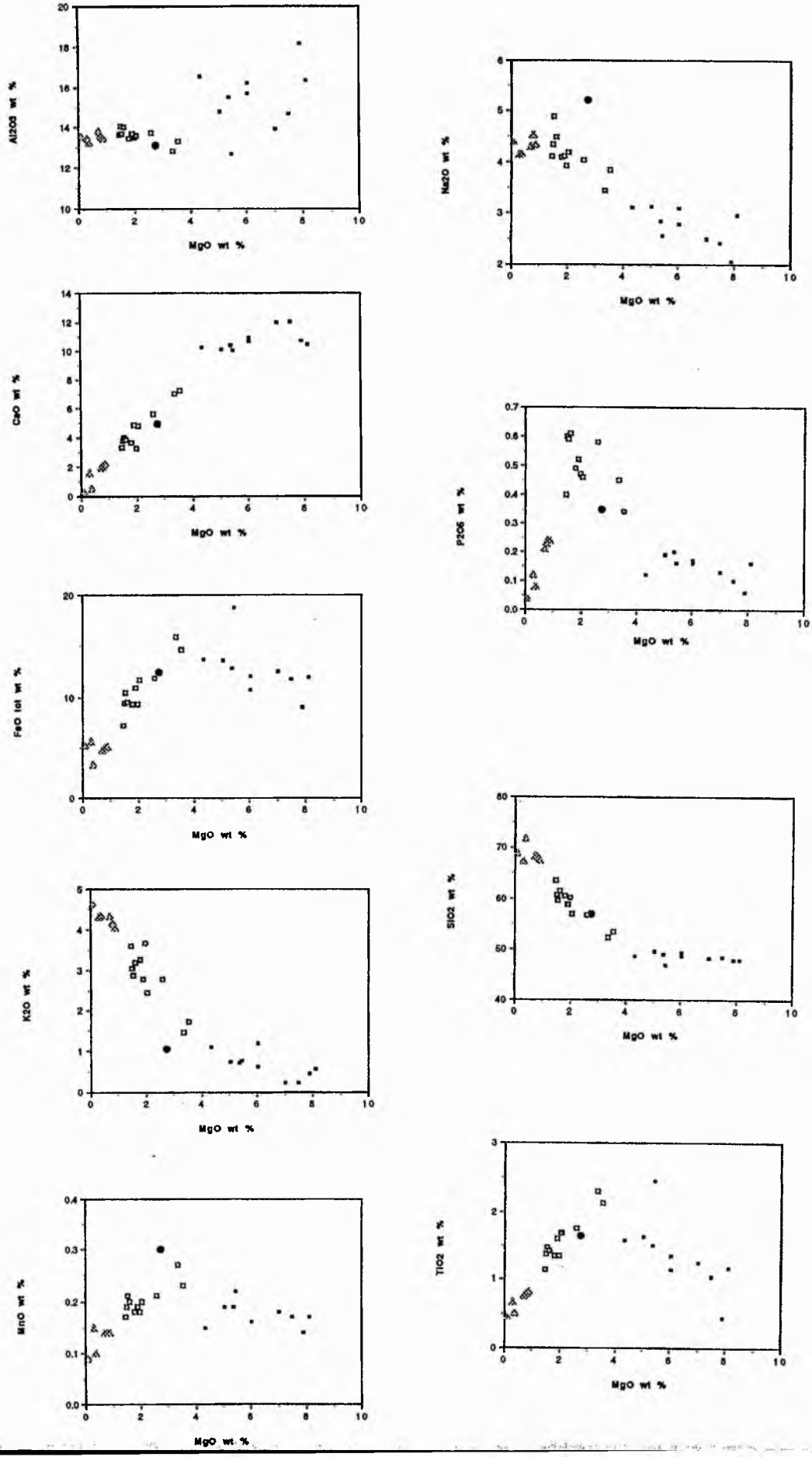

evidence, we can say that the petrogenesis of basic and acid-intermediate rocks is apparently distinct. This conflicts with Bailey's petrogenetic model.

A division, at 4 wt % MgO, between the two groups is made on petrographic grounds, with intermediate rocks being grouped with granophyres in one group and the gabbros comprising the other group. These two groups are now discussed separately.

9.2.2.1 Gabbroic rocks on the variation diagrams

The gabbros analysed in this study are displayed in figure 9.2. The rocks range from 4 to 8 wt% MgO, have a very narrow SiO_2 range (47.9-49.6 wt % SiO_2), and, with increasingly evolved compositions, show an increase in TiO_2, P_2O_5, Na_2O, MnO, K_2O, and FeO total. CaO and SiO_2 concentrations remain essentially constant across this range, while Al_2O_3 displays a wide variation in concentration between samples. One sample, GM7, has anomalously-high concentrations of TiO_2 and iron and low SiO_2 and Al_2O_3 concentrations. This is due to a high concentration of oxide minerals in the rock.

The graphs in figure 9.3 (MgO vs Plag % and Al_2O_3) relate chemical variations to modal mineral variations (see data in table 7.1). It can be seen that Al_2O_3 variation in the gabbros is closely related to plagioclase concentration. Gabbros with high Al_2O_3 concentrations are the ones with high modal proportions of plagioclase.

The lack of variation in SiO_2 content in the gabbros is problematic. It remains essentially constant throughout the gabbros, while modal mineral proportions vary greatly (plagioclase ranges from 34 to 62 %, and clinopyroxene varies from 9.5 to 26 %). An explanation for this could be found if both major mineral phases (plagioclase and pyroxene) had similar SiO_2 contents. This is not the case however; SiO_2 in pyroxene is typically 50% in this study, while that in plagioclase varies from 53 to 55 % (see tables 8.4 and 8.5).

Other factors must therefore be examined to account for the constant SiO_2 values throughout the gabbros. If the amount of quartz in the gabbros is considered (figure 9.4. MgO vs Px and Qz) then we can see that quartz appears in small amounts (upto 5%) on the rocks with highest pyroxene content, while it is absent in the rocks with highest plagioclase:pyroxene ratios. This could account for the constant SiO_2 values in the gabbros. For example when the plagioclase:pyroxene ratio falls, decreasing the overall SiO_2 content in the combined mass of these two minerals, quartz is present to top up the total SiO_2 content in the gabbros. The quartz is present usually as shapeless specks interstitially between cumulate plagioclase and pyroxene, in the patches of acidic mesostasis.

Figure 9.2. Gabbroic rocks on MgO vs FeO (tot) variation diagram

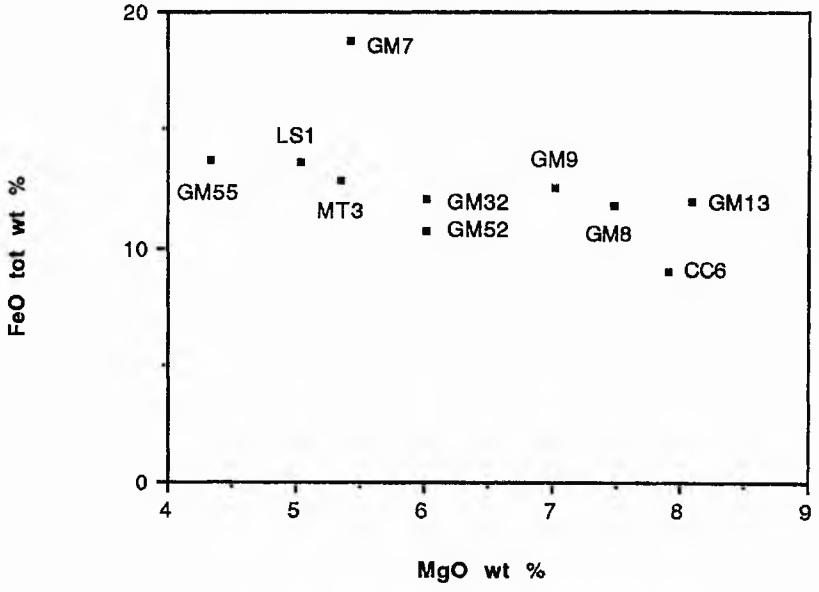

Figure 9.3. Graph showing the correlation between modal plagioclase content and wt % Al2O3 in the Glen More gabbros

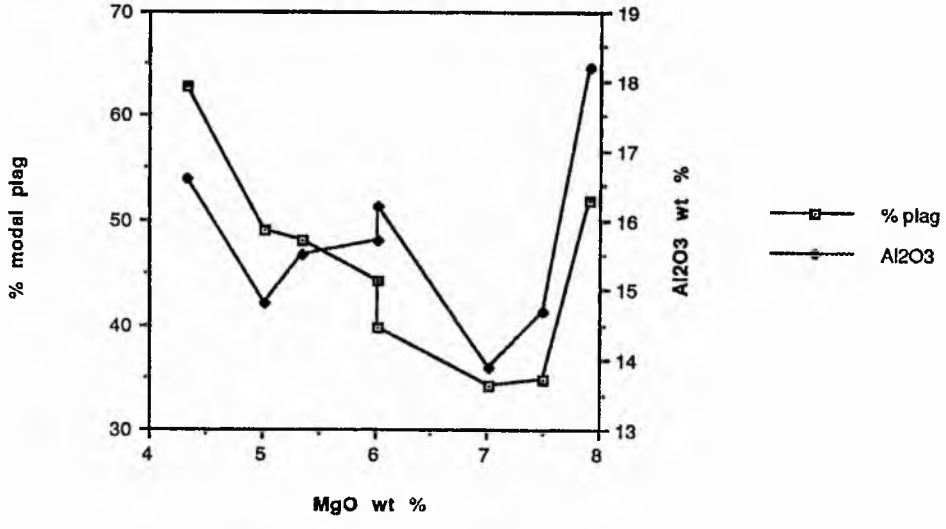

Figure 9.4. Modal clinopyroxene and quartz variation in the Glen More gabbros

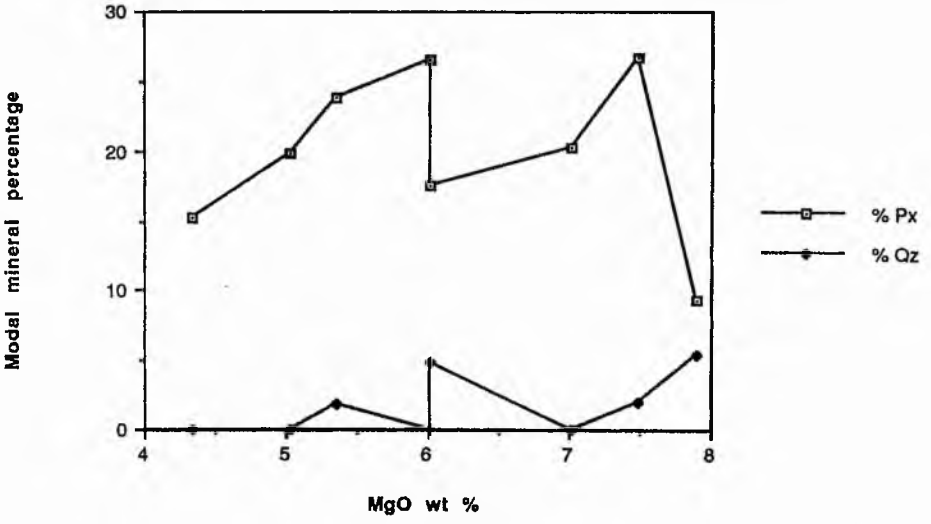

The enrichment of FeO total, TiO_2 and, to a lesser extent, MnO with decreasing basicity indicates removal of plagioclase-rich mineral assemblages from the parental magma, leaving the residual magma with increased concentrations of mafic elements. Forsteritic olivine crystallization takes more Mg^{2+} out of the magma than Fe^{2+}, resulting in iron enrichment with decreasing MgO. The AFM diagram in figure 9.5 clearly shows this iron-enrichment trend in the gabbros. The most iron-enriched samples on this trend are CG1 and GM4, both dioritic samples. The iron-enrichment trend in the gabbros shows considerable latteral spread. This could be accounted for by variation in plagioclase:pyroxene ratios in these rocks. Most rocks with a low ratio (GM8 and GM9) lie closer to the F-M axis, while those with a high plagioclase:pyroxene ratio plot closer to the A-apex. The appearance of CC6 (with a very high Plag:px ratio) is influenced greatly by the amount of chlorite in the sample which gives the rock a higher Fe-Mg value but is not reflected in the mineral content of the sample.

This evidence, combined with the plagioclase-rich nature of the gabbros, indicates that the variation in gabbroic whole rock compositions is consistent with crystallization of olivine, calcic-plagioclase, and diopsidic augite from a basic parental magma. The variations in modal abundances and the textures seen and described in chapter 7 point towards cumulate-style crystallization of minerals in the following order of importance; Calcic plagioclase, calcic augite, olivine, Fe-Ti oxides. The potential of this process is discussed further in chapters 10, 11 and 12.

9.2.2.2 Silicic and intermediate rocks on major-element variation diagrams

This group of whole rock compositions contains the specimens illustrated in figure 9.6. Rock types include quartz dolerites, dioritic and granodioritic intermediates, and granophyre, with a range of MgO from 0.1 to 3.5 wt%. With decreasing MgO, there is an increase in SiO_2, Na_2O, and K_2O and a decrease in TiO_2, P_2O_5, MnO, CaO, and FeO total. The most silicic sample is a granophyre, MT1, from the Ishriff ring-dyke which is the body immediately inside the Glen More ring dyke, and is also associated with the Beinn Chaisgidle igneous centre.

Variation diagrams show that these rocks plot along tightly-constrained straight lines. Table 9.2 shows R^2 (best fit) values for variation plots of rocks in this group.

Figure 9.5. AFM diagram for all rocks analysed. Note the iron-enrichment trend in the gabbros, and the straight-line trend between dioritic samples (CG1 and GM4) and granophyres (CG4). (Red = olivine gabbro, brown = quartz gabbro, green = intermediate rocks, yellow = granophyres.)

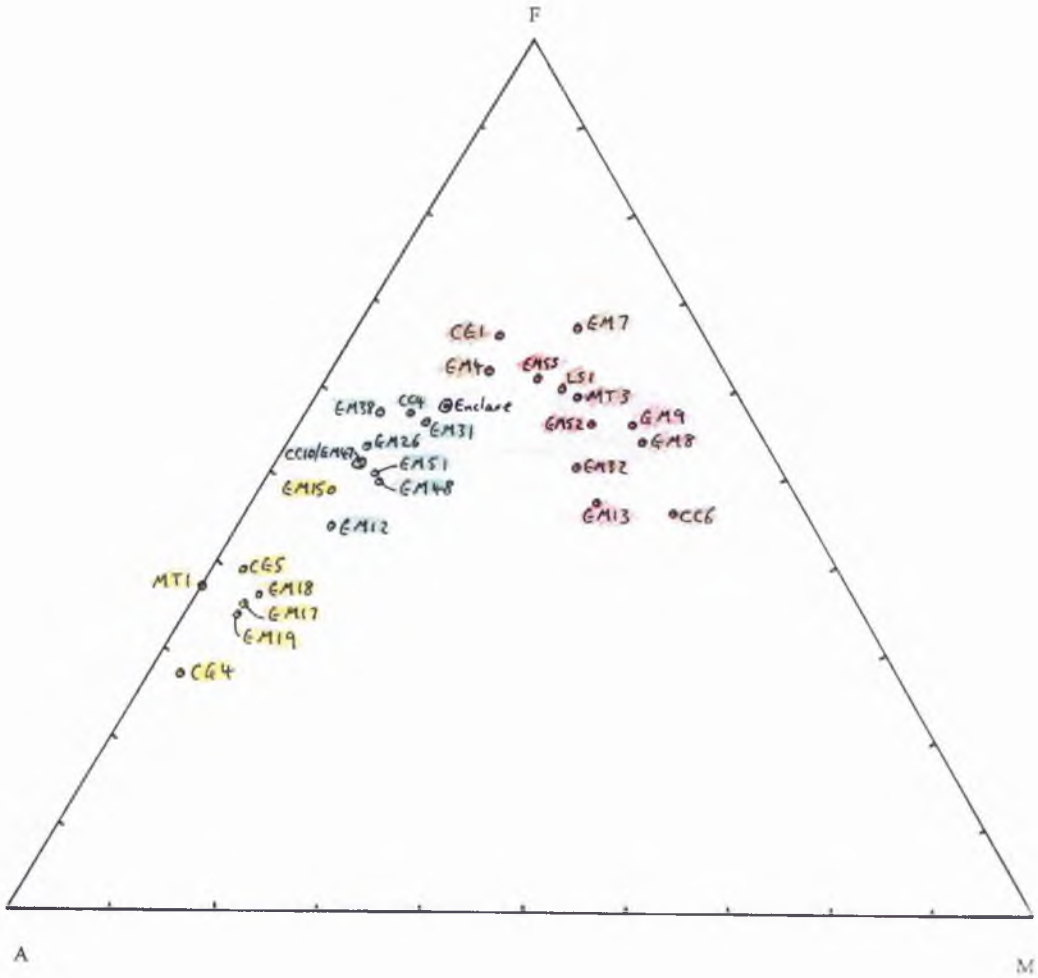

Figure 9.6. MgO and CaO variation in acidic and intermediate rocks.

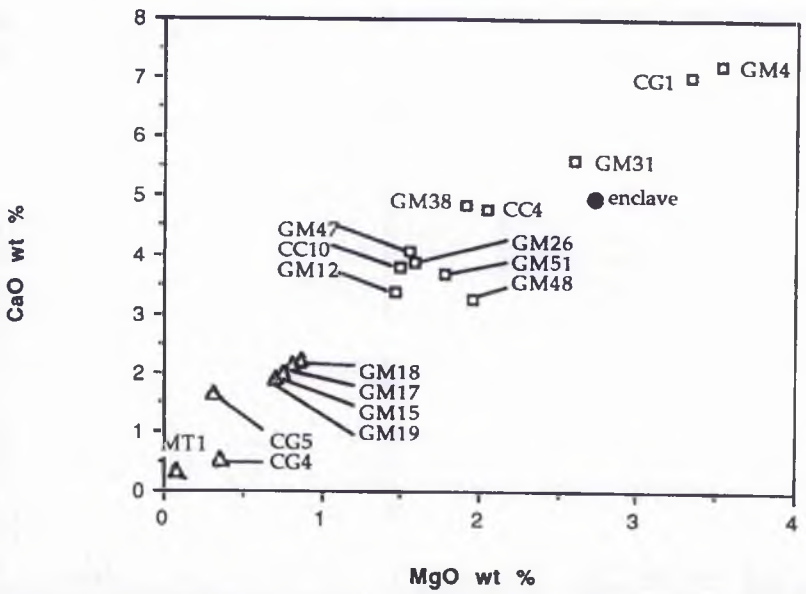

Table 9.2

Plot	R^2
MgO vsTiO_2	0.954
vsSiO_2	0.912
vs P_2O_5	0.425
vs FeO tot	0.905
vs CaO	0.955
vs MnO	0.843
vs Al_2O_3	0.076
vs Na_2O	0.385
vs K_2O	0.808

R^2 values close to 1, indicate a better fit of straight line. These data indicate that excellent straight line fits are seen for most of the major element oxide plots in this acidic-intermediate group. Poor fits include P_2O_5, Na_2O and Al_2O_3. Sodium and phosphorus deviation is possibly caused by deuteric alteration as both elements are relatively mobile. Aluminium varies as a result of variation in the proportions of plagioclase in the gabbros (see figure 9.3).

These variation patterns could be explained by either of the following processes:-

- Fractional crystallization of minerals from a ferro-dioritic parent magma with a composition close to that of GM4. If this were the case then we can imagine the rocks in the lower parts of the intermediate-acidic sequence to be dioritic cumulates, with residual liquids becoming more and more evolved and finally producing a granophyric magma at the top of the body.
- Mixing of a silicic and an intermediate magma to produce whole rock compositions that fall on a straight mixing line.

Field relations (the upper part of the granophyre is surrounded in a chilled jacket of granophyre, indicating that granophyric magma was intruded into the ring dyke fissure and not formed by in situ differentiation) and petrography (the blotchy heterogeneous character of the intermediate rocks) indicate that the second of the above possibilities is the most likely.

9.2.3 Major Element variations with altitude

9.2.3.1 Introduction

Earlier work on the Glen More ring dyke (Bailey et al, 1924 and Koomans and Kuenen, 1938) placed much emphasis on changes in petrography (particularly specific gravity) with

altitude. This information was used to propose the fractional crystallization model (Bailey et al 1924, Koomans and Kuenen 1938). The data presented in figure 9.7 (a-j) show major-element variations with altitude for rocks in this study. These data are discussed in the following section.

9.2.3.2 Data and discussion

On close inspection of figure 9.7 data above 450m are seen to fall approximately on straight line trends. These lines pick out the following trends:-

1) P_2O_5, MgO, FeO total, TiO_2, CaO and MnO decrease with increasing altitude.
2) Na_2O, K_2O and SiO_2 increase with altitude.
3) Al_2O_3 remains constant with increasing altitude.

On first inspection the samples from below 450m appear to follow no well defined patterns, but when their rock types are considered a certain degree of order can be made out of the apparently random distribution of data. The data can be split into two groups, one containing the gabbros, and the other containing the granophyres, with the intermediate samples falling into both groups. The gabbros are found upto 450m and the granophyres down to 220m, while intermediate rock types are seen from 140m to 530m. These data show that rock type is not strictly a function of altitude within the Glen More ring dyke. This contradicts the findings of Koomans and Kuenen (1938) who emphasized the smooth, uphill progression from gabbros to granophyres in the body, and used this to propose *in situ* crystal-liquid fractionation as the petrogenetic mechanism responsible for the distribution of rock types in the body.

9.2.4 Previous major element geochemistry.

9.2.4.1 Introduction.

Whole-rock, wet chemical analyses by Bailey *et al* (1924), Koomans and Kuenen (1938), and by Bor (1951) are the only previous chemical data available of rocks from the Glen More ring dyke. They were presented by Bor (1951) and by Marshall (1984) and are displayed in figure 6.05 in chapter 6. When plotted alongside the data from the current study (figure 9.8), previous whole-rock geochemical data frequently fail to fit closely with the trends outlined in section 9.2.3. Due to these discrepancies these data have not been considered in this study.

9.2.5 Major Element ratios (TiO_2/P_2O_5 vs FeOtot/MgO)

Bell (1983) reports that the TiO_2/P_2O_5 ratio of ferrodiorite (H344) from the Marscoite suite on Skye could only be produced by 95% fractional crystallization of a primitive tholeiitic basalt (Wager and Vincent, 1962. Wager, 1960). This ratio for the mafic microgranular enclave from GM17 in this study places it on the same fractionation trend as the Skye

Figure 9.7. Plots of major element concentrations against altitude for Glen More ring dyke samples. Note the split of data into two groups below 450m, with gabbros plotting as a distinct group. (Yellow = granophyre, green = intermediate, brown = quartz gabbros, red = olivine gabbro)

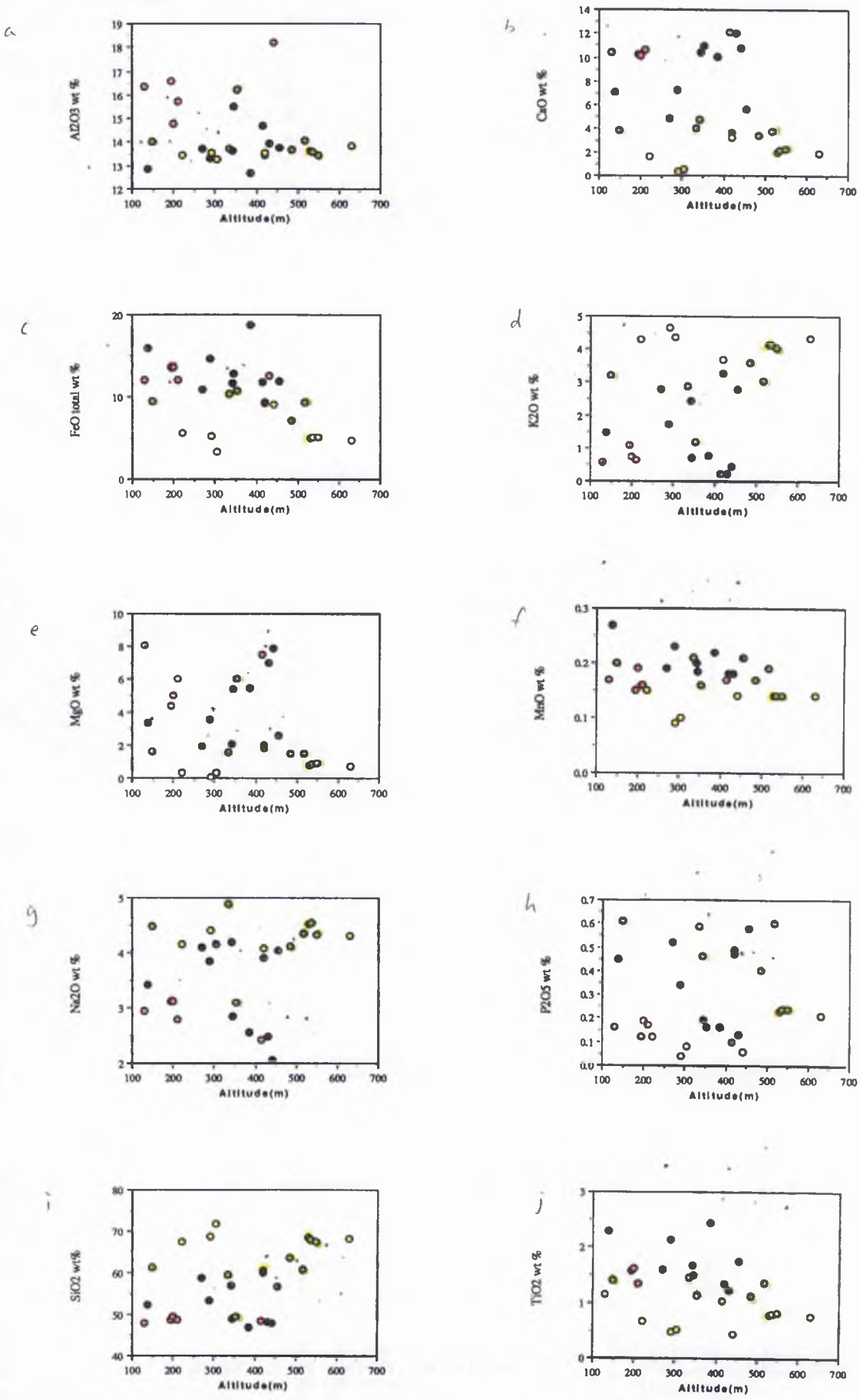

Figure 9.8. Variation diagrams containing data from this study and from Bor (1951). Note that in some plots (K_2O, SiO_2, CaO) the previous geochemical data reinforce the trends described in this study, while in others the data display a wider spread. (· = data from this study, ◆= data from Bor).

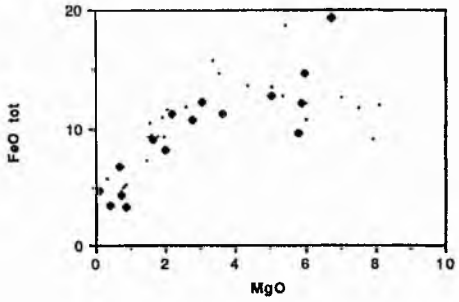

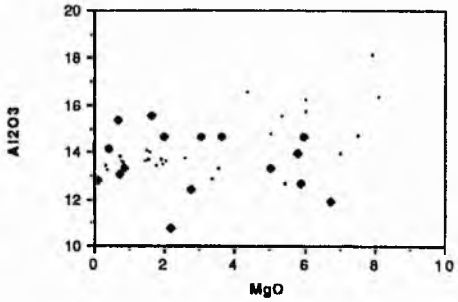

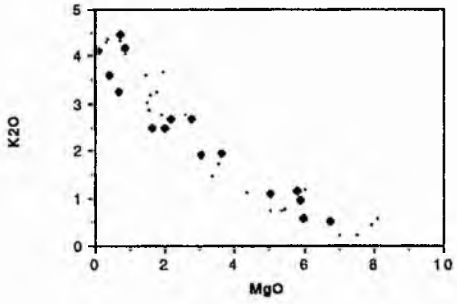

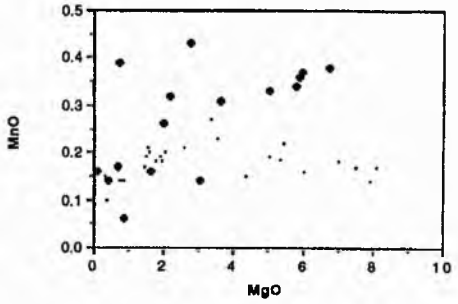

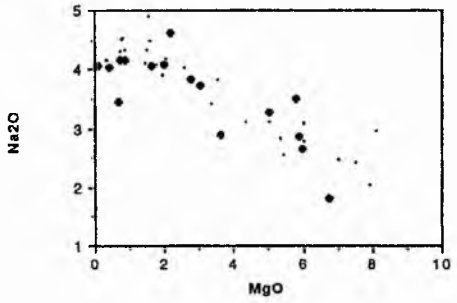

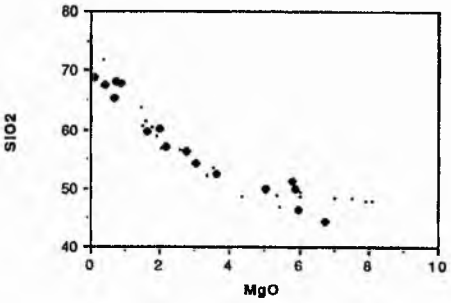

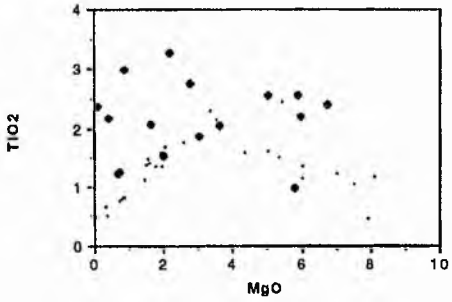

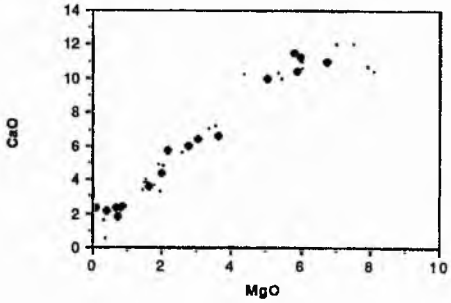

ferrodiorite (see figure 9.9 a). This position indicates that the mafic enclave composition could be derived by a lesser degree of fractional crystallization of a similar basaltic parental magma.

When plotted on a similar graph (figure 9.9 b), the rocks from Glen More produce a similar pattern to those from Skye. The composition of a mafic inclusion from the Loch Ba ring dyke (MS201X) is also very similar to that of the Glen More mafic enclave. The inclusions in the Loch Ba ring dyke are believed by Sparks (1988) to be from a zoned magma chamber. If the granophyre in the Glen More ring dyke evolved in a layered magma chamber, then this is also a possible origin of the enclaves and for the vertical compositional evolution in the granophyre. On the other hand the enclaves could also be the product of *in situ* crystal-liquid fractionation in the ring dyke fissure with the dioritic composition representing the residual magma composition following crystallization of basic rocks in the lower parts of the ring dyke. This residue could then have been mixed with a later intrusion of granophyric magma.

9.3 Trace Element Geochemistry

9.3.1 Introduction

In this section trace element concentrations from the 28 analysed rocks (see table 9.1) are displayed graphically against MgO wt %, against altitude, and as ratio-ratio and ratio-MgO plots. Patterns formed by these data have similarities with those observed in major element variation diagrams.

9.3.2 Element-Element variation diagrams

Figure 9.10 shows trace element concentrations (in ppm) plotted against MgO. The plots can be split into two types, A and B. Type A is typified by MgO vs Zr and includes the incompatible elements Y, Ce, Nb, Th, La and possibly Rb and Ba. Type B is typified by MgO vs Sr and also includes the compatible elements Sc, Ni and V. The plot of MgO vs Zr (type A) displays two groups of data points with a few intermediate points. The basic rocks (> 4 wt % MgO) have low Zr values, decreasing with increasing MgO. Acidic and intermediate rocks plot on a straight line with Zr increasing as MgO decreases. Two points (GM4 and CG1) regularly fall in an intermediate position between these two groups of samples. while GM38 and GM32 often have anomolous positions.

The type B plot includes a group of basic rocks with high concentrations of compatible trace elements (Sr, Sc, Ni, V)and another group (the acidic and intermediate rocks) showing decreasing concentrations of these trace elements with decreasing MgO. Data points CG1 and GM4 fall in intermediate positions on both type A and type B plots.

Figure 9.9a. TiO_2/P_2O_5 vs FeO_{tot}/MgO plot for a suite of rocks from Marsco, Skye (Bell, 1983).

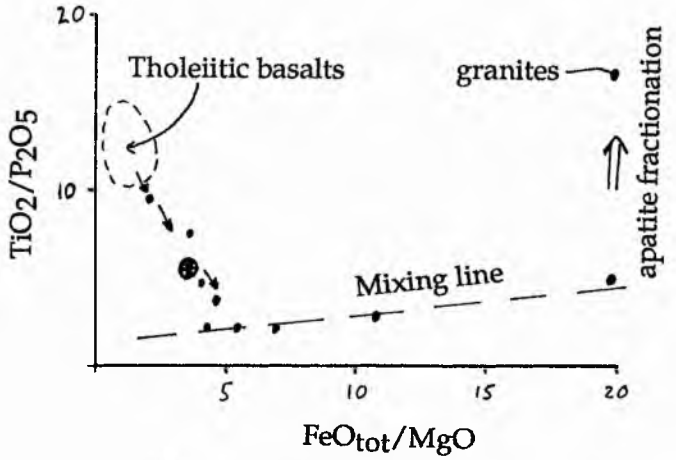

⊛ Dioritic enclave from Glen More granophyre

Figure 9.9b. TiO2/P2O5 vs FeO tot/MgO data for rocks from the Glen More ring dyke

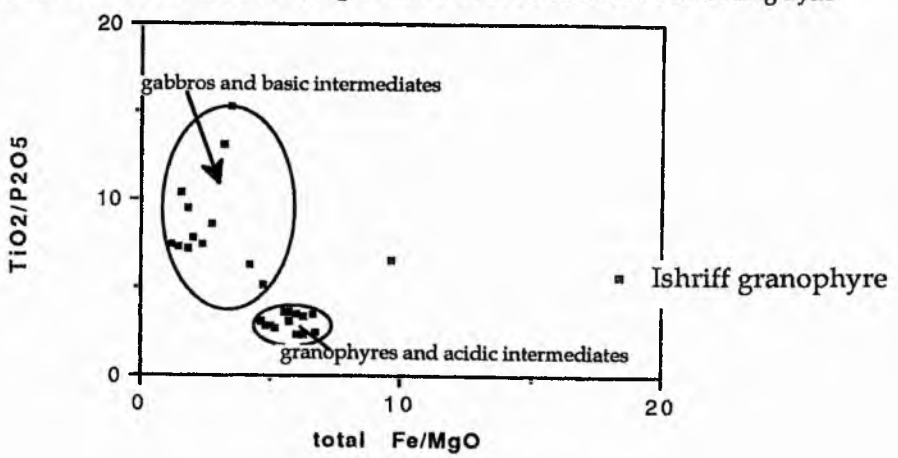

Figure 9.10. Trace element concentrations (ppm) plotted against MgO for rocks from the Glen More ring dyke. (■= gabbros, □= intermediates, △=granophyres, ● = ferrodioritic enclave).

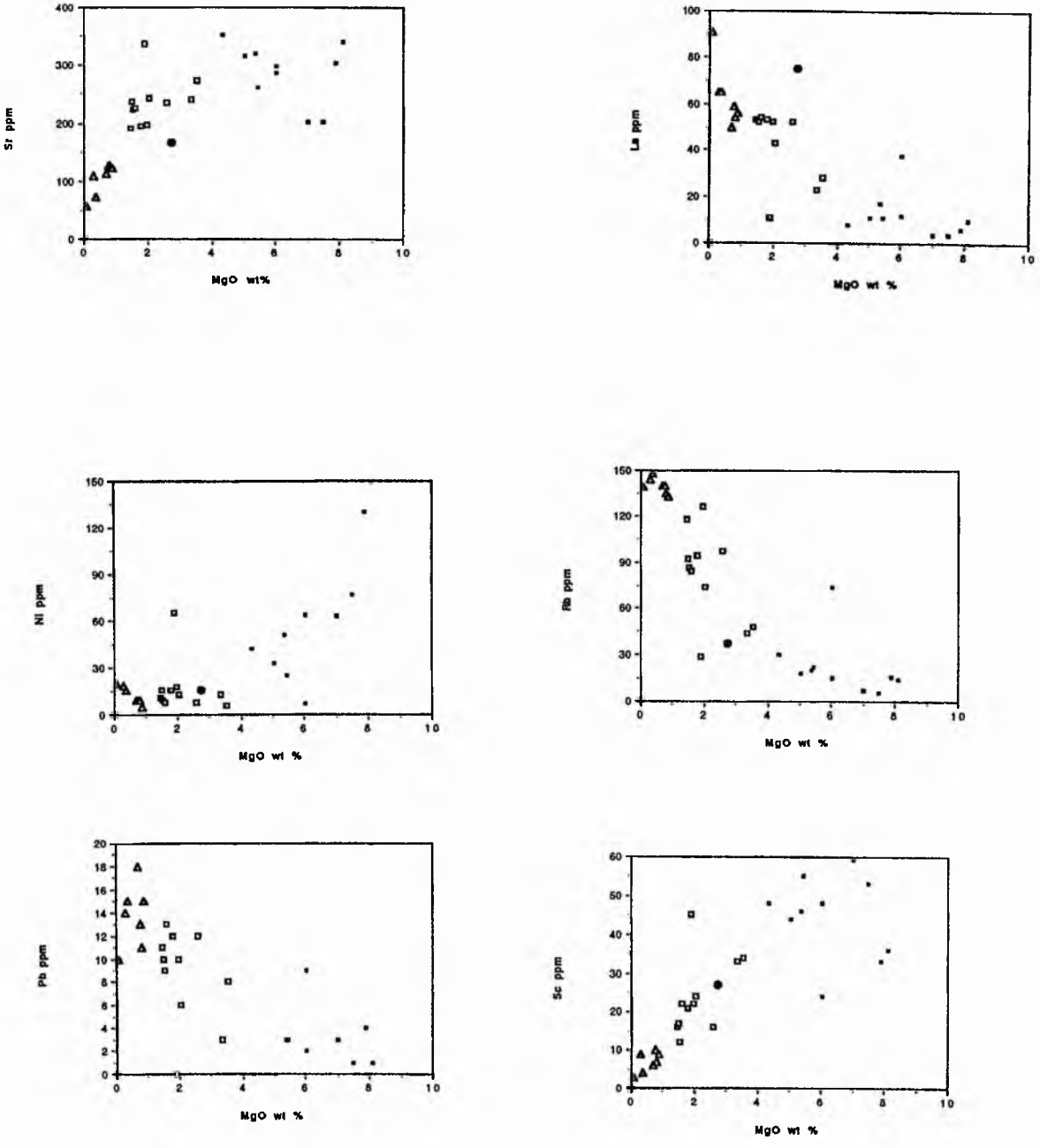

Figure 9.10. Trace element concentrations (ppm) plotted against MgO for rocks from the Glen More ring dyke. (■ = gabbros, □ = intermediates, Δ=granophyres, ● = ferrodioritic enclave).

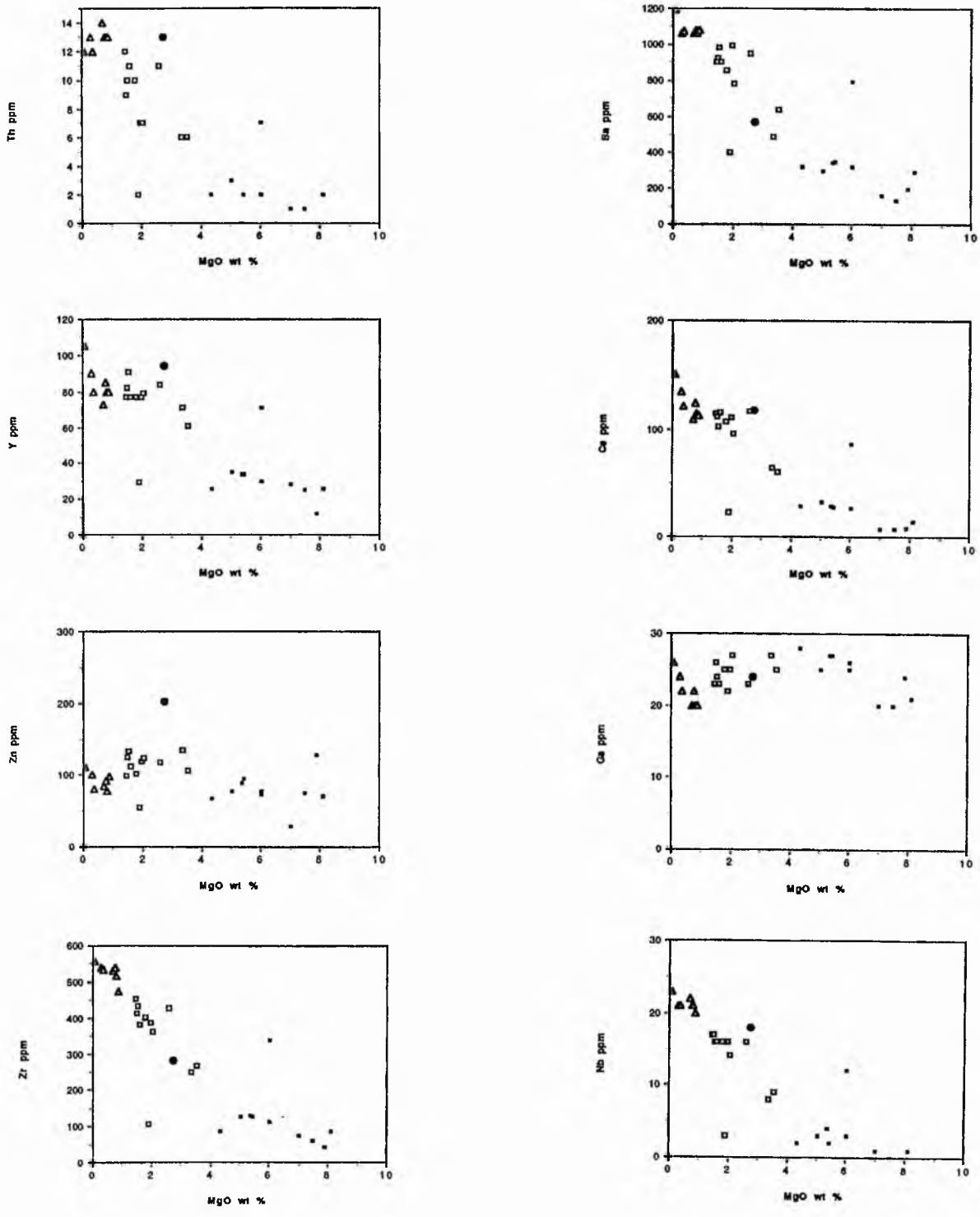

All trace element variation diagrams show distinctly different patterns for gabbros and intermediate-acidic rock samples. This distribution mirrors the spread of major element data described in section 9.2.

Two possible explanations are available for the high concentrations of incompatible elements in the silicic rocks. In partial melting of country rocks, the earliest melts will contain the highest concentrations of incompatible elements, decreasing with increasing proportions of melting. In contrast to this, during fractional crystallization the early residual liquids will show an increase in incompatible elements, increasing gradually with a greater degree of fractional crystallization (see figure 9.11).

The high concentrations of incompatible elements in the silicic magma could therefore be the product of a small portion of partial melting of crustal rocks, or a product of extensive fractional crystallization of a basaltic melt, or perhaps a combination of the two. If the rocks in the Glen More ring dyke were the product of *in situ* fractional crystallization of a basaltic parental magma there should be rocks of intermediate composition containing intermediate concentrations of incompatible elements. This is not the case. The silicic magma could, however, be the product of extensive fractional crystallization in a separate feeder body of magma and the intermediate magma has not been tapped. Fractional crystallization could have produced these silicic magmas at the top of a layered magma body which was then tapped by the Glen More ring fracture. In fact, recent work by Sparks (1988) on the Loch Ba ring dyke proposes that the rhyolitic magma which capped the underlying magma chamber was probably produced by extensive fractional crystallization.

9.3.3 Trace-Element ratio plots

9.3.3.1 Introduction

Plotting ratios of incompatible trace elements against a differentiation index or against another ratio is a technique used to identify groups of whole rock compositions connected by common petrogenetic processes (Winchester and Floyd, 1977). Such groups show spatial grouping on ratio-ratio or ratio-element plots. Zr, Nb, Ce, and La are used in these plots as they are relatively incompatible elements in mafic rocks. Ba and K are also used but, due to their high crustal abundance, their concentrations may have been affected by crustal contamination during magma evolution.

9.3.3.2 Data and Discussion

Figures in 9.12 (a-e) show the plots of selected trace element ratio data. If *in situ* fractional crystallization of a single magma body has produced the range of rock compositions seen

Figure 9.11. Schematic graph showing the behaviour of incompatible element concentrations with increasing degrees of melting and fractional crystallization.

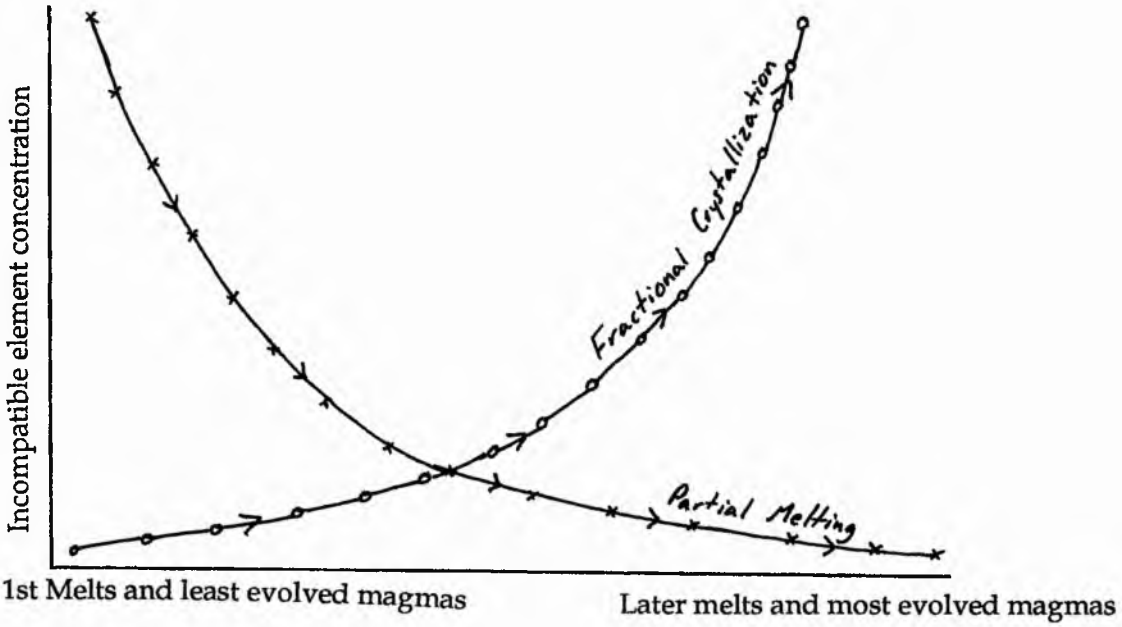

Figure 9.12a. MgO vs Ce/Nb for rocks from the Glen More ring dyke

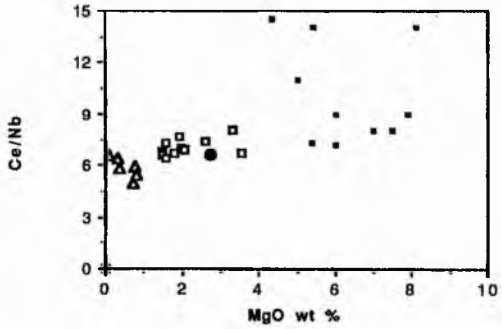

Figure 9.12b. MgO vs Zr/Nb for rocks from the Glen More ring dyke

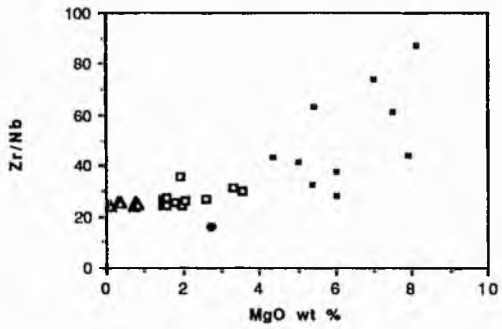

Figure 9.12c. Zr/Nb vs Ti/V for rocks from the Glen More ring dyke

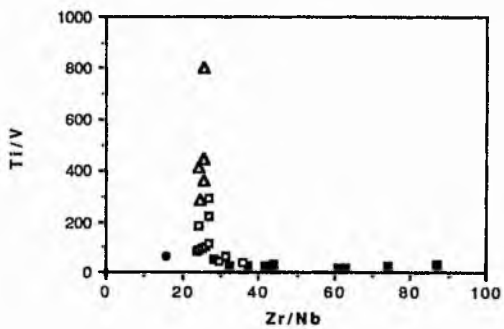

Figure 9.12d. Zr/Nb vs Ce/Nb for rocks from the Glen More ring dyke

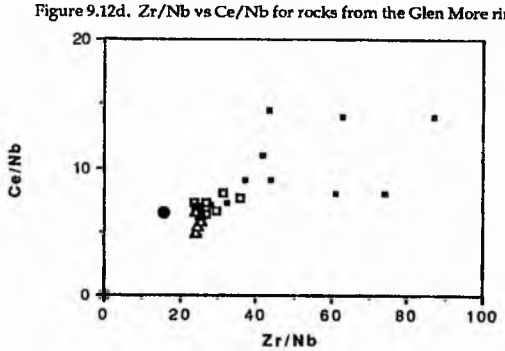

Figure 9.12e. MgO vs Ce/La for rocks from the Glen More ring dyke

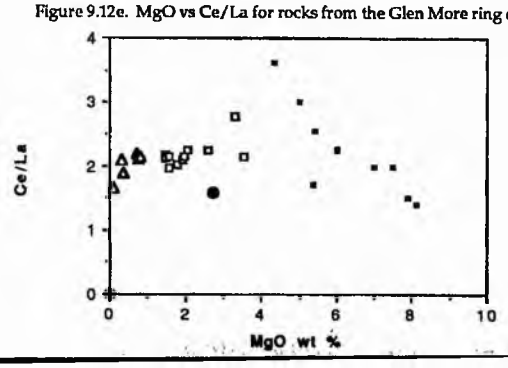

in the Glen More ring-dyke, and the rock compositions are those of former liquids, one would expect incompatible element ratios to remain essentially constant throughout the body. This feature is only seen within the acidic rock types (see plots of Ce/Nb vs MgO and Zr/Nb vs MgO). The scatter of ratio values within the gabbros implies that the gabbros examined do not represent a series of residual liquids left behind after the removal of gabbroic mineral assemblages. If this were the case we would expect the ratios to be constant throughout the gabbros. Other plots that display a similar pattern, and therefore infer that the acidic-intermediate rock sequence is linked by a common petrogenetic process, while the gabbros probably do not represent a series of residual liquid compositions, include Ce/Nb vs Zr/Nb and Ce/La vs MgO (see figures 9.12 d and e respectively).

The graphs in figure 9.12 show two separate groups of data points, with the rocks having distinctly different characteristics above and below 4 wt % MgO. As in previous plots, samples CG1 and GM4 often fall in positions which have some characteristics of both groups. In general the gabbros show a wider spread of ratio values, while the acidic and intermediate rocks tend to fall on more tightly constrained trends. The increase in the Ti/V ratio in the acidic rocks implies a decrease in V, or increase in Ti in the acidic rocks. This could be achieved if V was concentrated in the ferromagnesian minerals in the lower parts of the intermediate zone. Such ferromagnesian minerals are found largely in the basic portions of the intermediate rocks, and in the enclaves in the granophyres. The abundances of both of these decrease with increasing altitude, decreasing the amount of V in the rocks and resulting in an increase in the Ti/V ratio as the rocks get more acidic in the upper parts of the body.

9.3.3.3 Summary

Plots of trace-element ratios show patterns that re-inforce those seen on major and trace element variation diagrams, with two separate groups of data points being seen again. Acidic and intermediate rocks form a closely spaced group while the gabbros have a wider spread of data. This indicates two groups of rocks unconnected by a common petrogenetic process. Samples CG1 and GM4 again plot as intermediate compositions, with positions between the acidic and basic groups. Sample GM7 does not appear in anomalous positions in these ratio plots. Its anomalous major element characteristics are therefore probably due to modal concentrations of mafic minerals. The wide spread of ratio values in the gabbros may indicate that the whole-rock compositions are not those of a series of liquids residual from crystallization of gabbroic mineral assemblages from a basaltic magma.

Silicic magma, parental to the acidic rocks, could have been produced by either crustal melting and/or fractional crystallization in a feeder magma body. The blotchy appearance

of the intermediate rocks and their intermediate positions between diorite and granophyre on many of the variation diagrams point towards them being the product of mixing of granophyric and dioritic magmas.

9.3.4 Trace Element Variations with altitude

Trace element concentrations are plotted against altitude figure 9.13. At first glance there appears to be no pattern to the data in most of these plots. However, when the actual petrography of the samples is examined (see colour legend to the graphs) a division can be seen splitting the data points in the plots into two groups. In plots of altitude against Sc, V, Sr, and Ni all gabbros have high trace element concentrations while intermediates and granophyres have low concentrations of these trace elements. In all other plots (Zr, Y, Th, Rb, La, Ce, Pb, Nb and Ba) it is the gabbros that have low concentrations, while the intermediates and granophyres have higher abundances of these incompatible trace-elements. Within the intermediate-acidic group there is a general increase in incompatible trace-element concentration as the body is ascended, and a coinciding decrease in compatible elements over the same range. In the gabbros the opposite occurs and there is a decrease in incompatibles and an increase in compatible-element concentration as the body is ascended.

These data show that rock type (and therefore trace-element concentration) is not a function of altitude in the ring dyke - although gabbros are not found above 450m and granophyre is not seen below 200m. This contradicts the findings of Koomans and Kuenen (1938).

9.4 Incompatible Element Spiderdiagrams

9.4.1 Introduction

Spiderdiagrams provide on excellent method of displaying and analysing the behaviour of petrogenetically-important elements within suites of rocks (Thompson *et al* , 1984). In this section such data is presented and discussed for each of the rock types from the Glen More ring dyke. Possible links between the rock types are discussed, and possible sources of parental magmas are outlined. Normalizing data used are from Sun and McDonough (1989).

9.4.2 Data and Discussion

Figures 9.14 (a, b, c, and d) show selected element concentrations for gabbroic, intermediate, and acidic rocks. The elements used in the plots decrease in incompatibility from left to right (Thompson, 1982 and 1984).

Figure 9.13. Variation in trace element concentrations (ppm) with altitude. (red = olivine gabbro, brown = quartz gabbro, green = intermediate rocks, yellow = granophyres).

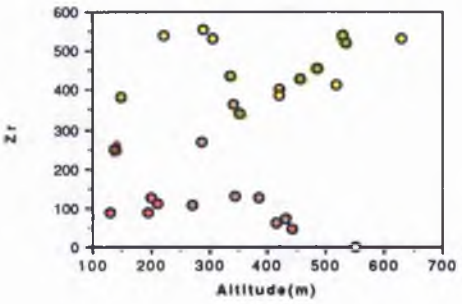

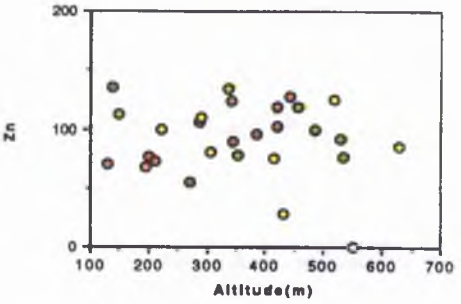

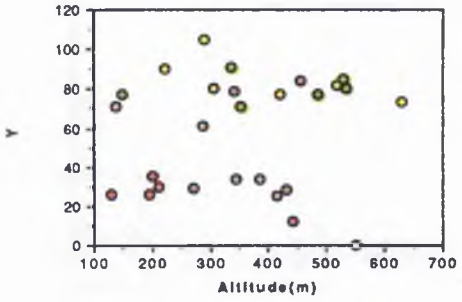

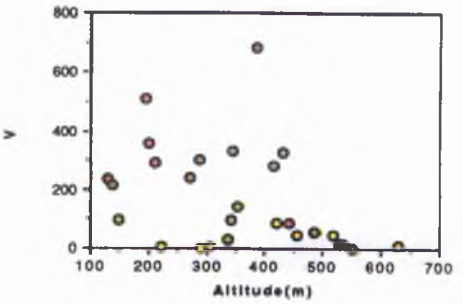

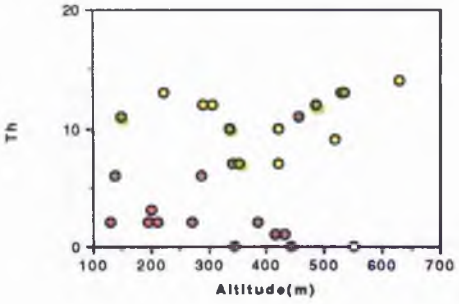

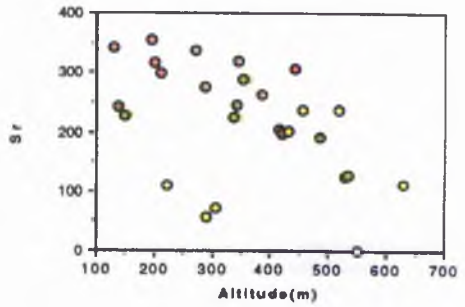

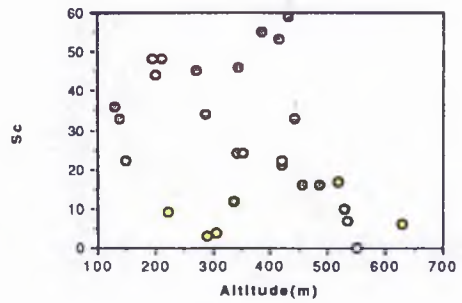

Figure 9.13. Variation in trace element concentrations (ppm) with altitude. (red = olivine gabbro, brown = quartz gabbro, green = intermediate rocks, yellow = granophyres).

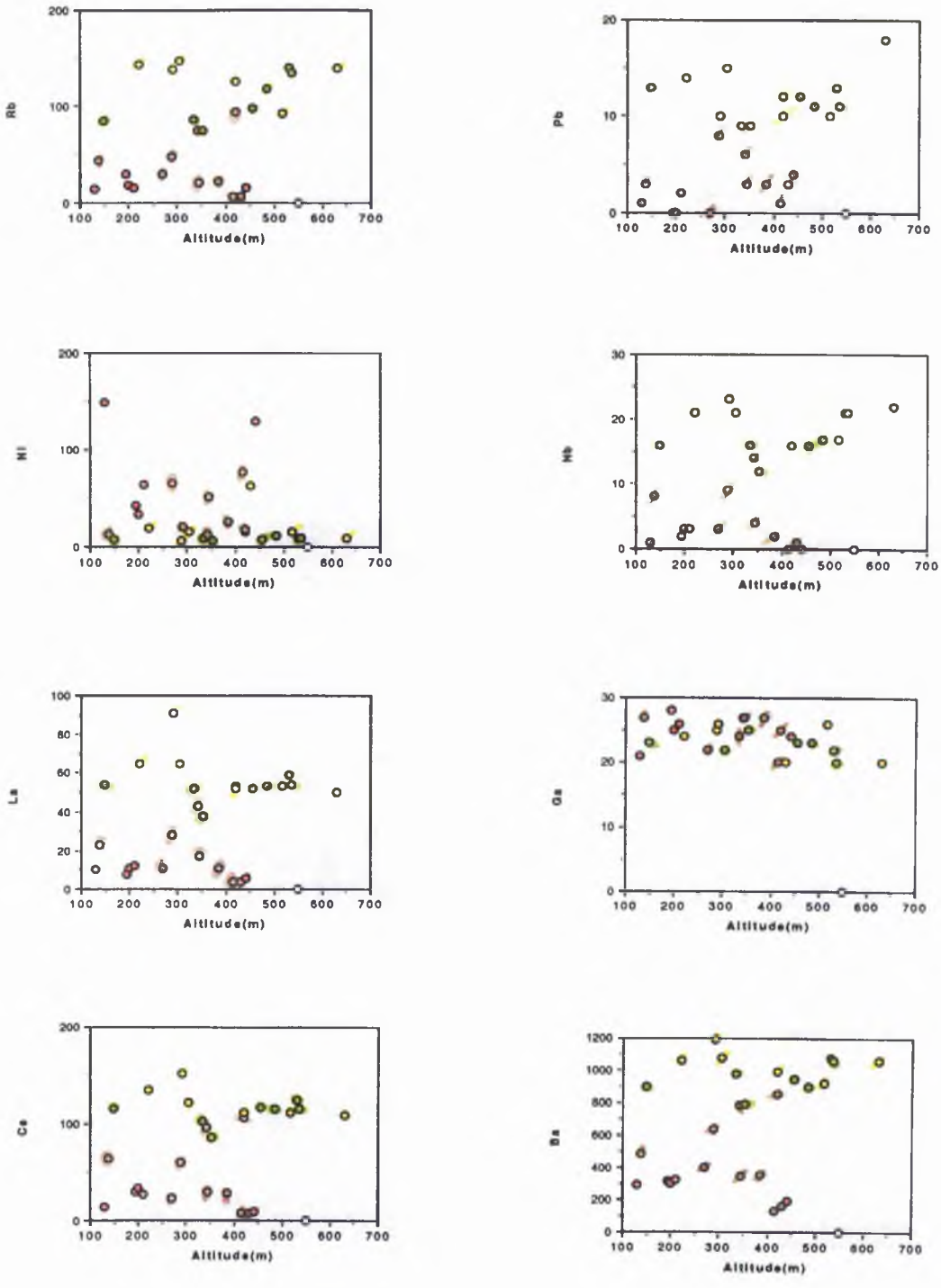

Figure 9.14A. Spiderdiagram for rocks representative of all types in the Glen More ring dyke.

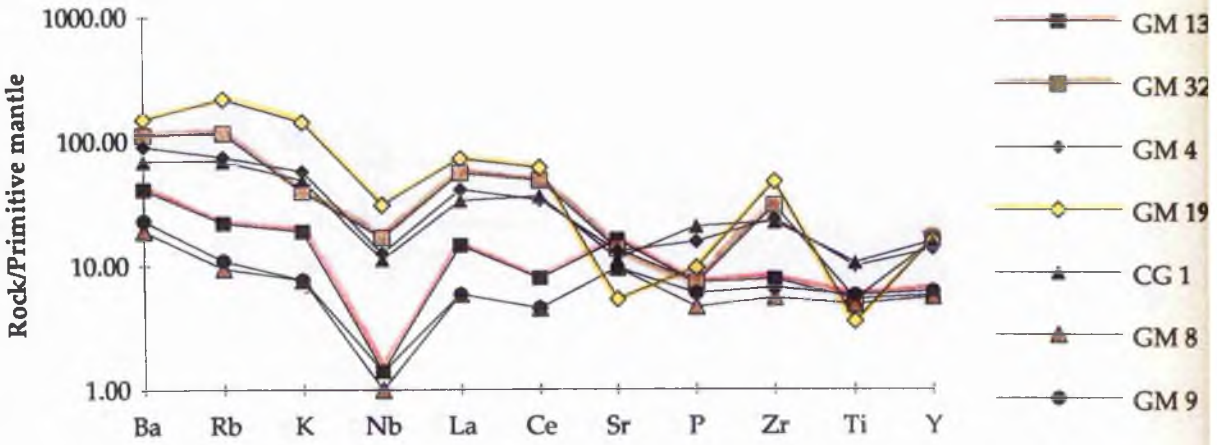

Figure 9.14B. Spiderdiagram of granophyres and acidic intermediates from the Glen More ring dyke

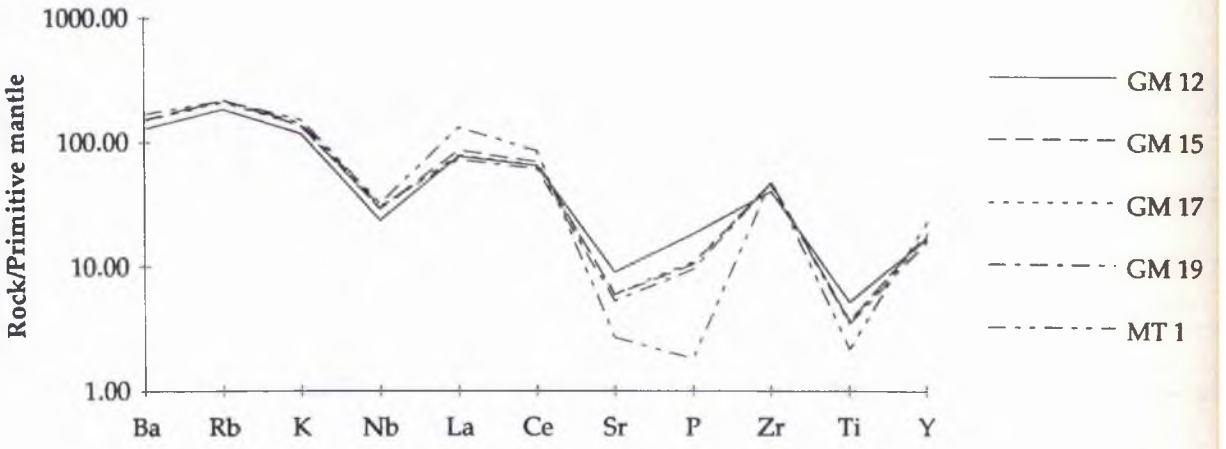

Figure 9.14C. Spiderdiagram showing the positions of intermediate rock types between granophyres and diorites

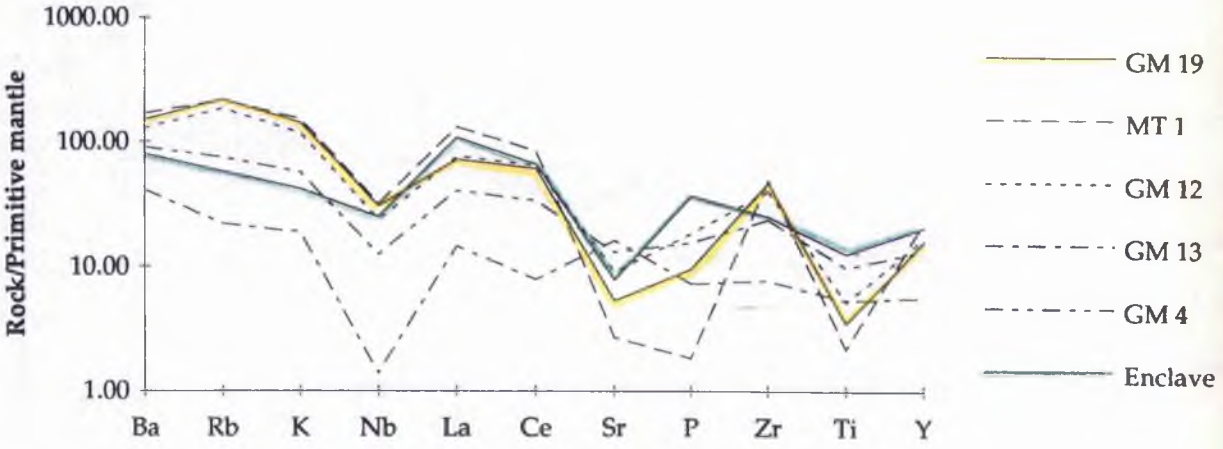

Figure 9.14D. Spiderdiagram showing the positions of dioritic samples between gabbros and granophyres

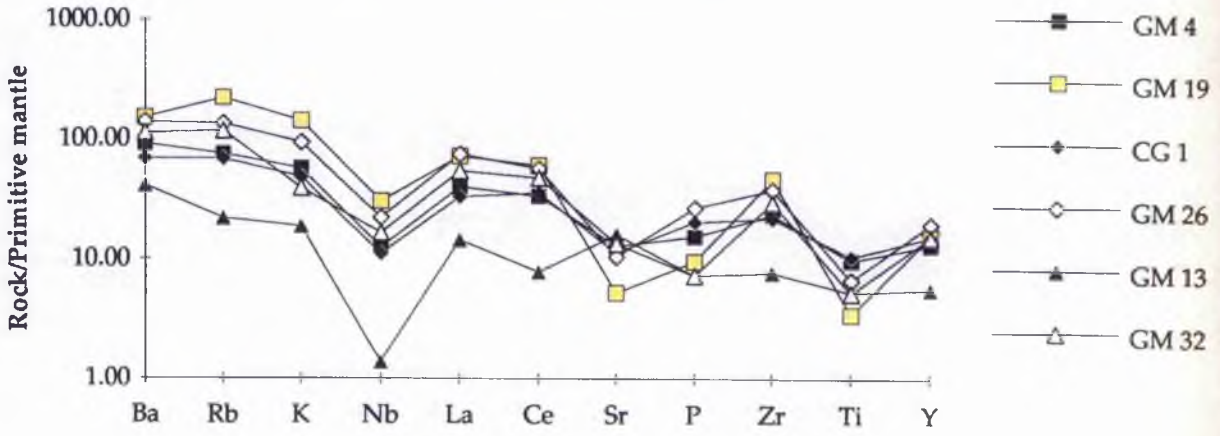

Figure 9.14a is a spiderdiagram for olivine gabbros, quartz gabbros and quartz dolerites and the granophyre GM19. The more evolved compositions on this diagram plot at increasing altitudes on the Y axis. The gabbros form a closely-spaced group of parallel lines. The parallelism of the gabbros suggests that they may be connected by fractional crystallization of a common parental magma (Thompson, 1982). A pronounced Nb dip seen in the gabbros is also present in GM4, GM32, and CG1, possibly linking these rocks to the gabbros by fractional crystallisation. Nb is incompatible in most rock-forming silicates except ilmenite and rutile and therefore becomes enriched during fractionation, possibly explaining the increasing amount of Nb in the more evolved gabbros.

All of the rocks examined are enriched in Ba, Rb, and K relative to the less incompatible elements. These elements have low concentrations in uncontaminated parental basaltic magmas but are found in higher concentrations in early partial melts formed by fusion of acidic crustal material (Thompson, 1982). Enrichment is therefore possibly due to contamination of a basaltic magma by partial fusion of material from the upper crust.

Samples GM4, CG1 and GM32 are the most evolved rocks with gabbroic characteristics. They have higher levels of incompatible elements than the rest of the gabbros and a relatively flat-lying trend on the right-hand side of the diagram. Dips in their trends occur at Sr, P and Ti, and are possibly due to low concentrations of plagioclase, apatite and ilmenite in these samples.

Sample GM4, texturally, has more affinity with the gabbros than with the blotchy intermediate rocks. It contains no textural signs of mixing with a granophyric magma. Spiderdiagram data rule out GM4 as a product of mixing GM32 and GM19 (figure 9.14a), as concentrations of Ba, Rb, Nb, La, Ce, and Zr are too low. This precludes GM32 as an end member of a mixing sequence in the acidic-intermediate rocks. It seems more likely that the intermediate end member of such a sequence has a composition close to CG1 or GM4 because these compositions have incompatible trace-element concentrations lower than all the intermediate rocks. Such a composition could be related to the gabbros by being the liquid residue left over after gabbro crystallization from an intermediate or basic parent magma in the ring dyke.

Figure 9.14b is a spiderdiagram for granophyres and the acidic intermediate rock types (GM12). Granophyres GM17, 15 and 19, and MT1 follow almost identical trends across the diagram. In contrast to the gabbros, these rocks show peaks and troughs on the right-hand side of the diagram, including dips at Sr, P and Ti (probably due to plagioclase, apatite and ilmenite fractionation). These rocks are greatly enriched in Ba, Rb and K compared with the gabbros, possibly indicating a higher degree of crustal contamination during magma genesis, or a large degree of fractional crystallization. The end result of

each of these processes is identical (i.e. high levels of Ba, Rb and K are produced in the melt) and the relative input of each could only be tested using isotopic studies.

Figure 9.14 c is a spiderdiagram showing representative samples from all the rock groups identified in the Glen More ring-dyke. MT 1, a sample from the granophyric Ishriff ring-dyke, is also plotted in this diagram, and shows very similar characteristics to GM 19. Sample GM12 is a granodioritic intermediate with blotchy character in thin section. The blotchy appearance suggests that this, and other intermediate samples, could be the product of mixing between intermediate and granophyric magmas. The position of GM12 in figure 9.14c backs this point up - as GM12 lies consistently between a dioritic sample (GM4) and a granophyre (GM19).

Data plotted on spidergrams again fall into two broad groups on either side of the line formed by the dioritic sample GM4. Gabbros have common characteristics and show parallelism of trends. The same can be said for the granophyres and acidic intermediates, but these contain different characteristics to the gabbros. Samples CG1, GM4, GM32 and GM26 (diorites or basic intermediate) fall at intermediate positions between the two main groups (see figure 9.14d). The four diorites and basic intermediates plot in the some order, relative to GM13 and GM19, throughout the spiderdiagram, with the progression from GM13 to GM19 being through the same sequence of samples for each element. On its own this pattern could be used as evidence for fractional crystallization, but if the textural characteristics of the samples are considered then CG1 and GM4 are homogeneous diorites, while GM32 and GM26 have a blotchy heterogeneous character. The intermediate positions of GM32 and GM26, combined with their textural characteristics may indicate that they are formed by mixing of granophyric and dioritic magmas. The composition of the granophyric magma was probably similar to GM19 or MT1, while the dioritic magma could feasibly have had a composition similar to GM4 or CG1. These latter two samples show no signs of mixing with granophyric magma, and could represent either a residual liquid of dioritic composition, left over from gabbro fractionation from a basaltic parent, or a dioritic magma composition from which gabbros have crystallized (in this latter case the dioritic liquid is the parental magma composition).

The origin of the acidic magma, typified by GM19 and MT1, is worth consideration here. Field relations (the chilled jacket of granophyre, and the veins of granophyre in the gabbros) show conclusively that the granophyre did not evolve by fractional crystallization of a gabbroic liquid *in situ* within the Glen More ring dyke fissure. However the parallel spider patterns in the region Ba-Rb-K-La-Ce suggest that it is possible to derive a granophyric magma by fractionation of a crustally-contaminated basic magma (e.g. GM8). Sr, Nd and Pb isotopes may give conclusive evidence regarding the origins of the magmas, but such investigation is beyond the scope of this study and so the origin of the acidic magma remains speculative. However, it is the case that recent work in

the British Tertiary Volcanic Province (Bell, 1983. Thompson, 1981 and 1983) suggests that although granites contain a crustal contamination signature, they are not primarily crustal melts, but are largely the products of magma chamber differentiation.

Accepting this to be so for the Glen More ring dyke granophyric magma, then it probably evolved by fractionation of a basaltic tholeiite in an underlying magma chamber. This could be a chamber which was older and more evolved than the one directly underlying the Beinn Chaisgidle centre, and could intermittently inject acidic magma into this chamber.

CHAPTER 10. Summary of evidence and possible petrogenetic schemes.

This chapter is a resume of the evidence found in chapters 6, 7, 8, and 9 of this thesis. The first section (10.1) lists the important findings of each of these chapters while the second part (10.2) outlines possible petrogenetic schemes that could be responsible for the vertical differentiation of this ring dyke. These schemes are based upon previous work on this body, and on work on other differentiated igneous bodies which could be applied to the Glen More body.

10.1 Summary of evidence

10.1.1 Field relations

- This is the latest intrusion associated with the Beinn Chaisgidle intrusive centre, and is therefore the last one before the intrusive focus migrated to the Loch Ba centre.
- Both the Loch Ba and the Beinn Chaisgidle centres display many granophyric intrusions and so acidic magma was readily available during the intrusive history on Mull. The intrusion of the gabbro-granophyre Glen More ring dyke was preceded by the intrusion of the granophyre Ishriff ring dyke (Bailey *et al*)
- Granophyre is seen above, alongside, and beneath the gabbros in the Glen More ring dyke. The hand specimen and thin section appearance of the granophyre does not vary between localities.
- Rocks of intermediate composition are only present between the gabbro and granophyre in the vertical section of the ring dyke at Cruach Choireadail.
- The granophyre has a 2-3m chilled, inclusion-free margin with the surrounding country basalts.
- At Loch Airdeglaiss the granophyre penetrates as fingers into the country basalts.
- Granophyre forms rectilinear veins in the gabbro, at Cruach Choireadail and Maol Tobar, which contain xenoliths and xenocrysts of gabbroic material.

10.1.2 Petrological and Textural Evidence

- Gabbros are plagioclase-rich olivine- and quartz-normative cumulates.
- No boundaries are exposed between olivine- and quartz-normative gabbros.
- There is a general decrease in grain size as the body is ascended.
- Intermediate rock types have a blotchy appearance which consists of contrasting portions of gabbroic and granophyric rock.
- The ratio of gabbroic to granophyric material decreases with altitude in the intermediate zone.
- The grain size of the gabbroic portion decreases with altitude, making it contrast more with the granophyre, because of the darker appearance of the basic portion as grain size decreases and ferromagnesium minerals become predominant.

• At Cruach Choireadail granophyre above the intermediate zone contains fine-grained ferrodioritic enclaves, but these are absent in the uppermost granophyre, and are not seen in granophyre at other localities. The enclaves have very fine-grained textures indicative of rapidly-quenched magma.

• The minerals in the basic portions show evidence of alteration where they come into contact with the granophyric portion.

10.1.3 Mineral Chemistry

• Olivine appears in the lowermost gabbros, is unzoned and forsteritic (Fo 68).

• Clinopyroxene shows a range of compositions within the augite compositional field. Augite crystals analysed in all olivine gabbros, and some quartz gabbros, and intermediates have very similar compositions (Wo 40 En 45 Fs 15). However some quartz gabbros and intermediates contain augite with more evolved compositions (Wo 28-48 En 27-42 Fs 15-36). These compositions have been produced in areas within intermediates where clinopyroxenes have been in contact with a more evolved, silicic magma. The crystals have re-equilibrated to be in equilibrium with their new surrounding melt. The evolutionary trend in clinopyroxene composition within the quartz gabbros may be the product of magma composition evolution, with the more Mg-rich clinopyroxene being produced early in the cooling history of the gabbro body, and the more Fe-enriched crystals forming later, at cooler temperatures, as the magma composition evolved.

• Plagioclase is labradoritic in the gabbros and is albitic in the granophyres and the acidic portions of the intermediate rocks. In the basic portions of the intermediate rocks plagioclase composition ranges from An45 to An75. The heterogeneous nature of this variation can be explained by the same mechanism as the variation in the clinopyroxene composition in the basic portions of the intermediate rocks.

10.1.4 Geochemical Evidence

• Gabbroic whole-rock analyses form a coherent trend which shows iron and titanium enrichment with decreasing MgO.

• Acidic and intermediate rocks plot on a straight-line trend, which can be explained by either fractional crystallization of a dioritic magma, or by mixing of granophyric and dioritic magmas. This latter mechanism would also explain the textural relationships in the acidic and intermediate rocks, and the variation in mineral chemistry.

• Two separate groups of data points are seen in plots, with a gap between them at 4 wt % MgO and 50 wt % SiO2. These values coincide with the composition of the most evolved quartz gabbro.

• Petrographic and chemical variation is not reliant on altitude, as has previously been indicated by Koomans and Kuenen (1938).

• Two distinct groups of data points are seen in most geochemical plots, suggesting that petrogenesis of basic and acid rocks is apparently distinct.

• Selected trace element ratios show a bimodal distribution. If the petrological variation was caused by differentiation of a single body of magma one would expect certain ratios to remain uniform through the body. This is not the case in this body.

• Certain intermediate composition samples plot at intermediate points between the basic and acid rock data groups in all geochemical plots.

• Trace element spidergrams pick out the following points:-

1) Parallel trends in gabbros and diorites indicate evolution by fractionation from a tholeiitic basaltic parental magma.

2) Granophyres could have evolved by extreme fractional crystallization of a crustally contaminated basaltic magma.

3) Intermediate composition rocks plot between granophyres and diorites and may result from mixing of these two end members.

10.2 Potential petrogenetic schemes responsible for the differentiated nature of the Glen More ring dyke.

The following are possible petrogenetic schemes for the formation of the petrological variation in the Glen More ring-dyke. The likelihood of these schemes is discussed in chapter 11 and 12. Some of the schemes outlined below are the ideas of, or are based on the ideas of, previous workers on the Glen More ring dyke. Others are ideas proposed for other differentiated bodies which may be applied to the body being studied here.

• 1 Bailey *et al* (1924) proposed the following petrogenetic scheme for the Glen More ring dyke:-

An undifferentiated basic magma was injected into the ring dyke fissure and the action of gravity during magma crystallization and consolidation caused the differentiation. "After crystallization had proceeded for some time, and had practically exhausted the magma as regards lime and magnesia, there still remained a residuum which retained its fluidity over a considerable range of temperature, so that there was, at this stage, a marked pause in the process of crystallization. Under such conditions, ample opportunity was afforded for migration of the fluid residuum under stress during the extended period that elapsed before crystallization was completed" (Bailey*et al* , p330). The microscopic appearance of the rocks at intermediate altitudes, with the plagioclase being altered by a more acidic mesostasis/residue is attributed to both the general albitization of rocks in Central Mull, and to the albitizing effect of the acid residual magma. Holmes (1936) criticized this theory because intermediate products of crystallization-differentiation are not seen, and also because there is no evidence in the gabbros of the acid residuum being squeezed out by the powerful deformative stresses needed to extract this liquid.

• 2 Nockolds (1934) ideas differed from the above in that he proposed that the primary tholeiitic magma was differentiated by crystallization in a deep reservoir to produce two contrasting magmas that intruded seperately, with the basic crystals reacting with the acid magma in the area where the two were in contact following the later intrusion of the acidic magma.

This model was developed further by Bor (1951) who said that the body was formed by two separate injections of compositionally contrasting magmas. First to be injected was a basic magma which underwent partial consolidation to form plagioclase-rich olivine and quartz gabbros and an intermediate residual liquid. A later injection of acidic magma underwent mixing with the intermediate residual liquid to form the blotchy intermediate rocks.

Holmes (1936) tends to agree with this model - with two contrasting magmas being available and being intruded separately (the basic one first). He adds that the magmas may have been generated separately or by fusion of acidic rocks by heat from the basic magma.

• 3 Koomans and Kuenen (1938) carried out chemical analysis of samples in the Glen More ring dyke and stated that the curves seen on variation diagrams could not be explained by hybridization of contrasting magma compositions (which would have produced straight mixing lines). Instead they propose that the variation is formed by gravitative sinking of augite, plagioclase and iron-ore, and the "peculiar microscopic aspect" of the intermediate rocks is attributed to "pneumatolytic emanations" from the lower parts of the ring dyke.

• 4 The intermediate zone is the product of mixing of granophyric and apatite-rich, dioritic magmas - the latter being produced by fractional crystallization of basaltic magma (Marshall, 1984). Marshall makes no mention of whether the contrasting magmas were intruded simultaneously or separately. Other work (Marshall and Sparks, 1984) proposes that magma mixing in other net-veined and mixed-magma ring intrusions in the British Tertiary Igneous Province is produced by simultaneous intrusion of compositionally contrasting magmas from vertically zoned magma chambers (eg. Loch Ba ring dyke and the St Kildan complex. See also Sparks, 1988).

• 5 A pulse of granitic magma infiltrates the interstices of partially consolidated gabbroic cumulates from below. This granitic pulse fills interstices and percolates up through the body to fill the top of the ring-dyke fissure. The upward percolation does not rely entirely on gravitational buoyancy, but instead on the magma pressure from below (cf. Moreau et al, 1987).

• 6 Simultaneous emplacement of two magmas, one basic the other acidic, with one of the following mechanisms being active, involving separation of contrasting magmas due to

density differences in the liquids (cf. Grossenbacher and Marsh [Zora ring intrusion, Gettysburg]):-

a) Flow differentiation in a feeder dyke. This could tap basic and acidic magma from different levels in a zoned magma chamber, bringing them together and causing mixing in the vertical feeder body. This mixing could be preserved between magma types in the ring dyke.

b) Buoyant rising of granitic blobs of melt. This is a product of immiscibility of magmas with large density and viscosity differences. The buoyant (low density and high viscosity) granitic blobs will rise through the denser, low viscosity basic melt and will coallesce near the top of the body.

• 7 Gabbro could have been injected into a body of granophyre. If the granophyre was only partially consolidated magma mixing could have taken place to produce the blotchy rocks in the intermediate zone.

All of the above schemes provide a mechanism for producing vertical differentiation of a magma body. Some of the schemes have already been questioned by other workers and are therefore less credible than others. The first section of chapter 11 outlines objections to the various schemes, and narrows down the possibilities that exist for the Glen More ring dyke.

CHAPTER 11 Major-Element Computer Modelling

11.1 Introduction

In this chapter the possible petrogenetic schemes described in chapter 10 are discussed and an attempt is made to evaluate the likelihood of the most probable schemes using geochemical modelling techniques.

Several of the petrogenetic schemes outlined in chapter 10 can be ruled out by evidence obtained in this study, combined with the opinions of previous workers. The arguments for and against these schemes are discussed in this section, while the geochemical modelling is described in sections 11.3 and 11.4.

11.2 Discussion of petrogenetic schemes

Reasons for rejecting the first petrogenetic scheme (Bailey *et al*, 1924) were raised by Nockolds (1934) and by Holmes (1936) and have already been outlined in chapters 6 and 10. Holmes' argument about deformative stresses being required to extract residual melt from the gabbros may now be obselete following recent work on the density and buoyancy of melts at crystal-liquid interfaces and in cumulate piles. This work shows that low-density melts may be able to convect away from their sources, so aiding melt extraction without the need for deformative stresses.

Field relations described in this study, are hard to ascribe to Baileys' original scheme for the Glen More ring dyke with the relationship of the granophyre to the gabbro being the most problematic point. Granophyric material is found above, below, and alongside gabbros; a fact hard to explain by crystallization differentiation, especially as the granophyre is also intrusive into the country basalts. Granophyre is intrusive into the gabbro as rectilinear veins which contain fragments of the gabbro, indicating that the gabbro was at least partially consolidated when the two were brought together. The granophyre also contains mafic enclaves, whose origin is hard to explain within the framework of the Bailey model, and, in the upper parts of the ring dyke at Cruach Choireadail, granophyre is surrounded by a jacket of chilled felsite. This latter point was observed by Bailey *et al.* but no comment was passed on the origin or petrogenetic significance of the enclaves. Chemical data presented in this current study suggest that the gabbroic and granophyric/intermediate rock groups have distinct petrogenetic origins, conflicting with the interpretation of chemical data in the Memoir.

The scheme based upon the work by Nockolds (1934) and Bor (1951) explains the mechanism by which the blotchy intermediate rocks were formed by mixing separately-injected gabbroic and granophyric magmas. This mechanism can also account for the

enclaves in, and the chilled margin around the granophyre. However, the order of intrusion of the magmas is problematic with this scheme. If granophyre is intruded first then it is difficult to account for the granophyric veins in the gabbros. Bor favours the initial intrusion of a gabbroic magma, followed, after some crystallization and consolidation, by the intrusion of a silicic magma into the top of the ring dyke. How to get such a magma to the top of the ring dyke fissure is an awkward problem to overcome however. Bor suggests intrusion of the acidic magma through a vertical channel that is now exposed at Loch Airdeglais. This is discussed further in chapter 12.

The order of magma intrusion also contains problems when considering the intrusion of other ring dykes around the Beinn Chaisgidle centre. Bailey *et al* did not determine the relative ages of the Glen More and the Ishriff ring dykes in the Memoir, but it has been assumed since (Emeleus, in Craig, 1991) that the Glen More body is the last major intrusion associated with the Beinn Chaisgidle intrusive centre, making it younger than the Ishriff ring dyke. If this is so, and if we assume that the first injection of magma into the Glen More ring fissure was basic in composition, then the magma chamber feeding the Beinn Chaisgidle centre has fed acidic, basic and acidic magmas into ring intrusions consecutively. This requires some considerable adjustment and re-adjustment of the magma composition that was tappable in the chamber and is the subject of part of the discussion in chapter 12.

The field relation objections to Baileys' model can also be raised as argu ments against the Koomans and Kuenen scheme. In addition to these arguments, the chemical data produced in chapter 9 of this study indicate that the gabbroic rocks and the acidic and intermediate rocks have discrete petrogenetic origins, and should therefore be treated separately, and not as one continuum of rocks produced by crystallization-differentiation (Bailey *et al* , 1924). Koomans and Kuenen (1938) propose that the geochemical data be considered as a single trend. They rule out hybridization of magmas on the grounds of a lack of straight-line mixing trends. However, if the data in this current study are treated as two distinct groups then a straight-line trend is seen connecting the intermediate and acidic rock compositions, meaning that magma mixing is a potentially active mechanism in the Glen More ring dyke.

Marshalls' proposal of the intermediate zone in the Glen More ring dyke being formed by mixing of granophyric and dioritic magmas certainly explains the textural aspect of the intermediate zone, but does not throw any light on the order of intrusion of acidic and basic magmas. However, if this mixing model is accepted, and if both magmas were intruded simultaneously, then a region of dioritic magma must have been present between the basic and the acidic ones in the feeder magma chamber before ring dyke formation. Factors that disagree with such a simultaneous intrusion mechanism include the

granophyric veins in the gabbros, and the sharp boundaries, with no evidence of magma mixing, between the gabbros and granophyres at Moal Tobar and Loch Airdeglais.

Moreau *et al* (1987) proposed the model involving upward filtration, driven by magma pressure, of granitic magma through a porous network of gabbroic crystals for the Taguei ring complex, Air, Niger. At this locality interstitial voids in the gabbros are filled with fine-grained granitic material, and the edges of gabbroic minerals which touch this later magma type show re-equilibration textures. This mechanism could be considered for the Glen More ring dyke because of similarities shown between it and the granophyric material in the interstices of the quartz gabbros.

Many olivine gabbros in the lower zone of the ring dyke on Mull contain no acidic mesostasis. If Moreaus' mechanism is to be applied to the body in this study then we should expect acidic material to occupy the interstices of gabbros throughout the body. This is not the case and leads us to assume that granitic melt has not percolated through the olivine gabbros, and that the acidic mesostasis in the interstices of the quartz gabbros is a residual melt trapped in the late stages of crystallization.

The simultaneous emplacement of mixed basic and acidic magmas, with gravity-driven separation after emplacement (Grossenbacher and Marsh, 1992), would appear to be a feasible mechanism to explain the partially-mixed intermediate zone, and the apparently density-controlled rock type distribution at Cruach Choireadail. However it fails to explain the rectilinear granophyre veins in the gabbro and the lack of magma mixing between adjacent outcrops of granophyre and gabbro at Maol Tobar and Loch Airdeglais. If the two magmas had been emplaced simultaneously then it seems reasonable to expect some degree of intermingling wherever they are in contact, unless the granophyre at Maol Tobar and Loch Airdeglais is part of a separate acidic intrusion unconnected with that at Cruach Choireadail.

The idea of gabbroic magma intruding into a ring dyke that already contains granophyre is difficult to use to explain many of the features of the body. Unless the mafic enclaves were already included in the acidic magma when it was intruded, it is difficult to envisage how they could originate. The origin of the granophyre veins in the gabbros is also probematic if the gabbroic magma was the second injection. The veins could be the product of back-veining, produced by fusion and remobilization of acidic material when a hot basic magma is emplaced next to it, but the rectilinear nature of the veins infers that the gabbros were solidified when granophyre was intruded.

As geochemical and petrographic evidence indicates that the petrogenesis of gabbroic rocks should be considered separately from that of granophyric and intermediate rocks, two questions need to be answered about the petrogenesis of the Glen More ring dyke.

1) What is responsible for the compositional variation in the gabbros?
2) What process can account for the straight-line variation trends seen linking the intermediates and granophyres?
The answers to these questions can then be linked together to produce a petrogenetic scheme for the overall evolution of the ring dyke.

From the evidence presented in chapters 6-9, and the work discussed above, the following schemes for petrogenetic evolution of the Glen More ring dyke are favoured, largely because they have the least evidence against them:-

1) The range of intermediate-acidic rocks is formed by magma mixing between granophyric and dioritic magma types.
2) Compositional variation in the granophyres may be caused either by differing proportions of mafic enclaves as part of the mixing scheme or by fractional crystallization within the upper parts of the granophyre.
3) Gabbro compositions are probably not representative of liquid compositions, but range from olivine gabbros to quartz diorites in composition. The question can therefore be posed; was the compositional variation present in magma when it was intruded into the ring dyke, or has it evolved by *in situ* differentiation caused by crystal-liquid fractionation of an initially homogenous magma in the ring dyke? (i.e. could the dioritic end-member of an acidic-intermediate mixing trend be the residual liquid from fractionation of gabbros from an initially-homogenous basaltic magma?).

An attempt is made in this chapter to evaluate the likelihood of these three hypotheses. This is done by examining the petrogenetic schemes using a least-squares mixing programme (MacGPP-MIX mass balance calculations, Geist, McBirney and Baker, 1989).

The input data for this modelling comprises major element compositions of whole rock analyses, and electron microprobe analytical data of cumulate mineral phases. The compositions of two other whole rocks are also used in order to estimate the composition of the magma parental to the gabbros in the Glen More ring dyke. These are the compositions of an early basic cone sheet (EX16) from Sidhean Dubh, to the south of Loch Spelve on Mull (GR 699271) which was suggested as a possible uncontaminated, primary, tholeiitic magma composition by A. C. Kerr (pers. comm), and the parental magma composition for the Skaergaard Intrusion, Greenland (Wager, 1960). These compositions were used in the modelling in the absence of any definite parental magma composition in the Glen More ring dyke (i.e. no chilled margins) in an attempt to estimate a suitable parental magma composition. In the modelling the compositions were used to see whether a dioritic end-member, similar to GM4, could be produced by fractional crystallization of the gabbroic mineral compositions described in chapter 8. The

compositions of these four whole rocks, and of the minerals used in this modelling are shown in table 11.1.

The potential of these magma compositions, and of some gabbroic whole-rock compositions, as parental compositions is examined in the following section (11.3) along with modelling involving the compositional evolution of the gabbroic rocks in the Glen More ring dyke. Section 11.4 examines the proportions of dioritic and granophyric magmas involved in producing the mixing trend in the acidic and intermediate rocks.

In the least-squares modelling (Bryan *et al*, 1972) the following basic equation is used:-

Magma A = Magma B + Minerals

The quality of fit of calculations is dependent on the sum of the squares of the differences between observed and calculated values for each of the major elements in the input data (i.e. "the sum of the squares of the residuals", Bryan *et al*, 1972). All elements were given equal weighting (i.e. importance) in the calculations. Only major elements were used, as trace element concentrations are not available for mineral analyses.

The computer output from the MacGPP-MIX programme comprises three parts:-

1) A table of unweighted analyses of the minerals and rocks selected for calculations.

2) Solution vectors are displayed as weight fractions of the mixing components (i.e. the parent magma, the minerals, and the daughter magma) together with the sum of the squares of the residuals. This latter part is a measure of the fit of the solution and is labelled R-Squared (R^2). R^2 values of less than 1 are considered reasonable, less than 0.3 is regarded as a good fit, and less than 0.1 is excellent. While modelling fractional crystallization, an increase in the number of minerals used in the calculations always results in a better fit. Therefore, only mineral phases actually seen in rocks are used in the calculations, although some are dropped from certain calculations to test whether particular minerals are more important than others during evolution of the gabbroic rock series. A percentage cumulate column gives the weight percentages of the minerals in the fractionated mineral assemblage.

3) A table giving the input parent and daughter compositions, the calculated daughter composition, and the residuals (differences between the actual and the calculated daughter compositions).

11.3 Possible Parental Magmas and a connection between acidic and basic groups of rocks

If it is accepted that the array of whole rock compositions in the acidic-intermediate range is produced by mixing acidic and intermediate magma compositions (see section 11.4) then the origin of the intermediate composition magma must be explored. Various possibilities exist for the origin of such a dioritic magma:-

Table 11.1. Composition of minerals and rocks used in GPP modelling.
See also table 9.1 for other whole rock compositions

	Olivine	Clinopyroxene	Plagioclase	Magnetite	Ilmenite	EX 16 (AC Kerr)	SK 4507 (Wager, 1960)	GM13	CC6
SiO2	36.5	51	51.3	0.5	0.5	48.24	48.08	47.9	47.9
TiO2	0.03	1	0	0	50	1.18	1.17	1.2	0.5
Al2O3	0.01	1.8	29.6	0.2	0	14.77	17.22	16.4	18.2
Fe2O3	0	1.84	0	68.9	4.2	3.78	1.32	5.32	4.04
FeO	30	7.36	0	30.8	42.2	8.82	8.44	6	4.5
MnO	0.6	0.3	0	0.2	1.4	0.2	0.16	0.2	0.1
MgO	31.8	15.2	0	0	0.5	7.33	8.62	8.1	7.9
CaO	0.14	20	12.9	0	0.7	11.89	11.38	10.4	10.7
Na2O	0.02	0.3	4.1	0	0	2.31	3.37	3	2.1
K2O	0.02	0	0.2	0	0	0.12	0.25	0.6	0.5
Total	99.12	98.8	98.1	100.6	99.5	98.64	100.01	99.12	96.44

(In GPP modelling FeO and Fe2O3 are combined as one total Fe value.)

1) The dioritic magma was intruded into the ring dyke from a magma chamber containing entirely dioriticmagma.
2) It is the product of differentiation of a basaltic magma in an underlying magma chamber, and was fed into the ring dyke above basaltic magma.
3) It is the product of differentiation of a basaltic magma in the dyke, before injection of the granophyric magma.

Magmas of intermediate composition are scarce in the British Tertiary igneous province, and dioritic ring intrusions are almost completely absent around the Mull central intrusive complex, suggesting that a source of such a magma was not available. Also, an intermediate magma composition could not be responsible for the less evolved mineral compositions seen in the Glen More gabbros. For these reasons the first of the above three options is least favoured.

This section therefore examines ways in which a dioritic magma could be derived from a basaltic magma by fractional crystallization, either in the ring dyke fissure or in the magma chamber underlying the Beinn Chaisgidle intrusive centre. This is done by exploring fractionation products (minerals and residual liquids) from potential parental magma compositions and comparing them with the rock and mineral compositions seen in the Glen More ring dyke.

As no chilled basic margins are exposed in the Glen More ring dyke, potential parental liquid compositions have to be surmised. Four possible parental magma compositions have been examined here; The Skaergaard parental magma, an uncontaminated, basic, tholeiitic cone sheet from Mull (EX16), and the most basic rocks analysed in this study (GM13 and CC6), both gabbros from Cruach Choireadail. The compositions of these rocks are displayed in table 11.1. Least squares mixing calculations were carried out for each of the above compositions, extracting olivine, augite, plagioclase, magnetite and ilmenite to evolve the composition GM4. Calculations are based upon the equation below and the results are shown in table 11.2.

Magma A = Magma B + Minerals,

where Magma A is the basic magma composition, Magma B is the composition of GM4, and 'Minerals' is the overall composition of the minerals that need to be extracted from Magma A to produce Magma B.

The data in table 11.2 can be split into four parts for each of the compositions examined. The first column of the results table (headed 'Solution') gives the proportions of each constituent needed to balance the equation (i.e. Magma A, Magma B, and Minerals). These values are converted to percentages in the next column (% of original volume). The third collumn calculates the percentage of each mineral in the cumulate mineral

Table 11.2. Modelling data for evolution of GM 4 from gabbro compositions

	EX 16	Solution	% of original volume	% of Cumulate
Magma B	GM 4	1	20	
Ilmenite		0.093	1.9	2.349
Magnetite		0.152	3.1	3.862
Olivine		0.515	10.4	13.044
Augite		1.261	25.5	31.947
Plagioclase		1.926	38.9	48.798
Magma A	EX 16	4.946	100	
R Squared		**1.578**		

	SK 4507	Solution	% of original volume	% of Cumulate
Magma B	GM 4	1	10.5	
Ilmenite		0.172	1.8	2.03
Magnetite		0.045	0.5	0.529
Olivine		1.65	17.4	19.455
Augite		1.712	18	20.175
Plagioclase		4.904	51.7	57.811
Magma A	SK 4507	9.484	100	
R Squared		**0.744**		

	GM 13	Solution	% of original volume	% of Cumulate
Magma B	GM 4	1	26	
Ilmenite		-0.037	-1	-1.283
Magnetite		0.166	4.3	5.749
Olivine		0.407	10.5	14.079
Augite		0.718	18.5	24.842
Plagioclase		1.635	42	56.612
Magma A	GM 13	3.889	100	
R Squared		**4.75**		

	CC 6	Solution	% of original volume	% of Cumulate
Magma B	GM 4	1	15.5	
Ilmenite		-0.144	-2	-2.64
Magnetite		0.222	3.4	4.06
Olivine		0.74	11.4	13.514
Augite		1.18	18	21.568
Plagioclase		3.475	53.7	63.5
Magma A	CC 6	6.472	100	
R Squared		**6.112**		

assemblage that must be crystallized from the basic magma to produce GM4. The final part of the output is the R Squared value for the calculation.

These data indicate the following points:-

- The Skaergaard parental magma represents a potentially better parental composition than the gabbros from the Glen More ring dyke, or the uncontaminated cone sheet.
- Approximately 90% crystallization of a tholeiitic basalt is required to produce 10 % of the original volume of magma with a composition of GM 4.
- This crystallization must be of plagioclase-rich mineral assemblages in order to produce the GM 4 liquid composition. This is consistent with the mineralogy of the gabbros in the Glen More ring dyke.
- It is proposed in section 11.4 that a magma composition similar to GM 4 is the basic end member of the acidic-intermediate mixing trend. This composition could be the product of fractional crystallization of a basaltic magma, either in the ring dyke, or in the underlying magma chamber system.

Although this modelling results in reasonable R Squared values for the compositions considered, it has been used over a wide compositional gap and for high degrees of fractional crystallization (>75 %). These are both far beyond the limits that least squares modelling is intended to test, and so the seemingly good results may be illusory. The results do, however, give an indication of the mineral assemblages that need to be produced if a dioritic residual magma is to be formed by fractional crystallization of a basaltic parent. These cumulate assemblages are similar to those seen in the Glen More gabbros, indicating a potential formation mechanism for such rocks.

In order to test more realistically the possibility of a dioritic magma evolving from a basaltic magma by crystal-liquid fractionation, it is neccessary to model a series of more closely-spaced compositions between a basaltic composition (GM13 or CC6) and a dioritic composition (GM4). This has been done by taking adjacent gabbro compositions on variation diagrams and calculating, using the GPP-MIX programme, what mineral assemblages have to be taken out of the more basic compositions to reach the more evolved compositions.

In chapter 8 it was suggested that mineral chemistry variation within the gabbros is minimal and that the variation in mineral chemistry is largely a product of interaction between primary gabbroic minerals and a secondary acidic magma in the intermediate zone. For these reasons the mineral compositions used in this modelling are all from gabbro GM13, the olivine gabbro type specimen.

The following sequence of gabbro compositions, based on MgO wt % values, has been examined here:-

GM 4 -GM 55-LS1-MT3- GM32-GM52-GM9-GM8-GM13-CC6

(most evolved) (least evolved)

In the modelling, minerals were extracted from the most basic rock compositions to derive progressively more evolved compositions. Mineral assemblages extracted were adjusted but always included at least three of the following; clinopyroxene, plagioclase, olivine, magnetite, and ilmenite. This alteration of mineral assemblage was done to test whether or not certain minerals were more important to the fractionation trend than others.

Part of the output of this computer programme is a list of mineral proportions in the fractionating assemblage, this list can be compared with modal proportions in the actual rocks. The output gives the proportions of these minerals that need to be taken out of (denoted by positive values) or added to (negative values) the basic magma composition to produce the less basic composition. Results of this modelling are summarised in table 11.3. Only calculations with an R^2 value of less than 1 are shown here.

As previously discussed, increasing the number of mineral phases to the fractionating assemblage produces a lower R^2 value for a given calculation, however a few exceptions exist in these calculations. GM 32 to GM52 have lower R^2 values with no pyroxene than they do with no olivine (0.705 vs 0.725). In other cases removal of clinopyroxene and olivine from the fractionating assemblage has little effect on the R^2 value. This suggests that these minerals are not as important as others in the fractionating assemblage responsible for the trends on the variation diagrams. Reasonable R^2 values are obtained, in some cases, by fractionating only plagioclase, magnetite and ilmenite. The addition of clinopyroxene and olivine has little effect on the resulting trend.

Examination of the results in table 11.3 shows that the range of whole rock compositions of the gabbros could have evolved by fractional crystallization of calcic-plagioclase-rich mineral assemblages from a basaltic parental magma, with smaller amounts of magnetite, ilmenite, calcic-augite and forsteritic-olivine , the end result being a dioritic residual magma.

11.4 Acidic and Intermediate rocks

Three possible schemes exist that could produce the array of whole rock compositions that fall on the straight-lines of variation diagrams in the acidic and intermediate rocks. These are:-

• *In situ* fractional crystallization of an intermediate magma with a composition represented by CG 1 or GM 4.

Table 11.3. Petrogenetic modelling data for possible fractionation trend of gabbros.

		Mineral as Percentage of Cumulate assemblage							
Magma B	**Magma A**	**Ilmenite**	**Magnetite**	**Olivine**	**Augite**	**Plagioclase**	**R Squared**	**% crystallization**	**% residual magma**
GM 4	LS 1	1.2	7.0	5.2	32.6	54.0	0.074	48	52
GM 4	MT 3	0.8	6.4	6.3	29.5	56.9	0.245	57	43
GM 4	GM 52	0.0	5.8	7.8	29.8	56.7	0.742	63	37
GM 4	GM 8	1.4	2.7	11.7	34.9	49.2	0.435	79	21
GM 4	GM 7	5.3	13.5	5.9	37.0	38.3	0.225	52	48
GM 55	GM 9	-0.3	2.7	8.4	59.2	30.0	0.38	38	62
GM 55	GM 8	-0.5	2.6	10.9	45.1	41.9	0.38	52	48
LS 1	MT 3	-0.3	5.2	9.0	22.4	63.8	0.159	17	83
LS 1	GM 52	-0.2	4.4	10.8	26.4	59.9	0.594	28	72
LS 1	GM 8	1.5	1.3	13.8	35.7	47.7	0.464	60	40
MT 3	GM 52	-3.0	3.4	13.1	30.7	55.9	0.217	13	87
MT 3	GM 8	1.7	0.9	14.4	37.7	45.3	0.717	53	47
LS 1	GM 7	25.2	45.5	9.5	58.6	-38.8	0.325	9	91
GM 32	GM 52	15.6	31.5	23.6	19.6	9.7	0.716	3	97
GM 9	GM 8	-0.9	2.6	14.0	28.0	56.4	0.088	23	77
GM 4	LS 1	2.2	7.2	NI	38.0	52.6	0.618	46	54
GM 55	GM 9	-0.2	2.1	NI	80.9	17.2	0.912	27	73
LS 1	MT 3	1.2	5.2	NI	30.3	63.3	0.369	14	86
GM 32	GM 52	81.9	121.4	NI	64.9	-168.2	0.725	1	99
LS 1	MT 3	-2.7	3.4	18.9	NI	80.4	0.458	9	91
MT 3	GM 52	-15.2	-5.1	44.5	NI	75.7	0.525	4	96
GM 32	GM 52	28.8	54.6	43.6	NI	-27.0	0.705	2	98
LS 1	MT 3	-0.7	1.5	NI	NI	99.2	0.806	5	95

- Mixing of acidic and intermediate magmas.
- Magma mixing with a degree of fractional crystallization.

The first of these three possibilities can be ruled out by the fact that a chilled jacket of granophyre exists in the upper parts of the ring dyke, indicating that acidic magma was injected into the ring dyke, and the textural make-up of the intermediate rocks favours the magma mixing process. This does not, however, rule out the possibility that the acidic magma evolved from a gabbroic or intermediate magma by fractional crystallization in a feeder magma reservoir. Such a process could have produced a range of magma compositions in a vertically stratified chamber. These could then have been intruded into the ring dyke either together (although field relations, i.e. veining, indicate that this was not the case), or separately, in one of two orders:-

1) Basic magma first. This then differentiates to produce a dioritic residue. Then granophyre intrudes.

2) Basic and intermediate magmas intruded together and underwent partial consolidation before the granophyre intruded.

Evidence is not available to separate between these two processes.

Textural evidence points towards mixing of acidic and intermediate magmas as the most likely mechanism of formation of rocks in the upper half of the Glen More ring dyke at Cruach Choireadail. This mechanism is tested here using least-squares modelling.

Potential end members of a mixing trend, identified from their positions on variation diagrams, are tested with all intermediately positioned compositions to find the most suitable end member compositions. Whole rock compositions falling at the ends of the acidic-intermediate sequence on Harker diagrams are CC 4, CG 1, GM 4, GM 31, and possibly GM 7, at the intermediate end, and GM 19, MT 1 and CG 4 and CG5 at the acidic end. The least-squares equation takes the following form in this modelling:-

Magma 3 = Magma 1 + Magma 2

where magma 1 is the intermediate composition (CC4, CG1, GM4, GM31 or GM7), magma 2 is the acidic composition (GM19, MT1, CG4 or CG5), and magma 3 is the composition of the blotchy, dioritic or granodioritic rock lying between magmas 1 and 2 on the variation diagrams.

All combinations of end members and intermediate compositions were tested. R^2 values and proportions of end members needed to produce the intermediates are given in table 11.4. These data show that intermediate end members GM7 and CG1 produce no R^2 values of less than 1, ruling them out as potential end members of a mixing sequence. The end members which provide a majority of the low R^2 values for the intermediate points are GM4 at the intermediate end, and CG4 at the acidic end. Points that fall very close to a line joining these two end members are GM31, 48, 51, 12, 18, 17, 15, and 19. The following reasons may account for compositions deviating from the mixing line:-

Table 11.4. Petrogenetic modelling of acidic-intermediate mixing trend

Basic End Member	Acidic End Member	Daughter	R Squared	Solution	% Basic end member	% acidic end member
GM 4	MT 1	GM 31	0.927	0.319	75.8	24.2
GM 4	MT 1	CC4	0.763	0.435	69.7	30.3
GM 4	MT 1	GM 38	0.496	0.558	64.2	35.8
GM 4	CG 4	GM 38	0.914	0.485	67.3	32.7
GM 4	GM 19	GM 12	0.3	2.586	27.9	72.1
GM 31	MT 1	CC 4	0.637	0.089	91.8	8.2
GM 31	GM 19	CC 4	0.892	0.086	92.1	7.9
GM 31	CG 4	CC 4	0.734	0.073	93.2	6.8
GM 31	CG 5	CC 4	0.807	0.09	91.7	8.3
GM 31	MT 1	GM 38	0.299	0.181	84.7	15.3
GM 31	GM 19	GM 38	0.546	0.198	83.5	16.5
GM 31	CG 4	GM 38	0.282	0.158	86.4	13.6
GM 31	CG 5	GM 38	0.503	0.198	83.5	16.5
GM 31	MT 1	GM 47	0.4	0.499	66.7	33.3
GM 31	CG 4	GM 47	0.605	0.418	70.5	29.5
GM 31	MT 1	CC10	0.609	0.5	66.7	33.3
GM 31	CG 4	CC 10	0.783	0.419	70.5	29.5
GM 31	GM 19	GM 12	0.185	1.631	38	62
GM 31	CG 4	GM 12	0.872	0.95	51.3	48.7
GM 31	CG 5	GM 12	0.845	1.571	38.9	61.1
CC 4	MT 1	GM 38	0.277	0.089	91.8	8.2
CC4	GM 19	GM 38	0.201	0.107	90.3	9.7
CC 4	CG 4	GM 38	0.212	0.082	92.4	7.6
CC4	CG 5	GM 38	0.243	0.104	90.6	9.4
CC 4	MT 1	GM 47	0.478	0.383	72.3	27.7
CC4	GM 19	GM 47	0.594	0.437	69.6	30.4
CC 4	CG 4	GM 47	0.51	0.324	75.5	24.5
CC4	CG 5	GM 47	0.908	0.422	70.3	29.7
CC 4	MT 1	CC10	0.501	0.382	72.4	27.6
CC4	GM 19	CC 10	0.705	0.434	69.7	30.3
CC 4	CG 4	CC 10	0.487	0.323	75.6	24.4
CC4	GM 19	GM 12	0.271	1.451	40.8	59.2
GM 48	GM 19	GM 51	0.502	0	100	0
GM 48	CG 4	GM 15	0.667	1.686	37.2	62.8
GM 48	GM 19	GM 15	0.187	41.436	2.4	97.6
GM 48	CG 4	GM 19	0.78	1.776	36	64
GM 51	CG 4	GM 15	0.487	1.677	37.4	62.6
GM 51	GM 19	GM 15	0.181	32.668	3	97
GM 51	CG 4	GM 19	0.731	1.788	35.9	64.1
GM 12	CG 4	GM 18	0.119	0.898	52.7	47.3
GM 12	CG 4	GM 17	0.318	0.993	50.2	49.8
GM 12	GM 19	GM 15	0.187	23.224	4.1	95.9
GM 18	CG 4	GM 17	0.08	0.045	95.7	4.3
GM 18	GM 19	GM 15	0.196	12.522	7.4	92.6
GM 17	GM 19	GM 15	0.201	15.249	6.2	93.8
GM 15	CG 4	GM 19	0.191	0.036	96.5	3.5

1) Hydrothermal alteration of the rocks.
2) Xenolith or Xenocryst presence in analysed rocks.
3) A degree of crystal-liquid fractionation during the post-mixing, cooling history of the magmas.

11.5 Summary

The following important points arise from this chapter:-

- The trend connecting the gabbro whole-rock compositions could be produced by fractional crystallization of plagioclase-rich mineral assemblages, containing minor amounts of olivine, augite, and Fe Ti oxides from a basaltic magma.
- After 90 % fractional crystallization of such a tholeiitic basalt the residual magma could have the composition of GM 4.
- GM 4 (a dioritic sample) and CG 4 (a granophyre) are the most likely end-member compositions of the mixing sequence which has produced the blotchy intermediate rock types.

CHAPTER 12. Discussion and synthesis of the petrogenesis of the Glen More ring dyke

12.1 Introduction

The original aim of this study was to examine the Glen More ring dyke as a potential site of *in situ* side-wall and floor crystallization with associated compositionally-driven convection. Such a mechanism could produce gabbroic cumulates and buoyant, progressively more evolved, residual magma which could produce intermediate and granophyric rock types in the upper part of the ring dyke. Petrographic and geochemical data provided in this thesis show that *in situ* crystal-liquid fractionation is not the cause of all of the petrological variations in the body. Instead this evidence supports mixing of compositionally-contrasted magmas injected into the ring-dyke fissure at separate times. Crystal-liquid fractionation can, however, be invoked as a formation mechanism for the range of compositions in the gabbros. This conclusion agrees with the work of Bor (1951) but contradicts Marshall's proposal (1984) of single injections of compositionally-contrasted magmas into ring dyke fissures.

Previous work on the petrological variation in the Glen More ring dyke has produced conflicting ideas to explain the vertical gabbro-granophyre differentiation in the body. Marshall (1984), in a study of the Mullach Sgar complex on St Kilda and the ring intrusions of Ardnamurchan, examined the Glen More ring dyke in brief detail, and proposed a mixed magma scheme for these bodies involving a single intrusion from a zoned magma chamber. Evidence of mixing of acidic and basic magma is available throughout the BTIP in numerous composite sills and dykes (in which basic magma was injected first), in net-veined intrusions, and in mixed magma ring dykes. A wide variation of frozen-in mutual relationships is preserved, involving a variety of magma compositions which appear to have been available throughout the development of the Tertiary igneous centres (Emeleus, in Craig 1991). Major and trace element data show that the magmas were cogenetic, that intermediate rocks formed by fractional crystallization are rare (most are formed by intermingling and mixing of magmas), and that the basic magma which mixes with the acidic magma is frequently ferrodioritic (Bell 1983). The processes involved in the formation of this range of magmas are closely linked with petrogenetic models for differentiated bodies, and are discussed in this section with special reference to the Glen More ring dyke.

A petrogenetic scheme that fits the evidence presented in this study is described in the latter part of this chapter (12.4). The evidence for this scheme is discussed in section 12.2, while the structural evolution of the body in relation to the Mull central intrusive complex and the nature of the underlying magma chamber is discussed in section 12.3.

12.2 Evidence for magma mixing during two injections into the ring dyke fissure.

12.2.1 Introduction

The evidence exposed in the field illustrates that magma mixing of granophyric and dioritic magmas has occurred in the Glen More ring dyke, and that it probably took place when two compositionally-contrasting magmas were brought together by separate injections into the fissure. This section discusses the petrographic and chemical evidence for magma mixing during two injections of magma into the ring dyke fissure.

12.2.2 Petrographic evidence for magma mixing

This section comprises three parts. 12.2.2a outlines the principles involved in magma mixing and the evidence for magma mixing in the British Tertiary igneous province. The next section (12.2.2b) discusses the petrographic magma mixing evidence from the Glen More ring dyke, and is followed by a view of how magma mixing may be brought about in the ring dyke fissure (section 12.2.2c).

12.2.2a Magma mixing and the British Tertiary igneous province

Previous accounts of mixed-magma igneous intrusions in the British Tertiary igneous province describe bodies in which the mixing takes place on a wide range of scales, to variable degrees, and between variable magma compositions (Bell, 1983; Vogel *et al* , 1984; Sparks and Marshall, 1986; Marshall, 1984). The degree of mixing preserved in these bodies depends on the rheological properties of magmas in contact with one another. Hot, low-viscosity magmas of similar compositions, brought together in a convecting body may mix thoroughly and quickly to produce a texturally and chemically homogeneous magma, with the resultant rocks containing no evidence of the mixing process. In contrast, if compositionally-contrasted magmas, at different temperatures, are brought into contact then the hotter will be cooled and begin to crystallize, it will become more viscous, and will therefore have great difficulty in mixing with the cooler host magma. This latter situation results in preservation of evidence of magma mixing, and is seen frequently in the British Tertiary igneous province (Marshall and Sparks, 1984).

The hurdle which needs to be overcome before magma mixing can occur involves the different physical properties of the two liquids once thermal equilibrium is reached. This barrier is governed by density, viscosity, temperature, and the low diffusion rate of chemicals in silicate melts. The mixing process can be split into two sub-processes; mechanical mixing and chemical diffusion. For two magmas to homogenize by chemical diffusion, they must remain superheated for a considerable time. Since one must cool in the other both cannot remain superheated, hence mechanical mixing is the main process

by which magmas are hybridized in the upper crust (Blake and Koyaguchi, in Didier and Barbarin, 1991).

The subject of magma mixing in the BTIP has been discussed extensively over the past ten years by many authors (Sparks and Marshall 1986, Bell 1983, Vogel 1982). This work describes a variety of mutual relationships preserved at the current erosional level in the BTIP. Sparks and Marshall (1986) discuss the constraints on mixing between compositionally-contrasted magmas. The diagrams in figure 12.1 a, b, and c are taken from this work and illustrate the compositional selectivity involved in magma mixing. Figure 12.1a shows data from rocks in the net-veined Mullach Sgar complex on St Kilda, and figure 12.1b indicates that only compositionally similar magmas, with relatively small temperature differences, are able to mix thoroughly. Magmas of contrasting composition have large physical barriers to overcome if they are to become homogenised. Figure 12.1 b shows that there is a lack of mixing of acidic magma with more mafic (>4wt% MgO) in the Mullach Sgar complex. This is consistent with findings in the Glen More ring dyke in this study.

Figure 12.1c summarizes different possible physical mixing situations . The important parameters are the initial temperature difference between magmas, and the proportion of mafic magma. The controlling factor is the viscosity contrast between mafic and silicic magmas after they have reached thermal equilibrium. This behaviour is discussed fully by Sparks and Marshall (1986) and by Blake and Koyaguchi (in Didier and Barbarin 1991) but, to summarize, three situations exist:-

1) Mafic magma viscosity remains lower than silicic magma viscosity on reaching thermal equilibrium. This requires a low initial temperature difference or a high proportion of mafic magma to provide superheat forthe system. Mixing is uninhibited.
2) Mafic magma crystallizes before thermal equilibrium is reached. This gives it a yield strength, creating a barrier to physical mixing. If it becomes solid, no physical mixing is possible (though digestion by reaction may ensue).
3) An intermediate situation with a limited degree of mixing between the mafic and acidic magmas.

12.2.2b Magma mixing evidence in the Glen More ring dyke

Petrographic evidence for magma mixing in the Glen More ring dyke occurs in two forms. One is the relationship between granophyre and partially consolidated gabbro, discussed in section 12.2.3., the other, discussed in this section, is on a smaller scale and involves the blotchy appearance of the intermediate rock types, and the ferrodioritic enclaves in the granophyric rocks. The Sparks and Marshall (1986) model can be applied to the mixing relationships seen in the intermediate and acidic rocks in the Glen More ring dyke.

FIGURE 12.1. Diagrams outlining the processes limiting mixing of compositionally-contrasting magmas (from Sparks and Marshall, 1986).

a) Plot of TiO2 vs MgO for rocks from the Mullach Sgar complex, St Kilda.

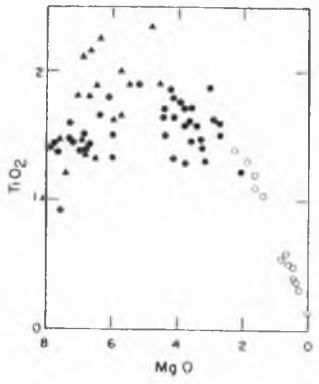

b) Schematic plot of TiO2 vs MgO showing the region in which magma mixing is prohibited. Compositions outside this zone are able to mix to varying degrees, accounting for the spread of data in the shaded region in figure 12.1a.

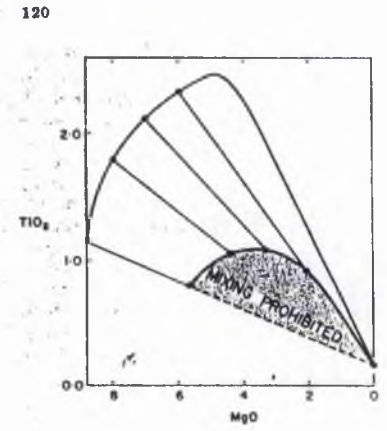

c) Composition mixing diagram illustrating the conditions leading to each of the three regions of viscosity (μ) contrast between relatively mafic (M) and felsic (S) magmas after they have reached thermal equilibrium.

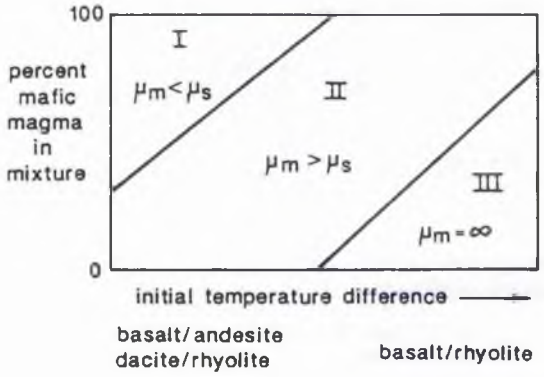

The rocks of the intermediate region, between 350m and 500m, have a heterogeneous blotchy appearance comrising discrete patches of diorite and granophyre, with resorption textures on edges of clinopyroxene and plagioclase crystals from the dioritic patches in contact with granophyric rocks. Mixing of dioritic and acidic magmas has not been complete. Vigorous mixing causes stretching out of included magma patches (Blake and Koyaguchi, 1991). This is not evident at Cruach Choireadail and so it appears that a less vigorous mixing regime operated and the dioritic magma has intermingled after partial crystallization, possibly as a crystal-liquid mush. The dioritic patches in the intermediate rocks are relatively rounded in shape, and do not show any signs of brittle deformation (i.e. no angularity), indicating that they were not rigid when they came into contact with the granophyre.

In the intermediate zone of the Glen More ring dyke there is a higher percentage of mafic magma in the mixture than in the upper granophyres. This means that its temperature here will have been higher after thermal equilibration than that higher up in the body. This will allow the mafic magma to crystallize more slowly in the dioritic part of the intermediate zone than in the granodioritic part, which has a higher proportion of acidic magma and has undergone less intermingling, probably on the boundary between areas 1 and 2 in figure 12.1c.

On chemical variation diagrams, the ferrodioritic enclaves plot at the intermediate end of the acidic-intermediate mixing trend, close to the whole rock composition GM4. The crystal morphologies in these enclaves suggest rapid crystal growth, and therefore fast cooling rates. This is consistent with a dioritic magma being surrounded by a cooler granophyric one and is a continuum of the mixing regime in the intermediate zone. In the granophyres a lower proportion of basic magma is preset which will become quenched on thermal equilibrium and mixing will be more limited than in the intermediate zone.

In the granophyres, ferrodioritic enclaves have been quenched and form rounded, ovoid patches. This indicates an intermediate initial temperature difference in a situation with a low proportion of mafic magma in the mixture, probably placing the mixture in the lower part of section 2 in figure 12.1 c.

Mixing in the Glen More ring dyke has taken place between granophyric and dioritic magmas, but not between gabbroic and granophyric magmas. Therefore the diorite must still have been partially molten (possibly as a crystal-liquid mush) to enable it to intermingle with the granophyre.

Evidence from geochemical modelling indicates that a magma of an intermediate composition is an unsuitable parental magma for the minerals found in the gabbroic

cumulates, and therefore rules out the possibility of gabbros and diorites forming by crystallization of an initial dioritic magma in the Glen More ring dyke.

New geochemical data for rocks from the Glen More ring dyke back up this magma-mixing interpretation. Major and trace element data for the acidic-intermediate group of rocks plot on straight lines on Harker-style diagrams. This trend could be produced by either fractional crystallization or by magma mixing. In the first situation, in order to satisfy the geometrical requirements of the trends, the fractionating mineral assemblage must include calcic-plagioclase, calcic-pyroxene, apatite and Fe-Ti oxides, with no potassium feldspar (in order to explain the increase in K_2O with decreasing MgO). These minerals are found in the intermediate rocks, but not as phenocrysts which have concentrated during fractional crystallization of an intermediate magma. Instead, the intermediate rocks have the appearance of intermingled magmas with discrete portions of dioritic and granophyric rock.

Whole-rock compositions do not plot on mixing lines between gabbroic and granophyric magma compositions. This is consistent with field evidence showing that the gabbro was more or less solid when granophyric magma was injected, and also fits the Sparks and Marshall (1986) mixing criteria, with such magmas being unable to mix due to large compositional and initial temperature differences.

Selected trace-element ratios, and plagioclase mineral chemistry display a bimodal distribution of data, split between gabbros, and intermediates and granophyres. This suggests contrasting sources of parental magmas of acidic and basic rocks, with the intermediate compositions resulting from mixing. This mixing is not between acidic and basic magmas, but instead is a product of intermingling of acidic and intermediate magma compositions.

The acidic rocks in the upper parts of the ring dyke at Cruach Choireadaill are not uniform in major and trace element composition. This phenomenon is also seen in the felsites of the Loch Ba ring dyke (Sparks 1988) and has been explained in that body as reflecting either a zoned top to the magma chamber from which magma was drawn, or as different amounts of contamination by a more mafic magma. At Cruach Choireadaill most of the granophyres that have been analysed contain ferrodioritic enclaves. The variable abundance of the enclaves could account for the compositional variation in these acidic rocks. On most geochemical plots the compositional range of the granophyres lies on a line between the most acidic sample (GM 19/MT 1) and the analysis of the ferrodioritc enclave analysis. This again supports a mixing scheme between granophyric and dioritic magmas as does the progressive decrease in enclaves upwards. Zoning at the top of an underlying magma chamber could also contribute to the variable composition of these rocks. Causes of such zoning could include crystal-liquid fractionation, wall melting, and

contamination of the melt by mixing with underlying, basic magmas. All of these mechanisms depend upon gravity-driven separation of magmas (Campbell and Turner, 1984).

12.2.2c Magma mixing with respect to magma intrusion into the ring dyke

In suggesting a magma-mixing scheme for the upper half of the Glen More body, the origin of the acidic magma is relatively simple to propose as much work on its origin has been undertaken in the Hebrides. Experimental work on Lewisian gneisses and Torridonian arkoses and shales (Thompson 1981, 1983) indicates that the acidic magmas in the BTIP have an input from melting of leucocratic portions of these rocks in the crust beneath the Tertiary intrusive centres, although trace element ratios indicate that fractional crystallization also has a major input in their development. Trace element data in this study (chapter 9) suggests a high partial melting input. The melting could be of amphibolite or granulite facies Lewisian rocks, or of Moine schists.

The origin of the other end member of the the mixing scheme is more problematic. If dioritic magma is the other end member in the intermediate rock sequence, then two possible origins exist for its source. These are:-
1) It is a residual product of a basic magma in the ring dyke fissure from which the gabbros have formed as cumulates.
2) It was injected at the same time as the basic magma from a compositionally-zoned magma chamber, where it was possibly formed by fractionation processes.

If both gabbroic and dioritic magmas had been injected simultaneously from a zoned magma chamber, one would expect to see mixing evidence and contact relationships between the two with blobs of dioritic magma in gabbros and *vice versa*.. Possibly due to the limited exposure, this is not seen in this body.

A compositionally zoned magma chamber beneath the Mull intrusive centre has been proposed for the Loch Ba centre (Sparks 1988), where a rhyolitic magma is thought to have overlain a sequence of magmas ranging from rhyolite at the top to at least mafic andesite at the base. The currently accepted view of the origin of this zoning is one of crystallization at the margins of the chamber producing buoyant liquids that separate and pond in the uppermost parts of the body due to gravitational separation combined with partial melting of country rocks (see figure 1.1 in chapter 1). These ideas have been based upon experiments with aqueous salt solutions (McBirney et al 1985, and Huppert et al 1986) and the process is thought to produce a superheated, crystal-free, stratified interior to the magma chamber. If this also happened in a chamber beneath the Beinn Chaisgidle centre, then it could be consistent with intrusion of a stratified sequence of olivine gabbroic, quartz gabbroic and quartz dioritic magmas into the initial fissure. This would

have to be from a chamber without a silicic top, as no silicic magma is seen that could have intruded at the same time as the basic magma.

Conversely, if the olivine gabbro-quartz gabbro-quartz diorite sequence developed *in situ* then the initial injection of tholeiitic olivine basaltic magma must have come from either an unzoned chamber or from a zoned one which has undergone recent mixing to homogenise the chamber. This latter possibility could be caused by the turbulent injection of a new pulse of magma into the chamber, destroying any previously existing stratification.

Therefore from the available evidence it is impossible to decide whether the gabbros are the result of emplacement of a zoned magma or *in situ* differentiation of an initially homogenous magma.

Gabbros in the ring dyke are plagioclase-rich cumulates, their whole-rock compositions plot on trends on variation diagrams, and they display parallelism of trends on spiderdiagrams. The dioritic sample GM4 also displays the same parallelism and lies on an extension of the gabbroic variation diagram trends. It shows no textural signs of having mixed with the granophyres or gabbros and so is interpreted as being derived by fractionation of tholeiitic basaltic parental magma. Sample GM4 and the ferrodioritic enclave analysed from the granophyres are thought to be of a composition very similar to the intermediate end-member of the acidic-intermediate mixing sequence and could be the link between basic and acidic groups of data points on the variation diagrams.

12.2.3 Petrographic evidence for a double injection mechanism.

12.2.3.1 Introduction

Bor (1951) and Marshall (1984) propose conflicting intrusion mechanisms for mixed magma ring intrusions. Bor proposes an initial gabbroic intrusion followed by the granophyre, while Marshall proposes a single injection of contrasting magmas from a zoned magma chamber. The current study supports the double injection mechanism, the evidence for which is discussed in the following section.

12.2.3.2 Field relations supporting two magma injections

At both Cruach Choireadail and Maol Tobar gabbro is veined by granophyre along rectilinear joints (possibly contraction joints). At Maol Tobar the granophyre contains xenoliths and xenocrysts of the gabbro, possibly broken off during intrusion of the granophyre. In other gabbro outcrops granophyre is seen interstitially, possibly where it has filtered into the network to fill intercumulus voids. Conversely this granophyre may be a residual product of crystal-liquid fractionation, with the granophyre constituting the trapped final melt fraction. At the localities near Loch Airdeglaiss, granophyre and gabbro

crop out closely together with no development of intermediate lithlogies. This evidence suggests strongly that the gabbro had solidified at these localities when the granophyre intruded.

In contrast to the above, in the Cruach Choireadail area the granophyre has come into contact with dioritic magma and has been able to intermingle, suggesting that solidification was incomplete when the granophyre intruded. An intermediate , dioritic, magma remained partially molten at the time of granophyre emplacement.

If granophyric magma existed in an underlying zoned magma chamber, it would have overlain any gabbroic magma in the chamber due to its density difference. On formation of a ring dyke fissure by block subsidence, one would expect the pre-existing layering to be preserved in an intrusion and for granophyric magma to be injected into the fissure above the gabbroic magma. Such layering is seen at Cruach Choireadail and at Choire Ghaibhre but not at Loch Airdeglaiss, where the granophyre occurs below and at the same level as gabbro. This suggests that the magma chamber underlying the Beinn Chaisgidle intrusive centre was not capped by acidic magma at the time of the initial formation of the Glen More ring dyke. It may have been stratified, however, with magmas ranging in composition from tholeiitic basalts to diorites. This fractionated sequence may have intruded to form the initial, basic part of the Glen More ring dyke (see previous section).

The origin of acidic magmas in the British Tertiary Igneous Province (see section 12.2.2 c) has been debated over the past decade (e.g. Thompson 1981, 1983). It is now commonly believed that magma chamber fractionation is dominated by side-wall and roof crystallization, with a degree of input from melting of sialic country rock. Recent work in the British Tertiary Igneous Province suggests that acidic and basic magmas are cogenetic and frequently existed together in one magma chamber (Bell 1983). Prior to the formation of the Glen More ring dyke, the Ishriff granophyric ring dyke was intruded, indicating that acidic magma was previously available in what was probably the same magma chamber which fed the Glen More fissure. The intrusion of the Ishriff ring dyke may have taken the acidic top from the magma chamber and left a basic magma chamber for subsequent intrusion into the Glen More ring dyke. Replenishment of the magma chamber by a tholeiitic magma during or after the Ishriff intrusion may have caused mixing and destroyed any stratification in the body to produce a homogenous tholeiitic basaltic magma chamber.

12.3 Structural Evolution of the Glen More ring dyke

12.3.1 Introduction

This section considers ring dyke formation mechanism (i.e. central block subsidence) with respect to the Glen More ring dyke, and proposes an intrusive model to fit in with the regional history of the Mull Central intrusive complex. This takes into account the northwestward migration of the intrusive centre.

12.3.2 A potential mechanism for a double intrusion of magmas (see figure 12.2)

It has been shown in this study that granophyric magma intruded into the Glen More ring dyke after the gabbroic magma, and that the gabbroic magma had already consolidated when this happened. The nature of the underlying magma chamber and the movement of central blocks into it are therefore important factors in explaining the nature of intrusions into the ring dyke fissure in Glen More.

For two intrusions of magma to occur in the Glen More body, reactivation of the ring dyke fissure must occur while magma is still present in the underlying chamber. The second event in the sequence has tapped a granophyric magma, while the initial one caused a tholeiitic basaltic magma or a layered basic magma to intrude into the fissure. If the initial block subsidence was into a compositionally zoned magma chamber then magmas of variable composition would be expected to intrude. This is a possibility with gabbroic and dioritic magma, but acidic magma was not present during the first intrusion, as this would have been at the top of the chamber and should therefore have intruded into the ring fissure above the gabbro and at the same time as it. Field relationships have shown that this is not the case.

Two possibilities exist to explain the magma plumbing system underlying the Beinn Chaisgidle centre during the intrusion of the Glen More body:-
1) Granophyric and gabbroic magmas were tapped from separate magma chambers.
2) The acidic magma was formed at the top of a layered magma chamber after an initial block subsidence caused emplacement of the gabbroic part of the body (see figure 12.2). The acidic magma was formed by either fractionation, country rock melting, by an acidic injection from another magma chamber, or a combination of these. Trace element data and spiderdiagrams suggest that the granophyric magma (GM19 and MT1) was produced by fractionation of a gabbroic magma, with a limited amount of contamination by fusion of silicic crustal material.

The presence of both acidic and basic magmas in the magma chamber beneath the Beinn Chaisgidle intrusive centre, throughout its history, is implied from the presence of both basic and acid ring intrusions. The magma type feeding these intrusions changes several

FIGURE 12.2. Sequence of events responsible for the differentiated nature of the Glen More ring dyke.

a) Initiation of ring-dyke fissure as pressure decreases in the underlying chamber. The underlying magma chamber contains either, (i) tholeiitic basaltic magma, or (ii) basaltic magma overlain by dioritic magma.

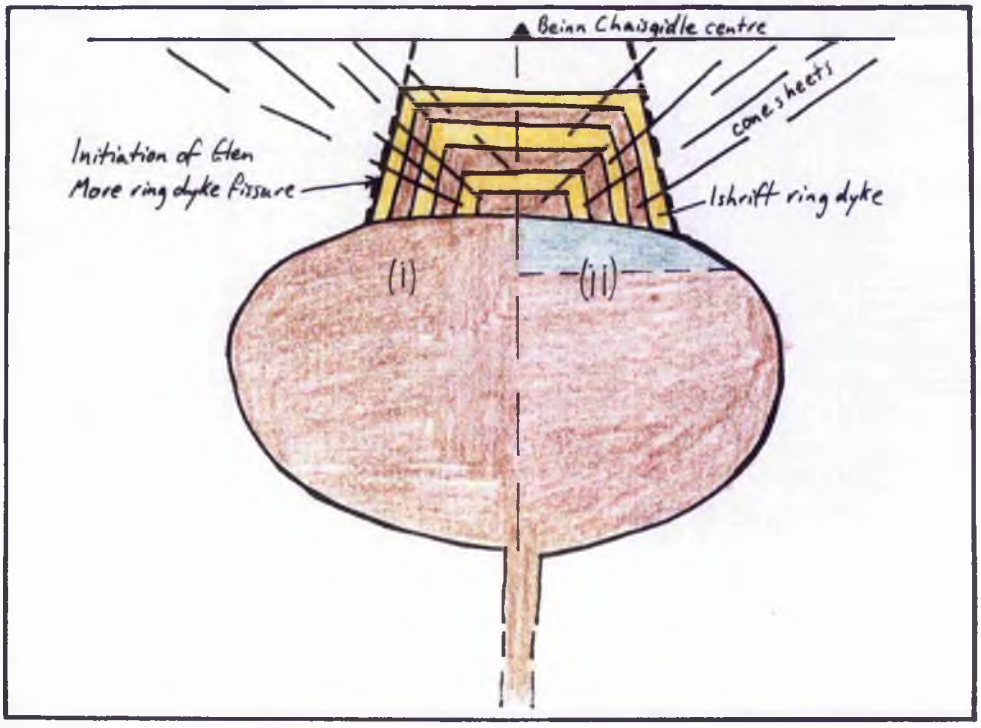

b) Subsidence of a central block comprising previously formed ring dykes (eg. Ishriff ring dyke) and screens of basalt. The underlying magma intrudes into the gap produced by subsidence.

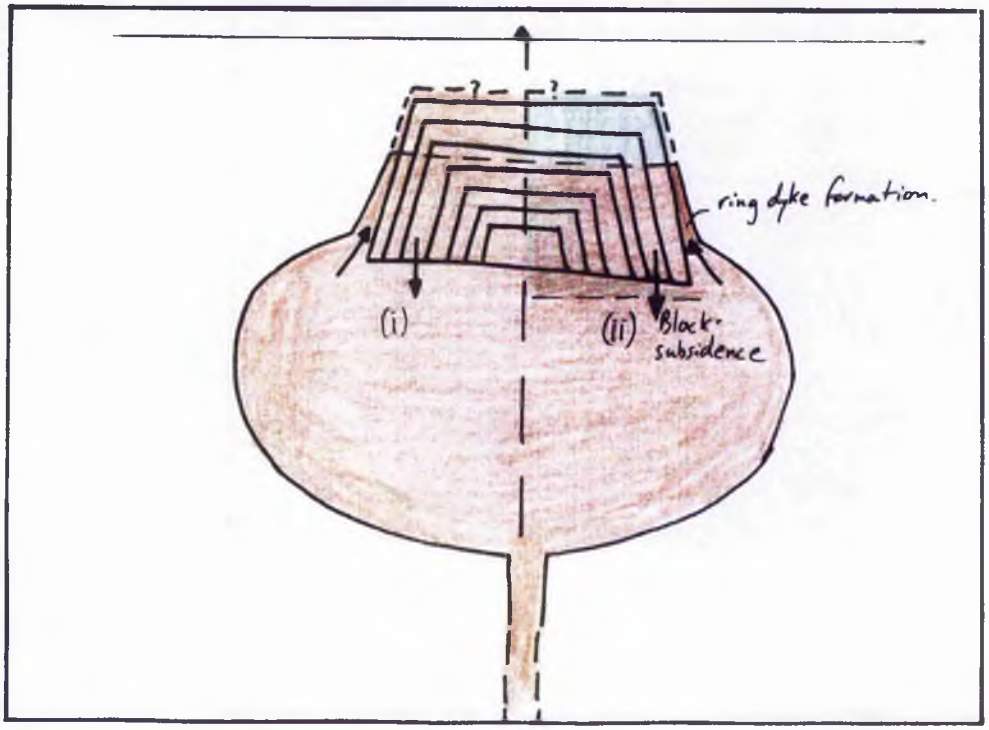

c) (i) Tholeiitic basaltic magma undergoes crystallization to form olivine and quartz gabbro cumulates and a dioritic crystal-liquid residual mush, or (ii) basaltic magma crystallizes to form gabbroic cumulates, and the dioritic magma cools to form a dioritic crystal-liquid mush. The end result of these two processes is identical. Meanwhile, the underlying chamber produces a silicic upper layer by side-wall crystallization, assimilation of silicic country rocks, and possibly injection of silicic magma from a more evolved chamber.

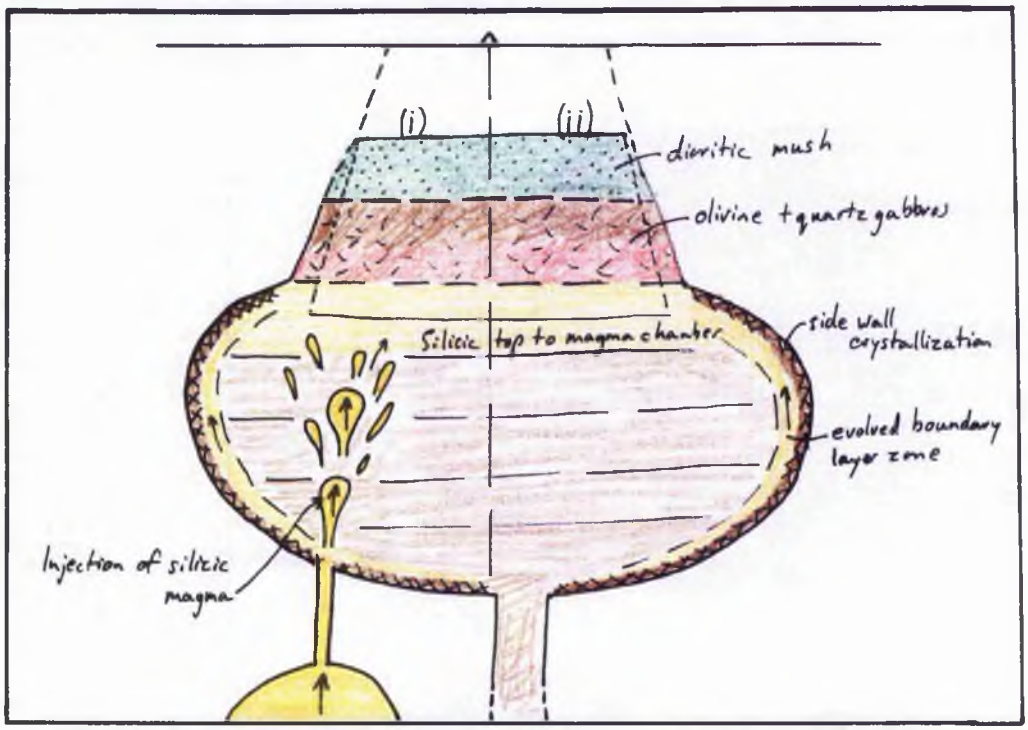

d) Reactivation of the ring dyke fissure, with the central block (containing the consolidated gabbro of the Glen More ring dyke and the initial central block) subsiding into the silicic magma at the top of the underlying chamber. This magma intrudes, possibly up a pipe-like structure at Loch Airdeglaiss, to the top of the ring dyke fissure and spreads out latterally. It intrudes into cooling joints in the gabbro and mixes with the dioritic crystal-liquid mush to form the intermediate zone.

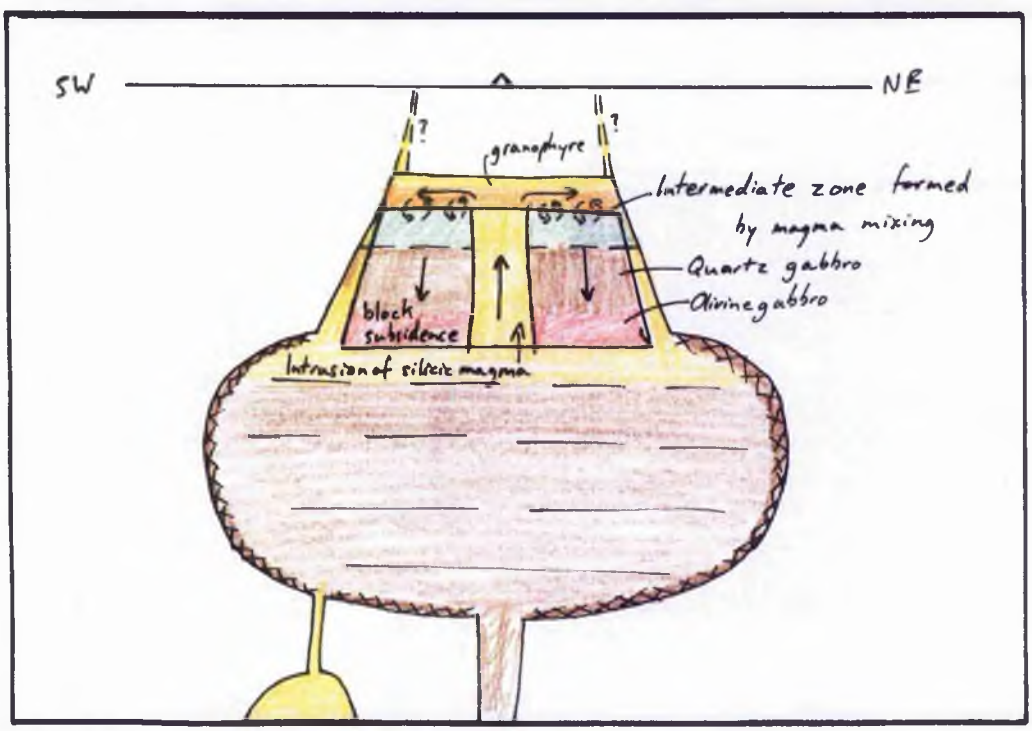

times during the activity of the Beinn Chaisgidle centre. The Glen More ring dyke is the last in the sequence of many ring intrusions, presumably all derived from the same chamber. The one preceding Glen More was the Ishriff ring dyke. an entirely acid dyke, indicating quite rapid and distinct changes in magma composition in the chamber.

This indicates that the magma chamber is capable of changing from acid to basic, and back to acid if the two-intrusion model is accepted for the Glen More ring dyke, very effectively. Three mechanisms can be thought of that may each be partially responsible for this:-
1) Side-wall and floor crystallization in the magma chamber with release of a low-density, more evolved magma which can convect buoyantly and pond beneath the top of the magma chamber (eg. Brophy, 1990).
2) Partial melting or assimilation of acidic country rocks to produce silicic magmas which will rise to the top of the chamber due to their lower density.
3) Silicic magma injected into the chamber from another magma body, and rose to the top of the magma chamber. The other magma chamber could be one in which silicic magma is produced by a combination of mechanisms 1 and 2.

As changes of magma at the top of the feeder chamber take place between consecutive ring dyke intrusions, a rapid process is required. Mechanism 3 is potentially the most rapid of the above options, and is therefore favoured here, possibly with a contribution from mechanisms 1 and 2.

One striking feature of the Glen More ring dyke is that it is only seen on the south side of the Beinn Chaisgidle centre, in an asymmetric outcrop pattern. This is characteristic of almost all of the ring dykes around this centre and could be due to either:-
1) the northern half of the ring dyke has been overprinted by later intrusions of the Loch Ba centre.
or, 2) the ring dyke were formed by subsidence of asymmetrical blocks and this semi-circular outcrop is their full development.
The first of these is favoured here as it is the easiest to explain.

Figure 12.2 is a series of schematic diagrams illustrating the sequence of regional events that have caused the petrological variations seen in the Glen More ring dyke. It is envisaged that the initial intrusion into the fissure was either a tholeiitic basaltic magma, or a series of magmas ranging from olivine-gabbroic at the bottom to dioritic at the top. This magma crystallized in the ring dyke to form olivine- and quartz-gabbros and a dioritic residual magma (figure 12.2a). Following substantial cooling and crystallization of the magma, when the gabbro was solid but the diorite was still a mush, there was reactivation of the ring fracture as the pressure in the magma chamber subsided. A second block subsidence event, with the central block this time including the solidified gabbro, formed a fracture which tapped acidic magma at the top of the underlying magma

chamber. This acidic cap to the chamber had evolved since the initial ring dyke intrusion at Glen More, by the processes described previously (figure 12.2b). This intruded up the southern side of the gabbros at Maol Tobar, filled the space alongside and above the gabbros in the ring dyke at Cruach Choireadail and Choire Ghaibhre, and intermingled with the residual dioritic magma mush (see figures 12.2c and d).

From a combination of the coarse grain-size in many of the intrusions in the central igneous complex, gravity and magnetic surveys (Bott and Tantrigoda, 1987), and from the inward dip of cone-sheets, which gives an estimated measurement to the top of the underlying magma chamber, depths of between 1 and 4 km have been estimated for crystallization of magmas in these intrusions (Emeleus, in Craig, 1991). This is supported by chemical analyses of olivine in this study (see chapter 8).

The acidic portion of the Loch Ba ring dyke is interpreted as an unerupted, welded tuff, and its ring fracture probably extended to the surface to feed eruptive vents (Sparks 1988). The Loch Ba and Glen More ring dykes are at approximately similar elevations and so it is conceivable that the Glen More fissure also extended close to the surface. If so, and if we assume that a certain amount of the injected acidic magma reached the surface and erupted, then the granophyres in the Glen More dyke were probably not the most acidic magmas in the underlying chamber, as these would have been the first to be intruded into the fissure in this second injection. In comparing GM19 (the least contaminated/most evolved composition sampled in the Glen More body) with MT1 (from the Ishriff ring dyke) and the Loch Ba sample (Sparks 1988) we can see that yet more acidic magmas were present beneath the Mull intrusive centres than are exposed in the Glen More ring dyke. This supports the view of the Glen More ring dyke feeding surface vents on its reactivation.

12.4 Sequence of events in the Petrogenetic Scheme (see figures 12.2 and 12.3)

1) Initial formation of Glen More ring dyke fissure. A central block of basalts and previously formed ring dykes and cone sheets subsides into an underlying chamber of tholeiitic basaltic magma or a zoned magma chamber which contains magmas ranging from olivine-gabbroic to dioritic in composition. The subsidence is probably associated with a decrease in pressure in the underlying magma chamber and occurs in a hypabyssal environment. Subsidence may be associated with the migration of the intrusive focus to the NW during the Tertiary period on Mull. The intrusion appears to have formed in an asymmetrical semi-circular fissure, but this may be deceptive as the northern half of the body could be overprinted by later intrusions.

2) Depending on the magma intruded into the fissure, either;

FIGURE 12.3. petrogenetic scheme for magma mixing in the Glen More ring dyke.

The second block subsidence event forces acidic magma to intrude alongside the subsided block, which contains the already consolidated gabbro cumulates, and above the dioritic mush. Granophyre veins form as the acidic magma intrudes into rectilinear joints in the gabbro. Mixing takes place between the dioritic mush and the newly emplaced acidic magma to form the intermediate zone, and dioritic blebs are quenched in the acidic melt to form elongate, rounded enclaves.

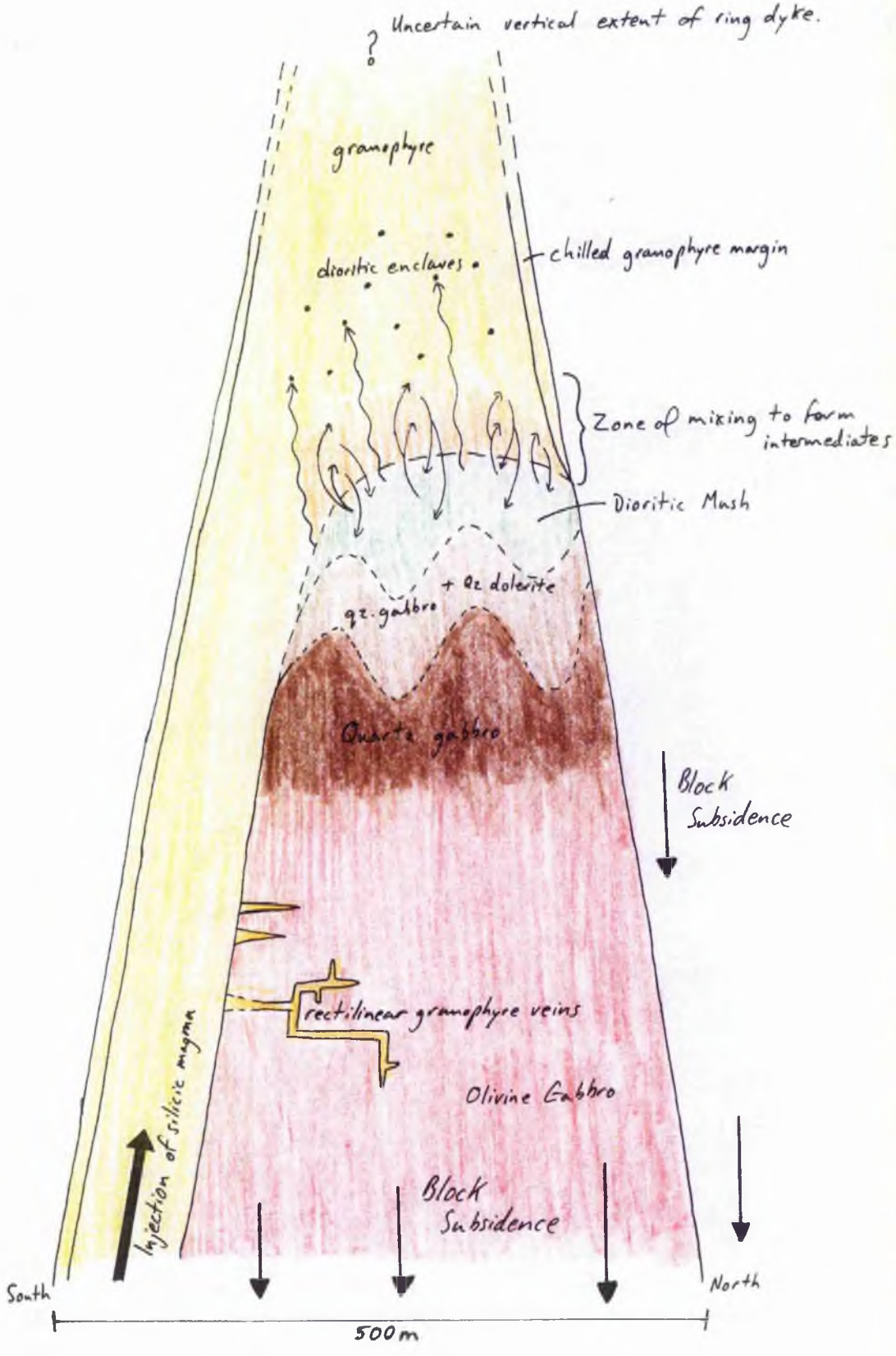

a) Crystallization begins as the tholeiitic magma cools. Fractionating mineral assemblages are dominated by calcic-plagioclase and also contain forsteritic olivine, calcic-augite, and Fe-Ti oxides. They form plagioclase-rich olivine gabbro cumulates with a quartz-normative gabbroic residual magma. This residue crystallizes as plagioclase rich quartz gabbros, leaving a dioritic residual magma above the olivine gabbros.
or b) the sequence of olivine-gabbroic, quartz-gabbroic, and dioritic magmas begin to crystallize. They cool until olivine- and quartz-gabbros are almost completely consolidated but dioritic magma remains, possibly as a mush, above then.
In (a) it is unclear whether *in situ* crystallization or crystal settling is responsible for the differentiation of the magma. Rectilinear jointing developes in the gabbros due to contraction during cooling, crystallization and consolidation.

3) The underlying magma chamber evolves into a zoned body with acidic magma beneath its roof. The acidic magma is of roughly the same composition as that which intruded into the Ishriff ring dyke before the gabbroic part of the Glen More ring dyke was intruded. The acidic top to the magma chamber could have developed by a variety of mechanisms. These include:-

- Fractional crystallization including side-wall crystallization and buoyant boundary layer release.
- Injection of melts derived by partial fusion of the acidic portions of Lewisian and Moine country rocks.
- Injection of acidic magma from another magma chamber.
- A combination of the above.

4) Migration of the intrusive centre towards the Loch Ba intrusive centre, causes a further decrease in pressure in the magma chamber beneath the Beinn Chaisgidle centre.

5) The Glen More ring dyke fissure reactivates due to this pressure decrease beneath the Beinn Chaisgidle intrusive centre.

6) The reactivation of the ring fissure causes subsidence of a central block (comprising the original central block and the solidified gabbros of the initial intrusion). The subsidence forms a gap, near to Loch Airdeglaiss, where acidic magma intrudes outside the original gabbro and fills gaps above the gabbros at Cruach Choireadail and Choire Ghaibhre. Acidic magma intrudes into joints in the gabbros and mixes with the dioritic magma residual from gabbro crystallization, producing a mixing zone containing patches of diorites in a fine-grained granophyre. Smaller blobs of dioritic magma were included in the acidic magma and quenched before they could mix thoroughly, due to the temperature difference with the cooler acidic magma.

Chapter 13. Summary and suggestions for further work

This chapter is a synopsis of the findings of this study. Some suggestions for further work to develop the findings of the preliminary experiments in this study are given in the final section of this chapter, along with suggestions for future work relating to the Glen More ring dyke, and the Mull intrusive complex.

In chapter one recent petrological, experimental and geochemical work on convective processes and its implications for differentiation processes in igneous geology was reviewed. Although it appears to be currently accepted that crystallization can produce density differences in magmas, sufficient to cause convection, chapter one points out that this process has not yet been demonstrated using experiments in silicate melts. The experimental work described in this study follows on from crystal dissolution experiments in rock melts carried out in this laboratory (Donaldson, 1993), and is the first known work of this type to examine boundary layer convection next to growing crystals in silicate melts.

This project was initially a three-pronged attempt to test for compositional convection in silicate melts. However due to the failure to find suitable glassy porphyritic material, and the findings about the Glen More ring dyke it has been necessary to write this thesis in two self-contained units, the first (part A) describing the experimental study, and the second (part B) detailing the petrography and petrogenesis of the Glen More body.

The experimental work initially followed a problem-strewn path until a relatively satisfactory experimental method was found. The experimental techniques attempted, the melt systems used, and the problems associated with each were described in chapter two. Each technique, with the exception of the wire-loop technique, produced convective phenomena that could be applied to magma chambers. The most successful technique used involved cementing crystal seeds to crucible floors with alumina cement to keep them *in situ* during crystal growth experiments.

Olivine growth experiments in a synthetic basaltic melt were reported in chapter 3. Thin compositional boundary layers, depleted in Co and Mg and enriched in Si, formed at crystal-liquid interfaces, and were detected above the crystal seeds. In longer duration runs Co-Mg-depleted melt was detected at the meniscus. As the crystal seeds do not come into contact with the meniscus (thus ruling out surface tension-driven convection) and a stabilizing temperature gradient exists in the charges, the Co-Mg-depleted melt must have attained its final position in the crucibles by compositional-driven convection associated with olivine growth. The relatively small compositional variation (upto 20 % decrease in CoO and MgO in melt above crystal

apexes) across thin (<50 μm) boundary layers is the product of the experimental design which encourages boundary layer convection at an early stage in its development. This stopped thick boundary layers forming and caused them to convect when only small depletions of Co and Mg existed.

The fluid dynamics associated with dissolution of hematite, through an intermediate layer of hoegbomite, were studied in chapter 4. Dissolution produced a dense, Fe-rich boundary layer that sank in the host melt. The presence of the dense melt above hematite seeds suggested that other convective processes can override the density differences. The action of bubbles rising through the crucibles was probably the main process responsible for this, although the rise of buoyant melt produced by hercynite crystallization on side-walls may also have affected movement of the dense melt.

The experiments in chapters 3 and 4 have both produced side-wall crystallization of hercynite. This crystallization caused a boundary layer zone of Co and Mg, or Fe and Mg depleted melt to form. The boundary layer zone remained discrete from the rest of the melt in the crucibles, probably due to its increased viscosity, and was able to rise up the side-walls and pond beneath the meniscus. Side-wall and floor crystallization of hercynite is directly analogous to crystallization of ferromagnesian minerals at the margins of magma chambers.

In chapter 5 the various convective phenomena seen in the two sets of experiments were likened to processes in magma chambers. Although the experimental crucibles cannot be regarded as mini-magma chambers the observations (buoyant boundary layer production and convention, bubble-aided convection of dense crystals and melt, and side-wall crystallization with the production of a buoyant boundary layer zone) prove that convection driven by density differences will take place in low viscosity silicate melts, and will therefore be active in magma chambers.

In the second part of this thesis a petrogenetic scheme for the evolution of the vertically-differentiated, gabbro-granophyre Glen More ring dyke was suggested after field and petrographic evidence had been re-examined and new geochemical data had been considered. The Glen More ring dyke provided arguably the best chance in the U.K. of testing for the effects of compositional convection in a vertically differentiated body.

Chapter 6 provided the background information for this study by reviewing the regional geological setting of, and previous work on, the Glen More body. Field relations from throughout the body were investigated and it was found that petrographic variation is not governed by altitude, as had been emphasized previously, but that granophyre is found above, alongside, below, and within the

gabbros. In chapter 7 petrographic descriptions were given for the type locality, Cruach Choireadail. Olivine gabbros are found at the bottom of the vertical section and granophyres at the top. Above the olivine gabbros, quartz gabbros merge into dioritic rocks with a blotchy appearance. The blotchiness comprises of a dioritic portion surrounded by granophyric material. The proportion of granophyre increases upwards in this intermediate zone until the rocks are entirely granophyric, containing small, rounded, ferrodioritic enclaves.

Electron-probe microanalysis of minerals in the Glen More rocks was reported and reviewed in chapter 8. Olivine compositions indicate that they crystallized from a basaltic magma under hypabyssal conditions. The small variation in clinopyroxene compositions in the gabbros is probably caused by slight evolution of magma composition either *in situ* or in the feeder magma chamber, becoming more Fe-rich moving from olivine to quartz-normative gabbros. A much wider spread in clinopyroxene composition was found in the quartz gabbros and intermediate rocks, and is thought to have been produced by the effect of acidic magma reacting with dioritic portions of the intermediate rocks. Plagioclase feldspar composition ranges from An_{70} in the olivine gabbros to An_5 in the granophyres. In the intermediate rocks there is a wide-range of compositions, probably caused by varying degrees of interaction of granophyric magma with a dioritic crystal-liquid mush.

The new geochemical data presented in chapter 9 show a range of compositions of gabbros describing an Fe-enrichment trend. This, combined with the mineral chemistry and the plagioclase-rich cumulate nature of many of the gabbroic samples, indicates that the gabbros could have evolved by fractional crystallization of a basaltic magma, or by cooling of a zoned basaltic-dioritic magma body. Dioritic, intermediate and granophyric rock compositions plott consistently on straight lines on variation diagrams. This fact combined with textural evidence strongly suggests a magma mixing origin for this range of rocks.

The evidence found in this petrographic study was summarized in chapter 10 and possible petrogenetic schemes for the evolution of the Glen More ring dyke were suggested. These schemes were discussed in chapter 11 and the most likely one was examined using a least-squares mixing programme. The modelling supports petrographic evidence and strongly suggests a petrogenetic scheme involving two injections of magma into the ring dyke fissure, basic followed by acidic, with mixing taking place between acidic and dioritic magmas at Cruach Choireadail. Mixing did not take place between granophyres and gabbros as gabbro had already consolidated when the granophyric magma intruded. The proposed petrogenetic scheme was discussed in chapter 12, along with its significance for the nature of the magma

chamber which fed the Beinn Chaisgidle intrusive centre. Magma mixing has been responsible for the petrographic variation in the Glen More ring dyke.

In summary, part A of this thesis provides evidence that begins to prove the importance of compositional-driven convection associated with crystallization in silicate melts. In order to evaluate the full effects of this process more experiments need to be carried out with other minerals, melt compositions and crystal orientations. The ability of high and low density melts to convect, both spontaneously and with the help of bubbles, has been proved. It seems probable that compositional convection will accompany crystallization in magma chambers, however it is unlikely that the overall compositional effects of this process can be differentiated from that of other crystal-liquid fractionation processes, unless the boundary layer melt remains discrete. This is unlikely if other convective processes (eg. temperature driven convection) are as active as has been predicted. Part B of this thesis has shown that the petrographic variations in the Glen More ring dyke are the result of mixing of acidic and dioritic magmas intruded during two separate events. The proposed petrogenetic scheme does not rule out the possibility of compositional-driven convection producing either ,a) a dioritic residual magma from fractional crystallization of gabbroic cumulates from an initially homogeneous basaltic magma in the ring dyke, or b) zoning in the underlying magma chamber involving magmas ranging from basic to intermediate in composition.

Suggestions for further work

As this has been the first experimental study of its type using silicate melts, it has been riddled with problems. However it has now provided a relatively successful means of observing boundary layer behaviour around fixed crystal seeds.

In order to observe boundary layers optically, larger compositional variations need to be produced than are seen in this study. To produce larger compositional variations, compositional-driven convection needs to be suppressed. Using a more viscous melt system is one way of doing this as bigger density differences would be needed to drive compositional convection. To do this larger degrees of Fe/Co depletion are needed, and these bigger compositional differences may produce colour differences in the glass produced on quenching. However olivine may not crystallize from more intermediate, viscous melts. Another method of producing thicker boundary layers, which may be detected more easily, is to suppress convection by overgrowing olivine on a horizontal surface so that a bigger thickness of melt has to develop before it becomes unstable and can convect (see figure 13.1). This would necessitate long duration runs at low degrees of supercooling much as would be expected in magma chambers. However, problems of melt reaction with crucible and cement might then

dominate behaviour. Furthermore, crystals do not ordinarily grow in nature with a large face horizontal, so inhibiting boundary layer release.

Side-wall crystallization of hercynite, a by-product of these experiments, has been very successful in producing a buoyant boundary layer near crucible walls. This phenomenon could be developed in further experiments using the Co basalt melt to grow olivine on a side-wall by inducing crystallization on the wall of a cold finger introduced into experimental charges (see figure13.2). Such experiments have been carried out in aqueous salt solutions (Turner and Gustafson, 1981). Problems that would have to be overcome include:-

1) If Al_2O_3 tubes were used then hercyite growth may be induced by high Al_2O_3 concentrations in the glass around the finger.
2) Surface tension associated with the contact between the finger and the melt's meniscus might drive convection.
3) Finding an affordable inert finger may prove impossible.
4) Bigger crucibles would have to be used and therefore more melt would need to be produced. If synthetic melt is used, much time will need to be devoted to its preparation, unless means of scaling up synthesis procedures can be developed.

Further work on the Glen More ring dyke could include the following:-

- A more detailed study of the chemistry of the enclaves in the granophyres. This may reveal compositional variation from enclave to enclave that throws more light onto their origin.
- A study of other ring dykes associated with the Beinn Chaisgidle centre to examine the compositional evolution of the magma chamber system underlying this intrusive centre.
- Isotopic studies may indicate whether the granophyric magmas were produced by fractional crystallization of more basic parental magmas or by fusion of the country rocks.

FIGURE 13.1. Possible experimental design for developing thick compositional boundary layers on a horizontal crystal nucleation and growth surface. This may allow enough Co-depletion to develop in a boundary layer in the synthetic basalt for the boundary layer to be more easily detectable in thin section.
T > 1250°C to allow slow crystal growth rates. X>>>Y.

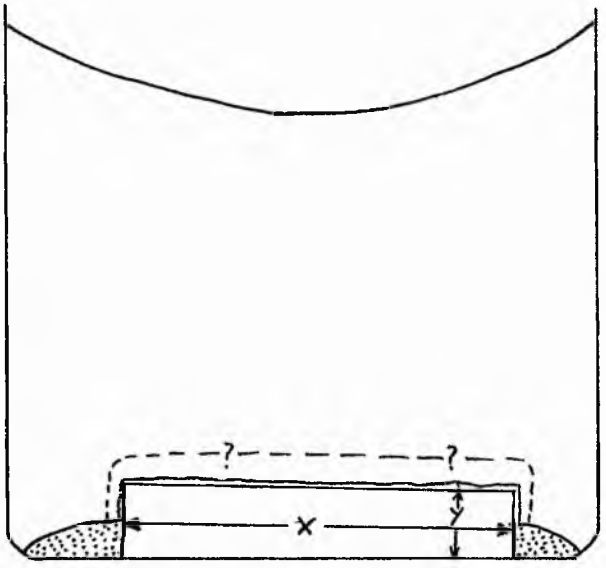

FIGURE 13.2. Possible experimental design to induce olivine crystallization on a cold finger in a basaltic melt.

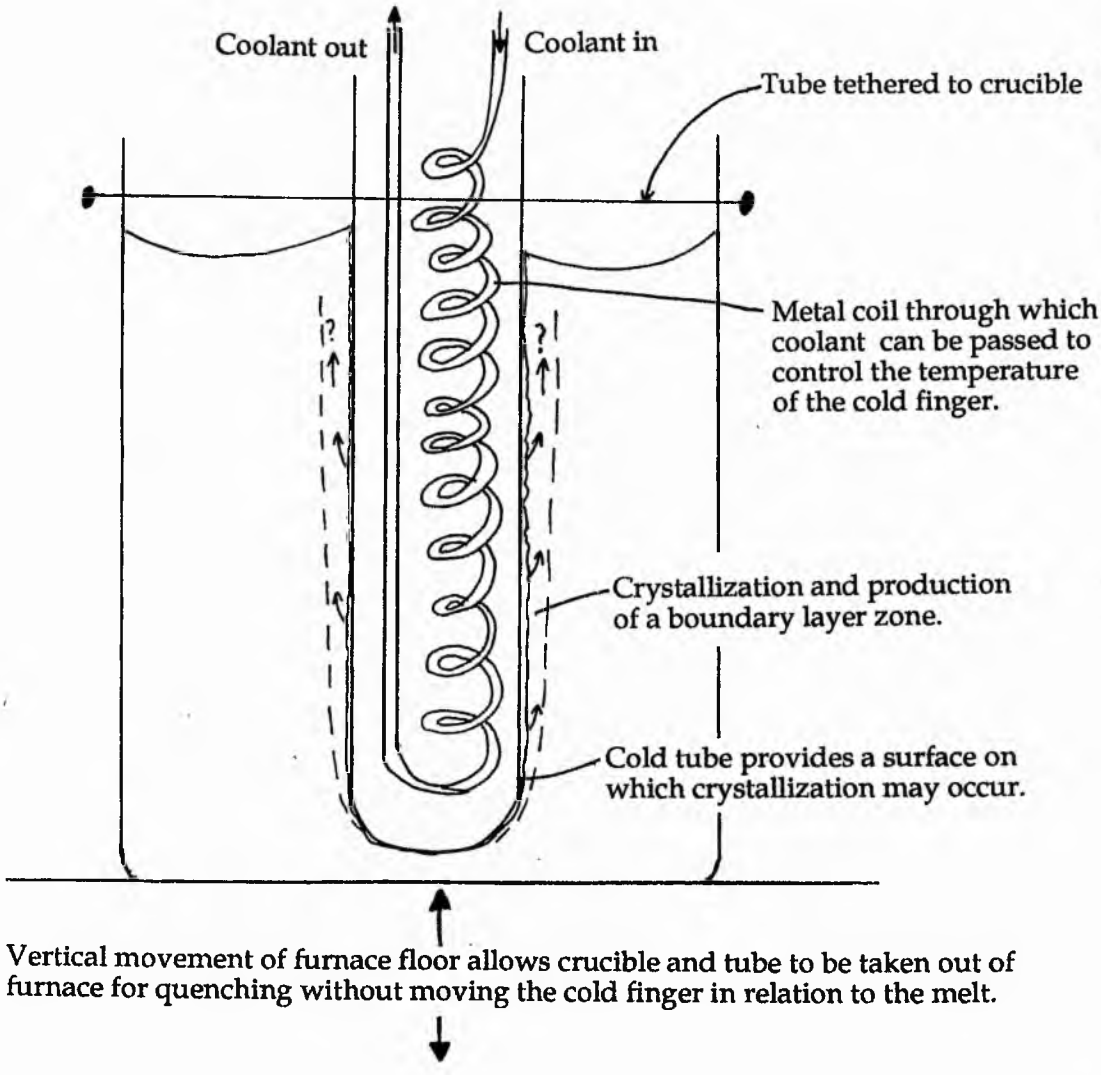

REFERENCE LIST

BAILEY EB, CLOUGH CT, WRIGHT WB, RICHEY JE, and WILSON GV. 1924. Tertiary and Post-Tertiary geology of Mull, Loch Aline and Oban. *Memoirs of the Geological Survey of Scotland.*

BARTLETT RN, 1969. Magma convection, temperature distribution, and differentiation. *American Journal of Science.* 267, 1067-1082.

BEDARD JH, KERR RC, and HALLWORTH MA, 1992. Porous sidewall and sloping floor crystallization experiments using a reactive mush; implications for the self-channelization of residual melts in cumulates. *Earth and Planetary Science Letters.* 111, 319-329.

BELL BR. 1983. Significance of ferrodioritic liquids in magma mixing processes. *Nature.* 306, 323-327.

BLAKE S and KOYAGUCHI T, in DIDIER J, and BARBARIN B (Eds) 1991. Enclaves and granite petrology. Developments in Petrology 13. *Published by Elsevier Press.*

BOR L. 1951. The Glen More ring dyke, Mull. *Unpublished PhD Thesis.* University of Cambridge.

BOTT MHP and TANTRIGODA DA, 1987. Interpretation of the gravity and magnetic anomalies over the Mull tertiary intrusive complex, NW Scotland.

BOTTINGA Y and JAVOY M, 1990. MORB degassing: bubble growth and ascent. *Chemical Geology.* 81, 255-270.

BOTTINGA Y and WEILL DH, 1970. Densities of iquid silicate systems from partial molar volumes of oxide components. *American Journal of Science.* 269, 169-182.

BOWEN NL, 1928. The evolution of the igneous rocks. Princeton University Press, Princeton.

BROPHY JG. 1990. Andesites from northeastern Kanaga Island, Aleutians. Implications for calc-alkalinefractionation mechanisms and magma chamber development. *Contributions to Mineralogy and Petrology.* 104, 568-581.

CAMPBELL IH, 1978. some problems with the cumulus theory. *Lithos.* 11, 311-323.

CAMPBELL IH *et al*, 1978. Crystal buoyancy in basaltic liquids and other experiments with a centrifuge furnace. *Contributions to Mineralogy and Petrology.* 67, 369-377.

CARRUTHERS JR, 1976. Origins of convective temperature oscillations in crystal growth melts. *Journal of Crystal Growth.* 37, 13-26.

CHAPMAN CA. 1966. Paucity of mafic ring dykes- Evidence for floored polymagmatic chambers. *American Journal of Science.* 264, 66-77.

CLOUGH CT, MAUFE HB, and BAILEY EB. 1909. The cauldron subsidence of Glen Coe and the associated igneous phenomena. *Quarterly Journal of the Geological Society of London.* 65, 611-678.

COONS WE, HOLLOWAY JR and NAVROTSKY, 1976.. Co^{2+} as a chemical analogue for Fe^{2+} in high temperature experiments in basaltic systems. *Earth and Planetary Science Letters.* 30, 303-308.

COONS WE and HOLLOWAY JR, 1979. Cobaltous oxide as a chemical analogue for ferrous iron in experimental petrology: An alternative solution to the iron-loss problem. *American Mineralogist.* 64, 1097-1106.

CORIELL SR *et al*, 1980. Convective and interfacial instabilities during unidirectional solidification of a binary alloy. *Journal of Crystal Growth.* 49, 13-28.

CORRIGAN and GIBB, 1979. The loss of Fe and Na from a basaltic melt during experiments using the wire-loop technique. *Mineralogical Magazine.* 43, 121-126.

CURRY RM, 1989. Mineral dissolution in silicate melts. *Unpublished PhD thesis, University of St Andrews.*

DALY RA, 1933. Igneous rocks and the depth of the earth. McGraw Hill, New York.

DARWIN CR, 1844. Geological observations on the volcanic islands visited during the voyages of the HMS Beagle. Smith Elder and Co, London.

DEER WA, HOWIE RA, and ZUSSMANN J, 1966. An Introduction to the rock-forming minerals. *Published by Longman Group Limited.*

DONALDSON CH, 1975. Calculated diffusion coefficients and the growth rate of olivine in a basaltic magma. *Lithos.* 8, 163-174.

DONALDSON CH, 1976. An experimental investigation of olivine morphology. *Contributions to Mineralogy and Petrology.* 57, 187-213.

DONALDSON CH, 1979. Compositional changes in a basalt melt contained in a wire loop of $Pt_{80}Rh_{20}$: effects of temperature, time and oxygen fugacity. *Mineralogical Magazine.* 43. 115-119.

DONALDSON CH, 1990. Forsterite dissolution in superheated basaltic, andesitic and rhyolitic melts. *Mineralogical Magazine.* 55, 67-74.

DONALDSON CH,1992. Compositional boundary layers, convection and liquid layering in silicate melts. *Final report of NERC grant GR3/6509.*

DONALDSON CH, 1993. Convective fractionation during magnetite and hematite dissolution in silicate melts. *Mineralogical Magazine.* 57, 469-488.

DONALDSON CH and HAMILTON DL, 1987. Compositional convection and layering in a rock melt.. *Nature.* 327, 413-415.

DONALDSON CH and HENDERSON CMB, 1988. A new interpretation of round embayments in quartz crystals. *Mineralogical Magazine.* 52, 27-34.

DUNHAM AC and WILKINSON FCF, 1978. Accuracy, precision and detection limits of energy-dispersive electron microprobe analyses of silicates. *Progress in Experimental Petrology, 1975-1978.* (Ed. WS Mckenzie) NERC publication No 11, 96-99.

EMELEUS CH, Tertiary Igneous Activity, in CRAIG GY. (Ed). 1991. The Geology of Scotland. 3rd Edition. *Published by the Geological Society of London.*

FENNER CN. 1937. A view of magmatic differentiation. *Journal of Geology.* 45, 158-168.

FERRY JM, 1985. Hydrothermal alteration of Tertiary igneous rocks from the Isle of Skye, NW Scotland. I- Gabbros. *Contributions to Mineralogy and Petrology.* 91, 264-282.

GEIST DJ, MCBIRNEY AR, BAKER BH. 1989. MacGPP. A program package for creating and using geochemical data files.

GROSSENBACHER and MARSH. 1992. The Zora ring intrusion, Gettysburg. *American Geophysical Union Fall meeting.* 73, No 43.

GROUT FF, 1918. Two phase convection currents in magmas. *Journal of Geology.* 26, 481-491.

GROVE TL and BAKER MB, 1983. Effects of melt density on magma mixing in calc-alkaline series lavas. *Nature.* 305, 416-418.

HARDEE HC, 1983. Convective transport in crustal magma bodies. *Journal of Volcanology and Geothermal Research.* 19, 45-72.

HARKER A, 1894. Carrock Fell: A study in the variation of igneous rock masses. Part 1. The gabbro. *Quarterly Journal of the Geological Society of London.* 50, 311-337.

HARKER A, 1909. The Natural History of igneous rocks. Methuen, London.

HELZ RT *et al*, 1989. Diapiric transfer of melt in Lilauea Iki lava lake, Hawaii: a quick, efficient process of igneous differentiation. *Geological Society of America Bulletin.* 101, 578-94.

HESS HH, 1960. Stillwater igneous complex, Montana: a quantitative mineralogical study. *Memoirs of the Geological Society of America.* 80

HESS PC, 1989. Origins of igneous rocks. Harvard University Press. Cambridge, Massachusetts.

HILDRETH W, 1981. Gradients in silicic magma chambers: implications for lithospheric magmatism. *Journal of Geophysical Research.* 86, 10153-10192.

HOFFMANN AW, 1980. Diffusion in silicate melts: a critical review. *In "Physics of magmatic processes" Ed. RB Hargraves,* Princeton University Press.

HOLMES A. 1931. The problem of the association of acid and basic rocks in central complexes. *Geological Magazine.* 68, 241-255.

HOLMES A, 1936. The idea of contrasted differentiation. *Geological Magazine.* 73, 228-238.

HOWARD LN, 1966. Convection at high Rayleigh numbers. *In: Gortler H (ed), Proc 11th International Congress of Applied Mechanics.* Springer, Berlin pp1109-1145.

HUNTER RH and SPARKS RSJ, 1987. The differentiation of the Skaergaard Intrusion. *Contributions to Mineralogy and Petrology.* 95, 451-461.

HUPPERT HE and SPARKS RSJ, 1988. The generation of granitic magmas by intrusion of basalt into continental crust. *Journal of Petrology.* 29, 599-624.

HUPPERT HE, SPARKS RSJ, WHITEHEAD JA, and HALLWORTH MA, 1986. Replenishment of magma chambers by light inputs. *Journal of Geophysical Research.* 91, 6113-6122.

HUPPERT HE, SPARKS RSJ, WILSON JR, and HALLWORTH MA. 1986. Cooling and crystallization at an inclined plane. *Earth and Planetary Science Letters.* 79, 319-328.

HUPPERT HE and TURNER JS, 1991. Comments on 'On convective style and vigor in sheet-like magma chambers. *Joural of petrology.* 32, 851-854.

HUPPERT HE, TURNER JS, and SPARKS RSJ. 1982. Replenished magma chambers: effects of compositional zonation and input rates. *Earth and Planetary Science Letters.* 57, 345-357.

IRVINE TN, 1980. Infiltration metasomatism, accumulate growth, and double-diffusive fractional crystallization in the Muskox intrusion and other layered intrusions. *In: RB Hargraves (ed), Physics of Magmatic Processes.* Princeton University Press, Princeton University, 325-383.

KOOMANS C, and KUENEN PH. 1938. On the differentiation of the Glen More ring dyke, Mull. *Geological Magazine* 75, 145-160.

LANGMUIR CH, 1989. Geochemical consequences of in-situ crystallization. *Nature.* 340, 199-205.

LASAGA A, 1981. Influence of diffusion coupling on diagenetic concentration profiles. *American Journal of Science.* 281, 553-575.

LOFGREN G, 1974. An experimental study of plagioclase crystal morphology: isothermal crystallization. *American Journal of Science.* 274, 243-273.

MCBIRNEY AR, 1979. Effects of assimilation: in *The evolution of igneous rocks; 50th anniversary perspectives.* Ed. Yoder HS jnr. Princeton University Press. 307-338.

MCBIRNEY AR. 1980. Mixing and unmixing of magmas. *Journal of Volcanology and Geothermal Research.* 7, 357-371.

MCBIRNEY AR, BAKER BH, and NILSON RH. 1985. Liquid fractionation, I. Basic principles and experimental simulstions. *Journal of Volcanology and Geothermal Research.* 7, 357-371.

MCBIRNEY AR, and NOYES RM. 1979. Crystallization and layering of the Skaergaard Intrusion. *Journal of Petrology.* 20, 487-554.

MARSH BD, 1988. Crystal capture, sorting and retention in convecting magma. *Geological Society of Americal Bulletin.* 100, 1720-1737.

MARSH BD, 1989A. Magma chambers. *Annual Review of Earth and Planetsry Science.* 17, 439-474

MARSH BD, 1989B. On convection style and vigor in sheet-like magma chambers. *Journal of petrology.* 30, 479-530.

MARSHALL LA. 1984. Origin of mixed magma and net-veined ring intrusions. *Unpublished PhD thesis.* University of Cambridge.

MARSHALL LA, and SPARKS RSJ. (1984). Origin of some mixed-magma and net-veined ring intrusions. *Journal of the Geological Society.* 141, 171-182.

MARTIN D, 1990. Crystal settling and in situ crystallization in aqueous solutions in magma chambers. *Earth and Planetary Science Letters.* 96, 336-348.

MARTIN D, GRIFFITHS RW, and CAMPBELL IH. 1987. Compositional and thermal convection in magma chambers. *Contributions to Mineralogy and Petrology.* 96, 465-475.

MERRILL and WYLLIE, 1973. Absorption of iron by Pt capsules in high-pressure rock melting experiments. *American Mineralogist.* 58, 16-23.

MOREAU C, BROWN WL, and KARCHE J-P. 1987. Monzo-anorthosite from the Taguei ring-complex, Air, Niger: a hybrid rock with cumuluc plagioclase and an infiltrated granitic intercumulus liquid? *Contributions to Mineralogy and Petrology.* 95, 32-43.

MORSE SA, 1973. The feldspar-magma paradox. In; Morse SA (ed), Nain Anorthosite Project, Labrador: Field Report 1972. University of Massachusetts. contribution 11, 113-116.

MURAS E T and McBIRNEYAR, 1973. properties of some common igneous rocks and their melts at high temperatures. *Bulletin of the geological Society of America.* 84, 3563-3592.

MUSSET AE *et al.* 1988. Time and duration of activity in the British Tertiary Igneous Province. In MORTON AC and PARSON LM (Eds) *Early Tertiary Volcanism and the opening of the NE Atlantic.* Geol. Soc. Spec. Publ., 39, 337-348.

NOCKOLDS SR. 1934. The production of normal rock types by contamination and their bearing on petrogenesis. *Geological Magazine.* 71, 31-39.

RAST DE *et al,* 1968. Triassic rocks of the Isle of Mull; their sedimentation, facies, structure and relationship to the Great Glen fault and the Mull caldera. *Proceeding of the Geological Society of London.* 1645, 299-304.

RICHEY JE. 1932. Tertiary ring structures in Britain. *Transactions of the Geological Society of Glasgow.* 19, 42-140.

ROEDER PL, and EMSLIE RF. 1970. Olivine-liquid equilibrium. *Contributions to Mineralogy and Petrology.* 29, 275-289.

ROHSENOW WM and CHOI H, 1961. Heat, mass and momentum transfer. Prentice-Hall, New Jersey.

ROSENBERGER F, 1979. Fundamentals of crystal growth I. macroscopic equilibrium and transport concepts. Springer-Verlag, Berlin.

SHAW HR, 1972. Viscosities of magmatic silicate liquids: An empirical method of prediction. *American Journal of Science.* 272, 870-893.

SHIRLEY DN, 1987. Differentiation and compaction in the Palisades Sill, New Jersey. *Journal of Petrology.* 28, 835-865.

SIGGURDSSON H and SPARKS RSJ, 1981. Petrology of rhyolitic and mixed magma ejecta from the 1875 eruption of Askja, Iceland. *Journal of Petrology.* 22, 41-84.

SIMKIN T and SMITH JV, 1970. Minor element distribution in olivine. *Journal of Geology.* 78, 304-325.

SKELHORN RR, MACDOUGALL JDS, and LONGLAND PJN. 1969. The Tertiary igneous geology of the Isle of Mull. *Geological Association Guides No.*20. Published by the Geological Association of London, Benham and Co. Ltd.

SPARKS RSJ *et al*, 1985. Postcumulus processes in layered intrusions. *Geological Magazine.* 122, 555-568.

SPARKS RSJ. 1988. Petrology and geochemistry of the Loch Ba ring-dyke, Mull (N.W. Scotland): an example of the extreme differentiation of tholeiitic magmas. *Contributions to Mineralogy and Petrology.* 100, 446-461.

SPARKS RSJ and HUPPERT HE, 1984. Density changes during fractional crystallization of basaltic magmas: fluid dynamic implications. *Contributions to Mineralogy and Petrology.* 85, 300-309.

SPARKS RSJ, HUPPERT HE, KOYAGUCHI and HALLWORTH M, 1983. Origin of modal and rhythmic igneous layering by sedimentation in a convecting magma chamber. *Nature.* 361, 247-249.

SPARKS RSJ, HUPPERT HE, and TURNER JS. 1984. The fluid dynamics of evolving magma chambers. *Philosophical Transactions of the Royal Society of London.* Series A310, 511-534.

SPARKS RSJ, and MARSHALL LA. 1986. Thermal and mechanical constraints on mixing between mafic and silicic magmas. *Journal of Volcanology and Geothermal Research.* 29, 99-124.

SPARROW EM *et al*, 1970. Observations and other characteristics of thermals. *Journal of Fluid Mechanics.* 41, 793-800.

STERN CR and WYLLIE PJ, 1975. Effect of iron absorption in rock melting experiments at 30 kbar. *American Mineralogist.* 60, 681-690.

STOLPER E and WALKER D, 1980. Melt density and the average composition of basalt. *Contributions to Mineralogy and Petrology.* 74, 7-12.

SUN S.-s and MCDONOUGH WF, 1989. Chemical and isotopic systematics of oceanic basalts; implications for mantle compositions and processes. In: *Magmatism in the Ocean Basins*, AD Saunders and MJ Norry, eds. *Geological Society Special Publication*, 42, 313-345.

TAIT SR, HUPPERT HE, and SPARKS RSJ, 1984. The role of compositional convection in the formation of adcumulate rocks. *Lithos*. 17, 139-146.

TAIT SR and JAUPART C, 1992. Compositional convection in a reactive crystalline mush and melt differentiation. *Journal of Geophysical Research*. 97, 6735-6756.

THOMPSON RN. 1969. Tertiary granites and associated rocks of the Marsco area, Isle of Skye. *Quarterly Journal of the Geological Society of London*. 124, 349-385.

THOMPSON RN. 1980. Askja 1875, Skye 56 MA: Basalt-triggered plinian, mixed-magma eruptions during the emplacement of the Western Red Hills granite, Isle of Skye, Scotland. *Geol. Rundschau*. 69, 245-262.

THOMPSON RN. 1981. Thermal aspects of the origin of hebridean Tertiary acid magmas. I. an experimental study of partial fusion of Lewisian gneisses and Torridonian sediments. *Mineralogical Magazine*. 44, 161-170.

THOMPSON RN. 1982. Magmatism of the British Tertiary Volcanic Province. *Scottish Journal of Geology*. 18, 49-107.

THOMPSON RN. 1983. Thermal aspects of the origin of Hebridean Tertiary acid magmas. II. Experimental melting behaviour of the granites at 1 kbar P_{H2O}. *Mineralogical Magazine*. 47. 111-121.

THOMPSON RN *et al*, 1983. Continental flood basalts, Arachnids rule OK?. In: *Continental Basalts and Mantle Xenoliths*, Hawksworth CJ and Norry MJ eds. 158-185.

TRITTON DJ, 1977. Physical fluid dynamics. Von Nostrand Reinhold, London.

TURNER JS. 1980. A fluid dynamical model of differentiation and layering in magma chambers. *Nature, London*. 285, 213-215.

TURNER JS and CAMPBELL IH, 1986. Convection and Mixing in magma chambers. *Earth Science Reviews*. 23, 255-352.

TURNER JS *et al*, 1986. Komaiites II: Experimental and theoretical investigations of post-emplacement cooling and crystallization. *Journal of Petrology*. 27, 397-437.

TURNER JS and GUSTAFSON LB, 1978. The flow of hot saline solutions from vents in the sea floor - some implications for exhalative massive sulphide and other ore deposits. *Economic Geology*. 73, 1082-1100.

VOGEL TA, YOUNKER LW, WILBRAND JT, and KAMPMUELLER E. 1984. Magma mixing: the Marsco suite, Isle of Skye, Scotland. *Contributions to Mineralogy and Petrology*. 87, 231-241.

WAGER LR, BROWN GM, and WADSWORTH WJ. 1965. Types of igneous cumulates. *Journal of Petrology*. 1, 73-85.

WAGER LR and DEER WA, 1939. The petrology of the Skaergaard intrusion, Kangerdlugssuaq, W. Greenland. *Medd on Gronland* 105, 1-352.

WALKER GPL. 1971. The distribution of amygdale minerals in Mull and Morvern (Western Scotland). In MURTY T and RAO SS (Eds) *Studies in Earth Sciences, West Commemoration Volume*. pp. 181-194.

WALKER *et al*, 1988. Adcumulus dunite growth in a laboratory thermal gradient. *Contributions to Mineralogy and Petrology*. 99, 306-319.

WALSH JN *et al.* 1979. Geochemistry and petrogenesis of Tertiary granitic rocks from the island of Mull, N W Scotland. *Contributions to Mineralogy and Petrology.* 71, 99-116.

WEILL DF and McKAY GA, 1975. Major and trace element trends during minor experiments of the crystallization of lunar melts. Abstract in *Lunar Science VI, Pt II.* 863-865. Lunar Science Institute, Houston, Texas.

WILSON M, 1993. Magmatic differentiation. *Journal of the Geological Society of London,* 150, 611-624.

WINCHESTER JA and FLOYD PA, 1977. Geochemical discrimination of different magma series and their differentiation products using immobile elements. Chemical Geology. 20, 325-343.

ZHANG *et al,* 1989. Diffusive crystal dissolution. *Contributions to Mineralogy and Petrology.* 102, 492-513.

Appendix A
Preparation of cobalt basalt analogue

Calculations of weights of starting materials were based on 1921 Kilauea basalt composition (GL-1921, Hill, 1969).

1) Analytical grade powders of SiO_2, Al_2O_3, MgO, TiO_2 and Co_3O_4, were weighed in to silica boats, dried separately for two hours at 500°C, cooled in a desiccator and then mixed thoroughly in a plastic bag.

2) $CaCO_3$ was weighed, dried at 500°C for two hours, and then heated at 1200°C overnight to thoroughly decompose it to CaO and CO_2.

3) $KHCO_3$ was decomposed at 200°C for two hours to produce K_2CO_3.

4) Na_2CO_3 was dried at 500°C and then mixed thoroughly, with the CaO, with a mortar and pestle. This mixture was heated slowly to 1200°C, from 800°C, in a $Pt_{95}Au_5$ crucible and held there for two hours.

5) The Na_2O-CaO mixture is mixed with K_2CO_3 with a mortar and pestle. The mixture is heated at 1200°C for two hours.

6) The CaO-Na_2O-K_2O mixture was then mixed with the other oxides in a bag and the whole batch was ground in the TEMA mill for three minutes to produce a fine, homogenous powder.

7) Fusion of cobalt-basalt powder was carried out in batches, in $Pt_{95}Au_5$ crucibles, for at least two hours at 1320°C (above the liquidus of the system). After fusion of all batches, the glass was ground in the TEMA mill and fused again for homogenization. Chips of the glass, after the two fusions, were made into a polished thin section and analysed using EPMA (See table 2.01 in chapter 2 for details of composition).

Appendix B

Method of making clay crucibles with internal handles

1) Liquid clay-slip is poured into a plaster mould of the crucible. The plaster absorbs water from the clay, producing a layer of partially dehydrated clay in contact with the plaster mould. The longer the clay is left in the mould, the thicker the layer of dehydrated clay becomes, and so the thickness of crucible wall produced can be varied.

2) After five minutes (less for thinner crucibles and more for thicker ones) the mould is turned upside down and the remaining liquid clay drained off. The partially dehydrated clay which remains in the plaster mould is allowed to continue drying for 24 hours at room temperature.

3) After 24 hours the crucibles are removed from the plaster mould, and after drying at room temperature for a further 48 hours, the handles for suspending a crystal are attached to the inner walls of the crucible. This involves attaching two small, moist, clay balls, with one of their sides flattened, to the opposite side of the crucible, about two-thirds of the way down the inner wall. These handles are then pierced vertically with a pin to make a hole through which wire can later be passed.

4) The crucible and attached handles are allowed to dry out at room temperature for 24 hours, prior to firing from room temperature to 1300°C at a rate of 200°C per hour. The crucibles are held at 1300°C for at least 2 hours. This elevated temperature is used because an earlier batch of crucibles, fired at 1000°C, cracked during the experiments, causing runs to be aborted.

5) After slow cooling to avoid shrinkage cracking, drilled crystal seeds were suspended in the crucible by threading and looping platinum wire through and around the crystals and the holes in the clay handles.

Appendix C. EPMA data from points analysed in olivine growth experiments.

Experiment Number	analysis	X (mm)	Y (mm)	SiO2	TiO2	Al2O3	CoO	MgO	CaO	Na2O	K2O	Total
CO 29	1	12.69	17.44	49.6	3.3	13.5	11.3	8.1	12.5	0.2	0.2	98.7
	2	12.21	17.44	49.6	3.3	13.6	11.4	7.7	12.4	0.3	0.2	98.5
	3	11.72	17.44	49.3	3.5	13.5	9.8	7.8	12.4	0.2	0.2	96.8
	4	11.22	17.44	46.0	2.9	12.6	5.9	7.4	11.2	0.2	0.2	86.4
	5	10.73	17.44	48.2	3.3	13.6	8.2	7.5	11.8	0.3	0.2	93.2
	6	10.21	17.44	49.6	3.4	13.6	10.4	7.7	12.8	0.2	0.2	97.8
	7	9.72	17.44	49.7	3.5	13.8	10.8	7.8	12.4	0.3	0.2	98.6
	8	9.22	17.44	43.1	2.9	12.5	5.0	7.2	9.7	0.2	0.2	80.6
	9	8.72	17.44	49.6	3.3	13.2	11.2	7.7	12.7	0.2	0.2	98.1
	10	8.24	17.44	49.9	3.6	13.5	11.2	8.0	11.9	0.3	0.2	98.6
	11	7.72	17.44	49.1	3.4	13.3	10.9	8.1	11.8	0.2	0.2	97.0
	12	11.26	18.30	50.1	3.5	13.5	1.3	8.0	12.4	0.3	0.2	99.3
	13	10.97	18.30	50.1	3.3	13.6	10.8	7.9	12.5	0.3	0.2	98.8
	14	10.72	18.30	50.0	3.4	13.9	10.2	7.8	12.1	0.2	0.2	97.9
	15	10.47	18.30	50.4	3.5	13.9	11.3	8.0	12.4	0.3	0.2	100.0
	16	10.23	18.30	49.7	3.6	13.7	10.9	7.9	12.6	0.2	0.2	98.8
	17	9.97	18.30	49.8	3.2	13.6	10.6	7.8	12.5	0.2	0.2	98.0
	18	9.72	18.30	49.7	3.1	13.6	10.8	7.6	12.6	0.3	0.3	98.0
	19	9.47	18.30	49.5	3.4	13.6	11.0	8.0	12.7	0.2	0.2	98.6
	20	9.22	18.30	49.9	3.5	13.6	11.4	7.9	12.6	0.2	0.3	99.3

Experiment Number	analysis	X (mm)	Y (mm)	SiO2	TiO2	Al2O3	CoO	MgO	CaO	Na2O	K2O	Total
CO 30	1	10.88	5.26	49.4	3.5	13.7	11.2	8.3	12.2	0.3	0.2	98.8
	2	11.12	5.26	49.0	3.4	14.0	11.4	8.1	12.5	0.3	0.2	98.8
	3	11.37	5.26	48.9	3.3	14.0	11.2	8.0	12.2	0.2	0.2	98.2
	4	11.62	5.26	49.1	3.4	13.7	10.9	8.1	12.3	0.3	0.2	98.0
	5	11.87	5.29	49.5	3.4	13.8	10.7	8.0	12.5	0.3	0.2	98.4
	6	12.12	5.29	50.0	3.4	13.9	11.0	8.1	12.3	0.2	0.2	99.1
	7	12.38	5.29	49.8	3.4	13.7	11.6	8.0	12.5	0.2	0.2	99.5
	8	12.62	5.29	49.7	3.4	13.7	11.2	8.1	12.6	0.2	0.2	99.0
	9	12.88	5.29	49.9	3.2	13.7	11.3	8.4	12.3	0.2	0.2	99.2
	10	13.13	5.29	49.1	3.6	13.3	11.5	8.4	12.5	0.2	0.2	98.7
	11	11.92	5.28	50.0	3.7	14.2	10.3	7.3	12.9	0.2	0.2	98.8

Experiment Number	analysis	X (mm)	Y (mm)	SiO2	TiO2	Al2O3	CoO	MgO	CaO	Na2O	K2O	Total
CO 31a	1	14.02	7.62	47.8	3.5	13.8	11.1	7.8	12.4	0.3	0.2	96.9
	2	13.78	7.62	49.8	3.4	13.3	11.1	7.9	12.3	0.2	0.2	98.1
	3	13.52	7.64	49.5	3.4	13.7	10.4	7.8	12.3	0.2	0.2	97.6
	4	13.27	7.64	50.2	3.3	14.1	11.1	7.8	12.5	0.2	0.2	99.4
	5	13.09	7.64	49.3	3.5	14.1	11.2	7.8	12.3	0.3	0.2	98.6
	6	12.90	7.63	49.9	3.5	14.2	10.9	7.8	12.4	0.2	0.2	99.1
	7	12.67	7.63	49.6	3.4	14.0	11.0	7.9	12.4	0.1	0.2	98.6
	8	12.02	7.63	49.3	3.1	13.9	11.0	7.9	12.4	0.2	0.2	98.1
	9	14.02	9.03	48.8	3.1	13.7	10.9	8.0	12.3	0.1	0.2	97.1
	10	13.55	9.03	49.6	3.3	13.9	11.4	8.0	12.3	0.3	0.2	98.9
	15	11.49	5.92	49.7	3.4	14.9	9.9	6.7	12.9	0.3	0.2	97.9
	16	11.44	5.93	49.3	3.4	14.3	10.8	7.9	12.7	0.4	0.3	98.9
	17	11.39	5.93	49.2	3.3	14.2	10.8	7.6	12.4	0.2	0.3	97.9
	18	11.28	5.93	48.9	3.5	14.0	10.7	7.7	12.2	0.2	0.2	97.3
	19	11.12	5.93	49.3	3.4	14.3	11.0	7.8	12.3	0.2	0.2	98.6
	20	10.85	5.93	49.6	3.5	14.4	10.7	7.8	12.4	0.2	0.2	98.8
	21	20.21	3.78	48.1	3.2	14.5	10.8	7.3	12.5	0.2	0.2	96.8
	22	20.00	3.78	48.7	3.3	14.4	10.9	7.7	12.5	0.3	0.2	97.9
	23	19.84	3.78	48.9	3.4	14.3	10.3	7.7	12.4	0.3	0.2	97.6
	24	19.52	3.78	48.9	3.5	14.1	11.0	7.9	12.0	0.2	0.2	97.7
	25	13.86	6.31	36.1	0.0	0.0	31.2	32.5	0.2	0.0	0.0	100.1
	26	13.37	7.07	50.2	3.7	15.0	10.0	6.6	12.8	0.3	0.3	98.8
	27	13.46	7.07	49.5	3.4	13.3	11.0	7.6	12.5	0.3	0.2	97.7
	28	13.51	7.07	49.0	3.5	14.0	10.7	7.5	12.3	0.2	0.2	97.4
	29	13.60	7.07	49.3	3.3	13.7	10.6	7.7	12.2	0.2	0.2	97.2
	30	13.90	7.07	49.2	3.1	13.8	11.1	7.9	12.3	0.2	0.2	97.5
	31	14.30	7.04	49.8	3.1	13.6	11.6	8.1	12.2	0.2	0.2	98.9

	32	13.92	5.02	49.2	3.4	14.3	10.7	7.8	12.2	0.2	0.3	98.0
	33	13.96	5.02	49.8	3.4	14.3	10.9	7.8	12.0	0.3	0.2	98.6
	34	14.07	5.02	49.8	3.4	14.1	11.1	7.8	12.2	0.2	0.2	98.9
	35	12.87	7.34	49.7	3.4	14.2	11.0	7.9	12.3	0.2	0.2	98.7
	36	12.58	7.37	49.6	3.2	14.3	11.1	8.0	12.3	0.2	0.3	99.0
	37	12.24	7.37	49.6	3.4	13.7	11.1	7.9	12.3	0.3	0.2	98.4
	38	11.73	7.38	49.5	3.5	13.3	11.3	7.9	12.4	0.3	0.2	98.2
	39	13.98	4.28	50.6	3.8	15.3	8.6	5.9	13.0	0.3	0.2	97.6
	40	14.00	4.28	49.6	3.4	14.1	10.9	7.4	12.3	0.2	0.2	98.1
	41	14.03	4.28	49.6	3.1	14.1	10.5	7.7	12.2	0.3	0.2	97.6
	42	14.05	4.28	49.7	3.3	14.2	10.5	7.8	12.3	0.3	0.2	98.2
	43	14.09	4.28	49.9	3.4	14.0	10.6	7.7	11.9	0.2	0.2	97.9

Experiment Number	analysis	X (mm)	Y (mm)	SiO2	TiO2	Al2O3	CoO	MgO	CaO	Na2O	K2O	Total
CO 31b	1	8.43	12.95	49.0	3.4	13.7	10.6	7.8	12.4	0.3	0.3	97.5
	2	8.37	12.95	48.9	3.3	13.9	10.6	7.9	11.9	0.3	0.3	97.0
	3	8.29	12.95	49.1	3.5	14.1	10.7	7.9	12.5	0.1	0.2	98.2
	4	8.19	12.95	49.1	3.5	14.1	10.5	7.8	12.0	0.2	0.2	97.4
	5	8.07	12.91	48.9	3.6	14.3	10.6	7.7	12.3	0.1	0.2	97.7
	6	7.95	12.91	48.6	3.5	14.1	9.3	7.7	12.4	0.2	0.2	95.8
	7	8.15	12.67	48.1	3.4	14.3	10.5	7.4	12.1	0.1	0.2	96.2
	8	8.09	12.67	48.8	3.5	14.0	10.7	7.9	12.2	0.3	0.3	97.4
	9	8.04	12.67	49.0	3.6	14.2	10.6	7.7	12.2	0.3	0.2	97.7
	10	7.72	12.67	49.3	3.4	14.1	11.5	7.8	12.5	0.3	0.2	99.0
	11	7.60	12.70	49.1	3.5	13.8	11.0	8.0	12.3	0.3	0.2	98.2
	12	7.31	13.03	49.1	3.4	14.0	10.7	7.9	12.4	0.3	0.3	98.0
	13	3.51	12.79	48.6	3.5	14.6	11.0	7.6	12.4	0.3	0.2	98.1
	14	3.58	12.61	48.4	3.4	14.4	11.3	7.8	12.2	0.3	0.2	98.0
	15	3.76	12.61	49.0	3.2	14.4	11.2	7.9	12.4	0.3	0.2	98.5
	16	3.97	13.43	48.5	3.4	14.3	10.9	7.8	12.5	0.3	0.3	97.9
	17	3.78	13.42	48.6	3.4	14.3	10.9	7.8	12.3	0.3	0.2	97.8
	18	3.58	13.42	49.0	3.6	14.5	11.3	7.7	11.7	0.3	0.2	98.3
	19	3.42	13.42	48.8	3.4	14.6	9.9	7.8	11.5	0.2	0.2	96.4
	20	3.30	13.41	48.1	3.5	14.3	10.1	7.7	12.5	0.3	0.2	96.7
	21	3.20	13.41	48.3	3.5	14.5	10.8	7.8	12.0	0.2	0.2	97.2
	22	3.06	13.41	48.3	3.4	14.9	10.7	7.6	11.9	0.3	0.2	97.5
	23	9.63	13.48	36.7	0.2	0.0	29.4	32.4	0.4	0.0	0.0	99.2
	24	9.66	13.48	49.3	3.3	14.0	11.0	7.9	12.6	0.2	0.2	98.5
	25	9.70	13.48	49.0	3.3	13.9	10.5	7.8	12.2	0.2	0.2	97.1
	26	9.73	13.48	48.8	3.5	13.9	10.8	7.6	12.1	0.2	0.2	97.2
	27	9.81	13.48	48.9	3.5	14.0	11.0	7.7	12.6	0.3	0.2	98.2
	28	9.42	13.56	49.1	3.4	14.2	10.9	7.7	12.6	0.2	0.2	98.3
	29	9.48	13.56	48.5	3.4	14.0	10.5	7.7	12.1	0.2	0.2	96.6
	30	9.55	13.56	49.4	3.4	14.1	10.9	7.7	12.6	0.2	0.2	98.5
	31	9.61	13.56	49.0	3.3	14.0	10.7	7.6	12.5	0.2	0.2	97.6
	32	9.67	13.56	49.0	3.6	14.0	10.8	7.7	12.6	0.3	0.2	98.2
	33	9.80	13.56	49.2	3.6	14.0	11.1	7.9	12.4	0.3	0.2	98.6
	34	15.05	19.57	49.3	3.4	13.9	11.2	7.7	12.3	0.2	0.2	98.1
	35	15.05	19.02	49.4	3.4	13.8	11.0	7.8	12.3	0.2	0.2	98.3
	36	15.05	18.02	48.8	3.1	13.9	11.1	7.9	12.2	0.2	0.2	97.5
	37	15.05	17.03	48.6	3.3	14.1	11.3	7.8	12.4	0.3	0.2	97.9
	38	15.05	16.02	48.8	3.3	14.1	10.8	7.7	12.2	0.3	0.2	97.5
	39	15.05	15.03	48.2	3.3	14.1	10.6	7.8	12.3	0.2	0.2	96.7
	40	15.05	14.02	48.2	3.4	14.0	10.8	7.9	12.2	0.2	0.2	97.0
	41	15.06	13.02	48.9	3.5	14.1	11.0	7.9	12.6	0.3	0.2	98.4
	42	15.06	12.02	48.8	3.3	14.3	11.3	7.9	12.4	0.2	0.3	98.5
	43	15.06	11.03	48.1	3.4	13.4	11.2	7.9	12.3	0.2	0.2	96.7
	44	15.01	10.00	47.9	3.1	13.6	11.2	8.0	12.1	0.2	0.2	96.3
	45	11.55	10.90	49.1	3.4	14.3	10.7	7.0	12.8	0.3	0.3	97.8
	46	11.57	10.90	48.6	3.4	13.9	10.9	7.6	12.4	0.2	0.2	97.3
	47	11.58	10.90	48.6	3.5	13.7	10.8	7.7	12.5	0.2	0.2	97.2
	48	11.60	10.90	48.6	3.1	13.6	11.1	7.7	12.4	0.3	0.2	97.0
	49	11.64	10.90	48.7	3.3	13.2	11.3	7.8	12.2	0.3	0.2	97.0
	50	11.76	10.90	48.7	3.3	13.7	10.9	7.8	12.1	0.2	0.2	96.9
	51	11.27	11.07	48.5	3.6	14.1	11.1	7.7	12.3	0.2	0.2	97.6

52	11.23	11.07	48.4	3.4	14.1	10.5	7.7	12.4	0.2	0.2	97.0
53	11.18	11.07	48.6	3.4	13.9	10.9	7.5	12.3	0.3	0.3	97.2
54	11.11	11.11	48.5	3.4	14.0	10.7	7.7	12.4	0.3	0.2	97.0
55	11.02	11.11	48.3	3.3	14.0	10.5	7.7	12.6	0.2	0.2	96.9
56	11.42	11.05	50.0	3.9	15.1	9.5	5.7	13.5	0.3	0.3	98.2
57	11.42	11.10	49.1	3.6	14.0	11.2	7.6	12.4	0.2	0.2	98.3
58	11.42	11.16	49.0	3.5	13.7	10.5	7.7	12.4	0.3	0.3	97.4
59	11.42	11.33	48.5	3.4	13.7	10.5	7.8	12.3	0.2	0.2	96.7
60	11.38	11.00	49.4	3.4	14.4	10.2	6.5	13.5	0.2	0.2	97.7
61	12.03	18.35	49.0	3.5	14.1	10.9	7.9	12.4	0.3	0.2	98.1
62	12.03	18.03	49.2	3.5	13.8	11.0	7.8	12.3	0.2	0.2	98.0
63	12.05	17.03	49.0	3.4	13.8	11.3	7.9	12.3	0.2	0.2	98.1
64	11.99	16.03	48.7	3.2	13.1	11.3	7.8	12.2	0.3	0.2	96.9
65	11.99	15.02	49.3	3.1	13.5	11.2	8.1	12.4	0.3	0.2	98.0
66	11.99	14.03	49.1	3.2	13.6	11.4	8.0	12.4	0.3	0.2	98.2
67	11.97	13.02	49.1	3.3	13.7	11.5	7.9	12.2	0.2	0.2	98.2
68	11.95	12.02	49.0	3.3	13.3	10.9	8.1	12.4	0.2	0.2	97.6
69	11.95	9.53	49.3	3.4	13.7	11.4	7.6	12.3	0.2	0.2	98.0
70	12.14	8.10	48.6	3.4	14.3	11.3	7.6	12.3	0.4	0.2	98.2
71	11.02	15.02	49.1	3.5	13.7	11.4	7.8	12.6	0.2	0.2	98.4
72	10.52	15.02	49.6	3.4	13.9	11.3	7.9	12.3	0.2	0.2	98.9
73	10.02	15.02	49.0	3.4	14.1	11.2	7.7	12.7	0.3	0.3	98.6
74	9.52	15.02	48.9	3.4	14.0	10.7	7.5	12.6	0.2	0.2	97.6
75	9.42	15.02	49.1	3.4	14.0	10.4	7.8	12.1	0.3	0.2	97.3
76	9.31	15.02	49.1	3.3	14.0	10.8	7.8	12.4	0.2	0.2	97.8
77	9.22	15.02	49.0	3.2	13.9	10.9	7.8	12.4	0.2	0.2	97.8
78	9.11	15.01	49.0	3.6	13.7	10.7	7.9	12.4	0.2	0.3	97.7
79	9.02	15.01	49.4	3.5	14.0	10.6	7.6	12.4	0.2	0.2	97.8
80	8.92	15.01	48.7	3.1	13.8	10.1	7.8	12.4	0.2	0.2	96.4
81	8.82	15.01	49.2	3.4	13.9	11.1	7.9	12.5	0.3	0.2	98.4
82	8.71	15.01	49.1	3.4	13.8	11.5	7.8	12.2	0.2	0.2	98.4
83	8.30	15.01	49.2	3.5	13.8	11.2	8.1	12.4	0.2	0.3	98.7
84	8.03	15.01	48.9	3.6	13.7	11.4	8.0	12.4	0.3	0.2	98.5
85	7.52	15.02	49.0	3.4	13.7	11.3	7.9	12.2	0.2	0.2	98.0
86	7.03	15.02	49.0	3.4	14.0	11.0	8.0	12.4	0.2	0.2	98.2
87	6.52	15.02	48.8	3.3	13.8	11.1	8.0	12.5	0.2	0.2	98.0
88	5.20	20.36	49.5	3.4	13.7	10.7	8.0	11.8	0.3	0.3	97.6
89	5.20	20.02	49.4	3.4	13.8	11.3	7.8	12.3	0.2	0.3	98.4
90	5.20	19.03	48.9	3.3	14.3	11.2	7.8	12.2	0.3	0.2	98.0
91	5.20	18.02	47.2	3.4	14.1	10.5	7.8	12.2	0.2	0.2	95.6
92	5.20	17.04	46.6	3.4	13.6	10.2	7.6	11.9	0.3	0.3	93.9
93	5.20	16.03	49.1	3.3	14.0	11.2	8.0	12.5	0.3	0.2	98.6
94	5.20	15.02	48.9	3.1	14.1	11.0	7.9	12.5	0.2	0.2	97.7
95	5.18	14.03	49.0	3.1	14.1	10.9	8.0	12.1	0.2	0.2	97.6
96	5.18	13.02	48.7	3.4	13.9	11.2	7.9	12.4	0.2	0.2	98.0
97	5.18	12.02	48.5	3.4	14.0	11.0	7.9	12.6	0.2	0.2	97.9
98	5.85	11.04	48.9	3.4	14.2	11.1	7.4	12.7	0.2	0.2	98.2
99	5.89	9.78	43.8	1.4	8.0	22.5	21.1	4.7	0.2	0.2	101.9
100	5.91	9.78	49.1	3.5	14.3	10.4	7.6	12.2	0.3	0.2	97.5
101	5.95	9.78	49.2	3.3	14.5	11.0	7.6	12.4	0.3	0.2	98.5
102	5.95	9.77	49.0	3.4	14.5	10.8	7.5	12.1	0.3	0.2	97.8
103	5.99	9.80	49.0	3.5	14.3	10.5	7.5	12.5	0.3	0.2	97.8
104	5.72	9.83	49.1	3.5	14.4	11.1	7.4	12.6	0.2	0.2	98.5
105	5.72	9.88	48.8	3.2	14.2	10.9	7.6	12.1	0.2	0.2	97.1
106	5.71	9.94	49.1	3.4	14.2	11.0	7.5	12.4	0.3	0.2	98.1

Experiment Number	analysis	X (mm)	Y (mm)	SiO2	TiO2	Al2O3	CoO	MgO	CaO	Na2O	K2O	Total
CO 32	1	11.33	15.18	49.0	3.5	14.6	10.7	7.7	13.1	0.5	0.3	99.3
	2	11.63	15.18	48.7	3.5	14.7	10.7	7.7	13.0	0.4	0.3	98.9
	3	12.02	15.18	48.8	3.4	14.8	10.9	7.6	13.0	0.1	0.3	99.3
	4	12.28	15.18	53.4	3.8	16.0	12.1	8.4	14.1	0.4	0.3	108.5
	5	12.53	15.18	48.5	3.4	14.6	10.3	7.6	13.0	0.4	0.3	98.2
	6	12.78	15.18	48.7	3.6	14.7	10.2	7.8	13.0	0.5	0.2	98.7
	7	13.03	15.18	54.3	3.8	16.2	11.8	8.6	14.2	0.6	0.2	109.8
	8	13.28	15.18	48.6	3.6	14.6	10.6	7.7	12.8	0.5	0.3	98.6

9	13.53	15.18	48.9	3.6	14.7	10.7	7.8	12.5	0.5	0.3	98.7
10	13.78	15.18	48.2	3.4	14.7	10.8	7.5	12.9	0.4	0.3	98.2
11	14.01	15.19	48.6	3.1	14.1	10.8	7.7	12.3	0.6	0.2	97.3
12	14.28	15.19	48.6	3.4	14.6	10.2	7.6	12.8	0.4	0.3	97.9
13	14.52	15.19	48.3	3.5	14.7	10.8	7.4	12.9	0.4	0.3	98.2
14	15.05	15.19	48.8	3.6	14.8	10.6	7.8	13.0	0.5	0.3	99.5
15	10.34	20.90	49.3	3.3	15.1	10.1	6.9	12.8	0.4	0.3	98.0
16	10.34	20.70	46.4	3.4	14.4	10.3	6.8	12.5	0.4	0.3	94.5
17	10.34	20.44	48.9	3.5	14.9	10.5	7.6	12.8	0.5	0.3	99.0
18	10.34	20.18	49.2	3.5	14.9	10.7	7.6	13.0	0.5	0.3	99.6
19	10.34	19.94	48.5	3.4	15.0	10.3	7.7	12.9	0.5	0.3	98.5
20	10.34	19.67	49.0	3.5	15.0	10.6	7.6	12.8	0.5	0.3	99.2
21	10.34	19.43	48.9	3.6	14.8	10.7	7.6	12.5	0.4	0.2	98.6
22	10.34	19.19	48.7	3.5	14.8	10.6	7.8	13.1	0.4	0.3	99.0
23	10.33	18.93	48.4	3.3	14.8	10.6	7.7	12.9	0.4	0.3	98.4
24	10.33	18.69	48.9	3.5	14.7	10.6	7.7	13.0	0.4	0.3	99.1

Appendix D

Sample list for rocks referred to in chapters 6 to 12

Sample Number	Grid Reference	Altitude (m)	Rock Type
GM7	59862999	385	quartz gabbro
GM13	60252962	130	olivine gabbro
GM9	59732996	430	olivine gabbro
GM8	59702990	415	quartz gabbro
GM52	60032975	210	olivine gabbro
GM55	60522952	195	olivine gabbro
GM32	59782994	352	dioritic intermediate
GM4	59942985	287	quartz gabbro
GM31	59793026	455	dioritic intermediate
GM38	59722964	270	quartz gabbro
GM26	59852986	335	dioritic intermediate
GM48	59773037	420	granophyre
GM51	59773037	420	granophyre
GM47	60042962	148	dioritic intermediate
GM12	59713016	485	granodioritic intermediate
GM18	59643044	550	granophyre
GM17	59653042	535	granodioritic intermediate
GM19	59503051	630	granophyre
GM15	59663040	530	granodioritic intermediate
LS1	634305	183	Quartz gabbro
CC1	59992986	265	quartz gabbro
CC2	59982986	270	quartz gabbro
CC3	59942992	320	quartz gabbro
CC4	59882989	342	plag rich quartz gabbro
CC5	59872997	381	plag rich quartz gabbro
CC6	59793008	442	quartz gabbro
CC7	59733037	497	granophyre
CC8	59832969	251	granophyre vein in quartz gabbro
CC9	59592963	351	dioritic intermediate
CC10	59683018	518	granodioritic intermediate
MT1	613299	290	granophyre
MT2	613298	344	contact between gabbro and granophyre
MT3	613298	344	olivine gabbro
MT4	613298	344	granophyre
LA1	62152903	146	quartz gabbro
LA2	62052898	168	quartz gabbro
LA3	62102900	155	granophyre vein in quartz gabbro
LA4	61952900	192	granophyre vein in quartz gabbro
LA5	617298	250	quartz gabbro
CG1	642337	137	quartz gabbro
CG2	642337	137	calcite vein
CG3	642337	137	granophyric vein
CG4	634346	305	granophyre
CG5	635345	222	granophyre

Appendix E.

Mapping geological data using UNIMAP 2000.

A guide compiled by Andrew Black for the School of Geography + Geology at St. Andrews University

MAPPING GEODATA USING UNIMAP 2000

A brief guide for Geography & Geology users

This note gives a step-by-step guide for the presentation of spatially distributed data using UNIMAP 2000 on a Sun workstation and output via the Geography & Geology Apple LaserWriter Plus. Details are, where necessary, specific to the Geography & Geology Department set-up.

INTRODUCTION

UNIMAP 2000 is one member of the UNIRAS suite of packages available on the Sun workstations in St Andrews. It is used to present spatially distributed data in a great variety of map types, although output can be produced quite easily with only a few basic commands. Full details are given (sometimes with less than perfect clarity) in the UNIRAS UNIMAP 2000 manual.

PREREQUISITES

a) Access to a userid for the Sun system

b) A data file with the X,Y and Z coordinates of points to be plotted. Ideally these should be in columns separated by spaces, in X,Y,Z order. Data is regular if collected at regular intervals on a fixed grid pattern, or otherwise (and more typically for field data) irregular.

c) Optionally, further data file(s) can be used to provide outlines within which the map data will be plotted. Column format, X, Y, recommended, again with space separation. Coordinates must be on same scale as X,Y values in primary data file.

STARTING THE SYSTEM

Log on to workstation pur1. No acceptable screen driver for the monochrome workstation monitors is currently available.
Enter the OpenWindows environment

```
pur1% openwin
```

Once the cmdtool and file manager windows have opened, SELECT the cmdtool window and start UNIMAP[1]:

```
pur1% setup uniras

pur1% unimap -d mx11 -m -f
```

[1] In the unimap command, -d mx11 specifies screen driver, -m mouse available, -f suppresses welcome message.

After a short delay, a black window with blue menu bar will appear. Commands are effected using a hierarchical menu structure: the main menu first displayed can be considered as the 'top' menu and more specific commands are found at lower levels in the 'tree' structure. Menu items can be selected by using the SELECT (left) mouse button, or by using the keypad arrow keys, <ENTER> and <Esc> (to move back up to higher menus). A command line at the bottom of the window also allows entry of numerical or text values where required.

Twelve menu items are displayed: these are the major areas of the system and a brief description of each is given before more detailed explanation.

DATA	Reads in the data to be mapped, along with any outlines.
INTERP	Used to interpolate irregularly distributed data onto a regular grid prior to mapping as a contour or line map.
CALCULATE	Mathematical operations for multiple Z-variables.
MAP	Controls the basic presentation of the data: select type of map.
OPTIONS	101 things you probably don't need to do.
PLOT	Plots the map: changes are not seen until this is done.
ARCHIVE	Restores / saves / deletes entire maps to / from file.
EXPORT	Allows export of maps to other applications.
HARDCOPY	Controls paper output of maps; allows PostScript files to be created for later printing.
LAYOUT	More detailed presentation commands than MAP.
HELP	On-line help.
EXIT	Exit from UNIMAP 2000.

PLOT and HELP are available at any level within the menu structure by typing at the command line.

TO PRODUCE A MAP

1: READ DATA

Select DATA from main menu and then either IRREGULAR or REGULAR depending on the nature of the data to be mapped. Select FORMAT from the new menu on the right, enter the number of Z variables to be read from the data file, COLUMN or ROW as appropriate and then key in the appropriate FORTRAN format of the data at the command line: if spaces separate all the values between each column, * (asterisk) will most easily indicate free format, otherwise type the appropriate code without enclosing parentheses, e.g. 2(I4),6(1X,F5.1) for a file containing X, Y then 6 Z variables with no spaces between the X and Y variables. Now select READ and type in the filename as prompted.

The default map area will be calculated such that the maximum and minimum X and Y values define the four sides of the rectangular plot. TABLE shows the range of all variables (X, Y, Z1, Z2 ...) and can be accessed

at most times by typing TABLE at the command line[2]. To adjust the map frame coordinates, use the AREA command and enter new maximum and minimum X and Y values. This may be particularly important if a basemap is to be added; otherwise such an outline may 'fall off' the edge of the map.

Two commands allow outline coordinates to be added, for different purposes. Reselect DATA from the main menu.

a) REGION is used to define an outline(s) inside (default) or outside of which Z values will be shown. Use FORMAT if necessary and then READ to specify the data file containing the outline.

b) BASEMAP, also available by selecting DATA on the main menu, allows an outline to be read for plotting on the map - REGION does not plot the outline itself. Read the file in as above.

FAULT is available in the same way; a file containing the line of a fault will allow rock strata to be handled across a fault. Use FORMAT and READ as above.

2: INTERPOLATION ***(only required for irregular data => contour/line map)***

If irregular data has been input, and a contour or line map is required, the irregular data values must be interpolated onto regular grid nodes, from which the isolines will then be plotted. Having chosen INTERPOLATE from the main menu, first choose the number of GRIDCELLS: too coarse a grid will give misleading patterns, so it is better to choose a high number of cells even though the processing time required will be longer. VARIABLE allows you to choose which Z variable is interpolated; 1 is the default. METHOD, OPTIONS and VARIOGRAM allow more control over the interpolation, and it is worth consulting the manual for an explanation of the methods available. However, the default method is normally acceptable; interpolation is effected by selecting DO from the menu. A new Z variable is created and is then available for plotting; TABLE will show its range of values.

3: MAP

VIEW sub-menu: choose 2D/3D/4D. 4D refers to one Z variable displayed as the height of a 3-dimensional surface, and a second Z variable being shown by the colour of the surface.

TYPE: choose from
- DOT: Z value shown by colour
- GRID: grid squares coloured for average Z value
- LINE: isoline map
- CONTOUR: colour-filled contour map
- IMAGE: fast grid map, poor quality

PROJECT: gimmick.

SMOOTH: contour smoothing option.

REDUCTION: allows plotting short-cut to save time; not really necessary.

VARIABLE: select which Z variable is plotted.

---

[2]This and other windows can be removed by clicking the blue top panel of the window with the ADJUST (middle) mouse button.

4D: select second Z variable for plotting on 4D map (surface colour).
STYLE: used to set two important parameters, especially for contour maps.

COLOUR: although the default settings on this option allow the best differentiation of Z values on-screen, once translated onto a monotone printer, the patterns are meaningless. For best representation of data on paper, set the following values:
Choose SCALE and select USER-DEFINED. Set Hue Start=0, Hue End=0; Lightness Start=100, End=50; Saturation Start=100, End=100. Highest Z values are shown with darkest shading, grading to lowest values as white. Use of Lightness End=0 would result in completely black shading on paper, but if more than about 4 classes of shading are used, it is difficult to differentiate from other shades.
To control the number of classes into which Z values are grouped, choose CLASS from the STYLE menu. NUMBER allows the number of classes to be set, INTERVAL the range in value for each class, EXTREMES the maximum and minimum of the grouping range, LIMITS sets the start and end values for each class individually, and STATIC sets these permanently so that the groupings are maintained for further data sets. Changing the number of classes shown on the map can radically alter its appearance; experimentation is recommended. Applies to all map TYPEs.

GALLERY contains pre-defined combinations of VIEW, TYPE and PROJECT.

Further changes to the appearance of the map will be made using the LAYOUT menu, but typing PLOT should now show a map close to the required finished product. To see the results of each change of settings, PLOT must repeatedly be keyed on the command line.

4: LAYOUT

More detailed changes can now be made to the map. Most of the menus are self-explanatory; the following notes relate to particularly useful features.
LEGEND: alters or removes characteristics of the key shown by default at the bottom left corner of the display. Often useful is to select CHANGE then DECIMAL to alter the number of decimal places shown for values in the legend.
POSTING: shows the position on the map for each data point. MARKER allows selection of appropriate symbol type; to show a small cross at each point, select CLD symbol, set size = 1.5 (or as desired; negative values are in pixels, positive in mm), colour to default white which prints as black and will only be seen clearly against all background colouring on hard copy if Lightness End value on MAP STYLE COLOUR SCALE »0 e.g. 50, and CLD index = 225 (+ symbol). Codes for other symbols are listed in Appendix B

of the manual. LABEL should be set to NONE if no value labels are required.
TITLE: allows main and sub-headings to be set with desired text, font, size, etc.
NOTES: allows extra text to be displayed at desired position.

5: HARDCOPY

Once an acceptable map has been produced, hard copy can be obtained by writing the map to a PostScript file then transferring it to an Apple Macintosh from which it can be printed on a laser printer.
DEVICE: select A4 PostScript, black & white or colour[3] as required.
ORIENTATION: default is landscape; portrait may require some scaling.
PATTERN: for best printing results, choose GREYTONE.
PLOTFILE: select YES, give a filename as requested, then answer NO to spool plotfile and delete spoolfile.
PLOT then writes the map image to the file named.

The plotfile will then be available for transfer and printing. Quit UNIMAP by typing EXIT at the command line if you are sure no further work is required (save your map using ARCHIVE if you might want to use it again later), and exit from OpenWindows.

TRANSFER OF POSTSCRIPT FILE

Using a Macintosh Classic, access the **telnet** folder and open the application **NCSA Telnet 2.3**. To copy a PostScript file from the Sun system, first log on to a Sun and then copy the file:
1. File menu: **Open Connection ...** Enter **purds** or another machine name in the **Session Name** window and click OK.
2. Follow the normal Sun login procedure as prompted.
3. Network menu: **Send FTP command** - wait for the **ftp>** prompt to appear[4].
4. ftp> **put filename** - and your file should be written to the Mac hard disk.
5. File menu: **Close Connection** to log off from the Sun, and **Quit** to leave Telnet.

PRINTING

The final stage to obtain hard copy of your map is to download the PostScript file now resident on your Macintosh hard disk onto the laser printer. Open the Cricket folder on fileserver-GEOLOGY1[5] and open the application SendPS.

[3]Colour PostScript files can be transferred to Macintosh disk and taken for printing to Reprographic Services.
[4]FTP: File Transfer Protocol
[5]Access the fileserver by selecting the **AppleShare** icon from the Chooser.

Choose **Download POSTSCRIPT® file ...** from the file menu, select the file for printing, and click **Download**. In a couple of minutes, your file will be printed on the LaserWriter.

REFERENCES

UNIRAS UNIMAP 2000 reference manual - one of many grey-covered spiral-bound UNIRAS manuals on shelf in Room 219
SunOS User Note 7, UNIRAS, available from the Computing Laboratory.

EXAMPLE MAP

Andrew R Black
April 1991

MAIN TITLE → APRIL – MAY FLOODS AS PERCENTAGE OF TOTAL

SUB-TITLE → 1959–88 adjusted

DATA IN, CLOCKWISE FROM

REGION 1ST POINT,

CONTOUR INTERVAL DOES NOT

EXTEND OUT TO TCP

BASEMAP 1ST POINT,

OUTLINE OF CLASSING

IS PRINTED ON MAP

PLOTTING

SIZE

LIGHTNESS

ABOVE	13.00
10.25 –	13.00
7.50 –	10.25
4.75 –	7.50
2.00 –	4.75
BELOW	2.00

MAP STYLE CLASS NUMBER 4

EXTREMES 2, 13

AREA MAP IN MIN X, Y SPACE CHANGED TO PLOT SPACE FOR BASEMAP